168(1), 2017

COMBUSTION ENGINES

Poznan University of Technology

Institute of Combustion Engines and Transport

POLAND, 60-965 Poznan, Piotrowo 3 str., tel. 48 61 6652207, fax. 48 61 6652204

Optical research of engine processes

Rapid Compression Machine - fully controled single combustion cycle (Otto and Diesel cycle)

Constant Volume Chamber (air pressure up to 100 bar)

LaVision HighSpeedStar 5 camera up to 200 000 fps

Continuum YAG solid-state laser

Data image post processing with DaVis software

Research on RDE (PEMS)

Gaseous exhaust emissions (CO, HC, NO_x)

Semtech DS, Ecostar (Sensors), M.O.V.E. (AVL)

Particle mass (PM) & number (PN) emissions

Micro Soot Sensor, Particle Counter (AVL),
Ecostar PM, Ecostar PN (Sensors), EEPS (TSI)

www.cel.put.poznan.pl

PTNSS Supporting Members
Członkowie wspierający PTNSS

BOSMAL Automotive Research and Development Institute Ltd
Instytut Badań i Rozwoju Motoryzacji BOSMAL Sp. z o.o

Motor Transport Institute
Instytut Transportu Samochodowego

The Institute for Sustainable Technologies
Instytut Technologii Eksploatacji

Institute of Aviation
Instytut Lotnictwa

Automotive Industry Institute
Przemysłowy Instytut Motoryzacji

The Rail Vehicles Institute TABOR
Instytut Pojazdów Szynowych TABOR

Institute of Mechanised Construction and Rock Mining
Instytut Mechanizacji Budownictwa i Górnictwa Skalnego

Institute of Logistics and Warehousing
Instytut Logistyki i Magazynowania

Industrial Institute of Agricultural Engineering
Przemysłowy Instytut Maszyn Rolniczych

AVL List GmbH

Solaris Bus & Coach S.A.

Air Force Institute of Technology
Instytut Techniczny Wojsk Lotniczych

COMBUSTION ENGINES

A Scientific Magazine

2017, 168(1)

Year LVI

PL ISSN 2300-9896

Editor:

Polskie Towarzystwo Naukowe Silników Spalinowych
43-300 Bielsko-Biała, Sarni Stok 93 Street, Poland
tel.: +48 33 8130402, fax: +48 33 8125038
E-mail: sekretariat@ptnss.pl
WebSite: http://www.ptnss.pl
Papers available on-line: http://combustion-engines.eu

Editorial:
Institute of Combustion Engines and Transport
Poznan University of Technology
60-965 Poznan, Piotrowo 3 Street
tel.: +48 61 2244505, +48 61 2244502
E-mail: papers@ptnss.pl

Prof. Jerzy Merkisz, DSc., DEng. (Editor-in-chief)
Miłosław Kozak, DSc., DEng. (Editorial Secretary for Science) – papers@ptnss.pl
Ireneusz Pielecha, DSc., DEng. (Technical Editor)
Krystyna Bubacz, MSc. (Proofreading Editor)
Wojciech Serdecki, DSc., DEng. (Statistical Editor)
and Associate Editors

Contents

Editor
Polish Scientific Society of Combustion Engines
43-300 Bielsko-Biała, Sarni Stok 93 Street, Poland
tel.: +48 33 8130402, fax: +48 33 8125038
E-mail: sekretariat@ptnss.pl
WebSite: http://www.ptnss.pl

Subscriptions
Send subscription requests to the Publisher's address.
Cost of a single issue PLZ30 + VAT.

Preparation for print
ARS NOVA Publishing House
60-782 Poznań, ul. Grunwaldzka 17/10A

Circulation: 700 copies.

Printing and binding
Zakład Poligraficzny Moś i Łuczak, sp. j., Poznań, ul. Piwna 1

The journal is registered in the Polish technical journals content database – **BAZTECH** www.baztech.icm.edu.pl

The journal is listed in the international database **IC Journal Master List** – **Index Copernicus** www.indexcopernicus.com

Declaration of the original version
The original version of the Combustion Engines journal is the printed version.

Papers published in the ***Combustion Engines*** quarterly receive 13 points as stated by the Notification of the Minister of Science and Higher Education dated 31 December 2015.

Cover
I – Chevrolet Volt Powertrain (*fot. www.netcarshow.com*), background (circuits – *allswalls.com*)
IV – Porsche Panamera turbo (*fot. caricos.com*)

Article citation info:
KAŁUŻNY, J., MERKISZ, J., GALLAS, D. et al. An innovative system for piston engine combustion with laser-induced ignition of the hydrocarbon fuel consisting carbon nanotubes. *Combustion Engines*. 2017, **168**(1), 3-14. DOI: 10.19206/CE-2017-101

Jarosław KAŁUŻNY
Jerzy MERKISZ
Dawid GALLAS
Tomasz RUNKA
Miłosław KOZAK
Ireneusz PIELECHA

CE-2017-101

An innovative system for piston engine combustion with laser-induced ignition of the hydrocarbon fuel consisting carbon nanotubes

The article proposes the concept of a new piston engine combustion system that is designed to meet future-oriented ecological requirements. The concept is to use ethanol as a fuel, in which a slurry of carbon nanotubes would be formed, which are characterized by the ability to ignite using a pulse of laser light fed into the combustion chamber. Modifying the shape of the light beam that penetrates the combustion chamber would allow to control the position and the size of the area in which the ignition of fuel would occur.

The originality of the concept is to combine the latest achievements in the field of nanotechnology in the construction of lasers and the production of biofuels, so as to contribute to improving the environmental performance of engines using the existing synergies.

The article discusses the prospects for the use of bioethanol as a fuel with zero carbon balance, a critical review of related research on light pulse initiated ignition of hydrocarbon fuels from carbon nanotubes was presented, and a review of studies of laser ignition for conventional fuels. The results of studies of carbon nanotubes suspensions in a variety of fuels conducted by the authors in order to seek solutions for the stable dispersions formation, that are resistant to nanotube agglomeration and sedimentation. The summary indicates directions for further research highlighting the importance of environmental impact.

Key words: *ethanol, carbon nanotubes, laser induced ignition*

1. Timeline of the development of internal combustion engines in automotive applications

Reciprocating internal combustion engines have been used in car drives for over a hundred years, but in recent years there has been a growing tendency to replace them with electric motors. These types of efforts are politically motivated or dictated by fashion – ecology and modernity, but are devoid of rational technical justification. It is also worth noting that neither the electric nor hybrid vehicles can be regarded as an invention of modern times.

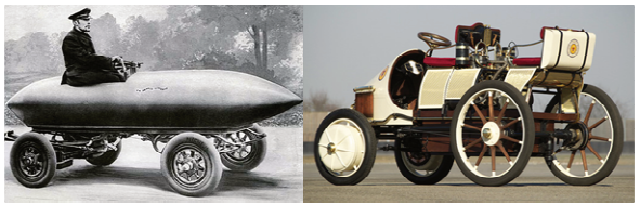

Fig. 1. Nineteenth century electric car, which for the first time exceeded the speed barrier of 100 km/h, and an early twentieth century hybrid diesel-electric vehicle

Road transport is one of the main sources of carbon dioxide and toxic air pollutants emissions. Air pollution continues to be a problem, especially in large cities, demanding an urgent solution. In this case the elimination of vehicles with combustion engines from city centers and replacing them with electric drive buses and taxis is an effective solution that can be quickly implemented. Such actions make sense, if they are local in nature, but striving for global replacement of combustion engines with electric motors as quickly as possible makes no sense. Well-to-wheel analysis indicates that as long as electricity is produced mainly in power plants burning fossil fuels the replacement of automotive internal combustion engines with electric motors will not bring a radical improvement in transport ecology. Currently about 67% of globally generated electricity is produced in power plants through the burning of fossil fuels. The development of renewable energy sources does not even compensate for the power lost due to nuclear power plants shut offs, as a result the share of energy derived from fossil fuels does not even decrease [47].

In the case of electric cars the unfavorable ratio of stored energy to the battery mass remains an unsolved problem. If coordinated action is planned and initiated the challenging technical task of dramatically increasing the battery electricity concentration could be realized in the future; as in the past a clearly defined plan allowed building a vehicle in a few years that allows man to fly to the moon.

An alternative to the search for solutions to increase the electricity concentration on board the electric vehicles is to improve the existing internal combustion engines. The authors believe that when determining further directions of automotive industry development the first consideration to take into account is the ratio of the expected benefits to the cost of a project and not its ambition. In this context, it is reasonable to strive for improvements to internal combustion engines; where the ecological and economic aspects play a special role. The environmental performance cannot, however, be seen as a formal meeting of the current tests requirements, but to ensure that the actual emission of toxic compounds is as small as possible in all operating conditions [38–40]. LCA analysis is an important issue. The paradigms presented above are the basis of the new piston engines combustion system concept proposed in the article.

2. Innovative ethanol combustion system

The presented concept involves the use of ethanol as a fuel, wherein a suspension would be formed from carbon nanotubes. Carbon nanotubes ignite under the influence of

a strong beam of light. Ignition of ethanol atomized and vaporized in the cylinder would follow from carbon nanotubes, ignited with laser light. The use of a laser would allow greater freedom in shaping the light beam, and therefore the fuel ignition would occur locally – in one or several locations in the cylinder, simultaneously or in a predetermined sequence. It would also be possible to initiate bulk ignition by splitting the laser beam, ensuring a sufficient concentration of energy. Likewise, operating a laser ignition system could be applied to other fuels, including gasoline or gaseous fuels. Choosing ethanol is dictated by its physical and chemical properties, and environmental characteristics that predispose it as fuel for future engines, as well as the ease of creation and stability of cnt suspensions in ethanol.

3. Ethanol as fuel for future engines

Ethanol is widely used as a petrol additive both in Europe and in the USA, while its share in the fuel does not normally exceed 5–10%. It is assumed that the maximum safe ethanol content in gasoline for the conventional automotive SI engines is around 10–15%. The Worldwide Fuel Charter recommends not to exceed 10% in its latest edition of 2013 [64]. Such fuel can be burned in standard spark ignition engines and the benefits from the addition of ethanol rely primarily on increasing the fuel resistance to knock, reducing greenhouse gas emissions and making the economy less reliant on oil. These benefits are obviously limited by the small share of ethanol in the fuel, but due to the total amount of fuel consumed it still has some economic importance. The world's largest ethanol producer is the US, where ethanol is produced mainly from corn, and the increase in production over the last decades was mainly due to its use as an additive to gasoline (Fig. 2).

Increasing the share of ethanol in fuel for SI engines or even using pure ethanol instead of gasoline is possible, but requires engine and fuel supply system adaptation. Changes in the fuel system boil down to increasing the material corrosion resistance and using seals resistant to ethanol. In the engine itself the changes needed to allow ethanol combustion involve the use of modified fuel mixture composition control software, in order to take into account the specific nature of the chemical reaction of ethanol combustion. These changes are sufficient, if ethanol is treated as a substitute for gasoline, especially in naturally aspirated engines of the older generation. This solution has been in use in Brazil for many decades, and experience shows that the use of ethanol, even as a standalone fuel without the addition of petrol, does not lead to serious operating problems. The only limit is the approximately 30% increased volume of ethanol fuel consumption compared to gasoline, and the need for extra starting fuel and/or fuel and air heating systems during start-up and warm-up phase of the engine. Vehicles adjusted for supply with any mixtures of ethanol and gasoline are called FFV (Flexible Fuel Vehicle). In the case of modern engines it also indicates a potential problem of lubricating oil dilution with ethanol and water condensing in the cylinders as a result of the intensive cooling due to ethanol evaporation. Warming the oil up to operating temperature, however, causes rapid evaporation of ethanol and restores the original oil properties [50]. The basic properties of ethanol relevant to engine operation are shown in Table 1.

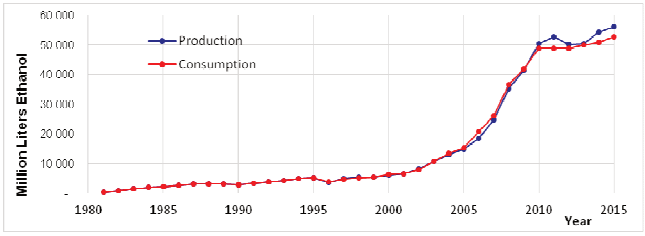

Fig. 2. Production and consumption of ethanol in USA [65]

Table 1. Properties of ethanol as engine fuel

Parameter		Ethanol	Gasoline 95
Density at 20°C	[kg/m^3]	789	750
Research octane number	–	109	> 95
Motor octane number	–	90	> 85
Heat of evaporation	[kJ/kg]	841	330
Heating value	[MJ/kg]	26.8	43.5
	[MJ/dm^3]	21.2	31.8
Stoichiometric air-fuel mixture	[kg_{air}/kg_{fuel}]	9.0	14.3
Distillation	[°C]	78	40–215
Flash-point	[°C]	13	– 43
Kinematic viscosity at 40°C	[mm^2/s]	1.2	0.5
Elementary composition	[% m/m]		
C		52.2	84.8
H		13.0	13.3
O		34.8	2.4

While ethanol was formerly treated as a substitute for gasoline – in Brazil, or as an organic additive – in Europe and the US, it is now turning out that ethanol can be a very attractive fuel for future engines [50]. With the continued trend of downsizing and further increase in boost pressure, and thus inevitably – pressure and temperature in the cylinder, ethanol may end up being a more suitable fuel than gasoline.

Engine downsizing is an effective method of reducing fuel consumption, and therefore the exhaust emissions of greenhouse gasses, and the obtained benefits are directly related to the degree of downsizing. The mechanical and thermal loads of engine components are the barrier to further increasing engine unit power, and in the case of SI engines also the problem of knocking, especially the so-called extreme knocking [62, 63, 70]. In the case of very large boost pressure even a single phenomenon of spontaneous mixture ignition initiated from hot components in the engine head (known as hot spots) can cause permanent damage to the piston-cylinder components [62]. As a result engines of this type use a two thermostats cooling system which ensures a lower temperature of the fluid flowing through the cylinder head in comparison to the rest of the engine block, sub-optimal compression ratios are used due to the engine efficiency, the air fuel mixture is deliberately enriched under maximum load conditions to cool the combustion chamber and the ignition is delayed [60]. All these activities lead to a significant deterioration in engine performance. As an extreme example of this is the ignition timing curve in the SI engine with direct fuel injection and

turbocharging range, as registered during the maximum acceleration road test at top gear and engine speed of 1,500 rpm. To prevent excessive pressure buildup and knock burning, the ignition in these conditions is delayed up to several degrees after TDC (Fig. 3).

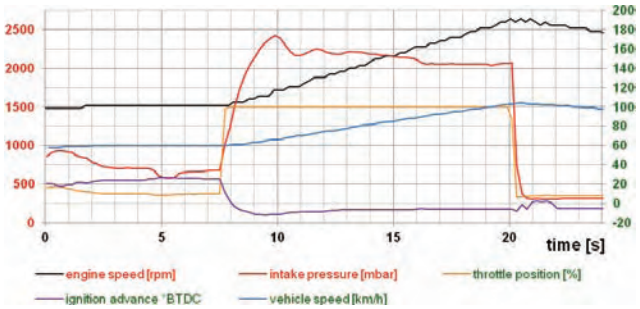

Fig. 3. The characteristic of selected parameters of a TSI type BLG engine during a maximum acceleration road test of a VW Golf, the parameters listed in the legend are color coded with the axis labels [30]

Regarding the relations described above, the characteristics of ethanol are extremely valuable, such as high octane number and a large vaporization heat, which contribute to the effective cooling of the cylinder fuel mixture [50]. An engine designed for ethanol fuel may have a higher compression ratio, thus significantly improving the overall efficiency under low and medium load, a similar effect relates to the accelerated ignition. On the other hand, under high load enriching the fuel mixture to cool the cylinder can be skipped, which in modern petrol-fueled engines of this construction like the TSI engine shown, significantly deteriorates their performance. It should be pointed out that resistance to ethanol knock depends on the engine operating conditions to a greater extent than it does for petrol. A parameter called the fuel sensitivity, representing the difference between the octane numbers RON and MON is about 10 for gasoline, and about 20 for ethanol.

The use of ethanol as fuel for internal combustion engines will not only reduce greenhouse gas emissions but is also beneficial in terms of nitrogen oxides emissions and hydrocarbons [53]. These benefits outweigh the negative consequences of increased emissions of acetaldehyde [23, 54]. One drawback of vehicles fueled with ethanol is the increased emissions by evaporation from the fuel supply system [19].

Developing industrial ethanol production on a mass scale is also justified by the fact that in the long term, it can become an energy carrier for fuel cells. For this application ethanol can be much more attractive than hydrogen, for which the chain of production, distribution, transportation and conversion into electrical energy is characterized by low efficiency and high environmental cost.

While today ethanol produced on an industrial scale comes from raw materials that could become food – corn in the US, sugar cane in Brazil or grain in Europe, it is possible to develop its production from wood waste or organic waste in the future.

European ethanol is usually produced from cereals and potatoes. In the US, Canada and China, the main raw material is corn. The largest amount of the world production of ethanol (approximately 60%), however, comes from the processing of sugar cane. This raw material is used, among others, in Brazil. The raw materials for bioethanol production can generally be divided into three groups [6]:

– containing sucrose: sugar cane, beetroot, sorghum, and some fruit,
– containing starch: wheat, rye, barley, potatoes, corn, rice, cassava,
– lignocellulosic biomass: energy crops, by-products from agriculture and the timber industry, paper and cardboard as fraction of municipal waste.

Bioethanol produced from last group raw materials belongs to 2nd generation of biofuels. While today ethanol on a commercial scale is produced mostly from materials which can be used for food purposes, the expansion of ethanol production from wood waste or discarded food remains is expected to grow significantly.

4. Carbon nanotubes

4.1. Basic information regarding cnt

Carbon nanotubes are one of the allotropic forms of carbon, such as: graphite, diamond, fullerene, graphene and a variety of amorphous variations. These allotropic varieties differ radically in their physical and chemical properties. Such differences arise from the spatial structure of crystalline carbon atoms and their interactions. The structure schematic of selected varieties of allotropic carbon are shown in Figure 4.

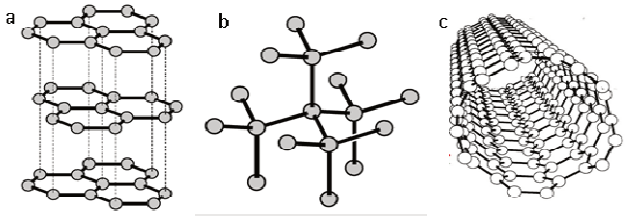

Fig. 4. Crystalline structure of graphite (a), diamond (b) and carbon nanotube (c)

The carbon nanotube shown in Figure 4 is a single-walled carbon nanotube (SWCNT), characterized by the simplest structure; a more common variant are, however, multi-wall carbon nanotubes (MWCNT) formed from concentrically superimposed single-wall nanotubes with different diameters. By purposefully adjusting the growth precursor selection of nanopowder metal as well as the atmosphere and temperature of the CVD (Chemical Vapor Deposition) process, it is possible to obtain both of these nanotube variants with lengths ranging from a few nanometers to many micrometers and a controlled diameter. The diameter of single-wall nanotubes is typically between 1 to 2 nm, multi-wall nanotubes have diameters from 2 to more than tens of nm, wherein the separation between successive concentric layers is fixed at 0.36 nm [9].

Graphite, diamond, and amorphous carbon form – sometimes imprecisely referred to as DLC (diamond like carbon) – all found industrial applications, including in the construction of internal combustion engines [59]. Carbon nanotubes were discovered in the '90s of the last century, but particularly intense development of nanotubes research

occurred at the beginning of the XXI century. A number of laboratories was established, which could grow, study, and develop nanotubes applications, but only a few of them have survived to this day [67]. Carbon nanotubes still primarily remain the subject of intensive applications research, and their industrial applications are relatively few in number as of yet [8, 10, 20]. The increase in carbon nanotubes production makes their price is halved every year [9, 67], and ceases to be a barrier preventing many of the possible industrial applications.

Because of their many functionally significant characteristics, from the engineering perspective, carbon nanotubes significantly exceed the best previously known conventional materials. It seems that their practical applications are limited so far because any engineering design can find a material characterized by a set of functionally essential characteristics. In this group of functionally significant characteristics the most crucial is the weakest feature, like the weakest link determines the strength of the chain.

4.2. Carbon nanotubes interaction with light

Among the many unique features that the carbon nanotubes possess is their ability to ignite under the impulse of light, e.g. a normal camera flash, was recognized relatively early. This phenomenon was found for single-wall carbon nanotubes grown in the CVD process, and untreated (pristine CNT) forming a small low density sample, giving it a "fluffy" appearance. The power density required to ignite a sample of SWNTs having a density of 0.2 g/cm^3 is about 100 mW/cm^2. In an attempt to understand the basic physical phenomena the role of light absorption with a broad wavelength spectrum was emphasized, extremely high heat conductivity typical of nanotubes, and the oxidation process. It was estimated that the local temperature of nanotubes must exceed 1500°C [1].

A purely thermal mechanism may be insufficient to describe the self-ignition of carbon nanotubes, especially when using a monochromatic light source such as a laser [3, 57]. In [58] attention was drawn to the fact that the nanotubes ignition under the influence of a light pulse is accompanied by a photo-acoustic effect, the resulting sound pressure level is sufficient to modify the structure of the nanotubes. Most importantly, however, it has been shown that the presence of iron nanoparticles, which are used as a catalyst for initiating growth of the nanotubes in the CVD process, is essential for the light-induced ignition of the nanotubes. These particles are usually not removed, and they are the main contaminant of nanotubes described as pristine cnt or industrial grade cnt, after the removal of these contaminants the nanotubes lose the self-ignition ability. In order to explain the process of light-induced spontaneous combustion it can be assumed that the iron nanoparticles oxidize generating heat which initiates a chain reaction [58]. Showing the key role that nanoparticles of iron play in this process also demonstrated that both single-walled and multi-walled nanotubes can ignite when exposed to light. In [56] a quantitative analysis of chemical reactions proposed in [58] was conducted, validating the assumed course of spontaneous combustion mechanisms.

An interesting case is described in [52] where spontaneous ignition of a polyurethane-nanotube composite was observed during Raman spectroscopy. The ignition was caused using a laser beam having a wavelength equal to 632.8 nm, and low output power typical for measurements with the Raman method. It was further noted that neither the nanotubes nor the polyurethane present in the composite underwent spontaneous ignition when illuminated with laser light on their own, not until they were combined into a composite with very high nanotube dispersion. The key factor towards explaining the ignition of the composite is that the carbon nanotubes used in it have the maximum light absorption wavelength of approximately 650 nm, similar to the laser wavelength. The polyurethane is transparent for this wavelength, but by surrounding the nanotubes it insulated them thermally from the environment, whereas the porosity of the composite allowed for oxygen-access and for the combustion to initiate [52].

By pulverizing the composite with the carbon nanotubes and the oxidizer sealed in the transparent resin a fuel additive can be made, which under the influence of light initiates combustion. Similar solutions were tested successfully in [5]. IDEM also indicated a quantitative relationship between the iron concentration in the nanotubes sample and the minimum light-initiated ignition energy. It has been shown experimentally that the phenomenon of light-initiated ignition of carbon nanotubes can be used for igniting liquid fuel. A particularly wide range of carbon nanotubes suspension concentrations, which can provide a light initiated ignition, was observed for methanol [5].

Carbon nanotubes are not the only nanomaterial for which the ignition can caused by a flash of light, a similar phenomenon was described for aluminum nanopowder [45].

In addition to the research relating to light-induced ignition of nanoparticles outlined above, a number of studies was performed aimed at the use of carbon nanotubes as an additive for engine fuel allowing light initiated ignition. The conclusions listed below can be formulated on this basis. Consideration should be given, however, that the dominant part of the studies conducted so far used xenon lamps as a light source; differing from the nanosecond Nd^{3+}:YAG laser in that they emit non-coherent out of phase light in a broad wavelength spectrum, with burst duration of at least a thousand times longer and a low energy density.

- Light induced ignition requires the lowest amount of energy when using single-wall carbon nanotubes with carbon content of over 40% [4].
- Using a xenon lamp in combination with different broadband filters, there was no strong correlation between the minimum ignition energy of the nanotubes and the wavelength of the incident light, thus photothermal nature of the ignition phenomenon was adopted [4].
- A strong relation between the pulse duration and the minimum energy required to initiate ignition was found, the shorter the pulse the less energy was needed [4].
- The use of carbon nanotubes and light induced ignition accelerates the process of gas burning (methane, ethane) and expands the flammability limits in comparison with spark ignition [23].

– The use of laser changes the nature of the mixture combustion process from deflagration to detonation [57].

4.3. Nanotubes in the piston engine combustion process

Carbon nanotubes are formed naturally in a piston combustion engine and their presence in the exhaust has been proven in studies presented in [21, 35–37]. The nanotubes present in the exhaust gas have a relatively short length, due to their short period of growth limited by the length of the combustion cycle [36]. The process of formation of nanotubes occurs intensively in spark ignition engine, powered by petrol or gas. In [2] it was demonstrated that growth of nanotubes can be purposefully continued outside the cylinder engine – on a metal plate placed in the exhaust system. Carbon nanotubes, same as soot, have the ability to adsorb the particles of toxic pollutants present in the exhaust gas to their surface as well as agglomeration.

It seems that especially important results were shown in [55], where it is indicated that the ferrocene [$Fe(C_5H_5)_2$] present in small amounts in the fuel causes a drastic increase in the emission of carbon nanotubes, where nanotubes present in the exhaust gases contain nanoparticles of iron with diameters of 5 to 10 nm. This process occurs intensively in diesel fuel with high sulfur content. The results are disturbing, because ferrocene is a widely used catalytic additive to diesel fuel; it is also used to increase the octane number of gasoline. The results obtained in [55] are completely understandable when considering the similarity of conditions in the cylinder of the running engine and the reactor deliberately growing nanotubes (cnt growth) in the CVD process, and iron nanoparticles are normally entered in this process as precursors for nanotubes growth.

The results shown in [55] indicate the need to exercise extreme caution in proposing such combustion systems concepts which require the addition of metallic nanoparticles into the fuel. The results of many of the conducted experiments lead to expect that nanotubes added to the fuel (fuel-borne) will have been burnt in the cylinder, causing relatively harmless carbon dioxide and carbon monoxide, whereas metallic additives can potentially become a source of secondary emissions, especially of carcinogenic nanotubes decorated with metallic nanoparticles. The indicated problem undoubtedly requires further studies. On the one hand, the action mechanism of carcinogenic carbon nanotubes and accompanying conditions have not yet been clearly understood, on the other hand, the results of recent work clearly indicate the beneficial effect of fuel metallic nano-additives in the combustion process.

In [51] the existence of a synergistic effect resulting from the simultaneous addition of carbon nanotubes and cerium oxide to fuel diesel engine was indicated. Significant benefits were obtained despite using low concentrations of both types of nanoparticles in fuel of up to 100 ppm. The carbon nanotubes act as a catalyst to accelerate the burning rate which results in decreased ignition delay and causes the lower heat release rate and advancement of the peak heat release rate. The cerium oxide nanoparticles act as an oxygen donating catalyst, which provides oxygen for the oxidation of carbon monoxide and absorbs oxygen for the reduction of nitrogen oxides [51]. The synergistic effect of the addition of functionalized carbon nanotubes and cerium oxide to biofuel for a diesel engine is also described in [41], more broadly, the issue of nano-additives to biofuels was discussed in [7, 48, 49].

Carbon nanotubes were also added to fuels for SI engines, which proved to be an effective anti-knock addition as well as raising the octane number [34].

In a number of works increases of the hot-plate ignition probabilities of ethanol due to the introduction of several different types of NP suspensions were found. Nanoparticles such as Al_2O_3, Fe_3O_4, and carbon nanotubes were tested [25, 26, 29]. In the engine operation aspect the most promising seems to be the observed rapid evaporation of the suspension of nanotubes in ethanol when compared to pure ethanol, [26, 29].

A relatively large number of publications relates to gas engines research in which the combustion process has been successfully modified through the addition of carbon nanotubes. A particularly valuable feature of nanotubes is in this case the acceleration of the lean mixtures combustion and extending the boundaries of the combustion of lean mixtures, as reported in [11–13].

4.4. Carbon nanotubes in hydrocarbons suspensions

Nanotubes are not solubilized, rather they are suspended as individual particles in the fluid, like an ink or paint. Carbon nanotube suspensions can be made in a number of ways, and with a number of fluids, where due to the method of suspending the solvents they can be split into polar and nonpolar. It is useful to start by modeling the nanotubes as rigid rods in a liquid suspension, to determine how far apart they may be for a given concentration.

When particles with a large aspect ratio (like carbon nanotubes) are dispersed in a solvent, they will rotate, due to the Brownian motion or in the presence of a velocity gradient (flow). This rotation creates a large effective hydrodynamic radius, and each nanotube sweeps through a spherical volume. For a nanotube with an aspect ratio of a = = L/d, the ratio (R) of the nanotube's actual volume V_{actual} = = (0.785 a d^3) to the volume of the swept sphere V_{sphere} = = (0.523 a^3 d^3) simplifies to: R = 3/(2a^2). Aspect ratios for carbon nanotubes are equal to ~2000. For example, MWCNT are often 20 microns long and 10 nm in diameter, and SWCNT are often 2 microns long and 1 nm in diameter. The volumetric ratio R for nanotubes of this aspect ratio is 4×10^{-5} vol%, which is less than 1 milligram per liter. At any greater concentration, the nanotubes will intrude upon each other's hydrodynamic spheres and hinder each other's rotation. This is the primary reason that nanotube suspensions are difficult to make and increase in viscosity quickly.

Nanotubes will interact with each other's hydrodynamic radius at any appreciable concentration. This would result in entanglement and the creation of large agglomerates, if there was no repulsive force to keep them from aggregating. When pristine nanotubes are suspended in hydrocarbons, they will aggregate and form a loose sediment on the bottom of the container, with a clear supernatant. To provide a repulsive force, it is necessary to electrically charge the nanotubes so that they repel each other and prevent agglomeration from occurring. This may not completely stop gravity-induced settling, but any sediment will then be made up of individual nanotubes, not agglomerates [68].

Pristine SWCNTs form „bundles" out of parallel-arranged, adjacent side walls of the CNTs. Multi-walled carbon nanotubes (MWCNT) are entangled in a chaotic tethered pattern of crossed fibers forming a mesh configuration [14, 28, 69]. The number of contacts which can form between neighboring MWCNTs increases dramatically with the length of the CNTs. Therefore, the binding of a clustered network of long MWCNTs is extremely strong, where each contact effectively acts as a cross-link fixing the network together [28]. The use of short CNTs therefore seems to be a simple and effective way that allows for obtaining a good dispersion. Figure 5 shows a comparison of the samples with ethylene glycol to which pristine MWCNTs were added. The CNTs were obtained using the same CVD process, but some of them have undergone a longer mechanical milling process, so that their length is much shorter. After adding the pristine CNTs the samples were only shaken by hand, they were not sonicated at all.

The dispersion of CNTs in low viscosity liquids, such as gasoline and ethanol can be effectively supported by the sonicating process. Ultrasonicating can effectively break SWCNT aggregates without damaging their structure; in the case of MWCNT effective breakdown of agglomerates is associated with the shortening of length of the CNTs predicted by theoretical considerations [28] as well as confirmed in several independent experiments. Both theoretical considerations [28] and experiments [14] indicate that after a long sonicating time a defined target length of the CNTs is obtained and the process of further shortening does not occur. The authors' own experiments show that the sonicating process is not effective in the case of viscous liquids such as lubricating oil or diesel fuel. In contrary to sonication, using dispersion by shear-mixing can be effective in viscous fluids [32].

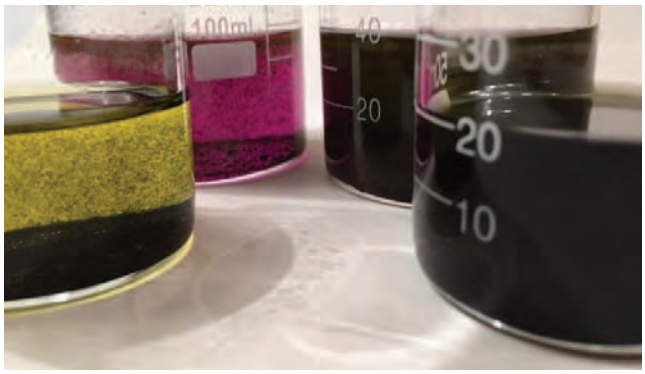

Fig. 5. Comparison of pristine MWCNT, long (5-20 µm, two on the left) and short (1-3 µm, two on the right) dispersion in ethylene glycol (Volkswagen Brake fluid DOT 4 two at the front and G13 cooling liquid concentrate two at the back)

Visual inspection of the nanotubes dispersion in hydrocarbons has a preliminary character, however, after conducting a series of experiments with different types of carbon nanotubes and various hydrocarbons, it can be concluded that using ethylene glycol allows for extremely easily obtaining relatively stable suspensions. In most cases, however, shortening of carbon nanotubes is not an effective method for obtaining a satisfactory dispersion degree and then the rule is to use different physical and chemical processes, with the aim to induce electric charge in the nanotubes. Electrically charged nanotubes repel each other, which impedes agglomeration, but does not always prevent sedimentation. Even if sedimentation occurs the resulting precipitate consists of individual nanotubes rather than their agglomerates, which makes redispersion dramatically easier.

In practice, it is extremely difficult to anticipate the ability of a certain type of nanotubes to form a suspension in a certain solvent. The multiple experiments by the authors lead to the conclusion, that among commercial fuels, the formation of a stable suspension in diesel fuel has proven the most challenging, similarly in vegetable oils. Obtaining a stable cnt suspension in commercial gasoline is much easier. However, even compared to gasoline ethanol is a very good solvent for the nanotubes. For this reason it is often used in many chemical treatment processes of nanotubes, and sometimes it is virtually impossible to obtain nanotubes sedimentation in ethanol, even after prolonged centrifugation [68]. An example of a bad solvents are Hexanes, seen in Fig. 6 which shows a sample of Hexanes, gasoline and ethanol in which that obtaining the dispersion of the nanotubes with the bamboo type structure was attempted, with diameter of about 30 nm and a length in the range of 1–5 microns. The nanotubes are electrically charged by the incorporation of COOH groups on their surface. ODA (Octadecylamine) and HATU were used in the preparation process among others. The illustrational, although representative nature of the results presented in Fig. 6 should be emphasized; the use of specific nanotubes and their preparation procedures can lead to a reversal of suspension quality obtained for gasoline and ethanol.

Visual inspection of the contents of sample no. 14 comprising a cnt suspension in ethanol does not allow to visually determine the presence of any agglomerates. Figure 7 compares pictures of the resulting dried fuel droplet from the sample no. 14 and 12 applied to a sheet of paper as seen by light microscopy.

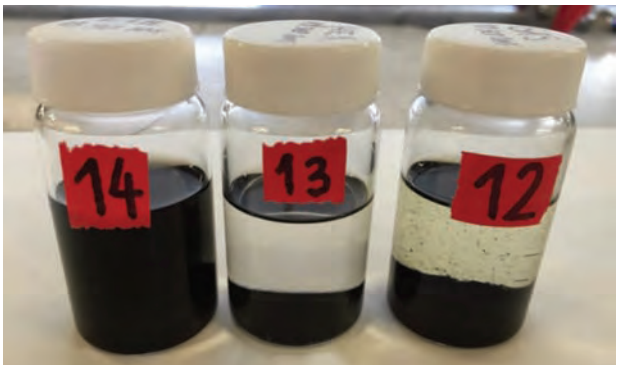

Fig. 6. Attempt at obtaining a similar concentration bamboo-structure MWCNTs solution, in ethanol (vial no. 14), hexanes (vial no. 13) and US commercial gasoline (vial no. 12)

An image obtained using a simple optical microscope allows for a clear illustration of the difference in size of the cnt agglomerates produced in the gasoline and the practically almost invisible agglomerates in ethanol. Further examination of specimen no.12 is pointless, agglomerates of nanotubes are so large that they would certainly cause improper operation of the fuel supply system of a modern

engine. It was found that for gasoline significantly better results can be obtained if the multi-walled nanotubes are replaced with single wall carbon nanotubes with a diameter of about 1.5 nm and a length in the range of 1–5 microns.

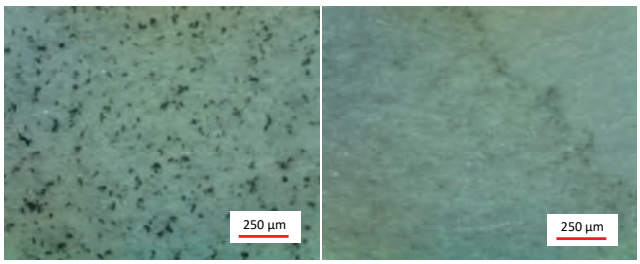

Fig. 7. Pictures of dried fuel drop on a piece of paper, the image from an optical microscope, at 60× magnification. On the left the fuel sample no. 12 (petrol), on the right no.14 (ethanol)

In order to prepare the sample for SEM to investigate the CNTs dispersion in hydrocarbons a drop of the solution was applied on an aluminum foil and evaporated at room temperature. The process of evaporation was associated with a temporary critical increase in the concentration of CNTs and as a result could have led to the agglomeration of CNTs on the surface of the aluminum foil, thus falsifying the results. It could certainly not, however, give a falsely negative test result for the presence of agglomerates [32].

Figure 8 shows an example of images obtained for ethanol with MWCNTs (as in vial no. 14), the results for the gasoline SWCNT are shown in Figure 9; all the images shown were made using a Field Emission Scaning Electron Microscope JEOL JSM-7001F.

The obtained images allow for the formulation of the comments listed below with respect to the suspension of nanotubes in ethanol.

– When using standard electron microscope it's impossible to measure the cnt agglomerates diameter in liquid fuel (not after evaporation), due to its high partial pressure.
– There is no easy way to measure the cnt agglomerates diameter in real fuel spray, but there are some laser light based method known in engine research, they could be adopted for this task. The laser wavelength set the resolution limit.
– The long time stability over weeks and months couldn't be tested during the short trial.
– The view focused on one of the biggest agglomerates (ca 30 micrometers diameter) shows large surface around covered with well dispersed CNT's. There are some smaller agglomerates or impurities visible in area around.
– The small CNT bundles of about 1 micrometer or less in diameter will be probably not filtered out in the engine fuel supply system. The bigger agglomerates can be probably easy removed by using the centrifuge or dissolved during longer sonicating process; eventually by using other, e.g. mechanical treatment methods.
– In the aspect of laser induced fuel ignition it is unknown if it's desired to keep the cnt's fully dispersed, or maybe the relatively small cnt bundles (1 micrometer or less) can improve the fuel ignition process. The agglomerates of diameter less than 1 micrometer will be probably not critical for the engine injection system, where the nozzle hole diameter is 100 micrometers or more.

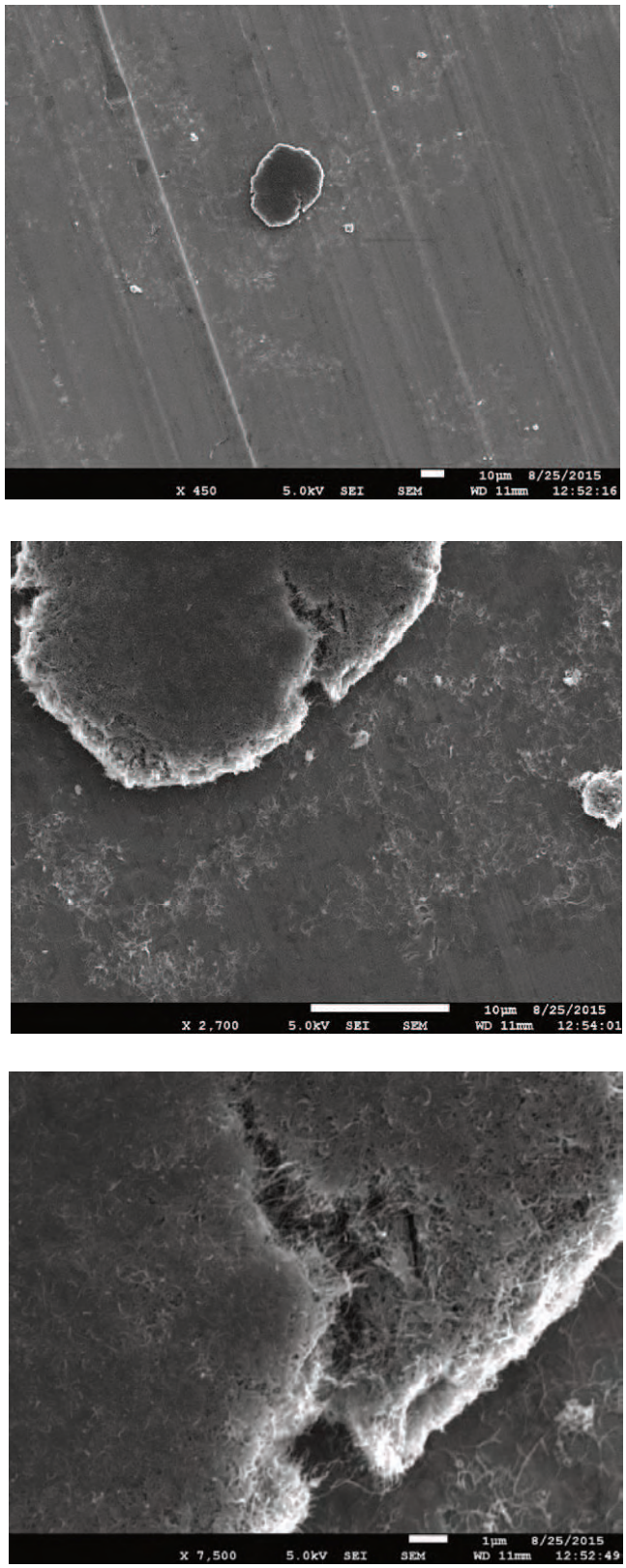

Fig. 8. MWCNT in ethanol (vial no. 14) subsequent images show increasing magnification

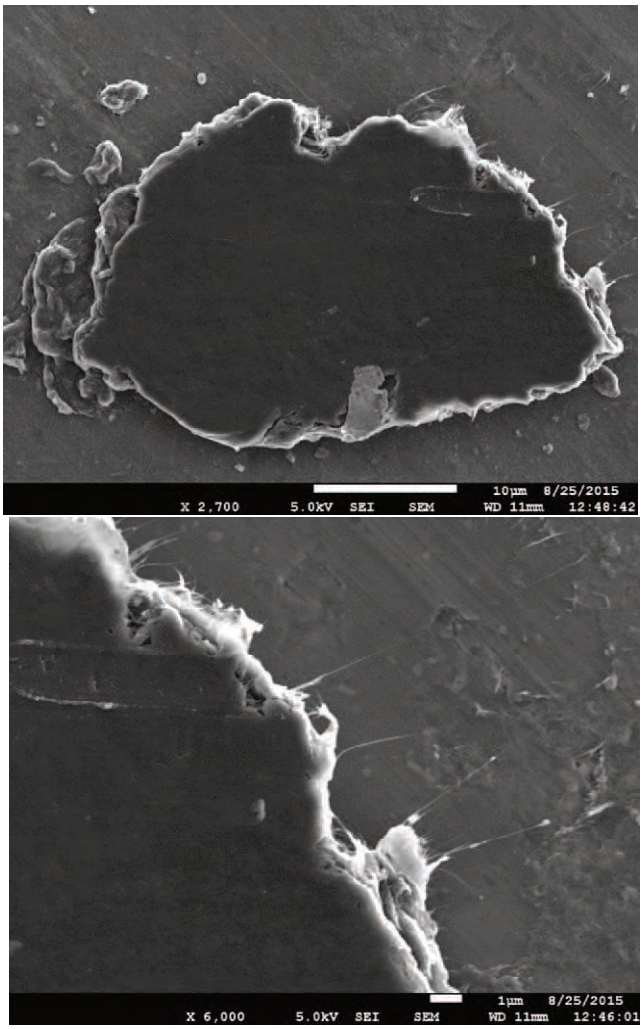

Fig. 9. SWCNT in commercial US gasoline subsequent images show increasing magnification

5. Laser induced ignition in IC engines

5.1. Experiences with the use of lasers in engine processes research

Lasers of various designs have been used for many years in research of in-cylinder processes, plentiful experience gained in these studies [71, 72] can be used in the ignition concept presented in this article. One of the simplest applications of laser in engine research is its use as a source of light to take a photograph of the fuel atomization process. The authors discussed their experiences in this field in [31]. It is worth noting that a great progress in laser technology has been made in the last decade, especially for Nd^{3+}:YAG lasers. An example of such a laser for laboratory research is shown in Figure 10 [31, 66]. Such a laser emits radiation at the wavelength of 1064 nm, the second harmonic generator can convert this wavelength into 532 nm. The laser light is generated in the course of pulses lasting several nanosecond. The pulse energy in the wavelength range 532 nm is equal to 300 mJ. The experience of the authors indicate that in order to achieve correctly exposed images of a fuel jet the impulse energy restricted to a few mJ is sufficient. Figure 11 shows a comparison of fuel jet photos lit with halogen bulbs and laser light. Pictures were made while maintaining the same parameters of the camera for quick photos. In the first case two lamps with 250 watt bulbs were used and in the second case the image illumination was realized with Laser Continuum Surelite SL II-10 [66].

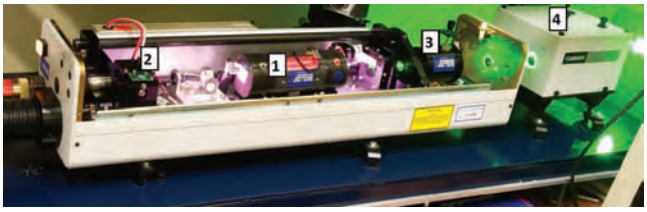

Fig. 10. Impulse Nd^{3+}:YAG laser with a second harmonic generator prepared for fuel atomization tests. 1: laser head with the rod and pumping lamp, 2: Q-switch, 3: second harmonic generator, 4: harmonic separator [66]

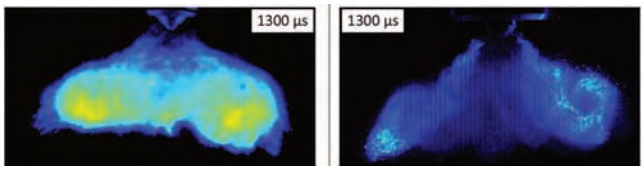

Fig. 11. Comparison between halogen lamps (left picture) and the laser (right picture) as a light source for illuminating the fuel spray injected into the pressure chamber, the two image frames were recorded after 1300 microseconds after the start of the injection [31]

In the authors' opinion, the laser light is more appropriate than a xenon discharge lamp light for the application concept of the ignition of hydrocarbon fuel with a suspension of carbon nanotubes discussed in this article. A number of the unique characteristics of laser light can be used with this solution, as listed below.

- Laser light is monochromatic, and the wavelength is important for its interaction with carbon nanotubes, as demonstrated by the results of Raman spectroscopy, and absorbance measurements [15, 16]. It is appropriate to use Nd^{3+}:YAG lasers in engine applications, because of their widespread use and the ability to generate harmonics with a wavelength of 532 nm, 355 nm and 266 nm. The use of light in the ultraviolet range may be advantageous due to their more intensive interaction with carbon nanotubes, however, the energy of these wavelengths is limited due to the enhanced harmonics generator circuit. In addition, delivering ultraviolet light to the cylinder may require the use of special glass screen, such as sapphire.
- Very small divergence of the laser beam allows for the beam to be focused by an optical system on any point in the combustion chamber. The beam can be formed in a targeted manner, for example to form a thin plane (light sheet) which can be used to force ignition not at a point, but in a controlled volume of the cylinder.
- The duration of the laser pulse is limited to a few nanoseconds and a high concentration of energy facilitates the ignition of nanotubes. The flash of a xenon lamp usually lasts longer than 100 microseconds, it is at least 10,000 times longer than a laser light pulse, so even a small laser provides an energy concentration that is virtually unattainable for any other light source. The tests in [17] indicates that a shorter pulse results in a significant reduction of the minimum energy required to ignite the nanotubes.

– The results of optical studies of in-cylinder processes indicate that contaminants originating from combustion and settling on the cylinder optical access window is one of the key problems. A laser beam directed through a glass window to the interior of the cylinder is effective in burning off impurities and ensure the transparency of the windows [27].

5.2. Experiences with laser ignition of conventional hydrocarbon fuels

The laser ignition as an alternative to the conventional ignition system, implemented with an electric spark between the electrodes of the spark plug, has been studied in conventional IC engines for many decades. The original motivation for using the laser system have been attempts to increase the efficiency of fuel burning in conventional engines and reducing emissions. Another factor accelerating the work on the use of laser ignition was a tendency for building lean-burning engines. In particular for engines burning gaseous fuels and the attempt to increase the exhaust gas recirculation level. There are numerous review articles, which examined in detail the results of many studies conducted on the use of laser ignition in engines burning a variety of hydrocarbon fuels [22, 42, 46], thus such a review of results will not be repeated in this article. It has been shown that the replacement of the conventional ignition system with a laser ignition system achieves considerable benefits in improved engine performance and operation. Appropriate technology has been successfully tested in laboratory conditions, but had never been used in mass production. It is worth noting that in terms of the application a breakthrough can be brought about by the development of laser technology observed in recent years. In particular reducing the production costs while maintaining high reliability, durability and resistance to harsh working conditions for Nd^{3+}:YAG lasers pumped with semiconductor diodes.

In most of the previous work on the laser ignition system an optical system was used to focus the laser beam in one or several points in the cylinder volume, which leads to the formation of plasma. The local energy density obtained in this way produced conditions somewhat similar to the conditions present between the electrodes of the spark plug at flashover time. The concept proposed in this article, where the aim of adding carbon nanotubes to fuel is a drastic reduction of the minimum ignition energy, should be stressed as a different solution. This way the relatively small energy laser beam does not have to be focused, but purposeful shaping of the beam could be used as a method to force the ignition in a controlled, much larger selected volume of space in the cylinder. Despite the distinct concepts presented here, the results of previous work on the laser ignition of conventional fuels shown below can be used for the realization of the concepts proposed in the article.

– Ignition of conventional fuel usually uses a laser beam with a pulse energy in the range of one to several tens of mJ. To achieve laser ignition of hydrocarbon fuels an power density (laser pulse intensity) in the range of 1010–1011 W/cm^2 is needed [61].
– Diode pumped Nd^{3+}:YAG lasers are typically used, with a primary wavelength of 1064 nm, second harmonic of 532 nm, but also CO_2 gas lasers emitting infrared later have been used successfully.
– The ignition volume in which a forced laser ignition occurs is greater than that of the spark between the electrodes of the spark plug, it is also true for focused laser beam ignition systems.
– In the case of previously conducted studies of conventional hydrocarbon fuels the non-resonant ignition mechanism plays a dominant role.
– No electrodes common for the spark plug ignition systems facilitates intentional shaping of the fuel dose movement in the cylinder in the compression process and then improves the spread of flame and reduces heat dissipation at the early stage of the flame development.
– It is assumed that four different mechanisms can lead to the laser ignition of fuel: thermal initiation, non-resonant breakdown, resonant breakdown, and photochemical ignition.
– In the case of previously conducted studies of conventional hydrocarbon fuels a dominant role is attributed to the mechanism of non-resonant ignition [61]. For a fuel with a suspension of carbon nanotubes, especially in the presence of iron oxide thermal ignition mechanism plays a crucial role, the authors attribute the potentially the most promising role to the occurrence of the other two effects in the presence of carbon nanotubes.

6. Conclusions

The development of the world economy and an increase in the number of cars forces a search for new, more environmentally friendly technical solutions for transport. The article presents the concept of a new piston combustion engine system. The originality of the concept is to combine the latest achievements in the field of nanotechnology in the construction of lasers and the production of biofuels, to use the existing synergies to contribute to improving the combustion engines environmental performance.

The concept presented in the article is the use of ethanol as a fuel where a suspension of carbon nanotubes would be formed, which are characterized by the ability to force ignition using a light pulse. A laser was chosen as the source of the light pulse, while changing the shape of the light beam penetrating the combustion chamber would allow control of the position and the size of the area in which the ignition of fuel would be induced.

The futuristic concept of an engine combustion system has been proposed because it allows achieving a number of synergistic benefits, the most important of them are listed below.

– Ethanol is a fuel with a high ecological potential, thus it is already widely used in the world as an additive to gasoline. The particularly attractive aspects of this fuel are the possible future methods of its production, which could achieve zero carbon dioxide emissions in the fuel production process.
– Properties of ethanol, such as a high octane number and high vaporization heat, make it a very attractive fuel for future engines regardless of the environmental benefits,

allowing for the further development of the concept of downsizing.
- The preliminary results in the article allow to conclude that among all the most common engine fuels ethanol allows for the creation of the most stable carbon nanotubes dispersions, effectively limiting the phenomena of agglomeration and sedimentation.
- The ability of carbon nanotubes to undergo ignition induced with a pulse of light is their unique feature. Independent studies have shown that nanotubes interacting with ferrocene may force the ignition of conventional hydrocarbon fuel with just the light of camera flash. A higher rate of combustion and wider flammability limits of the mixture (in a wider lambda range) is obtained this way compared with the conventional spark ignition.
- Replacement of the camera flash used by foreign authors with laser light allows taking advantage of the unique characteristics of laser light. Key advantages of the laser is a shorter pulse duration and energy concentration in the beam higher by several orders of magnitude and a unique opportunity to shape the laser beam with simple optics.

At the same time, problems that may hinder the practical application of the described concept have been identified.
- Carbon nanotubes are a relatively recently discovered material and therefore their impact on the environment and human health is not yet fully understood [35, 43, 44, 61]. Although nanotubes do not exhibit acute toxicity, and therefore they are for example intentionally introduced into the human body to accelerate the mending of broken bones [33], or are used to filter the air in the life support systems of spacecraft [18]. It is uncertain, however, whether or not they have any negative long-term health effects resulting from interaction with the human body.
- Many studies point to the carcinogenic effect of pristine cnt nanotubes growth in the cvd process, which have metal nanoparticles incorporated on their surface. Therefore the use of ferrocene in the presented concept combustion system should be restricted.

Further studies are necessary to verify the proposed concept, and in particular a fuel injection technique into the pressure chamber and then testing the engine is required. Regardless of the results of engine research it is necessary to shed light on the impact of nanoparticles emitted by the engine on the environment and human health. This issue is particularly relevant in a broader context, because nanoparticles are added to fuels more and more often – for both petrol and diesel fuel as anti-knock and soot oxidation catalyst additives.

Acknowledgements

The authors would like to thank all those who contributed to the final outcomes presented in the paper, by giving inspiration for the research, supporting laboratory tests, scientific cooperation, development and revision of the article. We are particularly thankful to David Carnahan, the president of NanoLab Inc., who was the exclusive supplier of CNT's used in our research.

The study presented in this article was performed within the statutory research.

Nomenclature

FFV	flexible fuel vehicle
SWCNT	single-walled carbon nanotube
MWCNT	multi-wall carbon nanotubes
CVD	chemical vapor deposition
DLC	diamond like carbon
NP	nanoparticles
ODA	octadecylamine

Bibliography

[1] AJAYAN, P.M., TERRONES, M., DE LA GUARDIA, A., HUC, V. et al. Nanotubes in a flash ignition and reconstruction. *Science*. 2002, **296**, 705.
[2] ALDAJAH, S., HAIK, Y., ELNAJJAR, E. A novel dual effect soot filtering system. *Jordan Journal of Mechanical and Industrial Engineering*. 2010, **4**, 75-78.
[3] ALUKER, E.D., KRECHETOV, A.G., MITROFANOV, A.Y., ZVEREV, A.S. et al. Understanding limits of the thermal mechanism of laser initiation of energetic materials. *The Journal of Physical Chemistry*. 2012, **116**, 24482-24486.
[4] BADAKHSHAN, A., DANCZYK, S. Ignition of nanoparticles by a compact camera flash. Air Force Research Laboratory Combustion Devices Branch, In-House Interim Report, September 2014.
[5] BADAKHSHAN, A., DANCZYK, S. Photo-ignition of carbon nanotube for ignition of liquid fuel spray and solid fuel. TMS Annual Meeting, 11-14.03.2012, Orlando, USA.
[6] BALAT, M., BALAT, H. Recent trends in global production and utilization of bio-ethanol fuel. *Applied Energy*. 2009, **86**, 2273-2282.
[7] BANAPURMATH, N.R., RADHAKRISHNAN, S., TUMBAL, A.V., NARASIMHALU, T.N. et al. Experimental investigation on direct injection diesel engine fuelled with graphene, silver and multiwalled carbon nanotubes-biodiesel blended fuels. *International Journal of Automotive Engineering and Technologies*. 2014, **3**, 129-138.
[8] BAUGHMAN, R.H., ZAKHIDOV, A.A., DE HEER, W.A. Carbon nanotubes – the route toward applications. *Science*. 2002, **297**, 787-792.
[9] BHUSHAN, B. Springer Handbook of Nanotechnology, third edition, Springer-Verlag, Berlin-Heidelberg 2010.
[10] BRAND, L., GIERLINGS, M., HOFFKNECHT, A., WAGNER, V. et al. Kohlestoff-Nanorörchen: Potenziale einer neuen Materialklasse für Deutschland; Technologieanalyse, VDI Technologiezentrum GmbH, Düsseldorf 2009.
[11] CARLUCCI, A.P., CICCARELLA, G., STRAFELLA, L. Multiwalled carbon nanotubes (MWCNTs) as ignition

agents for air/methane mixtures. *IEEE Transactions on Nanotechnology*. 2016, **15**, 699-704.

[12] CARLUCCI, A.P., STRAFELLA, L. Air-methane mixture ignition with multi-walled carbon nanotubes (MWCNTs) and comparison with spark ignition. *Energy Procedia*. 2015, **82**, 915-920.

[13] CARLUCCI, A.P., VISCONTI, P., PRIMICERI, P., STRAFELLA, L. et al. Photo-induced ignition of different gaseous fuels using carbon nanotubes mixed with metal nanoparticles as ignitor agents'. *Combustion Science and Technology*. Accepted for publication, posted online: 08.11.2016.

[14] CHAUVEAU, V. Le pouvoir lubrifiant des nanotubes de carbonne; *PhD dissertation*. L'Ecole Centrale de Lyon, 2010.

[15] CHEHROUDI, B. Activation and control of autoignition in HCCI engines using volumetrically-distributed ignition of as-produced single-walled carbon nanotubes. *SAE Technical Paper*. 2012, 2012-01-1691.

[16] CHEHROUDI, B. Minimum ignition energy of the light-activated ignition of single-walled carbon nanotubes (SWCNTs). *Combustion and Flame*. 2012, **159**, 753-756.

[17] CHEHROUDI, B. Nanotechnology and applied combustion: use of nanostructured materials for light-activated distributed ignition of fuels with propulsion applications. *Recent Patents on Space Technology*. 2011, **1**, 107-122.

[18] CINKE, M., LI, J., CHEN, B., WIGNARAJAH, K. et al. Development of Metal-impregnated Single Walled Carbon Nanotubes for Toxic Gas Contaminant Control in Advanced Life Support Systems. *SAE Technical Paper*. 2003, 2003-01-2368.

[20] Coordinating Research Council, Fuel Permeation from Automotive Systems: E0, E6, E10, E20 and E85. Final Report, 2006.

[20] DE VOLDER, M.F.L., TAWFICK, S.H., BAUGHMAN, R.H., HART, A.J. Carbon nanotubes: present and future commercial applications. *Science*. 2013, **339**, 535-539.

[21] DIKIO, E.D. Morphological characterization of soot from the atmospheric combustion of diesel fuel. International *Journal of Electrochemical Science*. 2011, **6**, 2214-2222.

[22] DODD, R., MULLETT, J., CARROLL, S., DEARDEN, G. et al. Laser ignition of an IC test engine using an Nd: YAG laser and the effect of key laser parameters on engine combustion performance. *Lasers in Engineering*. 2007, **17**(3), 1554-2971.

[23] FINIGAN, D.J., DOHM, B.D., MOCKELMAN, J.A., OEHLSCHLAEGER, M.A. Deflagration-to-detonation transition via the distributed photo ignition of carbon nanotubes suspended in fuel/oxidizer mixtures. *Combustion and Flame*. 2012, **159**, 1314-1320.

[24] FRIDELL, E., HAEGER-EUGENSSON, M., MOLDANOVA, J., FORSBERG, B. et al. A modelling study of the impact on air quality and health due to the emissions from E85 and petrol fuelled cars in Sweden. *Atmospheric Environment*. 2014, **82**, 1-8.

[25] FU, S., YU, L., HU, Y., WANG, C. et al. Impact of carbon nanotube suspensions on the hotplate ignition of liquid fuels. 2010 International Conference on Mechanic Automation & Control Engineering (MACE), 26-28.06.2010, Wuhan, China.

[26] GAN, Y., QIAO, L. Optical properties and radiation-enhanced evaporation of nanofluid fuels containing carbon-based nanostructures. *Energy Fuels*. 2012, **26**, 4224-4230.

[27] HAREL, S., KHAIRNAR, M., SONAWANE, V. Laser ignition system for IC engines. *International Journal of Science and Research*. 2014, **3**, 1551-1560.

[28] HUANG, Y.Y., TERENTJEV, E.M. Dispersion of carbon nanotubes: mixing, sonication, stabilization and composite properties. *Polymers*. 2012, **4**, 275-295.

[29] HUANG, Z., KAN, W., LU, Y., CHENG, T. et al. Effect of nanoparticle suspensions on liquid fuel hot-plate ignition. *Journal of Nanotechnology in Engineering and Medicine*. 2014, **5**, 31004-31004-5.

[30] KAŁUŻNY, J. Experimental applications of carbon nanotubes in the construction of internal combustion engines. Publishing House of Poznan University of Technology, Poznań 2013.

[31] KAŁUŻNY, J., CZAJKA, J., PIELECHA, I., WISŁOCKI, K. Investigations of the fuel injection and atomization with the use of laser illumination. *Combustion Engines*. 2013, **154**, 469-475.

[32] KAŁUŻNY, J., MERKISZ-GURANOWSKA, A., GIERSIG, M., KEMPA, K. Lubricating performance of carbon nanotubes in internal combustion engines – engine test results for cnt enriched oil. Internal Report.

[33] KAR, K.K., PANDEY, J.K., RANA, S.K. (Eds.) Handbook of Polymer Nanocomposites. Processing, Performance and Application Volume B: Carbon Nanotube Based Polymer Composites. Springer-Verlag Berlin Heidelberg, 2015.

[34] KISH, S.S., RASHIDI, A., AGHABOZORG, H.R., MORADI, L. Increasing the octane number of gasoline using functionalized carbon nanotubes. *Applied Surface Science*. 2010, **256**, 3472-3477.

[35] KOLOSNJAJ-TAB, J., JUST, J., HARTMAN, K.B., LAOUDI, Y. et al. Anthropogenic carbon nanotubes found in the airways of Parisian children. *EBioMedicine*. 2015, **2**, 1697-1704.

[36] LAGALLY, C.D., REYNOLDS, C.C.O., GRIESHOP, A.P., KANDLIKAR, M. et al. Carbon nanotube and fullerene emissions from spark-ignited engines. *Aerosol Science and Technology*. 2012, **46**, 156-164.

[37] MANOJ, B., SREELAKSMI, S., MOHAN, A.N., KUNJOMANA, A.G. Characterization of diesel soot from the combustion in engine by x-ray and spectroscopic techniques. *International Journal of Electrochemical Science*. 2012, **7**, 3215-3221.

[38] MERKISZ, J., PIELECHA, J. Selected experiences in RDE in Polish reality for different combustion engine applications. 4rd International Conference "Real Driving Emissions", Berlin 25-27.10.2016.

[39] MERKISZ, J., PIELECHA, J. Selected remarks about RDE test. *Combustion Engines*. 2016, **166**(3), 54-61.

[40] MERKISZ, J., PIELECHA, J., BIELACZYC, P., WOODBURN, J. Analysis of emission factors in RDE tests as well as in NEDC and WLTC chassis dynamometer tests. *SAE Technical Paper*. 2016, 2016-01-0980.

[41] MIRZAJANZADEH M., TABATABAEI M., ARDJMAND M., RASHIDI A. et al. A novel soluble nano-catalysts in diesel–biodiesel fuel blends to improve diesel engines performance and reduce exhaust emissions. *Fuel*. 2015, **139**, 374-382.

[42] MORSY, M.H. Review and recent developments of laser ignition for internal combustion engines applications. *Renewable and Sustainable Energy Reviews*. 2012, **16**(7), 4849-4875.

[43] MURR, L.E., BANG, J.J., ESQUIVEL, E.V., GUERRERO, P.A. et al. Carbon nanotubes, nanocrystal forms, and complex nanoparticle aggregates in common fuel-gas combustion sources and the ambient air. *Journal of Nanoparticle Research*. 2004, **6**, 241-251.

[44] MURR, L.E., GUERRERO, P.A. Carbon nanotubes in wood soot. *Atmospheric Science Letters*. 2006, **7**, 93-95.

[45] OHKURA, Y., RAO, P.M., ZHENG, X. Flash ignition of Al nanoparticles: Mechanism and applications. *Combustion and Flame*. 2011, **158**, 2544-2548.
[46] PHUOC, T.X. Laser-induced spark ignition fundamental and applications. *Optics and Lasers in Engineering*. 2006, **44**, 351-397.
[47] RAMACHANDRAN, S., STIMMING, U. Well to wheel analysis of low carbon alternatives for road traffic. *Energy & Environmental Science*. 2015, **8**, 3313-3324.
[48] RASHEDUL, H.K., MASJUKI, H.H., KALAM, M.A., ASHRAFUL, A.M. et al. The effect of additives on properties, performance and emission of biodiesel fuelled compression ignition engine. *Energy Conversion and Management*. 2014, **88**, 348-364.
[49] SARVESTANI, N.S., ROHANI, A., FARZAD, A., AGHKHANI, M.H. Modeling of specific fuel consumption and emission parameters of compression ignition engine using nanofluid combustion experimental data. *Fuel Processing Technology*. 2016, **154**, 37-43.
[50] SCHWADERLAPP, M., ADOMEIT, P., KOLBECK, A., THEWES, M. Ethanol und sein Potenzial für Downsizing-Motorenkonzepte. *MTZ*. 2012, **2**.
[51] SELVAN, V. ANAND, R.B., UDAYAKUMAR, M. Effect of cerium oxide nanoparticles and carbon nanotubes as fuel-borne additives in diesterol blends on the performance, combustion and emission characteristics of a variable compression ratio engine. *Fuel*. 2014, **130**, 160-167.
[52] SINGAMANENI, S., SHEVCHENKO, V., BLIZNYUK, V. Unusual ignition behavior of polyurethane/carbon nanotube composites with a He–Ne laser excitation (632.8 nm) during micro-Raman spectroscopy. *Carbon*. 2006, **44**, 2191-2195.
[53] SUAREZ-BERTOA, R., ZARDINI, A., KEUKEN, H., ASTORGA C. Impact of ethanol containing gasoline blends on emissions from a flex-fuel vehicle tested over the Worldwide Harmonized Light Duty Test Cycle (WLTC). *Fuel*. 2015, **143**, 173-182.
[54] SUNDSETH, K., LOPEZ-APARICIO, S., SUNDVOR, I. Bioethanol vehicle transport in Oslo as climate policy: what are the social economic costs resulting from acetaldehyde pollution effects? *Journal of Cleaner Production*. 2015, **108**, 1157-1167.
[55] SWANSON, J., FEBO, R., BOIES, A., KITTELSON, D. Fuel sulfur and iron additives contribute to the formation of carbon nanotube-like structures in an internal combustion engine. *Environmental Science & Technology Letters*. 2016, **10**, 364-368.
[56] SYSOEV, N.N., OSIPOV, A.I., UVAROV, A.V., KOSICHKIN, O.A. Flash ignition of a carbon nanotube. *Moscow University Physics Bulletin.* 2011, **10**, 66(5).
[57] TREWARTHA, S. Light ignition of carbon nanotubes for the initiation of energetic materials. *PhD Thesis*. 2015, Flinders University, School of Chemical and Physical Sciences.
[58] TSENG, S.H., TAI, N.H., HSU, W.K., CHEN, L.J. et al. Ignition of carbon nanotubes using a photoflash. *Carbon*. 2007, **45**, 958-964.
[59] VDI Richtlinie, VDI 2840, Kohlenstoffschichten Grundlagen, Schichttypen und Eigenschaften.
[60] Volkswagen SSP 359; 1.4l TSI Engine with dual-charging.
[61] WANG, J., ONASCH, T.B., GE, X., COLLIER, S. et al. Observation of fullerene soot in eastern China. *Environmental Science & Technology Letters*. 2016, **3**, 121-126.
[62] WILLAND, J., DANIEL, M., MONTEFRANCESCO, E., GERINGER, B., et al. Grenzen des Downsizing bei Ottomotoren durch Vorentflammungen. *MTZ*. 2009, **5**.
[63] WILLAND, J., SCHINTZEL, K., HOFFMEYER, H. Das Potential aufgeladener Ottomotoren mit Direkteinspritzung. *MTZ*. 2009, **2**.
[64] Worldwide Fuel Charter, 2013.
[65] www.afdc.energy.gov/afdc/data/
[66] www.continuumlasers.com
[67] www.nano-lab.com
[68] www.nano-lab.com/nanotubesuspensions.html
[69] XIE, H., LEE, H., YOUN, W., CHOI, M. Nanofluid containing multiwalled carbon nanotubes and their enhanced thermal conductivities. *Journal of Applied Physics*. 2003, **94**, 4967-4971.
[70] ZACCARDI, J-M., LECOMPTE, M., DUVAL, L., PAGOT, A. Vorentflammung an hoch aufgeladenen Ottomotoren; Visualisierung und Analyse. *MTZ*. 2009, **12**.
[71] ZHAO, H. Laser diagnostics and optical measurement techniques in internal combustion engines. *SAE International*, 2012, Warrendale, USA.
[72] ZHAO, H., LADOMMATOS, N. Optical diagnostics for in-cylinder mixture formation measurements in IC-engines. *Progress in Energy and Combustion Science*. 1998, **24**, 297-336.

Jarosław Kałużny, DSc., DEng. – Faculty of Machines and Transport at Poznan University of Technology.

e-mail: *Jaroslaw.Kaluzny@put.poznan.pl*

Prof. Jerzy Merkisz, DSc., DEng. – Faculty of Machines and Transport at Poznan University of Technology.

e-mail: *Jerzy.Merkisz@put.poznan.pl*

Dawid Gallas, MSc. – Faculty of Machines and Transport at Poznan University of Technology.

e-mail: *Dawid.Gallas@doctorate.put.poznan.pl*

Tomasz Runka, DSc. – Faculty of Technical Physics at Poznan University of Technology.

e-mail: *Tomasz.Runka@put.poznan.pl*

Miłosław Kozak, DSc., DEng. – Faculty of Machines and Transport at Poznan University of Technology.

e-mail: *Miloslaw.Kozak@put.poznan.pl*

Ireneusz Pielecha, DSc., DEng. – Faculty of Machines and Transport at Poznan University of Technology.

e-mail: *Ireneusz.Pielecha@put.poznan.pl*

Article citation info:
KOWALAK, P., ŻMUDZKI, S., BORKOWSKI, T. Marine diesel engine – a novel approach of indicated power determination and related uncertainty level. *Combustion Engines*. 2017, **168**(1), 15-20. DOI: 10.19206/CE-2017-102

Przemysław KOWALAK
Stefan ŻMUDZKI
Tadeusz BORKOWSKI

CE-2017-102

Marine diesel engine – a novel approach of indicated power determination and related uncertainty level

A proposal of a new method for marine engine indicated power determination, based on direct piston position, instead of crankshaft angular position measurement, was presented. With the aid of bond graph theory, it was proved, that the new method is equivalent to conventional method. To verify hypothesis, that the new method has potential of determined indicated power uncertainty reduction, simulated calculations were carried out. Results of calculations for two marine diesel engines: medium-speed, four stroke and slow-speed two stroke type, at assumption of engine crankshaft constant speed, were compared with results obtained by a conventional method. Data, collected by means of a typical portable, industrial, digital indicator on engines in service, were used for simulation. The uncertainties of engines indicated power determined by means of two methods were analysed. The indicated power uncertainty, achieved for conventional method, was nearly twice higher than for new proposed method. Finally, uncertainty structure was analysed and evaluated for both: new and conventional method of engine indicated power determination.

Key words: *marine diesel engine, indicated power, uncertainty*

1. Introduction

High demand to improve fuel economy and exhaust gas emission characteristics requires a new technology for engine control. Also, increased expectation of marine diesel engines reliability calls for sophisticated control and development of engine diagnostics systems. Computational modelling of crank shaft position and rotational speed fluctuations could be used as a basis for engine diagnosis. Certain parameters were found, such as crank friction or instantaneous engine speed that provide a better basis for fault engine assessment [4]. Also, balanced cylinder combustion is important for reliable, emission-compliant engine operation. Throughout the years, several engine balance techniques have been developed and efficiently utilized. Unfortunately, no clear-cut standard has been established for them. Combustion pressure is analysed for specific quantitative values like indicated mean effective pressure, maximum pressure, firing pressure angle, cycle variations, etc. and certain events location (valve closure and opening, peak rate of pressure rise, etc.), as well as process variation between cylinders. However, the principle aim is indicated power estimation for each cylinder and consequently total engine indicated power assessment. Engine cylinder pressure analysis may be used to balance and tune the engine: e.g. valve and fuel injection timing as well as fuel bulk and compression pressure.

Usually, low speed, large bore diesel engine is applied as a vessel's main propulsion and stays in a range of power from a few thousand kilowatts to over 80 MW. The main engine is one of the most expensive functional components of the ocean-going vessel. Daily fuel consumption of the most powerful marine engines may exceed 250 tons. Therefore, such responsible machinery should be monitored and controlled adequately. Any main engine malfunction involves enormous costs of excessive fuel consumption, repairs and even bigger costs of ship's trip delays and lost freight. One of the solutions used to meet these requirements is a real-time cylinder pressure monitoring system. Gas pressure appraisal in combustion chamber of reciprocating engine is mostly affected by two phenomena: the first of them are acoustic vibrations in a long duct, connecting combustion chamber with the sensor, the second is unreliable synchronization with the piston position. While the negative influence of acoustic vibrations can be solved by signal filtration with acceptable result, the problem of synchronization has not been solved yet satisfactorily. Instantaneous engine crankshaft rotational speed varies during the whole engine cycle. There are several possible ways of piston position estimation, presented in literature [1–3, 12, 13]. The majority of methods do not require a specific sensor placed inside the engine crankcase, but are based on the engine speed – measured by the typical pick-up mounted at flywheel. Supportive analysis of the cylinder gas pressure course [8, 12] is utilized too.

In order to monitor the overall engine output, the torque meter can be applied on the ship's main propulsion shaft. However, the determination of the indicated power in each cylinder unit brings more benefits indeed. In addition to the engine total indicated power, the balance of the engine load distribution between cylinder units needs to be evaluated too.

The indicated power is defined as a ratio of the indicated work generated in the single cycle to the time needed to generate that work [5]:

$$P_i = \frac{L_i}{\tau_c} = \frac{L_i \cdot \omega}{2 \cdot n_R \cdot \pi} \tag{1}$$

Generally, the principle of the indicated power determination strictly relies on the definitional formula (1). The method of indicated power determination has not changed much since the time of steam engines. Basically, the pressure course is integrated over the cylinder volume in order to determine the generated work per cycle and then the indicated power is determined. That solution comes directly from the classic definition and availability of engine cylinder gas pressure and crankshaft speed. Unfortunately, this method is still not sufficiently accurate in terms of modern requirements. One of the main reason is well-known prob-

lem of the engine's piston top dead center (TDC) determination, during combustion pressure measurement [6–10]. Position of the TDC is essential for proper assigning of the positive or negative value to the incremental indicated work that is calculated. In various publications it is estimated that 1° of a crank angle (CA) error in piston TDC determination, may lead to 3–10% of the determined indicated power inaccuracy [6–8]. As presented in [7], the TDC position standard uncertainty of 0.6° CA is achivable in a typical industrial conditions. There is a number of various methods aimed to increase the accuracy of pressure course with piston position synchronisation. Generally, they may be divided into two groups: pre measurement methods and post measurement methods. Installation of incremental encoders on the crankshaft may be an example of the first group. Also application of finite element method (FEM), for crankshaft torsional or vibratory deformation evaluation, is a kind of pre measurement method for increasing the accuracy of indicated power determination. The second group representative example is a rate of pressure rise dp/dα analysis. Unfortunatelly, presented exapmles provide limited improvement only, or they are selected for specific engines constructions or working conditions. Incremental encoders allow to reduce greatly the irregular shaft speed influence, however the problem of their static adjustment still remains unsolved. The method based on FEM analysis, requires detailed informations about the shaftline geometry, material and set of initial and boundary conditions data. Besides, enormous computational capacity is to be engaged for such model calculations, that makes it unavailable on board the vessel.

The concept of the thermodynamic TDC, understood as the one, detected by pressure course or heat flow analysis, was proposed [8, 12, 13]. However, the thermodynamic TDC differs from the real TDC [6, 8, 12, 13], by an angle φ, which is difficult to evaluate usually. As the main reasons, the heat exchange with cooled, engine chamber and loss of charge through the piston rings locks, are indicated [6, 13]. The dp/dα analysis gives quite satisfactory results for slow speed engines, where ignition occures after the piston TDC, however for medium speed engines, where ignition occures before piston TDC it is much less accurate.

Currently used method of indicated power determination exhibits one more disadvantage - difficulties with precise uncertainty estimation. Actually none of the commercially available, industrial indicators is equipped with manufacturer's specification regarding accuracy of calculated indicated power. Calibration certificate of the pressure sensor is attached eventually. This is mostly due to the complexity of the indicated power uncertainty evaluation and lack of standardised procedures [6, 7]. A proposal of a method for the indicated power uncertainty evaluation was presented in [7].

This paper is meant as a proposal of a method for indicated power determination, free of a major factor influencing the overall indicated power uncertainty – the TDC determination uncertainty.

2. Proposed method fundamentals

The problem of the piston engine's indicated power determination can be examined in terms of the bond graphs theory as a rate of energy transfer [9]. The bond graph representation of the piston engine's kinematics is shown on Figure 1.

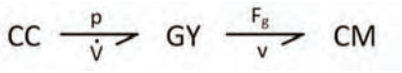

Fig. 1. Cylinder, piston and crankshaft assembly represented by a bond graph [9]

The power of the working gas in combustion chamber (CC) volume is described by a product of cylinder gas pressure p and rate of CC volume $\dot{V}$. The piston appears to be a bond graph node called gyrator (GY), where the rate of energy flow undergoes transformation from the energy of the working gas pressure into mechanical energy of the moving crank assembly. Following gyrator, the rate of energy transfer is described by a product of the force F_g, exerted on piston by working gas pressure, and piston speed v.

Consequently, the rate of energy transfer to the engine's crank mechanism CM and later, through engine's coupling, to the energy consumer. Assuming, that the rate of energy flow is transformed in the gyrator in a lossless process, it can be described by equation (2):

$$p \cdot \dot{V} = F_g \cdot v \tag{2}$$

For given combustion chamber geometry, known cylinder gas pressure and piston speed, the formula (3) for instant rate of energy transfer may be applied:

$$\frac{dE(t)}{dt} = F_g(t) \cdot v(t) = A \cdot p(t) \cdot \frac{dS(t)}{dt} \tag{3}$$

By integration, with respect to time, the indicated work of a cycle may be determined:

$$\int_0^{\tau_c} \frac{dE(t)}{dt} dt = A \int_0^{\tau_c} p(t) \cdot \frac{dS(t)}{dt} dt = L_i \tag{4}$$

Equations (3) and (4) prove that the indicated work may be evaluated from known cylinder gas pressure p, the piston speed v and piston area A. Consequently, the indicated power for one cylinder may be determined (5):

$$P_i = \frac{1}{\tau_c} \int_0^{\tau_c} \frac{dE(t)}{dt} dt = \frac{A}{\tau_c} \cdot \int_0^{\tau_c} p(t) \cdot \frac{dS(t)}{dt} dt \tag{5}$$

Specific technical means to observe the piston movement should be secured in order to apply the proposed method of the indicated power determination. Direct measurement of the piston speed might be problematic. A better solution is to utilise a number of known piston positions. From a series of recorded pairs: piston position and time, a function S(t), describing piston shift over the time can be elaborated and, consequently, piston velocity function v(t) can be established. Effectively, presented technique may be called as an observation method of the indicated power determination.

3. The uncertainty analysis

The overall uncertainty of the determined indicated power depends on the individual uncertainty components in equation (5). The piston area uncertainty as well as cylinder gas pressure measurement uncertainty are the same in new observation method as in the well-known conventional

method, based on the classic definition. The piston area A standard uncertainty type B is found from equation (6):

$$u_B(A) = \frac{\partial A}{\partial D_n} \cdot u_B(D_n) = \frac{\pi \cdot D_n}{2} \cdot u_B(D_n) \quad (6)$$

The dynamic pressure measurement accuracy problem is common for both methods, it is well described in literature [5, 6, 13]. It should be analysed in the same way regardless to the indicated power determination method applied. Consequently, pressure uncertainty has no influence on the difference in indicated power uncertainty between both described methods. To simplify analysis of the proposed method, which is concentrated on TDC determination issue, pressure measurement uncertainty is reduced to a single sample uncertainty which can be found from formula (7):

$$u_B(p) = \frac{R \cdot \Delta p}{100\% \cdot \sqrt{3}} \quad (7)$$

Typically, measured data are recorded at a fixed sampling rate. The relative uncertainty of the time interval measurement $u_r(dt)$ is quantitatively identical with the sampling rate uncertainty and usually given in the analogue-digital converter specification. Typical acquisition cards are equipped with clocks of basic frequency f_b= 5–10 MHz and relative stability of 100 ppm, that means: $u_r(f_b)$ = ± 0.01%.

In an industrial measuring devices, the typical sampling rate is 10–25 kHz, to secure sufficient time resolution of the measurement. The clock time interval uncertainty can be determined by means of the sampling rate parameters:

$$u_B(dt) = \frac{1}{f_s} - \frac{1}{f_s + f_s \cdot u_r(f_b)} \quad (8)$$

Assuming the sampling frequency of f_s = 10 kHz, thus for typical industrial application the clock time interval uncertainty amounts to $u_B(dt)$ = 10 ns.

The problem of the piston position uncertainty determination is closely related to the selected measurement technique. The review of linear position sensors available on the market allows for assumption that the measurement uncertainty of $u_B(S)$ = 0.1 mm is available. The finite number of piston positions S_i measured in the time domain can be approximated by a continuous function $\hat{S}(t)$. The overall uncertainty $u_B(S_p)$ of the piston position estimation (9) may be derived from the error propagation law as a singular value measurement uncertainty $u_B(S)$ and the approximating function $\hat{S}(t)$ mean square error which is a direct estimator of a fitting quality:

$$u_B(S_p) = \sqrt{u_B^2(S) + s^2\left(\hat{S}(t)\right)} \quad (9)$$

In time interval dt between consecutive samples i and i+1 piston displaces the distance:

$$dS_i = S_{i+1} - S_i \quad (10)$$

The uncertainty of the distance dS_i (10) is a function of both boundary positions S_i and S_{i+1} uncertainties. For a set of consecutive distances dS_i, a set A_S of starting positions $S_i \in A_S$ can be defined. Similarly, a set B_S of ending positions $S_{i+1} \in B_S$ can be defined too. Correlation coefficient $r(A_S, B_S)$ of both sets: A_S and B_S can be calculated accordingly. Subsequently the uncertainty of a distance dS_i can be determined form the formula for correlated values [10] (11):

$$U_B(dS) = \sqrt{u_B^2(S_p) + u_B^2(S_p) - 2 \cdot u_B(S_p) \cdot u_B(S_p) \cdot r(A_S, B_S)} \quad (11)$$

Since the piston position is described by means of a continuous approximating function $\hat{S}(t)$, the piston's speed function v(t) can be determined:

$$v(t) = \frac{d\hat{S}(t)}{dt} \quad (12)$$

The piston speed uncertainty can be determined with the aid of the formula (13):

$$u_B(v(t)) = \sqrt{\left(\frac{\partial v(t)}{\partial dt} \cdot u_B(dt)\right)^2 + \left(\frac{\partial v(t)}{\partial d\hat{S}(t)} \cdot u_B(dS)\right)^2} \quad (13)$$

Once the piston speed and cylinder gas pressure uncertainties are known, the rate of the energy flow uncertainty can be evaluated. Based on equations (3), (6), (7) and (13), the equation can be formulated:

$$u_B(\dot{E}) = \sqrt{\left(\frac{\partial \dot{E}}{\partial A} \cdot u(A)\right)^2 + \left(\frac{\partial \dot{E}}{\partial p} \cdot u(p)\right)^2 + \left(\frac{\partial \dot{E}}{\partial v} \cdot u(v)\right)^2} \quad (14)$$

In the presented method, to evaluate the cycle work, the rate of energy flow $\dot{E}$ must be integrated over the time (4). This is done by means of the numerical trapezoidal method usually. For the uncertainty determination, an uncertainty of the mean value of two consecutive values $\dot{E}_i$ and $\dot{E}_{i+1}$ should be determined first. The formula (15) for correlated input data can be applied, accordingly [10]. A set A_E of preceeding values $\dot{E}_i \in A_E$ and a set B_E of following values $\dot{E}_{i+1} \in A_E$ were defined and then a correlation coefficient $r(A_E, B_E)$ was calculated.

$$U_B(\dot{E}_{av}) = \sqrt{u_B{}^2(\dot{E}_i) + u_B{}^2(\dot{E}_{i+1}) + 2 \cdot u_B(\dot{E}_i) \cdot u_B(\dot{E}_{i+1}) \cdot r(A_E, B_E)} \quad (15)$$

For numerical integration, the elementary work is to be determined initially, its uncertainty can be expressed as:

$$u_B(\dot{E}dt) = \sqrt{\left(\dot{E}_{av} \cdot u_B(dt)\right)^2 + \left(dt \cdot u_B(\dot{E}_{av})\right)^2} \quad (16)$$

In consequence, the uncertainty of the indicated work of a single cycle can be defined from the equation:

$$u_B(L_i) = \sqrt{\sum_{j=1}^{j=k} u_B{}^2(\dot{E}_j dt)} \quad (17)$$

Finally, the single cycle indicated power uncertainty is assessed as follows:

$$u_B(P_i) = \sqrt{\left(\frac{\partial P_i}{\partial \tau_c} \cdot u_B(dt)\right)^2 + \left(\frac{\partial P_i}{\partial L_i} \cdot u_B(L_i)\right)^2} \qquad (18)$$

Final indicated power uncertainty equation (18) contains less variables and is much More convenient for a new approach, comparing to the conventional method [7] of indicated power determination. On the contrary to the conventional method [7], there are no factors, like a TDC sensor positioning, with unknown or difficult to evaluate uncertainties too. Consequently, a hypothesis may be formulated, that the new method might lead to the indicated power determination with lower uncertainty comparing to conventional method.

4. The simulation results discussion

The above presented uncertainty analysis of the proposed method was a subject to the validation test against the conventional method. The test was designed as a simulation calculation with the utilisation of data recorded by means of conventional method. The main goal of the validation was the comparison of indicated power and its uncertainty, resulted from common input but estimated with different methods. The original data sets for simulation calculations were collected for two marine diesel engines:

– medium-speed, four stroke – Hyundai Himsen H25/33,
– slow-speed, two stroke – MAN K90MC-C.

Both engines were in good service condition. The fuel injection valves were in the middle of their recommended working period. The exhaust gas temperatures, cylinder compression and maximum pressures did not indicate any related malfunctions to the leaky exhaust valves or piston rings.

Cylinder process data sets were collected by means of typical industrial digital indicator Premet XL® of Lemag GmbH, during engines service operation. Engines were operated for at least 1 hour at constant load before measurements were carried out. During measurements, engines load remained constant and several monitored operational parameters, like charging air pressure, proved it. The slow speed engine was equipped with the LEMAG Multiscan Sensor®, which is a type of incremental encoder, installed on the propulsion shaft. The sensor resolution is 360 pulses per revolution, that allows for substantial reduction of the shaft speed irregularity influences. The medium speed engine TDC was indicated by an inductive pick-up installed over a flywheel. Both: multiscan sensor and inductive sensor, prior to the measurement, were adjusted statically to the TDC of piston in cylinder unit No. 1, the closest one to the flywheel. The indicator presents the recorded set of measured data as an average pressure course calculated from the initially pre-set number of engine cycles. Even though it is a good practice to use the highest available number of cycles for average calculation, specifically for engines directly driving ship's propeller, too long time of indication increases the risk of recording engine load fluctuation due to influence of the sea swell. In case of engine driving electric generator, in industrial condition, there is similar risk caused by higher possibility of unexpected start or stop of a large electric consumer. For those reasons, the amount of observed cycles pre-set was chosen as 10 for every monitored engine. Utilised digital indicator allows only for post measurement TDC correction by means of pressure rise dp/dα analysis. However, such analysis was unreliable, specifically for medium speed engine due to advanced ignition. For this reason, it was decided to utilise uncorrected data for both engines. The influence of the pressure measurement uncertainty on the overall indicated power uncertainty was the same for both methods, therefore this complicated analysis was reduced to the sensor range and linearity only. Disturbances in the pressure measurements are independent on the indicated power determination method and therefore may be examined separately.

Recorded data sets were used to compare results of observation technique calculation, marked as method A, with outcomes given by the industrial indicator, which result was marked as method B. For further analysis and calculations only the single cylinder unit No. 1 data of each engine were considered. In both cases, it was assumed that the crankshaft angular speed was constant. This assumption was justified in case of slow speed engine due to installed incremental encoder, allowing to neglect the shaft rotational speed irregularity. The medium speed engine crankshaft speed irregularity caused a minor influence on the resulted indicated power uncertainty [7]. Additionally, this assumption allowed for an easier comparison of the uncertainty achieved. It is expected that the proposed method A, based on direct piston observation, should not be prone to the speed irregularity influence, while for measured engines this influence is limited. Finally, the indicated power and related uncertainties evaluations for both methods were carried out and presented in Table 1. Exclusively, in case of method B the uncertainties were evaluated by means of method proposed in [7]. The TDC positioning uncertainties were evaluated for typical industrial conditions.

Table 1. Results of indicated work and power calculations with their uncertainties

Engine type	Hyundai H25/33		MAN K90 MC-C	
Load	59%		80%	
Method	A	B	A	B
TDC uncertainty [7]	–	0.63° CA	–	0.57° CA
P_i	189 kW	182 kW	3991 kW	3850 kW
$u_B(P_i)$	±4.4 kW (±2.3%)	±12 kW (±6.8%)	±86 kW (±2.1%)	±180 kW (±4.8%)

For uncertainty determination, several values, listed in Table 2, had to be assumed. In case of time interval dt and pressure sensor range R, typical values of the industrial systems were accepted. Piston position approximating function $\hat{S}(t)$ was assumed with poor fitting quality, even if hypothetical sensor class, represented by the singular value measurement uncertainty $u_B(S)$, would exhibit higher precision.

Table 2. Basic assumptions for the observation method uncertainty evaluation

uB(dt)	10 ns
uB(S)	0.1 mm
$s\left(\hat{S}(t)\right)$	4 mm
R	25 MPa

The uncertainty distribution for the indicated power determination using methods A and B, of both marine engines are presented in Figs 1 and 2. The uncertainty of indicated power determined by means of the proposed technique – A, is considerable smaller than uncertainty established using the conventional method – B. The improvement is significant, approximately up to three times for medium speed engine and up to two times for slow-speed K90MC-C engine. In both methods, A and B the pressure measurement uncertainty is settled as main component. However, in case of a conventional method – B also other issues, described in details in [7], have a significant influence on the overall indicated power uncertainty.

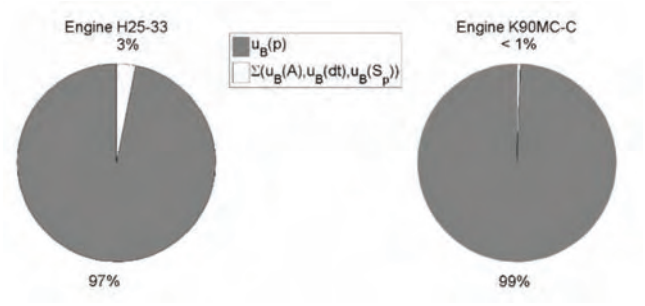

Fig. 1. Distribution of the indicated power uncertainties (method A) for marine engines – medium speed H25-33 and slow speed K90MC-C; $u_B(p)$ – cylinder gas pressure uncertainty, $u_B(A)$ – piston surface uncertainty, $u_B(dt)$ – clock time interval uncertainty; $u_B(S)$ – piston position uncertainty

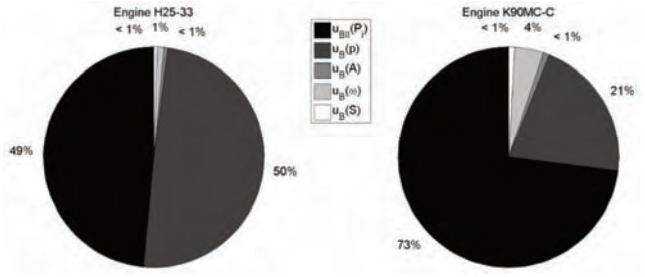

Fig. 2. Distribution of the indicated power uncertainties (method B) for marine engines – medium speed H25-33 and slow speed K90MC-C [7]; $u_{BII}(P_i)$ – indicated power uncertainty type B kind II, $u_B(p)$ – cylinder gas pressure uncertainty, $u_B(A)$ – piston surface uncertainty, $u_B(\omega)$ – crankshaft angular speed uncertainty; $u_B(S)$ – piston position uncertainty

Generally, the proposed method displays main component of the overall uncertainty as the pressure measurement uncertainty, with contribution of 97% to 99%. That makes a significant quality difference comparing to the conventional method. Also, the number of important factors is seriously reduced, that simplifies the uncertainty evaluation. However, it should be underlined that presented technique comprises essential assumptions: piston position samples are uniformly distributed and recorded over the entire stroke, and crankshaft rotational speed is constant over the entire cycle. In fact, the crankshaft speed irregularities [11] combined with the piston position observation difficulties will not allow for such optimistic result.

In the presented simulation, in case of both methods A and B, the uncertainty of type A [10] could not be evaluated due to lack of repeatedly collected data. It is expected however that, in case of the observation method, the value of type A uncertainty is significant. Principally, indicated power uncertainty type A is expected to include TDC position uncertainty, which is estimated on the base of the piston speed approximating function's $v(t)$ zero-crossing point.

5. Conclusions

Basically, new calculation technique should demonstrate advantages against current approach and observation method presents such potential of reducing uncertainty of marine engine indicated power. Additionally, proposed method substantially improves uncertainty calculation predictability. In presented simulation confirmation of significant uncertainty level reduction was achieved. Main factor influencing the overall indicated power uncertainty is cylinder gas pressure measurement uncertainty, which is responsible for over 90% of the overall uncertainty value. That is a qualitative improvement in comparison to the conventional method, where some, crucial for uncertainty evaluation factors are difficult to measure and evaluate.

The functional representation of the piston speed allows determination of the instant piston speed exactly at a time of every pressure sample, therefore difficult process of the pressure course synchronization with crankshaft angle is no more required. Finally, direct piston position measurement and consequent piston speed determination do not require additional piston's TDC determination. The piston TDC is automatically detected at the speed function zero-crossing points. The calculated functions of piston speed $v(t)$ and the rate of energy transfer $\dot{E}(t)$ seems to be very promising as a future diagnostic and engine performance evaluation tools.

Practical introduction of the proposed method may pose a real problem. Not only the difficult environment inside of the crankcase must be considered. Fulfilling of safety requirements (potential oil mist ignition) and classification societies acceptance may be difficult to overcome. From the other hand, proximity sensors, for a bearing monitoring systems, are currently successfully installed in large crosshead engines. This type of marine engines seems to be especially fit for the proposed method application. Access to the crosshead, which is rigidly connected to the piston is easy, and it allows for entire piston stroke observation.

Nomenclature

A	area of the engine piston [m^2]
A_E	set of incremental rate of energy flow preceeding values $\dot{E}_i$
B_E	set of incremental rate of energy flow following values $\dot{E}_{i+1}$
A_S	set of piston incremental travelling distances starting points S_i
B_S	set of piston incremental travelling distances ending points S_{i+1}
CC	combustion chamber

CM crank mechanism
dt time interval [s]
D_n nominal cylinder bore [m]
E energy [J]
$\dot{E}$ rate of the energy flow [J/s]
$\dot{E}_{av}$ average of the consecutive rate of the energy flow values [J/s]
f_b clock frequency [Hz]
F_g piston gas force [N]
f_s sampling frequency [Hz]
GY gyrator
k number of samples per engine working cycle
L_i indicated work [J]
n crank rotational speed [rps]
n_R number of crank revolutions per cycle
r correlation coefficient
R sensor measurement range [Pa]
s mean square error
S piston position (measured value) [m]
S_p estimated position of a piston [m]
$\hat{S}(t)$ approximating function of a piston position [m]
p cylinder gas pressure [Pa]
P_i indicated power [W]
u_A uncertainty type A
u_B uncertainty type B
u_r relative uncertainty
v piston speed [m/s]
$\dot{V}$ rate of combustion chamber volume change [m^3/s]
Δp pressure sensor's non-linearity error [% FSO]
τ_c cycle time [s]
ω crankshaft angular speed [rad/s]

Bibliography

[1] WANG, Y., LIM, T.C. An analysis of modal damping sources in reciprocating engine. *Journal of Sound and Vibration*. 2001, **242**(1), 179-193.
[2] NILSSON, M. Modelling flywheel-speed variations based on cylinder pressure [Master's thesis]. 2004, Linköping: Linköping University.
[3] TRAVER, M.L., ATKINSON, R.J., ATKINSON, C.M. Neural network-based diesel engine emissions prediction using cylinder gas combustion pressure. *SAE Technical Paper*. 1999, 1999-01-1532.
[4] TWIDDLE, J.A., JONES, N.B. A high-level technique for diesel engine combustion system condition monitoring and fault diagnosis. *Proceedings of the Institution of Mechanical Engineers Part I: Journal of Systems and Control Engineering*. 2002, **216**(2), 125-134.
[5] HEYWOOD, J.B. Internal combustion engines fundamentals. Singapore, 1988. McGraw-Hill.
[6] BROWN, W.L. Methods for evaluating requirements and errors in cylinder pressure measurement *SAE Technical Paper*. 1967, 670008.
[7] KOWALAK, P. Marine engine indicated power uncertainty determination. *Combustion Engines*. 2015, **161**(2), 3-13.
[8] STAŚ, M.J. An universally applicable thermodynamic method for T.D.C. determination. *SAE Technical Paper*. 2000, 2000-01-0561.
[9] CICHY, M. Silniki o działaniu cyklicznym podstawy teorii działania [Cyclic engines theory and fundamentals]. 1989, Gdańsk: Wydawnictwo Politechniki Gdańskiej.
[10] International Organization for Standardisation. 1995. Guide to the expression of uncertainty in measurement. Geneva: ISO.
[11] KOWALAK, P. Speed irregularity characteristic of low speed, two-stroke marine diesel engine applied as vessel's main propulsion. *Journal of KONES Powertrain and Transport*. 2008, **15**(4), 263-268.
[12] TAZEROUT, M., LE CORRE, O., ROUSSEAU, S. TDC determination in IC engines based on the thermodynamic analysis of the temperature-entropy diagram. *SAE Technical Paper*. 1999, 1999-01-149.
[13] WIMMER, A., GLASER, J. Indykowanie silnika [Engine's indication]. 2004, Warsaw: Instytut Zastosowań Techniki.

Przemysław Kowalak, DEng. – Institute of Marine Power Plants Operation, Faculty of Marine Engineering, Maritime University of Szczecin.

e-mail: *P.Kowalak@am.szczecin.pl*

Prof. Stefan Żmudzki, DSc., DEng. – Faculty of Marine Engineering, Maritime University of Szczecin.

e-mail: *S.Zmudzki@am.szczecin.pl*

Tadeusz Borkowski, DSc., DEng. – Faculty of Marine Engineering, Maritime University of Szczecin.

e-mail: *T.Borkowski@am.szczecin.pl*

Article citation info:
MERKISZ, J., RYMANIAK, Ł. Tests of urban bus specific emissions in terms of currently applicable heavy vehicles operating emission regulations. *Combustion Engines*. 2017, **168**(1), 21-26. DOI: 10.19206/CE-2017-103

Jerzy MERKISZ
Łukasz RYMANIAK

CE-2017-103

Tests of urban bus specific emissions in terms of currently applicable heavy vehicles operating emission regulations

The article presents a study of a city bus in real operating conditions (RDE) from the perspective of the latest regulations for the assessment of specific emissions compliance for heavy-duty vehicles (Euro VI standard). The object of the research was a serial configuration hybrid drive vehicle. Measurements were made in the real driving conditions in Poznan agglomeration. The latest mobile equipment PEMS was used for the measurements. This article presents the details of the EU 582/2011 Procedure in operational conformity assessment, the methodology of the study was discussed, and the obtained results were presented, both in terms of vehicle operating conditions and engine operation, as well as specific emissions evaluation.

Key words: *bus, drive system, hybrid, RDE, specific emissions*

1. Introduction

Buses have a significant impact on the environmental quality in urban areas, where there are large concentrations of people. This is due to the number of the vehicles in the considered group and the power used in their drive systems. The share of urban buses, non-urban buses, and tourist coaches from all the HDVs (Heavy-Duty Vehicle) in the European Union is 11%, while the estimated fuel consumption by these vehicles accounts for 15% of the consumption of all HDVs [12, 13]. The total number of registered heavy vehicles (including special vehicles) in Poland in December of 2014, was over 3.6 million units. Buses accounted for 106 057 units, of which almost 85% (89 996 units) were operated by public transport companies [3]. In 2000–2006, the number of registered vehicles remained at a similar level, reaching about 81 000 units, and in each subsequent year, their population increased by an average of 2.3%. 15 498 regular communication lines were operated in 2014, with a total travel length of 788 612 km, and transported nearly 431.5 million passengers. Due to the age distribution of the buses, vehicles of up to five years old constituted 8.1% of the total, buses in the age range of 6–15 years reached 28%, the remaining 45.7% was in the last age group, of up to 30 years [3].

For the approval of heavy-duty vehicles, in terms of compliance with the emission standards in the European Union, new Euro standards, from I to VI, were gradually introduced, supplemented with the EEV standard (Enhanced Environmentally Friendly Vehicle) for the Euro III–V. These rules expect for tests of only the combustion units themselves to be performed on an engine dynamometer, in defined static and dynamic measurement cycles. With the introduction of Euro VI (type approvals from 31.12.2012, first registration from 31.12.2013) new compulsory tests have been added: WHSC (World Harmonized Stationary Cycle) and WHTC (World Harmonized Transient Cycle), and replaced the previously used ETC (European Transient Cycle), ESC (European Stationary Cycle) and ELR (European Load Response) tests. The recent years of research work have indicated that the measurements quality and quantity of exhaust gases from internal combustion engines performed under laboratory conditions may differ from the actual vehicle emissions of the given category, including HDV [4, 5, 7, 8]. As a result continuous efforts are made to develop detailed and universal methods of emissions assessment in road conditions RDE (Real Driving Emissions). From the moment the Euro VI standard came into effect, it became necessary for manufacturers to perform road measurements to verify the operating conformity of heavy-duty vehicles powered by different types of fuels [1, 2, 9].

2. Legal regulations concerning the control of operational compliance of in-service HDV

The Euro V and Euro VI standards provide mileages and operating periods corresponding to the normal life span of a heavy vehicle. Minimal mileages for durability tests depending on the vehicle category and maximum mass are also compiled. The records are supplemented with data for determining the deterioration factors (more precise and unambiguous definitions are outlines in the Euro VI standard) [6]. Significant changes in the regulations occurred for the operational conformity control – at present it is necessary to perform emission measurements in real driving conditions, using PEMS type equipment. While previously, only combustion engines themselves were tested, after being removed from used vehicles.

The EU Regulation 582/2011 (Annex II) provides detailed description of the requirements for the operating compliance evaluation for engines or vehicles. Among the most important information it should be noted that the measurements need to be carried out on public roads in the EU, using normal driving patterns and loads. This means that the tests are conducted using the standard (the most common) operating conditions. It is also important to ensure that the driver has the appropriate driving skills and training for the given vehicle type, and it is best when the procedure involves a person who usually drives it. In the case when it is impossible to carry out tests under normal operating conditions it is possible to use other alternative routes. If there is insufficient information on a representative vehicle load an additional load is used to obtain 50–60% of the maximum vehicle load.

After the first registration of a complete vehicle is obtained, with a combustion engine which comes from the

approved group (family) of engines, the manufacturer must carry out field tests within an 18 month time frame and obtaining a mileage of at least 25 000 km [9]. According to [10], measurements have to be repeated periodically, at least every 24 months during the normal vehicle operation. The testing rejection and acceptance criteria, as a part of the compliance checks, is determined based on the number of tested vehicles, as relative to the total number of vehicles produced [9]. An inspection and testing of the used lubricating oils and fuels samples is included as supplementary procedures. It should be noted that the vehicle used for the measurement cannot be over-exploited, modified or improperly exploited.

The test route must include driving on urban roads (speed range: 0–13.89 m/s), suburban roads (13.89–20.83 m/s) and highways (over 20.83 m/s); the order can be changed should a legitimate case be made for doing so. The share in driving time for different conditions depends on the category of the tested vehicle (Table 1). These shares are determined with an accuracy of ±5% due to the difficulty of predicting the actual traffic conditions. Sampling is carried out continuously, and it begins even before starting the engine. While the data evaluation is carried out from the moment the coolant achieves the temperature of 343 K (70°C) or is stabilized within ±2 K in the span of 300 s. The measurement must be continuous and the data cannot be combined or modified. In addition to measuring the emissions intensity the acquisition of data from on-board diagnostic system must also be carried out in accordance to the guidelines [9]. It is imperative for the test on the realized route to perform work five times higher than during the WHTC test, or to achieve five times the CO_2 reference mass value of the same test.

Table 1. Shares of driving time in different conditions during operational compliance tests for heavy vehicles [9]

Category	Operating time share [%]		
	urban	suburban	highway
M_1, N_1	45	25	30
M_2, M_3 class I, II and A	70	30	0
M_2, M_3 others	45	25	30
N_2	45	25	30
N_3	20	25	55

The conformity factor is determined for the measuring windows which are devised two ways: based on the weight of CO_2, or based on the total work performed by the drive system. When issuing positive/negative decisions in the legislative process only the second variant should be used. The research involves the specific emission of gaseous compounds: CO and THC (for CI), NMHC and CH_4 (for SI) and NO_x (for CI and SI). Currently the weight and number of particles is not taken into account. In addition, it is necessary to measure exhaust gas mass flow, the engine operating parameters, the vehicle speed and its location, fuel flow rate, ambient conditions, etc. The legislation [9] also provides detailed information about the standards and functions, which the measuring equipment must meet, as well as a method of calibration, resetting, and self-diagnostics of instruments.

Pollutants specific emission evaluation is done using the moving averaging window method. Their determination is based on defining the mass flow rate of harmful substances emission for a subset of the complete data set, whose length is determined so as to correspond to the weight of CO_2 from the engine or the work measured on a test bench in transient operating conditions (WHTC test). Moving average is calculated for the time increment Δt, corresponding to the sampling period. The determined mass flow of emissions is expressed in mg/window [9]. For the method based on the work, the averaging windows are determined from the relation (Fig. 1):

$$W(t_{2,i}) - W(t_{1,i}) \geq W_{ref} \tag{1}$$

where: $W(t_{j,i})$ – engine work measured between the engine start and the time $t_{j,i}$ [kW·h], W_{ref} – engine work in the WHTC test [kW·h].

When calculating the value of $t_{2,i}$, the following relations must be met:

$$W(t_{2,i} - \Delta t) - W(t_{l,i}) < W_{ref} \leq W(t_{2,i}) - W(t_{1,i}) \tag{2}$$

where: Δt depends on the sampling frequency (1 s or less).

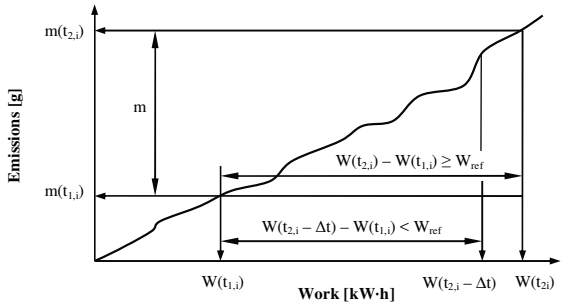

Fig. 1. Determining the measuring windows in the method based on the reference engine work [9]

In order for a measurement window to be considered valid, it needs to achieve an average power of more than 20% N_{emax}. Throughout the test, the percentage of valid measurement windows must be 50% or more. If this is not achieved the data evaluation must be repeated using lower power thresholds. This reduction is done in 1% increments, down to a level of 15% N_{emax}. Smaller values invalidate the test results. Specific emissions of pollutants are calculated for each measurement window using:

$$e_j = \frac{m}{W(t_{2,i}) - W(t_{1,i})} \tag{3}$$

where: e_j – specific emission j in i-th averaging window [mg/(kW·h)], m – mass of the exhaust component in i-th averaging window [mg], $W(t_{2,i}) - W(t_{1,i})$ – engine work in i-th averaging window [kW·h].

The vehicle operational conformity with regard to emissions CF (Conformity Factor) is calculated for all windows and for each considered component of exhaust gases according to the formula (4). To ensure the evaluation in any given averaging period was positive, the coefficients determined cannot be larger than 1.5. The vehicle itself is considered as meeting the legal requirements, provided

90% of the calculated CF values in the test fulfills this criterion.

$$CF = \frac{e_j}{L_j} \tag{4}$$

where: CF – conformity factor in the given averaging window [–], L_j – the permissible pollutant emission j in the WHTC test [mg/(kW·h)].

3. Research methodology in real operating conditions

3.1. Test vehicle

The study involved a city bus equipped with a series hybrid drive (Fig. 2). The drive system of the 18-meter vehicle used an internal combustion CI engine, with a displacement of 6.7 dm^3, a rated power of 209 kW at 2300 rpm, and a maximum torque reaching 1008 N·m at 1200 rpm. The vehicle is equipped with a traction motor with a power of 240 kW, and supercapacitors used to store the recovered braking energy, which is then used for acceleration. In addition, the bus uses electric drive solutions – in air compressor, radiator fan, power steering, door servos, as well as the air conditioning system. As a result, the power for the selected systems originates not directly from the internal combustion engine (mechanical drive), but from the electricity stored in the capacitors. The test vehicle meets the requirements of Euro V–EEV.

Fig. 2. Bus with a length of 18 m with a series hybrid drive system

3.2. Measuring equipment

Mobile device SEMTECH DS dedicated to the research in real traffic conditions was used in the measurements, it is classified in the PEMS group (Portable Emissions Measurement Systems). This device allows for making research measurements of spark and compression ignition engines that meet the Euro III and higher, and the principle of its operation is shown in Figure 3. The exhaust gases of the tested vehicle are directed to the exhaust mass flow probe, where the exhaust gas sample is taken. The taken gas sample is transported to a set of analyzers through heated conduits. The use of the heated conduit is to prevent condensation. The gases then go to the filter, where the particles are separated. Such a prepared sample is fed to the individual analyzers, each studying an individual exhaust gas component. The first FID analyzer (Flame Ionization Detector) is used to measure the hydrocarbons. In the next step the exhaust gas is cooled to a temperature of approx. 4°C and the sample volume is transported to the NDUV analyzer (Non-Dispersive Ultra Violet Detector) for the measurement of nitrogen oxides. Subsequently, the carbon monoxide and dioxide content is determined using NDIR analyzer (Non-Dispersive Infra-Red Detector). The last step is to electrochemically test the oxygen content in the exhaust gas. The analyzer can synchronize with the GPS positioning system, WLAN connection, and can communicate with the vehicle's OBD [11]. Using these road emission results it is possible to determine the vehicle fuel consumption using the carbon balance method.

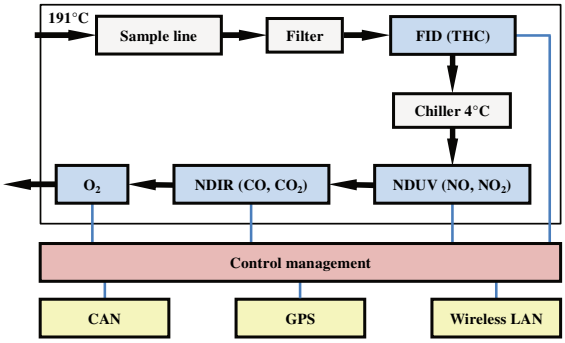

Fig. 3. SEMTECH DS operating schematic [11]

3.3. Test route

Measurements in real operating conditions required for the route selection to be representative of the tested vehicle type. The route is drawn on a map fragment in Figure 4.

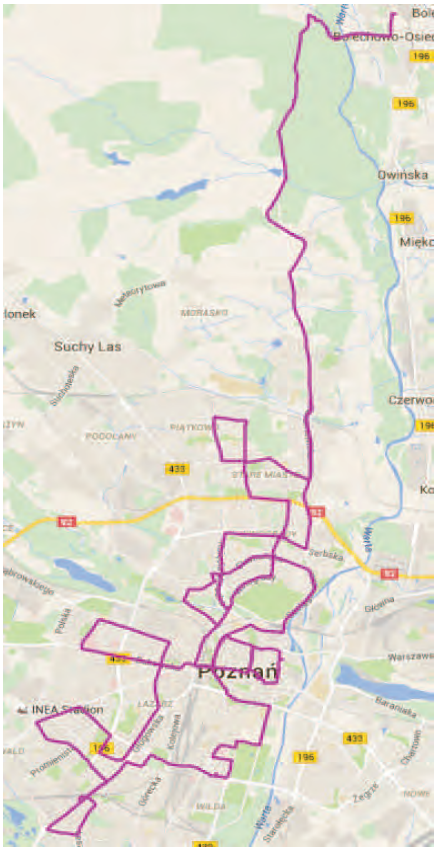

Fig. 4. The path of the test route used in the emissions test during real operating conditions (map created using GPS Visualizer [14])

The developed test route includes the sub-urban conditions, as well as the agglomeration center of the city, also using roads with speed limits above 50 km/h. The test route starting point was located in Bolechowo, it then led to the Poznan city center and ended in its northern part – the total distance of the route was 72.4 km. This considerable route length was driven by the need to obtain the minimum work value which had to be obtained during the test drive for the measurements to be valid according to [9] (at least five times the value obtained in the dynamic type approval engine test). The maximum relative elevation difference was 54 m, and the maximum slope did not exceed 5.2%. These factors had a direct impact on the values of the instantaneous and average velocity, the acceleration and the downtime of the vehicles tested.

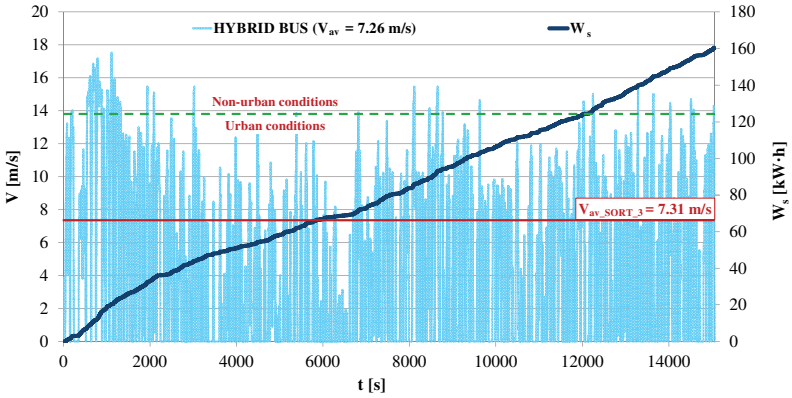

Fig. 5. The change in speed of a city bus on the test route with an added line representing the average speed of the SORT 3 road test

4. Research results

4.1. Analysis of the vehicle and engine operating conditions

For research purposes the specific emission of gaseous exhaust components: CO, THC and NO_x have been determined and compared to the EU Regulation 582/2011 [9], which refers to a group of heavy vehicles with Euro VI emission category. This allows checking whether the results obtained by this method correspond to the results obtained from all the data recorded during the test. It should be noted, however, that the test vehicle did not meet the Euro VI standard, and therefore, it was necessary to adopt some assumptions for the performed test procedure. The analysis was performed according to the previously described methods: using measurement windows defined using reference work measurements. The second method algorithm was not used, because the total weight of CO_2 produced by the combustion engines of the vehicles from laboratory tests was not known. Furthermore, the calculated results were referenced not only to the WHTC test, but also the ETC test. The presented discussion only refers to buses equipped with a hybrid drive, because the operating conditions of the combustion engine in such drives were the most reliable in terms of determining the measuring windows.

During the development of the test route it was assumed that it would consist of roads with an urban and non-urban character, ones with a sufficient possibility of obtaining an adequate vehicle speed (above 50 km/h, i.e. 13.89 m/s). However, the performed road tests have failed to meet the condition described in [9] regarding the shares of time driven in each type of road. To make the measurement compliant with the standard, it was necessary to achieve speed shares for the urban conditions of 70% and non-urban 30% with an accuracy of ±5%, whereas the performed test provided shares of 95.2% and 4.8% respectively. The resulting average speed value of the recorded drive (Fig. 5) was 7.26 m/s, and was most similar in this respect to the standardized non-urban test SORT 3 (7.31 m/s). This was primarily the result of local road conditions and congestion. Analyzing the current structure of roads in the Poznan agglomeration and its surrounding areas, it is difficult to unambiguously determine the route, which would meet the requirements of the existing standard. The use of highway section for the measurements would increase the share of non-urban speed, but this would conflict with the idea of reflecting the city buses operating conditions in everyday use.

Based on the operating parameters recorded by the CAN diagnostic system, it was calculated that the total work in the test cycle performed by the internal combustion engine was 160.4 kW·h. This value meets the requirements of the Regulation 582/2011, because it is close to nine times greater than in the WHTC test (legislation requires it to be at least five times greater). With regard to the dynamic ETC test for Euro V, taken into account for the needs of the research, the obtained results were more than five times greater. Characterization of the combustion engine and the cooperation with hybrid drive elements caused the resulting distribution of operating points had a specific pattern – increased density of measurement points can be seen for specific crankshaft speed values (Fig. 6). Maximum torque (1000 N·m) occurred in a limited speed range of 1600 and 1700 rpm, while for the interval of 2000 and 2100 rpm the highest torque value reached about 950 N·m.

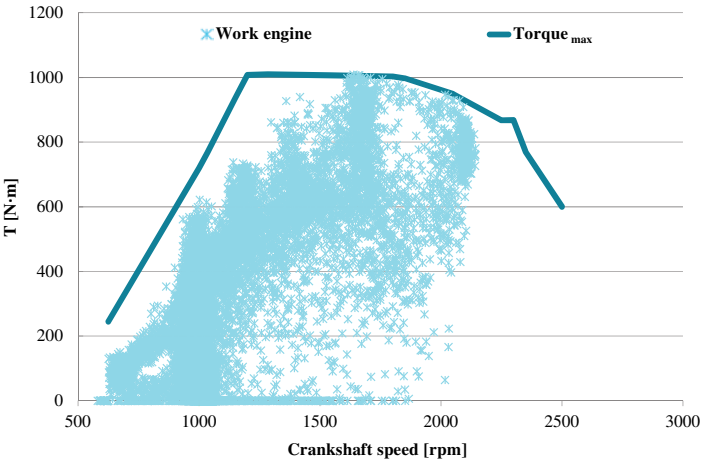

Fig. 6. Operating points of the combustion engine in the tested bus when the road measurements on the test route were made

4.2. Assessment of specific emissions in the measurement windows in the whole test route

Determination of parameters of the measuring windows in relation to the engine work shown in Figure 7. The determined values of specific emissions of gaseous exhaust components show that the values obtained in the context of EU Regulation 582/2011 are lower than during the entire measurement cycle (Fig. 8).

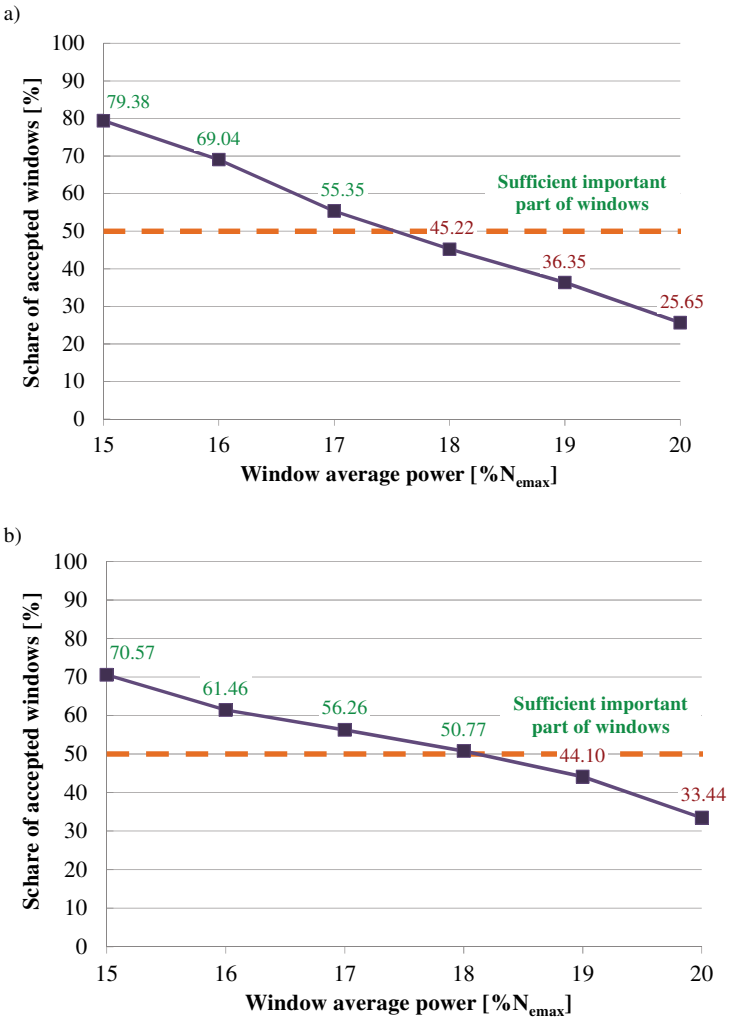

Fig. 7. The share of accepted measurement windows relative to the average power in the window [%N_{emax}] in tests: a) ETC, b) WHTC

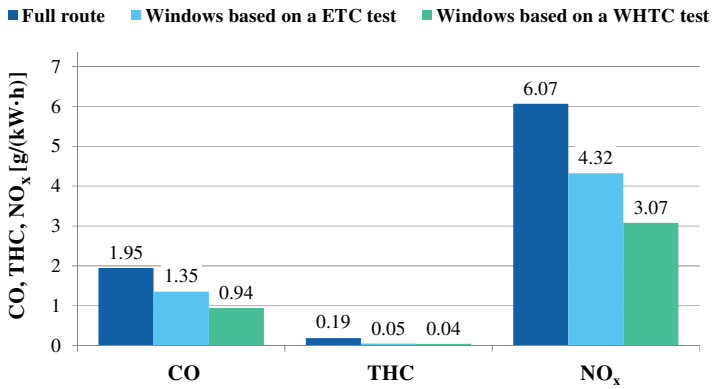

Fig. 8. Specific emission of CO, THC, NO_x and CO_2 obtained from the measurements made on the whole test route as well as in measuring windows (ETC, WHTC tests)

Due to the nature of urban traffic it is difficult to get a 50% share of the valid measurement windows, while maintaining the condition to get 20% of the N_{emax} value (Fig. 7). For this reason, it was necessary to decrease the value by 1% in accordance with the procedure described in [9]. In terms of ETC test the ability to assess the pollution generated for an average power measurement window of 17% N_{emax} (35.5 kW), whereas while referring to the WHTC the accepted windows had to be 18% of N_{emax} (37.6 kW). In the current dynamic type approval test there is less load on the engine and therefore the total work it generates is also smaller, which has a beneficial effect on the ability to determine the measurement intervals. It should also be noted that the engine used in the hybrid bus operated in the idle range to a lesser extent, and therefore the calculation of the average power of measurement windows it provides the best solution. In contrast, for a conventional drive, where the engine parameters are largely dependent on the conditions of vehicle movement it is more difficult, and sometimes impossible, due to the greater share of operating time in the area of smallest load and speed resulting from the characteristics of urban operation and visiting bus stops.

As required by [9] the research measurements were performed continuously and the complete collection of recorded data was used for the analysis. For the purposes of this research, the conformity factor was determined for the bus, while the calculations using the formula (4) were referred to the Euro V–EEV standard, as that was the standard used for the type approval of the tested vehicle. The averaged results for subsequent harmful exhaust gas components were: $CF_{CO} = 0.45$, $CF_{THC} = 0.4$ and $CF_{NOx} = 2.16$. For CO and THC over 90% of the obtained results had values of less than 1.5; while for NO_x only 32.4% of the windows measured met this condition. The internal combustion engine's operating parameters were favorable for use with the measuring windows because the engine was idle for a very limited amount of time. The lowest emission rates were achieved in the windows defined based on a WHTC test, which was the result of their shorter duration.

5. Conclusions

The operating conditions of city buses are specific due to the nature of the realized transport route, the line load and the number of stops on the route, and these parameters have a direct impact on the operating conditions of the drive systems used in the vehicles. Research pilot programs are currently conducted worldwide, and laws are introduced that codify the research of vehicle emissions in real operating conditions. The article presents a study of a hybrid city bus in light of the current legal rules on the operating compatibility – EU Regulation 582/2011. Due to the characteristics of the vehicles used for the research the following assumptions were made when analyzing the research results: the obtained values were compared to emission stand-

ards as well as the currently enforced Euro V–EEV tests. The results of this research indicate that the conformity factors CF obtained using the moving measuring windows method are different (the emission of pollutants is smaller) than for the whole test cycle. Moreover, based on the assumptions made for the measurements procedures, it can be stated that the assessment of the operational compatibility is often impossible to carry out for urban buses, due to the time requirements involving non-urban drive share.

Acknowledgements

The research was funded by the National Centre for Research and Development (Narodowe Centrum Badań i Rozwoju) – research project within the Applied Research Programme (contract No. PBS3/A6/25/2015).

Nomenclature

CF	conformity factor
e	emission of harmful exhaust components
EEV	enhanced environmentally friendly vehicle
ELR	European Load Response
ESC	European Stationary Cycle
ETC	European Transient Cycle
FID	flame ionization detector
GPS	global positioning system
HDV	heavy-duty vehicle
LAN	local area network
L_j	permissible emission of pollutants j in WHTC test
m	mass
NDIR	non-dispersive infrared
NDUV	non-dispersive ultraviolet
N_e	combustion engine power output
PEMS	portable emission measurement system
RDE	real driving emissions
SORT	standarised on-road tests
W	combustion engine work
WHSC	World Harmonized Stationary Cycle
WHTC	World Harmonized Transient Cycle

Bibliography

[1] ENGELJEHRINGER, K. Automotive emission testing and certification. past, present and future. *Conference materials: 2nd International Exhaust Emissions Symposium*, Bielsko-Biała 2011.

[2] FULPER, C. New Measurement techniques & procedures for measuring "real world" emissions with PEMS and PAMS. *2013 PEMS Conference & Workshop University of California*, Riverside 2013.

[3] Central Statistical Office of Poland: transport – wyniki działalności w 2014 roku. *Zakład Wydawnictw Statystycznych*, Warszawa 2015.

[4] MERKISZ, J., FUĆ, P., LIJEWSKI, P., ZIÓŁKOWSKI, A., RYMANIAK, Ł. The research of exhaust emissions and fuel consumption from HHD engines under actual traffic conditions. *Combustion Engines*. 2014, **158**(3), 56-63.

[5] MERKISZ, J., PIELECHA, J., NOWAK, M. Exhaust emissions from vehicles in real traffic conditions on the example of Poznan agglomeration. *Postępy Nauki i Techniki*. 2012, **15**.

[6] MERKISZ, J., RADZIMIRSKI, S. Nowe przepisy Unii Europejskiej o emisji zanieczyszczeń z pojazdów samochodowych. *Transport Samochodowy*. 2011, **2**, 41-70.

[7] NYLUND, N.O., ERKKILÄ, K., HARTIKKA, T. Fuel consumption and exhaust emissions of urban buses. *VTT Tiedotteita Research Notes 2373*, Helsinki 2007.

[8] PETROVIĆ, V.S., JANKOVIĆ, S.P., TOMIĆ, M.V., JOVANOVIĆ, Z.S., KNEŽEVIĆ, D.M. The possibilities for measurement and characterization of diesel engine fine particles – a review. *Thermal Science*. 2011, **4**(15), 915-938.

[9] Commission Regulation (EU) No 582/2011 of 25 May 2011 implementing and amending Regulation (EC) No 595/2009 of the European Parliament and of the Council with respect to emissions from heavy duty vehicles (Euro VI) and amending Annexes I and III to Directive 2007/46/EC of the European Parliament and of the Council.

[10] Regulation (EC) No 595/2009 of the European Parliament and of the Council of 18 June 2009 on type-approval of motor vehicles and engines with respect to emissions from heavy duty vehicles (Euro VI) and on access to vehicle repair and maintenance information and amending Regulation (EC) No 715/2007 and Directive 2007/46/EC and repealing Directives 80/1269/EEC, 2005/55/EC and 2005/78/EC.

[11] Sensors Inc. Emissions measurement solutions. SEMTECH® DS On Board In-Use Emissions Analyzer. Erkrath 2010.

[12] SHARPE, B., MUNCRIEF R. Literature review: real-world fuel consumption of heavy-duty vehicles in the United States, China, and the European Union. *International Council on Clean Transportation*, Washington DC 2015.

[13] The International Council on Clean Transportation (ICCT): Global transportation roadmap model (www.theicct.org/global-transportation-roadmap-model, access: 3.08.2015).

[14] http://gpsvisualizer.com (access: 29.10.2016).

Prof. Jerzy Merkisz, DSc., DEng. – Faculty of Machines and Transport at Poznan University of Technology.

e-mail: *Jerzy.Merkisz@put.poznan.pl*

Łukasz Rymaniak, DEng. – Faculty of Machines and Transport at Poznan University of Technology.

e-mail: *Lukasz.Rymaniak@put.poznan.pl*

Article citation info:
CIEŚLIK, W., PIELECHA, I. Analysis of the possibilities to achieve adiabatization process of combustion surrounded by inactive gases in RCM. *Combustion Engines*. 2017, **168**(1), 27-31. DOI: 10.19206/CE-2017-104

Wojciech CIEŚLIK
Ireneusz PIELECHA

CE-2017-104

Analysis of the possibilities to achieve adiabatization process of combustion surrounded by inactive gases in Rapid Compression Machine

In this work non-combustible gases impact on combustion processes studies is performed. Research was performed in a optically accessible rapid compression machine (RCM) under spark ignition engine conditions. The distribution of the swirl charge in the relation to adopted for analysis sequence of gas delivery to the chamber was varied with regard to the main injection. Authors investigate the influence of these sequence on the combustion and the ignition delay of the main injection and the overall combustion characteristics. The aim of this work is the experimental recognition of possibilities of creating combustible mixtures of light hydrocarbon fuels surrounded by non-combustible gases affecting the function of the inhibitor. Specifying the ability of preparation and combustion of mixtures in such systems enables the scientific analysis of adiabatization of the combustion process of fuel-air mixtures in the operating chambers. Theoretical analysis of the issues indicates possibility of obtaining such a stratification of the charge, that the inactive exhaust gases creating the outer ring surround the combustible mixture inside in such a way as to reduce the amount of heat exchanged between the working medium and the walls of the cylinder.

Key words: *exhaust* gas *recirculation, inactive gases, combustion fuels*

1. Introduction

The selected problem of assessing the emergence and spread of flame is critical for the search of new opportunities to reduce toxic emissions in spark ignition internal combustion engines [1, 2, 6]. The proposed system is associated with a reduction in the energy indicators, however, due to the nature of the combustion and the advantage in the form of lack of heat loss in exchange with the cylinder walls, investigation of the subject is justified. In order to improve the efficiency of combustion engines the proper preparation of the combustible mixture in the cylinder chamber is very important. Suitable conditioning of the combustion process may allow a fuel consumption reduction. One of the methods that can be used to achieve those demands is to use recirculated exhaust gas in order to introduce a controlled volume of non-combustible gases into the cylinder [6, 9].

In contrast to the classic solutions currently used in engines, the arrangement shown involves supplying the non-flammable gases in a strictly defined manner. Paper [10] describes the possibilities of stratification of fuel load with non-combustible gases (separation of air and exhaust gas) which influenced the Authors to choose the described combustion system concept. Different options for such a stratification is shown in Fig. 1. Stratification can be divided into longitudal (from the left), axial, and radial. Radial stratification (Fig. 1c) of the air and exhaust gases is the most suitable choice, from the point of view of the compression stroke, in terms of maintaining the stratification during piston movement. The interior region of the fuel-air mixture is encased in the exhaust gas region. Both of these regions are coaxial in the cylinder, and therefore the compression stroke should not disturb the load stratification (the separation of injected air and exhaust gas). In addition, if the angular momenta of the loads are be kept during the compression stroke then a mass of air and exhaust gas swirling in the same direction will result in a much longer lasting stratification of the mixtures at the end of the compression stroke.

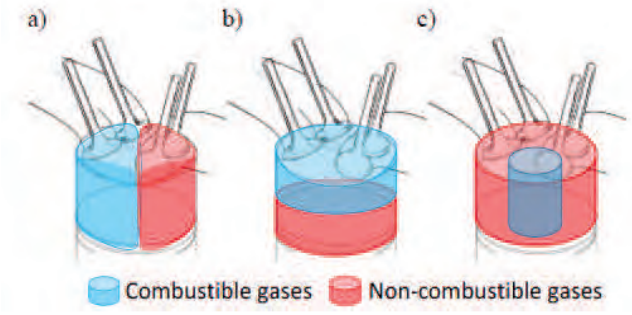

Fig. 1. Gases stratification modes: a) lateral, b) axial, c) radial [10]

The Authors performed simulations using the AVL Fire software preceding the experimental studies [5]. The results of these studies on different strategies to introduce gases into the combustion chamber were considered for possible initiation and control of the combustion process. In the analyzed cases, the aim was to achieve a strong wall guided flow, thus the calculations used the k-ξ-f model developed by Hanjalica et al. [7]. The summary of the article is a choice of strategy of exhaust gas supply into the engine cylinder.

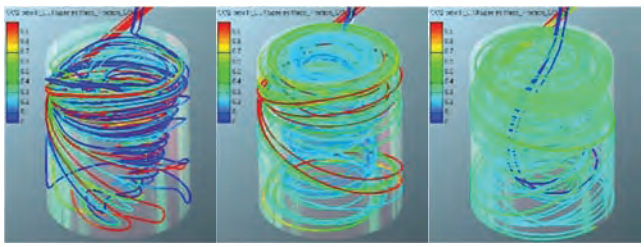

Fig. 2. Spatial distribution of the current lines during the sequence used in the study [5]

This article is a further research step taken by the Authors towards adapting the results of the simulation on a single cycle machine.

2. Research methodology

The test stand with a Rapid Compression Machine imitates the working conditions of the internal combustion engine with spark ignition, direct injection, and has been adapted to the needs of this research. Test stand parameters are shown in Table 1.

Table 1. Characteristic of RCM [8]

Quantity	Value
Stroke	89 mm
Bore	80 mm
Volume of combustion chamber	55 cm^3
Method of delivery non-combustible gases	solenoid valves
Compresion ratio	11
Type of combustion chamber	hemispherical chamber in the head + chamber in the piston
Optical access	from the bottom of the combustion chamber, quartz glass ϕ50 mm arranged in the piston

The adaptation of RCM, previously used by the Authors to study the dynamic [4] and optical processes, was to design an appropriate system implementing the injection of combustible and non-combustible gases into the combustion chamber (Fig. 3).

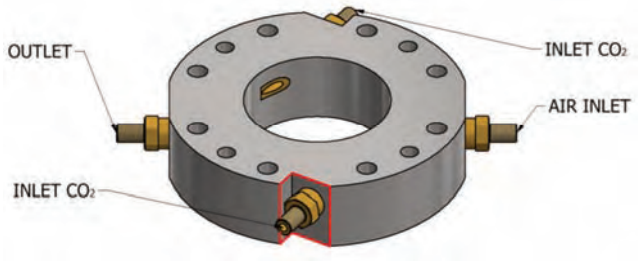

Fig. 3. Modified ring of RCM

The 3D model of the test stand with the elements necessary to carry out tests is shown in Fig. 4. In order to achieve a radial load stratification intake channels were added on the RCM periphery that fed non-combustible gases, controlled using solenoid valves, tangentially to the cylinder axis (13). Technical carbon dioxide was used as a non-combustible gas (9) with a purity of 99.95% by volume. The Rapid Compression Machine (8) operation is controlled using a sequencer (1, 2). An additional valve mounted in the head (12) is responsible for providing air in the spark plug area. In the first stage of the research presented in this article an outward-opening piezoelectric injector Siemens VDO (11) was located at the central point of the engine head. Spark plug (10) with the built in pressure sensor AVL GH13Z-31 is arranged in such a way that the formation and ignition of loads in RCM were carried out based on the spray guided combustion principle.

The elements used to perform tests on the present stand is:

- the high-speed camera (6) by LaVision, taking pictures with frequency of 5 kHz,
- piston displacement sensor – contactless potentiometric displacement sensor – Megatron LSR 150 ST R5k,
- the system for acquisition of measurements of fast-varying signals AVL IndiModul (4).

The obtained results: indicated (3) and optically measured (5) were processed using the following programs: AVL Concerto V4.5 and DaVis 7.2. The test results were compared with each other in relation to the recorded time.

3. Thermodynamic indexes of combustion process

A preliminary analysis of the impact of non-combustible gas injection into the combustion chamber is made on the basis of the indicated pressure registered in the combustion chamber. The system response has been shown in the form of the combustion process delay and a reduced increase of the maximum combustion pressure (Fig. 5).

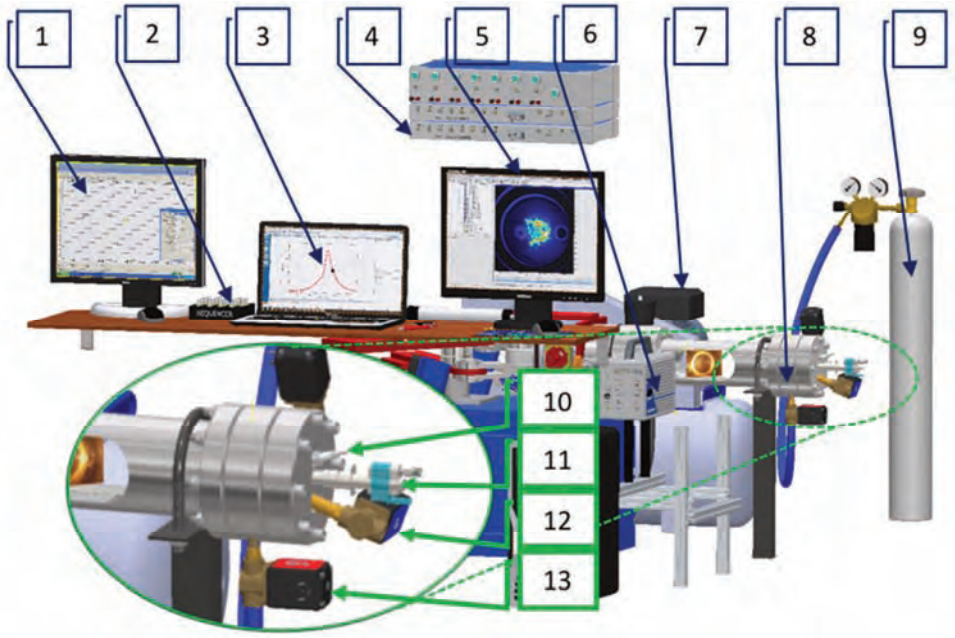

Fig. 4. Three-dimensional view of the measurement stand of Rapid Compression Machine

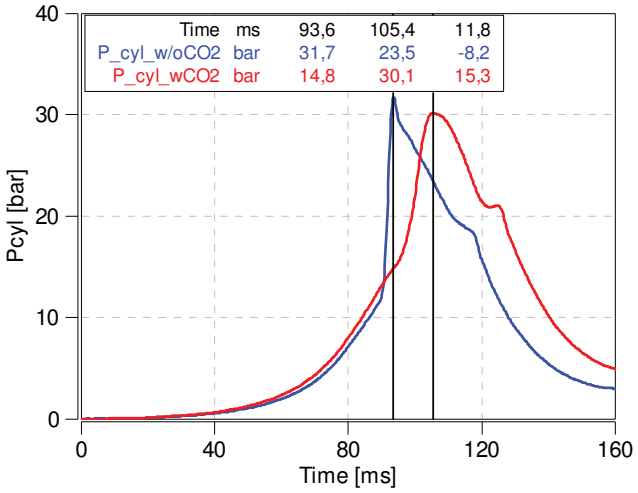

Fig. 5. The results of the measurements of the combustion pressure

In the arrangement without providing a non-combustible gas into the chamber, which serves as reference in studies, the maximum combustion pressure of 31.5 bar was acquired occurring within 93.6 ms after the piston movement began. Providing non-flammable gases into the combustion chamber in a selected sequence resulted in a delay of pressure increase of 11.8 ms and a reduction in the maximum pressure. Because of the previously cited articles, which demonstrated both the repeatability of RCM operation in the analysis of indicated parameters [4] and optical processes [3], the analysis covers two representative runs in which one is a reference run, and the second shows the effect of the proposed modifications. Figure 6 shows the heat release rate.

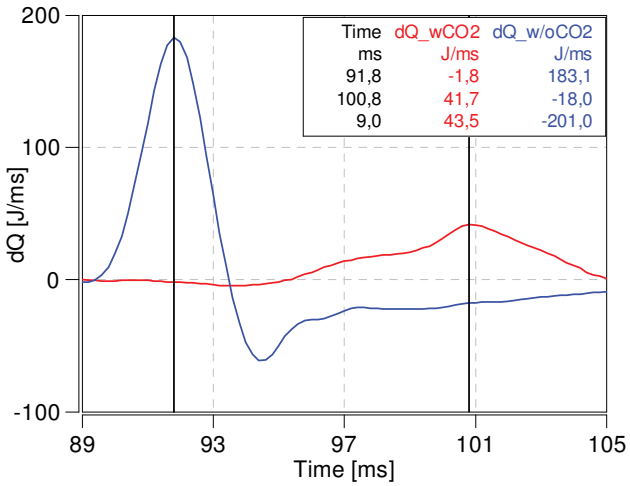

Fig. 6. Heat release rate

In this context, the fuel injection and combustion without the presence of non-combustible gases results in a large heat release rate with a maximum value of 183 J/ms. Using the load with recirculated exhaust gases strategy causes the combustion to be delayed significantly resulting in a far lower rate of heat release. Its maximum value is 41 J/ms, which is only 22% of the reference value.

4. Optical analysis of the combustion process

Optical test consisted of visual recording the combustion process in the RCM with a frequency of 5 kHz. In order to specify the area the flame takes up during combustion in a given system the recorded data was subject to digital processing consisting of: (1) defining the viewing window area mask and (2) counting the pixels whose radiation intensity was higher than the background noise. Then, by registering the triggered discharge on the spark plug, it was possible to determine a common time baseline for the indicator and optical research results (synchronization). Figure 7 shows the areas occupied by the flame in subsequent measurement attempts. Three functions relate to the classic combustion system without a supply of non-combustible gases and are marked in the article with the color blue, while the measurements using the supply system with non-combustible gases have been marked in red. The results of the calculated areas occupied by the flame have been again juxtaposed with pressure changes in the chamber. The results thus illustrate a direct correlation between the recorded test results of indicated pressure and the optical two-dimensional (flat) recording of the flame.

The reference measurements recorded a sharp flame size increase in the chamber, covering on average almost 100% of the viewing window located in the RCM piston. In this configuration, the flame is maintained for a long time in the whole viewing window, which indicates the long post-combustion process.

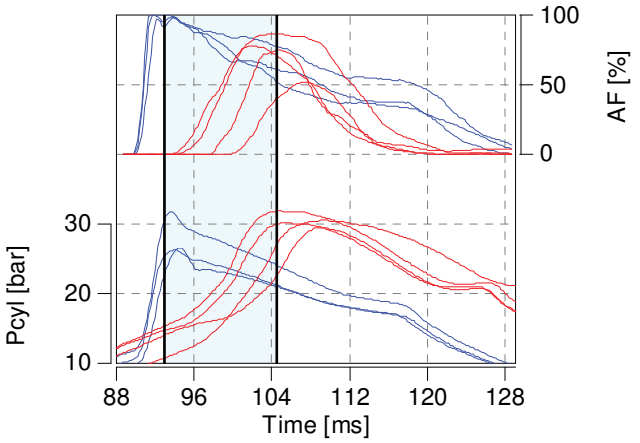

Fig. 7. The flame area in the combustion chamber with marked average times (indicated by black vertical bars) of the recorded maximum values

The supply of non-combustible gases into the combustion chamber resulted in the suppression of growth of both the intensity of the flame and its accumulation in the central part of the cylinder. In this case, the maximum area occupied by the flame reached 50 to 87% of the viewing window size. This indicates that the research concept has been reached and the flame was isolated from the cylinder walls.

Due to the extensive amount of data obtained in the course of this research further presentation of the results of optical tests in this article is limited to representative individual measuring points. Figure 8 displays the sequences of images of the flame development from the start of the ignition. Since the process was filmed with a frequency of 5

kHz, the time interval between images was 0.2 ms. In order to present the main features of the whole combustion process the chosen time interval between images shown in Fig. 8 is 2 ms. Comparison of the image timing and indicated test values made it possible to determine the flame image (in pictures) corresponding to the value Pmax for a given measurement point. These pictures are marked with circles.

The analysis of reference measurement images (left) reveals a sharp increase in pressure without the load motion and post-combustion flame around the cylinder walls.

The sequence of images of the combustion measurement in the vicinity of non-combustible gases (Fig. 8; right side) shows the development of the flame in the center of the cylinder. In addition, the flame is suppressed, and in contrast to the reference measurement, no long post-combustion near the cylinder walls was observed. Due to the design of the engine head, where the spark plug is located on the side, a clear swirling of the flames from the ignition point was observed, which corresponded to the turbulence created by the injection of carbon dioxide.

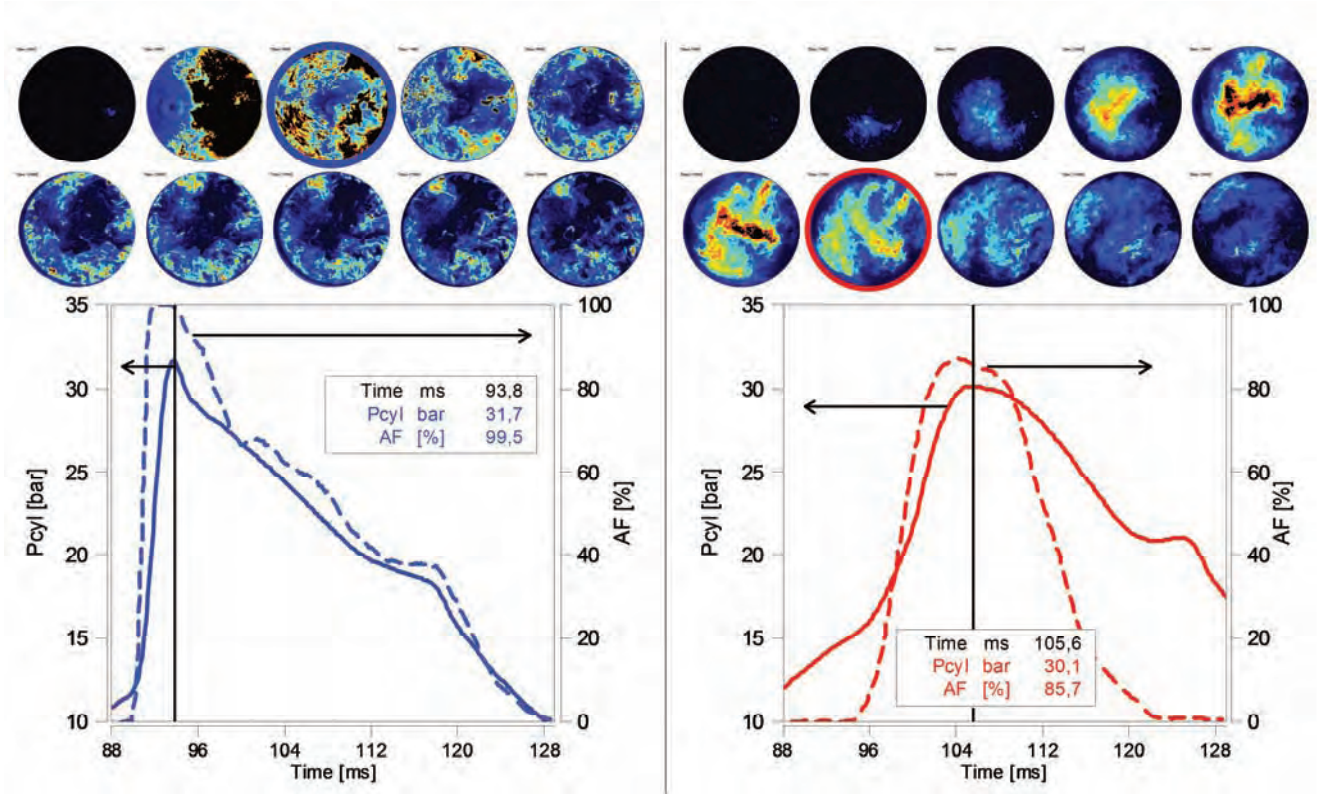

Fig. 8. A comparison of combustion: on the left – a reference measurement, on the right – measurement along with the injection of carbon dioxide

5. Summary

The assumed achievement of radial stratification, allowing the separation of the load in the combustion chamber in the spark ignition engine with direct petrol injection has been completed. The test results indicate that the flame access to the cylinder walls was limited. The resulting reduction in flame area ranged from 13% to 50% (for the four repeated tests of the combustion process). The proposed system is essential for carrying out further analyzes of the injection sequence effect, and to further develop the concept. In future projects, the Authors expect to use an engine head with a centrally positioned spark plug. This configuration will allow for better flame accumulation inside the cylinder volume.

Acknowledgements

The study presented in this article was performed within the statutory research.

Nomenclature

AF area of flame
EGR exhaust gas recirculation
CO_2 carbon dioxide
dQ heat release rate
Pcyl cylinder pressure
Pmax maximum cylinder pressure
RCM rapid compression machine

Bibliography

[1] ALGER, T. Gasoline Engine Technology for High Efficiency, *Southwest Research Institute*, San Antonio, 2014.

[2] ASAD, U., ZHENG, M. Efficacy of EGR and Boost in Single-Injection Enabled Low Temperature Combustion. *SAE International Journal of Engines*. 2009, **2**(1), 1085-1097.

[3] BOROWSKI, P., CIESLIK, W., PIELECHA, I., WISŁOCKI, K. Evaluation of the repeatability of combustion process in rapid compression machine using optical research. *XXII International Symposium on Combustion Processes*. 22-25.9.2015, Poland.

[4] CIEŚLIK, W., PIELECHA, I., BOROWSKI, P., WISŁOCKI, K. Evaluation of repeatability of rapid compression machine under selected conditions. *ECM 7th – European Combustion Meeting*.3-4.4.2015, Budapest.

[5] CIEŚLIK, W., PIELECHA, I., KAPUSTA, Ł. The concept of combustion system with use of recirculated exhaust gas in the spark ignition engine. *Combustion Engines*. 2015, **162**(3), 257-263.

[6] DINGELSTADT, R., EWERT, S., WERZ, M., TREMBLE, P. Potential of exhaust gas recirculation in gasoline engines. *MTZ*. 2014, **75**(9).

[7] HANJALIĆ, K., POPOVAC, M., HADŽIABDIĆ, M. A robust near-wall elliptic-relaxation eddy-viscosity turbulence model for CFD. *International Journal of Heat and Fluid Flow*. 2004, **25**(6) 1047-1051.

[8] PIELECHA, I. Modeling of gasoline fuel spray penetration in SIDI engines. *International Journal of Automotive Technology*. 2014, **15**, 47-55.

[9] TUTAK, W. Possibility to reduce knock combustion by EGR in the SI test engine. *Journal of KONES Powertrain and Transport*. 2011, **18**(3).

[10] WEI, H., ZHU, T., SHU, G., TAN, L., WANG, Y. Gasoline engine exhaust gas recirculation – a review. *Applied Energy*. 2012, **99**, 534-544.

Wojciech Cieślik, MEng. – Faculty of Machines and Transport in Poznan University of Technology.

e-mail: *Wojciech.Cieslik@put.poznan.pl*

Ireneusz Pielecha, DSc., DEng. – Faculty of Machines and Transport of Poznan University of Technology.

e-mail: *Ireneusz.Pielecha@put.poznan.pl*

Article citation info:
KORCZEWSKI, Z., RUDNICKI, J., ZADRĄG, R. Laboratory station for research of the innovative dry method of exhaust gas desulfurization for an engine powered with residual fuel. *Combustion Engines*. 2017, **168**(1), 32-37. DOI: 10.19206/CE-2017-105

Zbigniew KORCZEWSKI
Jacek RUDNICKI
Ryszard ZADRĄG

CE-2017-105

Laboratory station for research of the innovative dry method of exhaust gas desulfurization for an engine powered with residual fuel

Development of technology for exhaust gas desulfurization in marine engines using the dry method is, nowadays, a priority due to the calendar of introducing restrictions by the Directive of the European Parliament and of the Council 2012/33/EU of 21 November 2012. According to this directive, starting from 1 January 2015, inside the SECA (Sulphur Emission Control Area) the maximum sulfur content of marine fuels used on territorial seas is 0.1% per weight unit. But at the same time the directive allows for the use of exhaust gas desulfurization plant operating in a closed system. The ship equipped with the system will be able to use fuels with a high sulfur content, which will then be removed from the exhaust gas through an applied adsorber, and the reacted adsorbent is received by specialized services stationed in harbors. The International Maritime Organization has set a limit value of the emissions of sulfur oxides in exhaust gases of marine engines at 6 g/kWh (International Convention for the Prevention of Sea Pollution from Ships MARPOL 73/78 Annex VI, Regulation 14).

Contemporary methods of exhaust gas desulfurization in marine engines are all expensive methods (4-5 million euro). This is, among other reasons, due to the limited market audience, but primarily due to the monop-olized position of manufacturers offering fabrication and assembly of this type of marine ship installations. Proposed as part of a research project financed by the Regional Fund for Environmental Protection and Maritime Economy in Gdansk, the dry method (adsorption) reducing SO_x emissions in exhaust gases of marine engines, is an alternative, and a definitely cheaper and therefore competitive solution, compared to the wet methods (absorption), which are currently the most widely used in marine scrubber installations. Importantly, as confirmed by the results of the study, the proposed dry method, in addition to the effective reduction of sulfur oxides, also reduces emissions of nitrogen oxides and carbon monoxide.

The paper presents the configuration and measurement capabilities of the test station built under the project, as well as the representative results of the investigations so far. During the exhaust gas desulfurization test a sodium adsorbent (sodium bicarbonate) and its modifications were used in the process of mechanical, chemical, and thermal activation. Two physicochemical processes were studied during the development of the method:

- *of adsorbent's reaction on the chemical emission of the exhaust gas – the effectiveness of SO_x and NO_x compound removal, with various structural solutions in the process reactor,*
- *the impact of the adsorber on the emission source of sulfur oxides, that is, on the compression-ignition engine.*

Therefore, one of the priorities of the project, with a utilitarian significance, was to determine the impact of the inclusion of the desulfurization installation in the exhaust gas system on the energy ratios of the engine.

Key words: *compression-ignition engine, desulfurization of exhaust gas, dry method*

1. Introduction

Maritime transport is an essential element of the functioning and development of many sectors of economy in the world. It plays a major role in international trade and the transport of people. Ships transport more than 2/3 of the goods traded in the world. However, there exists the problem of air pollution caused by vessels that burn shipping fuel. High sulfur emissions originating from the combustion of heavy oil on watercraft contributes heavily to air pollution at sea and areas of port cities. This causes environmental damage in the form of acid rain and affects human health. As a result, the European Union is trying to fight the above issue by introducing new rules on the allowable limits for sulfur content in the fuel. It decrees the combustion of fuels with very low sulfur content, or alternatively, the use of exhaust gas desulfurization installations that meets the established requirements. EU, to meet this problem, issued a Directive of the European Parliament and of the Council 2012/33/EU of 21 November 2012, on sulfur content of fuels, which is the consequence of the International Convention for the Prevention of Pollution from Ships MARPOL 73/78 (Annex VI), signed and ratified by its Member States, where it was established that [7, 8]:

1. Inside the territory of SECA (Sulphur Emission Control Area), the maximum content of sulfur in shipping fuels used on the territorial seas is, as of January 1st, 2015, 0.1% per weight unit,
2. Outside of SECA territory, the maximum content of sulfur in shipping fuels is, as of January 1st, 2020, 0.5% per weight unit.

Of course, the cited directive is an attempt to reduce the environmental damage in the form of acid rains and the impact on human health, resulted from the high emission of sulfur coming from the combustion of residual fuel on vessels, which is largely responsible for the air pollution at sea and areas of port cities. The effect of the directive seems to be incommensurate, as it does not drastically influence the countries situated around the North Sea as it does the ones around the Baltic Sea. Baltic Sea, according to the above legislation, is treated as an inland sea, which is a special SECA area. At the current price difference between fuels with low sulfurization and the heavy fuel oil, which is about 70-80% in favor of the heavy fuel, the usage of fuel with low sulfurization does not have an economic justification and it can conceivably lead to changing the sea trade routes to avoid the SECA territories [8].

Of course there exist alternative solutions to this problem. In accordance with the directive 2012/33/EU, there is a possibility of using a exhaust gas desulfurization installation in a closed system. The ship equipped with such an installation will be able to use fuels with a high sulfur content, which will then be removed from the exhaust by the applied absorber, and the generated reacting sorbent will be collected by specialized services located in harbors. Currently on the market there is equipment supplied with scrubbing installations, which absorb the pollution from a gas mixture. However, the cost of such an installation is very high, ranging between 4-5 million Euro. In addition, the use of scrubbers is also associated with significant operating costs connected to frequent exchanges of the sulfur absorbent agent, as well as, while using the wet method, the machinery needs to be equipped with complex water installations, which not only have a significant energy requirements, but also considerably reduce the cargo holding capacity of the ship, limiting its viability to large vessels only.

An alternative to the wet methods (absorption) of exhaust gas desulfurization are the dry methods (adsorption), which have found common use in power industry, in the combustion of solid fuels, and they are based on the chemical binding of SO2 in a system: polluted gas – solid (sorbent). In the dry method, the adsorbent is directly injected into the flue or the combustion chamber, where it reacts with the acidic byproducts of the process. In the case of marine uses, the dry desulfurization technology is being developed in a few European institutes, among which the most influential results have been achieved by the 2006 TEFLES project (Technologies and Scenarios for Low Emissions Shipping) [7]. As per the analysis of available sources, the leading role in this study, completed with pilot implementations on board, is held by COUPLE SYSTEMS GmbH, which is a company that developed the original design of the installation marked DryEGCS (Dry Exhaust Gas Cleaning System) and the only one currently offering a product ready for installation on board of a ship [6]. In the presented solution, the desulfurization process is based on the chemisorption phenomenon, in which the adsorbent is a calcium hydroxide based substance, which, in a reaction with SO2, creates calcium sulfate (gypsum) and water. The used sorbent requires relatively high temperatures, which have a significant impact on the increase of sorptive capacity of calcium hydroxide.

In the solution proposed by the authors of the paper, sodium bicarbonate serves as the sorbent. The main advantage of using a sodium sorbent containing sodium bicarbonate is its exceptional sorption capacity to SO2 and other acidic pollutants of HCl and HF types, present in the gaseous products of fuel combustion. It also shows some capacity for removing nitric oxides, depending on the applied chemical modifiers. Sodium sorbents are characterized by their high reactivity in considerably lower temperatures (140 – 300°C) compared to other sorbents, e.g.: calcium (800°C). It has a substantial impact on the ability to use sodium sorbents for the reduction of gas pollution in installations with a direct injection of sorbent into the exhaust gas stream of a low temperature. A very high reduction efficiency of gaseous pollutants by the sodium sorbent results in using a smaller amount of the adsorbent agent and of after-reaction waste, thus reducing costs for both the transport and processing of sorption products [5].

2. The test station

An alternative method for limiting the sulfur emission into the atmosphere, possible to use on marine ships, is the process of chemisorption using an agent binding this type of pollutants. The process of dry cleaning the gas exhaust emitted by the marine ship engines proposed by the authors does not require an advanced installation, as it does not provide for the circulation of streams, commonly used in the wet methods. Suggested sorbent, in form of a synthetically made sodium bicarbonate ($NaHCO_3$) has the ability to bind acidic pollutants present in the gaseous products of fuel combustion into salts which have an industrial application. During a thermal dissolution, carbon dioxide and water are released from it, as shown in the reaction:

$$NaHCO_3 \rightarrow Na_2CO_3 + H_2O\uparrow + CO_2\uparrow \quad (1)$$

Crude, as well as pure sodium bicarbonate are produced by Soda Polska Ciech company, in Inowrocław. Sodium bicarbonate (trade name), also called the sodium hydrogen carbonate or, colloquially, bicarb, is a white, dry, fine crystalline powder. The molecular weight of this product is 84.02 and its density at 20°C ranges from 2.16 to 2.22 g/cm^3.

Increasing the activation of sodium bicarbonate is done by reducing the amount of water in its mass, which is achieved by drying in the temperature range of 50-60°C. Within these temperatures, bicarb doesn't undergo a dissolution into sodium carbonate and water, while the reduction of mass is similar and related to an insignificant loss of ammonium compounds. Another way of activating sodium bicarbonate is the mechanical activation where the diameter of the powder grains is reduced, making its reactivity higher. Currently used is the grinding of sodium bicarbonate in various types of mills: impact, antijet or electromagnetic. Grinding the grains of the adsorbent results also in changes of the specific surface structure. Depending on the employed method of activation, the specific surface increases as much as tenfold in relation to the base value [5].

The created porous structure of the adsorbent grains has a large specific surface, located inside of the microstructures of the dissolved sodium carboxide, which is the result of reducing the molar volume of sodium bicarbonate. The creation of a large specific surface of an adsorbent contributes to increasing its sorption capacity and as such, the adsorption of a larger amount of SO_2 from the waste gases.

Thus, while analyzing the sorption capacity of sodium bicarbonate it should be noted that it depends on the following:

- degree of dryness (water content),
- grammature of particles,
- specific surface of particles.

In addition to these factors, the contact time of the adsorbent with hot exhaust gases, that is the residence time of particles of sodium bicarbonate in the reactor chamber, seems equally as important. This time can be regulated depending on the method of feeding the adsorbent into the

reactor chamber, by a right selection of the chamber height or through a choice of speed with which the exhaust flows through the reactor chamber.

While designing the test station it was decided that two methods of feeding the adsorbent will be used (Fig. 1):

- through atomization inside the chamber and its gravitational fall,
- through the application of a fluidized bed.

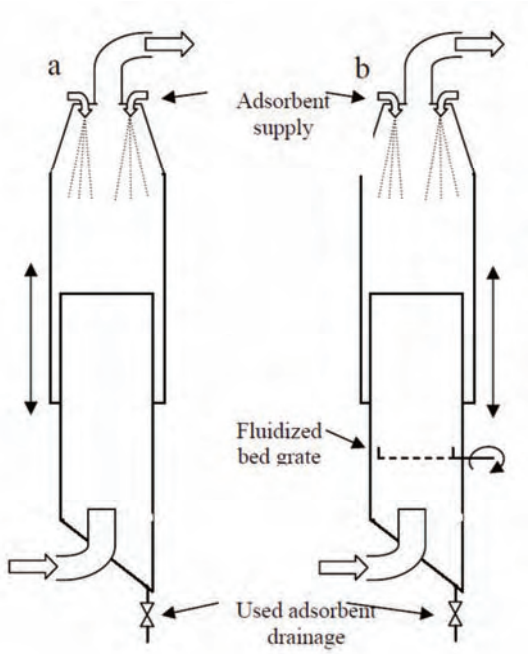

Fig. 1. The concept of the reactor structure: a) counter-current reactor, b) fluidized bed reactor

In the first case, while using the counter-current reactor, the time of the adsorbent's contact with the hot exhaust gases is essential for the optimal selection of the amount of the adsorbent being fed into the chamber. At the gravitational fall of the bicarbonate particles, except for their grammage (the diameter of the sodium bicarbonate particles ranges between 1 to 450 um, while the average diameter of these particles is around 140-150 um), an aerodynamic sedimentation will take place. This event will depend mainly on the specific surface of the adsorbent particles.

It can be assumed with a high probability that the nature of the fall, for both the gravitational and aerodynamic sedimentation, will proceed according to the normal schedule. The volatility of the aforementioned parameters of the adsorbent, that is, its grammage and the specific surface of its particles, is rather limited and as such the duration of the adsorbent's contact with the exhaust gases was decided to be regulated by lengthening of the path of its fall. For this reason, a double reactor blanket was suggested, which would allow a fluid increase of its length (height), and as such, lengthen the path and time of the fall of the adsorbent [1].

In case of using a reactor with a fluidized bed, it is essential to make the right selection of exhaust flow through the reactor, so that the conditions of a fluidized balance of adsorbent suspension would occur inside of the exhaust flow. Considering the limited capabilities for regulating the intensity of exhaust of the test engine, it was decided that a fan will be placed behind the reactor. Such placement is a result of the restrictions placed by the MARPOL convention and the ISO-8178 regulation [3, 4].

In accordance with these documents, it is prohibited to dilute fuel before the exhaust extraction point used for analyses.

For a correct conduct of a laboratory station, it is necessary to measure the following parameters:

- exhaust pressure before the reactor,
- exhaust pressure behind the reactor,
- exhaust pressure behind the filter,
- exhaust temperature inside of the exhaust manifold (behind the engine),
- exhaust temperature behind the exhaust heater,
- exhaust temperature behind the reactor,
- the concentration of toxic compounds inside of the exhaust manifold (behind the engine),
- the concentration of toxic compounds behind the reactor.

In addition to the above mentioned parameters, also realized is a measurement of the flow intensity of exhaust gas by measuring the volumetric air flow rate through the engine and measuring the volumetric fuel consumption.

Below is presented the measuring configuration of the laboratory station, which allows for the determining of emission values of basic exhaust components, in agreement with the ISO-8178 regulation, based on the E-3 and D-2 tests, which are intended for marine ship engines used according to the full-load and propeller characteristics [8]. It is also possible to conduct research in the broad scope of input parameter changes, both during set work conditions and during transient states. The overview of the station is shown in Fig. 2.

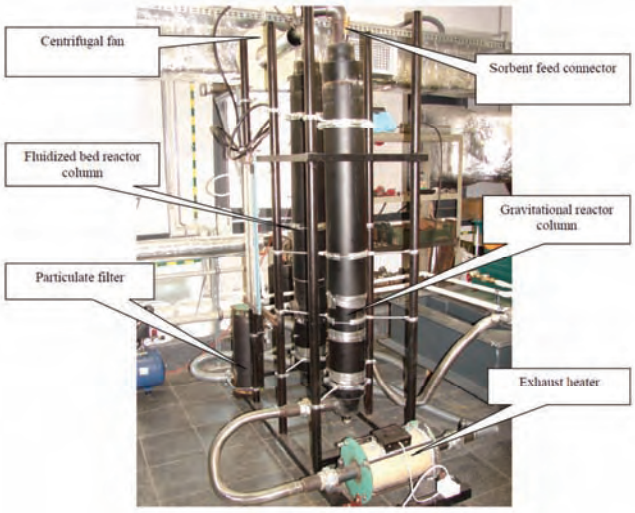

Fig. 2. An overview of the exhaust gas desulfurization station using the dry method

Considering the low power of the test engine powering the reactor (used was a single cylinder Farymann Diesel type D, with power of 6.9 kW), and therefore the small stream of exhaust and a high, compared to the employed engine, reactor volume, it was necessary to use an exhaust heater which would negate any heat loss. At first, the heat

loss was significant and it lead to decreasing the dew point which, in turn, resulted in the hydration phenomenon, thus reducing the sulfur oxide concentration before it reached the reactor chamber and which intensified the low temperature corrosion processes. Of course, considering the goal of the research, it was essential to keep a relatively high concentration of SO_2. Using the exhaust heater allowed the exhaust to stay at a temperature oscillating around 120°C. Aside from the heater, it was decided that thermal isolation made out of mineral wool would be used, which resulted in raising the exhaust temperature by another 20°C.

3. Initial research using the dry method of exhaust desulfurization

As mentioned before, the reactor station of the dry method of desulfurization cooperated with a single cylinder diesel engine Farymann type D, which was powered by fuel with an increased sulfur content.

The measurement of toxic compound concentration in the exhaust was conducted using an electrochemical exhaust analyzer KIGAZ 300 PRO made by Kimo company. In Figure 3, the placement of the sampling probe of the exhaust analyzer in the head of the reactor is shown [3, 4].

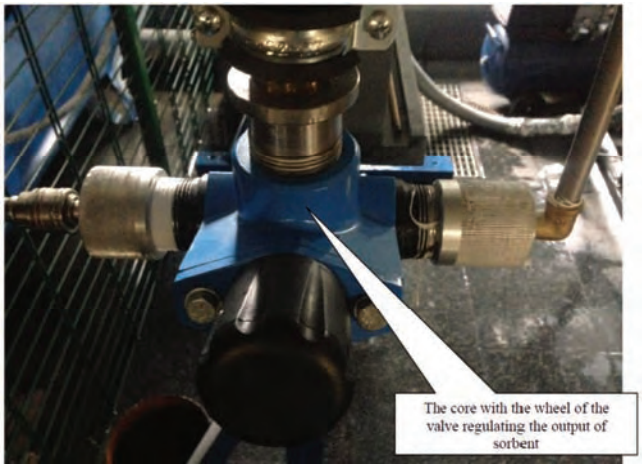

Fig. 3. A more detailed view of the head of the gravitational reactor

Research was conducted for two methods of feeding sorbent into the reactor:

- using a fixed bed with a limited fluidization phenomenon,
- through atomizing the sorbent inside of the reactor.

With the former method of feeding the reactor, a layer of around 10 mm of sorbent was laid on a grate installed inside of the reactor, which evenly covered the entire cross-section of the flue. This placement of sorbent forced a perpendicular flow of the exhaust stream through its layer. Considering the low speed of exhaust gases, the bed laid on the grate showed the qualities of a moving bed, characteristic of the initial stages of fluidized bed creation, when its surface undergoes loosening due to the passage of exhaust through it. After starting up the engine it was possible to note a brief, sudden increase in SO_2 concentration, after which the sulfur oxide concentration held for around 10 seconds before decreasing again and stabilizing at around 40 ppm. Increasing the thickness of the sorbent layer to around 20 mm resulted in a similar course of events, i.e. after about 10 seconds from the concentration extreme caused by starting up the engine, a decrease took place equal to the error value of the measurement noise of the analyzer. This value is maintained for around two hours, after which it gradually rose along with the decrease of sorptive abilities of the sodium bicarbonate. Figure 4 shows the initial effect of the reducing action of the sorbent for a bed thickness of 10 mm (bed 1) and for a bed thickness of 20mm (bed 2).

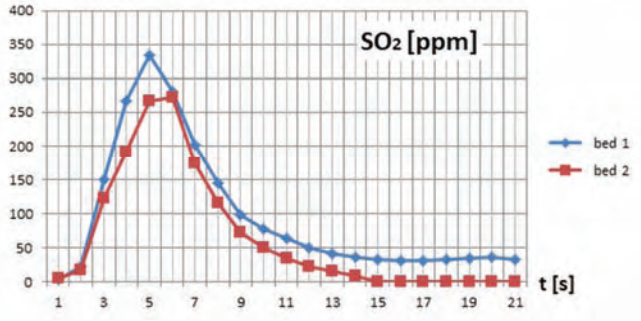

Fig. 4. Changes of sulfur dioxide concentrations while supplying the sorbent of a fixed bed

The latter method of feeding the sorbent was its atomization inside of the reactor chamber. In order to define the effectiveness of exhaust desulfurization using the dry method, an experiment was held for three settings of the valve controlling the output of the sorbent. Thus, the output of the sorbent was regulated by throttling the control valve at a set pressure (around 0.9 bar) of air supply. The degree of throttling was unambiguously defined through the measurement of the core height along with the wheel above the valve frame. Three settings were assumed, i.e.: ¾, ½ and ¼ of a core valve stroke. Additionally, in order to define the degree of exhaust stream dilution by the air supply and thus its impact on concentration values of particular toxic compounds, including of course the impact on sulfur oxides, the reactor column was fed only with air supply for the ¾ stroke setting. The view of the valve is shown in Fig. 5.

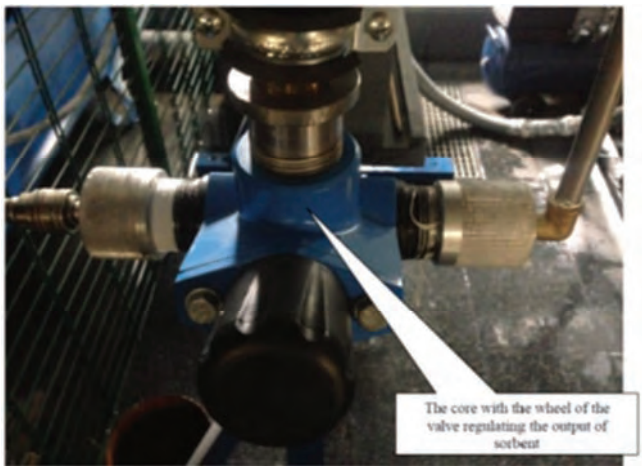

Fig. 5. View of the valve regulating the output of sorbent

The dilution degree is an essential value for at least two reasons. Firstly, as mentioned before, ISO-8178 regulation

and the MARPOL convention prohibit the dilution of exhaust has before the point of their extraction for analysis. Secondly, the dilution of exhaust with air supply can yield apparent indications, which lead to faulty conclusions. Analysis results are presented in Fig. 6.

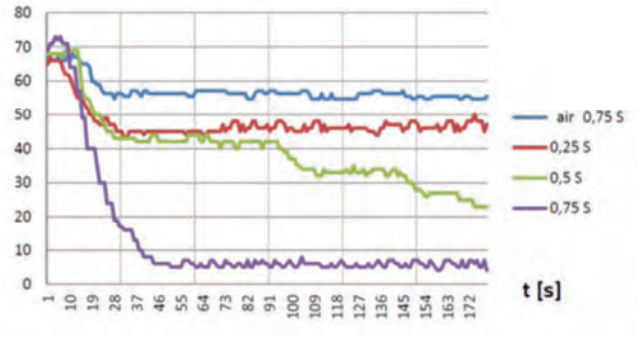

Fig. 6. Changes in concentrations of sulfur oxide with sorbent supply, where: 0.025S; 0.5S; 0.75S – degree of opening of the control valve; air 0.75S – air supply to the reactor at an opening of 0.75 valve stroke

In the case of sulfur oxide SO_2, the impact of exhaust stream dilution is not as sizeable, however, it is still vital and cannot be ignored (Fig. 6). After around 15 seconds of feeding air supply into the reactor column, a significant decrease in SO_2 concentration can be noticed.

The intensity of lowering the concentration, in comparison to the initial stage of the research is paradoxically higher (in an analogous example, concentration stabilization time was longer and amounted to around 15 seconds). After about another 10 seconds, concentration of SO_2 stabilizes and maintains level. At a valve throttle of ¾ of core stroke, lowering the concentration equals about 8–10 ppm, which comes to, respectively, 12–15% of the base value. The reason for it may be the decreased volume of the reactor column (about 60%), and at the same time the increased input of air supply into the exhaust stream going through the reactor.

It will also have an impact on the correct distribution of sorbent stream inside of the reactor column, and as such, its economic utilization. Currently the dose of sorbent is too high, which results in accumulation of unworked sorbent on the reactor walls, which in consequence changes the resistance of flow of the exhaust through the reactor, increasing the heat load of the engine. The influence of variable quantities of supplied sorbent on its reduction capacity are the most visible in case of SO_2. It seems to be obvious as sodium bicarbonate serves mainly as sulfur oxide reduction agent.

While analyzing Fig. 6, it can be noted that along with the increase of sorbent stream (the measurement is the degree of the throttle on the control valve), its sorptive capacity also increases.

As such, in the case of a valve set to ¼ of its core stroke, the reduction capacity is, respectively, 35%, and 68% for ½ core stroke. In the case of a valve set to ¾ core stroke, the SO_2 concentration inside of the reactor decreases to the level of the measurement noise error, i.e., the value of around 6–7 ppm. It constitutes almost 98% of the base value.

The changes of concentration of nitric oxide NO_x (Fig. 7), with the reactor getting air supply are similar (decrease in NO_x concentration by 15%). It may signify that it also has the same dilution characteristics on an exhaust stream inside of a reactor. Observing the reduction effect of sodium bicarbonate on the concentration values of nitric oxides NO_x (Fig. 7) its valuable capacities can be noticed, even though they are not as impressive (it should be mentioned that for the purposes of the research, a sodium bicarbonate with heightened NO_x sorptive capacity was used). The greatest sorptive capacity was observed for ¾ of core valve stroke, but very similar and comparable values were observed for the ¼ stroke and only slightly lower for the ½ valve stroke. The sorptive effectiveness for nitric oxides amounted to around 22%.

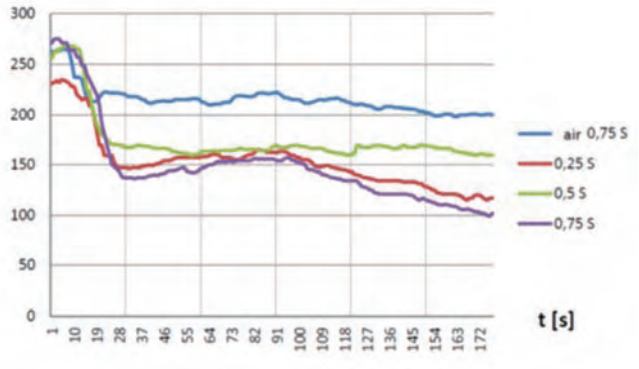

Fig. 7. Changes in concentrations of nitric oxides with a sorbent supply, where: 0,25S; 0,5S; 0,75S – degree of opening of the control valve; air 0.75S – air supply to the reactor at an opening of 0.75 valve stroke

Another issue that was analyzed during this research was the evaluation of sorptive effectiveness of the bicarbonate injected into the reactor. It was possible through determining the reaction time of the sorbent on the changes in SO_2 concentration. Tests were conducted three times and they resulted in a relatively significant repeatability. Slight differences of sulfur oxide concentration values and time it took the concentration to stabilize are most likely caused by the minimal differences in the amount of injected sorbent. These differences could also be caused by errors in the valve adjustment for the control of sorbent input into the reactor. A comparison of these timings is shown in a graphic form in Fig. 8.

With conditions presented in Fig. 8a, the engine was loaded with Ne = 0.9 kW. The value of sulfur oxides before the sorbent injection oscillates around 40 ppm while after its injection, the value decreases to around 14 ppm in a comparable time which amounts to 30-40 seconds, while for an engine load of Ne = 2.0 kW (Fig. 8b), the initial values of concentrations are around 120–140 ppm for SO_2 and decrease, after about 30 seconds, down to a value of 10–19 ppm.

Analyzing the changes of concentration values of SO_2 it should be noted that the nature of these changes is similar. The differences are caused by the significantly, by almost triple, higher concentrations of SO_2. This is because along with the shift of the load, the dosage of fuel increases while the SO_x concentration in the exhaust gas depends almost

solely on the amount of consumed fuel. An additional factor favorable to an increased sulfur oxide concentration is the increased combustion temperature, which also depends on the power load of the engine.

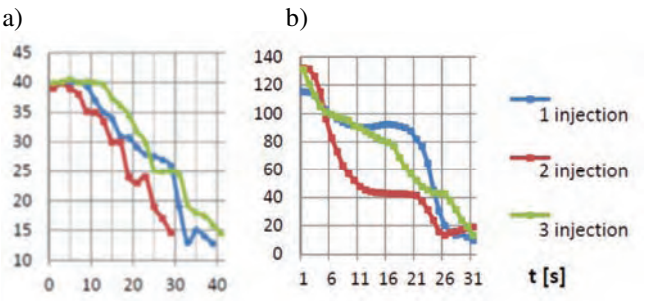

Fig. 8. Reaction time of the sorbent on SO_2 concentration, where: a) Ne = = 0.9 kW, b) Ne = 2.0 kW

As such it seems reasonable to come to the conclusion that the reactor capacity was largely oversized in relation to the size of the test engine used for powering the reactor.

5. Summary

Conducted research allowed for reaching the following conclusions:

1. The research confirmed the effectiveness of reduction impact of sodium bicarbonate as a sorbent for the reduction of oxides of not only sulfur, but also nitric oxides.
2. The suggested dry method is a competitive method relative to the wet methods used currently.
3. The research confirmed the validity of assumptions formulated during the creation of the laboratory station for testing the innovative dry method for the desulfurization of exhaust gas produced by a piston engine during the combustion of residual fuel.
4. The obtained results, on the level of quality reaction, are encouraging to conduct further research on the quantitative relations of a sorbent on the emission of reviewed sulfur, nitric and carbon oxides.
5. Encouraging is the perspective of research of dynamic reactions of bicarbonate sorbents on toxic compounds. Learning of the mechanisms of this phenomenon will allow the creation of a dynamic control of the sorbent output in case of the engine working during transient states. Such ability is not available to the wet method installations.

In order to continue with the research, it seems to be imperative to:

1. Conduct extensive optimization research, which would aim to help select the adequate amount of sorbent, necessary in the reduction of SO_x and NO_x. For the control parameter of the sorbent stream, not only output of the control valve should be considered, but also the supply pressure and the structure of atomizers. It should allow the free shaping of the sorbent stream, depending on the needs.
2. In order to eliminate the dilution of exhaust which could appear in result of feeding the reactor with a solvent by means of compressed air injection, research should be conducted using a gas neutral to the process of cleaning the exhaust, e.g.: nitrogen N_2 or carbon dioxide CO_2.

Bibliography

[1] DZIUBIŃSKI, M., PRYWER, J. Mechanika płynów dwufazowych. 2009, WNT, Warszawa.

[2] KORCZEWSKI, Z., RUDNICKI, J., ZADRĄG, R. Budowa stanowiska laboratoryjnego do badania innowacyjnej metody suchej odsiarczania spalin silnika zasilanego paliwem pozostałościowym. Projekt dofinansowany ze środków Wojewódzkiego Funduszu Ochrony Środowiska i Gospodarki Wodnej (WFOŚiGW) w Gdańsku – sprawozdanie z realizacji zadania, Gdańsk 2016.

[3] RUDNICKI, J., ZADRĄG, R. Problems of modelling toxic compounds emitted by a marine internal combustion engine for the evaluation of its structure parameters. *Combustion Engines*. 2015, **3**, 432-441.

[4] RUDNICKI, J., ZADRĄG, R. Problems of modelling toxic compounds emitted by a marine internal combustion engine in unsteady states. *Polish Maritime Research*. 2014, **21**, 57-65.

[5] SZYMANEK, A. Odsiarczanie spalin metodami suchymi, Europejski Fundusz Społeczny, Projekt „Plan Rozwoju Politechniki Częstochowskiej", Częstochowa 2008.

[6] VESTERGAARD, O.G. Comparing wet and dry exhaust gas cleaning systems. Bachelor project. Aarhus School of Marine and Technical Engineering. Denmark 2013.

[7] WALTER, J., WAGNER, J. Choosing exhaust scrubber system. Flensburg University of Applied Sciences, 2012.

[8] ZADRĄG, R., KNIAZIEWICZ, T. Identification of diagnostic parameter sensitivity during dynamic processes of a marine engine. *Combustion Engines*. 2015, **3**, 1007-1014.

Zbigniew Korczewski, DSc., DEng. – Faculty of Ocean Engineering and Ship Technology at Gdansk University of Technology.

e-mail: *zbikorcz@pg.gda.pl*

Jacek Rudnicki, DEng. – Faculty of Ocean Engineering and Ship Technology at Gdansk University of Technology.

e-mail: *jacekrud@pg.gda.pl*

Ryszard Zadrąg, DEng. – Faculty of Ocean Engineering and Ship Technology at Gdansk University of Technology.

e-mail: *ryszadra@pg.gda.pl*

Article citation info:
BABEL, M., KOSSOV, E. Model of exhaust system of a traction diesel engine with pulse supercharging on transient modes. *Combustion Engines*. 2017, **168**(1), 38-45. DOI: 10.19206/CE-2017-106

Marek BABEL
Evgeni KOSSOV

CE-2017-106

Model of exhaust system of a traction diesel engine with pulse supercharging on transient modes

A mathematical model of joint operation of a piston engine with pulse turbine drive, compressor as well as air supply of a diesel locomotive is presented in the article. This model in an integral part of the complex engine-generator power unit of a diesel locomotive in steady states and transient conditions, developed by the authors.

The periodic process in the exhaust manifold is represented as two specific characteristic ranges which encompass the process of forced exhaust and the scavenging process. The scavenging calculation is carried out jointly with the processes taking place in the inlet manifold of the engine, including inlet devices of the locomotive. The process of forced exhaust is calculated separately from the inlet processes and doesn`t require usage of empirical coefficients of impulsiveness. Both processes are represented as systems of nonlinear algebraic equations describe in the quasi-steady flow of working fluid in the elements of the inlet and exhaust tracts. The gas-dynamic calculation of the turbine in the transition process is conducted while taking into account changes in flow angles on the rotor blades. As a result of numerical calculation of the a8S22W diesel operational indices in transient modes, a satisfactory compliance of the calculated and the experimental results was obtained.

Key words: *diesel engine, locomotive, mathematical model, pulse supercharging, exhaust system, transient process*

1. Introduction

The analysis of the operating modes of the diesel engine shows that the engine runs on transient mode for a considerable part of the operation time.The transient modes, accompanying acceleration of the engine, are characterized by sharp increasing of fuel supply into the cylinder of engine and as a result by a reduction of the air excess coefficient λ, reduction of indicated efficiency η_i, significant peak temperature increase of exhaust gases T_t, incomplete combustion of fuel and other negative effects. A lot of such effects are excluded by using pulse supercharging.

Experimental studies of an operation of the diesel generator with pulse supercharging when momentary changes of load showed that the ratio of pressure in the inlet manifold P_s to pressure in front of the turbine P_t, is practically always larger than one throughout in the whole period of transient process. This parameter is one of the determining factors of the preference of using pulse supercharging system. The advantages of the pulse supercharging system are a better use of exhaust gases energy, which facilitates the increase in the torque of the turbine and improving the air supply of the diesel engine in the transient processes.

One of the most effective methods of studying the performance of the diesel locomotive engine with pulse supercharging in operation is a mathematic modelling of its working processes with a computer. It allows analysis of the working parameters of a diesel locomotive in exploitation, to determine and indicate the most efficient factors for improvement of the parameters already at the stage of design, tests and modernisation of engine systems.

This task can be achieved if the complex model of the engine-generator unit operation of a diesel locomotive in steady and transient modes is developed. This model should include a traction diesel engine – the piston part with its systems – inlet, exhaust and a turbocharger, locomotive transmission: – electric or hydraulic as well as auxiliary equipment on the vehicle. Development of such a model requires creation of mathematical models for above-mentioned components and systems. The model of the diesel locomotive power unit (system) obtained in this way will be used for simulation research (optimization) of influence of the revolution and power control system of the power unit on the energy efficiency of power transmission. Compliance of the model with the real processes, and also compactness and versatility of the description of processes for different types of engines and air aggregates are significant criteria of applicability of the mathematic model.

In [29] the authors reviewed 155 foreign publications concerning diesel engine simulations under transient operating modes in the open literature in the years 1971-2006. Most of these works (over 90%) concern simulation models of automotive engines as the research object, and about 5% marine engines. In this article, the authors summarize basic equations and modelling aspects concerning in-cylinder calculations, friction, turbocharger, engine dynamics, governor, fuel pump operation, and exhaust emissions during transients. The various limitations of the models are discussed together with the main aspects of transient operation (e.g. turbocharger lag, combustion and friction deterioration), which diversify it from the steady-state.

The general classification of the operating models of the piston engine cycle, known from the Polish literature, is described in [30], and the theoretical basics of fuel and air supply modelling of engines – in [35]. Implementation of mathematical models of diesel engine processes for simulation research of exhaust emissions are described in [12, 22, 26], and in publication [36], the model of diesel engine heat circulation is used for optimization of the research engine operation.

In the field of mathematic modelling of operation of automotive engines, most papers relate to control in engine systems with taking into account the transient modes [7, 13, 18, 24, 39].

A representation of conditions of the joint piston part and turbocharger operation in the form of calculations is a difficult task. It requires an accurate determination of the conditions of airflow and exhaust gases flow through the turbocharger. In [6, 19, 20, 27, 32], some alternative methods of solving the task are presented. They are different both in essence and accuracy.

The design of a model of the diesel with a turbocharger requires a mathematical description of the compressor and turbine. For solving this task, analytic methods [28, 31], which allow for calculating the hydraulic and thermal losses in the flow part of the turbine and turbocharger, can be used. Another method uses experimental characteristics of turbocharges for modelling, as functional relations – approximation of characteristics by polynomials of highest degree [8, 14, 15, 40].

Some mathematic models of the transient processes of diesel engines are based on the assumption that the diesel engine operation can be presented with a system of five differential equations [37]. The authors represented general differential equations without analysing the equations which express the relationship between concrete parameters of the engine. In [16], the mathematic model of the transient conditions of a marine diesel with pulse supercharging was elaborated based on the system of seven differential equations. The flow impulsiveness of exhaust gases is taken into account here by means of the correction factors obtained from experimental studies. The mathematical model of transient processes represented in [8] is also of interest. This model is based on a system of n differential equations for the piston part and of 6 equations describing the processes in the exhaust manifold in the case of using pulse supercharging. The mathematical models of transient modes of diesels in [38, 41] are based on similar principles. However, it is necessary to state that these models require a lot of computations and the presence of standard subprograms in the computer database. The precision of the model depends on the solution of the system of differential equations which is connected with the time of calculation.

For taking into account the pulsation of the mass flow which is delivered to the turbine at pulse supercharging, in [42] a coefficient α was entered, and to take into account the energy delivered at changeable pressure of gases, a coefficient β was entered. In [14, 15], impulsiveness of the flow of exhaust gases is taken into account with correction coefficients k_G, k_H and k_S for determining values of momentary growth of consumption of gas and pressure and also of changes in turbine efficiency. These coefficients are obtained based on analysis of diagrams of changes in gas pressures in the exhaust manifold for a certain number of engines. These coefficients are represented as approximate relations dependent on the pressure ratio π_k.

A systematization of coefficients type α, β, k_G, k_H, k_S is complicated due to large number of criteria, which have different effects on the shape of the curve of gases pressure in the exhaust manifold.

The authors of this article analysed the possibility of application of the existent mathematic model of the transient process of a diesel with the isobaric supercharging system [21] for the calculation of characteristics of the diesel with a pulse supercharging system.

The method of implementation static characteristics of diesel and supercharging aggregates in the mathematic model, as well as the calculation of a compressor and inlet system, are analysed in detail in [1, 21, 23]. A calculation of the transient processes performed in accordance with this method, while taking into consideration the pulse coefficients for determination of the power and the pressure of the turbine, showed that the condition $P_s/P_t > 1$ is not met, and the estimated time of transient process calculation is considerably prolonged [1]. The inclusion of calculations of the gas exchange process in this method, in order to achieve a more precise determination of the momentary values of gas parameters in the exhaust manifold, makes the mathematic model more complicated and useless for optimization calculations.

In [5, 9, 10, 25, 33], the authors described some interesting simulation models of diesel engine operation in steady conditions and transient states while using 1D models for turbocharger and chosen processes of diesel engines, and in publications [11, 17, 34] 3D CFD models. In these works, the research (modelling) object is, among others, a pulse-charged turbine in application for mainly automotive engines. In this scope of research, implementation of 1D and 3D models allows for effective simulation of the diesel engine processes chosen by the researchers. The object of research (modelling) and optimization calculations done by the authors of this article is the diesel locomotive power system, and the model of the exhaust system with pulse turbine supply is only an element of the above-mentioned complex model. Development of such a model implementing the 1-D modelling suggested by the researchers is a complex problem due to the variety of processes in the individual elements and systems of the diesel locomotive power unit and due to the limitation in the technical capabilities of computers. As it was indicated in the introduction to the chapter, the mathematical model should be compact, universal and suitable for multiple optimization calculations.

Given the above, the authors proposed a different approach to modelling of diesel engine exhaust system with pulse turbine supply which does not require implementation of differential equations for calculation of gas exchange, using experimental pulse indices or creation of complex, 1D or 3D models, e.g. for the piston part of the traction diesel engine, turbocharger.

2. Modelling of a diesel engine exhaust system

Based on modelling of the traction diesel engine, a quasi-steady model of working fluid flow in engine and turbocharging system elements was used [21]. The quasi-steady flow model allows for achieving satisfactory correspondence of the numerical calculation results to the experimental results [2, 32].

While creating the model it was proposed that the change in gas pressure in the exhaust manifold of diesel was dependent on time or on crankshaft angular velocity ω_d represents a periodic function with the period:

$$T = \omega_d \cdot \varphi^* \tag{1}$$

where ω_d, φ^* – crankshaft angular velocity and period of change in gas pressure.

The period of changes in gas pressure in the manifold φ^* will be equal to the value of phase shift of cylinder operation. We will assume that periodic process in the manifold may be represented in the form of some sequence of processes with the duration $\Delta\varphi$ inter-related by boundary conditions. There can be many such consecutive processes, however in relation with the processes in the inlet manifold, there are two specific periods: a process of forced exhaust (angle φ_{ex}–φ_{in}) and a scavenging process (angle φ_{in}–φ_{exe}, see Fig. 1a).

In the engine with pulse supercharging, the process of forced exhaust is completely isolated from the processes in the inlet manifold and it can be calculated based on the known methods if the parameters of the working fluid in the cylinder are set. The scavenging process is directly connected with the processes in the inlet manifold. In this work, it is suggested to calculate the scavenging process together with the processes in the inlet tract of the engine including the inlet equipment of diesel locomotive, air filter 1, compressor 2, intercooler 3, piston part 4, turbine 7 and exhaust equipment 8. (see Fig. 1b). The process of forced exhaust is calculated separately from the inlet processes. Both processes are presented by systems of nonlinear algebraic equations, which describe quasi-stationary flow of working fluid in the elements of the inlet and exhaust tracts. As in [21, 23], systems of algebraic equations are complemented by a system of differential equations, which describe changes in temperatures of heat carrier, of exhaust tract elements and of turbocharge rotor speed depending on time. The calculation of the flow of working fluid in the scavenging process and the exhaust process is carried out subsequently by taking the average values of pressure, temperature and working fluid flow rate in the corresponding periods with the assumed period $\Delta\varphi$ (see Fig. 1a). The initial parameters for a calculation of the exhaust tract with forced exhaust are the parameter values determined while calculating exhaust manifold during scavenging.

A working fluid flow rate (of air-gas mixture) in the diesel, G_{ag}, is represented by a sum of air flow rate in the scavenging process of cylinders, G_{sc}, and for filling cylinders from the moment of exhaust valves closure to bottom-dead-point, G_d.

It was assumed, that at the end of filling (in the cylinder) there will be a mass of working medium equal to the sum of the mass from the filling process and the mass present in the cylinders at the closure moment of the exhaust valves.

At pulse supercharging, $G_{SC} > 0$ which demonstrates why the pressure in the exhaust manifold behind the cylinder at the scavenging process will be determined by means of relation:

$$P_{10\,sc} = P'_6/\pi_d \tag{2}$$

where P'_6 – pressure of working fluid before inlet valves π_d – ration of intake manifold pressure and exhaust manifold pressure.

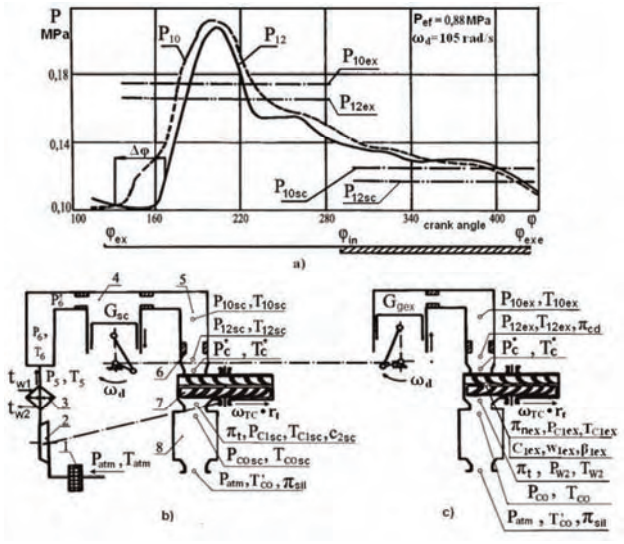

Fig. 1. Change in pressure in exhaust manifold (a) calculation model of a8C22 diesels with pulse supercharging at scavenging (b) and at free exhaust (c)

From the energy-conservation equation we determine the temperature of air-gas mixture in manifold at scavenging process (see Fig. 1b):

$$T_{10sc}\cdot(G_{sc}+G_{Vc})\cdot C_{pag}=T_6\cdot G_{sc}\cdot C_{pa}+T_{10ex}\cdot G_{Vc}\cdot C_{pex} \tag{3}$$

where G_{Vc} – working fluid flow rate at exhaust, which corresponds with the mass, contained in cylinders at the moment of opening of the exhaust valves; C_{pag}, C_{pa}, C_{pex} – heat capacity at constant pressure of air-gas mixture, air dose, working fluid at exhaust process, respectively; T_6 – temperature of air dose;

Working fluid flow rate,G_{Vc},can be determined from equation:

$$G_{Vc} = \frac{V_h \cdot \omega_d \cdot z_c}{(\varepsilon - 1)\cdot 2\pi \cdot \tau}\cdot \rho_{gex} \tag{4}$$

where V_h, ω_d– cylinder capacity and crankshaft angular speed; z_c, ε, τ – respectively: the number of cylinders, compression rate and the number of crank revolutions per power stroke;ρ_{gex} – gas density at temperature T_{10ex} and pressure P_{10ex}.

If we assume that heat capacity at a constant pressure of air-gas mixture, air dose and exhaust gases are constant and equal ($C_{pag} \approx C_{pa} \approx C_{pex}$), then from the equation (3) and (4) we obtain:

$$T_{10sc} = \left(T_6 \cdot G_{sc} + G_{Vc} \cdot P_{10ex} \cdot R_g^{-1}\right)/\left(G_{sc} + G_{Vc} \cdot \rho_{gex}\right) \tag{5}$$

In calculations it is assumed that at time $\Delta\varphi/\omega_d$ of scavenging, average gas flow rate G_g is determined by scavenging air flow rate G_{sc}. The pressure of working fluid before turbine P_{12sc} is determined from equation:

$$P_{12sc} = P_{10sc}/\pi_{cd} \tag{6}$$

where π_{cd} – pressure differential in conditional diaphragm 6 (see Fig. 1b).

The average working fluid flow rate at time $\Delta\varphi/\omega_d$ of forced exhaust is determined as a sum of gas flow rate G_d for filling cylinders and fuel mass flow rate b_{fc}.

$$G_g = G_d + b_{fc} \tag{7}$$

The temperature of the exhaust gases T_{10ex} is determined by the heat balance while taking into account the heat losses from incomplete burning of fuel according to the following equation:

$$T_{10ex} = \frac{b_{fc} \cdot H_u \cdot (\xi - \eta_i - \xi_1)}{G_g \cdot C_{pex}} + \frac{G_d}{G_g} \cdot T_{10sc} \tag{8}$$

where H_u – calorific value of fuel; ξ – available heat factor at the end of expansion process; ξ_1 –coefficient taking into account share of unburned fuel; η_i – efficiency indicator of diesel engine, and the gas pressure before turbine P_{12ex} – according to equation (6).

The temperature of gases before turbine T_{12sc}, T_{12ex} is determined by taking into account the heat exchange in exhaust manifold by means of method described in [21, 23].

A calculation of the turbocharger turbine at transient modes is of particular interest as a change of working fluid parameters can significantly change flow angles on the rotor blades (see Fig. 2). The pulsation of pressure in manifold and partial gas supply lead to the fact that the gas turbine works at constantly changing parameters of the gas before nozzles. Only the turbocharger shaft speed remains constant due to relatively large inertia moment of the rotor.

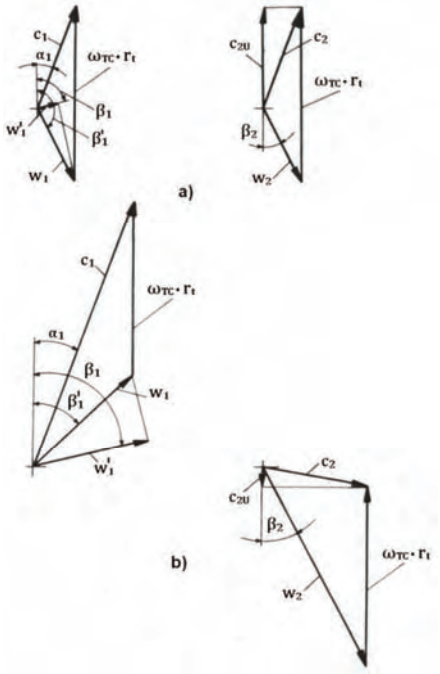

Fig. 2. Velocity diagrams at turbine rotor blades, inlet and exit at scavenging (a) and exhaust (b) – a8C22 diesel for ω_d = 52 rad/s, $\overline{P}_e$ = 0.25: α_1 – angle of flow exit from nozzle unit; β_1 – direction of shock-free inlet to the rotor blades; β'_1 – direction of relative velocity of flow at inlet of the rotor blades; β_2 – angle of flow exit from the rotor blades in relative motion

In this method, considering the gas-dynamic calculation of the turbine, it is assumed that the temperature of stagnated gas stream at the inlet of the rotor blades is determined by the relative rate w_1, (see Fig. 2), and the pressure of stagnated gas stream – by velocity w_1', which is the projection of the relative velocity w_1 in the direction β_1 of the shock-free flow of gas into the inlet of the rotor blades. The difference of kinetic energy at speeds w_1 and w_1' represents energy losses and turns to potential energy at isobaric process, therefore, the pressure of stagnated flow is determined by speed w_1'. Speed losses in the blades of the nozzle unit and rotor blades are taken into account by the coefficient of losses, and their values are determined according to method [1, 23].

Taking into account the stated assumptions and chosen method of calculating algebraic equations, the order of calculating the turbine is accepted as follows:

a) for a given value of working fluid flow rate, the parameters of stagnated flow stream at inlet of nozzle unit are determined as follows

$$T_c^* = T_{12} + \frac{G_g^2}{2} \cdot \frac{R_g \cdot T_{12}^2}{P_{12}^2 \cdot f_{em}^2} \cdot \frac{k_g - 1}{k_g}$$
$$P_c^* = P_{12} \cdot \left(\frac{T_c^*}{T_{12}}\right)^{\frac{k_g}{k_g - 1}} \tag{9}$$

where f_{em} – cross-sectional area of exhaust manifold.

b) from the equation of gas flow rate at adiabatic flow, the flow function $\psi_n$can be determined

$$G_g = f_n \cdot \frac{P_c^*}{\sqrt{R_g \cdot T_c^*}} \cdot \psi_n$$
$$\psi_n = \frac{G_g \cdot \sqrt{R_g \cdot T_c^*}}{f_n \cdot P_c^*} \tag{10}$$

where f_n – cross-sectional area of sector nozzle unit;

$$f_n = \frac{F_n}{z_{em}} \cdot \frac{\Delta\varphi}{2\pi \cdot \tau} \cdot z_c \tag{11}$$

where F_n – total cross-sectional area of nozzle unit; z_{em} – the number of exhaust manifolds which are connected to the turbine and have separate gas supply to the nozzle unit

$$\psi_n = \sqrt{\frac{2}{k_g - 1}\left[\left(\frac{P_{C1}}{P_C^*}\right)^{\frac{2}{k_g}} - \left(\frac{P_{C1}}{P_C^*}\right)^{\frac{k_g - 1}{k_g}}\right]} \tag{12}$$

c) using approximation of the flow function, we determine:

– pressure reduction in nozzle unit and parameters of working fluid at the outlet of nozzle unit

$$\pi_n = \pi_n(\psi_n) \tag{13}$$

– pressure P_{c_1} and temperature T_{c_1}

$$P_{c_1} = P_c^* / \pi_n$$
$$T_{c_1} = T_c^* \cdot \pi_n^{\frac{1 - k_g}{k_g}} \tag{14}$$

– absolute c_1 and relative w_1 flow velocities

$$c_1 = \varphi_1 \cdot \frac{G_g \cdot R_g \cdot T_{c_1}}{f_n \cdot P_{c_1}}, \qquad w_1 = \sqrt{c_1^2 + (\omega_{TC} \cdot r_t)^2 - 2c_1 \cdot \omega_{TC} \cdot r_t \cdot \cos\alpha_1}, \tag{15}$$

where φ_1 – the speed loss coefficient in nozzle unit

– relative gas velocity w_1' by the shock-free inlet and parameters of stagnation at the inlet of rotor blades

$$\beta_1' = \pi/2 - \arcsin\left(\frac{c_1 \cdot \cos\alpha_1 - \omega_{TC} \cdot r_t}{w_1}\right), \quad w_1' = w_1 \cdot \cos(\beta_1' - \beta_1), \quad T_{w_1}^* = T_{c_1} + \frac{w_1^2}{2} \cdot \frac{k_g - 1}{k_g} \cdot R_g^{-1}, \quad T_{w_1'}^* = T_{c_1} + \frac{w_1'^2}{2} \cdot \frac{k_g - 1}{k_g} \cdot R_g^{-1}, \quad P_{w_1}^* = P_{c1} \cdot \left(\frac{T_{w_1'}^*}{T_{C_1}}\right)^{k_g/(k_g-1)} \tag{16}$$

d) based on parameters of stagnation at inlet of rotor blades, we determine flow function ψ_t, turbine pressure ratio π_t, parameters of working fluid at the outlet of rotor blades, relative velocity of gas exhaust from rotor blades w_2 and components of absolute velocity c_2

$$\psi_t = \frac{G_g \cdot \sqrt{R_g \cdot T_{w_1}^*}}{f_t \cdot P_{w_1}^*}, \tag{17}$$

where f_t – cross-sectional area of sector rotor blades.

$$\pi_t = \pi_t(\psi_t), \quad P_{w_2} = P_{w_1}^*/\pi_t, \quad T_{w_2} = T_{w_1}^* \cdot \pi_t^{\frac{1-k_g}{k_g}}, \quad w_2 = \varphi_2 \cdot \frac{G_g \cdot R_g \cdot T_{w_2}}{f_t \cdot P_{w_2}}, \tag{18}$$

$$C_{2u} = w_2 \cdot \cos\beta_2 - \omega_{TC} \cdot r_t, \quad C_{2o} = w_2 \cdot \cos(\pi - \beta_2), \quad C_2 = \sqrt{C_{2u}^2 + C_{2o}^2}, \tag{19}$$

where φ_2 – speed loss coefficient in the rotor blades.

e) with the Euler`s formula, we determine specific work on the rotor blades L_{ad}, adiabatic heat drop H_t and internal efficiency of the turbine η_t

$$L_{ad} = \omega_{TC} \cdot r_t \cdot \left(w_1 \cdot \cos\beta_1' - w_2 \cdot \cos(\pi - \beta_2)\right), \quad H_t = \frac{k_g}{k_g - 1} \cdot R_g \cdot T_{12} \cdot \left(1 - (\pi_n \cdot \pi_t)^{\frac{1-k_g}{k_g}}\right), \quad \eta_t = L_{ad}/H_t\,. \tag{20}$$

Exhaust temperature and pressure at the outlet of turbine are calculated from the equation:

$$T_{co} = T_{w_2} + \frac{c_{2u}^2}{2} \cdot \frac{k_g - 1}{k_g} \cdot R_g^{-1}, \qquad P_{co} = P_{w_2} \tag{21}$$

A calculation of the exhaust tract and turbine parameters during a forced exhaust was performed by determining the work fluid flow rate throughout the engine, described in the [21].

From a calculation of exhaust process, the average working fluid flow rate in period $\Delta\varphi$ is known, and by means of that calculation we determine pressure P_{10ex} in the manifold 5 (see Fig. 1c).

As a first step of calculation, we set starting value of pressure P_{10ex}^I in the first approximation. With equation (8), we can determine a value of temperature T_{10ex}^I and calculate parameters of exhaust tract and turbine; as a result we receive values of pressure reduction in the conditional diaphragm π_{cd}, nozzle unit π_n, rotor bladesπ_t, and silencer π_{sil}. Then, we calculate a product of pressure reductions of working fluid at P_{10ex}^I, T_{10ex}^I:

$$\prod_1^n \pi_i = \frac{P_{10ex}^I}{P_{atm}} \cdot \frac{1}{\pi_{cd} \cdot \pi_n \cdot \pi_t \cdot \pi_{sil}}, \tag{22}$$

and we check the condition

$$\left|\prod_1^n \pi_i - 1\right| < \varepsilon_2, \tag{23}$$

If the condition (23) is not met with a given accuracy of calculations ε_2, we set a new value of the current value of pressure P_{10ex}^I and repeat the calculation.Otherwise, the average value of pressure P_{10ex} in period $\Delta\varphi$ is the value searched.

An average value of the exhaust gas flow rate throughout the engine can be calculated from relation

$$G_g = \sum_{i=1}^{i=n} \frac{z_c}{2\pi \cdot \tau} \cdot \Delta\varphi_i \cdot G_{gi}, \tag{24}$$

where n – number of periods $\Delta\varphi$.

After the calculation of the inlet system, piston part and exhaust system of diesel, we solve the system of equations which describes the diesel generator fuel supply and power control at transient processes. The system of equations includes a differential equation of power balance and systems of algebraic equations for the determination of the dependence of diesel generator power and limiting parameters of operational process of the diesel on an angular velocity of the diesel crankshaft. The mathematic model simulates functional connections used in control systems of angular velocity of the crankshaft and power of a diesel locomotive engine [3, 4, 21]. A calculation of transient and steady modes of diesel operation is carried out using a program, common for any diesel type. A general block diagram of that program is represented in Fig. 3.

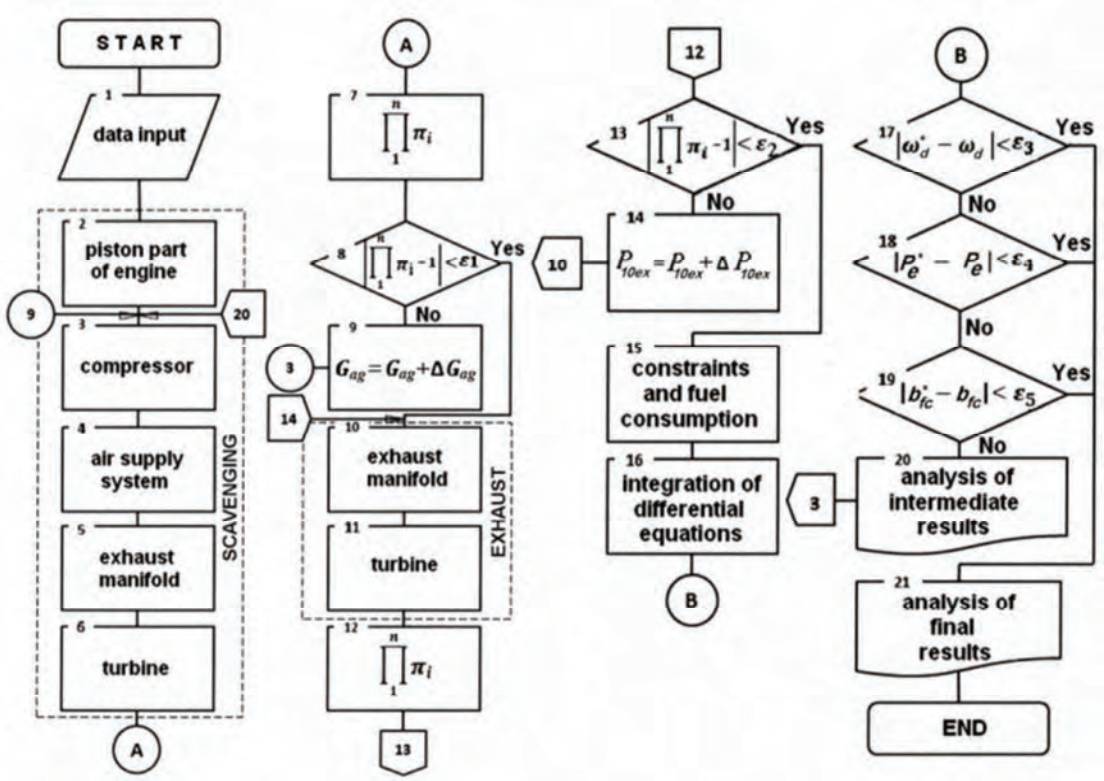

Fig. 3. Block diagram of calculation algorithm of transient process for diesels with pulse supercharging

The diesel operation mode and specific data are entered into the program in block 1 as an array of source data: array of constants, array of constants of the diesel engine and approximate experimental relations, like efficiency of diesel, characteristics of turbocharger compressors and turbines, etc.

In blocks 2–9, the calculation of air-gas mixture flow rate, G_{ag}, at set values of angular velocities of the diesel crankshaft and turbocharger rotor, temperatures and fuel supply is performed by means of system of nonlinear algebraic equations.

In blocks 10–14, the calculation of exhaust tract and turbine during the time of free exhaust is performed by means of system of nonlinear algebraic equations.

In block 15, a choice of possible increment of fuel consumption is performed according to system of differential and algebraic equations describing specific features of fuel feeding and load control system.

In block 16, an integration of differential equations describing changes the above-mentioned set values in time is done.

In blocks 17–19, actual values of angular velocity of crankshaft ω_d, effective power of diesel P_e and fuel mass flow rate b_{fc} are compared with the set ones ω_d^*, P_e^*, b_{fc}^*. In the case of their compliance with given accuracy, the transient process is considered to be finished. Otherwise, the calculation is continued with new values ω_d and ω_{TC}, starting from block 3.

In block 21, a print of output parameters is made and the calculation ends.

3. Validation of a diesel engine model

Using the demonstrated block diagram and method described in [21, 23], the performance calculation program of diesel locomotive engine with pulse supercharging on transient mode was made and debugged.

Before using the mathematic model for a calculation of transient modes of diesel engines, compliance of the model with the real objects on steady modes of operation was checked. To this purpose, the results of the numerical calculations were compared with the experimental data from the producer of the engines, HCP Cegielski, for exploitation and load characteristics of the a8C22W traction engines with the pulse turbine supply. Comparison of the calculations with the results of the experimental research showed a sufficient similarity of the results [2, 21]. The discrepancy between the calculated and experimental values is not greater than 2–4%. The differences occurring in the angular velocity of the turbocharger rotor, turbocharging pressure and air low rate under low load can be explained mainly by the shortage of experimental data of compressor (characteristics) within lower angular velocities of the turbocharger.

The evaluation of a mathematic model suitability at transient process was made by comparing operational indices of diesel obtained experimentally on the water braking resistor at rapid increase in the engine loading – switching of the driver controller from IV to XI position, to the numerical calculation data. Figure 4 presents a comparison of calculated and experimental time characteristics of the transient processes of an a8C22W diesel-generator unit for controlling revolutions and load realized on a SM31 diesel locomotive [2]. Figure 4 proves the sufficient

similarity of the results of simulation calculations to the results of experimental research. The greatest deviation of the calculated values is observed for the turbocharging pressure index between 4 and 6 second of the transient process period and is equal to 6%. The discrepancy between

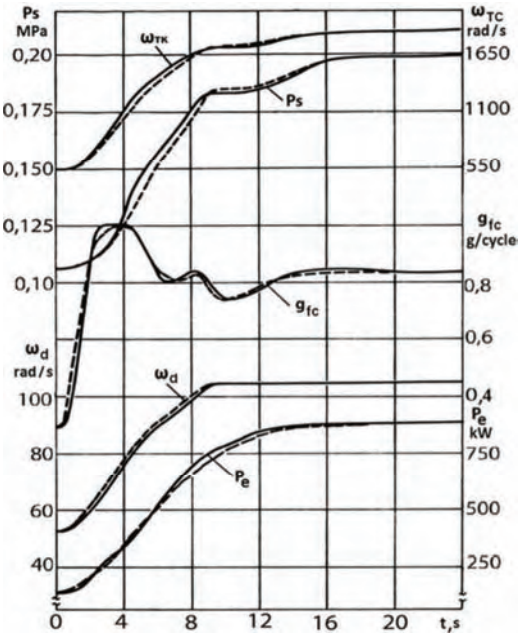

Fig. 4. Time characteristics of transient process in a8C22W diesel-generator unit: ω_d, ω_{TC} – angular velocity of crankshaft and turbine rotor; P_s – pressure of charge air; g_{fc} – fuel charge per cycle; P_e – effective power of diesel; continuous line – experimental data; dashed line – calculated data

the calculated and experimental values for the other performance rates of the diesel engine is not greater than 3%. These results allow the conclusion that the mathematical model reliably reflects the performance rate of the diesel locomotive traction engine both in quality and quantity. Summing up, the developed model can be implemented in optimization calculations of locomotive systems.

4. Conclusion

The developed mathematical models of interaction between the diesel traction engine and turbocharger supplied at variable pressure (including the authors' models), using the experimental pulse indices, provide a sufficient similarity of the numerical calculations to the experimental results in steady modes of the engine operation. In contrast, in transients modes the satisfactory similarity cannot be obtained. Inclusion of calculations of gas exchange processes into the models using differential equations or implementation of 1-dimension models, e.g. in the case of a turbocharger, makes the mathematical model complicated and unsuitable for optimizing calculations of locomotive systems.

The model of the exhaust system of the diesel traction engine with the pulsating supply of the turbocharger presented in this article was developed by the authors on the basis of a non-linear algebraic equations without the use of differential equations of the charge exchange process and gas exhaust, as well as of experimental, correction coefficients taking into account the pressure pulse of the exhaust gases. The assumption made by the authors for the development of the model are its specific features in comparison with existing methods of modelling of the exhaust systems of diesel traction engines. Confirmation of the validity of the adopted modelling assumptions is obtaining a satisfactory similarity of the results of numerical calculations to the actual runs, both in steady and transition stages. Moreover, the developed mathematical model gains compactness and versatility in terms of description of the processes in various types of traction engines and power aggregates.

The model of the traction engine exhaust constitutes an integral part of the complex model of the diesel locomotive power unit in steady operation and transient stages in exploitation [1, 3]. The complex model was used in the scientific-research works for simulation tests of influence of the power unit loading control on the energy efficiency of the power transmission. These research was aimed at evaluation of the modernisation effectiveness of the power unit loading control of diesel locomotive series SM31 [3, 4].

Bibliography

[1] BABEL, M. Повышение эффективности работы тепловозных дизелей а8С22 согласованием характе-ристик нагружения с режимами эксплуатации. Dissertation, Moscow, MIIT, 1989. m8.mech.pk.edu.pl/dissertation_babel/DR_Babel_spis_tresci.pdf

[2] BABEL, M. Zwiększenie efektywności pracy lokomotyw spalinowych SM31 w eksploatacji. *TTS Technika Transportu Szynowego*. 2012, **1-2**, 41-44.

[3] BABEL, M. Теоретические основы и методология выбора объемов и технологий модернизации тепловозов по критерию стоимости жизненного цикла. Dissertation, Moscow, VNIIZhT, 2014, www.vniizht.ru/fileadmin/site/files/Babel_doktorska_dissertacia.pdf.

[4] BABEL, M., SZKODA, M. Diesel locomotive efficiency and reliability improvement as a result of power unit load control system modernisation. *Eksploatacja i Niezawodność – Maintenance and Reliability.* 2016, **18**(1), 38-49.

[5] BELLIS, V., MARELLI, S., BOZZA, F., CAPOBIANCO, M. 1D simulation and experimental analysis of a turbocharger turbine for automotive engines under steady and unsteady flow conditions. *Energy Procedia*. 2014, **45**, 909-918.

[6] BERGLUND, S.A. Model of turbocharged engines as dynamic drivetrain members. *SAE Technical Paper*. 1993, 933050.

[7] BIANCHI, G.M., FALFARI, S., PAROTTO, M., OSBAT, G. Advanced modelling of common rail injector dynamics and comparison with experiments. *SAE Technical Paper.* 2003-01-0006.

[8] ВОЛОДИН, А.И. Моделирование на ЭВМ работы тепловозных дизелей. Москва, *Транспорт*. 1985, 217с.

[9] CHEN, H., HAKEEM, I., MARTINEZ-BOTAS, R.F. Modelling of a turbocharger turbine under pulsating inlet conditions. *Proceedings of the Institutionof Mechanical*

Engineers, Part A: Journal of Power and Energy. 1996, **210**, 397-408.
[10] CHIONG, M.S., RAJOO, S., ROMAGNOLI, A., COSTALL, A.W., MARTINEZ-BOTAS, R.F. Integration of meanline and one-dimensional methods for prediction of pulsating performance of a turbocharger turbine. *Energy Conversion and Management*. 2014, **81**, 270-281.
[11] CHIONG, M.S, PADZILLAH, M.H, RAJOO, S., ROMAGNOLI, A., COSTALL, A.W., MARTINEZ-BOTAS, R.F. Comparison of experimental, 3D and 1D model for a mixed-flow turbine under pulsating flow conditions. *Jurnal Teknologi*. 2015, **77**, 61-68.
[12] CHŁOPEK, Z. Modelowanie procesów emisji spalin w warunkach eksploatacji trakcyjnej silników spalinowych. *Prace Naukowe Seria „Mechanika"*. 1999, z. 173, Oficyna Wydawnicza Politechniki Warszawskiej, Warszawa.
[13] CHŁOPEK, Z., PIASECZNY, L. Uwagi o modelowaniu w badaniach naukowych. *Eksploatacja i Niezawodność – Maintenance and Reliability*. 2001, **4**(11), 47-57.
[14] DANILECKI, K. Założenia do modelowania turbosprężarki trakcyjnego silnika z pulsacyjnym zasilaniem turbiny. *Archiwum Motoryzacji*. 2006, **4**, 421-436.
[15] DANILECKI, K. Model systemu turbodoładowania trakcyjnego silnika o zapłonie samoczynnym. *Silniki spalinowe*. 2007, **3**(130), 36-48.
[16] FERENC, N. Modelowanie numeryczne procesu regulacji okrętowego silnika wysokoprężnego z uwzględnieniem nieliniowości. *Zeszyty naukowe Politechniki Śląskiej*. 1978, 567.
[17] GALINDO, J., FAJARDO, P., NAVARRO, R., GARCA-CUEVAS, L.M. Characterization of a radial turbocharger turbine in pulsating ow by means of CFD and its application to engine modelling. *Applied Energy*. 2013, **103**, 116-127.
[18] GUZZELLA, L., ONDER, CH. Introduction to modelling and control of internal combustion engine systems. *Springer Verlag*. 2nd Ed., 2010.
[19] IKEYA, N., YAMAGUCHI, H., MITSUBORI, K., KONDOH, N. Development of advanced model of turbocharger for automotive engines. *SAE Technical Paper*. 1992, 1992-02- 920047.
[20] KESSEL, J.A., SCHMIDT, M., SCHAFFNIT, J. Modeling and real-time simulation of a turbocharger with variable turbine geometry (Vtg). *SAE Technical Paper*. 1998, 1998-02-980770.
[21] KOSSOV, E., BABEL, M. Zagadnienia modelowania eksploatacyjnych warunków pracy trakcyjnych silników spalinowych. *Silniki Spalinowe*. 1988, **2**, 27-31, m8.mech. pk.edu.pl/articles/Artykul_SS_1988.pdf.
[22] KOWALSKI, J. Model procesu spalania w 4-suwowym silniku okrętowym. *Mechanik*. 2015, 10, 49-58.
[23] КОССОВ, Е.Е., СУХОПАРОВ, С.И. Оптимизация режимов работы тепловозных дизель- генераторов. *Трудыы ВНИИЖТ*. Интекст. 1999, 184 с.
[24] MA, H., XU, H., WANG, J. Real-time control oriented HCCI engine cycle-to cycle dynamic modelling. *International Journal of Automation and Computing*. 2011, **8**(3), 317-325.
[25] MACEK, J., VÁVRA, J., VÍTEK, O. 1-D Model of radial turbocharger turbine calibrated by experiments. *SAE Technical Paper*. 2002, 2002-01-0377.
[26] MARECKA-CHŁOPEK, E., CHŁOPEK, Z. Badania porównawcze emisji zanieczyszczeń z silników spalinowych o różnych zastosowaniach. *Transport samochodowy*. 2009, **9**,71-84.
[27] NIEWIAROWSKI, K. Tłokowe silniki spalinowe. Tom II. *WKŁ*. 1983. Warszawa.
[28] PANCHAREVSKI, G., IVANOV, V. Bestimmung der wärmeverluste in diffusor eines turbokompressors. *IV Symposium Klimatechnik, Belüftung Wärmeaustausch in Transportwesen – Tagungsmaterialen*. Politechnika Szczecińska. 1992.
[29] RAKOPOULOS, C.D., GIAKOUMIS, E.G. Review of thermodynamic diesel engine simulations under transient operating conditions. 2006, citeseerx.ist.psu.edu/view-doc/download?doi=10.1.1.466.5353&rep=rep1 & type=pdf.
[30] RYCHTER, T., TEODORCZYK, A. Teoria silników tłokowych. *WKŁ*. 2006, Warszawa.
[31] RYCHTER, T., TEODORCZYK, A. Modelowanie matematyczne roboczego cyklu silnika tłokowego. *PWN*. 1990, Warszawa.
[32] SERRANO, J.R., REYES, E., PAYRI, F. A Model for load transients of turbocharged diesel engines. *SAE Technical Paper*. 1999, 1999-01-0225.
[33] SERRANO, J.R., ARNAU, F.J., PIQUERAS, P., ONORATI, A., MONTENEGRO, G. 1D gas dynamic modelling of mass conservation in engine duct systems with thermal contact discontinuities. *Mathematical and Computer Modelling*. 2009, **49**, 1078-1088.
[34] SIGURDSSON, E., INGVORSEN, K.M., JENSEN, M.V, MAYER, S. Numerical analysis of the scavenge flow and convective heat transfer in large two-stroke marine diesel engines. *Applied Energy*. 2014, **123**, 37-46.
[35] SOBIESZAŃSKI, M. Modelowanie procesów zasilania w silnikach spalinowych. *WKŁ*. 2000, Warszawa.
[36] TUTAK, W. Modelowanie obiegu cieplnego tłokowego silnika spalinowego o zapłonie samoczynnym. *Modelowanie inżynierskie*. 2013, **49**, 73-78.
[37] ТИМАНОВСКАЯ, Л.К, СОБОЛЬ, В.Н., ПОГРЕБНЯК, В.В. Моделирование переходных процессов дизеля со свободным турбокомпрессором. *Двигатели внутреннего сгорания. Издание ХГУ*. 1975, вып. 21, 53-58.
[38] WATSON, N. Transient performance simulation and analysis of turbocharged diesel engines. *SAE Technical Paper*. 1981, 810338.
[39] WENDEKER, M., GODULA, A. Research on variability in control parameters for spark ignition engines in real-life operation. *Eksploatacja i Niezawodność – Maintenance and Reliability*. 2002, **16**(4), 12-23.
[40] WISŁOCKI, K. Badanie wpływu upustowej regulacji parametrów doładowania na własności trakcyjne turbodoładowanych silników spalinowych. Dysertacja, *Wydawnictwo Politechniki Poznańskiej*. 1986.
[41] ZELLBECK, H., WOSCHNI, G. Rechnerische Untersuchung des dynamischen Betriebsverhaltens aufgeladener Dieselmotor. *MTZ*. 1983, **3**, 81-86.
[42] ZINNER, K. Aufladung von Verbrennungsmotoren – Наддув двигателей внутреннего сгорания. Перевод с немецкого. Под редакцией Н.Н. Иванченко. *Ленинград, Машиностроение*. 1978.

Marek Babel, DSc., DEng. – Faculty of Mechanical Engineering, Institute of Rail Vehicles, Cracow University of Technology.

e-mail: *Marek.Babel@mech.pk.edu.pl*

Evgeni Kossov, DSc., DEng. – Joint Stock Company Railway Research Institute, Moscow, Russia.

e-mail: *voropaevamv@yandex.ru*

Article citation info:
WRÓBLEWSKI, E., FINKE, S. Test bench measurement of friction loss in combustion engine. *Combustion Engines*. 2017, **168**(1), 46-50. DOI: 10.19206/CE-2017-107

Emil WRÓBLEWSKI
Szymon FINKE

CE-2017-107

Test bench measurement of friction loss in combustion engine

The results of modeling and bench testing friction losses in the main engine kinematic nodes for different lubricating oil temperature values was presented in the article. The study was performed to evaluate the effect of lubricating oil temperature on the engine friction losses. In addition to friction losses in the crankshaft bearings and the piston rings in a cylinder-piston group the friction loss due to charge exchange in the cylinder, drive of timing system and the oil pump were measured. The obtained results show the course of the friction loss in the combustion engine. The research shows that the thermal state of the engine lubricating oil has effect on the amount of friction losses. Formulated conclusions allow to assess the impact of the oil temperature on the friction losses in the main friction nodes in combustion engine.

Key words: *combustion engine, piston, oil, lubrication, friction loss*

1. Introduction

Every year the number of vehicles on the roads and highways increases. Distances traveled by cars are often small, because the drivers move only in the urban area. In heavy traffic, a large number of lights on streets often creates congestion. In such traffic conditions, the engines of motor vehicles operate under idle and low loads, generating mechanical losses a relatively large value. It mainly translates into an increased amount of fuel consumption and exhaust emissions. Furthermore, referring to the small distances that the vehicle passes, it is not possible for an internal combustion engine to achieve optimum operating temperature. It has a great influence on the friction loss generated in the drive unit [1, 2].

Reducing friction losses has the effect of decreasing fuel consumption and increasing mechanical efficiency [1, 7]. One of the friction loss reduction method is the use of lubricating oils with reduced viscosity [3, 7]. This solution has a certain limitation. The use of oils with a very low viscosity may lead to deterioration of the lubricating properties which may lead to excessively rapid wear on the working elements or even contribute in seizing up of the motor [4].

The study of internal combustion engines, especially traction motors installed on the engine test bench has an important role in the understanding of the phenomena that occur in the engine, such as e.g. friction losses in the group piston-cylinder. Friction losses in a piston-cylinder largely depend on the thermal state of the engine. Mounting the engine on an engine test bench significantly changes the operating conditions. This results in structural changes for example in the engine cooling system. It should be noted that all changes are adaptive and should not change the course of events to those that occur in the driving vehicle engine [5]. A particularly important role played by the cooling system for the engine mounted on a dynamometer. The laboratory cooling system requires not only the ability to drain the excess heat under all operating conditions, but also the possibility of obtaining precise temperature stabilization.

Engine block coolant temperature determines the temperature of the cylinder and wall oil film covering the cylinder wall. It has a significant impact on the processes of friction occuring in the main engine friction nodes [5, 7]. Besides the node-piston rings and cylinder to total engine friction losses compared to the main part of the bearing and make the crank shaft of the engine. The basis for determining the temperature of the crankshaft bearing is not only the coolant temperature but also the temperature of the oil, usually measured in the oil sump [5].

The article presents the methodology and the results of model and bench testing friction losses in the engine combustion conditions of engine dynanometer variants for different temperatures of lubricating oil and engine speeds.

2. Model tests methodology of the friction losses in the combustion engine

The test bench of the model (Fig. 1) was built with a complete engine block FIAT 170A.046 with the crankshaft, connecting rods, pistons and engine head, in order to reproduce as closely as possible the actual working conditions of piston-engine crankshaft in the engine, while ensuring accurate measurement of torque under external drive.

Model test bench was built to measure friction loss in the piston-cylinder group composed of the modified internal combustion engine driven by electric motor from outside. The drive is transmitted through the measuring shaft which allows accurate torque measurement with high temporal resolution. In the engine camshaft is immobilized, leaving all valves in the closed position, there is also the immobilized crankshaft-driven coolant pump and an oil pump replacing them by outer system, driven by electric motors.

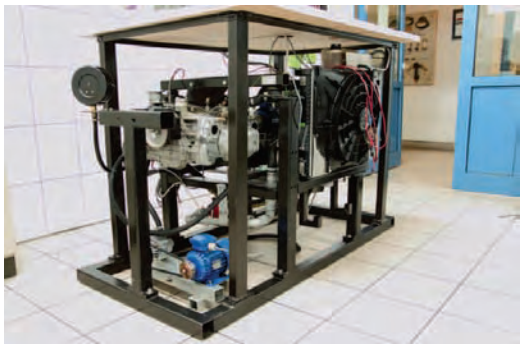

Fig. 1. View of the test bench

The changes made during each revolution of the crankshaft forces the repeating cycle of compression and expan-

sion of the fuel load confined within the cylinder, where in a portion of the fuel enters the crankcase due to leakage. With the valves closed engine loss charge in the cylinder can be supplemented by additional non-return valves mounted instead of spark plugs and called charge supplement valves. The design position allows you to close the valves or their opening to allow free air intake, ambient or bringing it under certain hypertension. Bringing the cylinder at the beginning of the stroke compressed air under increased pressure causes the increase in the maximum cylinder pressure. This is the method to simulate the actual increased engine load.

A very important element of the original system is to maintain a constant oil temperature of the heat exchanger oil-cooling liquid engine, the radiator and heater fluid and electrically powered pumps, coolant and oil. The PID controller makes it possible to maintain the desired oil temperature within ± 0.2°C, which ensures repeatability of the measurements. Diagram of stabilizing the oil temperature at the position shown in Figure 2, and the most important technical data positions in Table 1. A detailed description of the position of the model can be found in the literature [6].

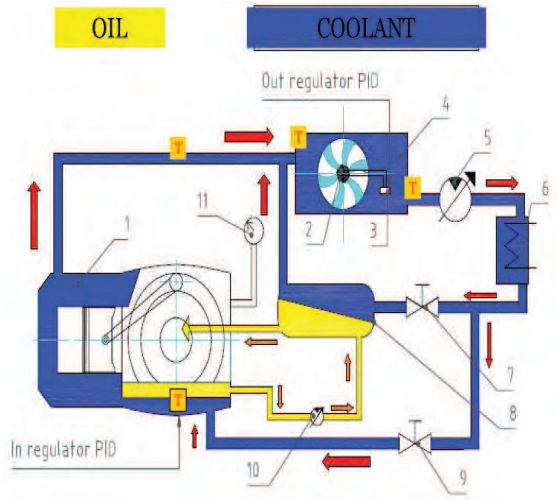

Fig. 2. Diagram of the oil temperature regulation system used on test bench

Table 1. Technical data

No.	Name
1	Engine Fiat 170A.046
2	Fan radiator fluid
3	Microprocessor control fan speed
4	Cooler
5	Liquid pump with a variable flow rate
6	Electric heating liquids
7	The ball valve of a small flow of liquid
8	The plate heat exchanger of a water / oil
9	The ball valve of a large flow of the liquid
10	Oil pump with variable flow
11	Manometer-pressure oil lubrication system

3. The results of friction losses model studies in the internal combustion engine

The approach adopted to the construction can capture the position of the torque with high accuracy and measurement frequency (Fig. 3), the measured torque is due to frictional losses in the piston-crank mechanism and is not significantly affected by the action of any other mechanism of the engine. Torque measurement is affected by the influence of thermodynamic phenomena that occur in the engine and charge blow-by to the crankcase.

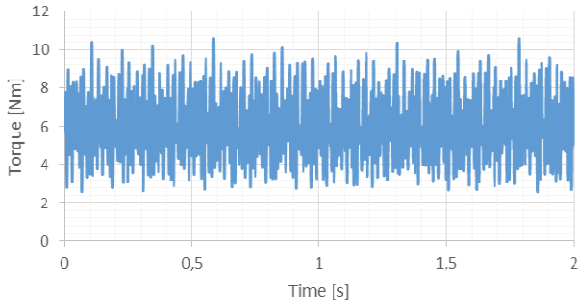

Fig. 3. Registered torque measurement at the speed of 2500 rpm and the oil temperature of 80 °C

The impact of these phenomena cannot be eliminated, but it can be assumed that their progress depends largely on micro-geometry for example or covering coats bearing surface of the piston and that allows mutual comparison of these variants in the range of manufactured friction losses. Model tests were carried out for the factory piston from Fiat engine 170A.046.

The measurements were made for the following conditions:

– engine speed 750-3000 rpm,
– temperature of the oil 50, 80 and 110°C.

As expected, resulting from the hydrodynamic lubrication theory of increasing the rotational speed increases the braking torque. A series of measurements were performed at intervals of several days, then they were averaged and summarized in Fig. 4–7.

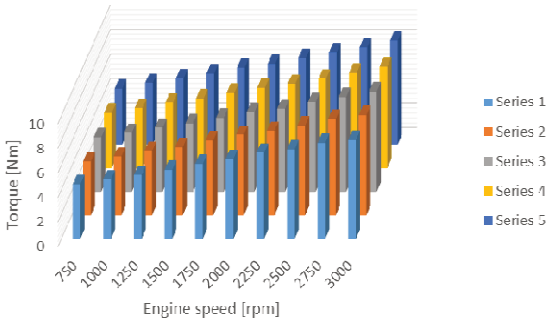

Fig. 4. Course of torque for the five series measuring – oil temperature 50°C

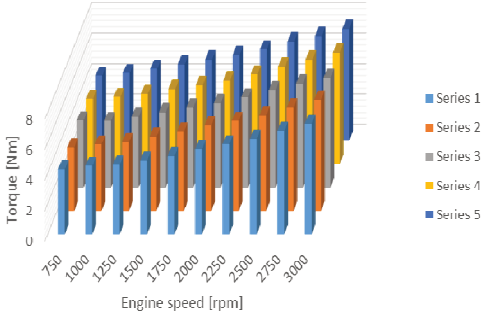

Fig. 5. Course of torque for the five series measuring – oil temperature 80°C

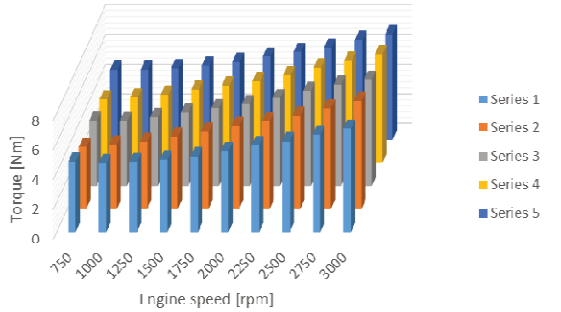

Fig. 6. Course of torque for the five series measuring – oil temperature 110°C

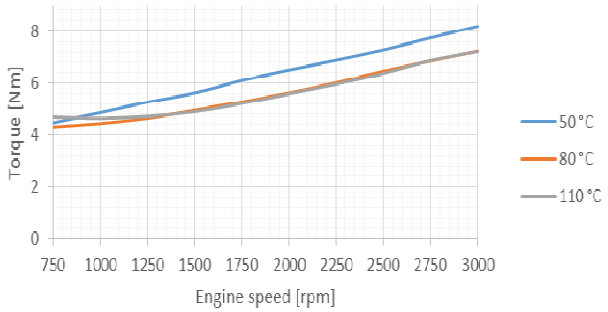

Fig. 7. The plot of averaged torque results for the five series of measurements as a function of oil temperature

On the basis of the results it can be seen that the magnitude of friction loss is higher for higher speeds of the engine.

Temperature 50 and 80°C observed increase in braking torque is a monotone throughout the rotation speed range. At these conditions, at an oil temperature of 110°C observation leads to the occurrence of a minimum braking torque. For the highest oil temperature speed increase will increase the total friction losses. This is a very important observation because when the engine speed increasing, due to the larger friction losses being converted to heat followed by rapid heating of engine components and lubricating oil, and this contributes to a reduction in viscosity, which may lead to the occurrence of boundary friction conditions.

4. Methods of friction losses bench tests in the internal combustion engine

The engine mounted on a test bench (Fig. 8) is manufactured by Volkswagen. Its basic parameters are shown in Table 2.

Table 2. The engine data installed on the test bench [8]

Built	five-cylinder, in-line
Displacement	2460 cm^3
Bore	81 mm
Stroke	95.5 mm
Compression ratio	18.0:1
The number of valves per cylinder	2
Max power	96 kW at 3500 rpm
Max torque	340 Nm at 2000 rpm
Built	five-cylinder, in-line
Displacement	2460 cm^3
Bore	81 mm
Stroke	95.5 mm
Exhaust aftertreatment	exhaust gas recirculation valve, catalyst

Research made on the engine are carried out, among others, to assess the impact of the thermal state of the engine lubricating oil on the friction losses.

Fig. 8. General view of the test bench

In studies conducted on the analyzed test bench engine, a key role is played by the system regulating the temperature of the engine coolant. This system differs significantly from the original cooling system, which is shown in Figure 9, which is used in vehicles, where it was installed abovementioned engine.

Research carried out in a motor are carried out, among others, to assess the impact of the thermal state of the engine friction losses. Therefore, the position is equipped with a cooling system that gives the possibility of making coolant temperature variants. It is presented in Figure 10.

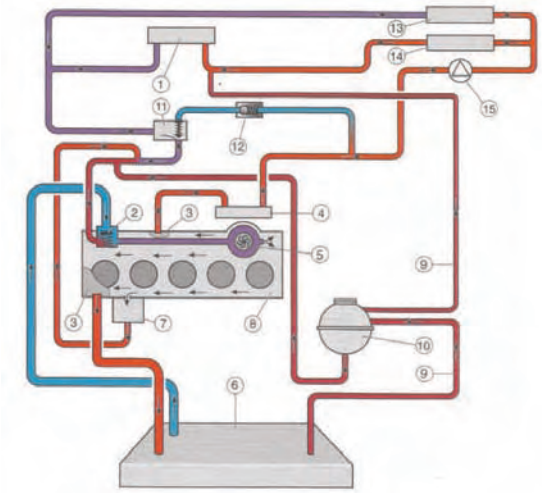

Fig. 9. The standard engine cooling system 2.5 TDI in the car utilitarian VW Transporter T5 [8]: 1 – first heat exchanger, 2 – coolant thermostat, 3 – cylinder head, 4 – exhaust gas recirculation cooler, 5 – coolant pump, 6 – cooler, 7 – oil cooler, 8 – cylinder block, 9 – vent pipe, 10 – expansion tank, 11 – heater coolant shut-off valve N279, 12 – non-return valve, 13 – second heat exchanger, 14 – supplementary coolant heater, 15 – recirculation pump

Engine cooling liquid, as in the case of installation in a vehicle, is located in a closed circuit. To its warm up two heaters with power of 10 kW are used. The controller that has been used is PID type. This controller is designed to establish and maintain a constant temperature of the cooling liquid in variable operating conditions of the engine. Liquid refrigerant for cooling water is supplied from the water mains. The water flows through the heat exchanger and thereby reduces the

temperature of the coolant. In the control panel, the engine can set the desired temperature of the liquid, which established after some time. Liquid temperature after stabilization of the thermal state should be approximately equal to the temperature of the oil. In the system before the conversion, the value of the coolant temperature can be adjusted significantly in a short period of time, but the time to stabilize the thermal state of the engine was relatively long.

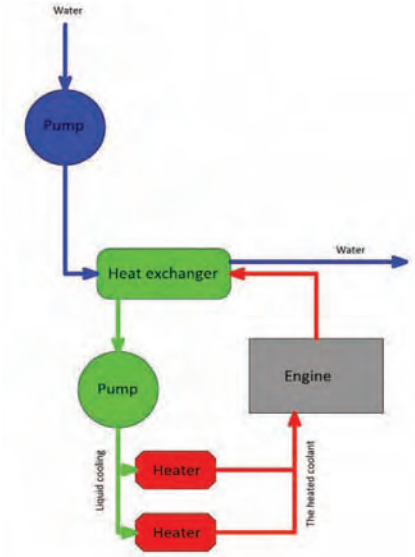

Fig. 10. Diagram of the primary control system of coolant temperature engine on a test bench

The lubrication system does not differ in the construction of the standard system used in the motor mounted in vehicles. The only differences are the temperature sensor in the oil sump and the manometer measures the pressure of the oil injected into the system behind the oil pump.

To the oil supply system are used the warp anchor holes shown in Figure 11, through which flows the oil to various bearings engine, and a transmission gear.

Return oil sump of the engine head is held primarily by the gear shown in Figure 12, and return channels in Figure 13.

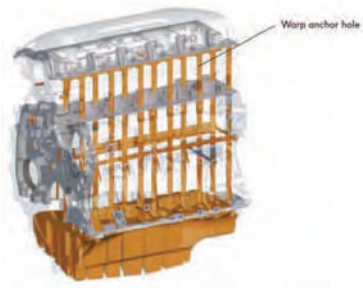

Fig. 11. Oil system power [8]

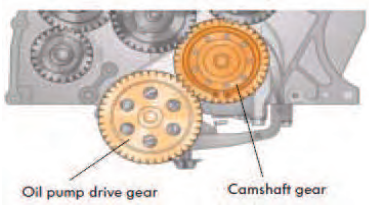

Fig. 12. Oil pump drive [8]

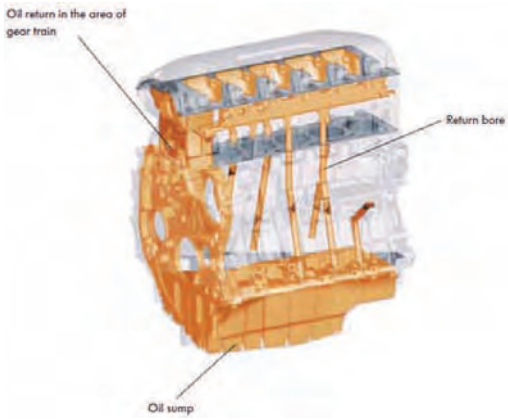

Fig. 13. Lubrication oil return [8]

5. The tests results of engine friction losses

Examining resistance of the internal combustion engine, in addition to frictional losses in the bearings of the crankshaft and a group of the piston rings and cylinder-piston unit were measured, also the friction loss due to charge exchange in the cylinder and air compression by the piston drive system in the oil pump.

The measurements were made for the following conditions:

– engine speed 800-2800 rpm,
– oil temperature 55-95°C.

The results torque and oil pressure were averaged and summarized in the graphs below.

Figure 14 presents a summary of the losses resistance engine resulting from the study for various temperatures of lubricating oil, which are dependent on engine speed. On the loss of resistance engine consists of friction losses in the group piston – rings – cylinder and crankset. In addition, exchange losses in the combustion chamber. Then there are also losses of the drive mechanism of the timing, oil pump and the inertia force of the piston.

The results obtained clearly map the course of the loss resistance of the motor during testing. It follows that the thermal state of the engine lubricating oil has a significant effect on friction loss.

From the graph in Figure 15 it can be concluded that the higher the oil temperature, the smaller is the mechanical resistance in a combustion engine. The reason for this is the lower viscosity of the lubricating oil. It is important to prevent excessive oil temperature, since too low viscosity can result in the direct cooperation of the moving parts up friction, and thus the mixed friction.

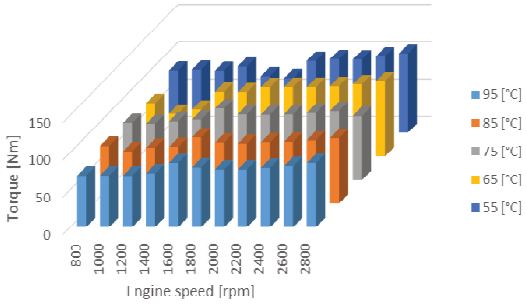

Fig. 14. The results of the motion resistance as a function of engine oil temperature

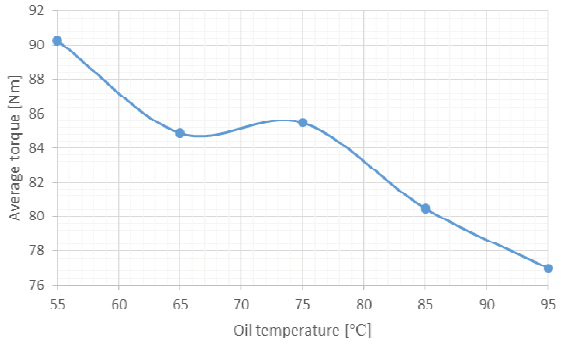

Fig. 15. Averaged torque curve as a function of oil temperature

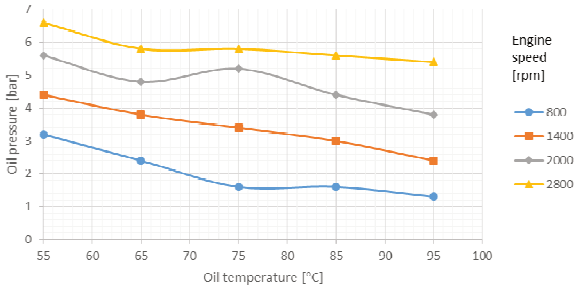

Fig. 16. The oil pressure as a function of oil temperature for different speeds

Also, the resistance losses of the engine depends the phenomenon of charge exchange. With the increase of the rotational speed increase the resistance losses of the motor.

Analyzing the diagram in Figure 16, it can be concluded that the temperature of the oil affects the oil pressure in the lubrication system. At a lower temperature of the lubricating medium pressure increases. The reason for this phenomenon is the viscosity of the oil. At lower temperatures, when the oil has a higher viscosity of the oil pressure must be increased in order to ensure the effectiveness of lubrication in friction. At higher temperatures the viscosity of oil decreases and the pressure which is necessary to deliver oil to the friction in the required amount is smaller.

6. Conclusions

The performed research lead to formulating the following conclusions:

- oil temperature measured in the oil sump is reliable in the description of the processes of friction,
- oil temperature has a big influence on the friction loss and other motion resistance in engine. This significantly improves the viscosity of lubricating oil, which decreases under the influence of temperature rise. The higher the viscosity of the oil is, the higher the friction loss in an internal combustion engine,
- oil viscosity is important for the operation of the oil pump. In case of a decrease in viscosity pump generates a higher pressure due to the lower resistance of the oil,
- engine coolant temperature and oil temperature regulate the engine that affects the friction losses,
- increasing speed is followed by rapid heating of the engine and oil. This is due to a higher relative velocity of the moving parts of the engine and as a result of the diffusion of higher temperature,
- increasing the speed at a relatively constant temperature of the oil increases the loss of mechanical resistance,
- for examineted relatively narrow temperature range of oil big changes in the total friction losses were observed. Purposeful independent control of the coolant temperature and oil temperature could significantly contribute to improving the mechanical efficiency of the internal combustion engine under very low loads and speeds.

Bibliography

[1] DEUSS, T., EHNIS, H., ROSE, R., KÜNZEL, R. Reibleistungsmessungen am Befeuerten Dieselmotor-Einfluss von Kolbenschaftbeschichtungen, *MTZ.* 2011, **4**.

[2] GOLLOCH, R. Untersuchungen zur Tribologie eines Dieselmotors im Bereich Kolbenring/Zylinderlaufbuchse, *VDI Verlag* GmbH, 2001, **12**, 473.

[3] ISKRA, A., KAŁUŻNY, J., BABIAK, M. Charakterystyka biegu jałowego w fazie nagrzewania silnika. *Wydawnictwo Politechniki Krakowskiej*, 2008.

[4] ISKRA, A., KAŁUŻNY, J., BABIAK, M. Wpływ temperatury cieczy chłodzącej i oleju na straty tarcia w tłokowym silniku spalinowym, *Czasopismo Techniczne*. 2012, 3-M, **8**, 109.

[5] ISKRA, A., WRÓBLEWSKI, E., BABIAK, M. Układ stabilizacji i regulacji stanu cieplnego silnika spalinowego w warunkach hamowni silnikowej, *Logistyka.* 2015, **3**, 1858-1864.

[6] KAŁUŻNY, J. Wpływ kształtu powierzchni nośnej tłoka na parametry filmu olejowego pokrywającego gładź cylindra. Praca doktorska, *Wydawnictwo Politechniki Poznańskiej*, Poznań, 2004.

[7] WRÓBLEWSKI, E., ISKRA, A., BABIAK, M. The influence of the thermal state of lubricating oil for friction in combustion engine. *Journal of Mechanical and Transport Engineering*. 2016, **68**(2).

[8] Zeszyt do samodzielnego kształcenia nr 305, Silnik 2,5 l R5 TDI.

Emil Wróblewski, MEng. – Faculty of Machines and Transport at Poznan University of Technology.

e-mail: *emil.z.wroblewski@doctorate.put.poznan.pl*

Szymon Finke, MEng. – Faculty of Machines and Transport at Poznan University of Technology.

e-mail: *szymon.a.finke@doctorate.put.poznan.pl*

Article citation info:
WRÓBLEWSKI, A. Multi-criteria fuel system optimization with an electronic control unit. *Combustion Engines*. 2017, **168**(1), 51-55. DOI: 10.19206/CE-2017-108

Aleksander WRÓBLEWSKI

CE-2017-108

Multi-criteria fuel system optimization with an electronic control unit

This paper presents the results of the multi-criteria synthesis of a diesel engine fuel system using the optimization method. The optimization criteria, functional restrictions and quality criteria have been selected. The efficiency of the proposed method was demonstrated using the example of a diesel engine with the Common Rail system.

Key words: *diesel engine, fuel system, solenoid injection, optimization*

1. Introduction

In technical design practice, various methods of optimization are frequently applied. First of all, approaches are verified on the basis of solving a simple problem – carrying out a series of calculations in order to determine system indicators for various single parameters [1, 2, 6, 13].

The economic aspects of applying virtual experiments are obvious. They allow combinations of parameters to be selected, a great number (up to 4,000 and more) of experiments to be performed and changes in parameters (pressure, displacement, temperatures) to be measured, which is sometimes not possible in practice. As a result, it helps to reduce the research time and design costs and to find optimal parameters for the entire object or its individual system.

The efficiency of the optimization solution depends on the reliability of the mathematical models applied and the dependencies between the variables. This article presents the results of an experiment obtained while determining the optimum parameters of the Common Rail system. Characteristics of most common mathematical models of this system are investigated, among others in [2, 3, 5, 8, 9, 10].

However, it should be indicated that no optimization method eliminates the human factor, i.e. so-called "expert advice". Expert advice plays a decisive role when choosing parameters, constraints and criteria, but also when selecting the result of the optimization process. Numerous studies have been published on the subject of optimization of the direct fuel injection system. Among them, the following studies can be distinguished [12, 14], where the authors apply methods based on constructing, in each point of the circuit, a functional model of the injection process and determining the search vector based on its analysis. To obtain regression equations, the theory of experiment design is used, making it possible to find the search direction with a limited number of calculations. In the complex "Wtrysk" [*Injection*] program [13], the method of optimizing system processes is formalized and reduced to the application of constrained non-linear multivariable function programming, including the method of penalty functions. As specified by the authors [10], since non-linear programming theory does not provide an answer to the question of what methods are better; several procedures should sometimes be used in parallel. Unlike the above-mentioned authors, who used vector analysis and regression equations, the study [11] uses linear models of the system in a multi-parameter and multi-criteria optimization algorithm. Based on the models or using computational and analytical methods for examining the impact of system parameters on the operating process factors, it is possible to choose and to justify the indirect criteria.

2. The aim and scope of the study, the object of research

The aim of the study is to optimize the injection process in a fuel system. To achieve this aim, an optimization method has been suggested, parameters significant for the injection process have been selected and functional constraints and quality criteria have been determined.

The object of the research is the injection process in the Common Rail (CR) fuel system. The system is equipped with an injector with a solenoid valve. The principle and characteristics of the system operation have been described in [7].

The operating principles of the injection system allow to formulate separate significant optimization tasks for the injector. After such a separation, the model (including the injector, fuel accumulator and fuel tube) can provide a basis for an efficient multi-parameter and multi-criteria optimization algorithm.

3. Optimization method

The modern method proposed by Sobol and Statnikov [15] was used for optimization purposes. This is a method based on computational scanning of the parameter space for the designed objects, which can be reduced to three stages:

Stage 1– constructing test tables. This stage does not provide for human participation. The procedure starts with N test points. The value of all criteria is determined at each point. Each criterion is composed of the test table. Tables are an analogue of statistical variation series.

Stage 2– choice of criteria constraints. This stage is carried out through the computer-designer dialogue. When reviewing each of the tables, the designer must set a constraint for each of the criteria.

Stage 3– checking the completeness of acceptable points. The stage is performed automatically.

3.1. Selection of sampling points

To date, the most popular method is one in which regular grids are used for the review of the multi-dimensional cube. However, uniform scanning of a multi-dimensional cube is optimal only in a one-dimensional case, at n=1 for the space. Regular grids are unsatisfactory at n=2. A precise model of the technical object contains a high number of

parameters in its description. It is known *a priori* that a considerable number of these parameters do not have any significant effect on the process. In an extreme situation, which often occurs, only one parameter has a significant impact, while others are negligible for a given criterion.

The distribution of N sampling points in which each of the parameters makes an evenly distributed sequence of N points at the given section should be considered optimal. Regular grids do not satisfy this requirement. Figure 1 presents a regular grid composed of N = 16 points. Points are evenly distributed. One point of the grid is placed in each of N small squares. The flaw of such a distribution is obvious. Evaluating the f(x1, x2) function, which is strictly correlated to one argument, we will obtain only four various values. In a multi-dimensional case, regular grids can provide even worse results, since the information loss when calculating f(x1…xn) increases. Determination of partial decisions for this problem will be possible through the use of random generators.

In this study [15], the authors propose a quite efficient distribution of points in space which solves this problem. As in the previous case, in the two-dimensional distribution composed of N = 16 points, one point is placed in each small square (Fig. 1). However, in this case, while calculating the function in grid points, we will receive 16 weights, which will provide a better view of the scale of function transformations. An optimum sequence always contains N = 2p points, where p – total positive number. An additional advantage of such a sequence is the possibility to double the number of sampling points.

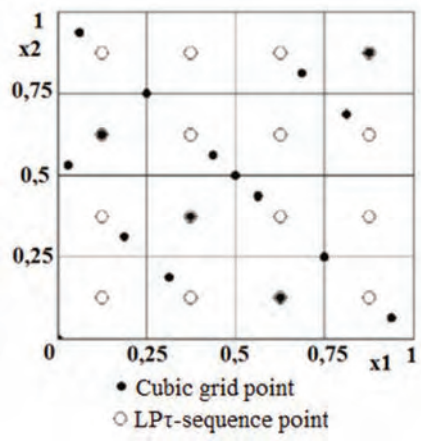

Fig. 1. Regular and improved grid at n = 2 (N = 16)

In [15], such a distribution is referred to as LPτ-sequence. To calculate the LPτ-sequence, the authors of this paper applied the following arithmetic algorithm. Using the numerator table, we can define r_j (l), for which m = 1 + [lni/ln2] is calculated after a set point number and then at each point and for each parameter j = 1, 2, ..., n is defined by a dimensionless value. The value of the parameter is calculated from the following equation:

$$q_{i,j} = \sum_{k=1}^{m} 2^{-k+1} \left\{ \frac{1}{2} \sum_{k=1}^{m} [2\{i2^{-l}\}] \cdot \left[2 \left\{ r_j^{(l)} 2^{k-1-l} \right\} \right] \right\} \quad (1)$$

In equations [z] – the entire z, {z} – a fraction of z. It is possible to determine the value of the j-th parameter in the i-th point of the n-dimensional space using a variable multidimensional cube with an edge of 1. Such an algorithm is integrated into the program for fuel system calculations.

3.2. Choice of injector parameters

Let us justify the choice of parameters and the scope of their changes. As it is known from [1–3], the process of injection in systems equipped with electronic control is highly affected by the following factors: – displacement of the injector elements; – propagation of pressure and deformation waves through fuel channels and injector elements; – spring vibrations; – physical phenomena accompanying the flow of fuel along small diameter channels (nozzle orifices, orifices of the control chamber); – fuel flow properties in low pressure tubes and related effects of connected masses, contacts and others.

By applying these factors, an improvement of the system operation can be expected. Previously conducted computational and experimental studies have made it possible to distinguish the basic structural and adjustment parameters of the system. Those parameters are shown in Table 1. These are initial set points situated in the centre of a n-dimensional parallelepiped. The choice of allowable fluctuation ranges for each of the parameters is made taking into account constraints related to the structure, production or operating conditions of the fuel system.

For instance, the value of the displacement of the valve cannot be lower than 0.025 mm (protection of the minimum distance between the magnet and the valve) on one side and more than 0.075 mm on the other (this is related to reducing the force while increasing the distance as a result of the operation). The minimum path of the needle and the stem is 0.125 mm. This reduction is related to the need to minimize the effect of the feasible cross-section area of the nozzle on the change of the fuel pressure also related to stem operation characteristics [5]. Within the ranges of the examined circulation, the transformation of each parameter from Table 1 was ± (40–50)%. This permits to investigate a wide scope of the multi-dimensional space and determines the direction for searching the optimum. Using the LPτ-sequence generator, sampling points were obtained and samples were marked in the tables. For the previous scanning of parameter space, 128 points were received.

Table 1. Fuel system parameters

1	Parameter	unit	value
2	Valve diameter	mm	1.3
3	Valve displacement	mm	0.05
4	Spring stiffness coefficient	N/mm	50
5	Valve socket angle	degree	100
6	Cross-section area of the intake orifice	mm^2	0.034
7	Cross-section area of the outlet orifice	mm^2	0.055
8	Piston diameter	mm	3.8
9	Piston length	mm	76
10	Diameter of the needle closing device	mm	1.6
11	Needle displacement	mm	0.25
12	Initial needle displacement pressure	MPa	5
13	Tube length	mm	220
14	Internal diameter of the tube	mm	1.5

3.3. Determining functional constraints

To determine the constraints while formulating the initial data to solve the problem of searching for optimum parameters, functional restrictions should be included. For the injector, functional constraints include the dependencies between the following parameters: –stem diameter exceeds the nozzle needle diameter, which is assumed at the constant level of 3.5 mm; – the feasible cross-section area of the inlet orifice of the control chamber is smaller than the effective cross-section area of the outlet orifice of this chamber; – the diameter of the needle closing device is smaller than needle diameter; – the speed of injector elements is reduced by hitting the support – run limiters. While solving the optimization, functional constraints can be taken into account in two ways.

The first method – after carrying out calculations, permits excluding from the analysis those points in which the value of the parameters is feasible. The second method – at the stage of formulating initial data the constraints indicated are taken into account by setting k1, k2, k3 coefficients, which involves dependencies of the above-mentioned parameters. The latter method is considered to be the best. It makes it possible to obtain a larger number of points for the criteria evaluation and reduces the time for solving the optimization.

3.4. Choice of quality criteria

Pursuant to reports by other authors (e.g. [10]), two decisive quality criteria should be ultimately selected for the injector – maximum injection pressure Pw and Qz fuel doses for control purposes. At the same time, Pw pressure should be at its maximum value. Let us explain the choice of the Qz criterion. In the control chamber, the fuel pressure is 25-150 MPa. The injection process takes place when the fuel is discharged from the control chamber to the fuel return system. Therefore, a lower volume of fuel is discharged with the lowest energy expense required for driving the fuel pump. However, there is a minimum value of Qz required for the safety of electromagnet cooling.

To obtain multiple Pareto points, which represent a single-dimensional variability on a plane, it is convenient for both criteria to aim towards the minimum, while maintaining a non-dimensional form. Let us introduce the following criteria: – Kp = Rz/Pw, where Rz – fuel pressure in the accumulator; – Kq = Qz/Qc, where Qc – fuel dose. Through the introduction of those criteria it is possible to evaluate the relative fuel rate on fuel control and to compare the Pw value with the Rz pressure level.

In problems with two criteria $\Phi 1 \rightarrow \min$, $\Phi 2 \rightarrow \min$, the decision consists in the so-called Pareto multitude of parameters; each such set is a solution to a single-criterion problem $\Phi 1 \rightarrow \min$ at $\Phi 2 = \text{const}$. Each set of parameters allowed after functional constraints (referred to as effective ones), corresponds to a point on a criteria plane (Kp, Kq) (Fig. 2). Pareto points on the criteria plane (Fig. 2) will correspond to the compromise curve section.

4. Optimization results

Let us demonstrate the final stage of the search for an optimum relation between CR injector parameters. As a result of scanning, out of the multitude of 128 acceptable points, 24 proved to be effective. Figure 2 shows the location of those points on the criteria plane (Kp, Kq). It can be seen that in each of those points, the efficiency of the injection process according to the criteria indicated (Kp = 0.912-0.941; Kq = 0.178-0.137) significantly surges in comparison to point 1 (Kp = 1.08; Kq = 0.447), which corresponds to the initial set of injector parameters (Table 1).

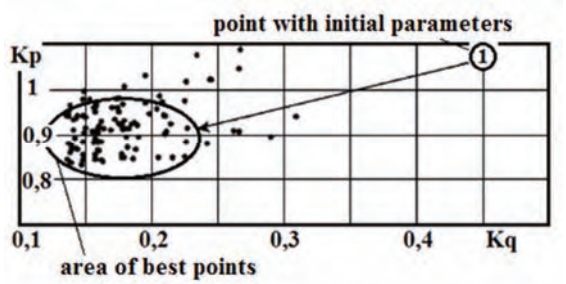

Fig. 2. Fragment of a distribution of sampling points on the criteria plane (Kp; Kq)

The compromise curve features three points, which are located on the by-passing curve A (Fig. 3) limited with lines D and E. The numbers of those points are – 61, 121, 106, and the part of the curve joining these points is the compromise confidence curve. Points № 48 and № 127 are also located on curve A, but curve A is not a compromise curve to the right of point № 106. Indeed, on a part of curve A separated with a dotted line there are points for which two criteria vary either up to the maximum or to the minimum side. For instance, for the minimum value of criterion Kq = 0.2, a point of intersection of curve A with the indicated weight of Kq should be found to obtain the best quality.

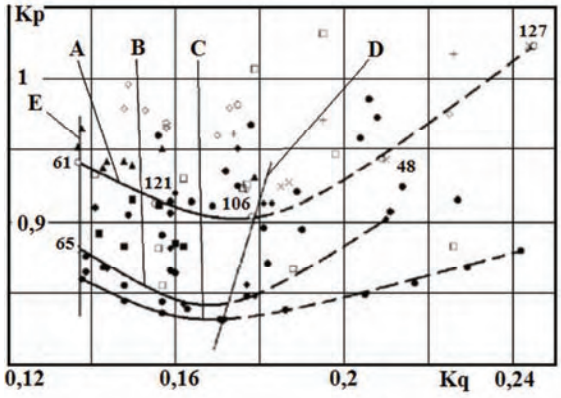

Fig. 3. Sampling points and compromise confidence curves on the criteria plane (Kp; Kq)

In point № 61, seven parameters are located near the centre of the scanned area, two parameters assume the maximum assumed values and two assume the minimum values. In point № 106, nine out of twelve parameters are located in the centre, two acquire the minimum value and one acquires the maximum. In point № 121, the number of mean values is eight, two assume the minimum and two assume the maximum values. In the obtained number of solutions, there exists an isolated point № 65 (Fig. 3). Ac-

cording to the quality criteria, this is the best point. However, five parameters of point № 65 assume the minimum acceptable value. The pin spring tensile pressure is 1.57 MPa, and the dimension of the valve range is 0.864 mm. Starting from the recommendation [15], also in view of the experience of the authors of the solution of this multi-criterion problem, this number would have to be increased up to 2-4 times, which will help to increase the efficiency of the optimization.

Partially, a solution to the problem is provided by the consistent optimization algorithm, the application of which to this problem is reduced to further refinement of the compromise curve. Additionally, the area of parameters in the vicinity of Pareto points № 61, 106 and 121 should be scanned. The centre of the new parallelepiped features the indicated Pareto point, the parameters of which can change within a narrow range of ± 15 %. In such a case, the volume of the scanned perimeter is reduced 106 times, and the number of sampling points, defined with the use of the LPτ-sequence generator, can be reduced to 16.

As a result of such refinement, many new allowable points have been obtained, located below A curve (Fig. 3), and a new compromise curve B was developed. It is interesting to note that point № 65 obtained during the previous scanning is situated on curve B and limits it on the left. Therefore, the procedure for refining the compromise curve should be repeated once again. At the same time, the area of points located in curve B, limited with lines D and E, should be scanned. The refinement results in curve C. The distance between curves B and C is slight, which indicates that the decision on abandoning the refinement of the compromise curve can be made.

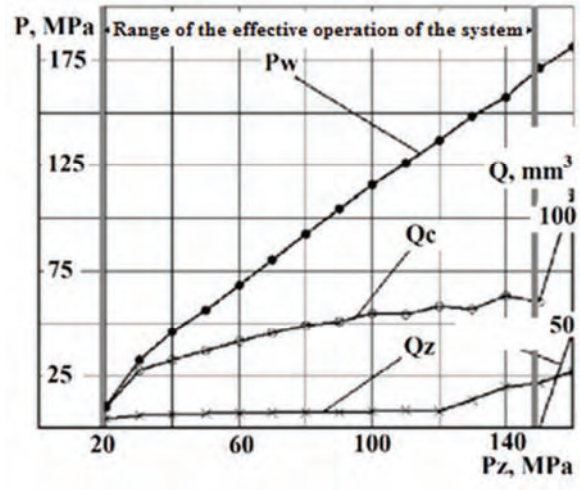

Fig. 4. Relation between injection parameters and pressure Rz for the system with an optimized injector

The obtained results indicate that curve A contains points with optimal parameters. The final point of the optimization solution is determination of the perimeter for the system operation with an optimized injector at pressure Rz change. Therefore, the values of parameters obtained for Pareto points on curve C were included in calculations, by setting the value of Rz, thus enabling calculation of dependencies between Pw, Qc, Qz and Rz. The maximum possible Rz was determined by the presence of unnecessary fuel rate Qp at the nozzle in the final phase of the injection. The obtained results make it possible to claim that the optimized system protects the fuel injection at minimum pressure of Rz = 20 MPa, and the maximum pressure of R = 150 MPa (Fig. 4).

The performed optimization of the injector permits increasing the injection pressure Pw in comparison to the pressure in the accumulator Rz by 15 % (Fig. 5).

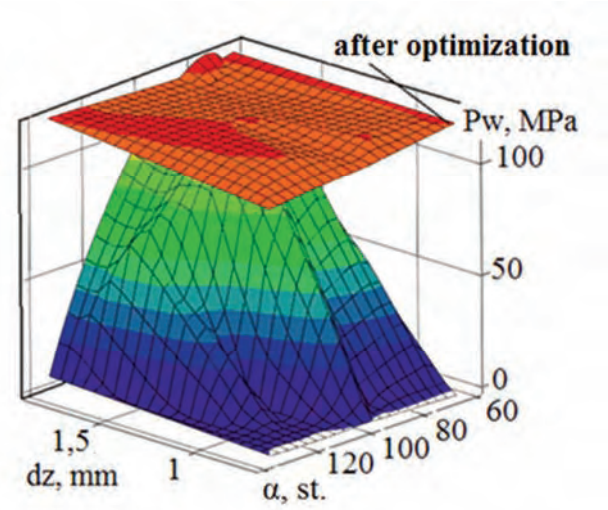

Fig. 5. The relation between injection pressure Pw, dz diameter and the injector valve socket angle (Pz = 100 MPa)

For all calculation points in the optimization process, a single-phase injection was set with electric pulse parameters (maximum value of current in the solenoid 17.5 A, and during the steady period 10 A, duration of the electric signal 1 ms).

5. Conclusions

1. A new method for multi-criteria optimization of the fuel system with an electronic control unit has been developed. It is based on computer scanning of the parameter change perimeter and construction of Pareto compromise curves.
2. The major parameters of the fuel system with the most significant impact on the injection process (Table 1) have been determined. Functional constraints have been formulated, along with the quality criteria – maximum injection pressure Pw and fuel rate on fuel control Qz, which enables evaluation of the injection process efficiency.
3. The fuel system optimization makes it possible to increase the maximum injection pressure Pw in comparison to the pressure level in Rz accumulator by 15% (Rz exceeds Pw in the initial system) and to achieve two-fold reduction of the fuel rate on fuel control.
4. The range of effective operation of the system in relation to pressure Rz has been determined. The system protects fuel injection at Rz pressure changes ranging from 20 to 150 MPa.

Nomenclature

CR common rail
LPτ sequence points in a multi-dimensional case
Pw maximum injection pressure
Pz fuel pressure in the accumulator
Qc fuel dose of injection
Qz fuel dose for control purposes
Kq, Kp quality criteria

Bibliography

[1] BIANCHINI, G.M., PELLONI, P., FILICORI, F., VANNINI, G. Optimization of solenoid valve behavior in common-rail injection systems. *Proc. of the SAE* 2000 World Congress, 2000-01-2042.

[2] BORCHSENIUS, F. STEGEMANN, D., GEBHARDT, X. Simulation of diesel common rail injection systems. *MTZ*. 2010, **6**, 42-45.

[3] COPPO, M., DONGIOVANNI, C., NEGRI, C. Numerical analysis and experimental investigation of a common rail-type diesel injector. *Journal of Engineering for Gas Turbines and Power*. 2004, **126**(4), 874-885.

[4] HU, Q., LOU, D., TAN, P., HU, Z. et al. Study on fuel injection parameters optimization for common rail diesel engine fueled with B20 biodiesel. *SAE Technical Paper*. 2014, 2014-01-2655,.

[5] Seykens X.L.J., Somers L.M.T., Baert R.S.G. Detailed modeling of common rail fuel injection process. *MECCA*, III. 2005, 30-39.

[6] STATNIKOV, R., BORDETSKY, A., STATNIKOV, A. Multicriteria analysis of real-life engineering optimization problems: statement and solutions. Nonlinear Analisys. 2005, **63**, e685-e696.

[7] Układ wtryskowy Common Rail Bosch. *WKiŁ*, Warszawa 2000.

[8] ВРУБЛЕВСКИЙ, А.Н., ГРИГОРЬЕВ, А.Л., ГРИЦЮК, А.В., ДЕНИСОВ, А.В.,. ЩЕРБАКОВ, Г.А. Особенности математического моделирования гидромеханических процессов ЭГФ. *ДВС*. 2007, **1**, 44-52.

[9] ВРУБЛЕВСКИЙ, А.Н. Математическая модель движения элементов и течения топлива в полостях низкого давления электрогидравлической форсунки. *Автомобильный транспорт – Харьков: ХНАДУ*. 2008, **22**, 109-117.

[10] ГРЕХОВ, Л.В., ИВАЩЕНКО, Н.А., МАРКОВ, В.А. Топливная аппаратура и системы управления дизелей. *Легион – Автодата*, Москва 2004.

[11] ГРИГОР'ЄВ, О.Л., Розробка універсальних методів гідродинамічного розрахунку, динамічного аналізу та оптимізаційного синтезу основних елементів паливної апаратури дизелів. Автореферат дис. докт. техн. наук. Харків. *НТУ* «ХПІ». 2004, **36**.

[12] ГОРБАНЕВСКИЙ, В.Е., КИСЛОВ, В.Г., БАШИРОВ, Р.М. и др. Дизельная топливная аппаратура: Оптимизация процесса впрыска, долговечность деталей и пар трения. *МГТУ*. Москва 1996

[13] КУЛЕШОВ, А.С., ГРЕХОВ, Л.В. Математическое моделирование и компьютерная оптимизация топливоподачи и рабочих процессов двигателей внутреннего сгорания. М.: изд-во *МГТУ*. 2000, **64**.

[14] МОРОЗОВ, Ю.В. Реализация заданных характеристик впрыскивания топлива путем оптимизации конструктивно-регулировочных параметров топливной аппаратуры: Автореферат дисс… докт. техн. наук. Харьков. *ХарГАЖТ*. 1998, **32**.

[15] СОБОЛЬ, И.М. СТАТНИКОВ, Р.Б. Выбор оптимальных параметров в задачах со многими критериями. *Наука*. Москва 1985.

Aleksander Wróblewski, DSc., DEng. – Faculty of Technical Sciences at University of Warmia and Mazury in Olsztyn.

e-mail: *Aleksander.Wroblewski@uwm.edu.pl*

Article citation info:
OSIPOWICZ, T., ABRAMEK, K.F. Diagnosing methods common rail fuel injectors. *Combustion Engines*. 2017, **168**(1), 56-61. DOI: 10.19206/CE-2017-109

Tomasz OSIPOWICZ
Karol Franciszek ABRAMEK

CE-2017-109

Diagnosing methods common rail fuel injectors

Article describes diagnose and research methods Common Rail system fuel injectors. Profesional diagnose modern fuel injectors is very dificult procedure. Basic theirs work parameter influencing on correctly work parameters are magnitude injection and return dosages by definite pressures prevailing in system and injetion times. Sometimes dosages during diagnose by coordinate task and actual fuel injector are correct but engine work is not proper. So that during diagnose should extend tests procedure in range varie work conditions. Fuel injectors work characteristics are one of method researching in whole range work. During researches has been used Continental fuel injector.

Key words: *CI engine, Common Rail system, fuel injector, high and low pressure system, engine diagnose, fuel combustion*

1. Introduction

Common Rail fuel injection system is very compound diagnosing process. These system assembles with many cooperating elements. There are apart from injection, intake, exhaust systems and everything is steered by engine controller with sensors and actuators. These whole system controls CI – engine work. When there are starting faults, diagnostic process begins with engine computer test, which not only rely on memory errors but actual parameters (if the engine work). It happens often that engine during vehicle test doesn't work, then one should suggest memory faults of controller. If actual parameters analysis and memory errors indicate that injection system is defected it should be whole low and high pressure system elements checked. One of the most exposes on damages whole system element is fuel injector. Its main tasks are spray and distribute fuel in combustion chamber at a given work moment. Injector nozzle influences on spraying and distributing quality. If injections holes are damage or pollute, work quality is deteriorated. Toxic substances in fumes increasing and whole combustion process is disrupt. The second factor influences on combustion process are injection dosages. There are injection and return dosages main work parameters of fuel injector. If these factors change outside of correct limits injector is fault. On these influence use precision elements and rest elements (springs, pads, inner sealers). The most reasons to speeding up use these elements are pollution and damp in fuel. So fuel injection diagnostic process should be investigate as quality and quantity.

2. Analysis modern fuel injectors construction solutions

There are known many varies classification modern Common Rail system fuel injectors [4]. But for something research, diagnose and repair possibility there is simply divide it as repairable and not repairable. Every fuel injector could be diagnose, but unfortunately on account of repair technology and original spare parts lack not every could be repair. It could be use fuel injectors producers like Bosch, Delphi, Denso and Continental in motor vehicles [2]. Bosch, Denso and Delphi companies produce electromagnetic and piezoelectric injectors and Continental company only piezoelectric [6]. It could be repair practically all electromagnetic injectors. Bosch fuel injectors generations 1.0, 2.0, 2.1, 2.2 and Delphi electromagnetic there are original spare parts and repair technology, injectors Bosch generations 2.16, 2.5 there are not original repair technology and spare parts but these injectors could be disassembly, clean, to seal and assembly. The same situation is with electromagnetic Denso injectors. There is no repair technology and original spare parts but it could be improve technical conditions. It is differently with piezoelectric injectors [5]. Delphi and Denso are not repairable, with Bosch it is hard to repair because of getting air in, and with Continental is a possibility to repair but difficult to regulate. There are original spare parts to Continental fuel injectors. Figure 1 presents piezoelectric Bosch fuel injectors.

Fig. 1. Piezoelectric Bosch fuel injectors

Piezoelectric Bosch fuel injectors are signed with numbers 0445115xxx, 0445116xxx or 0445117xxx. There are various generations 3.1; 3.2 and 3.3. This type of injectors are not repairable. Figure 2 presents disassembly on spare parts piezoelectric Bosch fuel injector.

Figure 3 presents electromagnetic Bosch fuel injector. These type of injectors are marked with number 0445110xxx CRI (cars) and 0445120xxx CRIN (lorries).

Fig. 2. Piezoelectric Bosch fuel injector disassemble on spare parts

Fig. 3. Electromagnetic Bosch fuel injector

Figure 4 presents electromagnetic Bosch fuel injector generation 2.1 disassembly on spare parts. CRI and CRIN injectors are built very similar. The differences are in magnitude of injection dosages. CRIN fuel injectors have larger on account of bigger engines. The most faulty elements are precision vapours on injector needle and steering piston. The leakage magnitude influence on injection and return dosages[1]. Fuel injector with worn out steering piston and nozzle is hard to regulate.

Figure 5 shows Continental VDO Siemens fuel injector. This type of injectors are very hard to regulate during folding up. The regulation comes down to screw the valve and piezoelectric element with appropriate torque. The range of correct torque is very small that's why these type of injectors very hard to regulate.

Figures 6 and 7 present electromagnetic and piezoelectric Denso fuel injectors. There are not many piezoelectric Denso fuel injectors in CI – engines. The most often it can be meet electromagnetic (Fig. 6B). These type of electromagnetic injectors are very similar to Bosch. It is easy to disassemble and repair in spite of lack of original spare parts.

Fig. 4. Electromagnetic Bosch fuel injector gen. 2.1 disassemble on spare parts

A B

Fig. 5. A – Piezoelectric Continental VDO Siemens fuel injectors, B – Continental fuel injector disassembly on spare parts

A B

Fig. 6. Denso fuel injectors A – piezoelectric, B – electromagnetic

Fig. 7. Electromagnetic Denso fuel injector disassembly on spare parts

Figure 8 presents electromagnetic Delphi fuel injector. These injector is very fast because of light valve. This is very important to create more dosages during one work cycle. Negative feature is easy valve damages. This construction is very light and delicate. Delphi injection systems need very good fuel quality and to clean whole system very often.

A B

Fig. 8. A – electromagnetic Delphi fuel injectors, B – electromagnetic Delphi fuel injector disassembly on spare parts

Bosch and Denso electromagnetic fuel injectors are similarly. There is possibility to regulate and repair both of them. The same situation is with electromagnetic Delphi injectors. Considerable difference between these injectors is construction. Electromagnetic Delphi fuel injector has very light steering valve therefore has shorter time of injection delay. Different situation is with piezoelectric fuel injectors. There is no technology to repair them. It is possible only to testing and eventually cleaning. Piezoelectric elements are very sensitive for work condition. It is very easy to damage them. For example piezoelectric Bosch fuel injectors get air in because of wrong engine dismantling. Continental fuel injectors are very easy to disassemble than clean and put together. The problem with them is very hard to regulate injection and return dosages because of precision screw in valve and piezoelectric element. Piezoelectric injectors have very short injection delay. Thanks to this feature generate more dosages on one engine work cycle. To high dosages divergence cause wrong engine work.

3. Diagnosing methods modern fuel injectors

Fuel injectors research process is looked into in two aspects. When the vehicle engine work or couldn't be turn on. If the engine works it is checked return dosages and actual engine parameters by using engine diagnostic scanner. If the actual parameters indicates not correct working fuel injectors, it is necessary to dismount and research on test bench. By not working vehicle it can be only read faults on engine diagnostic scanner. When faulty indicate on fuel injectors they are dismounted and test. There is very important to check every injection and return dosages. There are many instances that injectors on normal research test worked correctly but engine didn't work good and diagnose indicate on fuel injectors [3]. Then should make detailed injector research. It relies on making injector work characteristics. There are analytical methods of researching fuel injectors. These methods relies on calculating the magnitudes of injection dosages. These approaches are not correct because it is impossible to calculate and forecast injector work parameters. Fuel injector is the physical object compound with many elements and works in huge range of pressures and injection times. During defect faulty works only separate area very often. To find faulty area it is necessary to make injector work characteristic for example initial dosages. It has been researched engine with Continental injectors. There was a problem with irregular engine work between 1300–1800 min^{-1}. Engine diagnose indicates on fuel injectors failure. The standard test of fuel injectors was the first stage researches (Fig. 9). The results indicated that injectors were correctly therefore it has been made fuel injectors work test for initial dosages (Fig. 10–20). Initial dosages occur for very short injection time about 200 μs for various engine work conditions. Improper value causes deteriorating of combustion process. Figures shows that first injector had considerable higher dosages of the rest. It is noticeable on Fig. 12–16. Than it has been made two injectors work characteristics but only in initial and neutral gear dosages area (Fig. 21 and 22). Researches show that first injector had increased dosages values especially in range 200–400 μs. There is noticeable decrease of dosages values above injection time 450 μs particularly for injection pressures 45–55 MPa.

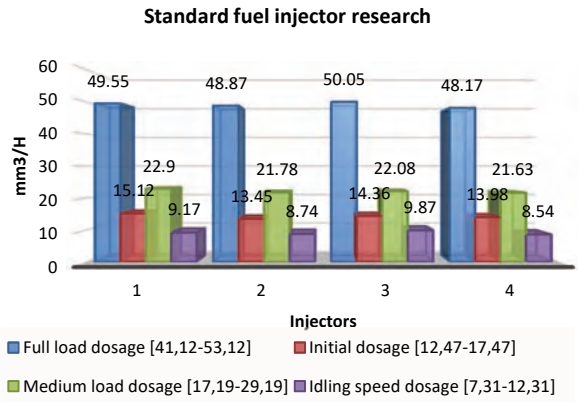

Fig. 9. Results of standard fuel injectors research

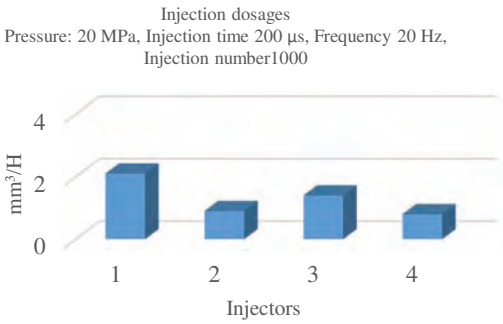

Fig. 10. Injector work test results. Pressure 20 MPa, injection time 200 µs

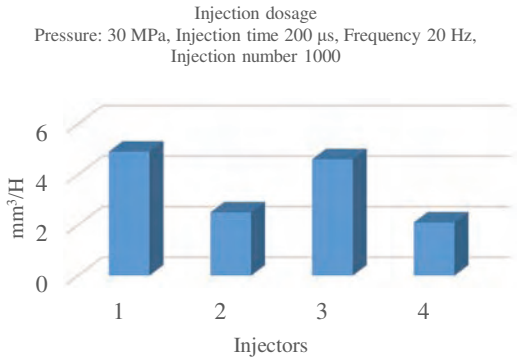

Fig. 11. Injector work test results. Pressure 30 MPa, injection time 200 µs

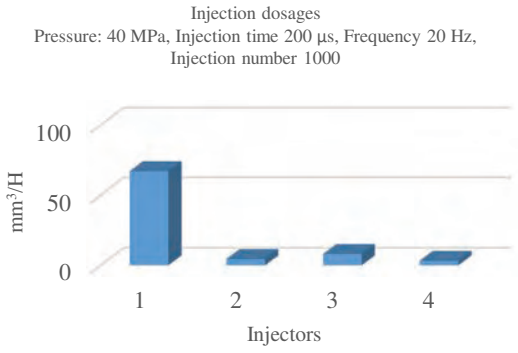

Fig. 12. Injector work test results. Pressure 40 MPa, injection time 200 µs

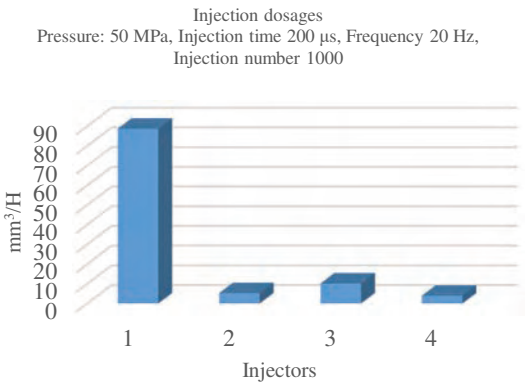

Fig. 13. Injector work test results. Pressure 50 MPa, injection time 200 µs

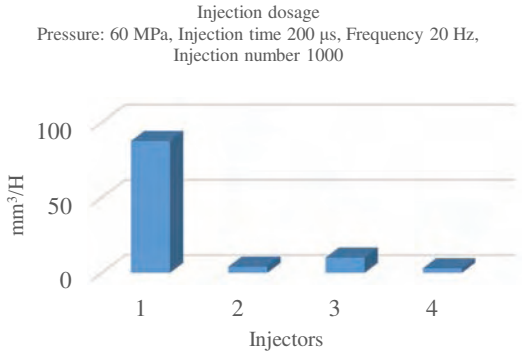

Fig. 14. Injector work test results. Pressure 60 MPa, injection time 200 µs

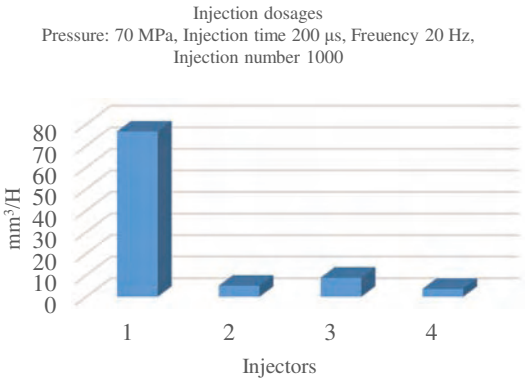

Fig. 15. Injector work test results. Pressure 70 MPa, injection time 200 µs

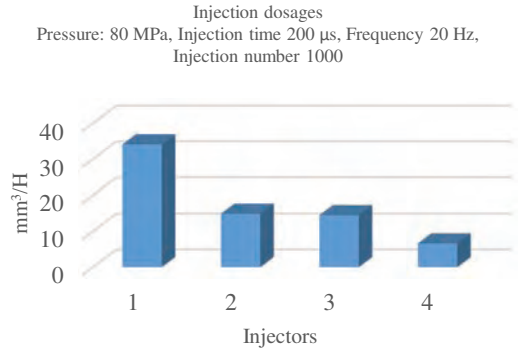

Fig. 16. Injector work test results. Pressure 80 MPa, injection time 200 µs

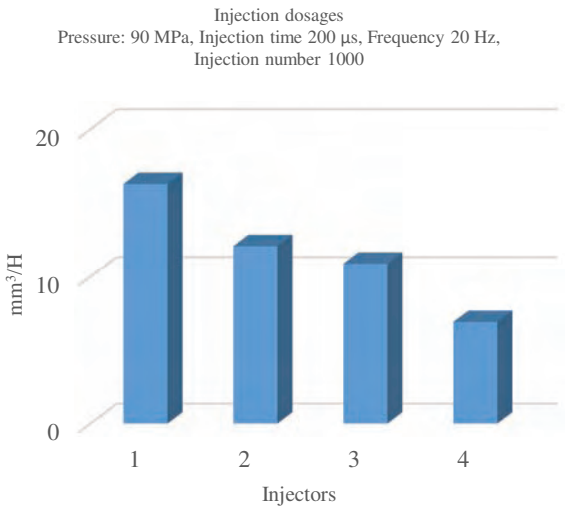

Fig. 17. Injector work test results. Pressure 90 MPa, injection time 200 µs

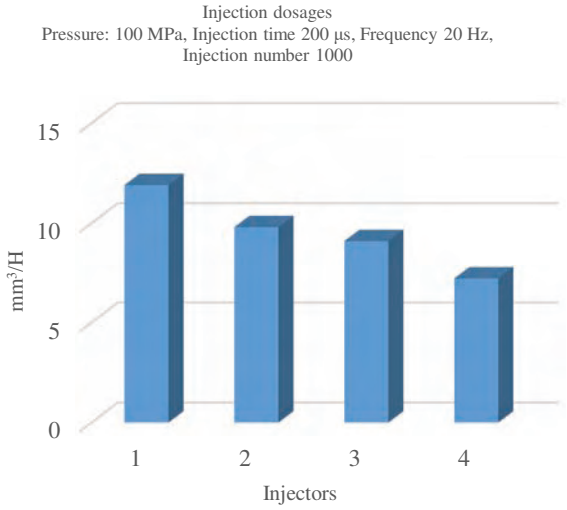

Fig. 18. Injector work test results. Pressure 100 MPa, injection time 200 µs

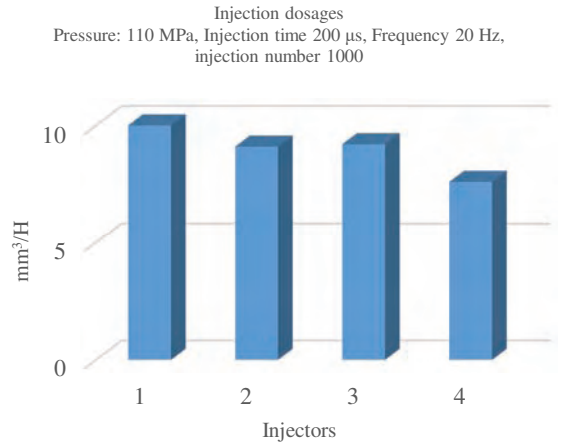

Fig. 19. Injector work test results. Pressure 110 MPa, injection time 200 µs

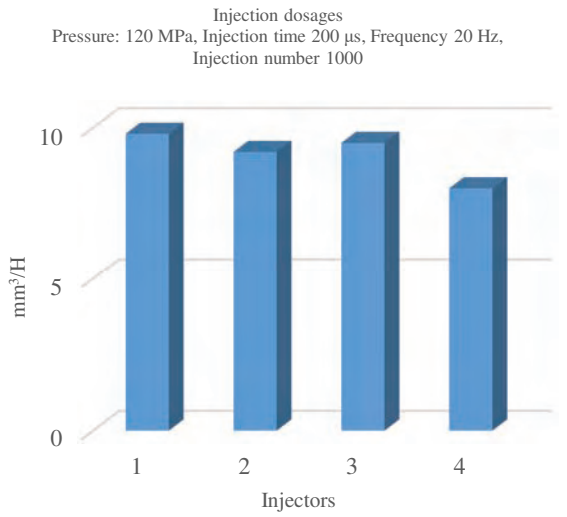

Fig. 20. Injector work test results. Pressure 120 MPa, injection time 200 µs

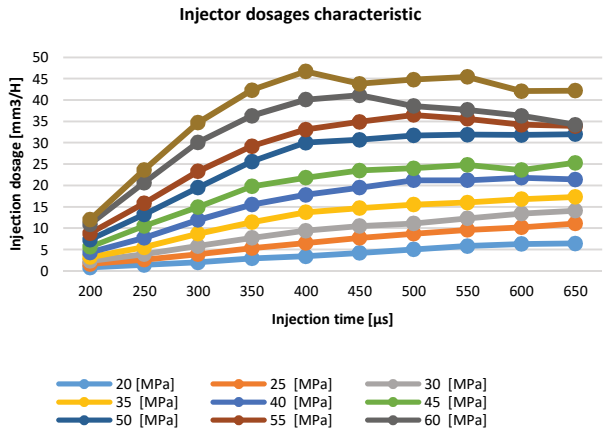

Fig. 21. Faulty injector work characteristic

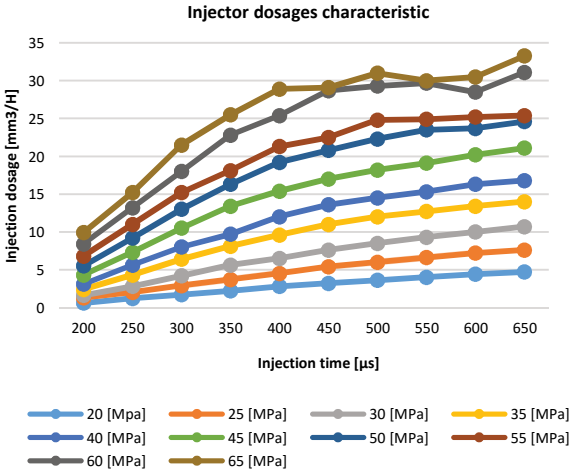

Fig. 22. Correct injector work characteristic

Fuel injectors work in varies dosages areas (Fig. 23). It means that every load of engine need appropriate fuel dosage by appropriate pressure. So that represents it has been

made fuel injectors dosages areas graph. This graph came into being in results own researches. The first stage of the researches was measuring injection and return dosages. Test came out positive and according to researches injectors worked correctly. But the problem was with engine work and diagnose indicated on problem with injector. Problems with engine started by 1500 min^{-1}.

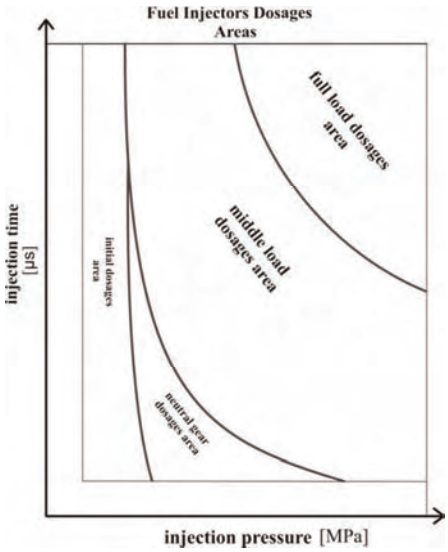

Fig. 23. Fuel injectors dosages areas [own study]

Engine work was irregular and it was heard strength clatting causing of predetonation combustion. One reason of detonation combustion is problem with initial dosages. So that after standard injectors test has been made research to check initial dosage. Initial dosages occurs by short injection times with various pressures. For Continental injectors initial dosages have time 200 μs Electrical test is very important by researching fuel injectors. For piezoelectric it must be made insulation resistance by voltage 100 V between connectors and to mass by voltage 250 V. Research showed that electrically injectors were correct.

4. Conclusion

The research objects were Continental fuel injectors. The research showed that detonation combustion and irregular engine work were caused to big initial injection dosage by 40–110 MPa system pressure. The reason of it were improper piezoelectric element effect in first injector. Electric and standard test didn't reveal fuel injectors defects. Only accurate tests uncovered the problem. It has been made injectors work characteristics for initial dosages. The research shows that first injector dosage by 200 μs injection time in the 40–110 MPa range were too high. The research has been made for 300 and 400 μs injection time in the same pressure range and all injectors worked correctly. There are two ways to improve engine work. The first is change the injector and the second is disassemble, clean, assemble and try to regulate to properly screw in piezoelectric element. The magnitude of injection dosages in Continental fuel injectors depends on piezoelectric element tighten moment. It is hard to make the regulation on account of element huge sensitive.

Nomenclature

CI	compression ignition
CR	common rail system
μs	micro seconds
H	one injection

Bibliography

[1] AMBROZIK, A., AMBROZIK, T., ŁAGOWSKI, P. Fuel impact on emissions of harmful components of the exhaust gas from the CI engine during cold start up. *Eksploatacja i Niezawodnosc – Maintenance and Realiability.* 2015, **17**(1), 95-99.

[2] GÜNTHER, H. Common Rail – Systeme in der Werkstattpraxis. Technik, Prüfung, Diagnose. *Bad Wörihofen: Krafthand Verlag Walter Schultz GmbH*. 2012.

[3] KNEFEL, T. Ocena techniczna wtryskiwaczy Common Rail na podstawie doświadczalnych badań przelewów. *Eksploatacja i Niezawodnosc – Maintenance and Reliability.* 2012, **14**(1), 42-53.

[4] OSIPOWICZ, T., ABRAMEK, K.F., STOECK, T. Testing of modern common rail fuel injectors. *Combustion Engines*. 2015, **162**(3), 688-694.

[5] OSIPOWICZ, T. Diagnosing Common Rail fuel injectors using fuel micro – doses. *Teka. Commission of Motorization and Energetics in Agriculture.* 2015, **15**(1), 61-64.

[6] OSIPOWICZ, T. Analysis of the costs and cost – efficiency of regeneration of modern fuel injection systems in CI engines. *Econtechmod. An International Quarterly Journal.* 2016, **5**(2), 45-50.

Tomasz Osipowicz, DEng. – Faculty of Mechanical Engineering and Mechatronics at West Pomeranian University of Technology.

e-mail: *Tomasz.Osipowicz@zut.edu.pl*

Karol F. Abramek, DSc., DEng. – Faculty of Mechanical Engineering and Mechatronics at West Pomeranian University of Technology.

e-mail: *Karol.Abramek@zut.edu.pl*

Article citation info:
ŚWIECZKO-ŻUREK, B., RONOWSKI, G., EJSMONT, J. Tyre rolling resistance and its influence on fuel consumption. *Combustion Engines*. 2017, **168**(1), 62-67. DOI: 10.19206/CE-2017-110

Beata ŚWIECZKO-ŻUREK
Grzegorz RONOWSKI
Jerzy EJSMONT

CE-2017-110

Tyre rolling resistance and its influence on fuel consumption

Rolling resistance of tyres is one of the major resistive forces acting on any wheeled vehicle. Unfortunately, it is also one of the forces very difficult to measure. It is estimated that in certain traffic conditions (like for example constant speed driving with slow or moderate speed) so called Rolling Resistance Impact Factor may be as high as 0.3. This means that reduction of rolling resistance by 50% would lead to 15% of energy savings. The paper presents road measuring method of tyre rolling resistance and unique equipment used by the Technical University of Gdańsk designed to perform measurements of passenger car tyres. It also discusses road pavement, tyre and environmental conditions influence on rolling resistance. Also selected data describing current situation related to rolling resistance on different road pavements and rolling resistance of modern passenger car tyres including tyres specially designed for electric and hybrid vehicles are presented.

Key words: *tyres, measuring methods, rolling resistance, fuel consumption, CO_2 emission*

1. Introduction

In order to move every vehicle must overcome resistive forces acting on it. Those forces are controlling the vehicle's performance and energy consumption. Lower value of resistance means better acceleration, higher speed and lower energy consumption leading to longer range and less costly operation of the vehicle.

Generally speaking, several resistive forces act or may act on a moving car. They are shown in Fig. 1. Some of the forces act on the vehicle all the time (rolling resistance, drag) some of them may not be present in a certain driving condition (inertia forces, up/downhill force, tow force).

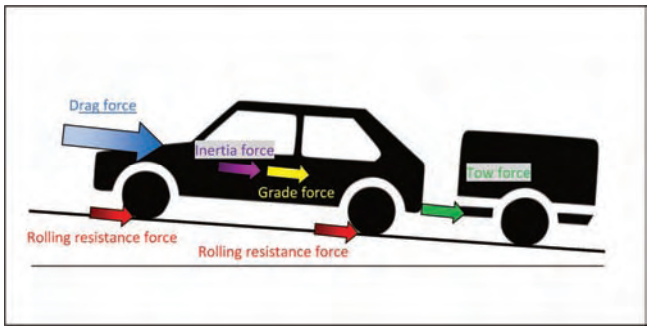

Fig. 1. Resistive forces acting on moving car

For different traffic conditions relative influence of the resistive forces may be very different. For example during driving in congested traffic the inertia force tends to dominate over other forces with rolling resistance force being the second important. During uninterrupted suburban driving with low or moderate speeds rolling resistance clearly dominates with aerodynamic drag force being the second, while at highway speeds it is the contrary. In mountain areas both grade and inertia forces may dominate other resistive forces.

This paper presents problems related to influence of tyre rolling resistance on overall energy (fuel) consumption and problems related to measuring of rolling resistance force which is one of the most complicated to measure parameter of tyre/road interface.

2. Rolling resistance force

Tyre rolling resistance (F_R) is the force resisting the motion of the tyre when it rolls on a road surface. It is mainly caused by non-elastic effects in tyre and slippage between the tyre tread and the pavement, which leads to dissipation of energy. Contrary to early diagonal tyres, rolling resistance of modern radial car tyres is not very much dependent on the speed (see Fig. 2), therefore for basic modeling used in this report it was assumed that rolling resistance is constant within low and moderates speed range and given by the equation (1).

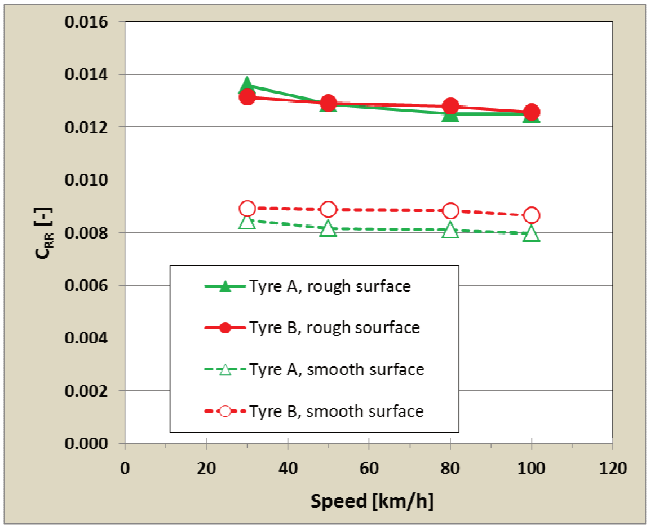

Fig. 2. Speed influence on tyre rolling resistance (results of laboratory measurements performed according to ISO standard)

$$F_R = C_{RR} * F_L \quad (1)$$

where: F_R – force of rolling resistance [N], C_{RR} – coefficient of rolling resistance [-], F_L – vertical load [N].

Rolling resistance depends on many factors related to road, tyre, and operating conditions. Most important influences of the road are: pavement texture, road unevenness and road stiffness. Most important influences of the tyre are: tyre size, rubber hysteresis, rubber hardness, construc-

tion of the belt and carcass, tread pattern and tread depths. Many operating conditions also influence tyre rolling resistance, especially: inflation pressure, air and pavement temperature, pavement wetness and tyre load.

3. Measuring methods of rolling resistance

3.1. General remarks

Tyre rolling resistance is very difficult to measure because it constitutes roughly only 1% of vertical force acting on the tyre. If desired accuracy is also 1%, for typical passenger car tyre loaded to 4000 N it is necessary to precisely measure forces in the range of 40 N with accuracy at least 0.4 N. This task which is difficult even in the laboratory conditions becomes extremely difficult in road conditions when many important variables are less controlled.

As an example of the problems it may be mentioned that if the vertical force loading the test tyre via force sensor is not exactly vertical but it is tilted by 20 seconds of angle the resulting measuring error is at about 1% of evaluated rolling resistance force – see Fig. 3.

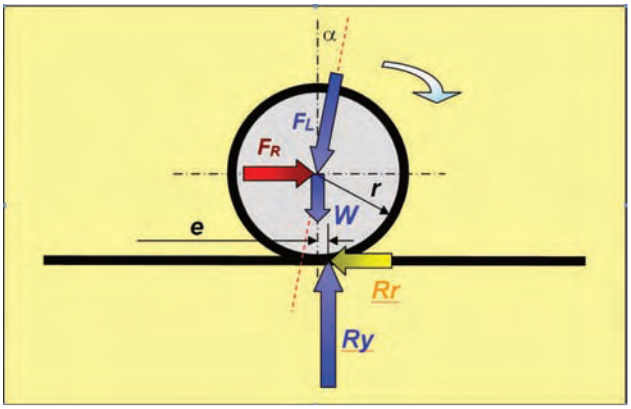

Fig. 3. Influence of imperfections in measuring system on accuracy of rolling resistance measurements

What is more, tyre rolling resistance is very sensitive to tyre inflation pressure and load [1], surface wetness [2] and temperature [3]. All those variables must be thoughtfully controlled during measurements and if it is not possible to control them (like for example temperature during road measurements), certain corrections must be applied.

3.1. Laboratory methods

Laboratory methods are based on so called "roadwheal facilities" which are big drums acting as "moving road" for tyres. One of the drum facilities used at the Technical University of Gdańsk is shown in Fig. 4.

General advantages of using drum facilities for rolling resistance measurements are as follows:

- measurements may be carried indoor with full control of ambient conditions,
- measurements are not biased by the driving style,
- easy adjustment of measuring conditions (load, inflation pressure, speed),
- low cost of measurements.

Fig. 4. Roadwheel facility with 1.7m diameter drum at the Technical University of Gdansk, Poland

Unfortunately there is a lot of problems related to the use of drums for rolling resistance measurements. Most important ones are listed below:

- road surface interfacing the test tyre is not flat but has certain curvature,
- there are serious problems with obtaining representative texture of the road pavement and special replica road surfaces must be manufactured,
- tyres have tendency to worn replica road surfaces and deposit rubber particles on them as there is no natural cleaning provided by changing weather conditions.

There are three commonly used laboratory methods of rolling resistance measurements, namely Force Method, Torque Method and Deceleration Method. All three roadwheel facilities at the Technical University of Gdańsk use torque method.

3.2. Road methods

Road methods are not so popular as laboratory methods because they are very difficult to carry out. Road methods are best suited for investigation of road surface influence on tyre rolling resistance. The most important advantages are:

- tyres roll on real road pavements so the phenomena related to the tyre/road interfacing are not distorted,
- road surface is flat so interaction between tyre and pavement is not impaired.

Despite very important benefits there are lots of problems related to the road methods. Most important ones are listed below:

- during measurements ambient conditions are difficult to control,
- there are a lot of sources of measurement errors like wind, road grade or acceleration/deceleration,
- performing measurements is time consuming and/or measuring equipment is very expensive,
- for some road methods it is not possible to make measurements on trafficked roads,

Road measurements may be performed using ordinary cars or trucks (sometimes with special conversions) or by

utilizing specially build trailers [4]. In contrast to the laboratory methods there is not a single standard regulating road measurements of the rolling resistance.

There are four basic road methods that may be performed with the use of ordinary vehicles [5]. The methods are:

- Coast Down Method,
- Power Train Torque Method,
- Fuel Consumption Method,
- Trailer Method.

Trailer method of rolling resistance measurements is the most versatile method and at the same time the most difficult one. At present there are only five known trailers that may make accurate measurements of rolling resistance of passenger car tyres. Two of them were built and are used by the Technical University of Gdańsk. One of the trailers called R^2 Mk.2 is generally considered to be the most advanced and most versatile on the world. The trailer is described in [6] and presented in Fig. 5 and 6. It makes measurements both in EU countries and in the USA [7].

Fig. 5. Test trailer R2 Mk.2 built by the Technical University of Gdańsk

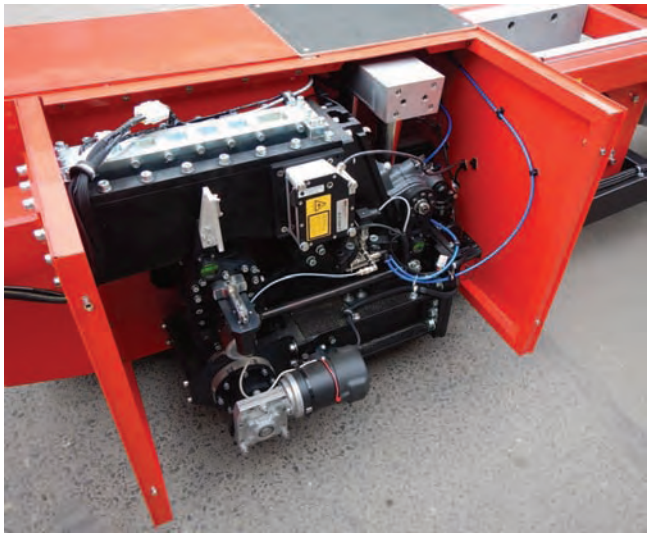

Fig. 6. Interior of the test trailer R^2 Mk.2

3.3. Rolling resistance coefficients for modern tyres and road pavements

In open literature most of the data related to tyre rolling resistance originate from measurements made on steel drums that are not representative for road conditions or measurements performed a long time ago by the coast down method. What is more, a few years ago a new concept of passenger car tyres was developed, namely "Blue Tyres" designed for electric and hybrid vehicles.

With a few exceptions most of the electric cars are developed for urban and suburban driving conditions where maximal speeds are rather restricted and high speed handling or tractions do not play a leading role in tyre ranking. For electric cars, especially low end and medium class it is however very important to ascertain as long operational range as possible because a typical electric car has only 120-150 km range. Adding 20-30 km of range to such a car due to low rolling resistance tyres may make remarkable difference for the driver.

It is interesting to note that, in fact there are two different "families" of tyres design for electric cars. First family has tyres that have similar sizes to tyres for conventional cars with internal combustion engines and the second family is composed with tyres developed for electric vehicles constructed in nonorthodox way. Those tyres have usually got very narrow tread and very big rim diameter – see Fig. 7.

Fig. 7. Tyres for electric cars; on the left – tyre of typical size for modern cars with conventional design, on the right – tyre for electric cars constructed in nonorthodox way

All results reported in this paper were obtained by using R^2 Mk.2 test trailer and measuring conditions described as "TUG measuring conditions" that differ slightly from existing ISO standards. At TUG conditions the vertical load acting on the tyre is set to 4 000 N, inflation pressure (regulated) is kept at the value of 210 kPa and speed is 80 km/h. All reported results are corrected to air temperature 20ºC.

Test tyres that were used for experiments are listed in Tab. 1. As there is no ISO standard for rolling resistance measurements on the road, Technical University of Gdańsk introduced several years ago set "informal reference tyres" that was adopted by most of the research institutes worldwide. Two of the tyres in the set (SRTT and AV4) are also used in ISO 11819-3 standard as reference tyres for tyre/road noise measurements. Tyre MCPR was selected as modern market tyre for medium class passenger cars while tyre BLUECO was selected as state of the art tyre specially developed for electric cars.

Table 1. List of tyres used during experiments

Tyre designation	Tyre description	Remarks
SRTT	P225/60R16 UNIROYAL Tiger Paw (Standard Reference Test Tyre)	Reference tyre passenger cars. All-season
AV4	195R14C AVON Super Van AV4	Reference tyre for light trucks
MCPR	225/55R16 MICHELIN Primacy HP	Informal reference tyre, summer tread
BLUECO	195/50R18 CONTINENTAL Blueco	Tyre designed for electric cars

In Table 2 selected results of rolling resistance measurements performed during the period 2015-2016 are presented. It is clearly visible, that tyre BLUECO exhibits coefficients of rolling resistance approximately two times smaller than coefficients of other tyres. A similar difference may be attributed also to pavement influence where rolling resistance measured on Surface Dressing 0/14 is about twice as big as rolling resistance on ISO Type DAC 0/6.

Table 2. Coefficients of rolling resistance for selected road surfaces measured at TUG conditions

Road pavement	Tyre			
	SRTT	AV4	MCPR	BLUECO
Stone Mastic Asphalt, SMA11	0.0086	0.0121	0.0110	0.0068
Stone Mastic Asphalt, SMA8 COOEE	0.0084	0.0112	0.0108	0.0064
Stone Mastic Asphalt, SMA6 COOEE	0.0078	0.0119	0.0105	0.0059
Dense Asphalt Concrete, DAC 12.5	0.0080	0.0121	0.0113	0.0053
Surface Dressing, SD 0/14	0.0133	**0.0161**	0.0160	0.0082
Surface Dressing, SD 8/10	0.0111	0.0147	0.0141	0.0074
Fine Surface Dressing,	0.0068	0.0110	0.0088	**0.0041**
Porous Hot Mix Asphalt, HMA	0.0088	0.0132	0.0130	0.0058
Portland Cement Concrete, PCC Conventional Diamond Grind	0.0076	0.0115	0.0109	0.0052
ISO Type DAC 0/6	0.0069	0.0107	0.0081	0.0045
Concrete block pavement (50 km/h)	0.0081	0.0116	0.0104	0.0050

When permutations of tyres and road surfaces are compared the difference between "the best" and "the worst" combinations is even bigger. The best combination of tyre/pavement is marked in Table 1 with green background color and C_{RR} for it is as low as 0.0041while the worst is marked with red color and C_{RR} is as high as 0.0161. Although both combinations are in some way extreme they show that in principle by playing with road pavements and tyres the rolling resistance may be quadrupled.

There is still ongoing discussion how to describe road surface texture in order to obtain good correlation with tyre rolling resistance. Commonly used Mean Profile Depth (MPD) in opinion of this authors is not appropriate as it treats each part of the texture profile in the same way. During interaction of tyre with pavement very often there is no contact between rubber of the tread and "valleys" of the texture as only summits of protruding aggregate interfaces with tyre. MPD is however calculated also in the areas where contact is not existing and this impairs correlation considerably. The authors believe that it is necessary to base texture estimator on enveloping procedures that account for properties of the tyre tread.

4. Rolling resistance influence on energy consumption

There are several simulation models used for estimation of energy consumption of light and heavy vehicles. They are usually very complicated and based on numerous input data that can be difficult to obtain. In the case of simulations reported in this paper it was not necessary to use very elaborate models as the goal is not to predict absolute energy consumption values but to evaluate relative changes of energy consumption attributable to rolling resistance changes.

In order to estimate the influence of rolling resistance on energy consumption a very simple mathematical model was created. It was assumed that changes of engine power due to the changes of rolling resistance will not have any influence on engine efficiency at given speed and torque so what follows is that changes of energy (fuel) consumption are proportional to changes of engine power.

The model used for evaluation is based on equations 2 and 3.

$$P = \left(F_R + F_D + F_I + F_G\right) \cdot V + P_0 \tag{2}$$

$$E = P \cdot t \tag{3}$$

where: P – power [W], F_R – rolling resistance force [N], F_D – drag force [N], F_I – inertia force [N], F_G – grade force [N], V – speed of the vehicle [m/s], E – energy [J], P_0 – during idling $P_0 = P_i$, during normal driving $P_0 = P_e$ (power necessary to rotate unloaded engine) [W].

Basic power necessary to drive a vehicle is calculated according to equation 2. If simulation is performed for conventional vehicle (diesel or petrol engine) the model evaluates when engine braking is present. Most of the vehicles are constructed in such a way that during engine braking fuel consumption is reduced to zero and this behavior is modeled in the algorithm. Algorithm also checks if the speed of vehicle is below 2 m/s and if so, the virtual "idling power" value is used (P_i). In the case of electric and hybrid vehicles equipped with KERS it is assumed that 50% of energy during "engine braking" is recovered.

To simplify the calculations, energy is calculated according to equation 3 with time interval of 1 s and summed for whole driving cycle. During idling fuel consumption for most of conventional cars is at about 0.5–1.4 l of fuel per hour. The authors estimate that virtual "idling power" value (P_i) that represents power necessary to idle the engine should be in the range of 0.4–1.3 kW for typical car engines. To rotate unloaded engine with certain rpm the virtual "rotation power" (P_e) is necessary. Estimations shows that depending on rotational speed the value of P_e is between 0.5–7.0 kW.

In order to simulate the influence of rolling resistance on overall energy consumption for conventional vehicles, six cars were selected as well as three hybrid cars and one electric car.

1. 2012 Jeep Liberty
2. 2010 Subaru Outback Wagon
3. 2009 Toyota Corolla
4. 2009 Chevrolet Aveo
5. 2009 GMC Sierra XFE
6. 2010 Ford Mondeo Estate
7. 2011 Chevrolet Volt (HYBRID)
8. 2010 Toyota Prius (HYBRID)
9. 2010 Honda Insight (HYBRID)
10. 2014 SMART (ELECTRIC)

Energy consumption simulations were performed for constant speeds: 30, 50, 70, 90, 110, 130 and 150 km/h as well as for urban driving cycle FTP 75. Calculations were performed for rolling resistance coefficients C_{RR} from 0.005 to 0.015 with increment of 0.001. Rolling resistance coefficient of 0.01 was considered as reference. The energy consumption calculated according to the algorithm does not account for efficiency of the engine and power train but it may be assumed that the efficiency will not change considerably for small and moderate differences in engine load due to changes in rolling resistance. Energy consumption for each rolling resistance coefficient was related to the energy consumption for the same driving conditions but calculated for reference rolling resistance coefficient of C_{RR} = 0.01. The resulting factor is called in this paper "Relative Change of Energy Consumption" and designated R_E. Values of R_E obtained for cars with internal combustion engines are presented in Table 3.

During urban driving the average speed is not high (34 km/h), but a lot of energy is consumed to accelerate vehicles. In conventional cars most of the energy during braking is lost. Also in low-emission vehicles this energy is not fully preserved by energy recovery systems. During urban driving R_E for conventional vehicles is on the same level as for constant driving with a constant speed of 110 km/h. For urban driving a decrease of the rolling resistance coefficient from 0.01 to 0.005 would lead to an 11% decrease of energy consumption for conventional vehicles.

In order to better describe the influence of rolling resistance on overall energy consumption the authors introduced “Rolling Resistance Impact Factor” (IFRR). This factor shows how much the energy consumption is influenced by a change in rolling resistance coefficient. For example, IFRR = 0.3 means that decrease of energy consumption will equal 30% of the decrease of rolling resistance. If the rolling resistance coefficient is reduced from 0.01 to 0.006 the energy consumption will be reduced by: (0.01–0.006)*0.3*100%, that is 12%. Impact Factors for different vehicles are presented in Table 4.

Table 3. Relative changes of energy consumption for conventional vehicles

C_{RR}	Constant speed driving							FTP-75
	30 km/h	50 km/h	70 km/h	90 km/h	110 km/h	130 km/h	150 km/h	
0.005	0.77	0.78	0.81	0.85	0.88	0.90	0.92	0.89
0.006	0.81	0.82	0.85	0.88	0.90	0.92	0.94	0.91
0.007	0.86	0.87	0.89	0.91	0.93	0.94	0.95	0.93
0.008	0.91	0.91	0.92	0.94	0.95	0.96	0.97	0.96
0.009	0.95	0.96	0.96	0.97	0.98	0.98	0.98	0.98
0.010	1.00	1.00	1.00	1.00	1.00	1.00	1.00	1.00
0.011	1.05	1.04	1.04	1.03	1.02	1.02	1.02	1.02
0.012	1.09	1.09	1.08	1.06	1.05	1.04	1.03	1.04
0.013	1.14	1.13	1.11	1.09	1.07	1.06	1.05	1.07
0.014	1.19	1.18	1.15	1.12	1.10	1.08	1.06	1.09
0.015	1.23	1.22	1.19	1.15	1.12	1.10	1.08	1.11

Table 4. Rolling Resistance Impact Factor for conventional, hybrid and electric vehicles

C_{RR}	Constant speed driving							FTP-75
	30 km/h	50 km/h	70 km/h	90 km/h	110 km/h	130 km/h	150 km/h	
Conv.	0.46	0.45	0.38	0.31	0.24	0.19	0.16	0.22
Hybrid	0.42	0.43	0.38	0.31	0.25	0.21	0.17	0.32
Electric	0.35	0.36	0.31	0.25	0.20	0.16	0.13	0.31

Generally for all types of cars the highest impact factor is predicted for low end medium speeds. Differences between conventional, hybrid and electric cars are mostly due to different sizes and weight of cars. For example electric car SMART has very low weight comparing to conventional vehicles and rolling resistance is proportional to the weight of the car and this may explain why rolling resistance impact factor for this car is lower.

Analyzing the results presented in Table 4 it is necessary to notice that the model does not account for energy losses due to cornering, or use of electric equipment like air condition, fans, lights. In opinion of this authors it is reasonable to assume that impact factor for slow, constant speed driving (up to 30 km/h) is at about 0.3 while for medium speed driving (30–90 km/h) it is at about 0.2.

4. Conclusions

Rolling resistance of car tyres plays a very important role in overall energy (fuel) consumption. This influence is especially essential for slow and medium speed driving. Rolling resistance measurements performed on numerous road pavements and using many modern passenger car tyres indicate that average coefficient of rolling resistance is close to $C_{RR} = 0.01$. it is however possible to find tyres and road pavements that are responsible for much higher coefficient, as high as $C_{RR} = 0.016$. This may increase fuel consumption during slow and medium, constant speed driving by 12–18%. On the other hand if special "low rolling resistance" road pavements and tyres designed for electric vehicles ("Blue type") are used it is possible to reduce C_{RR} to 0.004. Such dramatic reduction of tyre rolling resistance may decrease fuel consumption even by 20% during slow or medium speed driving.

Tyres designed for electric vehicles may in many cases be also used at conventional cars giving very substantial reduction of costs and emissions toxic gases and CO_2.

Acknowledgments

Research work reported in this article was sponsored by the Polish National Centre for Research and Development (NCBR) within the SPB project ROLRES (Grant Agreement PBS1/A6/1/2012) and Polish-Norwegian Research Programme CORE, project LEO (Grant Agreement 196195/ 2013).

Bibliography

[1] EJSMONT, J., TARYMA, S., RONOWSKI, G., ŚWIECZKO-ŻUREK, B. Influence of load and inflation pressure on the tyre rolling resistance. *International Journal of Automotive Technology*. 2016, **17**(2), 237-244.

[2] EJSMONT, J., SJÖGREN, L., ŚWIECZKO-ŻUREK, B. RONOWSKI, G. Influence of road wetness on tire-pavement rolling resistance, *Journal of Civil Engineering and Architecture*. 2015, **9**, 1302-1310.

[3] EJSMONT, J., TARYMA, S., RONOWSKI, G., ŚWIECZKO-ŻUREK, B. Influence of temperature on the tyre rolling resistance. *International Journal of Automotive Technology*. 2017 *(accepted for publication)*.

[4] SANDBERG, U. (editor) Rolling resistance – basic information and state-of-the-art on measurement methods, Deliverable #1, MIRIAM SP1, 2011.

[5] EJSMONT, J., ŚWIECZKO-ŻUREK, B. Methods of tire rolling resistance measurements. Troisième Congrès Tunisien de Mécanique COTUME'2014, Sousse 24-26 March 2014.

[6] ŚWIECZKO-ŻUREK, B., JASKUŁA, P., EJSMONT, J., KĘDZIERSKA, A., CZAJKOWSKI, P. Rolling resistance and tyre/road noise on rubberised asphalt pavement in Poland. *Road Materials and Pavement Design*. **18**(1), 2017, 151-167.

[7] EJSMONT, J., ŚWIECZKO-ŻUREK, B., RONOWSKI, G., WILDE, J. Rolling resistance measurements at the MnROAD facility. Round 2, Research Project Final Report MN/RC 2014-29, Minnesota Department of Transportation, USA.

Beata Świeczko-Żurek, DEng. – Mechanical Faculty at the Technical University of Gdańsk.

e-mail: *beazurek@pg.gda.pl*

Prof. Jerzy Ejsmont, DSc., DEng. – Mechanical Faculty at the Technical University of Gdańsk.

e-mail: *jejsmont@pg.gda.pl*

Grzegorz Ronowski, DEng. – Mechanical Faculty at the Technical University of Gdańsk.

e-mail: *gronowsk@pg.gda.pl*

Article citation info:
BOGUŚ, P., CIESZYŃSKI, M., MERKISZ, J. Multiresolution analysis of vibration signals acquired from locomotive Diesel engine for classification of engine states basing on signal statistical parameters. *Combustion Engines*. 2017, **168**(1), 68-72. DOI: 10.19206/CE-2017-111

Piotr BOGUŚ
Mateusz CIESZYŃSKI
Jerzy MERKISZ

CE-2017-111

Multiresolution analysis of vibration signals acquired from locomotive Diesel engine for classification of engine states basing on signal statistical parameters

The paper presents a method of classification of locomotive Diesel engine states basing on vibration signals taken from an engine body and using chosen statistical parameters calculated for the original signal and it wavelet multiresolution components. The researches presented in the paper concern estimation of an engine states before and after a general repair. The target application of the presented researches is an on-line diagnostic system which can complement standard OBD systems. To this purpose the applied methods should not base on complex analysis of some spectral, time-frequency or scalogram plots but rather on choosing single diagnostic parameters which are suitable for the fast on-line diagnostic. The results have showed the significant difference in distinguishing of engine work before and after a general repair using some chosen statistical parameters applied to vibration signals.

Key words: *vibration signals, Diesel engine diagnostic, multiresolution analysis, classification*

1. Introduction

A combustion engine is an example of a mechanical device which can run down. The engine diagnosis needs estimation of the technical state of an engine during it exploitation. Together with engines used in a car transport the locomotive combustion engines are nowadays also an important source of pollution. To reduce air pollution for passenger cars the OBD (on board diagnostic) norms and systems were introduced. The rail area is also partially regulated with several regulations considering limits on emission of combustion gases (for example, cart UIC 623 1-2-3 in Europe). But all the time there are no obligatory regulations for systems monitoring the emission critical damages that might play a similar role to that of the OBD for cars. Anyway, the coming years will show a tightening of norms and regulations regarding combustion gases emission regarding vehicles with heavy diesel engines like combustion locomotives. It is this imminent perspective that gives an impulse to research new detection methods that would be applicable in diesel locomotives and which base on vibration analysis [1].

The paper presents some researches on classification of different states of Diesel locomotive engine basing on vibration signals taken from an engine body before and after a repair. In the area of vibration signals analysis many specialized methods can be found. It is enough to mention about FFT spectrum, nonlinear analysis, short-time analysis and wavelets (see e.g. [2-9]). The results presented in the paper covers the application of multiresolution wavelet analysis into diagnostic of rail vehicle combustion engine with application of some chosen statistical parameters applied to the original signal and it wavelet multiresolution components.

The proposition of engine diagnostic presented in the paper bases on the indication of some diagnostic parameters which can be useful to distinguish engine different states by signal processing methods without considering details of mechanical engine processes. In this on-line analysis the applied methods cannot base on complex analysis of spectral, time-frequency or scalogram plots but they need choosing single diagnostic parameter which can be applied in a fast on-line diagnostic.

The results presented in the paper showed the significant difference in distinguishing of engine work before and after a repair using some of chosen shape parameters applied to vibration signals taken from an engine.

2. Multiresolution wavelet analysis

Wavelet analysis [7, 10] is nowadays a known signal processing method applied in broad range of problems and disciplines. Wavelets have also found an application in the area of analysis of broad class of mechanical signals (also vibration signals) for diagnostic aim [5, 6, 11–13].

In continuous wavelet transformation CWT [7, 10] the set of wavelets which create orthonormal base can be obtained by transformations of one special mother wavelet. In comparison with Fourier base functions the wavelets series is created by scaling (stretching or compressing) and by translation, while the Fourier base function are only scaled. Wavelets are better from traditional Fourier approach during analysis of signals which contain discontinuities and sharp non-periodic peaks. During processing of unsteady signals the Fourier analysis loses all information about localization in time of the given frequency components. The use of CWT while all calculations are done for all possible scales and translations gives the big amount of data. For this reason in practice the Discrete Wavelet Transformation DWT is used [7, 10]. In DWT a signal is transformed to discrete scales and discrete translations what gives a data reduction. What is worth to underline each DWT transformation can be interpreted as a special case of a filtering function [7, 10].

In effect using DWT transformation to the original signal S can make it decomposition into two terms: high frequency approximation term and low frequency approximation term. This operation can be repeated. For example, the structure of multiresolution decomposition of an original signal S on the level 5 can be described as $S = A_5 + D_5 + D_4 + D_3 + D_2 + D_1$ (see Fig. 1), where D represents low frequency component decomposed with a high scale and A high frequency components decomposed with a low scale.

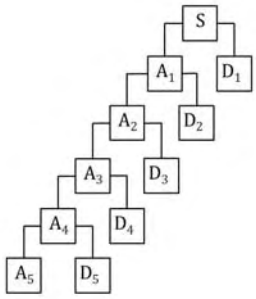

Fig. 1. The exemplary tree structure of multiresolution decomposition on level 5

3. Measurements

All experiments were done on Diesel locomotives ST44. The construction of ST44 locomotives is simple and a service is easy to performance. They have easiness of start in any circumstances and a big force. The ST44 locomotive was a typical combustion traction vehicle for railway in Poland 1949–1991. It appeared irreplaceable in winter conditions. Unfortunately it has also many disadvantages like a big fuel consumption, little fuel tank, high emission of combustion gases and high level of noise. The measurements were performed on two ST44 locomotives – number 2045 and 2061. The main calculations were done for data registered on both locomotives. The paper presents also some calculation performed for each locomotive separately. The number of performed registrations was limited by complexity of measurements and first of all by the general costs of researches.

The examinations were focused on Diesel engine 14D40 no 8849. The measurements were done under loading (on water resistor) for correspondingly adjustment power in determinate measurement points [1, 14]. The researches were performing basing on comparison of vibration signals recorded from an engine before and after the revision repair in a diagnostic station. Periodic repair consisted in full service of damaged parts and in replacement of damaged or wearing elements [14].

The acceleration measurements before repair of a Diesel engine were done by using acceleration sensors EGCS Entran Devices of the range ± 5 g. The signal was registered by cart PCL-818HD ADVANTECH with the sampling frequency f_{Hz} = 1004.0161 Hz/channel. The measurement after repair were done using the same sensors EGCS and new sensors PCB PIEZOELECTRONICS 393B04 where the signal was amplify by 3-channel signal conditioning amplifier and next registered using analogue to digital cart.

The sensors were mounted on an engine body in places which correspond to bearing sites of engine crankshaft (see Fig. 2). Each measurement points registered acceleration in vertical direction and transverse horizontal direction [14]. The measurements before the repair were performed under load on water recoil in the seven measurement points mounted on an engine body near of engine crankshaft bearing. In each measuring point acceleration was registered in two directions: vertical and horizontal transversal. The measurements after repair were also done under load on water recoil but in six points of sensors mounted on engine body. In this case acceleration was registered in the same two directions: vertical (Entran sensors) and horizontal transversal (PCB sensors).

Fig. 2. Sensors mounted on an engine body

4. Data analysis

Taking into account all configurations and all settings for horizontal case the full measurements gives finally 180 signals registered before and 120 signals registered after. Each of these signals was processing to find it multiresolution components. The calculations were performed in MATLAB for Daubechies wavelet rank 5 and multiresolution decomposition at 5-th level. The type of wavelet was chosen basing on literature remarks and some own experiments. From the point of view of diagnostic aims the 5 level of decomposition seems quite enough, because the analysis is usually performed on-line and this needs not very time consuming calculations.

In the considerations an original signal S after the decomposition consisted of 6 sub signals $S = A_5 + D_5 + D_4 + D_3 + D_2 + D_1$, where D_5 is a low frequency component decomposed with a high scale and successive D_5, D_4, D_3, D_2, D_1 are high frequency components decomposed with a small scale.

The example of signals and it multiresolution components are presented in Figs. 3-4. For each signal and its components, the following parameters were calculated:

- mean M, $X_1 = \frac{1}{n}\sum_{i=1}^{n} x(i)$ (1)
- variance VAR, $X_2 = \frac{1}{n}\sum_{i=1}^{n} (x(i) - X_1)^2$ (2)
- root-mean square RMS, $X_3 = \sqrt{\frac{1}{n}\sum_{i=1}^{n} x(i)^2}$ (3)

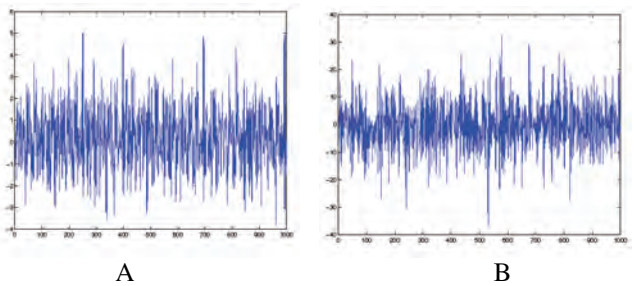

A B

Fig. 3. Exemplary vibration signal before (A) and after (B) an engine repair for horizontal transversal registration (the x-axis units are in number of samples; the y-axis units are in 10 m/s^2 ≈ g (A) and 1 m/s^2 (B))

- mean from absolute values MAV, $X_4 = \frac{1}{n}\sum_{i=1}^{n}|x(i)|$ (4)
- shape coefficient SC, $X_5 = \frac{X_3}{X_4}$ (5)

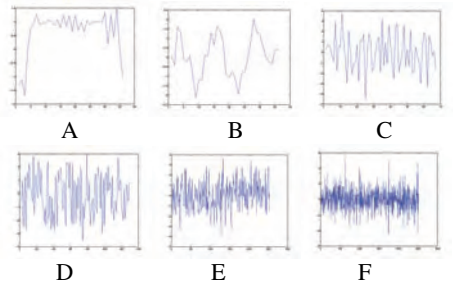

Fig. 4. Multiresolution components of signal A from Fig. 3 (before a repair) (the x-axis units are in number of samples; the y-axis units are in 10 $m/s^2 \approx g$)

5. Results

The general results for signal S and decomposition components A5, D1, D2, D3, D4 and D5 were showed that the most interesting are results are for horizontal registration (see Table 1). The Table 1 presents the averaged values of parameters X_1, X_2, X_3, X_4 and X_5 calculated for all signal cases (180 signals registered before and 120 signals registered after). Generally all parameters (except "Mean") for horizontal registration show the increase of parameter value after the repair. The values of parameters after a repair are higher in comparison with values before a repair, but only for horizontal registration. It is worth to underline that the values "before" represent a worn-out engine in a general bad state while values "after" represent the repaired engine in better general state.

The next step of the researches was a creation of a simple classifier to test if the chosen parameters can play a role of diagnostic parameters distinguishing engine state before and after the repair. Basing on the above observations above the three parameters: X_2 (Variance VAR), X_3 (Root-Mean Square RMS) and X_4 (Mean From Absolute Values MAV) for components S, D1 and D4 were chosen to build a classifier. It needs to define a threshold to distinguish the states of right and fault work of an engine and at the beginning the simplest way was taken into account.

Generally all parameters (except "Mean") for horizontal registration show the increase of parameter value after the repair. It is worth to underline that the values "before" represent a worn-out engine in a general bad state while values "after" represent the repaired engine in better general state. The next step of the researches was a creation of a simple classifier to test if the chosen parameters can play a role of diagnostic parameters. Basing on the above observations the three parameters: X_2 (Variance VAR), X_3 (Root-Mean Square RMS) and X_4 (Mean From Absolute Values MAV)

Table 1. The full results from two locomotives for horizontal registrations

		X_1	X_2	X_3	X_4	X_5
S	Before	0.054	3.298	1.733	1.547	1.257
	After	0.075	65.853	72.862	8.727	5.499
A5	Before	0.054	0.009	0.160	0.145	1.142
	After	0.075	2.268	1.879	1.172	1.265
D1	Before	-0.0000002	1.227	1.032	0.800	1.291
	After	0.000004	33.179	32.276	5.844	3.799
D2	Before	-0.0000005	1.114	0.987	0.767	1.291
	After	-0.000001	21.074	28.197	4.801	3.491
D3	Before	0.000003	0.676	0.768	0.611	1.256
	After	-0.0000005	8.109	9.955	2.954	2.390
D4	Before	-0.000006	0.243	0.471	0.374	1.265
	After	-0.00001	4.312	4.191	1.942	1.001
D5	Before	-0.000002	0.029	0.164	0.133	1.239
	After	0.000009	2.048	1.747	1.145	1.238

Table 2. The means and standard deviations of distribution of parameters X_2, X_3, and X_4 calculated for the cases before and after

		X_2	X_3	X_3
S	Before	3.298 ±2.298	1.733 ±0.571	1.547 ±0.513
	After	65.853 ±93.607	72.862 ±129.779	8.727 ±5.307
D1	Before	1.227 ±1.079	1.032 ±0.404	0.800 ±0.313
	After	33.179 ±43.655	32.276 ±52.626	5.844 ±3.425
D4	Before	0.243 ±0.142	0.471 ±0.144	0.374 ±0.119
	After	4.312 ±5.348	4.191 ±4.557	1.942 ±1.114

Table 3. The results of classification for signal S for gauss thresholds separately for locomotive 2045 and 2061

	X_2 Number (percentage) of classification as a		X_3 Number (percentage) of classification as a		X_4 Number (percentage) of classification as a	
	Proper	Improper	Proper	Improper	Proper	Improper
After both	95 (79%)	25 (21%)	110 (92%)	10 (8%)	110 (92%)	10 (8%)
2045	60 (100%)	0 (0%)	49 (82%)	11 (18%)	60 (100%)	0 (0%)
2061	40 (67%)	20 (33%)	50 (83%)	10 (17%)	50 (83%)	10 (17%)
Before both	11 (6%)	169 (94%)	4 (2%)	176 (98%)	16 (9%)	164 (91%)
2045	6 (7%)	84 (93%)	0 (0%)	90 (100%)	6 (7%)	84 (93%)
2061	13 (14%)	77 (86%)	0 (0%)	90 (100%)	4 (4%)	86 (96%)

Table 4. The results of classification for signal component D1 for gauss thresholds separately for locomotive 2045 and 2061

	X_2 Number (percentage) of classification as a		X_3 Number (percentage) of classification as a		X_4 Number (percentage) of classification as a	
	Proper	Improper	Proper	Improper	Proper	Improper
After both	108 (9%)	12 (10%)	110 (92%)	10 (8%)	110 (92%)	10 (8%)
2045	60 (100%)	0 (0%)	60 (100%)	0 (0%)	60 (100%)	0 (0%)
2061	41 (68%)	19 (32%)	50 (83%)	10 (17%)	50 (83%)	10 (17%)
Before both	13 (7%)	167 (93%)	11 (6%)	169 (94%)	12 (7%)	167 (93%)
2045	6 (0%)	84 (93%)	0 (0%)	90 (100%)	9 (10%)	81 (90%)
2061	0 (0%)	90 (100%)	2 (2%)	88 (98%)	5 (6%)	85 (94%)

Table 5. The results of classification for signal component D4 for gauss thresholds separately for locomotive 2045 and 2061

	X_2 Number (percentage) of classification as a		X_3 Number (percentage) of classification as a		X_4 Number (percentage) of classification as a	
	Proper	Improper	Proper	Improper	Proper	Improper
After both	110 (92%)	10 (8%)	110 (92%)	10 (8%)	110 (92%)	10 (8%)
2045	60 (100%)	0 (0%)	60 (100%)	0 (0%)	60 (100%)	0 (0%)
2061	50 (83%)	10 (17%)	50 (83%)	10 (17%)	50 (83%)	10 (17%)
Before both	9 (5%)	171 (95%)	7 (4%)	173 (96%)	6 (3%)	174 (97%)
2045	1 (1%)	89 (99%)	46 (51%)	44 (49%)	1 (1%)	89 (99%)
2061	7 (8%)	83 (92%)	5 (6%)	85 (94%)	6 (7%)	84 (93%)

for components S, D1 and D4 were chosen to build a classifier. It needs to define a threshold to distinguish the states of right and fault work of an engine.

At the beginning the simplest way was taken into account. The threshold was considered as a center between the parameter averaged value for the case before and the case after the repair. The results for this kind of thresholds appeared not perfect. But analyzing the original data more detailed it was noticed that resolutions of values for the state "after" was concentrated very broad in comparison with the values for the state "before" (see Table 2). Taking the "center" threshold gives a bad classification for signals before but better for signals after.

It can be seen from Table 7 that the standard deviations of parameters are approximately ten times bigger for the set of data "before". From the classifier construction point of view, it means that the threshold cannot be taken as a center of distance between before and after cases. To find the right threshold the Gaussian distribution was taken into consideration (find out that a mean and a standard deviation are enough to define a Gaussian distribution). This way a threshold should be define as a value, which is a coincidence point between two adjacent Gauss distributions, one for proper and the second for improper case. In other words, the threshold is a solution of equation created by equate two Gauss distribution with different means and standard deviations

$$G(x)_{\mu 2,\sigma 2} = G(x)_{\mu 2,\sigma 2} \tag{6}$$

These kinds of thresholds are calling in the paper as "gauss" thresholds. The results of classification for gauss thresholds were better but they all the time not satisfactory. The problem was in the fact that the set of all signal data were recorded on two locomotives but considered together. That's way the calculations were repeated for each locomotive separately.

Taking into account the center thresholds for each locomotive separately and classify all cases as improper (while the value of a parameter is below threshold) or proper (while the value of a parameter is above a threshold) separately for locomotive 2045 and 2061 give the results which are not satisfactory the same as for the analysis of data from two locomotives jointly. Here also can be noticed that resolutions of values for the state after are concentrated very broad in comparison with the values for the state before. Taking into account the means and standard deviations of distribution of parameters X_2, X_3, and X_4 calculated for the cases before and after for each locomotive separately the gauss threshold was using (threshold calculated basing on Gauss distributions). Considering gauss thresholds and classify all cases as improper (while the value of a parameter is below a threshold) or proper (while the value of a parameter is above a threshold) separately for locomotive 2045 and 2061 give the results of classification which are presented in Tables 3–5. These results are really the best and give a good perspective for using the above parameters and methods for classification of Diesel engine state.

Find that for classification performed in the paper a case was classified as improper while a corresponding value was below threshold and as a proper while the corresponding value was above a threshold. The state "before" represents a worn-out engine in bad conditions while state "after" represents the repaired engine in better general conditions. It strictly means that the values of Variance X_2, Root-Mean Square X_3 and Mean From Absolute Values X_4 of horizontal signal S and of it multiresolution components D1 and D4 are higher for proper engine working. At the same time the above parameters before the repair have significantly lower values (sometimes 10 or even 100 times) of standard deviation in comparison with the values for the same parameters for the case after repair. The resolutions of values for the state "after" are concentrated very broad in comparison with the values for the state "before". The bigger values of Variance, Root-Mean Square and Mean From Absolute Values show that the range of variability of the vibrations for repaired engine is higher. From practical point of view it seems that for the bigger values of the above parameters the engine is working "better". The sensors mounted on an engine body registered vibration signals which represent the influence of many vibration processes taken place in an engine, like combustion processes and functioning of engine parts. This is no way to distinguish between them and presented in the paper diagnostic base on the general indication of useful diagnostic parameters without finding the

relation to real mechanical engine processes. We can just say that the "better" working of an engine corresponds to better combustion and better working of engine parts.

6. Discussion

The analysis presented in the paper was performed to distinguish between different engine states corresponding to engine state before and after a repair using signal processing methods. For this analysis three parameters were eventually selected: Variance, Root-Mean Square and Mean From Absolute Values. The horizontal registration signals were chosen to analysis and in the calculations the original signal S and the two multiresolution components D1 and D4 were considered. The best results of classification were obtained for considering separately data from different locomotives. This shows that in this case the individual attributes of each signal can differ significantly for different signal source. In practice it means the classification and determination of thresholds should be performed separately for each locomotive engine. The even superficial analysis of the results is interesting and gives perspectives to practical application in combustion engine diagnostic. Although the results are very promising the great complexity and variety of possible measurement schemas need more experiments and researches before practical application in an on-line OBD diagnostic system.

Nomenclature

14D40	engine type
2045, 2061	locomotive numbers
A1–A5	multiresolution high frequency components of S
CWT	continuous wavelet transformation
D1–D5	multiresolution low frequency components of S
DWT	discrete wavelet transformation
FFT	Fast Fourier Transformation
M/X1	mean
MAV/X4	mean from absolute values
OBD	on board diagnostic
RMS/X3	root-mean square
S	original signal
SC/X5	shape coefficient
ST44	type of Diesel locomotive
VAR/X2	variance

Bibliography

[1] MERKISZ, J. Ecological aspects of combustion engines (Part 1 and 2). *Technical University of Poznań Publisher*, Poznań, Poland, 1998 and 1999 (in Polish).

[2] ABARBANEL, H.D.I. Analysis of observed chaotic data. *Springer*, 1996.

[3] BOGUŚ, P., MERKISZ, J. Short-time analysis of combustion engine vibroacoustic signals through pattern recognition techniques. *SAE Technical Paper Series* (2005), 2005-01-2529.

[4] BOGUŚ, P., MERKISZ, J. Misfire detection of locomotive diesel engine by nonlinear analysis. *Mechanical Systems and Signal Processing*. 2005, **19**, 881-899.

[5] BOGUŚ, P., MERKISZ, J. Wavelets application in combustion engine diagnostic. *Combustion Engines*. 2013, **154**(3), 226-231.

[6] BOGUŚ, P., DEDO, M., GRZESZCZYK, R., WRONA, A., MARKOWSKI, J., MERKISZ, J. Estimation of fuel spraying from diesel engine injector using multiresolution wavelet analysis of vibroacoustic signals. *Combustion Engines*. 2015, **162**(3), 264-270.

[7] GOSWAMI, J.C., CHAN, A.K. Fundamentals of wavelets. theory, algorithms, and applications. *John Wiley & Sons,* 2010.

[8] MITRA, S.K., KAISER, J.F. (eds.) Handbook for digital signal processing. *John Wiley & Sons*. 1993.

[9] SMITH, S.W. Digital signal processing: a practical guide for engineers and scientists. *BTC*. Warszawa, 2003 (in Polish).

[10] CHUI, K. Wavelets: A mathematical tool for signal processing. *SIAM Society for Industrial and Applied Mathematics*. 1997.

[11] AL-BADOUR, F., SUNAR, M., CHEDED, L. Vibration analysis of rotating machinery using time–frequency analysis and wavelet techniques. *Mechanical Systems and Signal Processing*. 2011, **25**, 2083-2101.

[12] PENG, Z.K., CHU, F.L. Application of the wavelet transform in machine condition monitoring and fault diagnostics: a review with bibliography. *Mechanical Systems and Signal Processing*. 2004, **18**, 199-221.

[13] TSEA, P.W., YANGB, W., TAMA, H.Y. Machine fault diagnosis through an effective exact wavelet analysis. *Journal of Sound and Vibration*. 2004, **277**, 1005-1024.

[14] BOGUŚ, P., SIENICKI, A., WOJCIECHOWSKA, E., MERKISZ, J. The comparison of vibroacoustic signals taken from an engine before and after repair. *Combustion Engines*, 2007-SC3, 300-306.

Piotr Boguś, DSc., DEng. – Department of Physics and Biophysics of Medical University of Gdańsk, Rail Vehicle Institute TABOR in Poznań.

e-mail: *Piotr.Bogus@gumed.edu.pl*

Mateusz Cieszyński, MSc. – Department of Physics and Bio-physics of Medical University of Gdańsk.

Prof. Jerzy Merkisz, DSc., DEng. – Faculty of Machines and Transport at Poznan University of Technology.

e-mail: *Jerzy.Merkisz@put.poznan.pl*

Article citation info:
WOJS, M.K., ORLIŃSKI, P., LASOCKI, J. The effect of alternative fuels injection timing on toxic substances formation in CI engines. *Combustion Engines*. 2017, **168**(1), 73-76. DOI: 10.19206/CE-2017-112

Marcin K. WOJS
Piotr ORLIŃSKI
Jakub LASOCKI

CE-2017-112

The effect of alternative fuels injection timing on toxic substances formation in CI engines

The present study describes selected issues associated with the emission level in toxic exhaust gases and fuel injection timing. The study was focused on the following types of fuels: Diesel oil (the base fuel) and the other fuels were the mixture of fatty acid methyl ester with Camelina (L10 – diesel fuel with 10% V/V FAME of Camelina and L20 – diesel fuel with 10% V/V FAME of Camelina) was used. Fuel injection advanced angle was set for three different values – the factory setting – 12° before TDC, later injection – 7° and earlier injection – 17°. The most important conclusion is that in most measurement points registered in the same engine operating conditions, the concentration of fuel NO_x in L10 and L20 increased but PM emissions decreased which is caused by active oxygen located in the internal structure of the fuel. This fact contributes to the rise in temperature during the combustion process. At the same time factory settings of the angle makes NO_x emissions lower and close to reference fuel.

Key words: *Biofuels, diesel engine, toxic substances*

1. Introduction

In the past few years there has been rapid development of public awareness and concern for the environment. Contamination of the environment has reached a level from which man had so far not met. It has been shown that the emission of harmful substances into the environment affects human life, the productivity of agricultural and natural ecosystems [15]. It has a direct impact on human health and contributes to respiratory illnesses; particularly allergies. Air pollution causes corrosion of metals and construction materials. Act adversely on the plants, disrupts photosynthesis and taints water and soil. On a global scale have an impact on climate change. The most characteristic examples of the risks are [5]:

- acid rains,
- the phenomenon of white smog (photochemical),
- black smog phenomenon (London),
- the greenhouse effect,
- decrease in the protective ozone layer.

Constantly tightening up the criteria for toxic exhaust emissions and decreasing oil resources are forcing the automotive industry to intensify research and finding for new technical solutions, offering the possibility of using alternative fuels and ensuring the least possible adverse impact of vehicles on the natural human environment. Reducing emissions of harmful compounds should focus primarily on reducing their formation in the engine (direct method), and then at their disposal (indirect method) [1, 2, 13, 14]. The main activities are focused on improving the combustion process in the engine by optimizing the design and implementation of additional systems, limiting the production of harmful substances in the combustion chamber. These activities are limited, since the primary task of the internal combustion engine is to produce energy in a highly effective and efficient way [5, 8, 12].

The article focuses on the impact of different fuels (ON, L10, L20) on formation of the toxic components at exhaust gases for different injection timing angles. This subject is moved mainly in Europe due to the origin of the plant used for production of L10 and L20 and partially was investigated by authors of publications as to the effect of the injection timing on combustion process [11]. The originality of presented research results is that the authors use to power the engine mixtures of diesel oil and fatty acid methyl esters - L10 and L20.

2. Experimental apparatus and procedure

The aim of the study is to analyze and evaluate the emission of toxic components in exhaust gases. Research was carried out on three fuels; namely, ON (diesel oil), L10, L20, and for three different angles of injection timing. Measurements related to the two standardized toxic components of exhaust gases: PM and NO_x were conducted. These two toxic components from the exhaust were designated from other components in the study because of the highest observed differences in their concentrations during tests on engine when engine was supplied with described fuels in different operation conditions.

Experimental tests were performed on a test bench in accordance with the C1 test procedure and ISO 8178 [3]. For the measurement of toxic components in exhaust gases AVL CEB II gas analyzer was used. The analyzer measures the concentrations of NO_x using CLD method – chemiluminescent sensor. It utilizes the phenomenon of emission of electromagnetic radiation of a wavelength 0,6-3 microns, accompanying the reaction of nitric oxide NO with ozone, O_3. The reaction produces radiation that can be converted later into an electrical signal. This signal is proportional to the intensity of the radiation, and thus the concentration of nitric oxide in the exhaust. Measurement of particulate matter was done in real time using the unit Horiba MEXA 1230. This device provides a continuous measurement of the components of the particulate emissions. Our research results show the sum of the weights recorded of soot and soluble organic molecules.

Three fuels used during the tests, namely ON, L10 and L20. Diesel fuel is the base fuel and the other fuels are ON and the mixture of fatty acid methyl ester with camelina, which could be, on grounds of its physicochemical properties, fuel substitute for pure ON [6, 7, 10]. It is known that

pure camelina ester is a promising future fuel because it belongs to the second generation of alternative fuels promoted and recommended for potential use in the European Union.

Table 1. Physical and chemical properties of three fuels ON, L10, L20

Parameter	ON (diesel oil)	L10	L20
Density [g/cm^3]	0.83	0.834	0.839
Viscosity [mm^2/s]	2.8	3	3,2
The calorific value [MJ/kg]	42.5	42	41
Cetane number	55	54	53

The test stand was based on the Perkins 1104C-E44T engine. It is a four-cylinder turbocharged diesel engine with direct fuel injection into the combustion chamber and liquid-cooling. This engine is electronically controlled, it has two ECU types: primary for engine and secondary for injection pump control. It is designed for working machines, agricultural tractors and power generators [4, 9, 10]. The tests measuring system consists of four measurement channels: (i) the pressure in the combustion chamber, (ii) the angle of rotation of the crankshaft, (iii) the toxic exhaust emissions, and (iv) the particulate emissions.

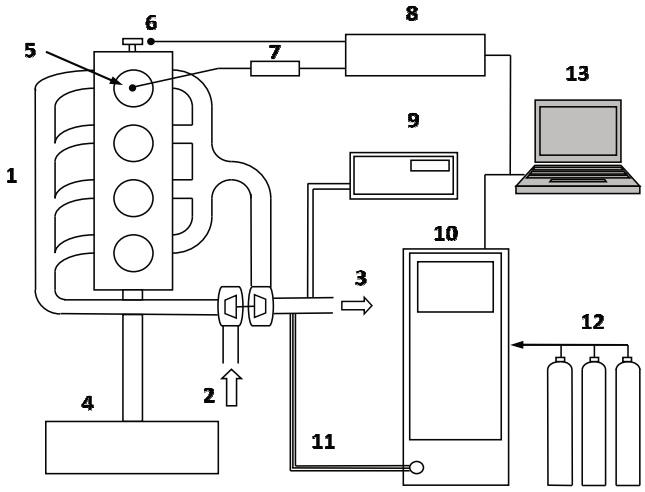

Fig. 1. Diagram of the test bench: 1 – engine PERKINS 1104C-E44T; 2 – air inlet; 3 – exhaust; 4 – brake; 5 – piezoelectric pressure sensor; 6 – crankshaft angle sensor; 7 – amplifier; 8 – indicating device; 9 – Horiba MEXA 1230 unit; 10 – AVL CEB II gas analyzer; 11 – heated route; 12 – reference gases; 13 – PC computer

3. Results and discussion

Because of the inaccuracy of instruments and testing methods, measuring result is always different from the actual measured values. Research was conducted on Perkins 1104C-E44TA and carried out using engine dynamometer and gas analyzers: AVL CEB II and Horiba MEXA 1230. Both analyzers have the same class of measuring which is 5% of maximum range of measurement.

The results are shown in Figures below. They presented as speed and load characteristics for n = 1400 rpm, that is crankshaft rotation speed of maximum torque. The results are presented for the three previously mentioned types of fuel (ON, L10, L20) at an angle of fuel injection timing set for three different values labeled – A, B, C. The injection advance angle A is the factory setting – 12^o before TDC, value B causes subsequent injection angle by about 5^o after A, and setting C is earlier injection of around – 5^o before A. Studies of toxic emissions for three fuels at three injection timing settings were conducted in accordance with test C1.

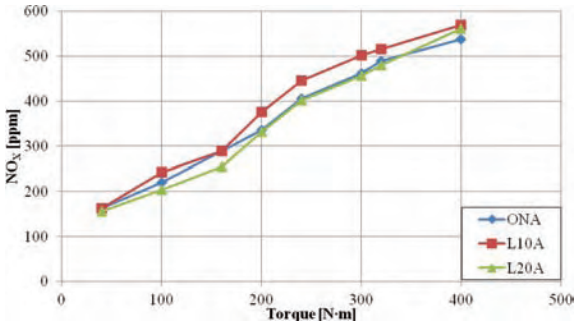

Fig. 2. NO_x concentration for injection timing A and n = 1400 rpm

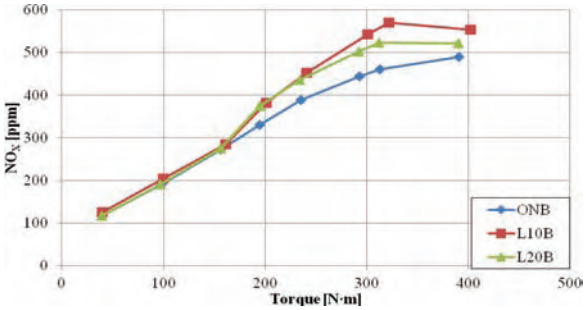

Fig. 3. NO_x concentration for injection timing B and n = 1400 rpm

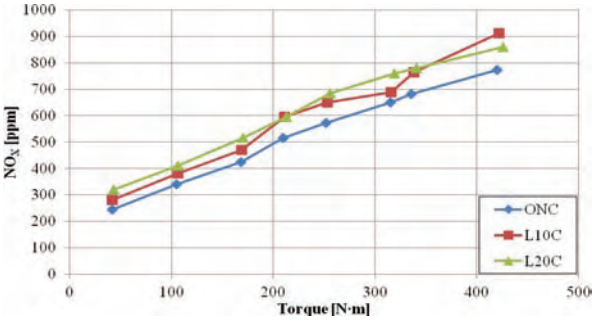

Fig. 4. NO_x concentration for injection timing C and n = 1400 rpm

Comparing the concentration of toxic components shows that for each injection angle, the highest concentration of the NO_x was observed in the case of fuel L20, whereas the lowest pertained to fuel ON. The biggest difference in NO_x formation was detected for fuels L20 and ON when injection timing angle C was set. Mentioned difference amounts to approx. 25%. (cf. Fig. 4).

The concentration of PM is the smallest in the case of fuel L20, and the largest for ON. The difference between the concentration of PM for fuel ON, and the concentration of PM for L20 when injection timing angle C was set (cf. Fig. 7) is approx. 35% for a maximum load of the engine.

The results shown in Figures 8–13 include speed and load characteristics carrying at n = 2000 rpm, that corresponds to the crankshaft rotation speed of the maximum power. Values of NO_x for all angles and fuels are almost identical. The lowest values of NO_x are obtained for angle B (cf. Fig. 9).

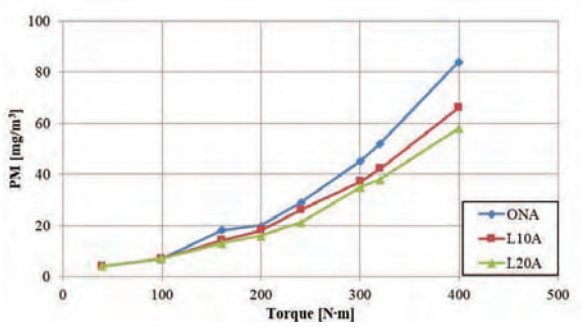

Fig. 5. PM for injection timing A and n = 1400 rpm

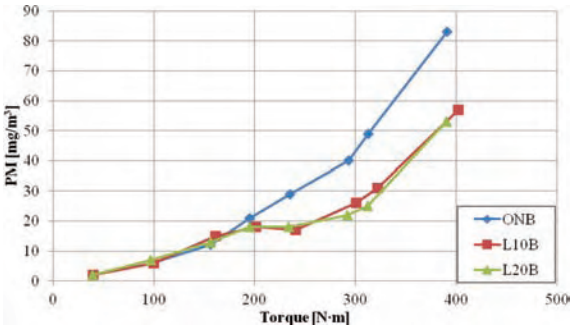

Fig. 6. PM for injection timing B and n = 1400 rpm

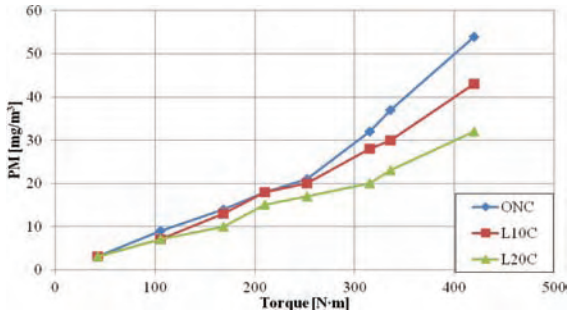

Fig. 7. PM for injection timing C and n = 1400 rpm

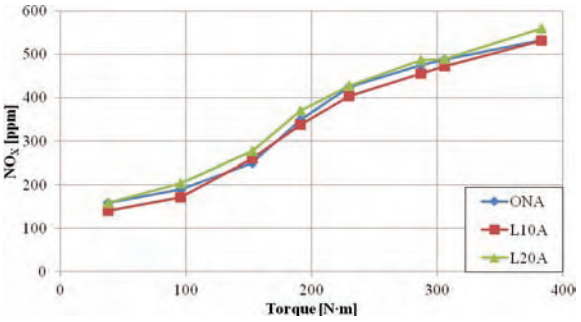

Fig. 8. NO_x concentration for injection timing A and n = 2000 rpm

The concentration of PM is the smallest for fuel L10, and almost identical for ON and L20. The difference between the concentrations of PM for fuel ON, L20 and L10 (cf. Figures 11 and 12) at injection timing angles A and B is approx. 60% for the maximum load of the engine.

In order to finally confirm the test results, the authors plan in the future to investigate the combustion process and associate it with the results of exhaust gas emissions levels.

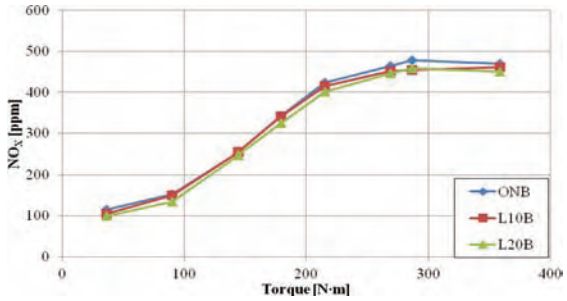

Fig. 9. NO_x concentration for injection timing B and n = 2000 rpm

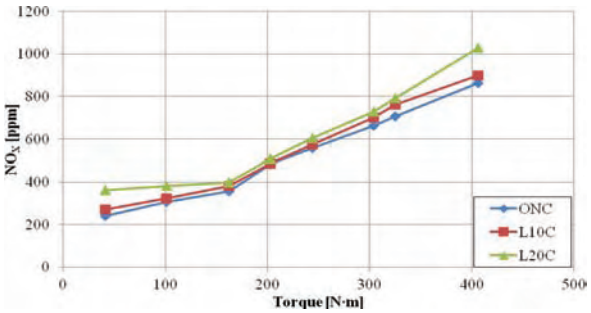

Fig. 10. NO_x concentration for injection timing C and n = 2000 rpm

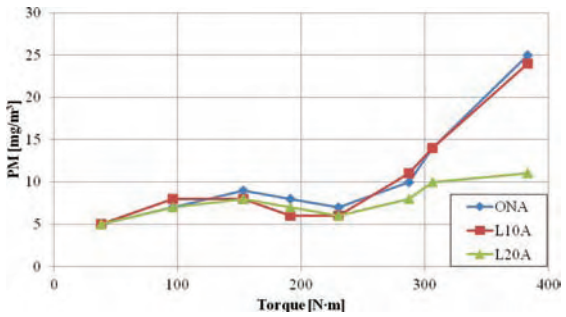

Fig. 11. PM for injection timing A and n = 2000 rpm

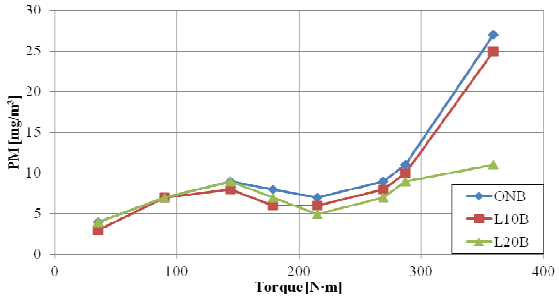

Fig. 12. PM for injection timing B and n = 2000 rpm

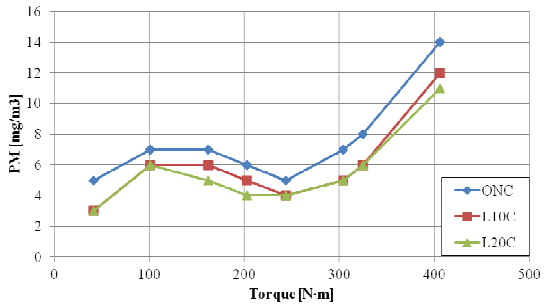

Fig. 13. PM for injection timing C and n = 2000 rpm

4. Conclusions

The results of experimental studies illustrate the difference in emissions of toxic components in exhaust gases (NO_x and PM). The study was carried out for two characteristic crankshaft rotation speeds (corresponding to maximum power and maximum torque of the engine) as a function of load. In addition, the study presented different setting of the fuel injection timing with respect to the concentrations of these two toxic components.

Analyzing the test results for two different characteristic speeds the following conclusion can be made:

- in most measurement points registered in the same engine operating conditions when fuel L10 and L20 is used, NO_x concentration increases, PM emissions decreases which is caused by active oxygen content in the internal structure of the fuels and thus contributing to the rise in temperature during the combustion process,
- the highest concentrations of NO_x and the smallest PM were recorded at maximum fuel injection timing angle (angle C). The reason for it was the advanced start of the combustion process (perhaps even before TDC) and thus causing the higher level of maximum pressure and temperature of the working medium in the combustion chamber.

Nomenclature

CLD chemiluminescent sensor method
ECU electronic control unit
FAME fatty acid methyl ester
L10 diesel fuel with 10% V/V fatty acid methyl ester of Camelina oil
L20 diesel fuel with 20% V/V fatty acid methyl ester of Camelina oil
NO nitric oxide
NO_x oxides of nitrogen
ON diesel fuel
PM particulate matter
TDC top dead center

Bibliography

[1] AGARWAL, A.K. Biofuels (alcohols and biodiesel) applications as fuels for internal combustion engines. *Progress in Energy and Combustion Science*. 2007, **33**, 233-71.
[2] AMBROZIK, A., AMBROZIK, T., ŁAGOWSKI, P. Fuel impact on emissions of harmful components of the exhaust gas from the ci engine during cold start-up. *Eksploatacja i Niezawodność – Maintenance and Reliability*. 2015, **17**(1), 95-99.
[3] AMBROZIK, A., ŁAGOWSKI, P. Podstawy sterowania i diagnostyki silników o zapłonie samoczynnym, *Wydawnictwo Politechniki Świętokrzyskiej*, 2016. Kielce.
[4] Instructions for Perkins 1100 Series. (IFP).
[5] KRUCZYŃSKI, S.W. Filtracja cząstek stałych w spalinach pojazdów samochodowych, *Instytut Naukowo-Wydawniczy SPATIUM*, 2011, Radom.
[6] KRUCZYŃSKI, S.W. Performance and emission of CI engine fuelled with camelina sativa oil. *Energy Conversion and Management*. 2013, **65**, 1-6.
[7] KRUCZYŃSKI, S.W., ORLIŃSKI, P. Combustion of methyl esters of various origins in the agricultural engine. *Indian Journal of Engineering and Materials Sciences*. 2013, **20**, 483-491.
[8] MOSER, B.R. Fuel property enhancement of biodiesel fuels from common and alternative feedstocks via complementary blending. *Renewable Energy*. 2016, **85**, 819-825.
[9] ORLIŃSKI, P, WOJS, M. K., MAZURUK, P. Budowa stanowiska do badań paliw eksperymentalnych płynnych wykorzystującego silnik rolniczy o zapłonie samoczynnym. *Zeszyty Naukowe Instytutu Pojazdów*. 2013, **1**(92), 167-172.
[10] ORLIŃSKI, P. Wybrane zagadnienia procesu spalania paliw pochodzenia roślinnego w silniku o zapłonie samoczynnym, *Instytut Naukowo-Wydawniczy SPATIUM*, 2013, Radom.
[11] ORLIŃSKI, P. Ocena wpływu zmiany kąta wyprzedzenia wtrysku na proces wydzielania ciepła w silniku rolniczym zasilanym biopaliwami. *Logistyka*. 2014, **3**, 4843-4854.
[12] PRZYBYŁA, P. Studium stosowania biopaliw gazowych do zasilania silników spalinowych, *Wydawnictwo Politechniki Śląskiej*. 2015, Gliwice.
[13] RAKOPOULOS, C.D., ANTONOPOULS, K.A., RAKOPOULOS, D.C., HOUNTALAS, D.T., GIAKOURNIS, E.G. Comparative Performance and emission study of DI diesel engine with vegetable oil. *Energy Conversion and Management*. 2006, **47**, 3272-87.
[14] REHMAN, H., PHADATARE, A.G. Diesel Engine emission and performance from blends of karanja methyl ester and Diesel. *Biomass and Bioenergy*. 2004, **27**, 393-297.
[15] REIF, K. Gasoline engine management: systems and components. *Springer Fachmedien*. 2015, Wiesbaden.

Marcin Krzysztof Wojs, DEng. – Faculty of Automotive and Construction Machinery Engineering at Warsaw University of Technology

e-mail: *mwojs@simr.pw.edu.pl*

Piotr Orliński, DEng. – Faculty of Automotive and Construction Machinery Engineering at Warsaw University of Technology

e-mail: *mwojs@simr.pw.edu.pl*

Jakub Lasocki, DEng. – Faculty of Automotive and Construction Machinery Engineering at Warsaw University of Technology.

e-mail: *j.lasocki@simr.pw.edu.pl*

Article citation info:
GĘCA, M. Cylinder-to-cylinder and cycle-to-cycle variation in combustion process in radial aircraft engine. *Combustion Engines*. 2017, **168**(1), 77-83. DOI: 10.19206/CE-2017-113

Michał GĘCA

CE-2017-113

Cylinder-to-cylinder and cycle-to-cycle variation in combustion process in radial aircraft engine

Cycle-to-cycle variation in combustion in a single cylinder of a radial engine has an impact on that in others and the entire engine. Steady- and transient-state engine operation was investigated, and the transient states were generated by cyclic changes in the timing of fuel injection to a given cylinder, having others operated on the same mixture composition. The measurement of pressure in the combustion chamber allowed for specifying indicated mean effective pressure (IMEP) in all cycles. The time series of IMEP were studied with mathematical techniques of non-linear dynamics, i.e. a wavelet transform and a multifractal analysis. Controlled disturbances in mixture composition in a single cylinder can have an impact on certain cylinders only. Cylinders 3, 5, 7 and 9 are most responsive to such disturbances, which proves their least cycle-to-cycle variation in combustion.

Key words: *radial engine, combustion, non-uniformity, cycle-to-cycle variation, wavelet analysis, multifractal analysis*

1. Introduction

Cycle-to-cycle variations in cylinder operation is typical of multi-cylinder engines. Performance of a next cylinder and combustion in a given cylinder are impacted by a design of a combustion chamber [1], pistons, a piston-crankshaft system, location of spark plugs and arrangement of cylinders [14]. Cylinders in the radial engine are arranged radially around the crankshaft, with their axes intersected at one point. Intake lines, connecting the compressor and heads of the carburetor-powered engine, are identical in shape but supply a differently composed air-fuel mixture, which is due to gravity acting on fuel drops and a fuel film. A mixture and fuel film move clockwise (lower cylinders) or counterclockwise (upper cylinders) with respect to gravity. The compressor moves by several degrees a fuel film in the same direction as its own rotation. Upper cylinders receive a lighter but lean mixture, whereas lower ones a heavier but richer mixture. A mixture of the air-fuel ratio larger than 1, i.e. $\lambda > 1$, or a lean mixture burns longer and makes an excessive increase in temperature of combustion chamber elements. As a result, it is difficult to maintain an appropriate head temperature in air-cooled radial engines and if temperature increases, knock occurs. The research by an American company, Radial Engines Ltd., a manufacturer of seven-cylinder radial engines Motors Jacobs R755B2 (202 kW) confirms an irregularly distributed mixture in cylinders, having analysed temperatures of exhaust gases in cylinders [22].

Multi-point fuel injection is the method to stabilize a mixture in steady states and to limit cycle-to-cyle variations in the operation of the combustion engine. Unfortunatelly, supplying the radial engine by injection cannot entirely be a solution here because more than 90% of fuel after injection settles down on intake system walls and only 10% of it reaches the cylinder in the first operating cycle. The rest of fuel evaporates with delay or reaches the combustion chamber in the liquid phase. Equilibrium, after which the mass of fuel injected into the intake system is the same as the mass of fuel which reaches the cylinder, is achieved after 6 operating cycles [19].

The irregular distribution of IMEP between cylinders in the ASz-62IR supplied by injection of Pb95 and Avgaz 100LL is discussed in [10].

Cycle-to-cycle variation is also impacted by the distribution of temperature on a cylinder surface. In the air-cooled radial engine, the cylinder head and liner are heated unevenly.

Cycle-to-cycle variation in the multi-cylinder engine can result from irregularly distributed any of the above factors in cylinders [15] as well as non-linear entire combustion (several possible courses of this process). The way the crankshaft-piston system in the radial engine is designed can differentiate a piston stroke. Each cylinder slightly differs in a degree of its compression and displacement.

The phenomenon of cylinder-to-cylinder variation is also impacted by cycle-to-cycle variation in combustion. The cyclical nature of processes follows from the nature of processes in the engine, i.e. the principle behind the operation of the piston internal combustion engine. Cycle-to-cycle variation in combustion may result in instability which reduces engine power [9, 11].

Cycle-to-cycle variation in combustion is especially high in SI engines. The sources of pressure oscillation were first classified by Heywood (the 1980s) as a degree of turbulence in the cylinder during combustion, a diversity of the amount of air and fuel, and the rest of exhaust gas in the cylinder as well as the local distribution of mixture around the spark plug [8]. The changed quality of a mixture has an impact on cycle-to-cycle variation [12].

A mathematical technique enables us to study time series and predict the future from the past. Data collected as time series give information on the past. Predicting the future from a statistical analysis is predicting possible behaviours. Importantly, predicting changes and tendencies can also become complicated if an investigated dynamic system has many solutions, which is a fundamental feature of non-linear systems. Slightly modified initial conditions or parameters of the system in non-linear systems can lead to a significantly modified response of the dynamic system, e.g. an internal combustion engine and its combustion.

Other interesting effects to be expected in non-linear systems are time synchronization and spacial location.

Importantly, the previous studies on the phenomena of irregularity and cyclical variation chiefly investigated automotive liquid-cooled engines and a single cylinder only. Unlike the radial engine, their intake ducts are arranged gravitationally.

The author proposed [4] a physically proven non-linear map as a model of cylinder-to-cylinder variation in the SI engine. He also discussed an approach of symbol rates statistics to digitize model and research time series. Other authors attempted [3] to synchronize cylinder-to-cylinder variation in automotive high-capacity engines. Cycle-to-cycle variation in combustion in the carbureted radial engine is investigated [2] to show significant differences in combustion in each cylinder and confirm cylinder-to-cylinder variation.

The methods to investigate time series of cylinder pressure with non-linear dynamics are efficient and allow for an in-depth understanding of an internal combustion engine. Cycle-to-cycle variation was examined by a number of researchers with the methods of non-linear dynamics to find out nonlinear aspects of variation [5]. The works using a wavelet transform and a multifractal analysis also followed this tendency [13, 18].

By investigating pressure in a given cylinder, it can be said that pressure clearly changes over time, both for its amplitude and frequency. Phase-frequency and time-frequency selections are sensible approaches to study the combustion engine bacause of rapid changes that occur at high frequencies and slow changes in low frequencies. This method is capable of defining positions of a filter on a time-frequency map by a scale factor and a window shift. If a window shifts towards high frequencies, its width decreases, which reduces resolution rate and increases time resolution and the other way round.

Recurrence plots method has been used to distinguish combustion dynamics of a multicylinder aircraft radial engine in the presence of cyclic perturbations in one of cylinders [6]. This paper follows non-linear methods to describe the mode of combustion in each radial engine cylinder. There are applied quantitative methods as a multifractal analysis and qualitative methods as a wavelet transform. These two approaches allowed for investigating an operating cycle in each cylinder and the impact of combustion in a given cyclinder on combustion in others.

2. Research object and the engine test stand

The research object is a four-stroke, air-cooled, gasoline aircraft engine – ASz-62IR (Fig. 1), manufactured at WSK "PZL-Kalisz". It is now a drive unit in the following aircraft: An-2, M-18 ”Dromader”, DHC-3 ”OTTER”, DC-3 “Dakota”, GAF-125 ”HAWK” and Y5. Our research engine has 9 radially-arranged cylinders with a total displacement of 29.87 dm^3. The engine is supecharged mechanically with a radial compressor driven from a crankshaft with a gear of 1:7. The maximum boost pressure is 0.14 MPa, and compression 6.4:1. The maximum power of approximately 745 kW (1,000 hp) is achieved at 2,200 rpm. The maximum fuel consumption at take-off power is approximately 300 kg/h. The engine is supplied with 9 electronically controlled injectors that inject fuel into all of the intake pipes.

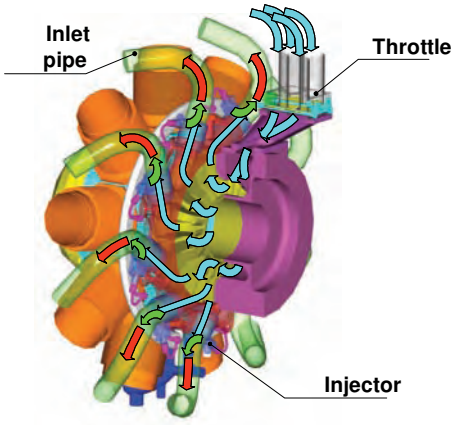

Fig. 1. ASz-62IR supplied by injection system

The engine section has a construction where our research engine is attached (Figure 2). Load is a four-bladed propeller with an adjustable angle of attack. Torque is measured by changing the position of counterweight. The so read reaction torque and regarding the factors behind the test stand enabled us to specify the torque generated by the engine.

To monitor the parameters of its performance, the research engine is equipped with sensors such as 4 pressure transmitters MPX4250 under the carburetor, 2 pressure transducers MPX4250 Motorola in each of the intake pipes at the compressor and head.

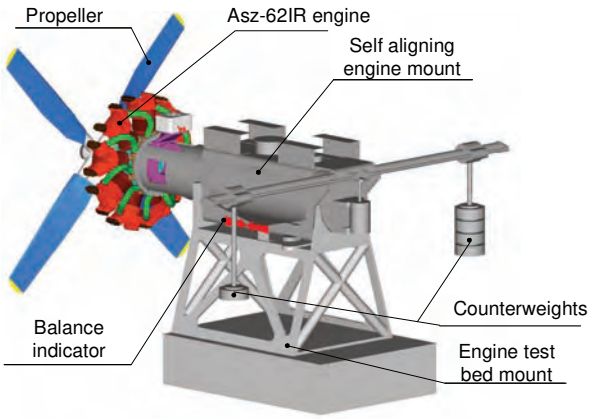

Fig. 2. Schematic of the engine section at the engine test stand

Combustion process was monitored with OPTRAND M 3.5 x 0.6 optoelectronic sensors installed in special adapters screwed in the central section of the head. This type of sensor monitors how the intensity of light from two adjacent fibers, one connected to the LED and the other to a photodetector changes. Any changes in the intensity of light received by the photo diode result from changes in the intensity of light reflected by a steel membrane which is deformed by pressure [21].

The cylinder pressure sensor consists of a pressure transducer connected to a signal transducer by means of an

optic fiber. The measurements of combustion pressure in each cylinder were synchronized and automatically performed in line with the signals from the magneto-inductive sensor to monitor engine speed and the position of a Honeywell crankshaft. Pressure signals were amplified and sent to an acquisition card to be archived on a hard drive.

3. Research methodology

3.1. Test stand research

The operation of the engine was studied in steady states, at constant speed and load as intake manifold air pressure. The measurements were performed for a middle operating range, i.e. speed n = 1,770 rpm and load ranging between a propeller characteristics and a full power characteristics at p_k= 0.094 MPa. At the measuring point, the engine generates a power of 353 kW and fuel consumption per hour is 109 kg/h (Figure 3). These conditions correspond to cruise speed of the airframe and are most frequent in operation.

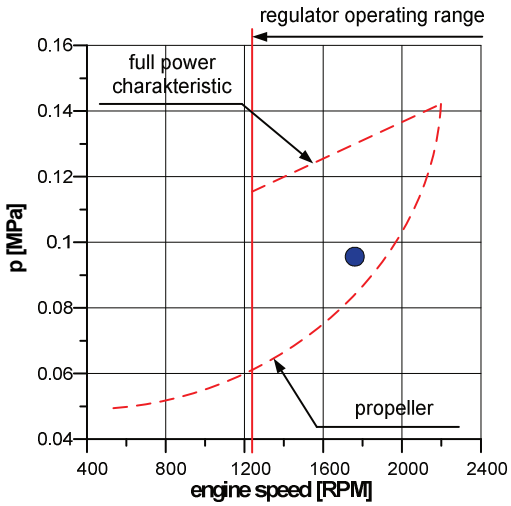

Fig. 3. Operating range and the measuring point [6]

Our transient investigation involved registering cylinder pressure during a case, in which one of considered cylinders was perturbed by changing the injection timing. Each of the cylinders was supplied by a mixture of λ = 0.7. The fuel injection timing was selected so as to obtain a given value of air-fuel ratio. This composition was achieved by selecting fuel injection time as t_1 = 7.8 ms. One of the cylinders was fuelled in a varying step way by changing the injection time every 10s from t_1 = 7.8 ms to t_2 = 5.84 ms according to the diagram given in Fig. 4 [6].

There were 9 measurement series in which a given cylinder was cyclically supplied according to the order of ignitions (Fig. 5). Pressures in 9 cylinders, i.e. 8 of them supplied by a mixture of constant composition and 1 by a mixture of disturbed composition were simultaneously registered at each measuring point.

There were also measurements in which one cylinder was supplied by a mixture of disturbed composition and the others were supplied by a mixture of λ = 0.7. Combustion chamber pressure was measured with a sampling frequency of 22 kHz (2 samples per one crankshaft rotation). Then, the IMEP for subsequent 1,000 cycles was calculated from each engine cycle. The surface area of the indicated pressure chart was calculated. A single sample shows measured pressure and displacement. The IMEP of a single cycle can be calculated from the formula:

$$\mathrm{IMEP(i)} = \frac{1}{V_s}\sum_{j=0}^{n-1}\frac{(P_{j+1}+P_j)}{2}(V_{j+1}-V_j) \tag{1}$$

where $(P_j + P_{1,j})$, (V_{j+1}, V_j) are respectively j+1 and j-th value of combustion chamber pressure and volume and n is the number of samples per cycle. This means that the calculation of IMEP is coordinated with the crankshaft position. The calculation data included the length of a connecting rod, a cylinder bore and the time of a single cycle.

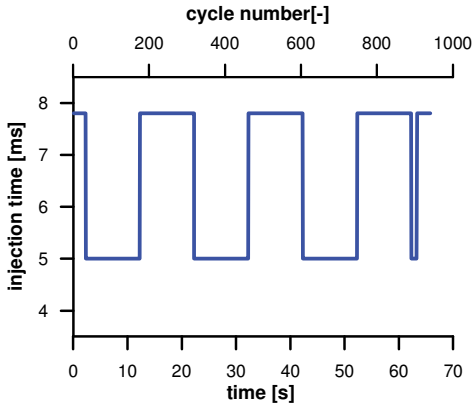

Fig. 4. Diagram of mixture composition disturbance in the individual cylinder [6]

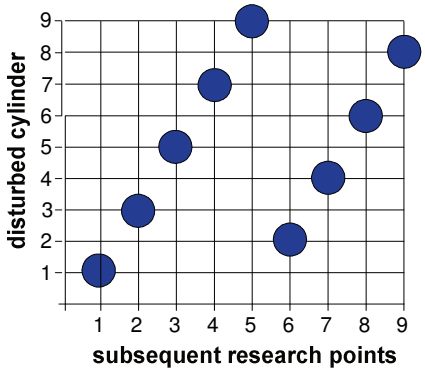

Fig. 5. Order of disturbances in mixture composition in the cylinders

3.2. Wavelet analysis

The wavelet transform can use any base function as a base function [17]. The Morlet function is most popular for its simplified mode of calculation. This method resembles a filtration with a constant relative bandwidth $\Delta f/f_s$. The parameters of scale a and transposition b determine the location of the filter on the time-frequency map. Bandwidth increases with the b to larger frequencies (frequency resolution of analysis decreases), and then time resolution increases and the other way round. This feature is used in a simultaneous analysis of various high- and low-frequency time steps and rapidly changing processes of low speed.

The Continuous Wavelet Transform (CWT) analyzed the time series of IMEP. The wavelet transform in relation to a wavelet function $\psi(\cdot)$ is defined as follows:

$$W_{s,n}(IMEP) = \sum_{i=1}^{N} \frac{1}{s} \Psi\left(\frac{i-n}{s}\right) \frac{(IMEP(i) - < IMEP >)}{\sigma_{IMEP}} \tag{2}$$

where < IMEP > is the mean and σ_{IMEP} is a standard deviation. A wavelet $\psi(t)$ is a base wavelet, n is a scale shift and s is a positive real number creating the scale. A wavelet power spectrum (WPS) of the time series of IMEP is defined as the square of the absolute value of CWT.

$$P_w(s,n) = \left|W_{s,n}\right|^2 \tag{3}$$

Our calculation uses as a base function the complex Morlet wavelet which consists of a flat wavelet modulated by the Gaussian function and is defined by the formula:

$$\Psi(\eta) = \pi^{-1/4} e^{i\theta_0 \eta} e^{-\eta^2/2} \tag{4}$$

The value of q_0 defines the number of oscillations in the wavelet to control time-frequency resolution. $\theta_0 = 2\pi f_0$ is defined as a wavelet degree where f_0 is a frequency center. Higher θ_0 improves frequency resolution but if lower, time resolution improves. Our analysis uses $\theta_0 = 6$. Such an approach results in a time and frequency resolution balance. The scale is also roughly equal to the period so the conditions of scale and time can be interchanged while investigating results.

3.3. Multifractal analysis

A multifractal analysis of IMEP oscillation consists of a specific spectrum of time series of IMEP against the Hölder exponent as a function of the Hausdorff distance. Its complexity can be evaluated by means of the width of a multifractal spectrum.

Following the procedure [16], the vicinity of each cycle and along a studied time series of IMEP (i + Δi) are investigated to find coefficient hi (incomplete number) capable of determining the corresponding discrepancy:

$$|IMEP(i) - IMEP(i + \Delta i)| \leq a_h \, \Delta i^{hi} \tag{5}$$

Factor a_h is related to exponent h_i which specifies a local internal separation. Generally, a multifractal analysis is based on a specific spectrum f(h) of all exponents h_i and precisely describes a quantitative behavior of a system. Formally, h defines the Hölder exponent and the probability of its decomposition, f(h), coincides with the Hausdorff distance of a dynamic system.

Figure 6 shows a sample method of specifying critical exponents for time series of indicated pressure when mixture composition was modified in cylinder 1. The red curve refers to the results from the multifractal analysis using a modified software code [7]. Across it, there is marked a tendency line (blue) calculated from a 4-level polynomial and least squares. The formula of a polynomial was entered into the MATHCAD to find the squares of the equation. Its complexity can be evaluated by means of the width of a specific spectrum, i.e. the value of critical exponents Δα.

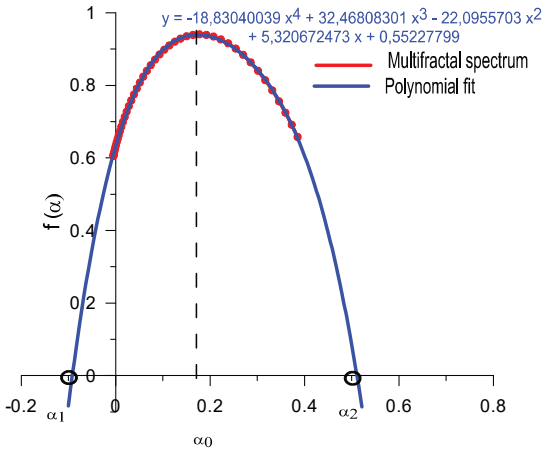

Fig. 6. Sample of a multifractal spectrum with critical exponents $\Delta\alpha$ and its most expected value of α_0 when mixture composition was modified in cylinder 1

4. Research results

In each series of our measurements, from 950 to 1,040 operating cycles were examined. Such a range was selected due to our research method in which the engine was held at a given operating point over a given constant period of time of 1 min. Such a period of time was selected to achieve a minimum of 900 operating cycles but it was limited by the size of the files with the measurements of several quantities to be saved.

IMEP was calculated from each of the registered cycles to create a time series of IMEP. Figure 7 shows a sample of a time series at a given measuring point when the mixture composition was disturbed in cylinder number 5.

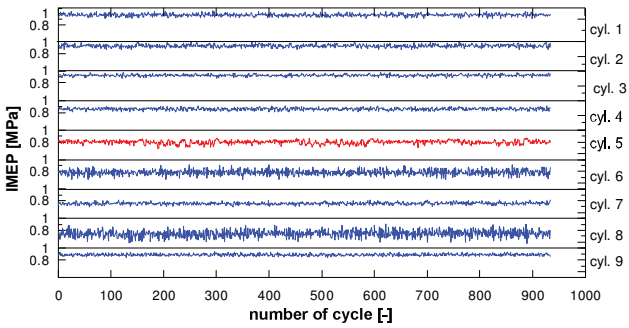

Fig. 7. IMEP time series in subsequent operating cycles when mixture composition was modified in cylinder 5

Figure 8 shows the research results of our MF analysis of the IMEP in the cylinders if the engine was driven by all of the cylinders supplied by a non-modified mixture composition of λ = 0.7. There were specified: a range of critical exponents Δα and its expected value α_0. The dotted line shows the maximum values of the exponents of our MF analysis (case without injection perturbations in cylinders).

Figure 9 shows the research results of our MF analysis with the operation of the engine with one mixture-modified cylinder, marked with the black circle, and the other cylinders supplied by a mixture of λ = 0.7. In addition, the dashed lines marked in all of the charts stand for the maxi-

mum values of the critical exponents of our MF analysis that occur if the engine is not disturbed by a modified fuel dose supplied into a given cylinder (see Fig. 9). The bottom right section of the figure shows again the research results of our MF analysis but for the modified cylinders only.

The results show that some of the modified cylinders can be distinguished by their extreme values of $\Delta\alpha$ and α_0. The maximum value of $\Delta\alpha$ for the modified cylinder no. 3 (a black circle) is due to a cyclically disturbed mixture composition.

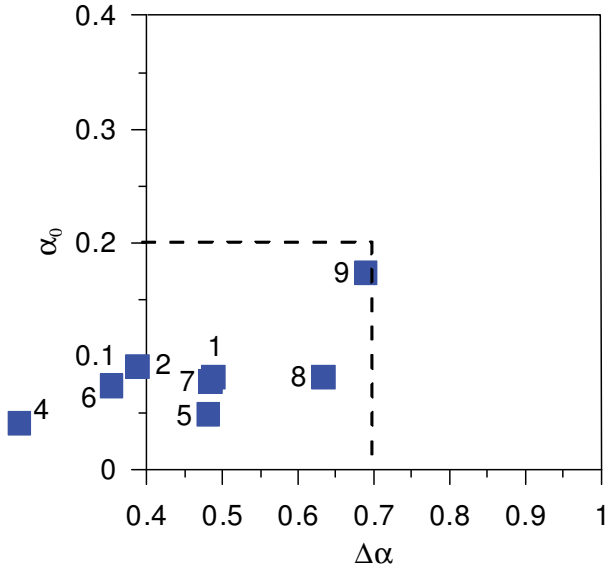

Fig. 8. Comparing an MF analysis of IMEP in the cylinders supplied by a mixture of non-modified composition of λ = 0.7 for 100 LL.

Disturbed cylinders no. 3, 5 and 7 show the highest value of $\alpha_0 \approx 0.3$, which indicates the least negative correlation and a higher correlation of pressure fluctuations. Most of the odd-numbered cylinders supplied by a mixture of modified composition shows large $\Delta\alpha$, which is related to a highly complex course of combustion. The course of pressure during mixture modification have complex response.

If the distributions of MF from Figures 9 and 10 (distributions of MF if no disturbances) are compared, the parameters clearly go beyond maximum $\Delta\alpha \approx 0.7$ and $\alpha_0 \approx 0.18$. This range always covers from 3 to 4 cases of indicated pressure out of 8 cases of failed cylinders. The repeating courses within this range are the courses of cylinders 6 and 8 (5 repetitions) and cylinders 4 and 5 (3 repetitions). Moreover, if the courses of the disturbed cylinders are investigated only, and despite a disturbance in mixture composition, cylinder 8 still operates as if the engine were not disturbed at all. If cylinder 2 fails, there are two courses (cylinders 8 and 9).

Their presence in the collection means that the IMEP proceeds in a comparable way, i.e. the largest negative correlation and low complexity.

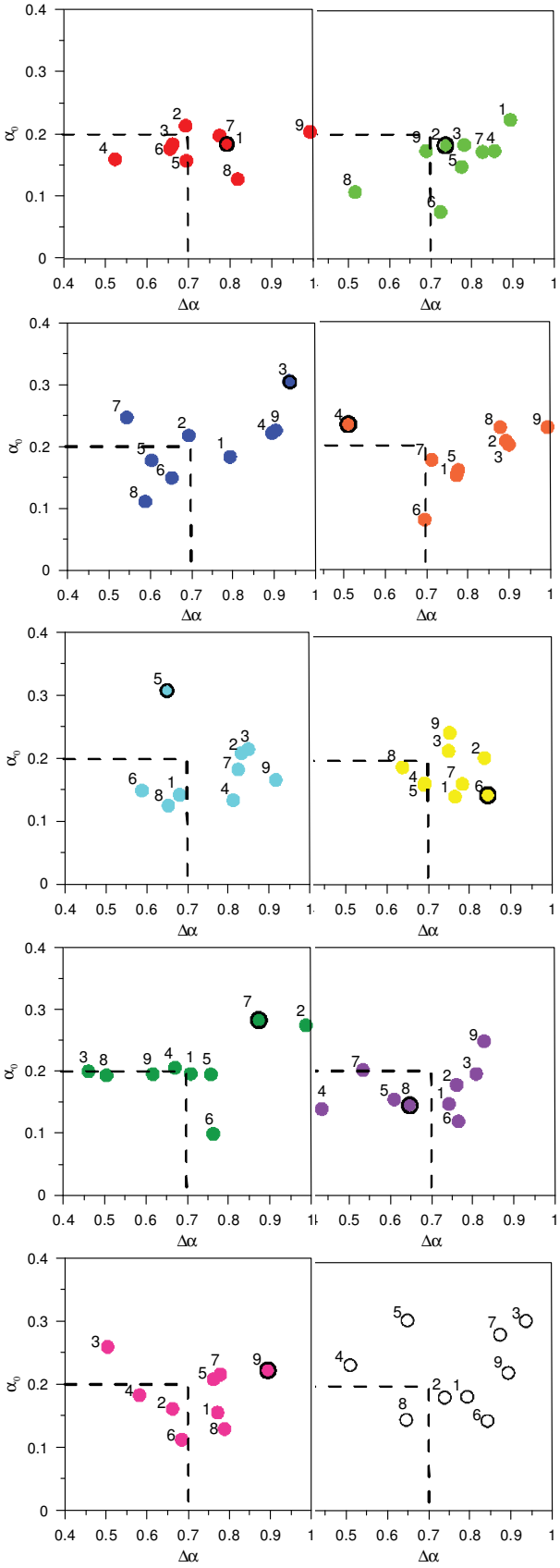

Fig. 9. Results of our MF analysis of the indicated pressure in each cylinder supplied by a mixture of modified composition (black circle), the other cylinders supplied by a mixture of λ = 0.7. The last graph (black points) summarizes the MF analysis for the disturbed cylinders only

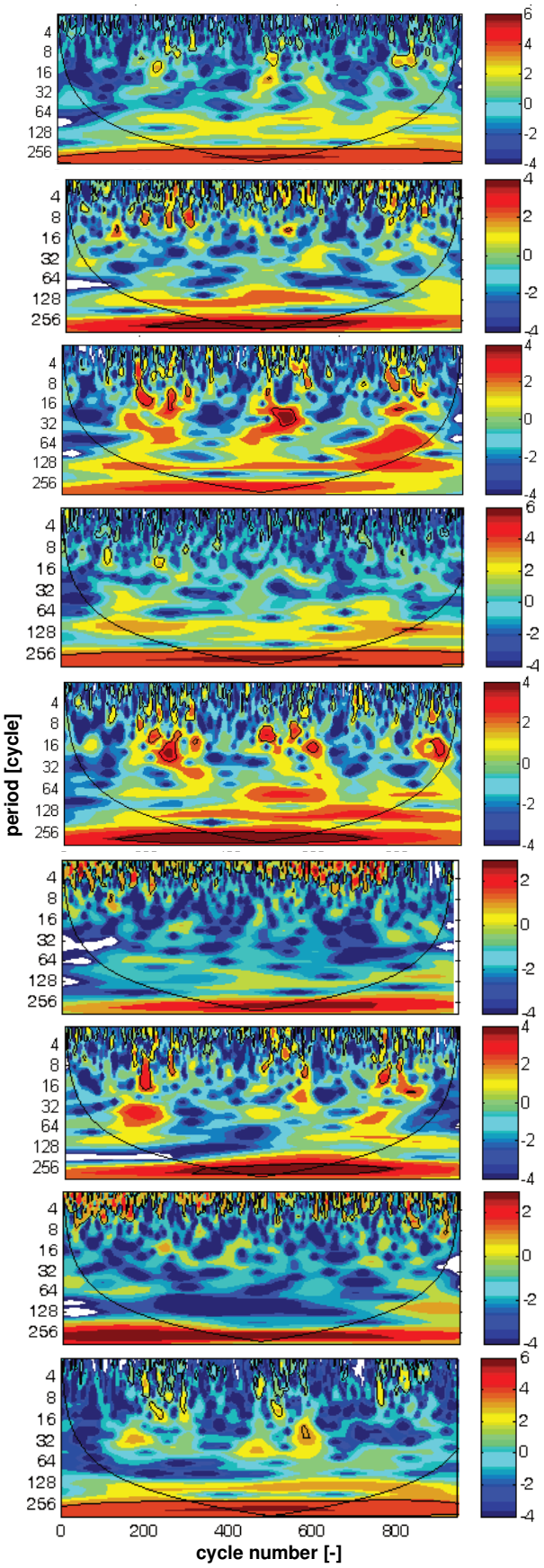

Fig. 10. Wavelet power spectrum for the IMEP in the cylinders supplied by a mixture of disturbed composition and the others supplied by a mixture of $\lambda = 0.7$

Cylinder-to-cylinder variation in operation is depicted in the wavelet power spectrum (Fig. 10) showing the pressure changes in the two domains at the same time, i.e. in domains of time and frequency (or the corresponding periods). The horizontal axis shows the subsequent numbers of successive cycles, whereas a vertical one shows a period (the inverse of frequency) in cycles. An associated power of a signal (relative to the option) is marked with colors in the figure. Red indicates the highest level of power, blue the lowest level, and other colors show middle values. The individual colors of the chart inform about dominant periods, which signal is stationary, and what its nature is (growth and disappearance of amplitudes or an intermittent signal).

The areas limited in the graphs by the black lines show a 95% certainty of red noise. The areas below the thin U-shaped line mean the cone of influence below which the edge effect is dominant so the results may not be reliable and should be applied with caution [20]. The period for the results in this area is less than 256.

Cycle-to-cycle variation in combustion occurs simultaneously in several different time scales as a result of nonlinear factors. Longer injection time results in oscillations to occur in a period ranging from 10 to 100 cycles. Such oscillations do not occur if mixture composition in the other cylinders remains the same.

Summary

A mathematical analysis of time series proves that if there are controlled disturbances in mixture composition in a single cylinder, certain cylinders only are responsive. Cylinders 3, 5, 7 and 9 are most responsive to disturbances, which proves that they show the least cycle-to-cycle variation in combustion. Cyclical modification in mixture composition are able to increase critical indicators of a multifractal analysis, i.e. a level of variation correlation and a complexity of its response). A wavelet analysis confirms graphically that combustion in cylinders supplied by a disturbed mixture is complex. There are significant differences in the level of cyclical variation in combustion in a single cylinder, which has an impact on a level of cycle-to-cycle variation in operation of the entire engine.

The methods to investigate a dynamic response of a system used in internal combustion engines need to be tested in other types of engines and for a different option of mixture composition disturbance to evaluate all of their advantages, typical irregularities in combustion. Investigating thoroughly the position of parameters of a multifractal spectrum/area for each time series of a given cylinder can be helpful in identifying and diagnosing an incorrectly operating cylinder.

Nomenclature

MF multifractal analysis
CWT continous wavelet transform
IMEP mean indicated effective pressure
SI spark ignition
λ air-fuel ratio
WPS wavelet power spectrum

Bibliography

[1] BERCKÜLLER, M., TAIL, N.P., GREENHALGH, D.A. The influence of local fuel concentration on cyclic variability of a lean burn stratified-charge engine. *SAE Technical Paper*. 1997, 970826.

[2] CZARNIGOWSKI, J., WENDEKER, M., JAKLIŃSKI, P. et al. Testing non-uniformity of the combustion process in a radial aircraft engine. *SAE Technical Paper*. 2007, 2007-01-2074.

[3] DAW, C.S., FINNEY, C.E., KENNEL, M.B. Symbolic approach for measuring temporal "irreversibility". *Physical Review* E 62. 2000, **2**, 1912-1921.

[4] DAW, C.S., KENNEL, M.B., FINNEY, C.E.A., CONNOLLY, F.T. Observing and modeling nonlinear dynamics in an internal combustion engine. *Phys. Rev. E.* 1998, **57**, 2811-2819.

[5] FOAKES, A.P., POLLARD, D.C. Investigation of a chaotic mechanism for cycle-to-cycle variations, *Combustion Science and Technology*.1993, **90**, 281–287.

[6] GĘCA, M., LITAK, G., CZARNIGOWSKI, J., PIETRYKOWSKI, K. Diagnostics of the aircraft radial engine by using Recurrence Plots method. *PTNSS CONGRESS 2009*, PTNSS-2009-SC-058, 133-140.

[7] GOLDBERGER, A.L. AMARAL, L.A.N., GLASS, L. et al. PhysioBank, physioToolkit, and physioNet components of a new research resource for complex physiologic signals, *Circulation*. 2000, **101**, E215, and the software provided on the webpage www.physionet.org/physio-tools/multifractal/

[8] HEYWOOD, J.B. Internal Combustion Engine Fundamentals, *MCGraw-Hill Science Engineering*. 1988.

[9] HU, Z. Nonlinear instabilities of combustion processes and cycle-to-cycle variations in spark-ignition engines, *SAE paper*. 1996, 961197.

[10] JAKLIŃSKI, P., WENDEKER, M., CZARNIGOWSKI, J. et al. Analiza ciśnienia indykowanego w gwiazdowym tłokowym silniku lotniczym zasilanym benzyną lotniczą 100LL i benzyną samochodową ES95, *Silniki spalinowe*. 009-SC2 Seria Specjalna, 2009, 162-170.

[11] KANTOR, J.C. A dynamical instability of spark-ignited engines, *Science*. 1984, **224**, 1233.

[12] LITAK, G., WENDEKER, M., KRUPA, M., CZARNIGOWSKI, J. A numerical study of a simple stochastic/deterministic model of cycle-to-cycle combustion fluctuations in spark ignition engines. *Journal of Vibration and Control*. 2005, 11371-11379.

[13] LONGWIC, R., SEN, A.K., GÓRSKI, K. et al. Cycle-to-cycle variations of the combustion process in a Diesel engine powered by different fuels. *Journal of Vibroengineering*. 2011, **13**, 120-127.

[14] MIKALSEN, R. ROSKILLY, A.P. A computational study of free-piston diesel engine combustion. *Applied Energy*. 2009, **86**, 1136-1143.

[15] MOULIN, P., CORDE, G. CHAUVIN, J., CASTAGNÉ, M. Cylinder individual AFR estimation based on a physical model and using Kalman filters. *SAE Technical Paper*. 2004, 2004-01-422.

[16] MUZY, J.F., BACRY, E., ARNEODO, A. Multifractal formalism for fractal signals: The structure-function approach versus the wavelet-transform modulus-maxima method, *Phys. Rev.* 1993, E **47**, 875-884.

[17] NEWLAND, D.E. Practical signal analysis: do wavelets make any difference! *Processings of DTC'97* 1997 ASME Design Engineering Technical Conference, September14-17, 1997, Sacramento, Kalifornia.

[18] SEN, A. K., LITAK, G., KAMINSKI, T., WENDEKER, M. Multifractal and statistical analyses of heat release fluctuations in a spark ignition engine. *Chaos*. **18**, 1-6.

[19] SZLACHETKA, M., GĘCA, M., WENDEKER, M., STĘPNIEWSKI, A. Badania porównawcze dynamiki filmu paliwowego w stanach dynamicznych silnika zasilanego benzyną oraz alkoholem etylowym, V Konferencja Naukowa Ekoenergia '2010, *Materiały konferencyjne – AUTOBUSY – Technika, Eksploatacja*, Systemy Transportowe, 2010, 95-102.

[20] TORRENCE, C., COMPO, G.P. A practical guide to wavelet analysis, *Bull. Amer. Meteor. Soc*. 1998, **79**, 61-78.

[21] www.optrand.com

[22] www.radialengines.com/fuel_injection/index.htm

Gęca Michał, DEng. – Faculty of Mechanical Engineering at the Lublin University of Technology.

e-mail: *m.geca@pollub.pl*

Article citation info:
WRÓBLEWSKI, P. Effect of asymmetric elliptical shapes of the sealing ring sliding surface on the main parameters of the oil film. *Combustion Engines*. 2017, **168**(1), 84-93. DOI: 10.19206/CE-2017-114

Piotr WRÓBLEWSKI

CE-2017-114

Effect of asymmetric elliptical shapes of the sealing ring sliding surface on the main parameters of the oil film

This article discusses the results of simulation studies of the effect of selected sealing ring sets with asymmetrical elliptical sliding surfaces on the oil layer thickness distribution over the whole operating range of an internal combustion engine. The problem of calculating the sliding surface coverage with visco-elastic oil film as well as in mixed friction conditions is discussed. The effect of asymmetrical elliptical sliding surfaces particularly on the dimensionless slip and squeeze indicators was determined, defining these surfaces ability to produce an oil film.

The research results presented in this article show that there exists a real possibility of friction loss re-duction in the cylinder and sealing rings contact area, while maintaining the oil film continuity between the sliding surfaces.

Key words: *rings with asymmetrical sliding surface shape, friction loss, oil film, quantification of lubricant oil consumption*

1. Introduction

During piston engine operation, the lubrication conditions of the piston and the rings mounted on it are constantly changing. Variable gas and mass forces acting on the piston rings along with the changing temperature affect the oil film performance. By performing simulation studies on the oil film thickness distribution for a given engine design, areas on the cylinder surface where the oil film may break can be identified. This results in the fluid friction to change into mixed friction, or even into boundary friction under extreme conditions.

The ring sliding surface oil film thickness affects the pressure distribution in the oil film. The sealing rings sliding surface shape becomes a key factor in this case. A significant factor affecting the oil film instantaneous pressure distribution is the shape of this piston rings sliding surface obtained on the individual sections of the total axial surface height. The greatest challenge is determining the top sealing ring sliding surface shape, so that it both ensures the oil film continuity and at the same time reduces friction losses. Significant reduction of friction losses in the internal combustion engine can be achieved by selection of the sliding surface shapes of both the top and bottom sealing rings. In addition, the theoretical predictions regarding the piston rings sliding surface oil coating impede the conditions associated with the instantaneous parameters of lubrication oil and the instantaneous temperature distribution on the surfaces of the kinematic pairs. It is very difficult to obtain the planned oil film thickness distribution by shaping the geometry of the piston rings sliding surfaces and shaping the ring operation parameters, due to the complex relationship between them. The minimum oil film thickness between the sliding surface of the piston rings and the cylinder wall depends on the shape of the sliding surface directly covered by the oil film and on the thickness of the oil layer on the cylinder wall surface before and after the ring passes it. The oil film distribution and the resulting friction type, in addition to the conditions mentioned above, will also be influenced by other factors related to the type of lubricating oil used as well as its viscosity and temperature characteristics, the instantaneous position of the sealing ring sliding surfaces within the piston groove and the oil film layers surface conditions.

Shaping the sliding surface of the piston rings directly affects the results of squeeze and slip, i.e., the instantaneous oil layer thickness left on the smooth surface of the cylinder wall after passage of the ring. The oil thickness in this area shapes the oil flow at the inlet to the next ring or to the same ring when returning through the cylinder. Depending on the shape of the sliding surface sections of this ring, the ring moves along the regions of various oil layer thickness at the piston's turning points. It can be stated, therefore, that a significant reduction in friction loss can be achieved primarily by setting the limit value of the minimum oil film thickness to be found on the cylinder wall after the ring passes, and the oil layer it leaves after its return just after the TDC. The thickness of the oil layer left behind by the top sealing ring at the piston's return point applies to a very short surface distance of the cylinder. The length of this section depends on the piston stroke and on the axial height of the upper ring. When analyzing these phenomena, it is also necessary to consider the forces from the gas acting on the upper sealing ring on this section of the piston path in the BDC direction, as well as the cylinder wall distance oil-coated by the bottom sealing ring moving towards the TDC in the previous stroke. The influence of these parameters must be taken into account when verifying the effect of the change in the sliding surface shape of the two sealing rings. Otherwise, the influence of these surfaces shape on the parameters defining the oil extrusion and lubrication effects may be misinterpreted.

Assuming that the sliding surface of the piston ring is not covered with the oil over its entire height, this area should be limited to just the section covered with the oil film. This requires describing complex surface shapes using appropriate mathematical functions or coefficients that define the approximate shape of the sliding surfaces. The asymmetric shape's effect of the piston rings sliding surface on their oil film coverage depends on the flow balance. In order to accurately analyze the effect of the sliding surface shape changes on the oily film distribution on its surface, the flow balance resulting from velocity areas should take into account.

The shape of the piston rings sliding surface should be chosen in a way that ensures an oil film coverage continuity of these surfaces throughout the whole engine cycle. On the sliding surface of the top sealing ring, the continuity of the oil film should be maintained especially in the angle range of 345 to 390° at the crankshaft. When analyzing such a crankshaft rotation angle range for the upper sealing ring, it is necessary to determine the path length just after TDC, on which the sliding surface of that ring moves on the oil layer left by its movement in the previous stroke. The distance to the end of this section, after which the sliding surface will encounter the oil layer left by the lower sealing ring before the piston's turning point also needs to be determined.

In the case of the most commonly used three ring piston design, in the suction and expansion strokes, the scraper ring moves over the oil layer accumulated on the cylinder wall and the remaining rings move over the layer left behind by the scraper ring. In the compression and exhaust strokes, the order of rings movement on the oil layer is reversed. The upper sealing ring moves only over the oil layer left by itself in the previous stroke, whereas the following rings move over the oil layer left by the preceding rings. In order to separate the sliding surfaces of the rings and the cylinder walls, a pressure must be created in the oil film that will determine its bearing capacity. In the expansion, exhaust and to some extent in the compression stroke, according to the pressure increase characteristic in the combustion chamber, the internal pressure in the oil film is influenced by the pressure of the gases acting on the inner surface of the piston ring. Depending on the adhesion of the ring sliding surface to the piston grooves surface resulting from the movement direction of the piston, it is the pressure from the space above or below the piston. In the intake stroke and to some extent the compression stroke the oil film pressure is affected by the ring's own elasticity and the distribution of specific pressures on the cylinder walls. The force exerted by the piston ring on the cylinder wall depends primarily on its geometrical dimensions, the type of material used, and the actual sliding surface covered by the oil film.

2. The problem of calculating the sliding surfaces oil coverage for an oil film with partially elastic properties

The effects of the temperature distribution, the lubricating oil dynamic viscosity, the specific pressure of the piston rings on the cylinder walls, the arrangement of all rings in the piston grooves and their geometrical dimensions on the piston rings sliding surface oil film thickness distribution are all well known. However, the currently produced synthetic oils are not perfectly viscous liquids and they do not show the elasticity that is manifested in compressibility. The partial elasticity of the oil results in different tangential pressures that affect the instantaneous friction forces occurring between the rings sliding surface and the cylinder walls [2]. In synthetic oils with elastic properties, there are other phenomena accompanying the distribution of the internal friction forces in the oil film, than in the mineral and semi-synthetic oils. The adoption of these features into the simulation model for the analysis of the influence of the sealing rings sliding surfaces shape on the oil film surface is very important, as the reciprocal stresses due to viscosity and elasticity that occur in the turning points of the piston movement tend to combine.

According to the oil layer swelling theory, known as the Weissenberg effect, these oils can increase the oil coverage of the sealing rings sliding surfaces [4]. Accurately determining the effects of this phenomenon requires detailed experimental research, including the aspects of covering these surfaces at the piston's turning point. In this respect, the effect of the sliding surface shape of the upper sealing ring plays a crucial role in shaping the thickness of the oil film related to its return stroke and scraping the oil into the combustion chamber in the compression and exhaust stroke. Taking into account the resilient properties of semi-synthetic and synthetic oils, the results can be expected to reduce the average friction losses in the oil film with a slight increase in losses at the piston turning points. Taking into account the resilient properties of these oils and evaluating their effect on the instantaneous oil film coverage of the upper sealing ring at the piston's turning points, an accurate mathematical model can be created to approximate the results that can define the effect of surface shape changes on the actual oil film coverage. Separation of the effects of these oils while simultaneously changing the shape of the sealing rings sliding surface requires experimental research.

In theoretical considerations this is not possible due to the error resulting from the introduction of the oil elastic modulus value into the mathematical model. Such a mathematical model would certainly make it possible to accurately predict the effects of changes in the rings sliding surfaces shape in terms of engine friction losses reduction while maintaining the durability of its kinematic connection of the main mechanisms and the engine timing. Another difficulty is creating a reliable mathematical description of the actual oil film volume at the piston's turning points, even if the oil is assumed to be only a viscous fluid.

Taking into account the theoretical considerations of the oil partially elastic one should also take into account the conditions when mixed friction occurs. For this purpose, an anisotropic friction model can be used, in which the value of the friction coefficient is calculated based on the slipping direction of the surface microroughness. At the moment the sealing rings sliding surfaces move on the cylinder walls, the main friction directions are perpendicular to each other. Such calculations use an elastic-plastic friction model.

These phenomena are broadly illustrated in the works of Maksak [12], which investigated the effect of tangential direction on the preliminary displacement values for metal surfaces, including spheroidal cast irons used for the production of piston rings. Based on the results of the Maksak study, it can be assumed that friction coefficient values decrease for samples with machining indications directed along the sliding direction, and increased – if the machining marks are perpendicular. In addition, displacement in the elastic range occurs only for a specific static load [15–17]. Thus increasing the static load resulting from the instantaneous changes in the piston movement direction will result in a macro-slip, preceded by the appearance of reciprocal elastic-plastic displacements in certain areas of the rings sliding surface and the cylinder walls. Displacement in the

elastic range is referred to as micro-slip and in these considerations concerns only the instantaneous friction between the rings and the cylinder walls. An unloading and reloading of the sealing rings sliding surfaces pressure will result in a permanent plastic displacement as a difference of total displacement and the elastic preliminary displacement.

According to Fredriksson's experimental research, reducing the roughness of the metal surfaces results in an increase in the friction coefficient in spite of the contact pressure being the same.

Considering the conditions described above, it is possible to determine the change in friction coefficients of spheroidal cast irons covered with selected piston ring protective coatings, depending on the method of shaping the asymmetrical sliding surfaces of the piston rings under instantaneous friction conditions. Adoption of the aforementioned conditions guarantees a precise theoretical definition of the effect of piston rings sliding surfaces shape change for fixed engine material and geometric requirements for the conditions where these surfaces are separated with visco-elastic oil film, as well as in mixed friction conditions. In addition, the mathematical modeling of the phenomena occurring at the piston rings sliding surfaces in mechanical friction conditions can be used to precisely predict the change in shape of these surfaces during the break-in period. Because every geometric change of the sealing rings asymmetrical shape affects the oil film thickness distribution on the cylinder wall surface over the entire engine life.

Currently, the most accurate available method for determining the impact of all the discussed conditions is exclusively experimental research of the piston ring operation with cylinder walls under certain engine operating conditions. It is worth mentioning that the measurements of piston rings sliding surfaces, piston and cylinder walls are the most important for guaranteeing the reliability of the obtained friction loss and oil film thickness results before, during, and after the completion of the tests.

3. Partial filling of the space beneath the asymmetric sliding surface with oil

Simulation studies on the asymmetric change in the piston rings sliding surfaces shape require the inclusion of many variables that are difficult to determine. However, irrespective of the shape of these surfaces, their oil film coverage area results from the flow balance. As mentioned previously, this balance also depends on the type of liquid used to separate the sliding surfaces.

In the assumed mathematical model [3] the oil exhibits viscosity but has no elastic properties. Taking into account such criteria at this stage of the study provides sufficient accuracy to determine the effect of the changes in the sliding surfaces shape on their oil film coverage. In all simulations, the asymmetrical shape of the sliding surface of both sealing rings is assumed in various combinations in the piston grooves. Based on the flow balance, it can be shown that the distribution of the oil film pressure affects not only the thickness of these film surfaces but also affects the position of the center and the angle values defining the selected parabolic shapes.

The sliding surfaces asymmetric spherical shapes with parabola peaks between 5 to 20 microns relative to the side edges of the rings and their different arrangements at axial ring heights were selected for the study. Based on experimental measurements of the actual piston rings shape, the selected asymmetrical spherical shapes are preserved for most of the samples over the entire circumference of the ring with a tolerance of about 1 micron. Such accuracy enables a real assessment of the effect of these surfaces shape change on friction losses and oil film parameters. On the other hand, repeatedly producing these surfaces in the ring cross-section at the technological stage is very difficult, since the asymmetric barrel shape error, i.e. the center of the parabola tip, and the height of the parabola with respect to the ring side edges, are in average between 3 and 5 microns. However, this is not a problem when selecting identical sliding surfaces for large production cycles for experimental purposes. The sliding surface shape of these rings around their circumference may be determined by means of profilers or visual-measuring devices.

The mathematical expression of asymmetric shapes similar to elliptic figures forces the assumption of certain distance values between the antipodal points of the ellipse, where the center of the line defined by these points, is the ellipse's center of symmetry relative to the transverse diameter and the conjugate diameter. Adopting elliptic shapes allow to determine the ellipse position center and the antipodal points distance that express the transverse diameter and the conjugate diameter values. In the case of asymmetrical shapes described using parabolic combinations, the comparison of friction losses and oil film parameters can be expressed based on the parabolic center position with its angle in that point defining the distance of the rings sliding surfaces from the cylinder surface. Manipulation of ellipsoidal angles and coordinates of their position and parabolic angles at the level of several micrometers of the ring cross section greatly influences the distribution of the velocity fields components at the starting and separating points of the oil film.

With the mathematical model used it is possible to analyze the phenomena accompanying the partial oil filling of the space under the piston rings sliding surface as well as the space between them by mapping the surface with straight line sections. As a result, a model simulating parabolic and sinusoidal surfaces using a specified number of broken curves was created. To make comparing the effects of implementing asymmetric parabolic or elliptical shapes possible, the values of the dimensionless slip and extrusion effects coefficients for these cross sections should be established. In the simulated type of reciprocating internal combustion engine, the manufacturer used a nose shape for the lower sealing ring and a symmetrical barrel shape for the upper sealing ring.

The dimensionless slippage and extrusion effects coefficients determine the rings sliding surface ability to form an oil film. It has been established so far that the highest values of slip rates have been obtained for stepped and two-step surfaces. On the other hand, the values of the extrusion coefficients increase as the interacting surfaces approach the parallel level. It is therefore justified to create a coeffi-

cient that would allow the sliding surface shape contours to be compared in terms of slip and extrusion coefficients. Due to the fact that the parallel position of the opposing surfaces may be unpredictable and vary during the entire engine life, it is important to adjust the sliding surface contours so that the values of the slip and extrusion effects are as large as possible within the limits set by the construction goals. The asymmetric contours arrangement defining the sealing rings sliding surfaces shape results in more favorable results than symmetric contours arrangement or the formation of circumferential grooves on these surfaces [16].

The upper sealing ring sliding surface contours should promote an asymmetrical shape with high slip coefficient values and low values of the extrusion coefficient. Contours characterized by a high value of slip coefficient should be located on the sliding surfaces on the crankcase side in the case of piston movement towards the TDC in the compression and exhaust strokes. Contours with small values of extrusion coefficient must be introduced in the opposite manner. Such a sliding surface design favors leaving an increased oil film thickness after the ring passage just before the piston's turning point. This provides reasonable conditions for liquid friction to occur along the return path of this ring before its sliding surface shape meets the oil layer left by the lower sealing ring. In this case, the contours with low extrusion coefficient values introduced on the sliding surface from the combustion chamber's side reduce the thickness of the oily film left behind by the ring in the intake and expansion strokes. This is acceptable since the upper sealing ring in the subsequent compression and exhaust strokes no longer generate as large gas forces as the expansion stroke. The reduced value of the gas force within this angle range on the crankshaft promotes the automatic increase of the oil film thickness by decreasing the specific pressure. Due to the fact that the load acting on the upper ring is smaller than at the piston's turning points just after the TDC, it is acceptable for the upper sealing ring to leave a thinner oil film within this crankshaft angle range. This improves the lubrication conditions of the upper sealing ring at the more heavily loaded crankshaft angles, resulting in the asymmetric position of the apex, i.e. the critical contour center at the axial ring height.

The contours of the lower sealing ring sliding surface should be able to achieve a high extrusion coefficient value and a low slip coefficient value. Contours with high extrusion coefficient values must be located on the sliding surface from the combustion chamber side, and the contours of the low slip coefficient values on the opposite side. This is caused by the shift of the critical contour center tip to the ring sliding surface part from the combustion chamber side. Such contour placement defines the shape of a sliding surface that favors oil scraping on the upper sealing ring slide surface during the compression and exhaust stroke due to the high value of the extrusion coefficient on that side of the ring. This sliding surface shape of the lower sealing ring reduces the oil film thickness left during its movement in the TDC direction. As a result, the lower ring moves over a reduced oil film thickness in the expansion stroke, where the load absorbed by the ring grows. This is very advantageous because the thickness of the oil layer left by the scraper ring is sufficient to ensure the continuity of the oil film and, in addition, the reduced oil thickness for this ring results in a reduction in friction loss in this crankshaft angle range.

These observations indicate the positive effects of modifying the contours defining the sliding surface shape for both rings and its effect on the slip and extrusion coefficient values. As noted, the position of these contours corresponding to the values of the slip and extrusion coefficients is different for each sealing ring, and should be selected based on the load transmitted by the respective ring in a given crankshaft angle region of the engine operating cycle.

The results of previous simulations did not clearly show the effect of sliding surfaces asymmetric contours angles on the values of slip and extrusion coefficients. An important parameter determining the value of these indicators beyond the contour angle is also the position of the critical contour center tip, where there is a change in the sectional effects of slip and extrusion. The offset of the critical contour center to the outer edge of the sliding surface profile directly affects the contour angle, and thus, it increases to the extrusion coefficient value.

Based on the previous model [2], approximative extrusion and slip effects coefficients can be determined for the entire sliding surface of a given ring. However, a thorough analysis of the phenomena occurring on surfaces with a parabolic curvature, and not solely rectilinear, requires the addition of additional approximation coefficients or an increase in the number of calculation steps of the current mathematical model, which will be the subject of subsequent studies.

Because of the complex relationship of the ring position with parameters characterizing the design of the engine components, its operating conditions and the properties of the oils, determining the coefficients approximating the phenomena resulting from the effects of slip and extrusion is preferred. Based on the assessment of these phenomena and the assumed changes in the ring's direction within the piston groove, tilt effect coefficients can be determined and linked to the slip and extrusion effects. The position of the ring is in particular influenced by the hydrodynamic pressure in the oil film and by the ring's own elasticity. To approximate the most important aspects of effective shaping of the upper sealing ring sliding surface by changing the value of the extrusion and slip coefficients, it is necessary to first determine the area of operation in which the mixed friction phenomenon can occur. The distance traveled by the upper sealing ring until it encounters the oil film left by the lower sealing ring during the return movement can be described by the equation:

$$a_{cpg}=a_{g\text{-}d}\pm a_{vg}\pm a_{vd}$$

The length of this path described in crankshaft degrees can be expressed by:

$$a_{OWK}=\frac{180}{S}\times a_{cpg}$$

where: a_{cpg} – distance from the oil film start point on the sliding surface profile of the upper sealing ring to the oil film separation on the sliding profile surface of the lower

sealing ring, $a_{g\text{-}d}$ – distance from the axial center of the upper sealing ring to the middle center of the lower sealing ring, a_{vg} – distance from the axial center of the upper sealing ring height to the oil film layer edge on the sliding profile surface, a_{vd} – distance from the axial center of the lower sealing ring height to the oil film separation on the sliding profile surface, a_{OWK} – the distance expressed in crankshaft rotation degrees, S – piston stroke.

For a 70 mm piston stroke internal combustion engine, this path averages out between 10 to 13° on the crankshaft just after TDC, depending on the shape of the sliding surface of the two sealing rings, their axial height and their respective positions in the piston. The shape of the top sealing ring sliding surface should allow for the thickest possible layer of the oil film behind the ring leading to the TDC on the path section covered by its return movement. This shape also needs to allow as little oil consumption as possible while reducing friction losses with respect to the reference ring sliding surface shape.

4. Analysis of oil film parameters and friction losses for selected sets of piston rings with asymmetric sliding surfaces

In the simulation studies, the asymmetric spherical shape of the lower and upper sealing rings was assumed. Simulation studies on oil film thickness and friction losses were made for the characteristic axes in the plane of the piston pins motion. The following sets of piston rings placement in the piston groove have been used:

- *reference ring set* – upper and lower sealing ring – reference shapes for the given engine,
- *ring set 1* – upper sealing ring – parabolic peak located in the crankcase side sliding surface and lower sealing ring – parabolic peak on the side of the combustion chamber – optimal ring set,
- *ring set 2* – upper and lower sealing ring – parabolic peak located in the sliding surface on the crankcase side,
- *ring set 3* – upper and lower sealing ring – parabolic peak located in the sliding surface on the combustion chamber side.

From the analysis of Figure 1, it is clear that the good oil film characteristics while reducing friction losses are obtained for the asymmetric spherical surfaces of the lower sealing ring with the center of the parabolic peak located in the sliding surface on the combustion chamber side – ring sets 1 and 2. Such a sliding surface shape of the lower sealing ring allows for the formation of a greater oil film thickness than in the reference shape and an oil film on the turning point of the upper sealing ring at about 15º on the crankshaft after the TDC, representing the expansion stroke, and a lower oil film thickness retained for the return movement of that ring in the BDC direction. Reducing the oil film thickness on the lower sealing ring sliding surface in the range of 20 to 180° on the crankshaft without the risk of mixed friction is very useful. It reduces the friction loss of this ring towards the BDC in the expansion stroke, while maintaining the conditions necessary to produce fluid friction throughout the entire crankshaft angle and at the maximum permissible load for the engine. The reverse situation occurs for the upper sealing ring. For this ring, the parabolic peak defining the asymmetric shape should be located on the crankcase side. Such a sliding surface shape of the upper ring provides less scraping of the oil to the combustion chamber in the compression and exhaust strokes, reducing friction losses and ensuring increased oil film thickness and retaining the film in the crankshaft angle of 0 to 15° after the TDC in the expansion stroke.

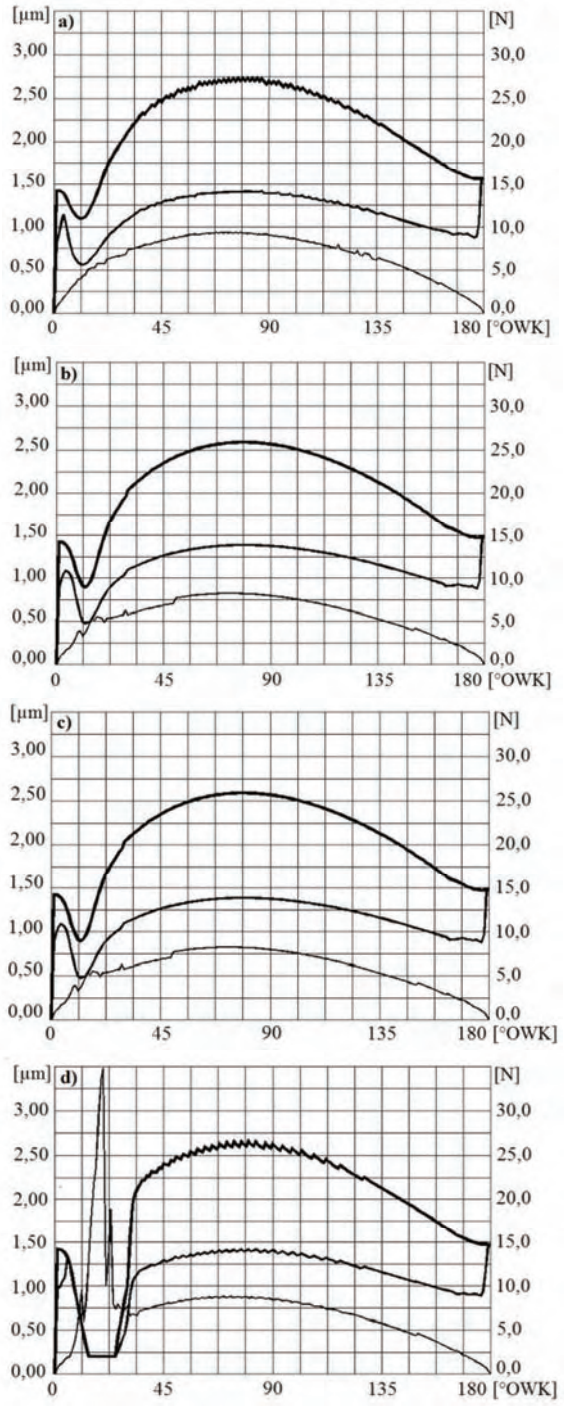

Fig. 1. The change in the oil film thickness, friction and the thickness of the oil layer left on the cylinder wall by the lower sealing ring after completing the TDC-BDC stroke; thick line – film, medium line – layer, thin line – friction, a) reference ring set, b) ring set 1, c) ring set 2, d) ring set 3

As shown in Figure 1, the insertion of the lower sealing ring with an asymmetrical sliding surface with the parabolic

peak on the side of the combustion chamber (ring sets 2 and 3) ensures oil film continuity just after the TDC in the expansion stroke. Within this angle on the crankshaft, the lower sealing ring has the highest gas force value, which can lead to breaking the oil film continuity. The analysis of Figures 1 and 2 leads to the statement that the oil layer distribution on the lower ring sliding surface for ring set 1 and 2 is similar to the reference distribution while simultaneously reducing the friction force in the return stroke of the ring.

Such a distribution of the oil film indicates a greater scraping of the oil by the lower sealing ring under the upper ring and leaving the reduced film thickness for the return movement of the piston. This sliding surface shape of the lower ring, in spite of the reduced oil film thickness, ensures continuity of its sliding surface coverage throughout the engine work cycle, especially just after TDC in the expansion stroke. Introducing the shape of ring set 3 for the lower sealing ring is not recommended. With this sliding surface shape, the oil film is broken off immediately after the piston's turning point, which promotes mixed friction and, in extreme cases, boundary friction. For this shape of the lower ring in the range of 5 to 34° on the crankshaft after the TDC in the expansion stroke, a sharp reduction in oil film thickness can be observed. This is due to the simulation program limitations and the reduction of these values to less than 0.200 μm. However, it is expected that such a slight surface roughness is impossible to obtain at the manufacturing stage and will probably result in mixed friction. Such a distribution of the oil film in this range of crankshaft angle is very unfavorable, because it affects the intensification of the operational wear of the lower sealing ring and cylinder wall sliding surfaces.

In addition, the lower ring sliding surface shape presented in ring set 3 increases the friction power of this ring by 1 W relative to the reference ring set and 4 W in relation to ring sets 1 and 2 at 3000 rpm. Increased friction losses for these ring sets result from breaking of the oil film continuity in the initial range of the crankshaft angle just after the TDC in the expansion stroke. From data in Table 1, it is clear that for ring set 1 the greatest reduction in friction losses is observed with respect to the reference set, while maintaining the favorable conditions for covering the sliding surfaces of the lower and upper sealing rings. For ring sets 1 and 2, the lower friction of the lower sealing ring N_2 is identical – it is equal to 20%, 11.11%, and 13.85% for engine speeds of 1000 rpm, 3000 rpm and 5000 rpm respectively.

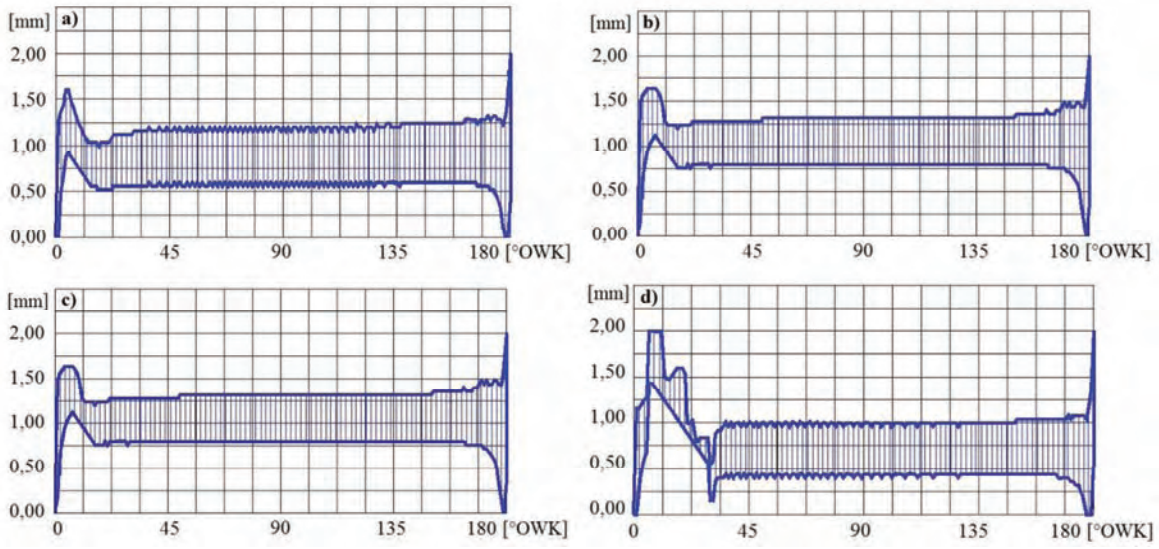

Fig. 2. Lower sealing ring sliding surface oil film layer after the TDC-BDC stroke; a) reference ring set, b) ring set 1, c) ring set 2, d) ring set 3

Table 1. Values of power and friction force for selected piston ring sets

Piston ring setup variant	Engine speed n [rpm]	Friction power of the upper sealing ring N_1 [W]	Friction power of the lower sealing ring N_2 [W]	Friction power of the scraper ring N_3 [W]	Friction power of a piston ring set N_{rsum} [W]	Friction force at 20° on the crankshaft after the TDC for the upper sealing ring [N]
Reference ring set	1000	10	5	6	27	4.3
	3000	60	27	36	159	8.4
	5000	142	65	83	374	11.1
Ring set 1	**1000**	**7**	**4**	**6**	**23**	**3.6**
	3000	**45**	**24**	**36**	**141**	**6.7**
	5000	**105**	**56**	**83**	**327**	**8.9**
Ring set 2	1000	8	4	6	24	3.9
	3000	47	24	36	143	7.3
	5000	108	56	83	330	9.9
Ring set 3	1000	7	4	6	24	3.6
	3000	46	28	36	146	6.6
	5000	108	65	83	339	8.8

Figure 3 indicates that the asymmetric shape of the lower sealing ring for ring sets 1 and 2 reduces the oil film thickness of that ring to below the thickness of the oil film of the scraping ring. For the reference ring a slight increase in oil film thickness is observed to above the film thickness value of the scraper ring. Such situation leads to the reduction of the friction losses for both sealing rings while maintaining the oil film continuity in the most heavily loaded areas from 0 to 50° on the crankshaft immediately after the TDC in the expansion stroke. By analyzing the graphs in Figures 1, 2 and 3 on the oil film distribution for the lower sealing ring, it can be stated that the use of asymmetrical shapes with the parabolic peak on the combustion chamber side makes it possible to significantly reduce friction losses while maintaining the oil film in all engine strokes. This means that this direction of piston ring sliding surface design enables high values of the extrusion coefficient and low values of the slip coefficient for these shapes. An important aspect of such modeling is the need to determine the whether the sealing rings retain their given shape after the adjustment of their sliding surface to the cylinder walls in engine break-in. In this case the decisive role in maintaining or slightly adjusting the sliding surface of the two sealing rings (at the level not exceeding 1–2 micrometers) plays the type of protective coating used on the sliding surfaces of the rings and the cylinder walls. The degree of changes in the original sealing ring sliding surface shape is affected by the thickness of the applied coating, friction wear resistance, sliding surface forming technology, surface roughness for all co-operating surfaces of the kinematic pairs, and the quality and viscosity of the applied lubricant.

The most favorable oil film distribution in the range of 332 to 390° on the crankshaft is obtained for ring set 1, as shown in Figures 4 and 5. In addition, the largest reduction in friction power for the upper sealing ring N1 was 30%, 25% and 26.06% for 1000 rpm, 3000 rpm and 5000 rpm respectively, and for the whole piston rings set N_{rsum}: 14.81%, 11.32% and 12.57% for 1000 rpm, 3000 rpm and 5000 rpm respectively. Reduction of friction in 20° on the crankshaft after TDC for upper sealing ring is – 16.28%, 20.24% and 19.82% for 1000 rpm, 3000 rpm and 5000 rpm respectively.

In Figures 4 and 5 for ring set 1, the continuity of the upper sealing ring sliding surface oil layer can be observed throughout the entire crankshaft angle range, particularly from 360 to 390° on the crankshaft. For ring set 2, the upper sealing ring sliding surface is shifted away from the combustion chamber side in movement towards the TDC in the compression and exhaust stroke, which promotes the scraping of larger amounts of oil in this engine operating range and increases the consumption of the engine oil. Such a situation not only reduces the engine operation economy, but also damages the sliding surface interaction of this ring with the cylinder wall, as shown in Figures 4 and 5. For this

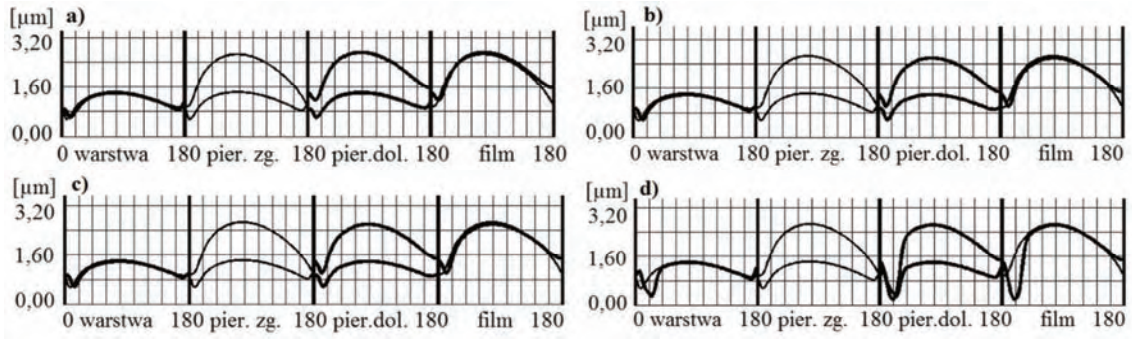

Fig. 3. The oil film layer distribution for the lower sealing ring and the scraper ring after the TDC-BDC stroke; a) reference ring set, b) ring set 1, c) ring set 2, d) ring set 3

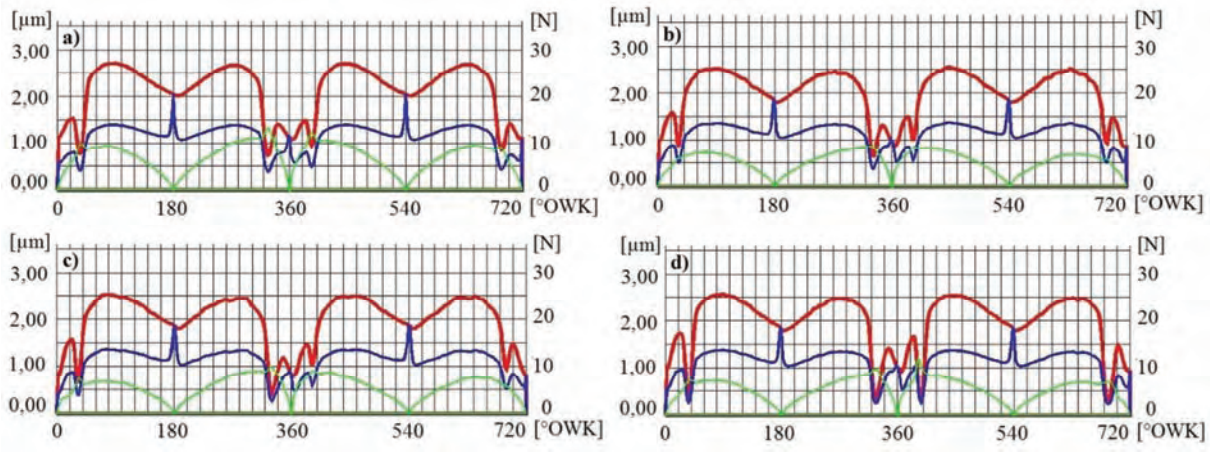

Fig. 4. Changing the upper sealing ring oil film coverage – blue line, oil film thickness – red line, friction forces – green line as a function of the crankshaft angle; a) reference ring set, b) ring set 1, c) ring set 2, d) ring set 3

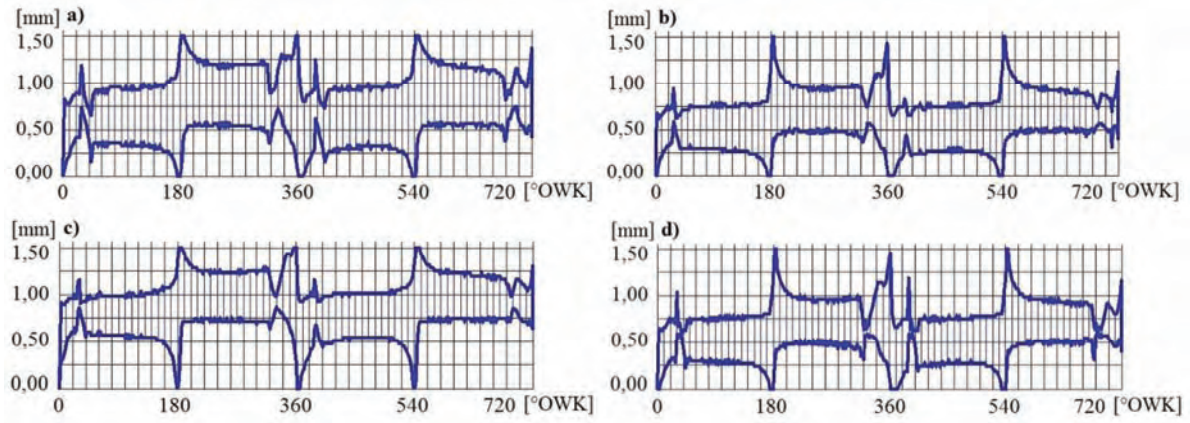

Fig. 5. Change in the upper seal ring sliding surface oil film coverage for characteristic axes in the plane of the piston pins motion; a) reference ring set, b) ring set 1, c) ring set 2, d) ring set 3

combination, the thickness and width of the oil film coverage between 330 and 335° on the crankshaft before TDC in the compression stroke is significantly reduced. It is particularly dangerous to reduce the oil film coverage of the top sealing ring sliding surface in the plane of its largest point of this surface, i.e. the peak of the parabola just before the TDC at 334° on the crankshaft in the compression stroke and at 387° on the crankshaft in the expansion stroke. In these areas, despite favorable engine operating conditions, there will certainly be a break in oil film continuity.

The areas of reduced oil film coverage and reduced oil layer thickness on the upper sealing ring sliding surface are varied and are not a reference point for a larger group of asymmetric piston rings. These areas depend on many individual piston-crank design factors and the actual engine operating conditions. However, the example of reducing the coating and the oil layer thickness for these ring sets indicates some tendencies for changes in these parameters that occur when shaping the geometry of the asymmetrical piston rings sliding surfaces.

From Figures 4 and 5 as well as Table 2, it can be seen that ring set 3 exhibits unacceptable variations in the thickness and coverage of the sliding surface oil film of these rings. A sharp reduction in oil film surface coverage is observed at 326° on the crankshaft in the compression stroke and at 391° on the crankshaft in the expansion stroke. A breach in the oil film continuity occurs at these points. Based on the data in table 2, it can be stated that there is no constant crankshaft angle value for different asymmetrical shapes and their combinations that would define the minimum oil film thickness. The value of this parameter, depending on the different asymmetrical shapes cooperation conditions and various operating conditions of the engine, is shifted closer or further from the TDC. This is shown in Figure 5 – by the blue line, where the minimum oil film thickness for ring sets 1, 2 and 3 is different. For example, for ring set 1, it is approximately 336° on the crankshaft in the compression stroke and 389° on the crankshaft in the expansion stroke, for Pack 2 at approximately 333° on the crankshaft in the compression stroke and 391° on the crankshaft in the expansion stroke, and for ring set 3 at approximately 326° on the crankshaft in the compression stroke and 395° on the crankshaft in the expansion stroke.

Table 2. Oil film thickness values at 5° and 10° on the crankshaft after the TDC in the expansion stroke for selected ring sets

Piston ring setup variant	Engine speed n [rpm]	Oil film thickness 5° after TDC [μm]	Oil film thickness 10° after TDC [μm]
Reference piston ring set	1000	0.657	0.711
	3000	1.084	1.168
	5000	1.580	1.633
Ring set 2	**1000**	**0.427**	**0.520**
	3000	**0.880**	**1.017**
	5000	**1.148**	**1.322**
Ring set 3	1000	0.322	0.500
	3000	0.803	0.995
	5000	1.259	1.433
Ring set 4	1000	0.455	0.531
	3000	0.918	1.041
	5000	1.179	1.344

It can therefore be considered that the lower the oil film thickness encountered by the upper sealing ring in the piston movement towards the TDC in the compression stroke and to the BDC in the expansion stroke, the larger the distance of the crankshaft angle between points defining the minimum oil film thickness. If the oil film thickness encountered in both directions is large enough, both points defining the minimum film thickness for the upper sealing ring slide surface are approaching the crankshaft angle near the TDC. This is a valuable observation that indicates that the susceptibility of the points of minimum oil film thickness in the compression and expansion strokes closely depends on the shape and the asymmetry of the opposing sliding surfaces of both the sealing rings. This dependence is also repeated for other geometric dimensions of piston-crank assemblies, which justifies the practical application of this relationship to a wider group of engines.

It can also be noted that in considering the oil layer distribution on the two sealing rings sliding surfaces, in numerical methods significant parameters should not be linearized. The goal should be to precisely express the change of the gap between the kinematic pairs surfaces that limit the lubricant wedge. Linearization of the two opposing surfaces shape geometry may lead to a significant error resulting in misinterpretation of the change in this parameter and its effect on the oil film distribution on the piston rings sliding surface. Similar recommendations also apply

to the speed of the wedge thickness change. In these cases increasing the parameters and auxiliary parameters accuracy, that result from the hydrodynamic lubrication theory, greatly increases the complexity of the mathematical model used in the numerical calculations.

5. Quantitative oil consumption analysis for selected asymmetrical ring sets sliding surfaces

In the performed simulations it has been assumed that the asymmetric shape of the upper sealing ring sliding surface in a given position, moving in the compression and exhaust strokes, moves along the oil layer that it left on the cylinder wall surface in the intake and expansion strokes. The approximate amount of oil that is partially evaporated or burned during the hot gases is taken into account in the mathematical model defining the oil consumption. It is assumed that the additional amount of oil consumption depends on the distance of the tip leading the asymmetric shape of the upper sealing ring towards the combustion chamber and from the instantaneous oil temperature value near the TDC before the expansion stroke, with the height of the piston sliding surface from the piston head to the end of the upper realing ring. The instantaneous actual oil temperature in this range of engine performance also depends on the thermal conductivity of the material applied to the upper sealing ring, piston head, piston and cylinder surface, pressure and temperature generated before and after the expansion stroke in the combustion chamber, and fuel concentration in the oil after a given period of its operation in the engine.

For the given engine kinematic assemblies geometry and the assumed values of the temperatures in the combustion chamber, the data defining the thermal conductivity of the spheroidal cast iron and the selected aluminum alloy used in the manufacture of the pistons, the geometrical data of the main engine assembly, for the duration of combustion flame acting on the cylinder walls surface from its ignition to decay, just before and during the exhaust stroke, and for the ignition temperature of synthetic oil with a dynamic viscosity of 0.0152 Pa×s in the range of 200 to 250°C, the total amount of oil consumed due to its combustion in the cylinder will hypothetically increase from 16% to 19%. The percentage value of the amount of oil consumed depends on the gas force, and will certainly increase with the rise in the isochoric pressure increase factor, that is to say, for supercharged engines.

The analysis of the data in Table 3 indicates that, for ring sets 1 and 3, the total oil consumption is much lower than for the reference ring set. This is due to the asymmetric shape of the upper sealing ring with the sliding surface parabolic peak located on the crankcase side. The more oblique angle of the parabola defining the given elliptical shape on the sliding surface on the combustion chamber side results in less oil scraping to the combustion chamber in the expansion and exhaust strokes. This is due to the use of asymmetric shaped contour surfaces of the upper sealing ring with large values of the slip coefficient and small values of the extrusion coefficient. Oil consumption is one of the most important parameters determining the practical application validity of the two sealing rings asymmetrical shapes located in the piston grooves. Each attempt to reduce the friction loss of a piston ring set affects the oil consumption and oil film thickness, and the thickness of the oil film influences the durability of the main engine assemblies.

6. Conclusions

Using the data obtained from the simulations, the following conclusions can be made:

- Analyzing the most important effective shaping aspects of the upper sealing ring sliding surfaces by changing the extrusion and slip coefficients values, it is necessary to determine the area of its operation in which mixed friction may occur. This means that the distance traveled by the upper sealing ring must be defined until the oil film left behind by the lower sealing ring is encountered during its return movement for the given engine design.
- The mathematical description of asymmetrical elliptic shapes forces the acceptance of certain values of the distance between the antipodal points of the ellipse, i.e. the pairs of points whose midway point defines the center of the ellipse's symmetry relative to the transverse diameter and the conjugate diameter. The accepted elliptic

Table 3. Specific and hourly oil consumption and the quantity of oil scraped into the crankcase and combustion chamber for each engine stroke for selected piston ring sets

Piston ring setup variant	Engine speed n [rpm]	Specific oil consumption g_o [g/kWh]	Hourly oil consumption G_h [g/h]	The volume of oil scraped into the combustion chamber in the intake stroke V_1 [mm^3]	The volume of oil scraped into the combustion chamber in the compression stroke V_2 [mm^3]	The volume of oil scraped into the combustion chamber in the expansion stroke V_3 [mm^3]	The volume of oil scraped into the combustion chamber in the exhaust stroke V_4 [mm^3]
Reference ring set	1000	9.5	1.2	0.008	0.027	0.060	0.010
	3000	13.54	3.1	0.006	0.022	0.031	0.017
	5000	20.79	5.7	0.006	0.026	0.058	0.016
Ring set 1	**1000**	**15.89**	**1.6**	**0.022**	**0.034**	**0.074**	**0.024**
	3000	**13.72**	**3.2**	**0.015**	**0.020**	**0.056**	**0.020**
	5000	**17.60**	**4.9**	**0.013**	**0.018**	**0.044**	**0.018**
Ring set 2	1000	26.96	2.7	0.007	0.067	0.022	0.033
	3000	23.10	5.4	0.004	0.041	0.021	0.026
	5000	51.92	14.3	0.004	0.083	0.028	0.023
Ring set 3	1000	16.07	1.6	0.024	0.035	0.138	0.024
	3000	13.58	3.2	0.015	0.019	0.079	0.020
	5000	17.67	4.9	0.015	0.018	0.064	0.018

shapes allow to define the common center of the ellipse position and the distance of the antipodal points that express the transverse and conjugate diameters.

- The shape contours of the upper sealing ring's sliding surface should be characterized by a high slip coefficient value and a low extrusion coefficient value. Contours characterized by a high value of slip coefficient should be located on the crankcase side sliding surface. In case of piston movement in the direction of TDC in the compression and exhaust stroke, contours with small values of the extrusion coefficient must be placed on the opposite side. The contours of the sliding surface of the lower sealing ring should be in the opposite positions relative to the contours of the sliding surface of the upper sealing ring.
- Using the right sliding surfaces asymmetrical contours of both the sealing rings reduces the friction power of the entire piston ring assembly of the N_{rsum} by: 14.81% at 1000 rpm, 11.32% at 3000 rpm and 12.57% at 5000 rpm. It also affects the reduction of friction in 20° of the crankshaft after TDC for the upper sealing ring by: 16.28% at 1000 rpm, 20.24% at 3000 rpm and 19.82% at 5000 rpm.
- Reduction of the oil film thickness encountered by the upper sealing ring when piston moves towards the TDC in the compression stroke and to the BDC in the expansion stroke results in a distance increase of the crankshaft angle points defining the minimum oil film thickness. If the thickness of the oil film encountered in both piston movement directions is large enough, both points defining the minimum film thickness for the upper sealing ring slide surface are approaching the angle on the crankshaft near the TDC.
- Using an appropriately selected asymmetrical sliding surface shape of the upper sealing ring can lead to a slight increase in specific and hourly consumption of the engine oil between 1000 to 3000 rpm, while maintaining an approximate value of this parameter at speeds of 2500 to 3500 rpm and a significant decrease in the value of this parameter above 3500 rpm – even over 15% while maintaining good lubrication conditions for all piston rings throughout the entire engine speed range.
- The theoretical assumption of the oil partial elasticity should be considered simultaneously with the mixed friction conditions – in the asymmetric analysis of the sliding sealing rings shape contours – due to the reduced oil film thickness and the angular value of this parameter position in the compression and expansion strokes. Hypothetically, one can use an anisotropic friction model or an elastic-plastic model of orthotropic friction to include these assumptions.

Bibliography

[1] AKALIN, O., NEWAZ, G.M. Piston ring-cylinder bore friction modelling in mixed lubrication regime: Part I – Analytical results. *J Tribol* 2001, **123**(1), 211-218.

[2] ISKRA, A. Rozkład filmu olejowego na gładzi cylindrowej silnika spalinowego, *Rozprawy* nr 181, Politechnika Poznańska 1987.

[3] ISKRA, A. Efekty sprężystości olejów syntetycznych a straty tarcia w silniku spalinowym, *Journal of KONES'97*, Warszawa–Nałęczów 1997.

[4] JAKUBIAK, L., GEMBARA, J. Ocena sprężystych własności olejów smarnych i ich wpływ na parametry współpracy tłoka z cylindrem w silniku spalinowym. *KONSSPAL*. Wrocław 2000.

[5] SERDECKI, W. Analysis of ring pressure distribution on a deformed cylinder face. *Journal of POLISH CIMAC*. Energetic aspects, 2012, **7**(1), Gdańsk.

[6] STYLES, G., RAHMANI, R., RAHNEJAT, H. et al. In-cycle and life-time friction transcience in piston ring-liner conjunction under mixed regime of lubrication. *Int J Engine Res*. 2014, **15**(7), 862-876.

[7] TAULOR, R.I. Squeeze film lubrication in piston rings and reciprocating contacts, Institution of Mechanical Engineers, *Journal of Engineering Tribology*, 2015, UK.

[8] TIAN, T., WONG, V.W., HEYWOOD, J.B. A piston ringpack film thickness and friction model for multigrade oils and rough surfaces. *SAE*. 1996, 962032.

[9] TIAN, T. Dynamic behaviors of piston rings and their practical impact – part ii: oil transport, friction, and wear of ring/liner interface and the effects of piston and ring dynamics. *Proc. Inst. Mech. Eng., Part J: Journal of Engineering Tribology*. 2002, **216**.

[10] WOLFF, A. Numerical analysis of piston ring pack operation of a marine two-stroke engine. *Combustion Engines*. 2011, **3**.

[11] WOLFF, A., PIECHNA, J. Numerical simulation of piston ring pack operation in the case of mixed lubrication. *The Archive of Mech. Engineering*, 2005, LII(33).

[12] MAKSAK, W.I. Microsliding and Contact Stiffness of Metallic Bodies, *Nauka*, Moskau 1975.

[13] FREDRIKSSON, B. Experimental determination frictional properties in araldite b contacts, Rep. LiTH-IKP-R-061, Linköping Institute of Technology, 1975.

[14] ETSION, I. Revisiting the Catteano-Mindlin concept of interfacial slip in tangentially loaded compliant bodies, Trans. ASME, *Journal of Tribology*. 2010, **132**, 020801-1-020801-9, 2010.

[15] LIOU, J.L., LIN, J.F. A modified fractal microcontact model developed for asperity heights with variable morphology parameters. *Wear*. 2010, **268**, 133-144.

[16] WRÓBLEWSKI, P., ISKRA, A. Geometry of shape of profiles of the sliding surface of ring seals in the aspect of friction losses and oil film parameters. *Combustion Engines*. 2016, **167**(4), 24-38.

Piotr Wróblewski, MEng. – Faculty of Machines and Transport at Poznan University of Technology.

e-mail: *piotr.je.wroblewski@doctorate.put.poznan.pl*

Article citation info:
STELMASIAK, Z., PIETRAS, D. The evaluation of the irregularity of the combustion process in the SI engine fueled with petrol and ethanol. *Combustion Engines*. 2017, **168**(1), 94-99. DOI: 10.19206/CE-2017-115

Zdzisław STELMASIAK
Dariusz PIETRAS

CE-2017-115

The evaluation of the regularity of the combustion process in the SI engine fueled with petrol and ethanol

In the paper are presented results of a research work concerning automotive spark ignition engine fueled with ethyl alcohol. The research was performed on a Fiat 1100 MPI engine adapted to dual fuel feeding. Injection of ethyl alcohol was accomplished in area near inlet valve with use of original injectors, the same as used in case of gasoline feeding. The subject-matter of the study was to compare smoothness of engine operation fueled with alcohol in relation to parameters of the engine fueled traditionally with gasoline. There were analyzed combustion parameters calculated on the basis of recorded indicated diagrams of successive individual combustion cycles and averaged diagrams of successive 50 cycles. Performed investigations are pointing at smooth engine operation running on neat alcohol, and on improvement of performance parameters such as effective power and overall efficiency.

Key words: *ethyl alcohol, overall efficiency, engine smoothness, combustion pressure, indicated pressure*

1. Introduction

Obligation of usage of biofuels results from accomplishment of the National Indicative Targets (NCW in short), which assume gradual increase of reproducible fuels in total volume of engine fuels [1–3]. According to decree of the Polish Government on the NCW of the 20.07.2013, energetic fraction of biofuels in the year 2017 should amount to 7.8%, while in the year 2018 should reach level of 8.5% [3].

The alcohols belong to primary biofuels (used mainly in spark ignition engines) and esters of unsaturated fatty acids used to fueling of self-ignition engines [5–8].

Simple alcohols, like methyl and ethyl, can be produced from a biomass, reproducible source of energy, possible to be obtained in very high quantities [9, 12]. Ethyl alcohol can be obtained in fermentation process of vegetable raw materials (cereals, potato, sugar cane, cassava) and cellulose from a wood waste. It seems that in future, in Polish domestic conditions, methyl alcohol produced from coal or natural gas can also play an important role [13, 14, 18]. A future can be foreseen also for developed during the recent years technology of synthesis of methanol from carbon dioxide and hydrogen.

Products of combustion of methyl and ethyl alcohols are carbon dioxide and water, while the process proceeds according to the following reaction:

$$CH_3OH + \frac{3}{2}O_2 \rightarrow CO_2 + 2H_2O \quad (1)$$

$$C_2H_5OH + 3O_2 \rightarrow 2CO_2 + 3H_2O \quad (2)$$

Mass fraction of carbon atoms in a molecule of alcohols is lower comparing to traditional fuels and amounts to 0.375 for methyl alcohol, and to 0.520 for ethyl alcohol, while in case of gasoline and diesel fuel such ratio amounts approximately to 0.845–0.850. Anyhow, taking into consideration differences in calorific values, obtainment of the same unit of energy from alcohols will result in a slight, within limits 2%, reduction of CO_2 emissions comparing with gasoline [14–16].

Alcohols, due to their perfect properties, mainly due to high octane number, high heat of vaporization and high combustion rate, can be successfully used both in spark ignition engines (as a neat fuels, or as additions to traditional fuels), and in self-ignition engines as additions combusted simultaneously with diesel oil [10, 11, 17, 19]. Advantages of alcohols have resulted in research studies on feeding of engines with alcohols, conducted in many worldwide research centers.

Spark ignition engines in European conditions are the most often fueled with mixtures of anhydrous ethyl alcohol or its esters with gasoline [1, 14, 18]. Due to susceptibility of alcohol-gasoline mixtures to stratification in low temperatures and in presence of water, total contents of alcohol or duration of usage of the mixtures are limited. Due to such reasons, fueling of spark ignition engines with pure ethyl alcohol is especially attractive, because in such case it is possible to use water-down alcohols, and cost of their production is lower. Fueling with pure alcohol enables to take full advantage of high knock resistance of alcohols, allowing increase of compression ratio, increase of overall efficiency and unit power of the engine [15, 18, 19]. Such direction is especially developed in Brasil, where are running some 2 million cars fueled with ethyl alcohol produced from cassava and sugar cane [14].

Common usage of multipoint injection of light fuels has created a new possibilities of usage of alcohol additive to gasoline, or alternating use of alcohol or gasoline to feeding of engines. After some modifications of engine's feeding system, start-up of the engine and its heating can occur when the engine is fed with neat gasoline, and further engine operation can occur with alcohol fueling. In such engines the compression ratio can be increased with 2.0–3.0 units, what should increase engine efficiency. The research studies show that also in area of partial engine loads, efficiency of the engine fueled with neat alcohol is higher, what have a significant effect in case of automotive spark ignition engines operated in urban conditions.

In this study are presented results of investigations of automotive engine of the FIAT 1100 MJT type fueled with ethyl alcohol. Special attention was paid on parameters of combustion process, calculated on the basis of recorded indicated diagrams from successive cycles of individual combustion courses and averaged diagrams for 50 succes-

sive cycles. Selected parameters were used to assessment of smoothness of engine operation in successive cycles, so called cycle by cycle, and to assess changes in pressure course during combustion. As a reference values were implemented the same parameters as obtained during engine fueled with neat gasoline.

Performed investigations are pointing at a stable operation of the engine running on pure alcohol, and improvement of operational parameters such as effective power and overall efficiency.

2. Engine test bed

The investigations were performed on four cylinder, spark ignition engine with multipoint fuel injection of the Fiat 1100 MPI brand. Technical data of the engine are specified in the Table 1.

Table 1. Technical data of the Fiat 1100 MPI engine

Engine type	Fiat 1100 MPI
Bore x stroke	70 x 72 mm
Swept capacity	1108 ccm
Compression ratio	9.6
Rated power/rpm	40 kW/5000 rpm
Maximal torque/rpm	88 Nm/3000 rpm

Factory made engine was adapted to the dual fuel feeding with gasoline and alcohol. To perform it, in suction manifold of the engine were installed additional injectors for each cylinder. Original injectors (positioned close to inlet valve) served to injection of alcohol, while additional injectors to injection of gasoline. In course of the investigations, due to alternating fueling with alcohol or gasoline, were used original injectors only, positioned near the inlet valve. Scheme of prototype suction manifold is presented in the Fig. 1.

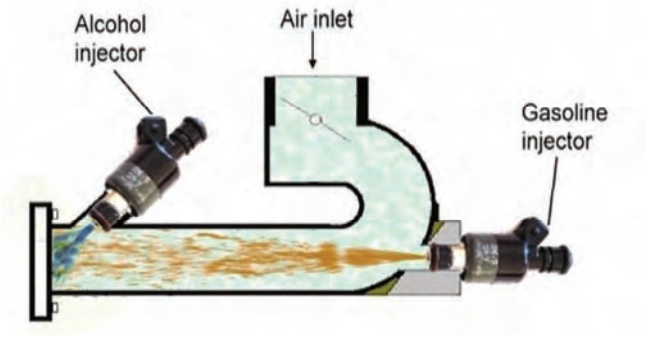

Fig. 1. Scheme of prototype inlet manifold of Fiat 1100 MPI engine

For the purpose of engine indication, in cylinder head of the second cylinder one drilled a hole for adapter of not-cooled sensor made by the AVL. To recording of quick-changing pressures in the combustion chamber one make use of the INDIMETER 619 system made by the AVL.

In the test stand one installed a system to automatic acquisition of measurement data to the Excel calculation sheet. To needs of the testing, in the test stand one installed a dual system of fuelling for the alcohol and for the gasoline. Each from the systems was equipped with individual fuel pump and pressure stabilization system, and system to measurement of fuel consumption. Fuelling system enabled control of instantaneous consumption of the fuels, what considerably facilitated selection of engine adjustment and recording of time of consumption of a determined dose of the fuel. View of the test stand is presented in the Fig. 2.

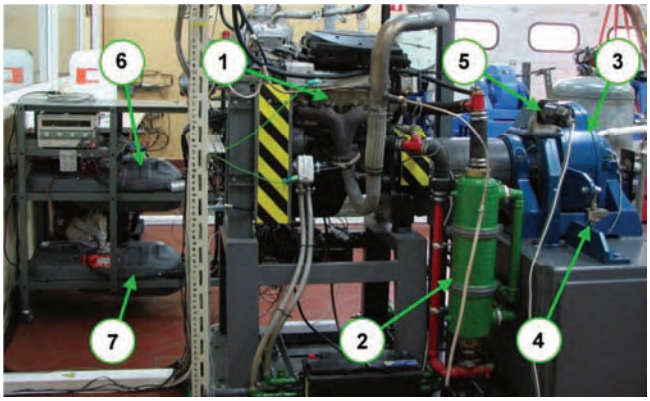

Fig. 2. Test stand – general view: 1 – research engine of Fiat 1100 MPI type, 2 - radiator, 3 – eddy-current engine brake made by Schenck, 4 – transducer of engine load, 5 – engine speed sensor, 6 – alcohol tank, 7 – gasoline tank

3. Analysis of results of the investigations

Comparison of overall efficiency of the engine shown in the Fig. 3 indicates what in complete range of engine loads the efficiency, when fueled with ethyl alcohol, was higher than efficiency of gasoline fueling. Especially significant differences are present in area of medium and maximal engine loads, where increase of the efficiency in range of 1.5–2.5% of absolute values was observed.

a)

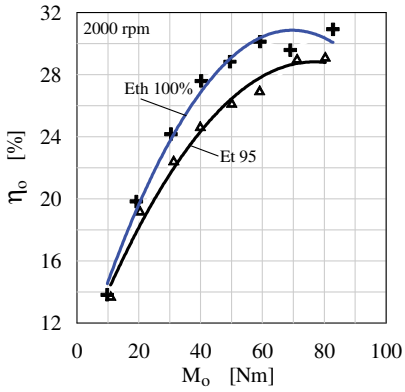

b)

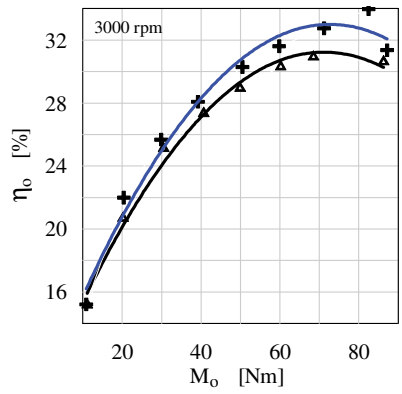

Fig. 3. Comparison of overall efficiency of the Fiat 1100 MPI engine fueled with Et 95 gasoline and ethyl Eth 100% alcohol

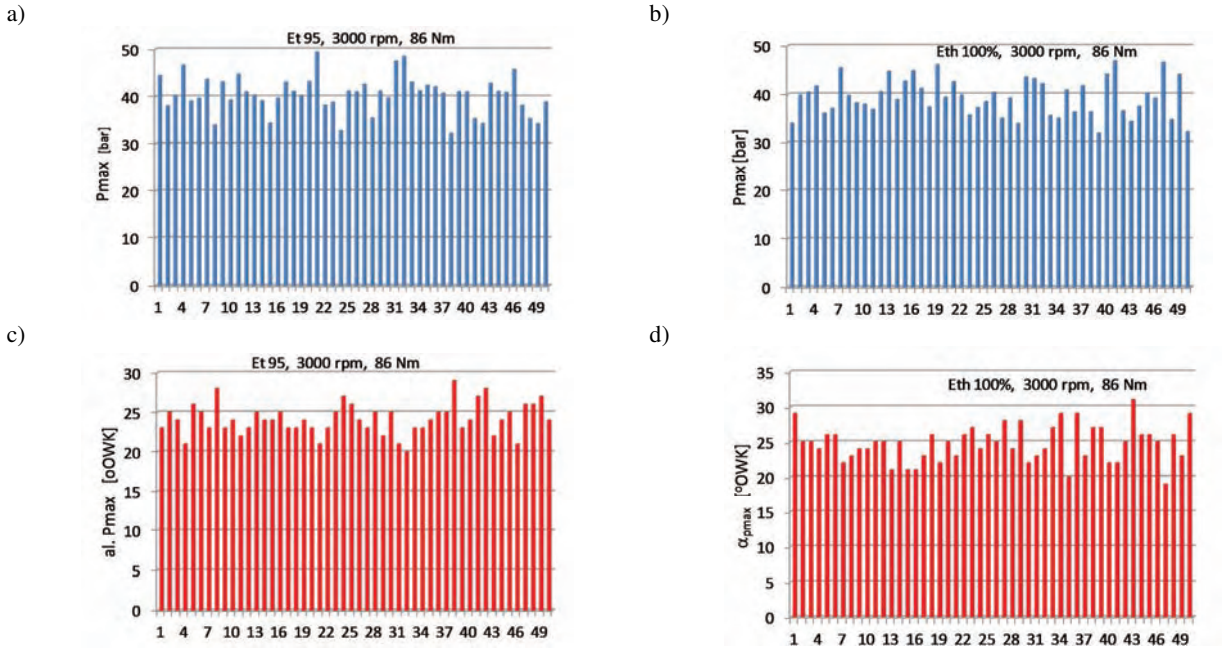

Fig. 4. Comparison of maximal combustion pressures and angles of their occurrence in the Fiat 1100 MPI engine fueled with Et 95 gasoline and Eth 100% alcohol

In the Figure 4 is presented comparison of maximal combustion pressures and CR angles corresponding with points of maximal pressure for 50 successive cycles of engine operation for the both types of fueling. From analysis of the Fig. 4 is seen that at full engine load the levels of maximal pressure for gasoline and alcohol are similar. Simultaneously, it can be seen a slightly bigger fluctuations of maximal pressure in case of gasoline, Fig. 4a.

In majority of cycles, maximal combustion pressures are developed for the angles of 20–25° CR after TDC, Fig. 4c and 4d. However, there are existing cycles in which the maximal pressures were developed later, while in case of ethyl alcohol such phenomenon occurs in distinctly bigger number of cycles, Fig. 4d.

Values of average maximal pressures for 50 successive cycles of engine operation for changing engine loads are shown in the Fig. 5a. The average pressures were calculated according to the following dependency:

$$\overline{p}_{max} = \frac{\sum p_{max-i}}{n} \tag{3}$$

where: p_{max-i} – maximal pressure of a successive cycle, n – number of analyzed cycles.

From comparison of the Fig. 5a results that in complete range of engine loads change, similar values of mean pressures are present for the both fuels. Such tendency was also seen for other investigated rotational speeds.

As a repeatability measure of successive operational cycles are used standard deviation of maximal combustion pressures and variability factor calculated from the following equations:

$$\sigma_{Pmax} = \sqrt{\frac{\sum (p_{max-i} - \overline{p}_{max})^2}{n-1}} \tag{4}$$

$$s_p = \frac{\sigma_{Pmax}}{\overline{p}_{max}} \tag{5}$$

where: σ_{Pmax} – mean standard deviation, s_p – pressure variability factor.

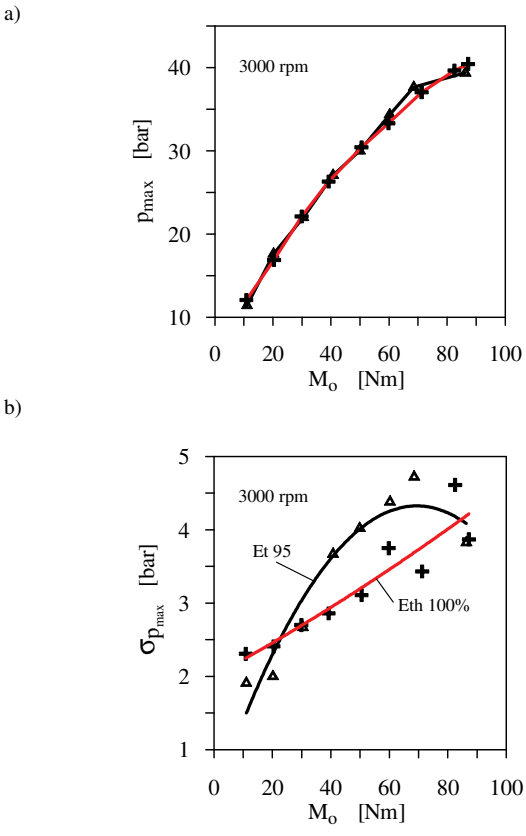

Fig. 5. Comparison of average value of maximal combustion pressures and mean standard deviation of combustion pressures in the Fiat 1100 MPI engine fueled with Et 95 gasoline and Eth 100% ethyl alcohol

Comparison of standard deviation values shown in the Fig. 5b and comparison of pressure variability factor shown in the Fig. 6 indicate that the engine fueled with ethanol in range of medium and maximal engine loads is characteristic of a higher repeatability of operation from one cycle to another. It speaks for more uniform and stable operation of the engine with such type of fueling, comparing with standard fueled with gasoline. Only in area of the lowest engine loads are present more bigger fluctuations of the pressure, what can be caused by reduction of temperature of the charge, connected with a higher heat of vaporization of alcohol and prolonged time of flame stabilization after ignition.

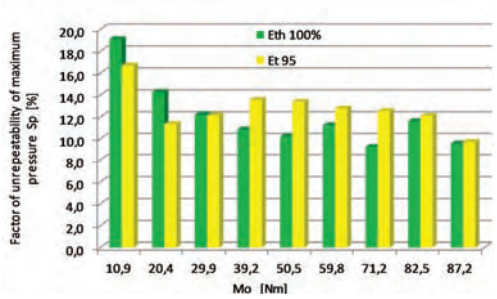

Fig. 6. Comparison of variability factor of maximal combustion pressures in the Fiat 1100 MPI engine fueled with Et 95 gasoline and Eth 100% ethyl alcohol

Noisiness of engine operation when fueling with gasoline and ethyl alcohol is similar, what can be proved by similar values of pressure growth rate dp shown in the Fig. 7. In the both Figures 7a and 7b are seen, in case of the both fuels, a distinct differences of the dp in range of 1.0–1.3 bar/ms with maximal values of the dp amounting to 1.8 bar/ms. It is worth to pay attention on lack of distinct correlation of the runs with minimal growths of the pressure dp and with CR angles of the maximal pressure shown in the Fig. 4c and 4d. It suggests changing combustion rate of the charge after ignition, similar for the both fuels, which character is clearly stochastic.

The mean indicative pressure was calculated from the following formula:

$$p_i = \frac{1}{V_d} \int_0^{720} p \frac{dV}{d\alpha} \tag{6}$$

where: p_i – mean indicated pressure, V – cylinder volume, p – instantaneous pressure of the working medium in cylinder.

a)

b)

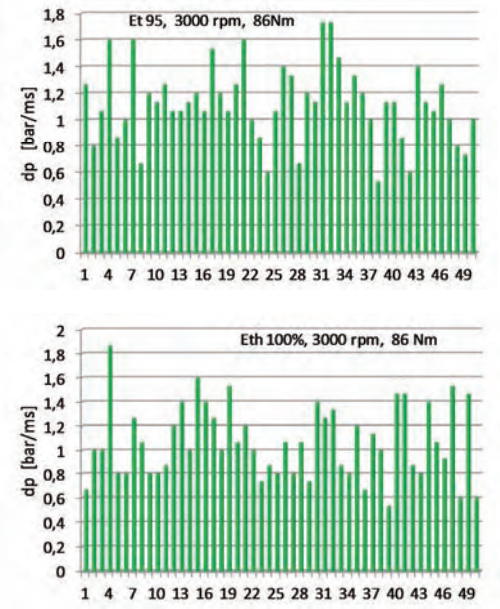

Fig. 7. Comparison of pressure growth rate during combustion on the Fiat 1100 MPI engine fueled with Et 95 gasoline and Eth 100% ethanol

a)

b)

c)

d)

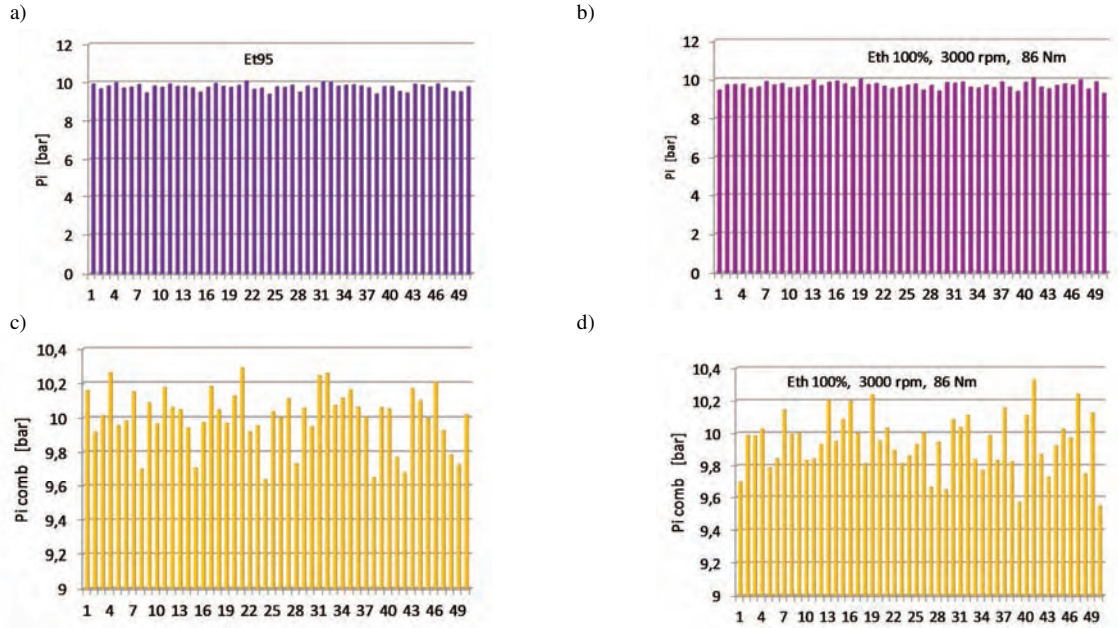

Fig. 8. Comparison of changes of mean indication pressure of complete cycle of p_i and high pressure portion of the cycle $p_{i\,comb}$ in the Fiat 1100 MPI run on Et 95 gasoline and Eth 100% ethylene alcohol

From comparison of the pressures shown in the Fig. 8a and 8b is seen that at constant engine load, fluctuations of the pi in successive cycles of engine operation are very low and are similar for the both fuels. Analysis of relative factor of variability of the p_i shown in Fig. 9 tells that in range of medium and maximal engine loads the fluctuations of pi for the both fuels are similar and their values are lower than 2%, what should be considered as a small changes, comparing with the ones met in a spark ignition engines.

A little bit higher values of the fluctuations are present for the mean indicated pressures of high pressure portion of the cycle pi comb (calculated from the formula (6) only for CR angles for which instantaneous pressure in the cylinder is higher than atmospheric pressure $p > p_a$), because their values can approach to 6% of the mean value. Also in such case, however, value and character of the changes are similar for the both fuels.

Comparison of pressure runs for individual cycles during combustion of gasoline and ethyl alcohol is presented in the Fig. 10. With black colour are marked runs with maximal pressure similar to the mean value calculated from 50 successive cycles of engine operation, while with dotted lines are depicted runs of the maximal pressures lower than the mean pressure, and with solid lines are depicted maximal pressures higher than the mean pressure. The comparisons were made for low engine load M_o = 10 Nm and the load closer to the maximal one M_o = 86 Nm.

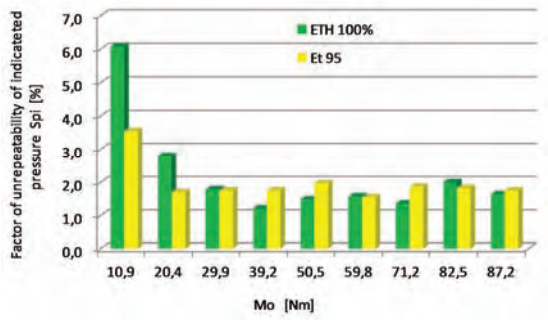

Fig. 9. Comparison variability factor of mean indicated pressure in the Fiat 1100 MPI engine run on Et 95 gasoline and Eth 100% ethyl alcohol

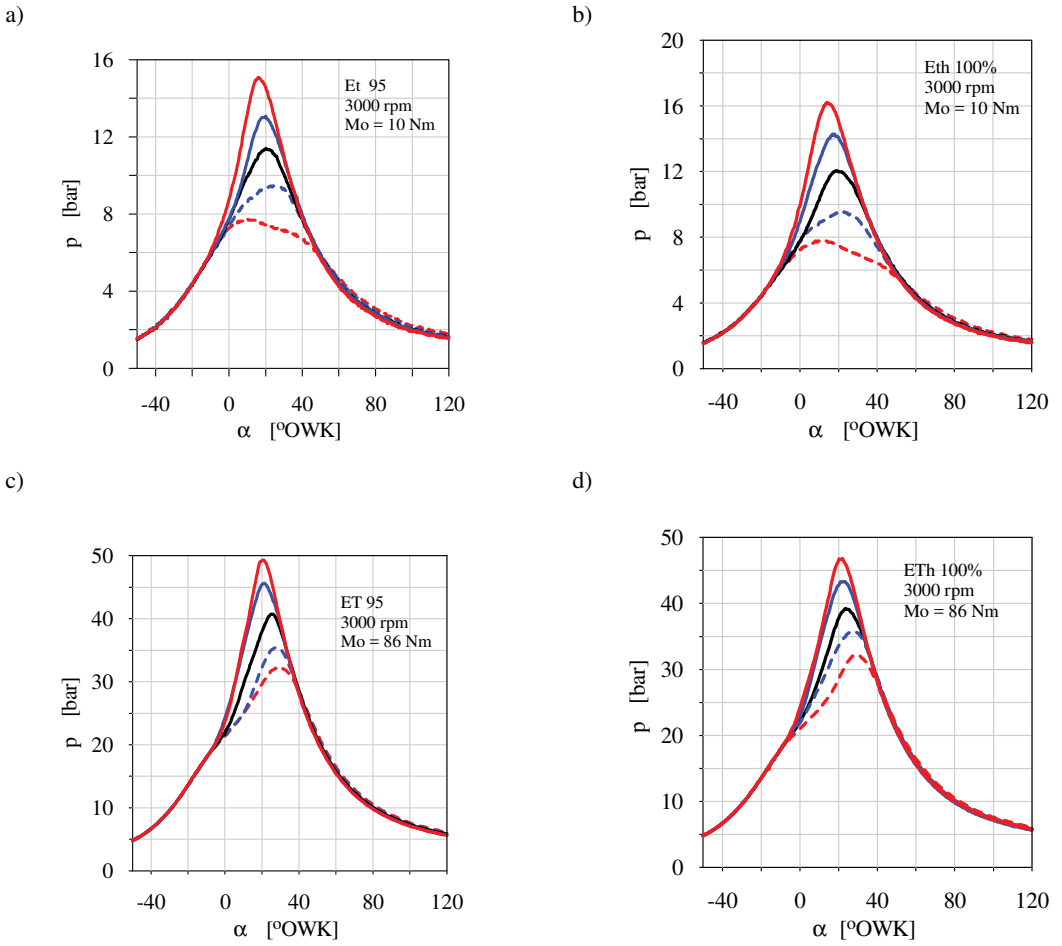

Fig. 10. Comparison of pressure runs in cylinder of the engine run on gasoline and ethanol: rotational speed 3000 rpm, minimal load10 Nm and maximal load 86 Nm

From the comparison is seen that a lower maximal combustion pressures are accompanied by more late CR angles of completion of kinetic combustion phase (when the maximal pressure is reached), this phenomenon is more clearly seen in case of low engine loads. For the load of M_o = 10 Nm, in case of the cycles with low pressure it can be seen protracted combustion process accompanied by a higher pressures in more late phases of the combustion.

The comparison presented in the Fig. 10 shows that in case of two investigated fuels the both runs of combustion with high pressure and with low pressure are similar.

4. Summary

Usage of ethyl alcohol to fueling of automotive spark ignition engine results in increased overall efficiency of the engine. Increase of the efficiency occurs in complete range of changes of engine load and rotational speed and amounts to 1.5–2.5% of absolute values. Further growth of the efficiency can be achieved by increasing compression ratio of the engine, what will enable to take advantage of high knock resistance of ethyl alcohol.

Fueling with ethyl alcohol doesn't result in any significant changes in area of maximal combustion pressure as well as noise level of engine operation, values of average maximal pressures and pressure growths dp are similar. Changes in maximal pressure p_{max} in successive cycles of engine operation are similar for alcohol and gasoline, and their character is distinctly stochastic.

Quantitative change of maximal pressures defined by mean standard deviation σ_{Pmax} and factor of variability of pressures s_p indicate that fluctuations of maximal pressure for gasoline in area of medium and maximal engine loads are higher, what can testify for improvement of smoothness of engine operation run on ethyl alcohol.

In area of low engine loads, when the engine was run on ethyl alcohol, it was observed a worsening of smoothness of engine operation from cycle to cycle. Probably it was caused by reduction of temperature of the charge due to a higher heat of vaporization of ethyl alcohol comparing to gasoline, what had an effect on duration of flame stabilization after ignition of combustible mixture. This issue shall be investigated in course of a further research.

Performed investigations indicate that ethyl alcohol can be used as a pure fuel to modern spark ignition engines. Adaptation scope of the engines to alternating fueling with gasoline and alcohol is small, whereas alcohol fueling can be implemented in selected fleets of cars, or periodically in our climatic zone. It will enable to comply with the National Indicative Targets in range of usage of biofuels and will bring measurable economic benefits due to possibility of usage of water-down alcohols.

Bibliography

[1] BACZEWSKI, K., KOŁDOŃSKI, T. Paliwa do silników o zapłonie iskrowym. *WKiŁ*, Warszawa 2005.

[2] BORYCHOWSKI, M. Produkcja i zużycie biopaliw płynnych w Polsce i na świecie – szanse, zagrożenia, kontrowersje. *Roczniki Ekonomiczne Kujawsko–Pomorskiej Szkoły Wyższej w Bydgoszczy*. 2012, **5**, 39-59.

[3] *Biuletyn Urzędu regulacji Energetyki,* 2010, 2.

[4] Ethanol Internal Combustion Engines. ETSAP Energy Technology System Analysis Programme. *Technology Brief,* June 2010.

[5] GMYREK, J. Bioetanol w realizacji NCW w PKN ORLEN S.A., *Konferencja „FUEL'S ZOOM – BIOETANOL"* Kraków 27-28 kwietnia 2010 r.

[6] KOWALEWICZ, A. Emission characteristics of compression ignition engines fuelled with RME/DF and ethanol. *Journal of KONES.* 2004, **11**(1-2).

[7] KOWALEWICZ, A., PAJĄCZEK, Z. Eco-diesel engine with additional injection of ethanol. *Archives Combustionis.* 2003, **23**(3-4).

[8] LÁBAJ, J., BARTA, D., LENHARD, R. CFD simulation of glycerol combustion in diesel engine. *Prague. Institute of Thermomechanics AS CR*, ISBN 978-80-87012-14-7, 2008, 35-50.

[9] LARISCH, J., STELMASIAK, Z. Dual fuelling SI engine by mixing alcohol and gasoline. *Combustion Engines.* 2013, **3**.

[10] MCNEIL, J., DAY, P., SIROVSKI, F. Glycerine from biodiesel. The perfect diesel fuel. *Process Safety and Environmental Protection – ELSEVIER.* 2012, **90**, B, 3.

[11] MCNEIL, J. Efficient combustion of glycerol and other low cetane fuels in the diesel engine. The Institution of Diesel and Gas Turbine Engineers publication. *Power Eng*. 2011.

[12] PAŃCZYSZYN, T. Forum roślin energetycznych. Produkcja biopaliw płynnych – potencjał surowcowy. Poznań, 12.02.2010.

[13] RYCHLIK, A., KIBALCZYC. Ł. Zastosowanie gliceryny do zasilania tłokowych silników wysokoprężnych dużej mocy. *Combustion Engines*. 2015, **3**.

[14] SEMIKOW, J. Studium dwupaliwowego zasilania silnika o zapłonie iskrowym benzyną i alkoholem. *Praca doktorska*, ATH Bielsko-Biała, 2012.

[15] STELMASIAK, Z., LARISCH, J., SEMIKOW, J. Some aspects of dual fuelling SI engine with gasoline and alcohol *12th EAEC European Congress Bratislava EAEC.* 2009, June 29-July 1.

[16] STELMASIAK, Z., SEMIKOW, J. The possibilities of improvement of spark ignition engine efficiency through dual fueling of methanol and gasoline. *Combustion Engines*. 2010, **3**, 59-67.

[17] STELMASIAK, Z. A new concept of dual fuelled SI engines run on gasoline and alcohol. *The Archives of Transport*. 2011, **2**, 73-85.

[18] STELMASIAK, Z. Applications of alcohols to dual-fuel feeding the spark-ignition and self-ignition engines. *Polish Maritime Research.* 2014, **3**, 86-94.

[19[WESTCOTT, P.C. Ethanol expansion in the United States. How will the agricultural sector adjust? *Economic Research Service.* May 2007.

Zdzislaw Stelmasiak, DSc., DEng. – Faculty of Mechanical Engineering at University of Bielsko-Biala.

e-mail: *zstelmasiak@ath.bielsko.pl*

Dariusz Pietras, DEng. – Faculty of Mechanical Engineering at University of Bielsko-Biala.

e-mail: *pietras@ath.bielsko.pl*

Article citation info:
SICZEK, K., SICZEK, K. Studies on the dynamics the valve train with machined valve springs. *Combustion Engines*. 2017, **168**(1), 100-109. DOI: 10.19206/CE-2017-116

Krystian SICZEK
Krzysztof SICZEK

CE-2017-116

Studies on the dynamics the valve train with machined valve springs

An analysis of the literature for currently used solutions of valve trains in internal combustion engines and analytical studies on the dynamics the valve train of the internal combustion engine provided with machined valve springs were carried out. The aim of the study was to compare the dynamic parameters of the two valve trains for the established internal combustion engine: the first one equipped with machined springs and the second one with coil springs. The numerical models for investigated valve trains, using the Finite Element Method and additional mathematical relationships were developed and presented in the article. The article describes the results of the researches and formulated conclusions.

Key words: *dynamics, valve train, combustion engine, machined spring, finite element method*

1. Introduction

The valve train is a very important subsystem in the combustion engine treated as the system for change of the chemical energy of combustion into mechanical one. Its design has varied with time becoming more complex due number of valves per cylinder, number of cams per valve, number of valve springs etc. There was observed tendency for downsizing and use of lightweight parts as valvetrain components. The control of mechanical valve trains sometimes includes electric motor or hydraulic units driving phasers used to change valve timing. The stiffness, dimensions and mass of valve springs are critical for operation of mechanical and some advanced types of valve trains, i.e. electromechanic or electromagnetic one. The one aim of the present study is to investigate the dynamical parameters of machined valve springs with some geometrical parameters like these of classical coil valve springs.

During studies were investigated components the valve train from the combustion engine used i.e. for tribological studies [1]. The scheme of such valve train is shown in the Figure 1. Inlet valves operate under fully variable control.

Fig. 1. The scheme of valve train from the engine for tribological studies

The two models of the chosen valve train but with different valve springs were elaborated using the Finite Element Method. Dynamical parameters obtained for the valve train with machined valve springs were compared with those for valve train with classical coil springs.

2. Types of valvetrain

The pushrod valve train systems can be used not only in both SI or CI four-stroke combustion engines with classical valve timing and combustion process, but also in similar engines with:

- modified combustion process by varying valve timing via the phasor [2–10],
- modified combustion process by varying valve timing via other methods [11–13],
- modified combustion process by varying valve lifts via different cams [14–32],
- modified combustion process by continuously varying valve lifts [33–34],
- modified combustion process and the pneumatic energy accumulator [35].

There are five most often met types of valve train system with poppet valves.

- The Direct Acting OHC Valve Train (Fig. 2a), also known as the Bucket Style Follower OHC. It is used in i.e. Ford Ztec, Olds Quad 4. This type has: high rigidity during functioning which enable to be used at high engine speeds, high friction because of contact between cam lobe and tappet surface, high values of inertial masses [36].
- The End Pivot Rocker Arm OHC Valve Train (Fig. 2b), also known as the Finger Type Follower OHC. It is used in i.e. Ford Modular, Pinto and Ranger 4 Cyl., Mitsubishi 4G63, GM Ecotec, Chrysler 2.2L. This type has: low friction because of rolling contact between cam and rocker arm, high friction for sliding contact, high sensitivity at rocker arm oscillation, small values of acceleration due to cam concavity which doesn't permit to be used at high engine speeds, small cam profile due to rocker ratio [36].
- The Centre Pivot Rocker Arm OHV Valve Train (Fig. 2c), used in i.e. Honda B18, Porsche. It is characterized by low friction for rolling contact between cam and

rocker, high sensitivity at rocker oscillation, low stiffness as a function of rocker ratio [36].
- The Centre Pivot Cam Follower OHV Valve Train (Fig. 2d) which has similar characteristics with the third type [36]. It is used in Ford Escort CVH.
- The Pushrod OHV Valve Train (Fig. 2e). This type is very flexible because of the length of the pushrod and can't be use at high engine speeds [36]. It is used in the GM 556-hp 6.2L LSA V8 OHV engine of the Cadillac CTS-V.

The friction due to valve train system represent 7.5-21% of total engine friction loss [36].

The variation of the first type is the Double OverHead Cam (DOHC) Valve train, sometimes called "Twin Cam" or "Double Cam", used in most modern cars.

A DOHC engine has usually two camshafts and 4 valves per cylinder. There exists also the configuration with five valves per cylinder. One camshaft operates intake valves installed on one side, while another camshaft controls outlet valves on the opposite side. Camshafts can be installed further apart from each other. This allows the inlet valves to be at a larger angle from the outlet valves, which results in a more direct air flow through the engine with less obstruction. A DOHC engine produces more power out of smaller engine volume. It is used in i.e. 3.5-liter V6 DOHC engine of the 2003 Nissan Pathfinder.

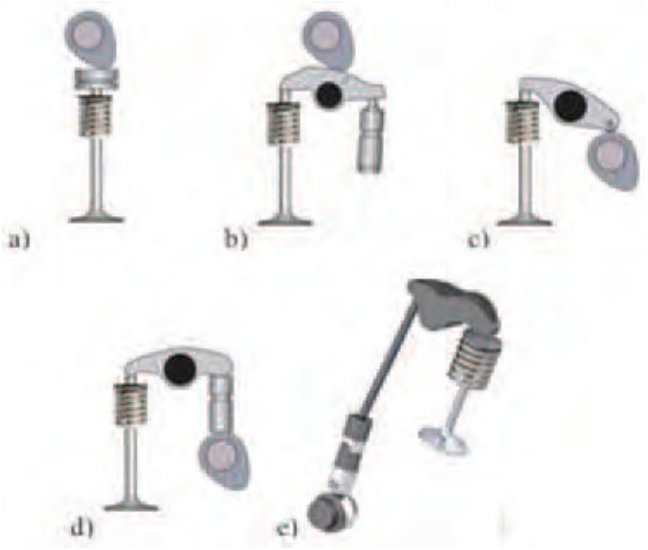

Fig. 2. Types of Valve Train: a) Direct Acting OHC, b) End Pivot Rocker Arm OHC, c) Centre Pivot Rocker Arm OHV, d) Centre Pivot Cam Follower OHV, e) Pushrod OHV [36]

3. Classical types of valve springs

The functions of valve springs are presented in [37].

Some typical winding shapes of coil springs are shown in [38]. Helical coil springs with different winding shapes are usually used [39].

Some typical cross-sections of a valve spring wire are shown in [38]. Elliptical cross-sections allow a reduction of the overall height. Multi-arc profiles (MA) are generated from several circular segments with differing radii and center points. Compared to elliptical cross sections, MA profiles has better stress distribution and allow better utilization of the material.

According to [40], the use of MA profiles in combination with beehive winding reduces the spring forces in a valve train by 13%. According to [37], the valve closing load is conveyed axially along the spring, which stresses the material principally in torsion. For the valve, open and the valve closed conditions, the ratio of spring loads is usually in the region of 2:1.

Spring end coils are ground flat and square with the spring axis and are also diametrically opposed, to minimize an inherent tendency towards bowing of the spring during its compression.

According to [38], nearly without exception valve springs of current engines have a progressive behavior. This behavior is mainly caused by a non-constant pitch between adjacent coils. The coils with a lower pitch come into contact earlier than coils with a higher pitch. The active part of the spring is reduced resulting in increasing total spring stiffness with increasing compression of the spring. The characteristic becomes progressive and resonant frequencies increases.

According to [37], if the frequency of load coincides with the natural vibration frequency of the valve spring itself, a phenomenon known as spring 'surge' may develop because of resonance effects. According to [41], springs with asymmetric shapes are less prone to surging because of lower moving masses and geometrical reasons.

According to [38] the further reduction of the moving mass can be obtained using conical valve springs. The smaller spring fixings and collars are possible, and the solid length is marginally shorter. They have the less progressive characteristics than the cylindrical springs.

Beehive springs are a combination of cylindrical and conical springs. The moving mass is reduced by the conical part and the cylindrical part provide progressive characteristic.

The methods to reduce valve spring surging are presented in [37]. According to [42], the pneumatic valve springs are used, for example, in high-speed Formula One racing engines. Pneumatic valve springs enable high rotational speeds of up to 20000 rpm due to their progressive characteristic and the reduced number of moving parts.

According to [43], the stock valve springs can operate to about 5,500 to 6,000 rpm, but beyond that it is needed stiffer springs, double springs or even triple springs depending on the engine design. The design, materials and methods of manufacturing for valve springs are presented in [37]. The failure modes of valve springs, especially fatigue, are presented in [44–46].

4. Machined valve springs

The pushrod valve train systems can be used with classical valve springs replaced with machined valve springs, which strategy is used in the other devices [47]. The machined springs can possess the same free length, mean diameter and thickness equal to the diameter of the wire. This allows for the use of some original components like valves, keys, spring retainers in the valve train.

One example of use the machined spring was reported in [48], where was presented a displacer spring and displacer/spring assembly for use in a free-piston Stirling engines (FPSE). The machined spring provided enhanced structural

accuracy which, in turn, leads to the elimination of lateral and side loads as compared to prior art wire-wound helical springs.

The analysis was carried out for machined springs with parameters like those for coil valve springs. Each valve in the analyzed valve train mated with the set of two springs: the outer and the inner. The free height for those springs was of 40.86 mm. For outer spring the outer diameter was equal 27.5 mm, the wall thickness was of 3.75 mm. For the inner spring, the outer diameter was of 20 mm and the thickness was of 2.6 mm. The spring rate of the original coil spring set was equal 55 N/mm, so such rate of machined spring set should be close to that value. The geometry of machined springs was shown in the Figure 3.

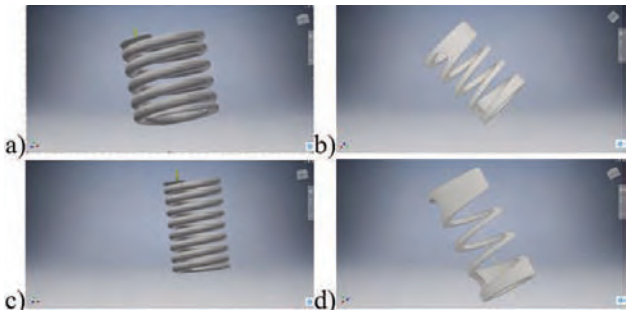

Fig. 3. Coil springs: a) outer, c) inner and machined springs: b) outer, d) inner used in the analyzed valve train

5. The model of analyzed valve train

The model of analyzed valve train consists of two drives: the first for inlet valve and the second for outlet one. Model was elaborated with FEM. The geometrical parameters were as in the original configuration. The valve stroke was of 9 mm. The analysis was carried out with the constant rotation speed of the camshaft and for two variants: the first with coil springs and the second with machined springs. Except springs, each component was modelled using stiff finite elements connected to the other components by the elastic-damping joints or contact elements. The friction coefficient in the contact between sliding surfaces was assumed to be constant and equal 0.1 and between rolling surfaces to be constant and equal 0.03. The material of stiff elements was assumed to be steel with the equivalent: Young modulus E = 210000 MPa, Poisson ration ν = 0.3 and density ρ = 7,800 kg/m^3.

It was assumed, that the stiffness between cam and the follower is the sum of the stiffness $k_{r\text{-}c}$ in contact between roller and cam and the stiffness $k_{r\text{-}f}$ in contact between roller and the follower. The stiffness in contact between pushrod and follower was equal to half the pushrod stiffness $k_{pushrod}$. The stiffness in the contact between pushrod and rocker arm was the sum of half the pushrod stiffness $k_{pushrod}$ and the stiffness k_{raps} of part the rocker arm on the pushrod side. The stiffness between the rocker arm and valve was the sum of the stiffness k_{ravs} of part the rocker arm on the valve side and half the valve stiffness k_{valve}. The stiffness between the rocker arm and the axis was equal to the axis stiffness k_{axis}. The stiffness between valve and its insert was equal to half the valve stiffness k_{valve}. The damping coefficient values in each contact zone was assumed to be the same and equal 5 Ns/m.

To estimate the stiffness $k_{r\text{-}c}$ in the contact between roller and the cam, the FEM sub-models of the camshaft were elaborated and presented in the Figures 4 - for the inlet valve and in the Figure 5 - for the outlet one. The camshaft was loaded by the force F with linearly raised values up to 1,000 N. The camshaft was fixed on the cylindrical surfaces 1 and 2. For the given i-th value of the force F(i), the displacement $d_{r\text{-}c}(i)$ of the middle point on the cam surface was computed. Then the stiffness $k_{r\text{-}c}$ for the step number i of the analysis was estimated as the ratio of such force value F(i) and displacement $d_{r\text{-}c}(i)$.

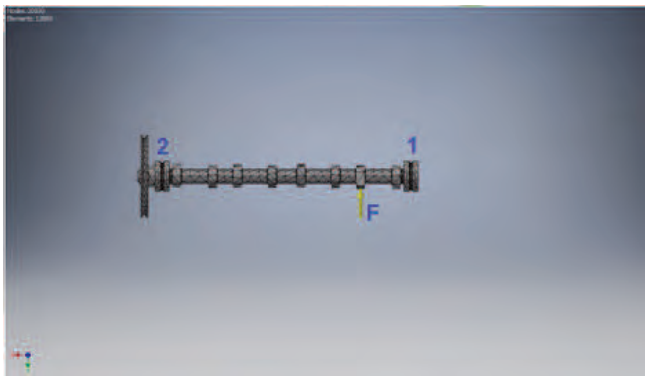

Fig. 4. The grid of finite elements for the sub-model of the camshaft loaded by the force *F*, for the case of inlet valve

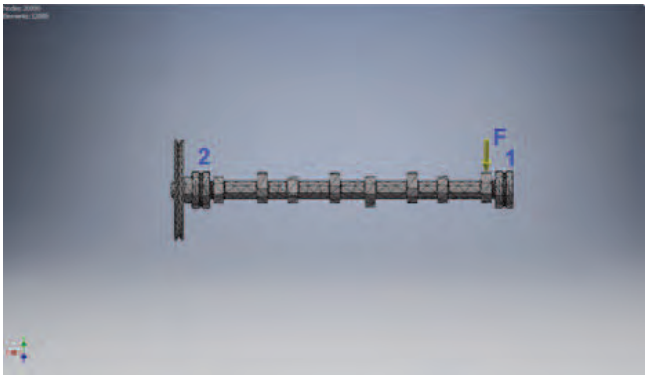

Fig. 5. The grid of finite elements for the sub-model of the camshaft loaded by the force *F*, for the case of outlet valve

To estimate the stiffness $k_{r\text{-}f}$ in the contact between roller and the follower, the FEM sub-model of the follower was elaborated and shown in the Figures 6. The follower was loaded by the force F with linearly raised values up to 1,000 N and uniformly distributed along the roller axis. The follower was fixed on the inner spherical surface 1 mating with the pushrod. For the given i-th value of the force F(i), the displacement $d_{r\text{-}f}(i)$ of the middle point on the roller axis surface was calculated. Then the stiffness $k_{r\text{-}f}$ for the step number i of the analysis was estimated as the ratio of such force value F(i) and displacement $d_{r\text{-}f}(i)$.

As mentioned earlier, assumed stiffness values in the contact between pushrod and the follower and in the contact between pushrod and rocker arm were the same. To estimate the stiffness in such contacts, the FEM sub-model of the pushrod was elaborated and presented in the Figure 7. The pushrod was loaded by the force F with linearly raised values up to 1,000 N. The pushrod was fixed on the outer

spherical surface 1 mating with the rocker arm screw. For the given i-th value of the force F(i), the displacement $d_{push-rod}(i)$ of the middle point on the inner pushrod surface was obtained. Then the stiffness $k_{pushrod}$ for the step number i of the analysis was estimated as the ratio of such force value F(i) and displacement $d_{pushrod}(i)$. The stiffness values in the contact between pushrod and the follower and in the contact between pushrod and rocker arm were equal the half of obtained stiffness $k_{pushrod}$.

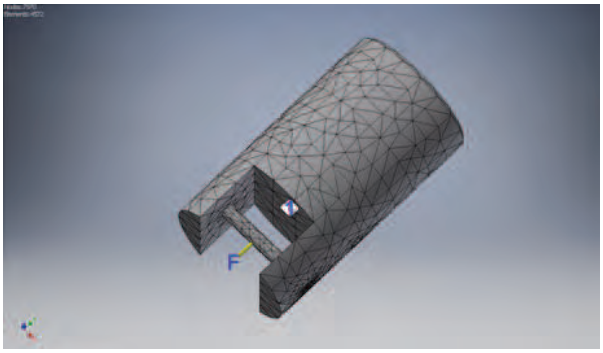

Fig. 6. The grid of finite elements for the sub-model of the follower loaded by the force *F*

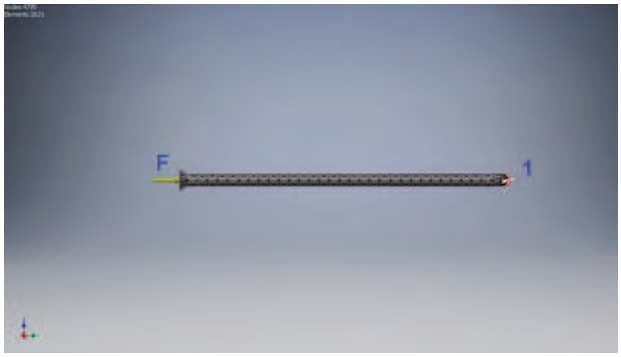

Fig. 7. The grid of finite elements for the sub-model of the pushrod loaded by the force F

To estimate the stiffness k_{raps} of the rocker arm on the pushrod side, the FEM sub-model of the rocker arm was elaborated and presented in the Figure 8. The rocker arm was loaded by the force F with increasing values up to 1000 N and acting along the axis of the rocker arm screw. The rocker arm was fixed on the semicylindrical surface 1 and on the axis the bearing surface 2. For the given i-th value of the force F(i) the displacement $d_{raps}(i)$ of the loaded point the rocker arm was calculated. Then the stiffness k_{raps} for the step number i of the analysis was estimated as the ratio of such force value F(i) and displacement $d_{raps}(i)$.

To estimate the stiffness k_{ravs} of the rocker arm on the valve side, the FEM sub-model of the rocker arm was elaborated and shown in the Figure 9. The rocker arm was loaded by the force F with linearly raised values up to 1,000 N and acting along the axis of the valve. The rocker arm was fixed on the inner cylindrical surface the screw hole 1 and on the axis the bearing surface 2. For the given i-th value of the force F(i), the displacement $d_{ravs}(i)$ of the loaded point the rocker arm was computed. Then the stiffness k_{ravs} for the step number i of the analysis was estimated as the ratio of such force value F(i) and displacement $d_{ravs}(i)$.

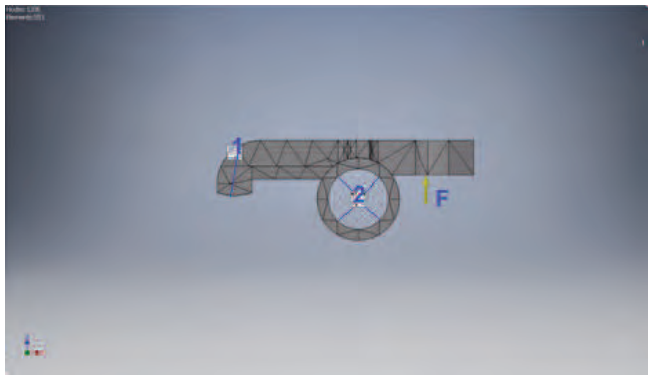

Fig. 8. The grid of finite elements for the sub-model of the rocker arm loaded by the force *F* on the pushrod side

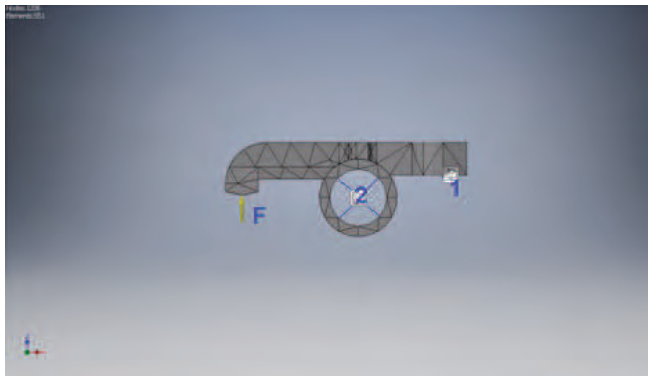

Fig. 9. The grid of finite elements for the sub-model of the rocker arm loaded by the force F on the valve side

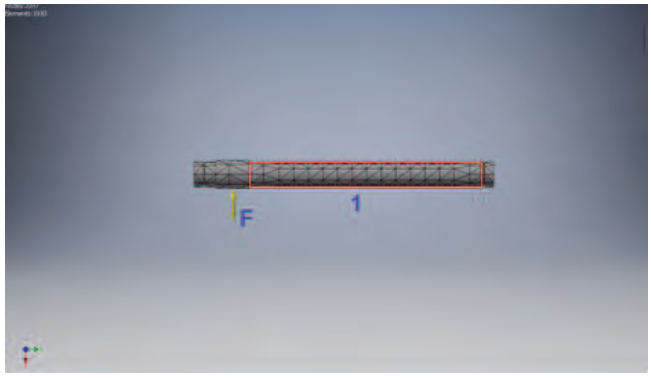

Fig. 10. The grid of finite elements for the sub-model of the rocker arm axis loaded by the force F for the outlet valve case

To estimate the stiffness k_{axis} of the rocker arm axis, the FEM sub-models of the rocker arm axis were prepared and shown in the Figure 10 for the inlet valve and in the Figure 11 for the outlet one. The rocker arm was loaded by the force F with linearly raised values up to 1,000 N and uniformly distributed along the axis of rocker arm bearing. For the outlet valve, the rocker arm was fixed on the cylindrical surface 1. For the inlet valve, the rocker arm axis was fixed on the cylindrical surfaces 1 and 2. For the given i-th value of the force F(i), the displacement $d_{axis}(i)$ of the loaded point the rocker arm was obtained. Then the stiffness k_{axis} for the step number i of the analysis was estimated as the ratio of such force value F(i) and displacement $d_{axis}(i)$.

To estimate the stiffness k_{valve} of the valve, the FEM sub-model of the valve were prepared and shown in the

Figure 12. The valve was loaded by the spring force S with linearly raised values up to 400 N and by the pressure from the gas in cylinder with values up to 7 MPa. The valve was fixed on the conical seat surface 1. For the given i-th value of the force S(i) and gas pressure p, the displacement $d_{valve}(i)$ of the valve tip was computed. Then the stiffness k_{valve} for the step number i of the analysis was estimated as the ratio of such force value F(i) and displacement $d_{valve}(i)$.

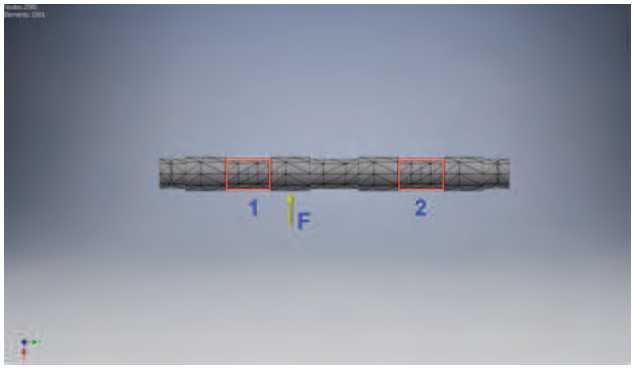

Fig. 11. The grid of finite elements for the sub-model of the rocker arm axis loaded by the force F for the inlet valve case

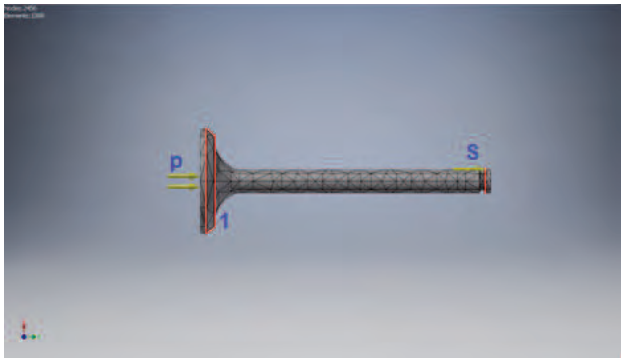

Fig. 12. The grid of finite elements for the sub-model of the valve loaded by the spring force S and gas pressure p

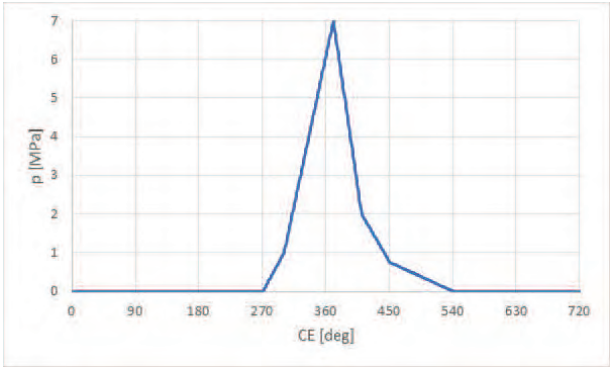

Fig. 13. The modelled course of gas cylinder pressure *p* against crankshaft rotation angle CE

The modelled course of gas pressure *p* against the crankshaft rotation angle CE was shown in the Figure 13.

The coil springs was modelled using joints with values of the stiffness and the damping coefficients equivalent to those of real valve springs. The machined springs were also modeled using FEM, but with the elastic solid finite elements. The grid of finite elements for the machined springs was shown in the Figure 14.

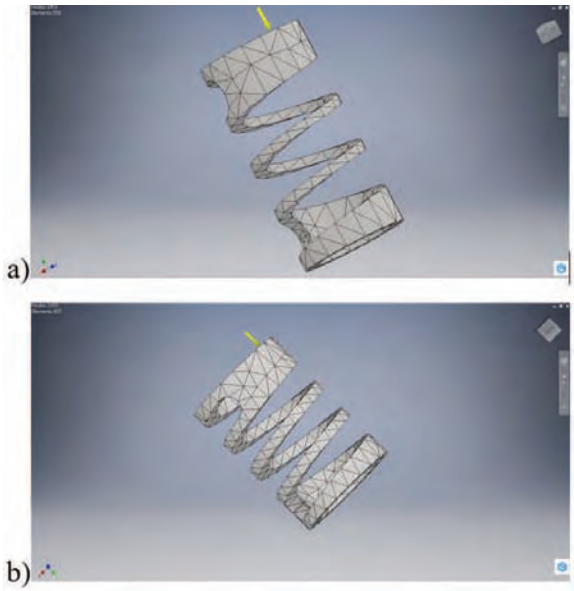

Fig. 14. The grid of finite elements for machined springs a) large and b) small applied in the model of the analyzed valve train

One of the spring front surface was fixed and the force F was applied to the opposite front surface. The force was evenly distributed over the circumference the spring front surface. The value of the force was constant for the each case of analysis, but varied up to reaching the spring deflection equal 12 mm. The distributions of displacements and von Misses stresses were recorded for each case of analysis.

Also, the modal analysis was provided for machined springs. One of the spring front surface was fixed and the spring was preloaded by the initial displacement of 6 mm along the spring axis. It was calculated the modal frequency values and equivalent modes of spring deformations.

6. Results

The resulted values of displacement $d_{r\text{-}c}$ of points the camshaft sub-model loaded by the force F = 1,000 N was presented in the Figure 15, for the inlet valve and in the Figure 16, for the outlet one. The corresponding estimated stiffness $k_{r\text{-}c}$ value was equal 37,000 N/mm for inlet valve and 2,380,000 N/mm for the outlet one.

The calculated values of displacement $d_{r\text{-}f}$ of points the follower sub-model loaded by the force F = 1,000 N was presented in the Figure 17. The corresponding estimated stiffness $k_{r\text{-}f}$ value was of 26,000 N/mm.

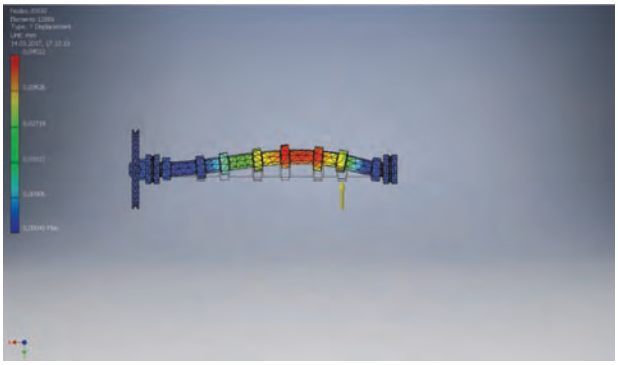

Fig. 15. The displacements of points the camshaft sub-model loaded by the force F = 1,000 N, for the case of inlet valve

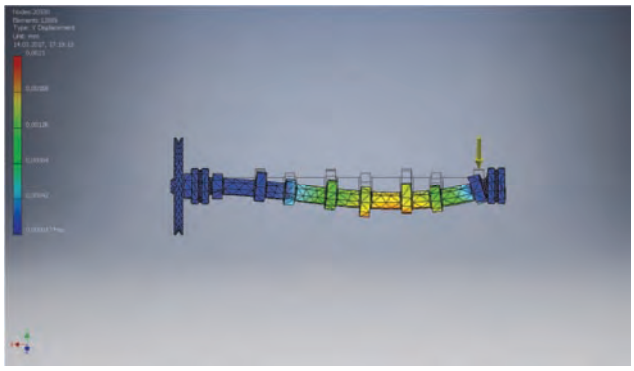

Fig. 16. The displacements of points the camshaft sub-model loaded by the force F=1,000 N, for the case of outlet valve

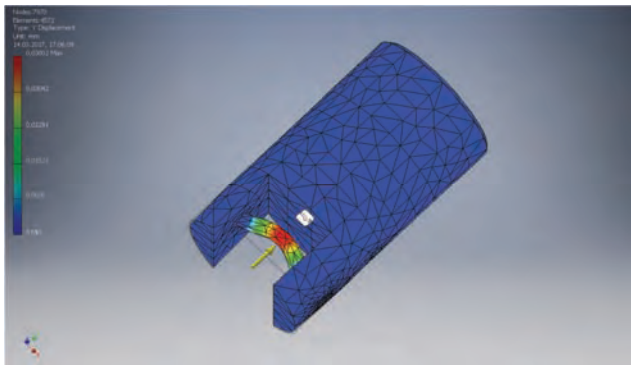

Fig. 17. The displacements of points of the follower sub-model loaded by the force F = 1,000 N

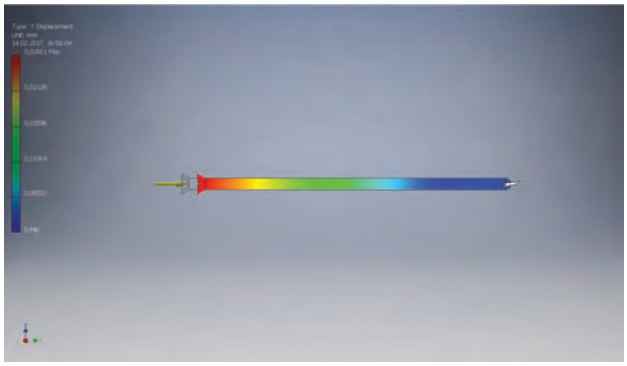

Fig. 18. The displacements of points the pushrod sub-model loaded by the force F = 1,000 N

The resulted values of displacement $d_{pushrod}$ of points the pushrod sub-model loaded by the force F = 1,000 N was presented in the Figure 18. The corresponding estimated stiffness $k_{pushrod}$ value was equal 38,000 N/mm.

The calculated values of displacement d_{raps} of points the rocker arm sub-model loaded by the force F = 1000 N on the pushrod side was shown in the Figure 19. The estimated stiffness k_{raps} value was of 189,000 N/mm.

The resulted values of displacement d_{ravs} of points the rocker arm sub-model loaded by the force F = 1,000 N on the valve side was presented in the Figure 20. The estimated stiffness k_{ravs} value was equal 100,000 N/mm.

The calculated values of displacement d_{axis} of points the sub-model of the rocker arm axis loaded by the force F = 1,000 N was shown in the Figure 21 for the outlet valve and in the Figure 22 for the inlet one. The estimated stiffness k_{axis} value was equal 1,520,000 N/mm for the outlet valve and 1,250,000 N/mm for the inlet one.

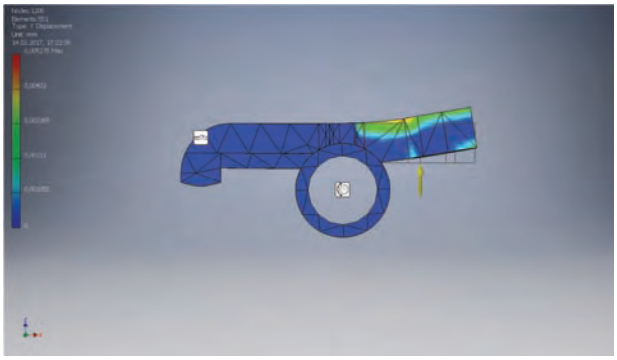

Fig. 19. The displacements of points the rocker arm sub-model loaded by the force F=1000 N on the pushrod side

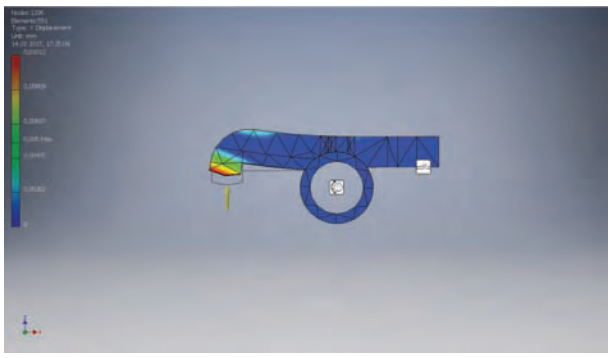

Fig. 20. The displacements of points of the rocker arm sub-model loaded by the force F=1000 N on the valve side

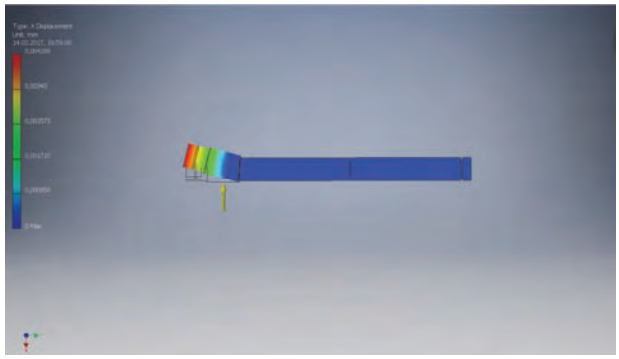

Fig. 21. The displacements of points the sub-model of the rocker arm axis loaded by the force F = 1000 N for the outlet valve

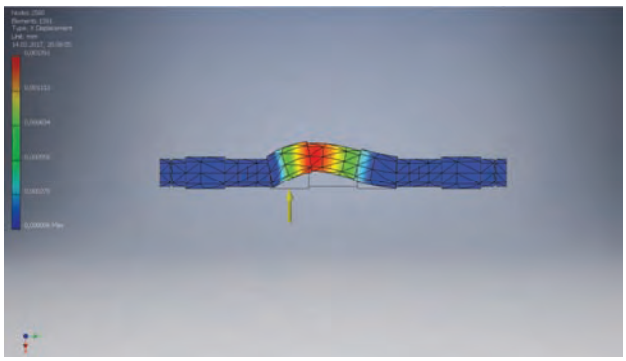

Fig. 22. The displacements of points the sub-model of the rocker arm axis loaded by the force F = 1000 N for the inlet valve

The resulted values of displacement d_{valve} of points the valve sub-model loaded by the force S = 330 N and gas pressure p = 7 MPa were shown in the Figure 23. The estimated stiffness k_{valve} value was equal 1,520,000 N/mm for the outlet valve and 150,000 N/mm for the inlet one.

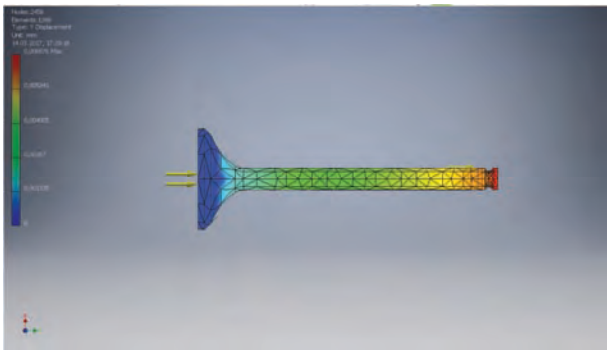

Fig. 23. The displacements of points of the valve sub-model loaded by the force S = 330 N and gas pressure p = 7 MPa

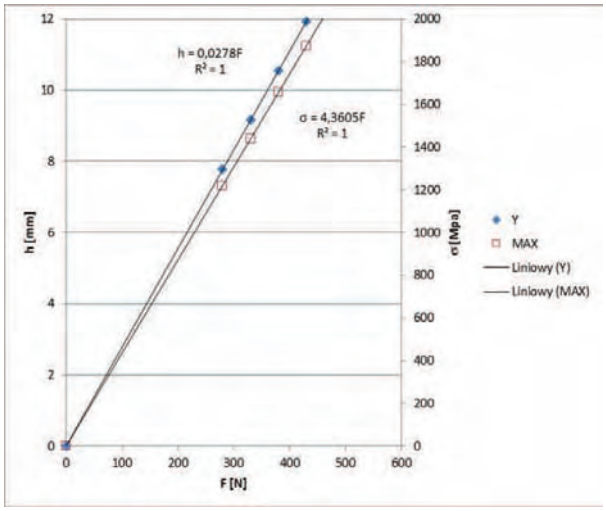

Fig. 24. Displacement and maximum von Misses stress against loading force for the large machined spring

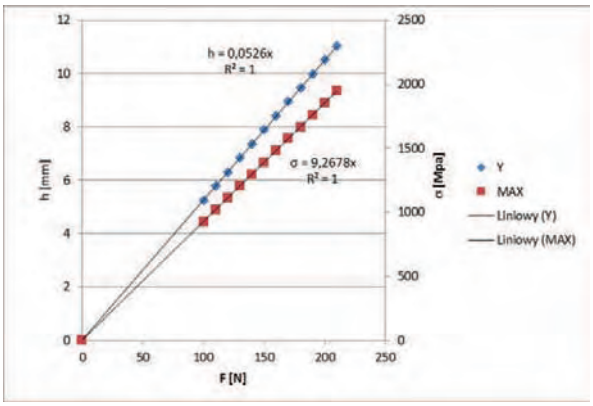

Fig. 25. Displacement and maximum von Misses stress against loading force for the large machined spring

The resulted values of displacements and maximum von Misses stresses as a function of loading force were presented in the Figure 24 - for the large machined spring and in Figure 25 – for the small machined spring. The obtained courses were of the linear nature. The spring rates were equal the inverse of the slope the function h(F). For the large spring its rate was equal 36 N/mm and for the small machined spring the rate was of 19 N/mm. As the springs operate in parallel configuration, so equivalent rate of the spring set was equal 55 N/mm.

The obtained distributions of displacements for the large machined spring loaded with the force F were shown in the Figure 26 and in the Figure 27 – for the small one. Maximal displacement in both cases was about 9.5 mm.

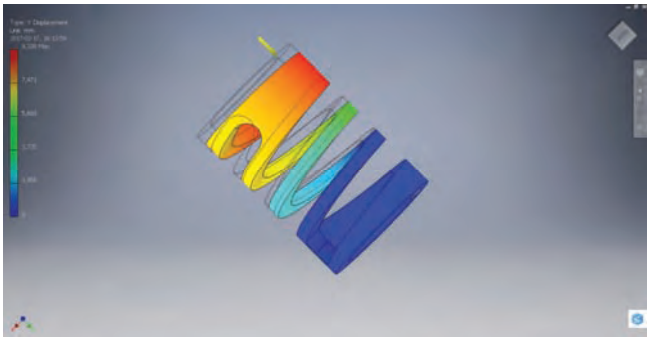

Fig. 26. Distribution of displacements for large machined spring loaded with the force F equal 430 N

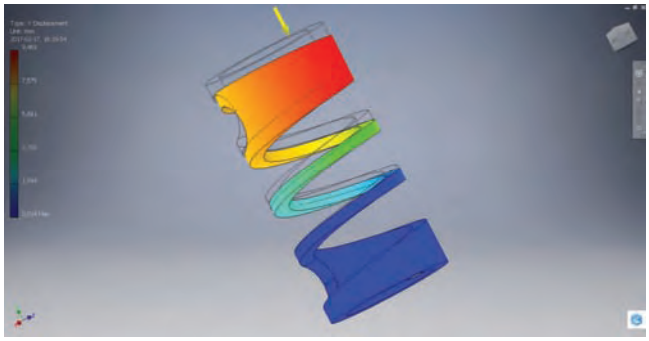

Fig. 27. Distribution of displacements for small machined spring loaded with the force *F* equal 180 N

The corresponding von Misses stress distributions were shown in the Figure 28 – for large spring and in the Figure 29 – for the small one. The maximum von Misses stresses for the large spring loaded by the force F = 430 N was of 1582 MPa and for the small spring loaded by the force F = 180 N was of 1,668 MPa. The points of maximal von Misses stresses were located near the inner diameters of springs.

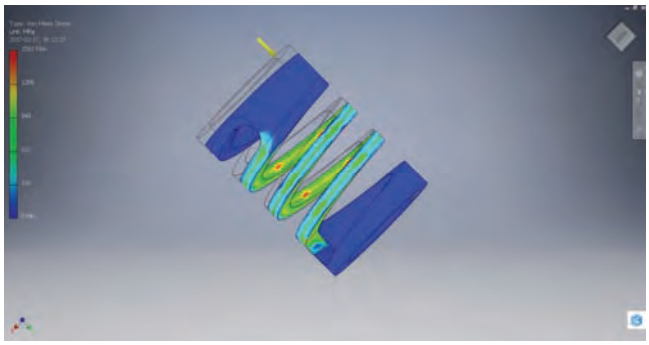

Fig. 28. Distribution of von Misses stresses for large machined spring loaded with the force F equal 430 N

The obtained courses of the inlet valve lift and acceleration against time were presented in the Figure 30 – for the coil valve springs and in the Figure 31 – for the machined springs. The use of machined spring resulted in the twice lower amplitude of small vibrations with the high frequency, probably due higher weight of the machined spring in comparison to the coil one.

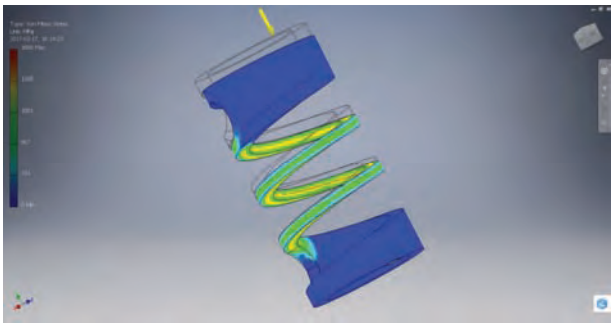

Fig. 29. Distribution of von Misses stresses for small machined spring loaded with the force F equal 180 N

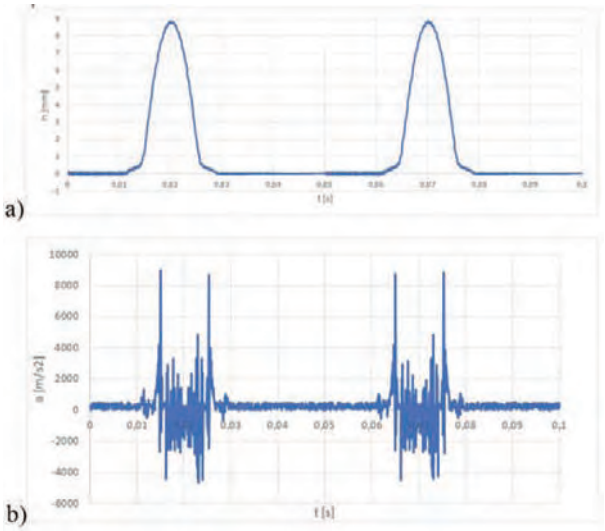

Fig. 30. Courses of the inlet valve a) lift and b) acceleration against time for the coil valve springs

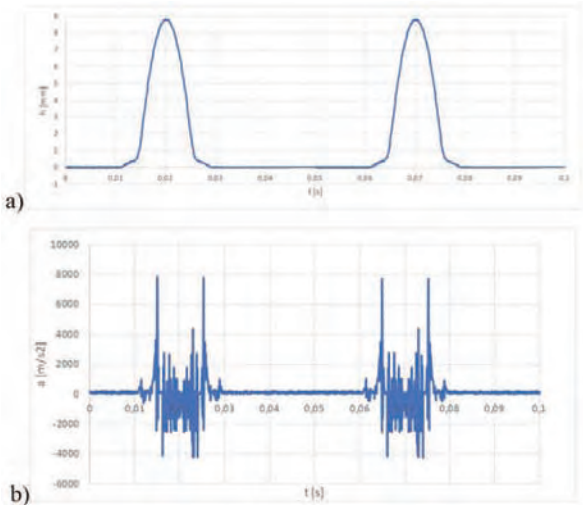

Fig. 31. Courses of the a) lift and b) acceleration of the inlet valve against time for the machined valve springs

The obtained courses of the outlet valve lift and acceleration against time were presented in the Figure 32 – for the coil valve springs and in the Figure 33 – for the machined springs. The use of machined spring resulted in the twice lower amplitude of small vibrations with the high frequency, probably again due higher weight of machined spring in comparison to the coil one. The occurrence of gas pressure in the beginning of valve opening resulted in the 1.5 times lower amplitude of small vibrations with the high frequency in comparison to the case of the inlet valve.

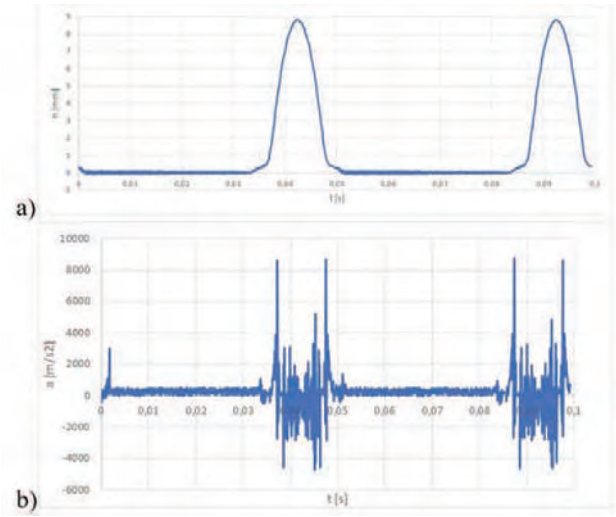

Fig. 32. Courses of the a) lift and b) acceleration of the outlet valve against time for the classical valve springs

Modal frequency values were calculated for the range 0-700 Hz, as current engines can operate with the speed up to 19,000 rpm [49]. The obtained modal frequency values for inner and outer machined springs were shown in the Table 1. For common engines operating with the speed up to 6,000 rpm the existence of spring resonances was hardly to observe.

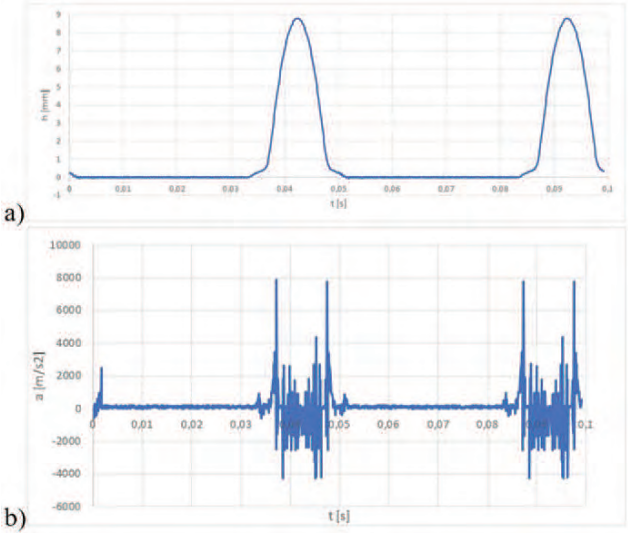

Fig. 33. Courses of the a) lift and b) acceleration of the inlet valve against time for the machined valve springs

Table 1. Modal frequency against number of mode for machined springs

Number of mode	Modal frequency [Hz]	
	Inner spring	Outer spring
1	211.97	165.26
2	285.43	170.52
3	287.80	268.63
4	352.89	365.23
5	413.26	707.05
6	422.41	711.28
7	589.11	1031.54
8	619.59	1301.54
9	619.58	1370.11
10	684.17	1710.77

The obtained modes were presented in the Figure 34 for the inner machined spring and related modal frequencies.

4. Summary

The use of machined valve springs against classical coil springs resulted in the obtaining almost the same spring stiffness. The increased mass of machined springs did not make important changes in the lift and acceleration of inlet and outlet valves. Only small decreasing of amplitude the small vibrations with high frequency was observed during motion the valves. For the engines operating with the common speed range up to 6,000 rpm the machined spring resonances cannot exist.

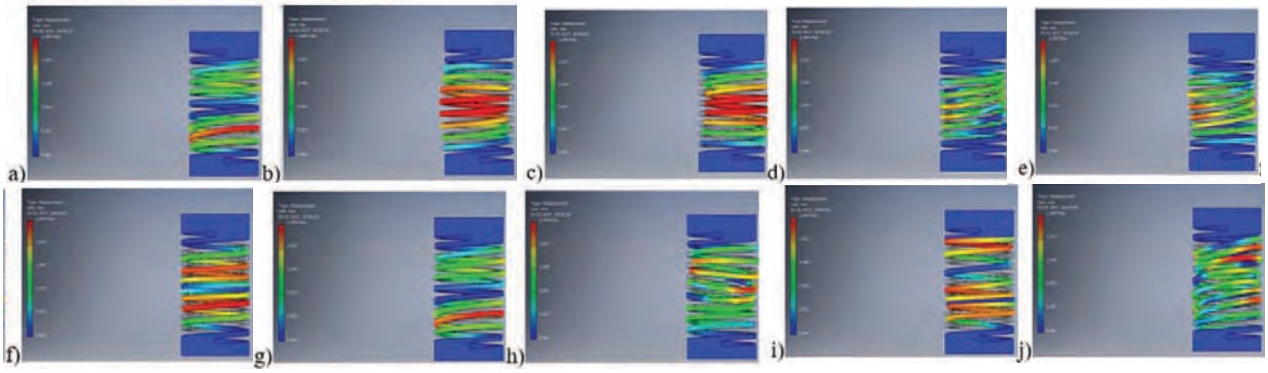

Fig. 34. Modes of the inner machined spring for the different values of modal frequency: a) for the mode number 1, b) for the mode number 2,…, j) for the mode number 10, respectively

Nomenclature

FEM finite element method
CE engine crankshaft rotation angle
OHC over head cam
OHV over head valve
DOHC double over head cam
MA multi-arc
SI spark ignition
CI compressed ignition

Bibliography

[1] CLENCI, A.C., HARA, V., STANESCU, N-D., BIZILAC, A., NICULESCU, R. Analytical synthesis and computer-aided kinematic analysis of a continuously variable valve lift mechanism. *AProc. IMechE Part C: J. Mechanical Engineering Science*. 2017, **231**(2), 309-325.
[2] JOHANSSON, B. Förbränningsmotorer del 2, 2004.
[3] KRÜGER, K. Einfluss hydraulischer Nockenwellenversteller auf die Dynamik von Ventil- und Steuertrieben, DI Dissertation, Technischen Universität München, 2009.
[4] HEISLER, H. Advanced Engine Technology. *SAE International*, Warrendale, PA, 1995.
[5] GROHN, M. The new camshaft adjustment system by Mercedes Benz – design and application in 4valve engines. *SAE Technical Paper* 901727, 1990.
[6] MORIYA, Y., WATANABE, A., UDA, H., KAWAMURA, H., YOSHIOKA, M. A newly developed intelligent variable valve timing system – continuously controlled cam phasing as applied to a new 3 liter inline 6 engine. *SAE Technical Paper* 960579, 1996.
[7] JÄÄSKELÄINEN, H. Variable valve actuation. 2011, DieselNet. www.dieselnet.com (2012-06-5).
[8] STONE, C.R., KWON, E.K.M. Variable valve timing for IC engines. *Automotive Engineer*. August/September 1985.
[9] PARKER, P.H. The variable valve timing mechanism for the Rover K16 engine. Part 2: application to the engine and the performance obtained. *Proceedings of the Institution of Mechanical Engineers, Part D: Journal of Automobile Engineering*. 2000, **214**(2), 207-216.
[10] VON JOHANN-GEORG, U., FIEDLER, O., Vo§ H., Motor fur Porsche 968. *Motortechnische Zeitschrift* 1991, **52**(12).
[11] STOFFREGEN, J., Motorradtechnik: Grundlagen und Konzepte von Motor, Antrieb und Fahrwerk Populär. *ATZ/MTZ-Fachbuch Springer Vieweg Populär. Kraftfahrzeugtechnik, Springer-Verlag*. 2012.
[12] Ventiltrieb: Systeme und Komponenten, Mahle GmbH, *Springer-Verlag*, 2012.
[13] INOUE, K., NAGAHIRO, K., AJIKI, Y., KISHI, N. A high power, wide torque range, efficient engine with a newly developed variable valve lift and -timing mechanism. *SAE Technical Paper* 890675, 1989.
[14] LANCEFIELD, T., LAWRENCE, N., AHMED, A., BEN HADI HAMOUDA, H. VLD a flexible, modular, cam operated VVA system giving variable valve lift and duration and controlled secondary valve openings, SIA-IFP (2006).
[15] my.ms-motorservice.com/fileadmin/media/kspg /Broschueren/Produktbroschueren/ Pierburg/Variabler_Ventiltrieb/Bro_Var_Ventiltrieb_EN_web.pdf (available 2017.02.12).

[16] YAMAGUCHI, J. Super-economy lean-burn engines from Mitsubishi and Honda – techbriefs. *Automotive Engineering*. 1991, 11(99).
[17] asia.vtec.net/spfeature/vtecimpl/vtec1.html (available 2017.02.12).
[18] paultan.org/2006/03/13/2006-honda-civic-18-sohc-i-vtec-engine/gevtec.html (available 2017.02.12).
[19] www.honda.co.jp/tech/auto/engine/20i-vtec/index (available 2017.02.12).
[20] paultan.org/2006/03/13/2006-honda-civic-18-sohc-i-vtec-engine (available 2017.02.12).
[21] www.autozine.org/technical_school/engine/vvt_2.htm (available 2017.02.12)
[22] www.mitsubishi-motors.com/corporate/about_us/ technology/performance/e/mivec.html (available 2017.02.12).
[23] paultan.org/2007/04/17/honda-files-advanced-vtec-patent (available 2017.02.12).
[24] outlander.kiev.ua/manual/Outlander_2.4_AT_MT/11C.pdf (available 2017.02.12).
[25] www.datsuncr.com/motores-nissan-datsun.html (available 2017.02.12).
[26] www.neovvl.com/whatisneovvl.php (available 2017.02.12).
[27] www.sr20-forum.com/vvl/40827-ve-factory-nissan-cam-specs.html (available 2017.02.12).
[28] paultan.org/2008/02/06/proton-waja-campro-16-premium-cps-details (available 2017.02.12).
[29] MILOVANOVIC, N., DAVE, B., GEDGE, S., TURNER, J. Cam profile switching (CPS) and phasing strategy vs fully variable valve train (FVVT) strategy for transitions between spark ignition and controlled auto ignition modes. *SAE Technical Paper*. 2005, 2005-01-0766.
[30] ZHAO, H. HCCI and CAI engines for the automotive industry. *Elsevier*. 2007.
[31] www.delphi.com/manufacturers/auto/powertrain/gas/valvetrain/2step (available 2017.02.12).
[32] www.yamaha-motor.eu/designcafe/de/ (available 2017.02.12).
[33] www.nissan-global.com/EN/TECHNOLOGY/OVERVIEW/vvel.html (available 2017.02.12).
[34] ThyssenKrupp techforum Juli 2004 (available 2017.02.12).
[35] DABROWSKI, A., GLOGOWSKI, M., KUBIAK, P. Improving the efficiency of four-stroke engine with use of the pneumatic energy accumulator – simulations and examinations. *International Journal of Automotive Technology*. 2016, **17**(4), 581-590).
[36] BALL, A.D., DOWSON, D., et al. Cam and follower design. In: *Tribology Series*. 1988, **14**, 111-130.
[37] NUNNEY, M.J. Light and heavy vehicle technology. *Elsevier*, 2013, 514.
[38] HUBER, R. Dynamics of variable valve trains and extrapolation methods for time-stepping schemes. PhD Thesis, Technischen Universität München, 2012.
[39] VAN BASSHUYSEN, R., SCHAFER, F. Internal combustion engine handbook: basics, components, systems, and perspectives. *SAE International*, 2004.
[40] MUHR, T.H. New technologies for engine valve springs. *SAE Technical Paper*. 1993, 930912.
[41] HILLIER, V. Hillier's fundamentals of motor vehicle technology. Nelson Thornes, 6 edition, 2004.
[42] SEMET, W. Entwicklung einer pneumatischen Ventilfeder für hochdrehende Serienmotoren, PhD thesis, Universität Stuttgart, 2007.
[43] Pick-a-Part: Selecting valvetrain components for a performance build. *Engine Builder*, February 2014.
[44] SUDHAKAR, K.V., Failure analysis of an automobile valve spring. *Engineering Failure Analysis*. 2001, **8**(6), 513-520.
[45] YU, Z-W., XU, X-L. Failure analysis on diesel-engine valve springs. *Journal of Failure Analysis and Prevention*. 2009, **9**(4), 329-334.
[46] PATEL SUJAL, V., PAWAR SHRIKANT, G. Failure analysis of exhaust valve spring of C.I. engine. *International Journal of Engineering Research & Technology (IJERT)*. 2013, **2**(3).
[47] BOEHM, G.L. Wire springs versus machined springs. A comparison, *PE* – 15 SEP 14 – Version 16, Helical Products Co. MW Industries, Inc. Santa Maria, USA.
[48] Machine spring displacer for Stirling cycle machines, *Patent* US7017344 B2.
[49] www.f1network.net/main/s107/st66401.htm (available 2017.02.12).

Krystian Siczek – Faculty of Electrical, Electronic, Computer and Control Engineering at Lodz University of Technology.

e-mail: *Krystian.Siczek@p.lodz.pl*

Krzysztof Siczek, DSc., DEng. – Faculty of Mechanical Engineering at Lodz University of Technology.

e-mail: *ks670907@p.lodz.pl*

Article citation info:
BALICKI, W., GŁOWACKI, P. Causes of the powerplants failures installed on Polish civil aviation aircraft. *Combustion Engines*. 2017, **168**(1), 110-121. DOI: 10.19206/CE-2017-117

Włodzimierz BALICKI
Paweł GŁOWACKI

CE-2017-117

Causes of the powerplants failures installed on Polish civil aviation aircraft

Currently in Poland about 2,500 different engine types are installed on the aircraft. In the years 2008-2016 powerplants failures caused nearly 600 aviation events. Aborted flight or emergency landing, especially in the case of aircraft powered by a single piston engine occurred. The objective of the article was to determine the failure causes and assessment of their impact on the flight safety. Engine faults were assigned to particular types of powerplants, for example turboshaft, piston, etc. Causes of the failures were examined, assigning ATA chapter to each of them. Also human factor was taken into account. According to the ICAO methodology, aviation safety engine systems essential for flight safety and theirs impact on the safety risk was determined. The results of the analyzes presented in this article are useful for managing the national aviation safety and supervising SMS in aviation organizations. The article shows that preventive measures to raise the level of aviation safety should be taken. This is the first comprehensive analysis of the powerplants failure causes and an evaluation of their influence on the level of aviation safety in Poland.

Key words: *powerplant, aircraft engine failure, safety risk*

1. Introduction

The hitherto operational experience indicate that to the greatest extent powerplant determines airplanes and helicopters safety of flying. Still significant number of aircraft engines exploitation is a subject of the guaranteed by manufacturers service life (so-called "hard time") [8, 9]. Such a time is usually determined by the manufacturers carrying out test-bed endurance programs where the engine is run day and night, cycling through a specified and purposely over-punishing schedule of so many hours at full power, so many at idle, so many at cruise. During the manufacturer's tests the engine is run on the test bed in a manner which is purposely more severe than ordinary operator will use. Often engines are tested in the flying beds as well as high altitude test-cells. During tests engine durability, especially resistance on uncontained failure of the fan, compressor and turbine cases are checked. Also resistance of the fan blades against bird strike is examined.

The hard time exploitation method requires technical inspections and engine overhaul conducting after its work for a certain period of time (regardless of the actual technical condition of the engine). After a guaranteed by manufacturer life the engine is subject of a cassation. The advantage of this method of operation is the possibility of a relatively simple overhaul and maintenance tasks planning, spare parts purchasing and new engines acquisition scheduling. This system, however, is expensive, because often unnecessary maintenance tasks have to be carried out, reduces aircraft operational readiness, requires removals of a serviceable engine parts (risk of damage during these works), in brief, increases engine direct maintenance cost.

It was noted that the degree of engine wear depends not only on the number of its working hours, but also on variety of difficult to evaluate factors like environmental conditions (eg. dust, salt, humidity), and aircraft flight profile. Also level of training and individual pilot psychophysical characteristics are engine condition influencers. An attempt to take into account the influence factors related to engine operating conditions was the use of appropriate statistical tools.

The development of a safe for aircraft application measurement and registration technologies, enabled introduction of the on-condition exploitation method applied for airframes, powerplants and specific aircraft parts. The possibility of obtaining reliable records of the registered parameters resulted, in turn, in the development of data interpretation methods. For the equipment reliability evaluation mathematical statistic methods in a wider range were applied [5, 7, 11]. The reliability function allows a determination of the system continued operation probability. The quality of the assessment depends on the obtained data credibility, samples volume, that is, from the experience gained during operation of a specific equipment type.

In order to present equipment reliability various indicators are used, which include inter alia time between failure, time between overhaul or factor describing the number of its failures per 1000 operating hours [5, 6, 12].

The aircraft engines exploitation practice is to maintain the required level of the flight safety. For this purpose, in addition to the assessment of the engine's technical condition, identification of its installations significantly affect the flying safety is carried out. The risk associated with the frequency of their faults is determined, which is important one of the elements of aviation safety management system (SMS).

The identification of aircraft and engines systems was simplified by the introduction in 1956 standard numbering system ATA 100 developed by Air Transport Association (ATA) [4]. This rely on aircraft and engines systems description by giving them a two-digit number, eg. Chapter 73 – fuel supply and flow control, chapter 74 – ignition, chapter 80 – starting etc. This system has expanded in 1999 by adding two more digits to indicate each group, defining the specific subsystems, eg. in the chapter 71 – powerplant (general) separated: 7110 – cowling, 7120 – mounts, 7150 – electrical harness etc. During the encoding of events caused by powerplant, recorded in the data base ECCAIRS as SCF-PP, the authors used the numbering system identical for large aircraft, small and helicopters.

2. Research methodology

In order to analyse various types of the powerplants influence on flight safety, data contained in the ECCAIRS were reviewed. This database is conducted by SCAAI and ULC. Contains aviation event reports sent by the organizations involved in air operations. It is very extensive – contains over 7000 events in air traffic reported between 2008 and 2016. Reported aviation incidents are coded according to ICAO aviation occurrence categories [1, 2].

Events caused by powerplants coded as SCF-PP were divided depending on engine type (piston, turboprop, turboshaft and turbine). As the number of Polish registered aircraft was changing between 2008 and 2016, factor in order to objectify the data analysis was introduced (equation 1).

$$K_{1000TYPE} = \frac{1000 \cdot LZ_{TYPE}}{LSP_{TYPE}} \quad (1)$$

where: LZ_{TYPE} – number of aviation events caused by turboshaft, turboprop, turbine and piston engines in certain year, LSP_{TYPE} – number of registered aircraft powered by specified above type of engine in certain year.

Proper safety management lies not only in an identification of essential safety parameters and prediction of their level, but also requires an estimation of safety risk connected with selected safety indicators.

In order to assess safety risk, it is necessary to estimate the probability that the consequences of hazard will come to effect during aircraft operations. In literature five point probability table is frequently used [13]. The Tab. 1 includes five categories, which describe the probability related to an unsafe event.

Table 1. Safety risk probability [13]

Likelihood	Meaning	Value
Frequent	Likely to occur many times (has occurred frequently)	5
Occasional	Likely to occur sometimes (has occurred inferequently)	4
Remote	Unlikely to occur, but possible (has occurred rarely)	3
Improbable	Very unlikely to occur (not known to have occurred)	2
Extremely Improbable	Almost inconceivable that the event will occured	1

The next step is a safety risk severity assessment, which is a potential harm that might occur as a consequence of the identified hazard. Tab. 2 from [13] has been utilized in order to evaluate safety risk as a consequence of a potential event caused by any powerplant system.

Based on the two tables above, safety risk assessment could be performed. Usually it is performed utilizing Tab.3 Safety risk assessment matrix, which is a combination of severity/probability

Events caused by particular type of powerplant system were assigned by authors and shown in the safety risk assessment tables (Tab. 5, Tab. 10, Tab. 13, Tab.16), which are presented in the chapters disscusing each engine type.

Table 2. Safety risk severity [13]

Severity	Meaning	Value
Catastrophic	Equipment destroyed Multiple deaths	A
Hazardous	A large reduction in safety margins, physical distress or workload such that the operators cannot be relied upon to perform their tasks accurately or completely Serious injury Major equipment damage	B
Major	A significant reduction in safety margins, a reduction in the ability of the operators to cope with adverse operating conditions as a result of an increase in workload, or as a result of conditions impairing their efficiency Serious incident Injury to persons	C
Minor	Nuisance Use of emergency procedures Operating limitations Minor incident	D
Negligible	Little consequences	E

Table 3. Safety risk assessment matrix [13]

Risk probability		Risk severity				
		Catastrophic A	Hazardous B	Major C	Minor D	Negligible E
Frequent	5	5A	5B	5C	5D	5E
Occasional	4	4A	4B	4C	4D	4E
Remote	3	3A	3B	3C	3D	3E
Improbable	2	2A	2B	2C	2D	2E
Extremely improbable	1	1A	1B	1C	1D	1E

There was 557 reported events between 2008 and 2016 caused by all engine types installed on Polish registered aircraft.

Figure 1 shows an annual number of reported aviation events caused by powerplant types considered in this article.

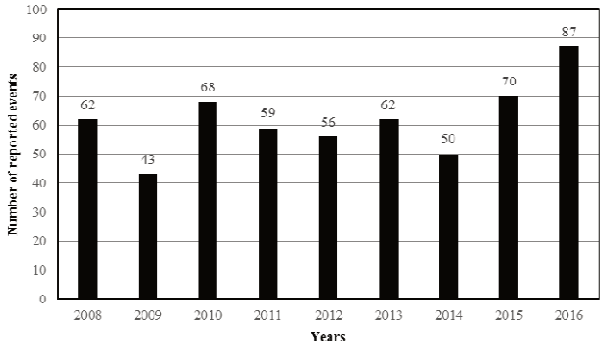

Fig. 1. Number of reported aviation events caused by powerplants installed on Polish registered aircraft

Figure 2 shows changes of the coefficient K_{1000} for aviation events occurred within 2008-2016, for all powerplant types. The below presented figures are showing increased trend of the reported aviation occurences per 1000 registered aircraft for last two years. Such a situation

is different considering various engine types. Next four chapters contains detailed information of aviation events have occurred for each of the powerplant type since 2008.

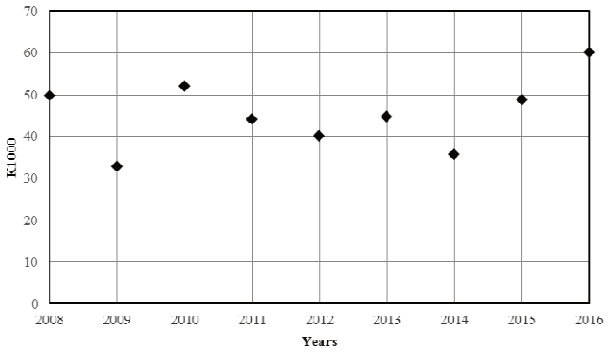

Fig. 2. Changes of the coefficient K1000 for SCF-PP aviation occurrence categories

3. Aviation piston engines

Piston engines will be a suitable and popular engine choice among personal airplane owners for many years. From a manufacturing and engineering perspective, the reciprocating engines found in piston aircraft are far less complex than turboprops. Piston aircraft are generally smaller aircraft, seating no more than six passengers, and are well suited for relatively short missions of 500 kilometers or less. There are many piston engine models being currently in operation in Poland. All of them are installed on aircraft which are operated in general aviation. Tab. 4 contains information about numbers of each installed engine model.

Table 4. Model and number of the piston engines

Engine model	Number of installed engines
Austro Engine	5
Bombardier Rotax	101
Continental	208
de Havilland Gipsy Major	3
Franklin	23
Jabiru	2
Limbach	4
LOM	46
Lycoming	492
PZL Kalisz ASZ62	120
PZL Kalisz AI14	94
PZL Kalisz M11	7
PZL Kalisz WN3	3
Rolls Royce	20
Rotor Way RI	4
Simonini Victor	1
Subaru EA	4
Thielert TAE125-01 Centurion 1.7	7
Titan CC340	4
Vedeneyev M14 P	35
Verner 1400	1
Volkswagen 1600	1
Walter Mikron III	3
WSK PZL Rzeszów PZL3 SR	1
Total	**1189**

Figure 3 shows view of the contemporary utilized typical aviation piston engine with description of its main parts [3].

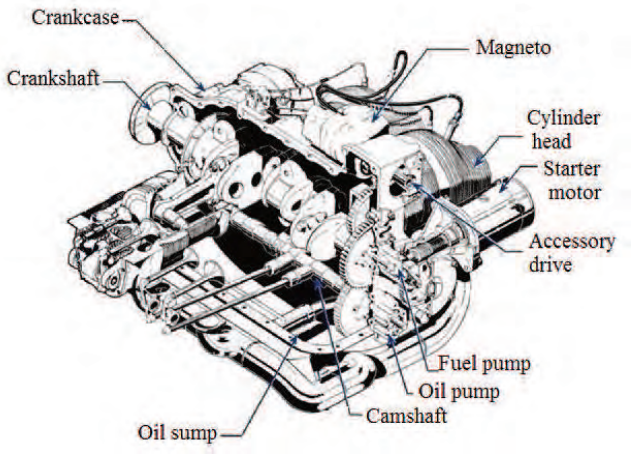

Fig. 3. Four cylinders, horizontally opposed, air cooled aviation piston engine

3.1. General information

There was totally 207 aviation events caused by piston engines in 2008-2016. **Due to the fact that almost 95% of the piston engines powered aircraft are single engine airplane each failure is not the only a threat to the flying crew safety, but most importantly for individuals on the ground.**

Figure 4 shows an annual number of reported aviation events caused by piston engines. Figure 5 shows changes of the coefficient $K_{1000pist}$.between 2008-2016.

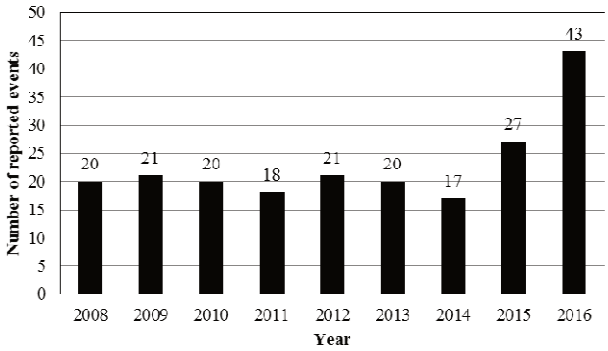

Fig. 4. Number of events caused by piston engines installed on Polish registered aircraft between 2008-2016

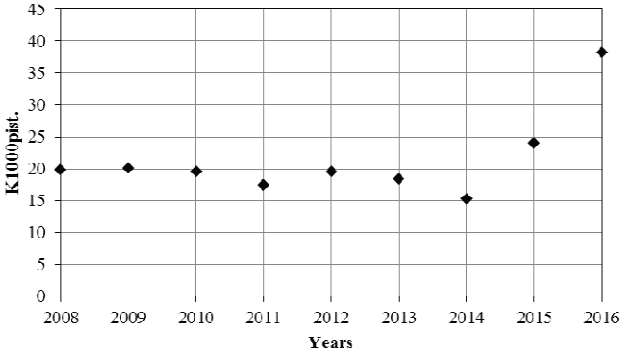

Fig. 5. Changes of the coefficient $K_{1000pist.}$

It has to be pointed out that for last two years sudden, significant increase in number of events caused by this

engine type is observed. From 17 in 2014 to 43 in 2016 – more than twice.

Figure 6 gives (in percent) information during which aircraft maneuver and how often reported event caused by piston engine took place in 2008-2016. It is unacceptable that the vast amount of the powerplant reported failures occurred during aircraft movement. Only 15% of them were detected during routine maintenance tasks.

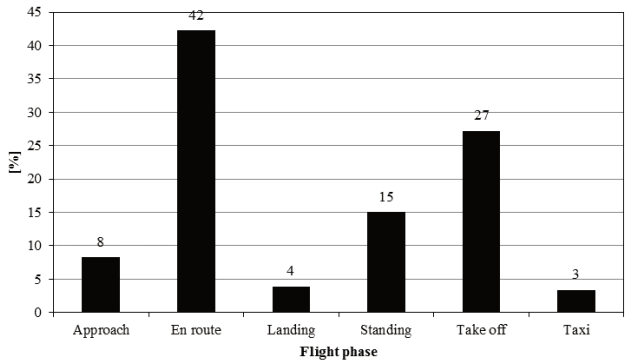

Fig. 6. Flight phases share when piston engine malfunction took place

Figure 7 shows reported system defects frequency in percent assigned to the certain ATA chapter for the piston engines in the 2008-2016.

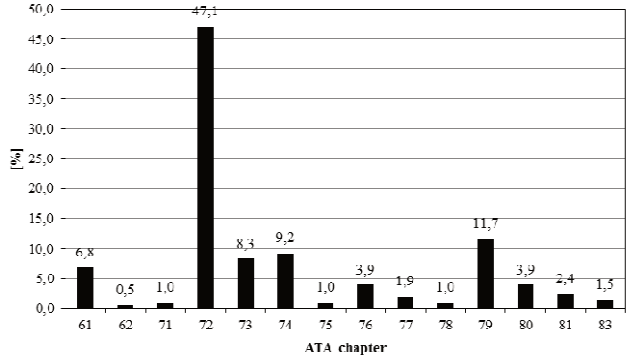

Fig. 7. Share of each powerplant system events coded by ATA 100 chapter between 2008 and 2016

The above Fig. 7 shows "share" of the certain ATA chapter in percent in the total volume of the piston engines reported events. It was assumed that the most frequently occurred event – ATA chapter 72 has occurrence probability level equel 5. Next 79, 74 and 73 level 4, 61 level 3, 76 and 80 level 2 and the remaining 62, 71, 75, 77, 78, 81 and 83 level 1. According to the methodology described in the introduction (Tab. 1, Tab. 2 and Tab. 3) to each from the above ATA chapters safety risk severity was assigned, based on events consequences described in the ECCAIRS reports. Then safety risk assessment matrix was developed for piston engines operated in Poland. Results of the analysis are presented in the Tab. 5.

Every item presented in the red field requires immediate actions, which have to be taken on the country level in order to mitigate safety risk connected with the highlted in red engine systems coded in ATA 72, 74 and 79 chapters. Engine systems marked in yellow are acceptable based on risk (moderate risk) mitigation. However, a schedule for performance of safety assessment has to be prepared in order to find ways to bring down safety risk to low. In this way aviation authority can develop or order program implementation of safety risk mitigation, in our case on Country level. Below are discussed in details "red" ATA chapters.

Table 5. Safety risk assessment matrix for piston engine systems

ATA chapter		Index
No.	Contents	
61	Propellers/propulsors	3C
62	Main rotor(s)	1D
71	Powerplant general	1C
72	Engine-reciprocating	5B
73	Engine-fuel and control	4C
74	Ignition	4B
75	Bleed air	1E
76	Engine controls	2C
77	Engine indicating	1C
78	Exhaust	1E
79	Oil	4B
80	Starting	2D
81	Turbines	1E
83	Accessory gear boxes	1D

3.2. ATA chapter 72

There were 97 reported aviation events in the ATA 72 chapter between 2008-2016. Figure 8 shows an annual number of reported events as a result of piston engine failures coded in that chapter.

Figure 9 gives (in percent) information during which aircraft maneuver and how often failure of the piston engine in the ATA 72 chapter took place between 2008-2016.

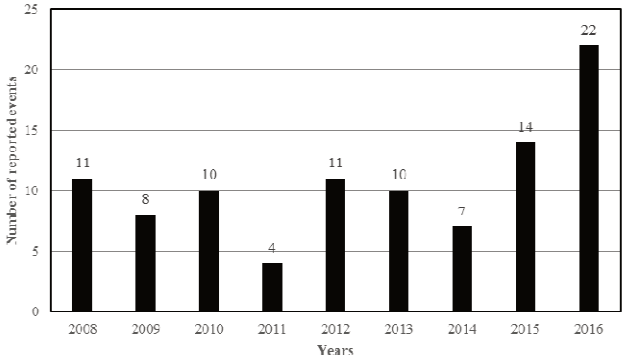

Fig. 8. Number of events caused by piston engines installed on Polish registered aircraft in the ATA 72 chapter between 2008-2016

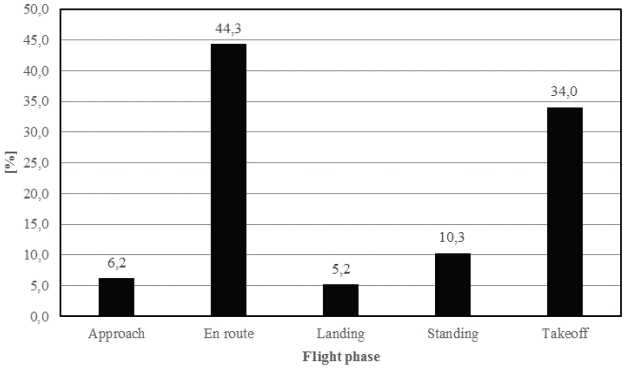

Fig. 9. Flight phases share when powerplant malfunction ATA chapter 72 took place

Majority failures concern ATA sub charters 72-20-00 power section and 72-30-00 cylinder section. As a result of the engine failure serious events took place. Table 6 shows in numbers result of the piston engines malfunction, symptoms observed and precursors of the powerplant defect, where it was confirmed.

Almost 50% out of the total (207) occurrences caused by powerplants can be assigned to the engine itself (see Fig. 7). Most of the events are connected with powertrain and cylinder systems. The events were caused by cracked exhaust valves. Also carbon deposit was observed on them. Other occurrences were caused by different failures of the cylinders. It can be presumed that those damages were mainly due to engines overheating that resulted from an improper exploitation.

3.3. ATA chapter 74

During 2008-2016 there was 19 events caused by ignition system. All of them in the two ATA sub chapters 74-10-00 electrical power supply and 74-20-00 distribution. First includes magnetos, second spark plugs.

Figure 10 gives information during which aircraft maneuver a failure in the ATA 74 chapter took place within 2008-2016. The Tab. 7 shows in numbers result of the engine ignition system malfunctions, symptoms observed and precursors of the powerplant defects, where it was confirmed.

Spark plugs during post event checks were found with carbon deposit, few wrongly fitted, which again is an evidence of careless maintenance or failure to meet engine exploitation procedures. More than 70% of ignition system malfunctions jeopardized flight safety as 13 aborted flights or emergency landings occurred.

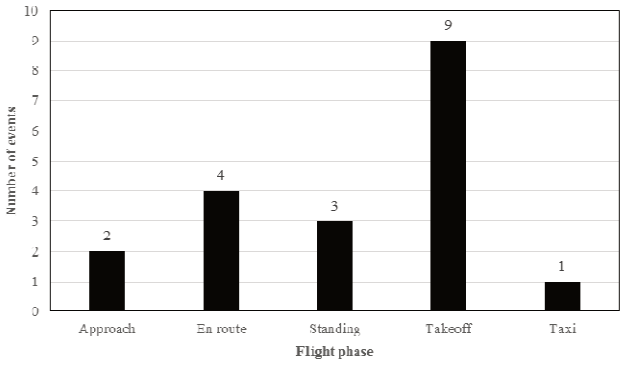

Fig. 10. Flight phases share when powerplant malfunction in the ATA 74 chapter took place

3.4. ATA chapter 79

Between 2008-2016 there was 23 events caused by engine oil system. Figure 11 gives information during which aircraft maneuver a failure coded in the ATA 79 chapter took place within 2008-2016.

The Tab. 8 shows in numbers result of the engine oil system malfunctions, symptoms observed and precursors of the powerplant defects, where it was confirmed.

Improperly installed or connected oil pipes causing leaks are the main, but not the only reason, for the reported events connected with the engine oil system. Most of them occurred due to maintenance imperfections. Oil system faults had a significant impact on flight safety. It needs to be mentioned that in 23 cases, in the years 2008-2016 out of the oil system malfunctions, 19 of them resulted in aborted flights or emergency landings.

Table 6. Confirmed roots of the piston engines failures coded in the ATA 72 chapter which caused aviation event

No	Mulfunction result	No	Symptom	No	Confirmed precursor
14	Emergency landing	27	Loss of power	4	Exhaust valve
51	Aborted flight	24	Unstable engine work	5	Cylinder
3	Aborted takeoff	2	Engine overheating	5	Crancase
2	Ground roll stopped	11	In flight shut down	4	Crankshaft
		1	Engine vibration	1	Camshaft
				2	Connecting rod

Table 7. Confirmed roots of the piston engines failures coded in the ATA 74 chapter which caused aviation event

No	Mulfunction result	No	Symptom	No	Confirmed precursor
3	Emergency landing	8	Unstable engine work	10	Spark plug
10	Aborted flight	4	Loss of power	5	Magneto
		2	Engine vibration	1	Electrical wire

Table 8. Confirmed roots of the piston engines failures coded in the ATA 79 chapter which caused aviation event

No	Mulfunction result	No	Symptom	No	Confirmed precursor
15	Aborted flight	3	Loss of power	6	Improper maintenance
4	Emergency landing	4	Oil pressure low	6	Metal chips in the oil filter or on detector
1	Ground roll stopped	3	Oil temperature high		
1	Aircraft elements damage	2	Engine vibration		
		1	Oil pressure high		
		3	Oil leak		
		1	Not extended nose gear		
		1	Oil chip indication		

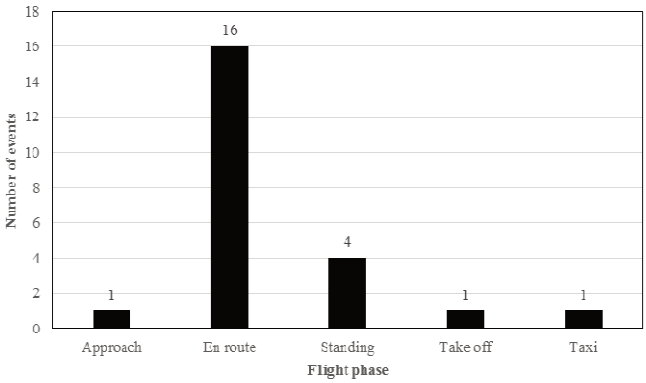

Fig. 11. Flight phases share when powerplant malfunction in the ATA 79 chapter took place

The above descriptions presented leading to the conclusion that piston engines require changes in the current exploitation system in order to improve flight safety. In addition to the existing maintenance and operational requirements already included in the manufacturers' manuals such a system should introduce new tasks like, for example, engine vibration or flight parameters monitoring. It seems that also more insightful supervision of the maintenance tasks execution as well as way of flying is required. This will not have only a positive economic impact for general aviation operators, but also intangible, like improvement of the flight safety, technical culture and sense of responsibility of aviation technical staff and pilots.

4. Turboprop engines

Turboprop engines are source of power for aircraft operated in general and commercial aviation. Turboprop aircraft are generally most efficient at altitudes of 6000 to 9000 meters and at average speeds of 450 km/h to 600 km/h. Turboprops tend to be larger than piston aircraft with greater passenger capacity – and more fuel on-board – and are more likely to be found flying distances of up to 2000 km. It seems that turboprops will be used widely for a long time, both short and medium distances. Table 9 presents number of installed turboprop engine models on Polish registered aircraft.

Today's turboprop engines are characterized by a huge power range (300-11000 kW) and a variety of design forms. These are now mostly single-rotor with axial or axial compressors with a radial stage, and a large share (among small and medium power engines) of separate power turbines.

Table 9. Model and number of the turboprop engines

Engine model	Number of installed engines
PRATT AND WHITNEY PT6A FAMILY	53
PRATT AND WHITNEY PW 150	20
PRATT AND WHITNEY PW 124	10
GENERAL ELECTRIC CT7 5A2	28
HONEYWELL TPE331	3
IVCHENKO AI24 VT	4
LOM M601 E	4
Total	**122**

Figure 12 shows scheme of the contemporary utilized popular Pratt &Whitney PT6 turboprop engine with description of its main parts, covering the power range between 430 and 680 shaft kilowatts [8, 9].

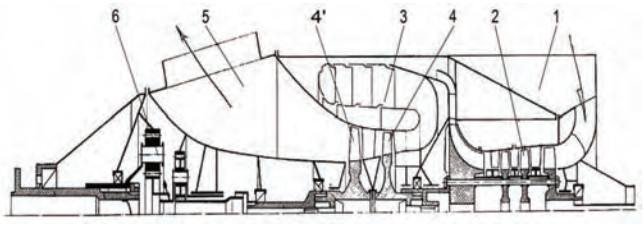

Fig. 12. Design scheme of PT6 turboprop engine: 1 – air inlet, 2 – compressor, 3 – combustor chamber, 4 – compressor powered turbine, 4' – power turbine 5 – exhaust, 6 – reduction gearbox

4.1. General information

There were 101 aviation events caused by turboprop engine malfunction. It has to be emphasized that in Poland almost 95% of turbo-propops are twin engines aircraft, so results of a powerplant failure are not so dangerous like for single engine aircraft.

Figure 13 shows an annual number of reported aviation events caused by turboprop engines. Figure 14 shows changes of the coefficient $K_{1000tprop}$ during 2008-2016.

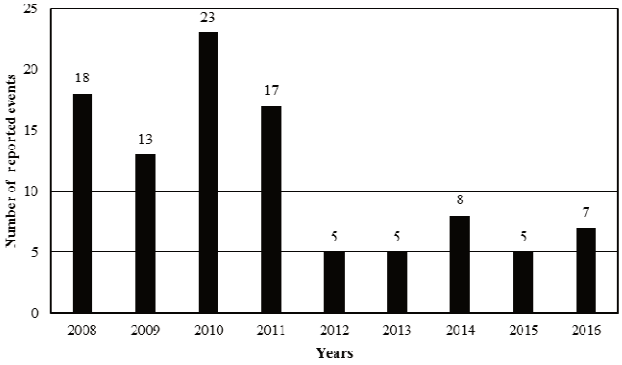

Fig. 13. Number of events caused by turboprop engines installed on Polish registered aircraft between 2008-2016

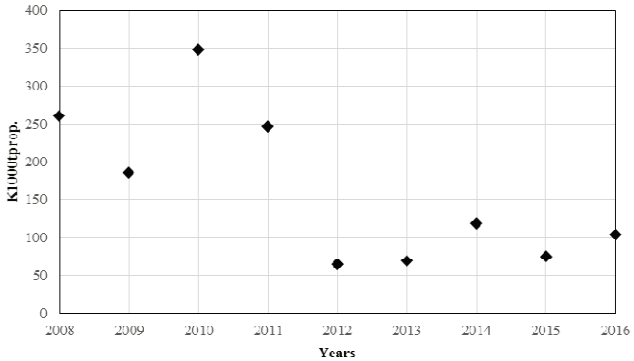

Fig. 14. Changes of the coefficient $K_{1000tprop}$

Above pictures are showing sudden decrease in number of events as well as coefficient $K_{1000tprop}$ from 2012 without turboprop aircraft fleet size changes. Reason for such level of safety increase is one of the operators aircraft fleet a

change to another turboprop aircraft type powered by different engine model.

Figure 15 shows reported system defects frequency in percent assigned to the certain ATA chapter for the turboprop engines in the years 2008-2016. Figure 16 gives (in percent) information during which aircraft maneuver and how often reported event caused by turboprop engine took place within 2008-2016.

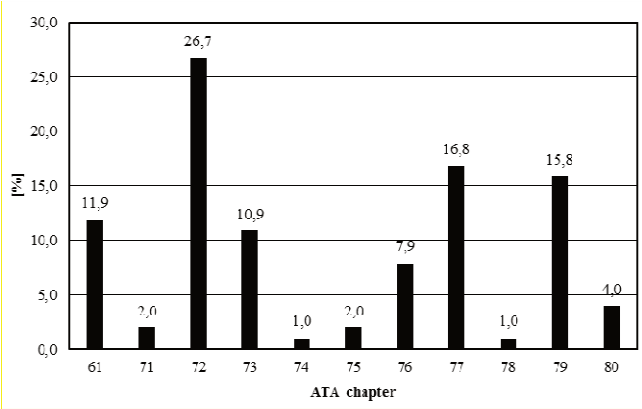

Fig. 15. Share of each powerplant system events coded in the ATA 100 chapter between 2008 and 2016

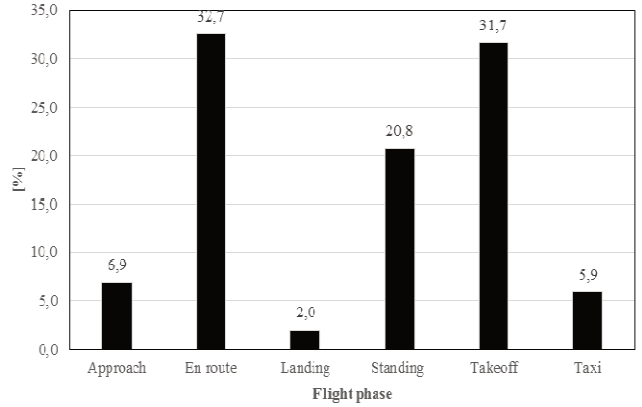

Fig. 16. Flight phases share when powerplant caused event took place

Figure 15 shows in percent "share" of the certain ATA chapter in the total volume of the turboprop engines reported events. It was assumed that the most frequently occurred event – ATA chapter 72 has occurrence probability level equel 5. Next, 77 and 79 level 4, 61, 73, 76 level 3, 80 level 2 and the remaining 71, 74, 75, 78, level 1. According to the methodology described in the Introduction (Tab. 1, Tab. 2 and Tab. 3) to each from the above ATA chapters safety risk severity was assigned, based on events consequences described in the ECCAIRS reports.

Then safety risk assessment matrix was developed for turboprop engines operated in Poland. Results of the analysis are presented in the Tab. 10.

Table 10. Safety risk assessment matrix for turboprop engine systems

ATA chapter		Index
No.	Contents	
61	Propellers/propulsors	3D
71	Powerplant general	1E
72	Engine	5D
73	Engine-fuel and control	3D
74	Ignition	1E
75	Bleed air	1E
76	Engine controls	3D
77	Engine indicating	4D
78	Exhaust	1E
79	Oil	4C
80	Starting	2E

Similarly like for piston engines, turboprops systems marked in yellow are acceptable based on risk (moderate risk) mitigation. However, a schedule for performance of safety assessment has to be prepared in order to find ways to bring down safety risk to low. Especially when so many engine systems fall in moderate risk level. The Tab. 11 shows in numbers result of the turboprops system malfunctions, symptoms observed and precursors of the powerplant defects, where it was confirmed.

Turboprops failures, which caused aviation events were mainly due to medium level of engine parts reliability and durability. There were only seven confirmed maintenance faults.

5. Turboshaft engines

There are 135 helicopters powered by turboshaft engines registered in Poland. Fourteen of them are in MTOM > 5700 kg class. Most of them is powered by engines models like: Allison 250C20, different kinds of P&W 206, Turbomeca Arrius 2F and Arriel 2B1. Also manufactured in Poland PZL-10W and GTD-350 are being in exploitation.

Mainly twin engine helicopters are utilized. Tab. 12 presents number of installed turboprop engine models on Polish registered helicopters.

With the constant number of helicopters, the number of events reported to the ECCAIRS database have increased since 2008 (Fig. 18), as a consequence also coefficient $K_{1000tshaft}$, proportionally has increased (Fig. 19).

Table 11. Confirmed roots of the turboprop engines failures which caused aviation event

No	Mulfunction result	No	Symptom	No	Confirmed precursor
25	Aborted flight	12	In flight shut down	6	Auto feather unit/governor
19	Aborted takeoff	12	Unstable engine work	4	Starter generator
4	Ground roll stopped	5	Low oil pressure	5	Torque indication
6	Emergency landing	1	High oil pressure	4	EGT indication
		2	Engine vibration	7	Wrong seals/tubes installation
				6	PCU/HMU/EEC failure
				3	Compressor blades damage
				1	Turbine blade damage

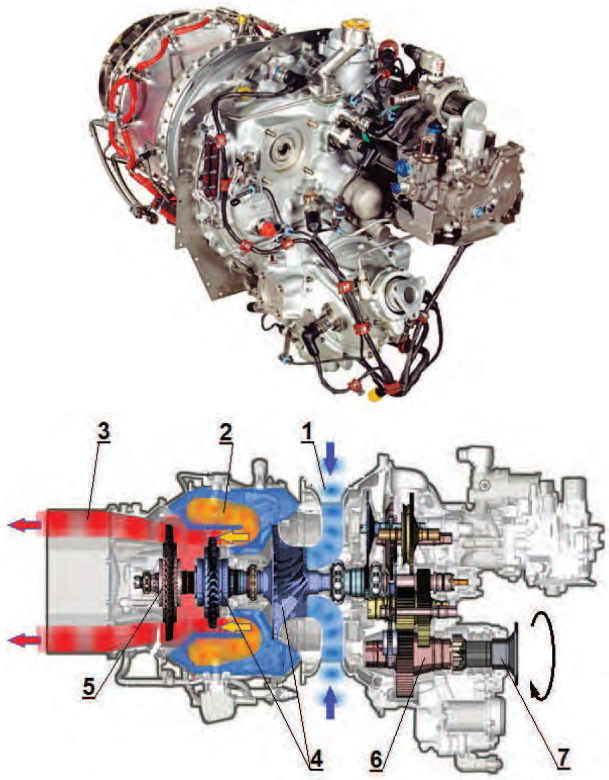

Fig. 17. View and cross-section of the PW 206 turboshaft engine: 1 – air inlet, 2 – combustor chamber, 2 – compressor, 3 – exhaust, 4 – radial compressor and turbine, 6 – reduction gearbox, 7 – shaft [17]

Table 12. Model and number of the turboshaft powerplants

Engine model	Helicopter type	Number of helicopters
PW 206 B2	EC-135	25
GTD-350	Mi-2	24
Turbomeca Arriel 2 B1	EC-130	11
Turbomeca Arrius 2F	EC-120	11
PZL-10W	W-3	7
GE T-700	S -70i	6
Allison 250 C20B	Bell-206, Mi-2 Kania, H-369	5
Allison 250 C20R2	SW-4	5
Turbomeca Arriel 2 D	AS-350; EC-130	4
PW 206 B3	EC-135	4
PW 207 D	Bell-427; Bell-429	4
R-R 300	Robinson 66	4
Allison 250 C47B	Bell-427	4

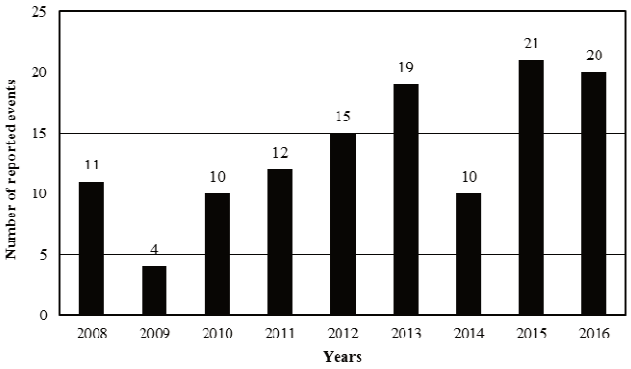

Fig. 18. Number of events caused by turboshaft engines installed on Polish registered aircraft between 2008-2016

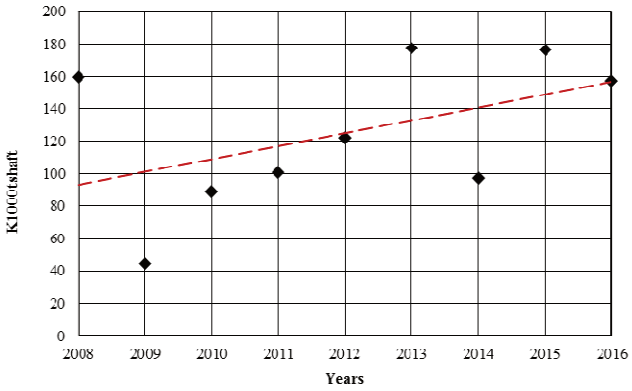

Fig. 19. Changes of the coefficient $K_{1000tshaft}$ and the trend line

A more accurate analyzes of the events shows that most of them concerns engine oil system (ATA 79 chapter) and ATA 72 chapter. This order is preserved both in terms of number of events and percentage share (see Fig. 20 and 21).

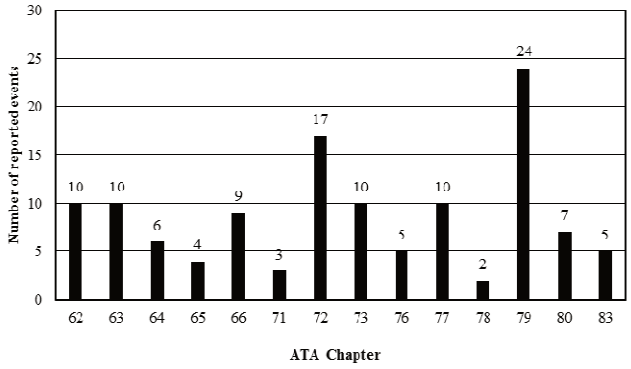

Fig. 20. Number of the turboshaft engine system events coded in ATA 100 chapter between 2008 and 2016

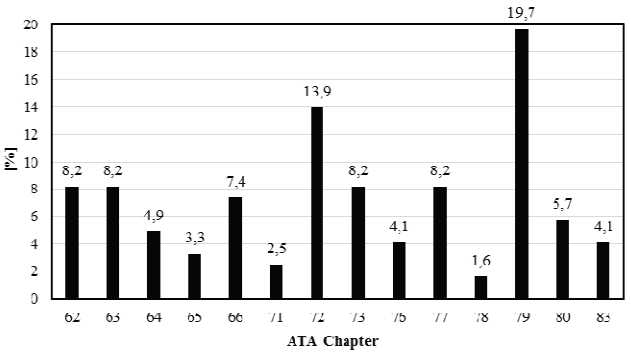

Fig. 21. Share of turboshaft engine system events coded in ATA 100 chapter between 2008 and 2016

The positive thing is that as many as 2/3 of all turboshaft malfunctions were detected during routine maintenance checks and less than 1/5 during flight, which shows Fig. 22.

Using a method described in Chapter 2 (Tab. 1 and Tab. 2), a safety hazard assessment chart for turboshaft engines was developed (Tab. 13). It includes engine systems (coded according to ATA100) failures were mentioned in the incident reports. The most frequent failures are related to the oil system (ATA chapter 79), when malfunctions of the ex-

haust system (ATA chapter 78) are rare. Oil system faults had a significant impact on flight safety. It needs to be mentioned that in the years 2008-2016 six of the oil system malfunctions ended in aborted mission, two emergency landings and one aborted takeoff. For helicopters that carry out rescue missions (HEMS), aborted flight may mean serious consequences for victims who may not be able to get medical help right away.

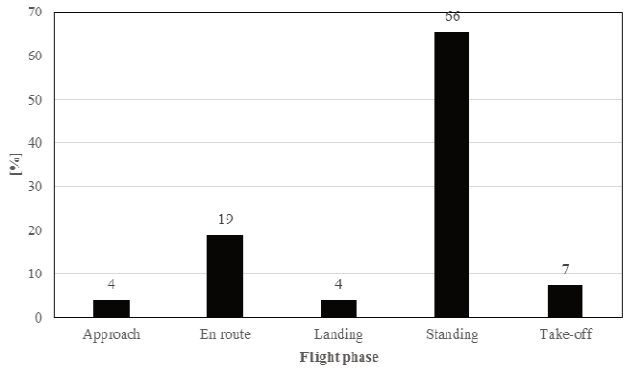

Fig. 22. Flight phases share when turboshaft engine malfunction took place

Even worse are the events related to the engine itself (ATA 72 chapter). In two cases, the sudden loss of power caused a catastrophe and complete destruction of the helicopters. Compressor surge has also been reported during startup at high ambient temperature. Also maximum torque exceedance in the drive transmission units, and a dozen or so cases of compressor blades damage by FOD hashappened. There have also been 3 cases of the rotor blades damage due to engine open covers or unplugged exhaust pipes.

Table 13. Safety risk assessment matrix for turboshaft engine systems

ATA chapter		Index
No	Contents	
62	Main rotors	3D
63	Main rotors (drive)	3D
64	Tail rotor	2D
65	Tail rotor (drive)	2D
66	Rotor blade and tail pylon folding	3C
71	Power plant general	1D
72	Engine	4C
73	Engine-fuel and control	3C
76	Engine controls	2D
77	Engine indicating	3C
78	Exhaust	1D
79	Oil	5D
80	Starting	3D
83	Accessory gear boxes (engine driven)	2D

Summary of the causes, symptoms and effects of major events involving turboshaft engines are contained in the Table 14. One of the most common causes are electrical wire connection breaks in the connectors. Electrical installations for helicopter engines operating at high vibration levels are particularly susceptible to the disconnection of contacts due to, for example, contamination by marine pollutants. At the same time, modern engine control systems cannot operate properly without rpm signal (FADEC turns off), as almost all control functions operate on this signal.

Ordinary occurrence for helicopter propulsion systems is the "oil chips" signal. In many cases it turns out that the chip detectors are so sensitive that they respond to the "dust" generated during the normal wear of the gears (even a case was reported of the piece of synthetic thread from the fabric detection). The causes of damage to the powerplants are also faults of the maintenance staff: improper assembly of components (gaskets, bolts), not closed engine covers (rush during dispatch).

6. Turbojet engines

Currently there are 94 Polish registered aircraft powered by jet engines, 80 of them fall into MTOM > 5700 kg class [16]. Details are shown in the Tab. 15. Figure 23 presents representative of the most popular worldwide turbofan engine family CFM56.

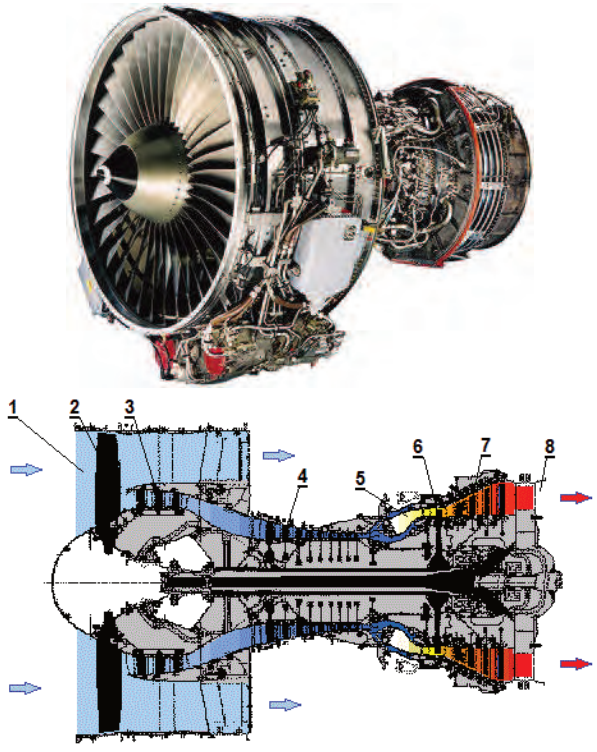

Fig. 23. Basic features of modern turbofan engine [18]: 1 – engine inlet, 2 – fan, external duct, 3 – low pressure compressor internal duct, 4 – high pressure compressor air, 5 – combustion chamber, 6 – high pressure turbine, 7 – low pressure turbine, 8 – exhaust

Table 14. Confirmed roots of the turboshaft engines failures which caused aviation event

No	Mulfunction result	No	Symptom	No	Confirmed precursor
13	Aborted flight	7	Engine chips	20	Main gearbox tapping
10	Emergency landing	6	Unstable engine work	21	Electrical connection missing
3	Aborted take off	5	In flight shut down	12	Foreign object damage
		3	Oil pressure or temperature	7	Incorrect bolt/gaskets installation
		3	FADEC fail		

The aircraft jet propulsion usually consists of two engines placed under the aircraft wings or at the rear of the fuselage. Currently on Polish registered aircraft mostly turbofan engines are installed. They have superior fuel efficiency over single shaft engines, which are only used in military applications on aircraft of the 50's.

Table 15. Type and number of the aircraft powered by jet turbine powerplants

Engine model	Aircraft type	Number of aircraft
GE CF-34	Embraer ERJ 170 and 190	26
CFM-56 serie 3, 5 and 7	Boeing 737 and Airbus 321	24
PW serie 300, 500 and 600	Cessna 510 Embraer 500 Falcon 2000 Learjet 60	8
IAE V2527	Airbus 320	6
Trent 1000	Boeing 787	6
Williams FJ44	Cessna 525 Beech 390 Raytheon 390	6
Allison AE3007	Embraer EMB 135 and 145	5
Honeywell AS907	Bombardier 100	4
Honeywell TFE731	Gulfstream 150 Learjet 45 Hawker 750	3

Number of reported events as well as factor $K_{1000jet}$ since 2011 have stabilized (Fig. 24 and 25).

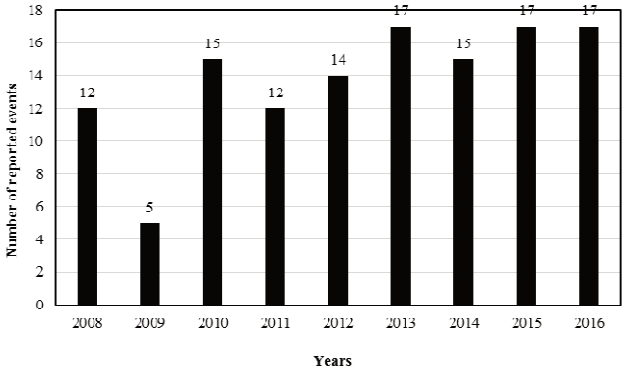

Fig. 24. Number of events caused by turbojet engines installed on Polish registered aircraft between 2008-2016

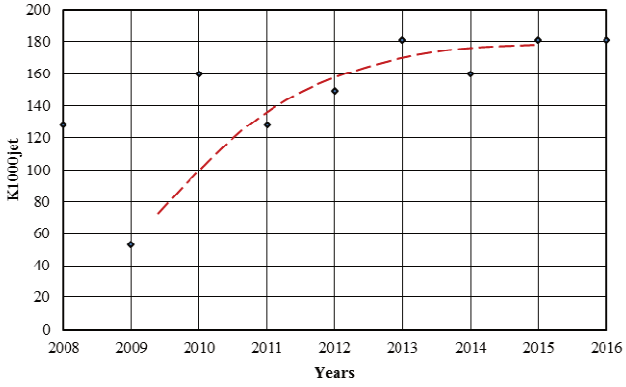

Fig. 25. Changes of the coefficient $K_{1000jet}$ and the trend line

Figure 26 presents number of reported events in each ATA 100 chapter dedicated to powerplant systems. Fig. 27 shows reported system defects frequency in percent assigned to the certain ATA chapter for the turbojet engines in the years 2008-2016. Fig. 28 gives (in percent) information during which aircraft maneuver and how often reported event caused by turbojet engine took place between 2008-2016.

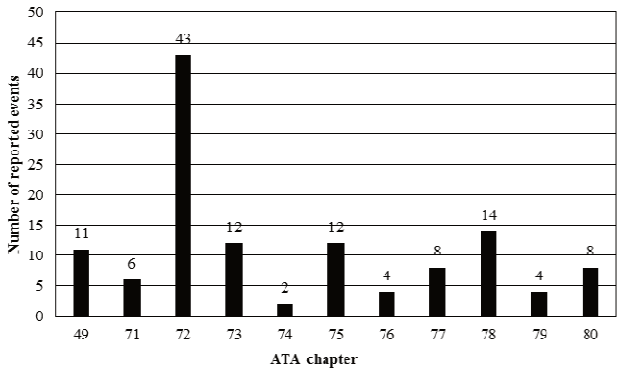

Fig. 26. Number of the turbojet engine system events coded by ATA 100 chapter between 2008 and 2016

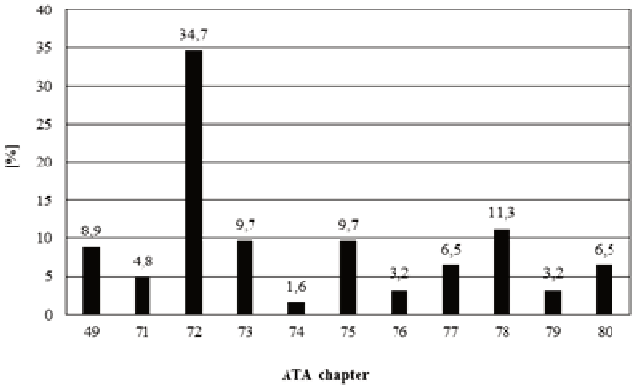

Fig. 27. Share of turbojet engine system events coded by ATA 100 chapter between 2008 and 2016

Figure 27 shows "share" of the certain ATA chapter in percent in the total volume of the turbojet engines reported events. It was assumed that the most frequently occurred event concerns engine design parts coded in ATA chapter 72, next are events in the ATA chapters 78, 75 and 73. The most serious consequences are caused by events related to the engine itself (chapter ATA 72). In 43 cases, 10 ended with aborted flight, 4 aborted takeoffs and 1 emergency landing. The reason was usually the sudden increase in engine vibration, compressor surge, also exhaust temperature limit exceedances, and thrust differences between engines causing the aircraft drift during takeoff. Borescope inspections performed during routine maintenance detected damage to the fan blades and compressor blades caused by foreign objects (FOD).

Failures of the exhaust (ATA chapter 78) caused aborted takeoff (5 out of 14 events). One aborted flight and one emergency landing took place. During routine maintenance checks usually thrust reverser sensors mulfunction were reported.

Problems with the fuel flow are very important for flight safety as this is the main parameter of the engine control. In the fuel flow control system (ATA chapter 73), clogged filters (5 out of 12 cases) or fuel pump failures (3 cases) were an events reason.

Malfunctions of the engine bleed system (75 ATA chapter) are most likely due to incorrect operation of the control valves. The inability to open such a valve results in, for example, the failure of the de-icing installation or the cabin pressurization system. Leakage of this valve causes that hot air flows into the engine nacelle and, for example, activates a fire alarm. A relatively common cause of malfunction of several airframe systems is the jamming of the valve that opens the air bleed from the compressor. This valve works in harsh conditions: the air temperature can exceed 400 °C and the pressure difference reaches dozens of bars.

It has to be taken into consideration for those involved in the SMS that more than 60% of the reported events have occured during different aircraft flight phases (Fig. 28). Some organizational projects has to be undertaken in order to increase failures detectability level during maintenance.

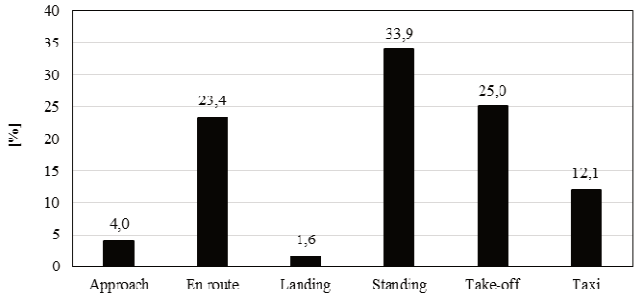

Fig. 28. Flight phase share when turbojet engine malfunction took place

Using a method described in Chapter 2 (Tab. 1 and Tab. 2), a safety hazard assessment chart for turbojet engines, similarly like for other engine types, was developed (Tab. 16). The most frequent failures are related to the engine itself (ATA chapter 72), when malfunctions of the ignition system (ATA chapter 74) are rare.

Similarly like for previously analysed types of the engines, turbojet engine systems marked in yellow are acceptable based on risk (moderate risk) mitigation. The Tab. 17 shows in numbers result of the turbojets system malfunctions, symptoms observed and precursors of the powerplant defects, where it was confirmed.

Unfortunately there are also cases of service negligence. Quite a bizarre event was lack of one of the fuel filters on engines across one aircraft fleet. Other cases of this kind include improper mounting of the VSV mechanism resulting in damage to it, no connection between the actuator and the vane ring etc.

Table 16. Safety risk assessment matrix for jet engine systems

ATA chapter		Index
No	Contents	
49	Airborne auxiliary power	4D
71	Power plant general	3E
72	Engine	5D
73	Engine-fuel and control	4D
74	Ignition	1E
75	Bleed air	4C
76	Engine controls	2B
77	Engine indicating	3B
78	Exhaust	4D
79	Oil	2B
80	Starting	3D

7. Conclusions

The factors $K_{1000TYPE}$ values, excluding piston engines are similar for all considered in the article powerplant types. They are in the range between 100 and 150.

For piston engines, this value increased in 2016 and its value now is 60. This is due to the relatively small number of reported events assigned to the number of airplanes. The reason for such situation is probably the lack of willingness to report all aviation occurrences by general aviation operators. Also, the number of notifications about engine defects, potentially threatening flight safety, found during maintenance inspections is disquietingly low for general aviation. This may indicate low quality level of the maintenance. Reasons for this situation require serious analyzes. Especially due to the fact that in general aviation mostly single-engine aircraft are operated.

The quality of the method described in the article can be improved by referring the number of events to the engine working hours. At present there is no flight hour data aggregated in one place. They are recorded in the aircraft technical logs. Also knowledge of the engine production dates would help in carrying out more accurate analyzes.

Table 17. Confirmed roots of the jet engines failures which caused aviation event

No	Mulfunction result	No	Symptom	No	Confirmed precursor
24	Aborted flight	9	Reverser disagree	15	Sensor damage
18	Aborted taxi	7	EGT incorrect	8	Jamming out the air valve
15	Aborted take off	5	Vibration too high	4	Foreign object damage
5	Emergency landing	5	FADEC fail		
		7	Fuel filter bypass or fuel pressure too low		

Nomenclature

ATA	Air Transport Association
ECCAIRS	European Coordination Center for Accident and Incident Reporting Systems
FADEC	full authority digital engine control
SCF-PP	system component failure – powerplant
SCAAI	State Commission on Aircraft Accidents Investigation
SMS	safety management system
VSV	variable stator vanes
ULC	Polish Civil Aviation Authority

Acknowledgments

The work is financed from the Institute of Aviation statutory fund (Project no 21944).

Bibliography

[1] Aviation Occurrence Categories, Definitions and Usage Notes., International Civil Aviation Organization, Common Taxonomy Team, October 2013 (4.6).
[2] Annual Safety Review 2014, European Aviation Safety Agency, Safety Intelligence & Performance Department, Cologne, Germany 2015.
[3] Aviation technician advanced training program Continental engine theory. 2005, Teledyne Continental Motors, Inc.
[4] ATA Specification 100 – Specification for Manufacturers' Technical Data, Publications Department Air Transport Association (ATA) of America, Inc. Washington, DC 20004-1707 USA.
[5] BALICKI, W., GŁOWACKI, P. Aircraft engines – analysis of reported systems failures in Polish Aviation during years 2008-2015. *Journal of KONES Powertrain and Transport*. 2016, **23**(1), 31-37.
[6] BALICKI, W., GŁOWACKI, P., KAWALEC, M. Assessment of the airframe systems affecting safety risks caused by large aircraft. *Journal of KONES Powertrain and Transport*. 2016, **23**(1), 39-46.
[7] BALICKI, W., GŁOWACKI, P., LOROCH, L. Safety performance indicators assessment for small aircraft airframe systems. *Journal of KONES Powertrain and Transport*. 2016, **23**(2), 31-38.
[8] BOLIŃSKI, B., STELMASZCZYK, Z. Eksploatacja silników turbinowych. WKŁ, Warszawa 1981.
[9] CHEDA, W., MALSKI, M. Techniczny poradnik lotniczy. Silniki. WKŁ, Warszawa 1984.
[10] KEBA, I.W. Diagnostika aviacionnych gazoturbinnych dvigatieliej. Transport, Moskwa 1980.
[11] LEWITOWICZ, J. Podstawy eksploatacji statków powietrznych. T. 3. ITWL, Warszawa 2006.
[12] LOROCH, L. Bezpieczeństwo lotnictwa krajowego w działalności Instytutu Lotnictwa. „Bezpieczeństwo i niezawodność w lotnictwie. Rozwój lotnictwa w regionach". NOT, Radom 2015.
[13] Safety Management Manual (SMM), Doc. 9859, AN/474, Third edition ICAO 2012.
[14] PETTIT, D., TURNBULL, A. General Aviation Aircraft reliability Study. NASA Langley Research Center, Hampton, Virginia 23681-2199, February 2001.
[15] WIŚNIOWSKI, W. XX lat programu samolotów lekkich i bezpieczeństwa (PSLiB). *Transactions of the Institute of Aviation*. 2014, **3**(236).
[16] www.ULC.gov/pl/regulacja-rynku/3724-statystyki-wg-portow-lotniczych.
[17] en.wikipedia.org/wiki/Pratt_%26_Whitney_Canada_PW200.
[18] www.cfmaeroengines.com/engines/cfm56/

Paweł Głowacki, DEng. – Center of Space Technologies of the Institute of Aviation.

e-mail: *Pawel.Glowacki@ilot.edu.pl*

Włodzimierz Balicki, DEng. – Center of Space Technologies of the Institute of Aviation.

e-mail: *Wlodzimierz.Balicki@ilot.edu.pl*

Article citation info:
BRZEŻAŃSKI, M., MARECZEK, M., SUTKOWSKI, M. et al. A 4-stroke spark-ignition engine fuelled with low quality gas. *Combustion Engines*. 2017, **168**(1), 122-124. DOI: 10.19206/CE-2017-118

Marek BRZEŻAŃSKI
Michał MARECZEK
Marek SUTKOWSKI
Wojciech SMUGA

CE-2017-118

A 4-stroke spark-ignition engine fuelled with low quality gas

Huge amount of by-products is still considered as waste and is simply disposed, for example by-product gas is usually flared. Political and social pressure to reduce air pollution and national needs for energy security make these waste fuels interesting for near-future power generation. Unfortunately most of these waste fuels, even when liquefied or gasified, have very low quality and can hardly be used in high-efficiency power systems. Among main challenges are low calorific value and composition fluctuation. Additionally very often there is a high content of sulphur, siloxanes, tars, etc., which have to be removed from the fuel.

Modern 4-stroke gas engines designed for power generation applications provide very high efficiency, high reliability and availability. Unfortunately, these gas engines require high quality fuel with stable composition. Horus-Energia together with Cracow University of Technology developed a novel gas supply system HE-MUZG that can adapt to current gas quality and change engine settings accordingly.

This article will present results from the HE-MUZG system tests on modern 4-stroke spark-ignition gas engine. Tests focus on low quality gas, such as gas with low calorific value, gas with very low methane number and gas with very big variations of calorific value. Test results compared with performance of that engine in the original configuration show huge improvements. Moreover the HE- MUZG system is easy to implement in commercial gensets.

Key words: *engine, genset, low quality gas*

1. Introduction

Modern 4-stroke gas engines are designed to operate with high reliability and high efficiency. It is possible due to fact that they utilise advanced combustion systems supported by sophisticated control system. For example, a 20-cylinder spark-ignition gas engine can be equipped with more than 200 various sensors which gather continuously information about engine operation, combustion characteristics and help to optimise control settings such like air-fuel-ratio, ignition advance etc. On one hand such complex control systems provide ultimate engine performance but on the other hand high quality of gas is required. Usually gas quality requirements include calorific value, methane number, methane or inert gas content etc. It is possible to tune engine for specific fuel but tuning may influence engine performance: available power, efficiency, emissions etc. There is a strong limitation for using fuels with very low methane number or very low calorific value, because these parameters determine available power of the engine. Operation at very reduced power makes solution not feasible – engine becomes very expensive in respect to available power and additionally engine efficiency decreases significantly. Even more problematic is situation when gas parameters change significantly or if the changes are rapid because control systems of typical gas engine can hardly adopt.

Novel gas supply system HE-MUZG was developed by Horus-Energia together with Cracow University of Technology. The system can be mounted on typical stationary gas engine and can automatically adjust own settings if fuel properties change. The results of broad tests are presented in this paper.

2. Test facility

The tests were held at Horus-Energia test facility, which is arranged for genset testing. The test facility is equipped with gas mixing station that creates possibility to mix several components and create almost any gas composition required for tests. Additionally, the gas mixing station is equipped with specially built control system that can generate very rapid change of fuel composition between set points defined by user. The test engine MAN E2876 LE302 was combined with Marelli MJB 250 LB4 generator as it is in the original genset configuration. The basic data of the engine and the genset in original configuration are presented in the Table 1 and the Figure 1 shows general view of the test facility.

Table 1. Basic data of the engine and the genset in original configuration (provided by manufacturer) [1, 5]

Engine type	4-stroke, turbocharged, spark-ignition, 2-stage mixture cooler
Cylinder configuration	6 cylinders in-line
Cylinder bore	128 mm
Piston stroke	166 mm
Compression ratio	11:1
Mean effective pressure	13.1 bar
Fuel supply system	Gas mixer in front of turbo-charger's compressor
Nominal air-fuel equivalence ratio (λ)	1,6
Engine speed (50 Hz genset application)	1500 rpm
Nominal power (engine)	210 kW
Nominal power (genset)	200 kW
Genset efficiency (at 50% load)	32.0%
Genset efficiency (at 75% load)	35.2%
Genset efficiency (at 100% load)	37.1%

The test program covered following stages:

- engine optimisation for operation on methane,
- engine operation on gas with very low calorific value,
- engine operation on gas with very low methane number,
- engine operation on gas with significant and fast change of calorific value.

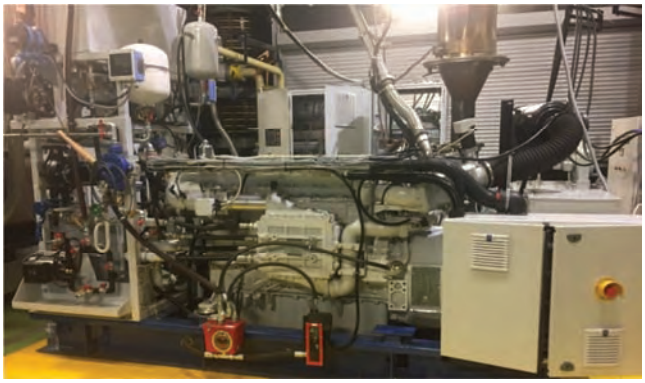

Fig. 1. General view of the MAN E2876 LE302 engine at the Horus-Energia test facility

2. Test results

The first stage of tests showed that HE-MUZG fuel supply system enables operation with higher genset efficiency than with original fuel system. The results are presented in Table 2 and in the Figure 2.

Table 2. The genset efficiency measured during tests with HE-MUZG fuel supply system

Engine load	Genset efficiency
0%	0.00%
25%	27.00%
50%	35.30%
75%	37.80%
90%	38.41%
100%	38.63%

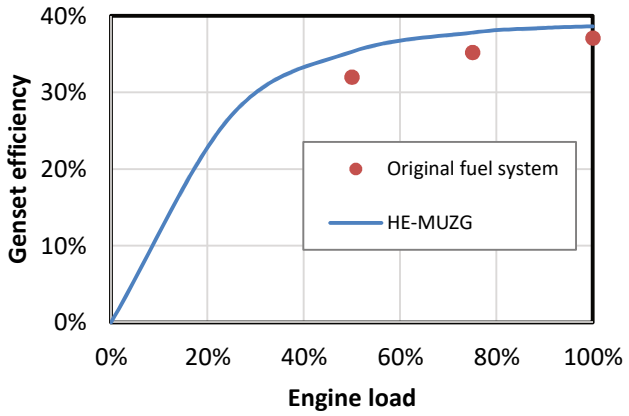

Fig. 2. The genset efficiency for original fuel system and measured during tests with HE-MUZG fuel supply system [1]

In the second stage methane was mixed with carbon dioxide to reduce gas fuel calorific value. The main target was to check how low can be gas calorific value that still enables stable genset operation. According to the engine manufacturer requirements, the gas with lower heating value (LHV) at least 32 MJ/m^3 is required for engines tuned for natural gas and the gas with LHV higher than 18 MJ/m^3 is required for engines tuned for bio-gas [4]. During test it was important not only to achieve stable engine operation but also to keep NO_x emission within allowed limit, i.e. 250 ppm at 5% oxygen content in the exhaust gas [2]. The results are presented in Table 3 and in the Figure 3.

Table 3. NO_x emissions for genset operation on fuel with wide range of LHV

CH_4 content in fuel	CO_2 content in fuel	Fuel LHV [MJ/m^3]	NO_x emission [ppm] (adjusted to 5% O_2)
100%	0%	36.0	146
75%	25%	27.0	165
65%	35%	23.4	171
50%	50%	18.0	185
43%	57%	15.5	207

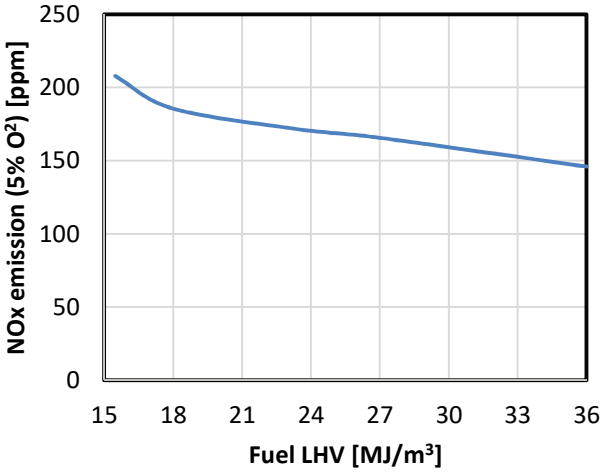

Fig. 3. NO_x emission at 5% O_2 for wide range of fuel LHV

Results show that the HE-MUZG system enables stable engine operation in wide range of fuel calorific value. It is important to highlight that the test genset was equipped with the engine originally tuned for operation on natural gas and the HE-MUZG system enabled operation with range of fuel calorific value wider even if compared with tuning of that engine for operation on biogas. Moreover NO_x emissions do not cross allowed level for whole fuel calorific value range. However at very low LHV NO_x emissions are significantly higher. The reason is that for fuel with very low LHV engine was tuned to operate at richer mixture than for fuel with higher LHV.

The next stage of tests was focused on low methane number. This is very important aspect, because lot of waste gas fuels contain heavier hydrocarbons or significant amount of hydrogen. These components reduce fuel methane number rapidly which creates problems with engine stable operation, engines cannot reach nominal power or operation can be simply impossible. According to manufacturer's requirements, engine can reach nominal power for fuels with methane number at least 80 and for pure propane engine can reach maximum 71% of its nominal load, which corresponds with 143 kW of the genset electrical power [4, 6]. As fuel for these tests pure propane was used. The results are presented in Table 4 and in the Figure 4.

Table 4. The performance of the genset fuelled with propane

Genset power [kW]	Engine load	Genset efficiency
0	0%	0%
45	23%	27.24%
90	45%	34.48%
135	68%	37.41%
162	81%	38.55%
180	90%	38.63%

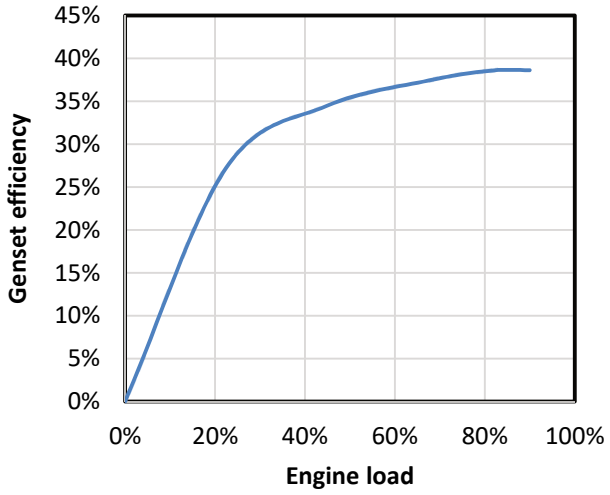

Fig. 4. The efficiency of the genset fuelled with propane

It was impossible to reach engine nominal power when engine was fuelled with propane due to the engine knocking, but the engine with the HE-MUZG system easily reached power higher than guaranteed by manufacturer for original fuel supply system. Moreover, the genset efficiency reached during operation on propane was higher than during operation on methane.

The last stage covered tests of engine operation during very fast changes of fuel composition. For this purpose mixture of methane and carbon dioxide was used. The original fuel supply system can tolerate changes of gas calorific value not faster than 0.002 MJ/m^3 per second and not more than 20% of the LHV set point. The gas composition was changed in a way that methane content was decreasing from 90% to 50% and then it was increasing from 50% to 90% with the same rate upwards and downwards. This corresponds to change of gas LHV between 32.337 MJ/m^3 and 17.965 MJ/m^3. The tests covered ramp times from 167 s down to 29 s, which covers methane content fluctuations from 0.24% per second to 1.38% per second. It can be presented also as fuel LHV variation from 0.086 MJ/m^3 per second to 0.496 MJ/m^3 per second. As the acceptance criteria for stable genset operation the generated electricity frequency variation (ßf) was selected, according to ISO 8528-5 norm. The norm defines operation as stable when ßf parameter is not greater than 2.5%. The shortest ramp time when the genset could fulfil stable operation criteria was 38s, which corresponds to CH_4 content change 1.05% per second and LHV change 0.378 MJ/m^3 per second. This results is approximately 190 times faster and covers range twice wider than allowed for standard engine setting. Moreover, for ramp time equal to 29 s, the ßf parameter was equal to 3%, which means only slight deviation from the norm and fluctuations of methane content of 1.38% per second and LHV fluctuations even 0.496 MJ/m^3 per second can be accepted in other applications for the engine.

Conclusions

The HE-MUZG fuel supply system tests showed that system improves gas engine operation characteristics and makes engine more flexible for fuel quality. Even for good quality gas the system brings benefits by improving engine performance.

The HE-MUZG extends limits for accepted fuel parameters. The system makes possible use of fuels with LHV 15.5 MJ/m^3, improves engine operation with fuels with low methane number providing better knock resistance and higher efficiency. Additionally system is very adaptive and fast responding for current gas quality, which is reflected in enabling the engine stable operation even when fuel LHV fluctuates almost 0.5 MJ/m^3 per second. The HE-MUZG fuel supply system can tolerate not only 200 times faster fluctuations but can also adopt do LHV changes in twice wider range than standard fuel supply system.

As next steps further system tests and optimisation are scheduled.

Bibliography

[1] Cogeneration unit HE-EC-200/263-MG200-GZ data sheet.
[2] Genset emission requirements www.dieselnet.com
[3] ISO 8528-5 – Generator Set Standard Operating Limits.
[4] Minimum Requirements to Gas Quality for MAN – NG/Special Engines.
[5] Natural Gas Engine MAN E 2876 LE 302 Technical Data.
[6] Performance of MAN Gas Engines tuned for propane with 500 mg/m^3 NO_x emission settings.

Prof. Marek Brzeżanski, DSc., DEng. – Faculty of Mechanical Engineering at Cracow University of Technology.

e-mail: *mbrzez@pk.edu.pl*

Michał Mareczek, DEng. – Faculty of Mechanical Engineering at Cracow University of Technology.

e-mail: *Michal.Mareczek@mech.pk.edu.pl*

Marek Sutkowski, DEng. – Engine Portfolio Team within Technology & Solution, Wärtsila Finland Oy.

e-mail: *Marek.Sutkowski@wartsila.com*

Wojciech Smuga, MEng. – Research and development department – HORUS Energia Sp. z o. o., Sulejówek.

e-mail: *w.smuga@horus-energia.pl*

Article citation info:
PARCZEWSKI, K., ROMANISZYN, K.M. The proposition of utilisation the vehicle in 1:5 scale to construction and testing of an autonomous vehicle. *Combustion Engines*. 2017, **168**(1), 125-128. DOI: 10.19206/CE-2017-119

Krzysztof PARCZEWSKI
Kazimierz M. ROMANISZYN

CE-2017-119

The proposition of utilisation the vehicle in 1:5 scale to construction and testing of an autonomous vehicle

In the near future, vehicles will be moving autonomously with little participation or completely without the driver affecting on the vehicle move. Task of driver will be limited to identify the end point of the vehicle route. Vehicles, to meet this challenge, must be equipped with the control systems and supervising the movement of the vehicle, reacting onto the movement of pedestrians and other vehicles, road signs, time of day and weather conditions. The movement of the vehicle will be controlled and driven by a system on board a vehicle, but will also be required to tracking the vehicles position and its movement parameters using of the vehicle satellite navigation systems. In addition, the motion trajectory of the vehicle will be determined and any deviation from the target track will be corrected.

The article presents a proposal for determining the trajectory of the vehicle based on the control points specified by the coordinates of the location of the vehicle and ways of correcting the trajectory of the vehicle. For this purpose was utilized the vehicle in scale.

Key words: *autonomous vehicle, determining the trajectory of the vehicle, the correction of the vehicle motion trajectory*

1. Introduction

The main task of the autonomous vehicle is to carry passengers and cargo from a specific starting place to the particular ending position. In addition, the vehicle must react to the situation on the road, pedestrians, vehicles and road signs. This vehicle also must adjust their speed to the road conditions, speed up or slow down and to keep in their road lane. These properties require the development of an autonomous vehicle control system that is able to respond to traffic conditions in every situation by adjusting the speed and direction of vehicle motion. For this reason, the control of the autonomous vehicle is a complex issues, which consists of a number of different tasks. These tasks can be analysed and implemented separately.

Fig. 1. The measurement equipment mounted on the vehicle in scale

In the Department of Internal Combustion Engines and Vehicles of University of Bielsko-Biala was built vehicle in a scale of 1: 5, which has been used to study the vehicles stability. For this purpose, was used the theory of similarity and π-theorem of Buckingham [3,5]. To describe the parameters of the vehicle and its movement were used the dimensionless variables, normalized using the basic units like: length, mass and time.

Presented vehicle in scale, in addition to the requirements such as the maintenance of conditions similarity to the full size vehicle (geometric, kinematic, dynamic and structural similarities), the behavior of the similarity of the test research, was designed to drive defined route with a defined speed. From these tasks we saw that is required to build a specific control system for our vehicle. This system will could control the vehicle motion, to ride vehicle in scale after a certain, imposed from the top track and be able to make adjustments to the realized trajectory of motion. In addition to the evaluation parameters of vehicle movement was necessary to select of the measuring equipment with low weight and small size while maintaining the required measurement accuracy.

1.1. Description of the vehicle in scale

For the build of the vehicle in scale was used an existing radio controlled vehicle in scale 1:5, Himoto Raptor, which was modified resulting from the need to meet the requirements of similarity to the full-size vehicle.

The vehicle in scale it was equipped with an internal combustion engine with a capacity of 26 ccm, centrifugal clutch, gearbox, powertrain with central gear and differentials on front and rear axle in the basic version. The driving torque is transmitted via a shaft to the gearbox and then through the shafts to front and rear differentials and through driveshaft on the wheel. Wheels consist of the rim of the plastic and rubber tires with stiffening inserts. The frame was made of aluminum sheet metal profiled, reinforced in the rear part. The basic version of vehicle has allowed riding with maximum speed of 70 kph. Suspension both front and rear are based on two wishbones with coil springs. The brake is mounted on the output shaft of the motor in the form of a single disk-compressible during braking. Servo motor controls the engine speed and brakes. The second servo motor is used to control of the steering system, it is connected to the longitudinal steering rod. The vehicle is controlled by radio (Fig. 1).

In order to maintain the conditions of similarity with respect to the full-size vehicle (the truck with a high-lying center of mass), it was done a number of modifications on

the vehicle in scale. These modifications has included: increasing the wheelbase, change the position of the center of mass, changes the mass moments of inertia, changes the suspension of both the front and the rear axle from the independent to dependent, changing tires with characteristics similar to use in the real vehicle. Description of the vehicle after these modifications and methodology of conduct found in [10, 11, 14, 16]. This vehicle was equipped with measuring apparatus Racelogic VBOX with module IMU and two antennas GPS/GLONAS.

The basis of the analysis was to use a model of the human driver that allows to achieve the desired action.

2. The models of human driver

In literature we can find models the human driver with a high complexity, allowing the inclusion of driver reaction time, delays resulting from the reaction of vehicle systems or correction of the track resulting from the nature of cooperation of tires with the road [7–9]. The following is the relationship describing the general model of the human driver [1].

$$H(s) = h(\tau_D \cdot s + 1 + \frac{1}{\tau_I \cdot s}) \cdot e^{-\tau_L \cdot s} \tag{1}$$

where: h – constant of proportionality, τ_L – driver's reaction time, τ_D – differentiation time constant, τ_I – integration time.

In this study, we focused on passing the points lying on the track of the vehicle in scale and a possible correction of the assumed trajectory. For this purpose were used simpler models of human driver: a compensation [15], and anticipatory model [1, 6, 13].

2.1. The compensation model of human driver

The compensating models of human drivers are relatively simple. The aim of their activities is to minimize the deviation of the position of the vehicle from the established track. In this model, the task of the human driver is the correction of the position of the car, which would lead to driving on the specified path. The basic equation describing the control of the vehicle can be presented in a form that allows the selection of the angle of rotation of the steering wheel [16]:

$$\alpha(t) = P_y \cdot y(t) + P_\alpha \cdot \alpha_0(t) \tag{2}$$

where: P_y and P_α – amplification factors of the human driver model, defining the sensitivity of the model to the lateral and angular deviation, α_0 – the current angle of deviation the car from the predetermined direction, y(t) – the current value of the coordinate describing the lateral deviation of the vehicle from the predetermined direction.

2.2. The anticipatory model of human driver

The anticipatory model of human driver is based on the assumption that the driver observes the road some distance ahead of the vehicle L(m) and evaluates the deviation of lateral position of the vehicle from the established route ε (Fig. 1, 2) [1, 6, 13].

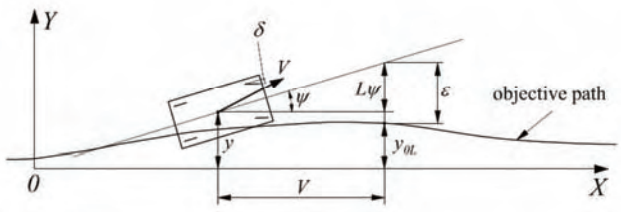

Fig. 2. The motion of the vehicle using of the anticipatory driver model

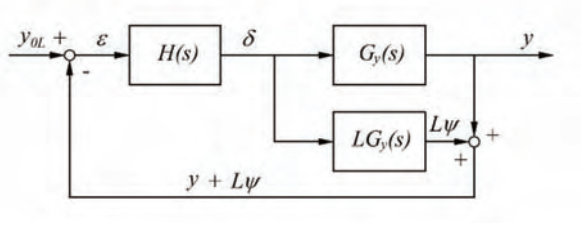

Fig. 3. The simple block diagram of a driver-vehicle system [1]

The estimated lateral displacement of the transverse component y_{0L} is the distance traveled by the vehicle at time t = L/V in certain traffic conditions. Hence the mathematical description of the human driver model:

$$\alpha(t) = P \cdot \beta(t - t_R) \tag{3}$$

$$\varepsilon = y + L\beta - y_{0L} \tag{4}$$

$$\beta(t) = \frac{1}{L}[\varepsilon - (y - y_{OL})] - \alpha_0 \tag{5}$$

Reński [11] proposes the following solution to the problem presented above:

$$\alpha(t) = \frac{P}{L} \cdot \varepsilon \cdot (t + \frac{L}{V} - t_R) - \frac{P}{L} \cdot (y - y_{OL})(t - t_R) - P \cdot \alpha_0 \cdot (t - t_R) \tag{6}$$

where: P – amplification factors of the human driver model, t_R – driver's and steering system reaction time, β – angle between the longitudinal axis of the vehicle and the position of the point of observation, y – the vehicle's position in the global coordinate system, y_{0L} – estimated position of the vehicle (at the point of observation) after adjustment driving path, ε – estimated lateral displacement of the vehicle at the point of observation L, α_0 – angle of longitudinal axis of the vehicle from the direction of the track, α – required steering angle, L – distance of the point of observation.

3. Controlling of the vehicle in scale

To drive was used the specially built system consisting of a microprocessor controller and servomotors. In the memory of controller was stored setting of servomotor to carburetor throttle and clamping the braking system and also servomotor to control of turning wheel angles. They have been saved the procedures specifying how to accelerate and stop the vehicle. In the memory of the controller has been saved also procedures to control the speed and direction of travel of the vehicle during the test. These proce-

dures are similar to ISO tests but they have adapted to the size and speed of the vehicle in scale. Were made the location system of the vehicle utilizing the vehicle positioning system GPS assisted by the accelerometers and magnetometers to the realization driving after a specified path. In the first version of the system was used microcontroller Arduino II [4]. The proposed system allow for the ride of the vehicle after a predetermined track only at relatively low speeds.

4. Tests of the vehicle in scale

The application of the model the human driver to control of the vehicle in scale resulted from the vehicle path deviation of movement from the established track. This was due to disruptions caused by unevenness of the track, by various coefficient of adhesion of the driving wheels, by external forces as well as the phenomena occurring during twist maneuvers, such as: changing of load on left and right side of the vehicle, changing the suspension geometry, or the characteristics of the tires.

In the case where the direction of motion of the vehicle is affected by interference the external, a correction needs to establish of the position of the vehicle and its direction of movement. Under the direction of K. Romaniszyn was developed controller equipped with a GPS chip, allowing the collection of information on the position and direction of the vehicle motion [3]. Efforts were made to use the compensating model of the human driver and ultimately create a system of autonomous control the direction of the vehicle movement.

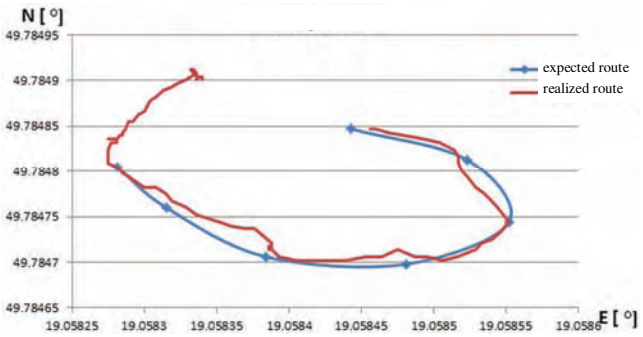

Fig. 4. Comparison of the preset and has made track of the vehicle physical model [3]

For this purpose was used the Arduino microcontroller, GPS antenna, and a number of actuators allowing for "programming" the trajectory of the vehicle by determining the selected waypoints. These selected points, have been achieved by the vehicle with the specified accuracy. The correction of the vehicle path was carried out by changing the twist angle of the steered wheels. Figure 4 shows the "programmed" and the real path of the vehicle in scale during test "ride the circular path".

The use of anticipatory model of human driver, presented in the work of M. Abe [1] requires the determination of the characteristics of tires, longitudinal and lateral speed of vehicle, center of mass, yaw ratio and twist angle of the steered wheels. During road tests of the vehicle in scale was used testing equipment of Racelogic VBOX 3i. This equipment allows for measurement of the position of the vehicle, its speed and direction of movement. Since the measured variables are required to determine the amendments of the wheel steer angle, based on the anticipatory model of human driver it is possible to make adjustments to the path of vehicle. Ongoing works allow determining the adjustment of the vehicle path. A simulation was performed using the results of measurements of the motion of the vehicle while driving along a circular path. Figure 5 shows the difference between the predetermined and realized radius of driving, during the test "ride on a circular path".

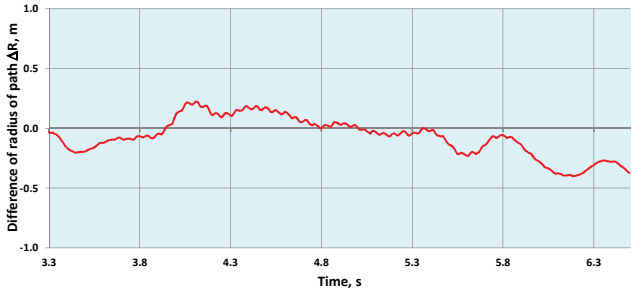

Fig. 5. The difference between predetermined and realized radius of driving, during the test "ride on a circular path"

Based on these graphs, you can attempt to make a correction of angle δ_e. this correction will be introduced with a delay resulting from the characteristics of the control system of the vehicle in scale.

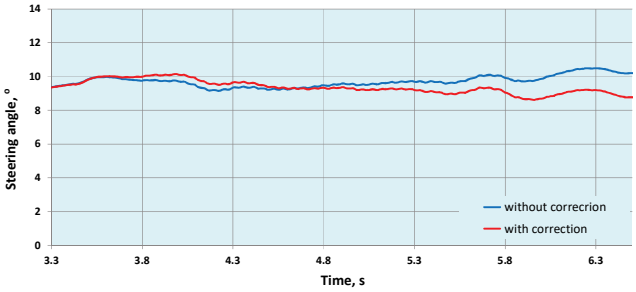

Fig. 6. Steering angle: real and corrected, during the test "ride on a circular path"

The use of a simplified driver model allows for an trajectory adjustment which simulates the behavior of the human driver. Figure 7 shows the realized path, after which vehicle in scale was driving and simulated circular path after correction of steer angle.

Due to accept the simple model of the human driver, the proposed adjustment does not take into account the delayed reaction time of the vehicle to changes in the controller settings. This influence should also be estimated and included in the amendment of control parameters vehicle.

5. Summary and conclusions

In this article was presented the preliminary considerations regarding the possibility of construction an autonomous vehicle based on a testing of the vehicle in scale. In such a vehicle may be tested solutions used subsequently in the autonomous vehicle. This article presents possible to use human driver models allowing moving along a specified route or making some adjustments of motion direction

of the vehicle. Studies were carried out using a vehicle in the scale of 1:5.

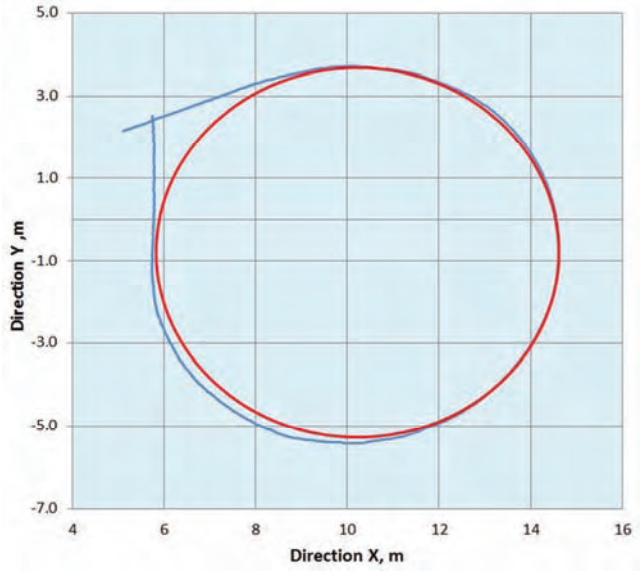

Fig. 7. The vehicle path: real (from the test) and corrected, during the test "ride on a circular path"

The control system based on the position signals from the GPS, which uses a compensation driver model turned out to be little accurate, due to the low frequency determining vehicle position and relatively slow actuators. However, the use of the more efficient measuring apparatus may allow to increase the accuracy of control of the vehicle and eventually to apply it to the autonomous vehicle.

The use of anticipatory model of human driver allows you to make adjustments to the track of the vehicle. From the simulations carried out using the results of measurements made while driving in a circular path indicates that the majority of motion parameters of the vehicle requires filtering with low-pass filter frequency to 6 Hz. The application of the proposed solution requires the use of actuators with a short response time. Delays resulting from the reaction speed of actuators require estimating and taking into account in the applicable adjustment of control parameters.

Ultimately, the planned modifications to the vehicle in scale by incorporating a system of speed control and steer angle with greater accuracy and speed of execution.

Despite this, the authors believe that the results of both of the tests are promising and believe that further research in this area is justified.

Bibliography

[1] ABE, M. Vehicle handling dynamics. Theory and application, II ed. *Elsevier*, Oxford 2015, 281-300.
[2] AUGUSTYNOWICZ, A. Modelowanie typu kierowcy samochodu. *Wydawnictwo Politechniki Opolskiej*. Opole 2009.
[3] BAKER, W.E., EESTINE, P.S., DODGE, F.T. Similarity methods in engineering dynamics. Theory and practice of scale modeling, *Spartan Books*. New Jersey 1978.
[4] BOGUSZ, M., BIELENIN, D. Projekt i badanie autonomicznego system sterowania do modelu pojazdu. *V Konferencja Inżynier XXI w.* Bielsko-Biała. 2016.
[5] BUCKINGHAM, E. On physically similar systems: Illustration of the use of dimensional equations. *Physics Review*. 1914, **4**, 345-376.
[6] BUŁKA, D., WALCZAK, S., WOLAK, S. Antycypacyjny model kierowcy zastosowany w programie do symulacji ruchu i zderzeń pojazdów V-Sim. *V Konferencja „Problemy bezpieczeństwa w pojazdach samochodowych"*. Kielce 2006.
[7] KROMULSKI, J., SZCZEPANIAK, J., PAWŁOWSKI, T. Model układu sterowania ze sprzężeniem zwrotnym (człowiek–agregat rolniczy) w aspekcie bezpieczeństwa ruchu. *Journal of Research and Applications in Agricultural Engineering*. 2011, **56**(2), 101-104.
[8] LOZIA, Z. Analiza ruchu samochodu dwuosiowego na tle modelowania jego dynamiki. Monografia. *Prace Naukowe Politechniki Warszawskiej*. Transport, 1998, **41**.
[9] MACADAM, C.C. Understanding and modeling the human driver. *Vehicle System Dynamics*. 2003, **40**(1-3), 101-134.
[10] PARCZEWSKI, K., ROMANISZYN, K.M. Układy kierowania mobilnych modeli pojazdów wykorzystywanych do badań dynamiki ruchu pojazdów. *Logistyka.* 2015, **4**, 789-800.
[11] PARCZEWSKI, K. Analiza możliwości wykorzystania modelu fizycznego pojazdu do oceny stateczności ruchu pojazdów wielkogabarytowych. *Wydawnictwo Akademii Techniczno-Humanistycznej w Bielsku-Białej*. Rozprawa naukowa 52, Bielsko-Biała 2014.
[12] PROCHOWSKI, L. Mechanika ruchu. *WKŁ*, Warszawa, 2005, 289-291.
[13] REŃSKI, A. Identification of driver model parameters. *International Journal of Occupational Safety and Ergonomics*. 2001, **7**(1), 79-92.
[14] ROMANISZYN, K.M., WNĘK, H. Symulacja dynamiki ruchu na mobilnym modelu samochodu. *Pomiary Automatyka Kontrola.* 2010, **3**, 240-243.
[15] STAŃCZYK, T.L., JURECKI, R. Modele kierowcy, możliwość ich wykorzystania do analizy sytuacji przedwypadkowych. *IV Konferencja „Problemy bezpieczeństwa w pojazdach samochodowych"*. Kielce 2004.
[16] WITAYA, W., PARINYA, W., KRISSADA, C. Scaled vehicle for interactive dynamic simulation. *Proceedings of the 2008 IEEE International Conference on Robotics and Biomimetic.* Bangkok, 21-26.02.2009.

Krzysztof Parczewski, DSc., DEng. – Faculty of Mechanical Engineering and Computer Science at University of Bielsko-Biała.

e-mail: *kparczewski@hth.bielsko.pl*

Prof. Kazimierz Romaniszyn, DSc, DEng. – Faculty of Mechanical Engineering and Computer Science at University of Bielsko-Biała.

e-mail: *kromaniszyn@ath.bielsko.pl*

Article citation info:
ANDRYCH-ZALEWSKA, M. Improving the environmental performance of the internal combustion engine by the use in-cylinder catalyst. *Combustion Engines*. 2017, **168**(1), 129-132. DOI: 10.19206/CE-2017-120

Monika ANDRYCH-ZALEWSKA

CE-2017-120

Improving the environmental performance of the internal combustion engine by the use of in-cylinder catalyst

The problems of using the inner surfaces of a combustion chamber as catalytic converters in order to reduce the harmful exhaust emissions were discussed in this paper. The proper choice of the catalyst is one of the most important issues. The interaction between the burned mixture and the catalyst is not limited by the kinetics of the chemical reactions but depends primarily on the flow rate of the reactants to the catalyst surface during combustion. The lifespan of a catalytic layer is determined by the application technique, where plasma spraying is the most popular and most accessible method. However, when it comes to the catalytic coating durability, it is not an efficient option, as ion implantation is indicated shows greater potential in this respect. In this research the coating of aluminum-titanium and chromium-nickel have been applied to the engine head and the piston crown. Then the modified catalytic parts were used in a CI combustion engine and the obtained emission results were compared with the reference results. Another set of tests was performed for an SI engine, powered with gasoline and methane, where the piston crown was covered with a thermal layer of zirconium oxide and a catalytic layer of platinum. The beneficial effects of these in-cylinder catalysts on exhaust emissions and the possible problems in the wide spread use of such solutions have been presented.

Key words: *IC engine, catalyst, in-cylinder catalysis*

1. Introduction

Reciprocating internal combustion engines are now a common source of power in the drives of motor vehicles, machinery and equipment. They were initially used as stationary engines, but then, thanks to their many advantages, they started also being used in vehicles. The pursuit to get more and more engine power output, improved work indicators, to reduce the engine weight and its harmful effects on the environment are just some of the targets for engines today. All of these aspects also substantially affect the engine development process, including its individual components and subsystems. These requirements are also the reason driving change in the proper operating method of internal combustion engines, with the aim to achieve these benefits while maintaining a low environmental impact.

For an internal combustion engine, the nature of its operation determines the formation of harmful exhaust gases, where the proper execution of the combustion process tends to be the primary source of these pollutants. Increasing emphasis on reducing the negative impact of combustion engine vehicles on the environment, both from the legislative institutions of individual countries as well as their communities, drives the search for ever more sophisticated technical solutions for the internal combustion engine, which will ensure environmental impact reduction and allow meeting current emission standards. Among such efforts, the ones that reduce the emissions in exhaust gases after they leave the internal combustion engine are essential, i.e. the advanced exhaust aftertreatment systems.

Due to the nature of operation of such systems (obtaining the high required operational temperature) places them ever closer to the engine. However, these activities are aimed at reducing the pollutants that have already formed (been produced) in the combustion engine. On the other hand, careful consideration should be given to measures which are technically feasible and which would influence the reduction of pollutant production at their source – that is, in the combustion chamber of the engine – by adding catalysts as close to the combustion process as possible.

2. The concept of using an in-cylinder catalyst

The process of combustion and heat release in combustion engines generates effects of a physical and a chemical nature, that to a large extent determine the engine operational properties. The most essential physical effect of the combustion process for the engine, is primarily the combustion quality (how much energy contained in the fuel is released), and how effectively it is used, the value of the crank dynamic loads the and the noise generated. The chemical effects mainly relate to the composition of the exhaust gases, especially the content of toxic substances. Currently, due to the environmental protection regulations the control of these substances is among the main requirements for the operation of internal combustion engines.

The conditions in which combustion occurs, should primarily ensure the complete release of fuel energy (complete combustion) with the fullest possible use of the air and maintaining the exhaust gases as pure as possible. From the engine, thermodynamic cycle analysis, it follows that the utilization efficiency of the heat released in the engine during combustion is related to its position in time. As a result the conditions required for the full fuel energy release, along with its use, and for obtaining low dynamic crankshaft loads while maintaining low noise level oppose each other. Therefore, every technical solution to this problem must be a matter of compromise between these aspects. Another factor affecting this compromise is the exhaust gas composition, which must now meet the established legal requirements.

In the first stage of self-ignition delay a stream of atomized fuel is subject to preparatory reactions which result in spontaneous combustion centers appearing in different locations on the fuel stream surface. Oxidation in this stage can be represented as a slow burning process without a visible flame or pressure increase. This process is exothermic, so heat is produced, where part of it heats the air-fuel mixture, and part is dispersed to the combustion chamber

wall. Heating the mixture accelerates the reaction, which leads to further production of heat and oxidation. Under certain conditions, the amount of heat generated becomes equal to the amount of heat dispersed, leading to a thermal balance which corresponds to the mixture ignition temperature. Such thermal equilibrium quickly disappears as the mixture is heated further as a result of the increasing pressure and temperature, which finally results in the self-ignition and combustion of the fuel.

For the reaction to start, collision of reactive particles is necessary. In fact, not all collisions cause a reaction to occur between the particles. The particles have finite speeds, which means that only a certain number of them causes a reaction to occur. Effective collisions are defined as only those collisions, where the total collision energy is higher than the average energy, specific for a given temperature. The activation energy is the energy surplus, which molecules need to have in the moment of impact in order to enter into a chemical reaction, and is the primary factor in determining the course of that reaction. The lower the activation energy, the greater the reaction rate constant and the faster the reaction. To help overcome the energy barrier associated with the activation energy, either additional energy can be delivered to the reaction (for example through heating) or a substance can be used (a catalyst), which readily reacts with the substrate (lower activation energy) and the resulting compound can easily transform into the final product (also low activation energy). After the substrates transform into products the catalyst completely regenerates, thus it is possible to sometimes encounter the claim that the catalyst is a substance not taking part in the reaction but merely facilitating its course.

Based on such analysis it can be concluded that the improvement of environmental and economic operating parameters of combustion engines mainly depend on the proper execution of the combustion process, which is highly dependent on the activation energy and the presence of a catalyst that increases the chemical reaction rate. Therefore, it is proposed that such "internal" catalyst is used as a structural element of the combustion chamber.

3. Possible applications overview

Studies by Karuppasama and Mageshkumara [5] related to engine components coated with aluminum, titanium, nickel and chromium compounds deposited via plasma spraying (Fig. 1). The parameters of the investigated engine were as follows:

– four-stroke single cylinder CI engine,
– cylinder diameter – 80 mm,
– piston stroke – 110 mm,
– compression ratio – 16,
– liquid cooling,
– engine speed (const.) – 1500 rpm.

The study was conducted for fixed engine speed and variable load. The concentration of carbon monoxide (Fig. 2), hydrocarbons (Fig. 3) and nitrogen oxides (Fig. 4) have been determined as well as specific fuel consumption (Fig. 4) for the following test conditions:

– elements of the engine head and piston crown without a catalytic layer,
– parts of the engine head and the piston crown covered with aluminum and titanium compounds (Al–Ti),
– parts of the engine head and the piston crown covered with nickel and chromium compounds (Ni–Cr).

Fig. 1. The elements of engine covered by means of plasma spraying

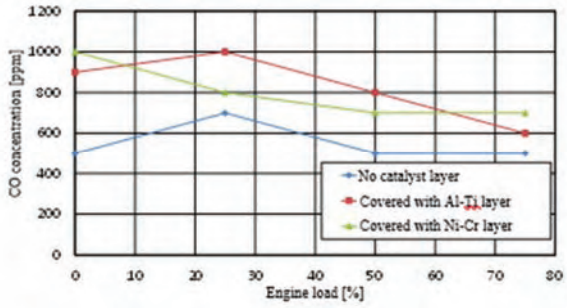

Fig. 2. The concentration of carbon monoxide as a function of engine load

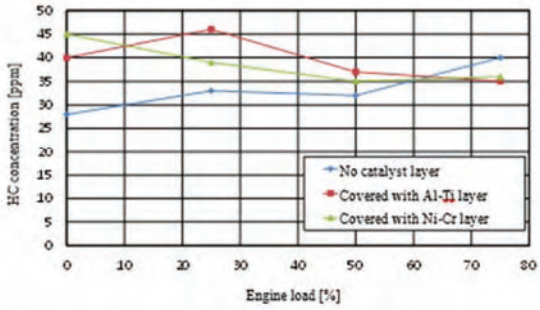

Fig. 3. The concentration of hydrocarbons as a function of engine load

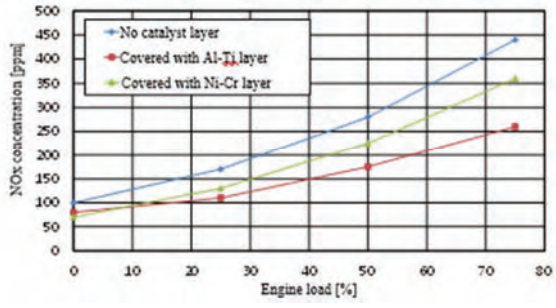

Fig. 4. The concentration of nitrogen oxides as a function of engine load

Based on the research results, it has been confirmed that the Al–Ti and Ni–Cr catalytic layers:

– adversely affect the concentration of carbon monoxide (CO) and hydrocarbons (HC) in the exhaust gas. For hydrocarbons, a 10% reduction has been observed for the highest engine loads,

– reduce the emission of nitrogen oxides (NO_x) in the entire range of engine loads by approx. 30%, which is of particular importance for compression ignition engines,
– reduction in specific fuel consumption by about 15% over the entire tested engine load range.

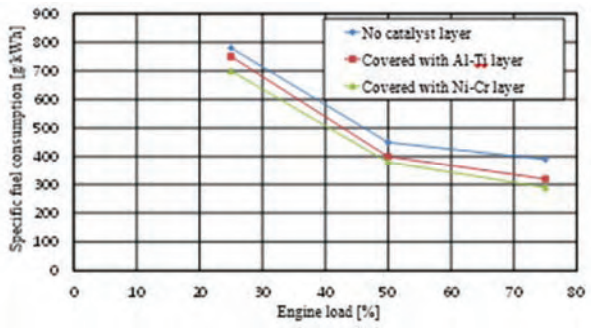

Fig. 5. Specific fuel consumption as a function of engine load

Research by Soltic and Bach [9] related to the issue of internal catalysts used in spark ignition engine powered with methane. The basis for the performed analysis of this issue was the difficulty of methane reduction in the catalytic reactor, due to the fact that it is the most stable molecular hydrocarbon, while keeping the methane in the catalytic reactor at an excess air ratio greater than 1.

Two pistons with different catalytic layers were tested:
– platinum layer with a thickness of 20 nm,
– porous zirconium oxide layer with a thickness of 0.6 mm to increase the temperature of the catalytic surface and thus catalyst reactivity (Fig. 6). The catalytic platinum layer was applied in a magnetron sputtering process (Fig. 6).

Figure 7 shows the surface of the piston after applying a zirconium oxide layer via thermal spraying. The desired thickness of the thermal surface was obtained through grinding.

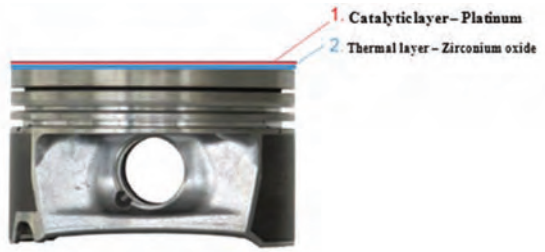

Fig. 6. Method of covering the piston with catalytic and thermal surfaces

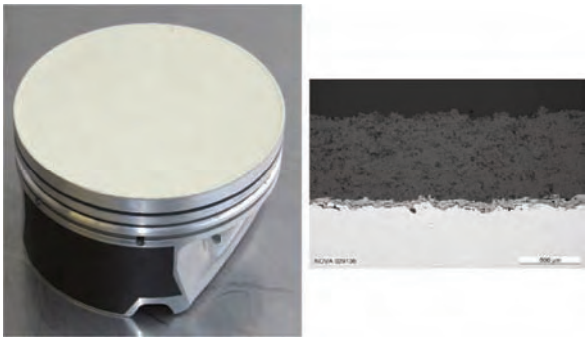

Fig. 7. Piston surface coated with zirconium oxide

The test was carried out on a research station that enabled maintaining stable air parameters (temperature and humidity) and the measurement of engine performance as well as hydrocarbons concentration in the exhaust gas. In the study a 4-cylinder, spark ignition engine fueled with gasoline and methane with a displacement of 2 dm^3 was used.

Measurements of hydrocarbons, carbon monoxide and nitrogen oxides concentrations in exhaust gas were performed at the following parameters: lubricating oil temperature greater than 90°C, air temperature of 24°C, humidity of 47%. Measurements were taken at 2500 rpm for different values of the excess air ratio (0.9, 1.0, 1.1) and various ignition timing settings. After 28 hours of operation, the catalytic coating was evaluated for signs of wear. Damp areas formed by the effects of the engine oil have been found on the piston crowns (Figure 8).

Fig. 8. State of the catalytic surface after 28 hours of operation

In this research the authors did not notice any significant changes in the nitrogen oxides concentration in the exhaust gas, regardless of the fuel used and the excess air ratio (Fig. 9). Similar results have been reported with respect to the carbon monoxide concentration in the exhaust gas – irrespective of the fuel used and the excess air ratio there were no significant concentration changes (Fig. 10).

An increase in the hydrocarbons concentration has been confirmed regardless of the fuel used and the excess air ratio value – this was a result of the catalytic coating application. The result of the study was the adsorption and desorption properties determination of the thermal coating layer (zirconium oxide). With a high internal cylinder pressure, the coating takes in a significant mass of methane ($1.74\ 10^{-3}$ g per cylinder). At low pressures, methane is released directly into the exhaust, increasing its content as a result (Fig. 11).

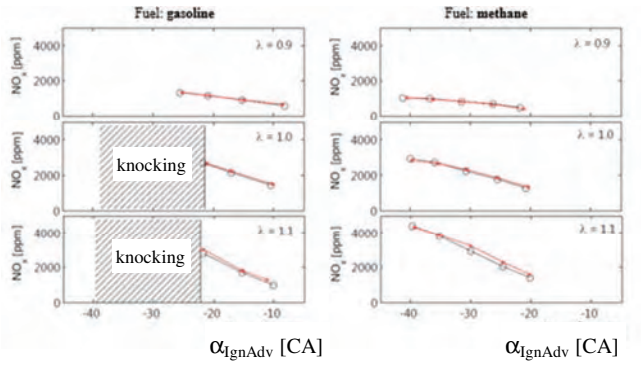

Fig. 9. Nitrogen oxides concentration in the exhaust gas of petrol and methane fueled engine

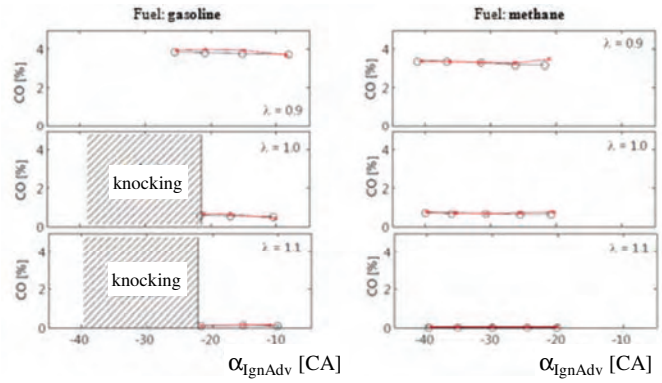

Fig. 10. Carbon monoxide concentration in the exhaust gas of petrol and methane fueled engine

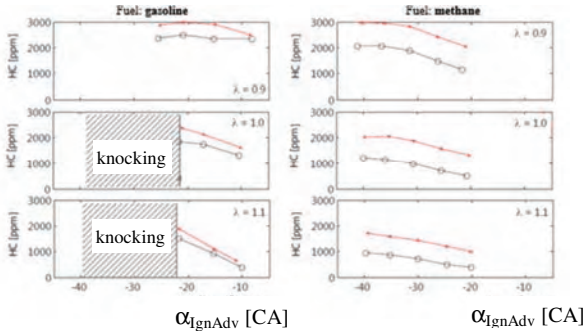

Fig. 11. Hydrocarbons concentration in the exhaust gas of petrol and methane fueled engine

The study concluded that the thermal and catalytic layers would withstand the thermal and mechanical stress present in the cylinder of the spark-ignition engine. There was a significant hydrocarbons concentration increase in the exhaust gas due to the use of a piston covered with a catalytic layer. There were no changes in concentrations of other pollutants (nitrogen oxides and carbon monoxide).

4. Conclusions

From the presented overview of the possibilities of using in-cylinder catalysts in internal combustion engines, the following conclusions can be drawn:

– One of the most important issues is the choice of an appropriate catalytic converter depending on the engine type (spark ignition, compression ignition). Individual elements or compounds are characterized by different operating temperature ranges in which they reach the highest efficiency. Due to the change in the catalytic surface efficiency depending on the temperature in the cylinder, ensuring a sufficiently high catalysts efficiency for the entire engine load range is challenging. This is due to the fact that the temperature in the cylinder also changes depending on the engine load.
– The interaction between the combustible mixture and the catalyst is not limited by the kinetics of the chemical reactions, but rather depends on the rate at which the reactants are delivered to and from the catalyst during the combustion process. This aspect can be improved by introducing turbulence into the cylinder charge.
– The lifespan of the catalytic surface depends on the coating method. Plasma spraying is the most common and most readily available, but it does not work well for catalytic coating. Ionic implantation is most often considered as a high potency solution for this problem.

Bibliography

[1] BANNIKOV, M.G., DRAPER, P.H, CHATTHA, J.A. et al. Reduction in NO_x emission of diesel engines by in-cylinder catalysis. *Proc. Instn Mech. Engrs, Part A: J. Power and Energy*. 2003, 217.
[2] GUO, H., MURAKAMI, H., KURODA, S. Thermal cycling behavior of plasma sprayed segmented thermal barrier coatings. Materials Transactions. 2006, **47**(2), 306-309.
[3] HEJWOWSKI, T. Comparative study of thermal barrier coatings for internal combustion engine. *Vacuum*. 2012, **2**(12).
[4] HU, Z., LADOMMATOS, N. Reduction of unburnt hydrocarbon emissions from spark ignition engines using in-cylinder catalysts. *Proc Instn Meeh Engrs, Part D: Journal of Automobile Engineering*. 1996, 210.
[5] KARUPPASAMY, K., MAGESHKUMAR, M.P., MANIKANDAN, T.N., et al. The effect of thermal barrier coatings on diesel engine performance. *ARPN Journal of Science and Technology*. 2013, **3**(4).
[6] MELLO, J.P., BEZAIRE, D., SRIRAMULU, S., WEBER, R. Performance and economics of catalytic glow plugs and shields in direct injection natural gas engines for the next generation natural gas vehicle program. Final report. *National Renewable Energy Laboratory*. NREL/SR-540-34286, 2003.
[7] NEDUNCHEZCHIAN, N., DHANDAPANI, S. Effects of in-cylinder catalytic coating on the performance of a two-stroke spark ignition engine. *Indian Journal of Engineering & Materials Sciences*. 2001, 8, 1-7.
[8] NORMAND, B., FERVEL, V., CODDET, C., NIKITINE, V. Tribological properties of plasma sprayed alumina–titania coatings: role and control of the microstructure. Surface and Coatings Technology. 2000, 123, 278-287.
[9] SOLTIC, P., BACH, C. Catalytic piston coating. *Conference Gas Powered Vehicles*. Berlin 30.09–1.10.2010.
[10] TAYMAZ, I., CAKIR, K., GUR, M., MIMAROGLU, A. Experimental investigation of heat losses in a ceramic coated diesel engine. *Surface and Coatings Technology*. 2003, 169-170, 168-170.

Monika Andrych-Zalewska, MEng. – Department Vehicles Engineering at Wroclaw University of Science and Technology.

e-mail: *Monika.Andrych@pwr.edu.pl*

Article citation info:
PARCZEWSKI, K., WNĘK, H. The influence of vehicle body roll angle on the motion stability and maneuverability of the vehicle. *Combustion Engines*. 2017, **168**(1), 133-139. DOI: 10.19206/CE-2017-121

Krzysztof PARCZEWSKI
Henryk WNĘK

CE-2017-121

The influence of vehicle body roll angle on the motion stability and maneuverability of the vehicle

The article discusses the impact of design solutions of vehicle suspensions into angles of body roll. It was shown which type of suspensions is better from this point of view. There were examined the dependence of the suspensions parameters on the vehicle body roll angle. The influence of camber angle on the force transmitted to the tire contact with the road surface was analysed. The lateral forces were measured on the test stand. There was tested dependency of lateral forces from the sideslip angle for different angles of camber. Was analysed change of lateral forces generated by camber angle on the vehicle which was made on a scale ~ 1:5 during tests carried out on the testing track. For this purpose, two tests have been selected: first one allowing the measurement in steady motion conditions, the second one with dynamic change of direction of vehicle motion. The graphs show the effect of camber angles on the controllability and stability of the vehicle motion.

Key words: *stability of vehicle motion, suspensions, the interaction of the road and tires, the roll angle of vehicle body*

1. Introduction

One of the tasks of the suspension of the vehicle is the appropriate wheel movement relative to the vehicle body. The controllability and stability of vehicle motion is influenced by: the stiffness and damping of suspension elements, suspension kinematics motion and changes the wheels angles. The solutions of design of suspensions affect the load and wheel inclination while performing various maneuvers by the vehicle. During analyzing the interaction of the wheel with the road surface, it can be determined which of the suspension construction is the most preferred for use in various types of vehicles. For this purpose, was conducted the study of dynamics of the physical model in a scale of 1:5, in which were assembled various types of suspension on the front and rear axles. This model fulfills criteria of similarity to medium truck [1, 2, 11, 14].

Tires parameters were determined during the tests on the test stand: stiffness in the longitudinal direction, transverse and radial and angular stiffness. In addition, were compared various parameters of the vehicle suspension: vertical stiffness and roll stiffness while maintaining the gross vehicle weight and moments of inertia. During the testing on the testing track were analyzed behavior of the vehicle during tests: the first one – driving on the circle track (quasi-static driving conditions) and the second one – sudden changes of vehicle direction (dynamic driving conditions) [5, 6]. The study allowed to determine the effects of the suspension on the vehicle behavior [10].

2. Influence of the kinds of suspension on the co-operation of the tire with the road surface

The total force transmitted by the wheel on the road surface consists of the normal force and tangential forces (driving or braking, and lateral force). The maximum values of tangential forces are limited by the conditions of the adhesion [13]. The lateral force depends on the wheel angular stiffness and its inclination. Figure 1 shows a comparison of different kinds of vehicle suspensions during driving in a circular track.

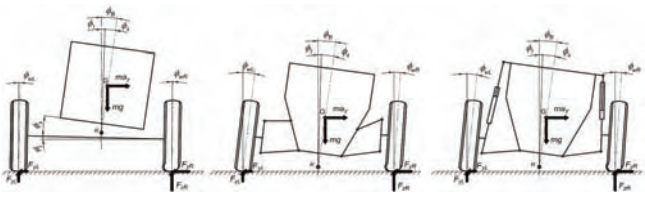

Fig. 1. Comparison of vehicles with different kinds of suspensions on a curvilinear track [own study]

In the case of dependent suspensions, camber angle is usually smaller than that of the car equipped with the double wishbone in suspensions. Suspensions equipped with McPherson's columns, generate slightly less camber angles. The vehicle body inclination angles depend on the kinematics and stiffness of the suspensions and are usually smaller for vehicles equipped with dependent suspensions. The use of anti-roll bar increases the angular stiffness of the vehicle. The anti-roll bar increases the angular stiffness of the suspension on the axis of the vehicle and protects it from excessive angles of body roll. During driving on a bend of the road, vehicle under the influence of the centrifugal forces incline towards the outer wheels. The anti-roll bar operates to reduce the differences of instantaneous loads on the elastic elements of suspensions of the wheels on one axle and reduces roll angles [13].

In vehicles equipped with suspension with rigid axles change camber depends on the susceptibility of the tires and the road surface irregularities. In the case of vehicles with independent suspensions angle of wheel inclination depends on the suspension geometry changes resulting from the vertical movement of wheel and the lateral inclination of the suspension. Figure 2 shows the camber angle according to the inclination of the vehicle body for different kinds of suspension: double wishbone, McPherson's column, and rigid axle [own study].

2.1. The parameters of the vehicle suspensions

For the analysis were chosen dependent suspension currently used in SUVs, vans and trucks, and an independent suspension with double wishbones of different lengths used in passenger cars and vans. The test method was used to

determine the vertical and angular stiffness of the suspension and roll damping of suspension. The measurement results of suspensions stiffness are given in Table 1.

Table 1. Comparison of parameters of the vehicle physical model equipped with various types of suspension [own research]

Parameter		Dependent suspension		Independent suspension	
		front axle	rear axle	front axle	rear axle
Vertical stiffness	K_s, N/m	1910	1550	2980	5240
Vertical stiffness	K_t, N/m	1680	1680	1680	1680
Suspended mass	m_s, kg	9,329	13,688	8,839	13,818
Unsuspended mass	m_{us}, kg	1,667	1,648	2,662	2,783

The following figures show the impact of vehicle body inclination angle to the wheels camber angles for different types of suspension, taking into account the correction caused by the anti-roll bars.

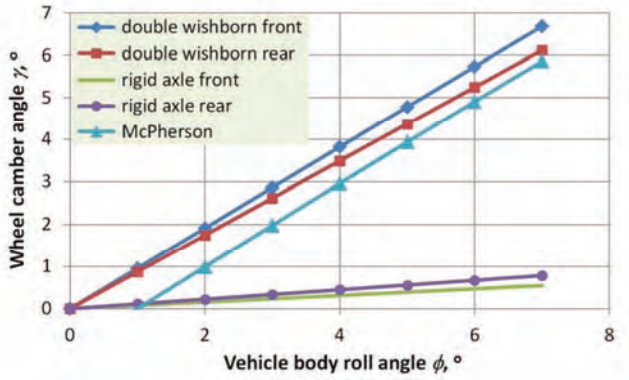

Fig. 2. The angle of wheel camber γ as a function of vehicle body roll angle ϕ for different types of suspension (including the impact of tire deflection) [own research]

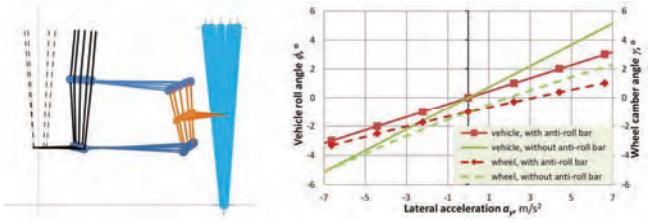

Fig. 3. The wheel camber changing γ resulting from vehicle body roll angle ϕ equipped with suspension with double wishbone [own research]

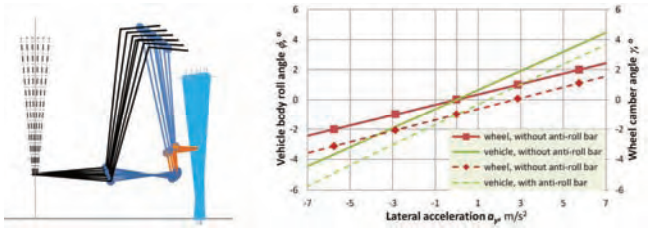

Fig. 4. The wheel camber changing γ resulting from vehicle body roll angle ϕ equipped with McPherson suspension [own research]

2.2. The parameters of the vehicle suspensions

Figure 5 schematically shows the inclination of the car due to a lateral force.

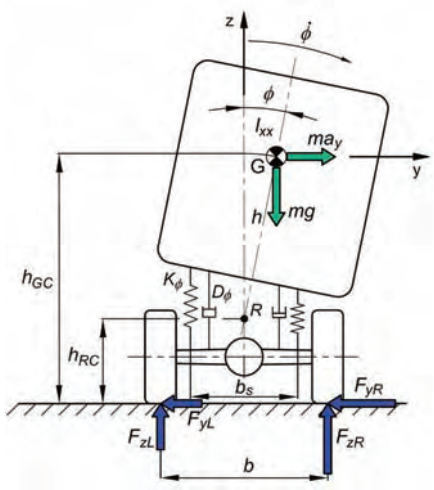

Fig. 5. The inclination of the vehicle caused by the lateral force [11]

The impact of tires deflection was omitted. Taking equation for the sum of lateral force and equation for the sum of moments about the roll centre it can be determined the impact of the location of centre of gravity on roll angle of the vehicle.

$$F_{yf(r)} = m_s \cdot (\dot{V} \cdot \sin\beta + V \cdot \dot{\beta} \cdot \cos\beta + V \cdot \psi \cdot \cos\beta) = m_s \cdot a_y \tag{1}$$

$$\begin{aligned} M_{RC} = {} & m_s \cdot g \cdot (h_{GC} - h_{RC}) \cdot \sin\phi \\ & - D_\phi \cdot \dot{\phi} - K_\phi \cdot \phi - K_{\phi\_ARB} \cdot \phi + \\ & + m_s \cdot (\dot{V} \cdot \sin\beta + V \cdot \dot{\beta} \cdot \cos\beta + V \cdot \psi \cdot \cos\beta) \cdot \\ & (h_{GC} - h_{RC}) \cdot \cos\phi = 0 \end{aligned} \tag{2}$$

For small roll angles ϕ it can be assumed that $\sin\phi \approx \phi$ and $\cos\phi \approx 1$, and that the lateral offset of centre of gravity, caused by inclination of the body, is so small that can be neglected. The equation (2) was used to determine how the lateral acceleration affects on the roll angle of the vehicle body (assuming that the lateral motion of the vehicle body is relatively slow).

$$\begin{aligned} \frac{M_{RC}}{b_s} \approx {} & \frac{1}{b_s} \cdot (m_s \cdot a_y \cdot (h_{GC} - h_{RC}) - \\ & D_\phi \cdot \dot{\phi} - K_\phi \cdot \phi - K_{\phi\_ARB} \cdot \phi) = 0 \end{aligned} \tag{3}$$

$$a_y = \frac{D_\phi \cdot \dot{\phi} + (K_\phi + K_{\phi\_ARB}) \cdot \phi}{m_s \cdot (h_{GC} - h_{RC})} \tag{4}$$

Hence, the simplification:

$$\phi \approx (a_y \cdot (h_{GC} - h_{RC}) \cdot m_s - D_\phi \cdot \dot{\phi}) \cdot \frac{1}{K_\phi + K_{\phi\_ARB}} \tag{5}$$

Analysing the equation (5) it can be stated that the roll angle of the vehicle body to a large extent, determined by the lateral acceleration, the distance from vehicle centre of gravity to the roll centre and ratio of the mass to the roll stiffness of the suspensions (including the influence of the anti-roll bar).

Taking into account the deflection of tires, it will result in an increase in the roll angle of a few percent for trucks to several percent for passenger cars. Based on of research carried at the Laboratory of the Department of Internal Combustion Engines and Vehicles in University of Bielsko-Biala, was determined the maximum roll angle ϕ_t, resulting from the deflection of tires: for passenger cars ~ 1.3 ° and for trucks ~ 0.7 °.

Figures 6–8 shows the influence of the lateral acceleration, distance of centre of gravity from the roll centre and the suspension roll stiffness and damping.

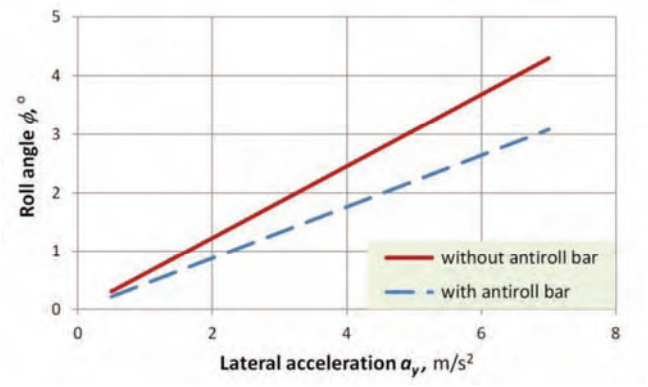

Fig. 6. The impact of lateral acceleration on the vehicle roll angle (for a full-size vehicle) [own research]

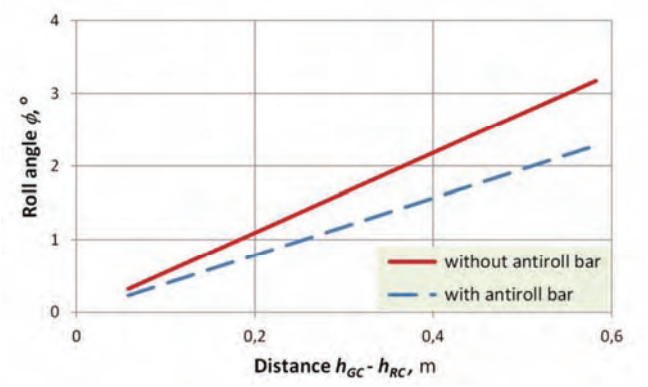

Fig. 7. Impact at vehicle roll angle of distance from centre of gravity to the roll centre (for a full-size vehicle) [own research]

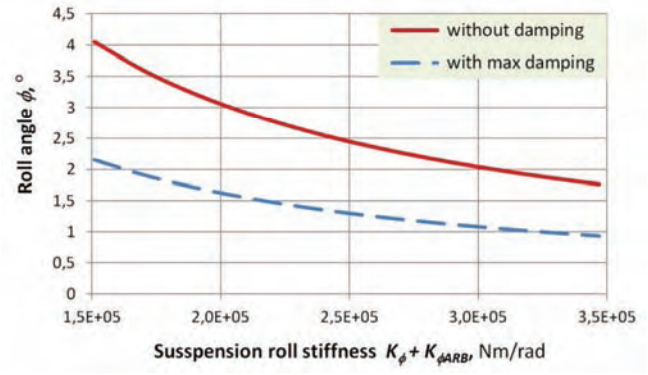

Fig. 8. The impact at vehicle roll angle of the roll stiffness of suspension (for a full-size vehicle) [own research]

On the vehicle roll angle also affects the product of roll rate and roll damping stiffness, in the dynamic states, it creates a temporary decrease in the roll angle. In Figure 8 is shown as dashed line, which represents the possible impact of roll rate and roll damping to temporarily change the roll angle (e.g during turning manoeuvre).

The maximum value of the roll angle for cars and trucks is about 4 to 7°, with the largest impact on the roll angle has lateral acceleration ~56%, slightly lower distance from centre of gravity to roll centre ~46% and the minimum ratio of weight to suspension roll stiffness ~8%. Taking into account the deflection of the tire can change the roll angle to ~4%. Moment of inertia of the vehicle body will cause a delay of rolling. The use of anti-roll bars of the front and rear axles will cause a reduction in the roll angle of up to 30%.

On the basis of this analysis, it can select the appropriate type of vehicle suspension with high and low located centre of gravity above ground. In the sports vehicle and passenger cars distance from the centre of gravity to the roll centre is relatively small and can be used suspension, in which the effect of vehicle body inclination on the roll angle is greater. In cars with a high located centre of gravity for example SUV and trucks should be used suspension, in which the inclination of the vehicle body has a little effect on the wheel camber angles.

3. The impact of wheel camber angle on the transmission of forces on the tire contact with the road

Changes in camber angles cause a change in footprint the tire contact with the road and affect on change of the value of lateral force transmitted to the road [8,9]. Because the side force is limited by the terms of adhesion, and depends on the wheel load, the cornering stiffness $K_{\alpha i}$ will not be constant and will vary.

Lateral force between wheel and ground depends on the sideslip angle α and camber angle γ and is described by equation (6a) [4]. For larger sideslip angles R. Jazar [7] recommends the use of a simplified equation (6b), taking into account the non-linear curve of the lateral force:

$$F_{yi} = -K_{\alpha i} \cdot \alpha_i + K_{\gamma i} \cdot \gamma_i \tag{6a}$$

where i – an index indicating the i-th wheel

$$F_y = -K_\alpha \cdot \alpha \cdot \left(1 - \frac{1}{3}\left|\frac{K_\alpha \cdot \alpha}{F_{yM}}\right| + \frac{1}{27}\left(\frac{K_\alpha \cdot \alpha}{F_{yM}}\right)^2\right) + K_\gamma \cdot \gamma \tag{6b}$$

The wheel camber angle will cause a change of the tire footprint on the roadway and thus the formation of the lateral force component depends on the camber angle γ. In addition, will appear some point shift reaction force F_z from the wheel axis. In Figure 10b was shown the impact of wheel camber angle on the tire footprint shape on the roadway.

When vehicle is driving with lateral acceleration under steady state conditions (e.g. during cornering), on the vehicle operates the centrifugal force, which can be determined

from equation $F_y = m \cdot a_y$. This lateral force can be decomposed into components acting on the front and rear axles.

$$F_y = F_{yf} + F_{yr} \tag{7}$$

The forces acting on the front and rear axles, for small sideslip angles of wheels, can also be determined from equation:

$$F_{yf} = F_y \cdot \frac{a_2}{L_w} \tag{8a}$$

$$F_{yr} = F_y \cdot \frac{a_1}{L_w} \tag{8b}$$

Based on the analysis equation (6b) can be seen that when the vehicle is moving on the curvilinear track under steady state conditions (fixed side force), the increase of camber angle, will affect the decrease value of lateral force and at the same values of this force the value of wheel sideslip angle α will be increased.

Sideslip angles of the wheels can be determined from equations (9a) and (9b) [3].

$$\alpha_f = \frac{W_f}{g \cdot K_{\alpha f}} \cdot a_y - \frac{K_{\gamma f}}{K_{\alpha f}} \cdot \gamma_f \tag{9a}$$

$$\alpha_r = \frac{W_r}{g \cdot K_{\alpha r}} \cdot a_y - \frac{K_{\gamma r}}{K_{\alpha r}} \cdot \gamma_r \tag{9b}$$

They were defined functional dependencies of wheels camber angle as a function of vehicle body roll angle and a vehicle body roll as a function of lateral acceleration, based on the results of research and analysis for various types of suspensions. The values of tires cornering stiffness and camber stiffness were determined from measurements on the test stand [10].

4. The impact of wheel camber angle on the transmission of forces on the tire contact with the road

Lateral force measurements were conducted on a test stand [10] using the tire used in physical model for various wheel sideslip angles α at fixed value of camber angles γ (in the range of 0 to 10 deg).

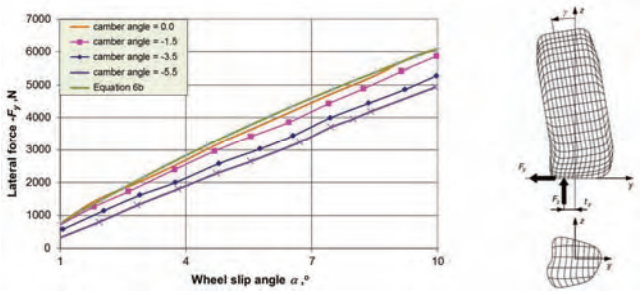

Fig. 9. a) Lateral force on the wheel contact with the road Fy at various wheel camber angles γ, depending on the wheel sideslip angles α (for a full-dimensional vehicle) [own research], b) The lateral and vertical force and a footprint of the contact on the road surface caused by wheel camber angle

Figure 9a shows a comparison of the lateral force determined from the equation (6b), and obtained from measurements on the test stand [10]. The lateral force – F_y decreases with increasing camber γ from a few to several percent, proportional to the wheels sideslip angle.

The values of angular stiffness of tire and camber stiffness were determined on the basis of measurements which were made on the test stand. The values shown in table 2 were obtained from measurements and were multiplied by scale factors of similarity (for full-dimensional vehicle).

The impact of the vehicle body roll angle on stability and steerability of the vehicle were verified during the tests of physical vehicle model at scale ~1:5, conducted on the test track.

Table 2. The stiffness of tire for full-dimensional vehicle determined on the basis of the tire of the physical model [own research]

Parameter		Front axle	Rear axle
Vertical stiffness	K_z, N/mm	923	1151
Lateral stiffness	K_y, N/mm	70	82
Cornering stiffness	K_α, N/rad	68800	76000
Camber stiffness	K_γ, N/rad	3305	3569

The influence of the vehicle body roll angle on the stability and steerability of the vehicle were verified during the tests of the vehicle model in a scale performed on the test track.

5. Analysis of influence of the camber angle on the dynamics of vehicle motion based on tests of the physical model

5.1. Measurements of stability and steerability performed with using the vehicle model

During measurements of stability and steerability of vehicles are used standardized research tests: driving in a circular path at a steady-state condition (ISO 14792) [5], step steering input (ISO 14793) [6], dynamic stability of the vehicle motion (AVTP 03-160 – test of avoid an obstacle on the road) and other [12]. For study were chosen two tests based on the driving on a circular path in steady-state conditions and test of a response on sudden change of the steering wheel rotation.

For testing was used a physical model of the vehicle made on a scale ~1:5, which fulfilled criteria of similarity to the commercial vehicle (LCV) [11,14]. Using the theory of similarity, were chosen the trajectory and the parameters of motion to the scale of the vehicle. The runs of the tests has been programmed in the controller of model.

On the vehicle model was mounted measuring equipment VBOX 3i Racelogic based on GPS technology, allowing for registration of the trajectory and parameters of the motion: velocity, longitudinal and lateral acceleration, angular velocity of vehicle motion about axis passing through centre of gravity and roll angle of the vehicle [15]. Figure 10 shows a model prepared for the tests. During the tests on the model were assembled various types of suspension and additionally also were mounted anti-roll bars on the front and rear axles.

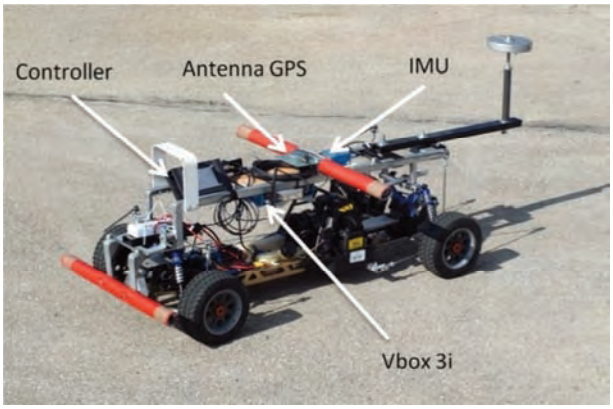

Fig. 10. The physical model of the vehicle on a scale ~1:5 with mounted measuring apparatus

5.2. Analysis of influence of camber angle on the vehicle stability and steerability

During the tests, after the start the vehicle was moving straight for about 3 seconds to achieve the required speed and then performed a manoeuvre of turn right and for about four seconds was moving along a circular path, would then return to the straight track and stop. Steering angle of wheels, velocity and duration of individual manoeuvres were programmed and performed by the controller. This test allows for conducting research under conditions of dynamic changes of motion direction and during the driving on a circular path in steady-state conditions.

Figure 11 shows the run of the velocity during transient and steady-state motion.

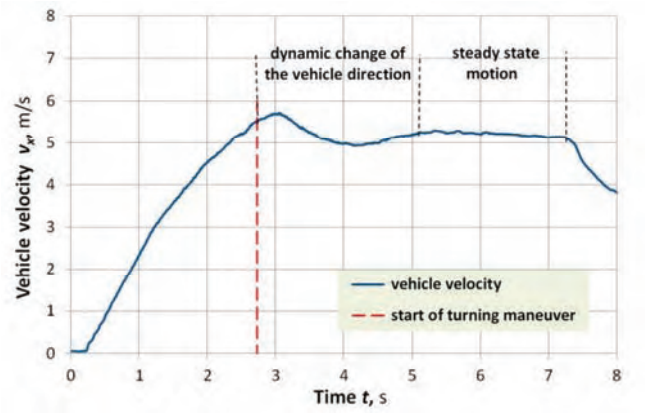

Fig. 11. The run of vehicle motion velocity during the test. [own research]

The following figure shows the vehicle body roll angle (Fig. 12) depending on mounted suspension in the vehicle. The red curve shows the vehicle body roll angle with mounted dependent suspension at front and rear axles. The curve of blue colour shows the vehicle body roll angle with independent suspension for both axles and the green one shows the vehicle with independent suspension (two wishbones) mounted on the front axle and with the rear rigid axle. The body roll angles are greatest in a vehicle with independent suspension ~13° and the smallest in the vehicle equipped with dependent suspension ~7°. In the first case, with the independent suspension on both axles, the roll angle in the initial phase of the turning reached to 13° and then decreased up to 6°. In the case of independent suspension on the front axle and dependent on the rear one (green curve) roll angle reached up to 9° in the initial phase of the manoeuvre, order then to decrease to 4°. While a vehicle was equipped with a suspension with rigid axles (red curve) the roll angles were of ~7° to fall in the final phase to 2.5°.

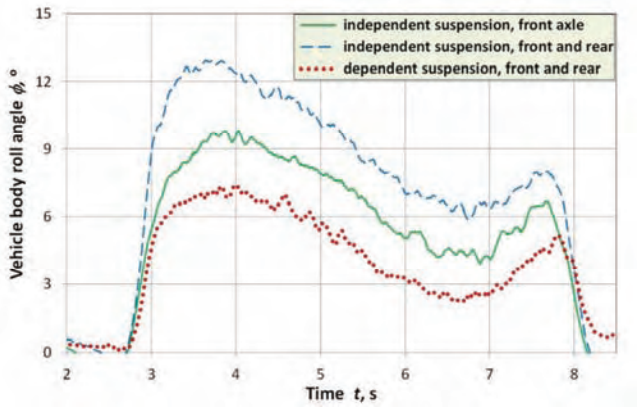

Fig. 12. The run of the vehicle body roll angle during the test. [own research]

Figure 13 shows influence of the camber angle on the side slip angle of wheels.

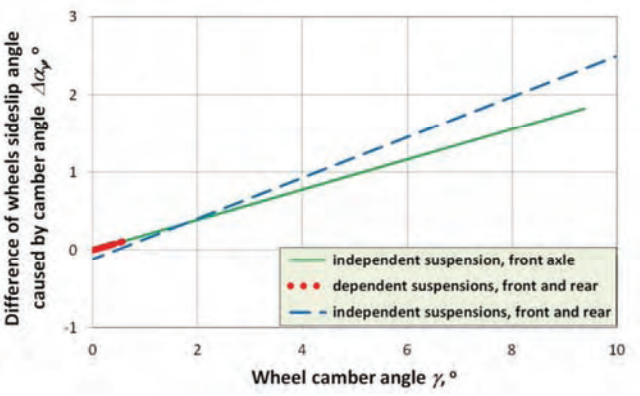

Fig. 13. The influence of camber angle γ on the difference of wheels side slip angle – Δα [own research]

Camber angles have an influence on the side slip angles, and their change does not exceed ~3° for a vehicle equipped with an independent suspension on both axles, ~1.75° for the vehicle with independent suspension on the front axle and dependent on the rear one, and ~0.3° for a vehicle equipped with dependent suspension on both axles. Figure 14 shows difference of side slip angles of wheels of the front and rear axle for different suspension types mounted on the vehicle. The vehicle equipped with different suspension on the front and the rear axle had oversteer characteristics. The vehicle had understeering characteristics for other combinations of the suspensions.

Vehicle with different suspension of front and rear axles in the initial part of the test (dynamic change of the direction of motion) clearly tightened the turn. A vehicle equipped with independent suspension on both axles in the initial part of the test increased the radius of curvature of the track. A vehicle equipped with a dependent suspension to a much lesser extent increased the radius of the track. In

the part of the test, while the vehicle was moving in steady-state condition, radii of curvature of the tracks were very similar.

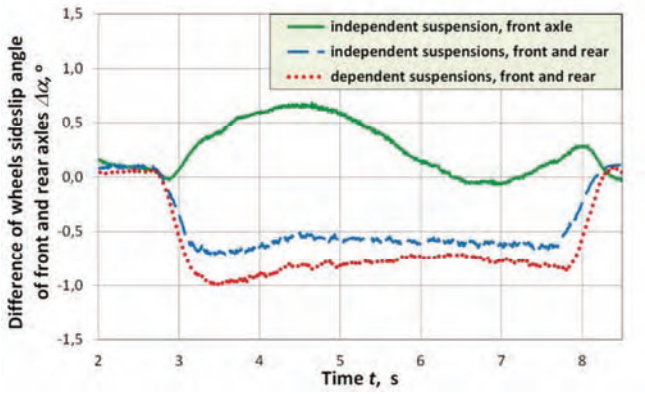

Fig. 14. The influence of roll angle ϕ on the difference of wheels side slip angle of front and rear axles. [own research]

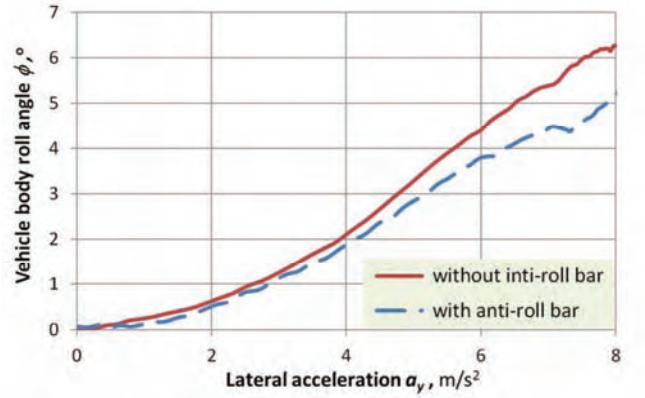

Fig. 15. The influence of anti-roll bars on the vehicle body roll angle. [own research]

The application of anti-roll bars in the suspensions of vehicles reduces the roll angles (Fig. 15). During the tests of the model has been observed reducing of the vehicle roll angle more than 1 degree (about 15%). This was due to increase reactions forces on the unloading wheels (at large roll angles, even up to 40%) and in result the improvement of lateral stability. The use of anti-roll bars allowed the transfer the larger driving forces during the intense turn manoeuvres (even at high lateral accelerations). During the road tests was observed a slight decrease of the trajectory radius of the vehicle motion, resulting from better load distribution on the sides of the vehicle.

6. Summary and conclusions

In vehicles equipped with suspension with rigid axles the change of the camber angle results from the compliance of the tires and the road surface irregularities. In the case of vehicles with independent suspension the camber angle also depends on the suspension geometry changes resulting from its the vertical movement and from the vehicle body roll angle. Changes of camber angles will change the contact patch the tire with the road and affect to change of the size of lateral force transmitted on the road surface.

On basis of conducted tests and studies it can be concluded about choosing the right type of suspension for vehicles with high and low centre of gravity position. In the sport vehicles and classical passenger cars the distance between the roll axis and the centre of gravity is relatively small and can be used suspensions, in which the influence of vehicle body roll angle on the camber angle is greater. In cars with a high position of gravity centre, for example multipurpose vehicle (SUV – sport utility vehicle) and trucks (CV – commercial vehicle) should be applied suspension, in which the vehicle body roll angle has little effect on camber angles.

Larger camber angles effect on increasing the side slip angles. The application of different suspensions can cause variation of side slip angles difference of front and rear axle and thereby affect on understeer and oversteer of the vehicle. This is particularly apparent when dynamically changes direction of the vehicle motion. During the driving in a circular path at steady-state condition influence of the applied suspension is much less felt. The use of independent suspensions on the front and rear axle in trucks results in a significant increase in vehicle roll angle, which increases the risk of vehicle rollover and deteriorates the properties of vehicle motion, both in quasi-static and dynamic conditions.

The use of anti-roll bars on the front and rear axles results in decrease the vehicle roll angles and thereby improving cooperation the wheel with the road surface, and increasing steerability and stability of the vehicle.

Nomenclature

α	sideslip angle of wheel, °, rad
$\Delta\alpha$	difference of wheels sideslip angle of front and rear axles, °, rad
$\Delta\alpha_y$	difference of wheels sideslip angle caused by camber angle, °, rad
β	vehicle slip angle, °, rad
γ	camber angle of wheel, °, rad
ϕ	roll angle of the vehicle body, °, rad
ϕ_s	roll angle of the sprung mass, °, rad
ϕ_t	roll angle of the vehicle body caused by tire, °, rad
$\dot{\phi}$.	roll rate of the vehicle, 1/s
$\dot{\psi}$.	yaw rate of the vehicle, 1/s
a_1, a_2	distance of the centre of gravity from the front/rear axle, m
a_x	longitudinal acceleration ($a_x = \dot{V}$), m/s^2
a_y	lateral acceleration, m/s^2
b	wheel tread, m
b_s	lateral separation between the springs, m
C_γ	tire camber stiffness, N/rad
C_α	tire cornering stiffness, N/rad
C_z	tire vertical stiffness, N/m
C_y	tire lateral stiffness, N/m

D_ϕ roll damping of suspension, Nms/rad
$F_{sL(sR)}$ vertical force acting as a result of the deflection of the left (right) spring, N
F_{yf}, F_{yr} lateral force acting on the front/rear wheel, N
$F_{yL(R)}$ lateral force acting on the left wheel (right), N
F_{yM} maximum value of the lateral force, N
$F_{zL(zR)}$ vertical force acting on the left wheel (right), N
g gravity acceleration, m/s^2
h distance between the center of gravity and the roll center, m
h_{GC} height of the center of gravity above the ground, m
h_{RC} the height of the roll center above the ground, m
i an index
K_ϕ the roll stiffness of suspension, Nm/rad
K_{ϕ_ARB} additional roll stiffness suspension caused by a anti-roll bar, Nm/rad
k_s suspension stiffness, N/m
k_t vertical tire stiffness, N/m
k_α cornering tire stiffness, N/rad
L_w wheelbase ($L_w = a_1 + a_2$), m
M_{RC} sum of moments about the roll centre, Nm
m mass of vehicle ($m_{us} + m_s$), kg
m_s „sprung" mass of vehicle, kg
m_{us} „unsprung" mass of vehicle, kg
R roll centre point,
r the radius of the track, m
R_y, R_z the reactions operating in the roll centre, N
V the speed of a moving vehicle, m/s
W_f, W_r load of front/rear axle, N

Bibliography

[1] BAKER, W.E., EESTINE, P.S., DODGE, F.T. Similarity methods in engineering dynamics. Theory and practice of scale modeling. 9th ed. New Jersey: *Spartan Books*. 1978, 83-142.

[2] BUCKINGHAM, E. On physically similar systems: Illustration of the use of dimensional equations. *Physics Review*. 1914, **4**, 345-376.

[3] GILLESPIE, T.D. Fundamentals of vehicle dynamics. 1st ed. Warrendale: *SAE*. 1992, 198-219.

[4] GUZEK, M., LOZIA, Z., REŃSKI, A. The influence of angular stiffness of suspension on the lateral stability of the two-axle vehicle on the example of light comercial vehicle. *Zeszyty Naukowe Instytutu Pojazdów*. Politechnika Warszawska. 1998, **3**, 17-29.

[5] ISO 14792:2003. Heavy Commercial vehicles and Articulated Buses. Steady state circular test.

[6] ISO 4138:2012. Passenger cars. Steady-state circular driving behavior. Open-loop test methods.

[7] JAZAR, R.N. Vehicle dynamics. Theory and application. 2nd ed. New York: *Springer*. 2008, 135-151.

[8] LOZIA, Z. A two-dimensional model of the interaction between pneumatic tyre and an uneven road surface. *Vehicle System Dynamics: International Journal of Vehicle Mechanics and Mobility*. 1988, **17**(1), 227-238.

[9] LUTY, W., PROCHOWSKI, L. The possibility of transferring lateral forces by the tires of a truck on a bend of the road. *Zeszyty Naukowe Instytutu Pojazdów*. Politechnika Warszawska. 2004, **3**(54), 61-70.

[10] PARCZEWSKI, K., WNĘK, H. The tyre characteristics of physical models used to investigate vehicles lateral stability. *Proceedings of the Institution of Mechanical Engineers, Part D: Journal of Automobile Engineering*. 2015, **229**(10), 1419-1426.

[11] PARCZEWSKI, K, WNĘK, H. Using mobile scaled vehicle to investigate the truck lateral stability. *Eksploatacja i Niezawodnosc Maintenance and Reliability*. 2013, **15**(4), 415-421.

[12] PIENIĄŻEK, W. Selected issues of research on the vehicle stability and steerability. *Zeszyty Naukowe Instytutu Pojazdów*. Politechnika Warszawska. 2010, **3**(79), 29-43.

[13] REŃSKI, A. Vehicles active safety. The suspension, steering and braking systems. 1st ed. Warszawa. *Oficyna Wydawnicza Politechniki Warszawskiej*. 2011, 1-36.

[14] ROMANISZYN, K.M. Mobilne modele samochodów do badań stateczności. *Logistyka*. 2012, **3**, 1927-1934.

[15] ROMANISZYN, K.M. Comparison of dynamic parameters of a special-purpose vehicle with different centre of gravity locations. *Zeszyty Naukowe Instytutu Pojazdów*. Politechnika Warszawska. 2010, **1**(77), 291-299.

Krzysztof Parczewski, DSc., DEng. – Faculty of Mechanical Engineering and Computer Science at University of Bielsko-Biała.

e-mail: *kparczewski@hth.bielsko.pl*

Henryk Wnęk, DEng. – Faculty of Mechanical Engineering and Computer Science at University of Bielsko-Biała.

e-mail: *hwnek@ath.bielsko.pl*

Article citation info:
JAWORSKI A., LEJDA, K., MĄDZIEL, M. Emission of pollution from motor vehicles with respect to selected solutions of roundabout intersections. *Combustion Engines*. 2017, **168**(1), 140-144. DOI: 10.19206/CE-2017-122

Artur JAWORSKI
Kazimierz LEJDA
Maksymilian MĄDZIEL

CE-2017-122

Emission of pollution from motor vehicles with respect to selected solutions of roundabout intersections

The article concerns the assessment of emmision of selected two-lane roundabout functioning in the city of Rzeszow and its alternate turbo version. In the work was considered four scenarios that represent two different in terms of traffic congestion time of day. The results of the emission of selected components of the exhaust gas (NO_x and particulates PM10) were obtained on the basis of calculations of emission model VERSIT+ Enviver. While the input data for the calculations were taken from the modeled options of roundabouts in the Vissim program. The results from the Enviver program were compared to calculations from mesoscopic model COPERT 5. The results show that the overall reduction in average speed, as well as increased frequency of braking and sudden acceleration, directly contribute to the growth of harmful emissions. However, with respect to comparision of turbo roundabout in regard of currently running two-lane roundabout can be observed reduction of selected components of exhaust gases emission about approx. 1/3.

Key words: *emission, roundabout, traffic, urban transport, microsimulation*

1. Introduction

As the number of motor vehicles continues to increase, so too does the total emission of toxic exhaust gas components. This leads to a deterioration in air quality and people's health. Notwithstanding the fact that steps have been taken to remedy this problem by establishing relevant standards and executing a number of social campaigns and research projects, emissions from road transport still pose a significant threat. Road transport emissions depend on many factors, including traffic volume, road and car features, weather conditions, drivers' behaviour and the type of intersections. At intersections, vehicles usually slow down or stop, causing disruption in traffic flow. Roundabout intersections are safe and effective, and can also improve traffic flow compared to conventional signalized intersections. However, it is not certain, to what extent different solutions of this kind can reduce emissions of toxic chemicals from car exhaust fumes [4, 6, 8].

The aim of this study is to determine the volume of pollutants emitted by means of road transport for a selected Rzeszów roundabout which is heavily burdened with traffic. At present, the roundabout has two lanes but a turbo roundabout option was additionally modelled to compare emission outputs. In order to obtain traffic-related results, a microsimulation of traffic flow was carried out in Vissim software using the actual traffic values obtained from the traffic count points existing in the city. In total, 4 scenarios representing two times of the day with different traffic volumes were collated. The traffic results obtained were used to determine the amounts of toxic components: nitrogen oxides (NO_x) and particulate matter (PM10) emitted by motor vehicles. A COPERT 5 emission model was adopted to verify the emission results obtained by Enviver software.

2. Methodology of the study

The intersection chosen for exhaust emission analysis was a two-lane roundabout at the crossing of Warszawska, Marszałkowska, Rycerska and Lubelska streets in Rzeszów. The roundabout has four main entrances, three of which having two lanes. The entrances on the side of Warszawska, Lubelska and Marszałkowska streets are marked by high traffic volumes, whereas the traffic at the entrance from Rycerska street is light. The traffic on the two-lane entrance roads during the times of commutes and returns home makes the intersection access roads jam over a distance of about 100 m from the roundabout entrance. The intersection is shown in Fig. 1.

During the measurements, pedestrian traffic was very light and was therefore passed over in further analysis. All the road traffic measurements were taken on 18 Dec. 2015. The intersection geometry data were taken from a satellite photograph found in Google Maps. The photograph was appropriately scaled so that it could be processed in the Vissim traffic microsimulation software. Traffic volume numbers for individual roundabout entrances were obtained from the database of a vehicle weight pre-selection system. Two times of the day were chosen for the testing of emissions. The first time from 8:00 to 9:00 am represents the morning peak hours, whereas the second time from 8:00 to 9:00 pm is marked by light traffic. Total traffic volumes for all roundabout entrances are charted in Fig. 2.

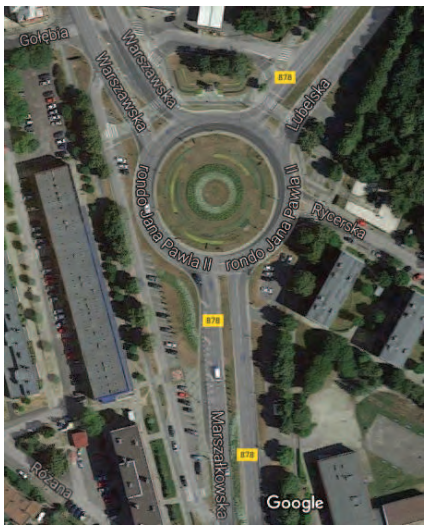

Fig. 1. A view of the selected intersection

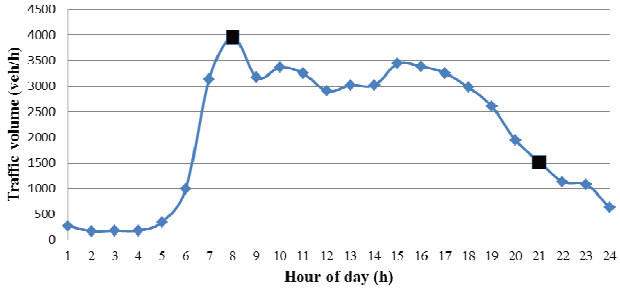

Fig. 2. Aggregate daily traffic volume for selected roundabout at the day of research (black squares means selected part of the day)

2.1. Modelling traffic and related emissions

Models of traffic and exhaust gas emission can be divided by their detailed scales as follows: macroscopic (regional), mesoscopic (local) and microscopic (intersections, street stretches). Whereas, models of exhaust gas emission can be differentiated, according to traffic congestion (average speed, vehicle density), to form the following 3 types: A, B and C. A models require input data for particular road situations defined as speed profiles. The data are generated by B models when emissions processes are modelled. Both A and B models are suitable for micro-level analysis. Whereas C models contain standard driving patterns in their emission model and are suitable for mesoscopic application [11].

PTV Vissim, a microsimulation traffic modelling tool was chosen to estimate emissions at the intersection. Based on the traffic data from Vissim, the emission of toxic exhaust gas components was calculated using TNO Enviver Enterprise. These tools and the models created in them provide reliable data for microscopic emission simulation [1–3, 5]. Additionally, the results obtained were collated with a mesoscopic emission model from COPERT 5 software.

The VERSIT+ emission model, which is used in Enviver software, is a multiple regression model in which the driving cycle of a given vehicle is a variable (A emission model). This model requires that speed profiles are first obtained in Vissim in order to provide a basis for estimation of emission coefficients (g/km) for different vehicle classes [10]. VERSIT+ contains a series of 246 emission model classes, the algorithms of which are appropriately determined for each vehicle category and each type of toxic exhaust gas component. Using the vehicle data, Enviver can calculate types of emissions like CO_2, NO_x and PM10. As opposed to the emission factors derived from the New European Driving Cycle (NEDC), the speed profiles used in this model are representative for the actual road conditions [9]. The emission factors ($E^F_{j,k,l}$) are derived from multiple linear regression in order to find empirical relationships between emissions, speed profiles and dynamic variables [12].

Exhaust gas emissions from road transport [g/h] for a specific exhaust gas constituent from one or more road sections are calculated using this equation [13]:

$$TE_j = \sum_{k,m}(E^F_{j,k,l} * TV_{k,m} * L_m) \quad (1)$$

where: $E^F_{j,k,l}$ – average emission factor [g/km], j – exhaust gas component, k – vehicle class, l – speed profile, $TV_{k,m}$ – traffic volume [vehicles/h], m – road section, L_m – road section length [km].

In the case under study, NO_x and PM10 emissions were calculated in a spatial resolution of 5x5 m using Enviver software. The emissions were estimated for urban conditions, that is, the model allowed for a certain proportion of vehicles which were characterized by increased emission of pollutants in exhaust gas due to the phenomenon of engine cold start.

The duration of Vissim traffic simulation was set to 3600 s. Two classes of vehicle were adopted, namely cars (which made up 80% of all vehicles) and trucks plus buses (20%). The car class was made up of 40% of vehicles with petrol engines, 47% of vehicles with Diesel engines and 13% of LPG-powered vehicles. The average vehicle age for cars was set to 8 years. For the truck and bus class, it was assumed that 82% of the vehicles had Diesel engines and 18% were CNG-powered buses. The average vehicle age for this class of vehicles was set to 9 years. Emission classes for these vehicles are presented in Fig. 3.

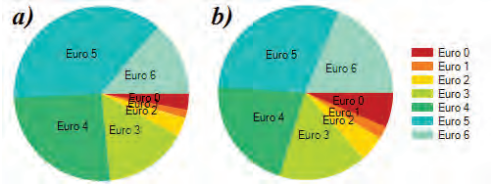

Fig. 3. Emission classes for selected vehicles; a)passenger car's b)trucks and buses

The modelled variants of roundabout intersections are presented in Figures 4 and 5.

Fig. 4. Vissim model of existing two-lane roundabout

Fig. 5. Vissim alternative model of turbo roundabout

The modelled turbo roundabout introduces a modification for Rycerska street: its entrance and exit become wider to include an additional lane. The main direction of the traffic flow in this roundabout is the stretch from Marszałkowska to Lubelska streets for its highest total traffic volume.

The traffic volume data for the individual entrances were set in accordance with the actual values collated in Table 1. Whereas parameters related to the right of way were set in the tool in accordance with the data in Table 2.

Table 1. The traffic volume for selected street entries in selected hours of the day, with the division on the analyzed scenarios

Scenario	Day	Hour	Street entrances	Traffic intensity (veh/h)
A1	18th December 2015	8:00-9:00am	Warszawska	1507
			Marszałkowska	1453
			Lubelska	1000
			Rycerska	100
A2		08:00-09:00pm	Warszawska	462
			Marszałkowska	761
			Lubelska	296
			Rycerska	47
A3	The data as for A1 scenario (optional turbo roundabout)			
A4	The data as for A2 scenario (optional turbo roundabout)			

Scenarios A1 and A2 represent a real road situation that occurred during the measurement of traffic volume in the subject roundabout. Whereas scenarios A3 and A4 are their alternative equivalents to the turbo roundabout option.

Table 2. Priority rules for the simulation

Roundabout type	Lubelska/Marszałkowska streets		Warszawska/Rycerska streets	
	Headway (m)	Critical gap time (s)	Headway (m)	Critical gap time (s)
Two-line roundabout	3.5 (outer lane)	2.7 (outer lane)	2 (outer lane)	2 (outer lane)
	3.8 (inner lane)	3.2 (inner lane)	2.6 (inner lane)	2.9 (outer lane)
Turbo roundabout	3.5	2.7	2 (outer lane)	2 (outer lane)
	–	–	2.6 (inner lane)	2.9 (outer lane)

It should be stressed that the first 5 minutes of the simulation were excluded from the analysis due to insufficient model saturation. The simulation starts with a null number of vehicles, so, a certain phase of saturation of the road network is needed at the beginning. If this "model warm-up" phase were not allowed for, the true road data would not coincide with the data obtained during the simulation [5, 8].

2.2. Assessment of the model

The emission outputs from Enviver were collated with the results from the Computer Programme to Calculate Emissions from Road Transport (COPERT 5). COPERT 5 is a model basing its results on the average speed of the vehicles which have passed through a given stretch of the selected route [7]. It is classified as a C-type emissivity model [11]. It is used primarily for calculation of emissivity for a given region or country. It can also be also as a reference model for other microscopic models. In the subject study, the average vehicle speeds obtained from VISSIM formed the input data for the COPERT model. For the scenarios under study, these data are as follows: A1 – 13.1 km/h, A2 – 34.4 km/h, A3 – 20.7 km/h, A4 – 37.8 km/h.

In summary, Figure 6 shows the overall implementation pattern of the emissivity test procedure for the selected roundabout.

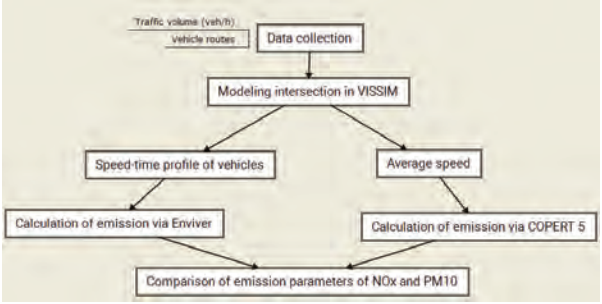

Fig. 6. Diagram of the procedure for selected modelled roundabout scenarios

3. Results of testing

The data needed to determine speed-time profiles for each of the vehicles were obtained from VISSIM and had a time resolution of 5 s. These data were essential for ENVIVER to calculate average vehicle speeds for a grid of with a resolution of 5x5 m. This provided data for speed changes that occur when vehicles enter the roundabout (Fig. 7).

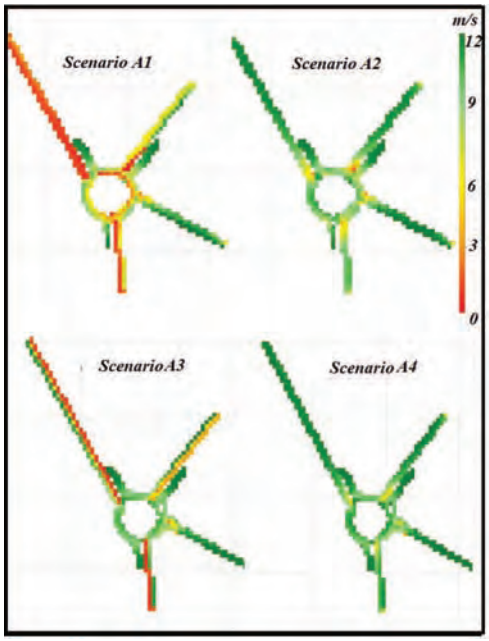

Fig. 7. Resulting average speed of vehicles for considered scenarios

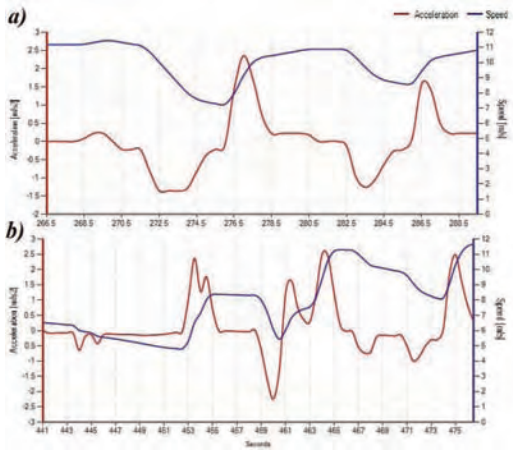

Fig. 8. Speed-acceleration pattern for selected vehicles; a) free flow traffic conditions b)saturated traffic conditions

For example, Figure 8 presents speed and acceleration profiles for vehicles under different road congestion conditions.

From Figure 8b, or the case of severe traffic congestion, it can be seen that vehicles need more time to pass through the same road stretch compared to the case of a low level of traffic congestion (Fig. 8a). This is due to the fact that the vehicles perform more braking and acceleration operations and this in turn translates directly into an increase in harmful emissions. If the passage times for both the cases are collated, it can be seen that the time lengthens by 35% for traffic congestion conditions.

3.1. Results of emission estimation

The impact of low speeds and, hence, of traffic congestion on car emissions are well reflected in microscopic models.

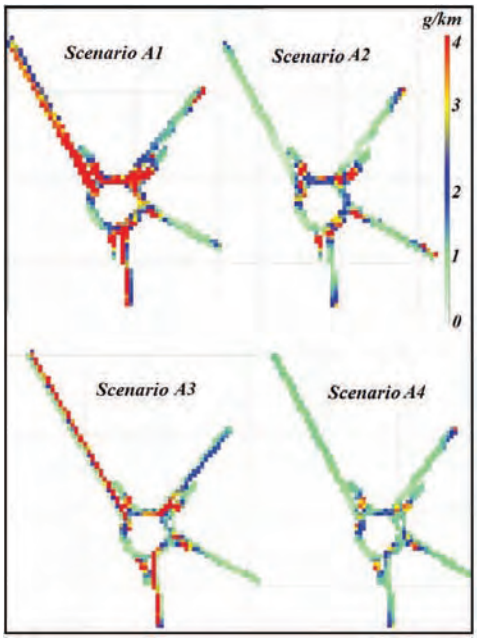

Fig. 9. NO_x emission results for considered scenarios with spatial resolution of 5x5 m

From Figures 9 and 10 it is easy to notice on which intersection access roads the most massive traffic jams take place and how they influence the emission levels for the selected constituents of vehicle exhaust fumes. In places where the emission is marked red and yellow, vehicles move at low speed, stop for a moment and accelerate one by one, thus contributing to increased emissions. This takes place mainly in the case of congestion as in scenarios A1 and A3, in access road stretches with the highest traffic volumes. Whereas scenarios A2 and A4, in which the traffic flow is smooth, have definitely lower emission levels than scenarios A1 and A3. This is directly due to a lower number of vehicles and to the constant speed maintained by them while passing through the intersection, without the need to brake or accelerate suddenly.

The results of total emissions and emission factors for NO_x and PM10 are presented in Fig. 11 and 12. Emissions are lower by approximately 70% for evening hours compared to the morning peak hours for both the exhaust gas components under study.

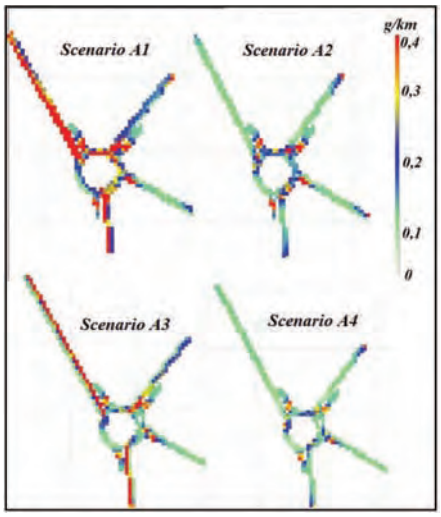

Fig. 10. PM10 emission results for considered scenarios with spatial resolution of 5x5 m

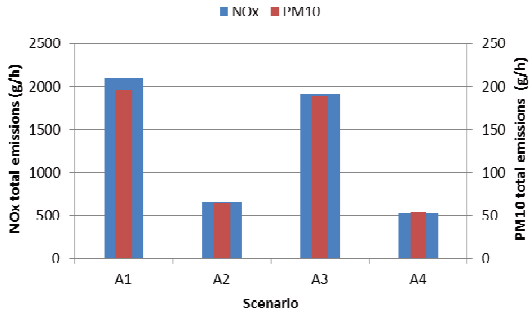

Fig. 11. Total NO_x and PM10 emissions for considered scenarios

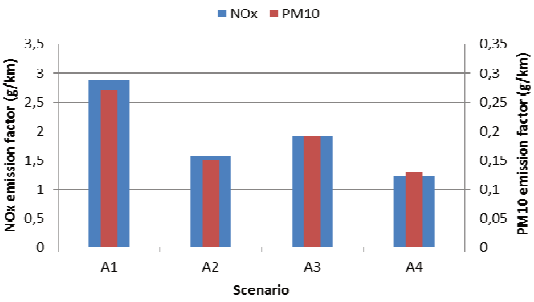

Fig.12. Emission factors for NO_x and PM10 for considered scenarios

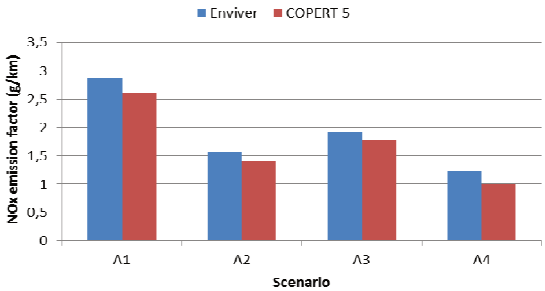

Fig.13. Comparison of Enviver and COPERT 5 emission factors

The results obtained in ENVIVER were compared to the results from COPERT 5 in order to verify them. Figure 13 shows that the NO_x emission outputs from Enviver and COPERT 5 are near to each other. Differences in the emis-

sion calculations as performed by the VERSIT+ model range from 7 to 18% compared to COPERT 5. These two models differ mainly in that VERSIT+ calculates different emission factors for various road situations which are marked by similar average speeds but different dynamics [12]. VERSIT+ uses driving patterns for specific local situations which it takes from Vissim, while COPERT 5 calculates averaged driving patterns. Therefore, Enviver should reproduce micro-level emissions better [3]. The scenarios with severe congestion and high emission levels involve the greatest deviations from the emission outputs.

4. Conclusions

According to the results, the total exhaust gas emission in the area under analysis confirms that the emission significantly changes throughout the day. For the selected exhaust gas components, i.e. NO_x and PM10, the total emission is 3-4 times higher for heavy traffic hours (scenarios A1, A3) compared to the hours outside the peak hours (scenarios A2, A4). It's certainly connected with the traffic volume and on the consequent of road conditions as well. During the morning peak hours, the emission factor for NO_x increases by 35-45%, and for PM10 – by 32-43%.

With regard to the comparison between the existing two-lane roundabout and the alternative option of a modelled turbo roundabout, an increase in average speed by 38% can be noted under morning congestion conditions. This translates into a decrease in the emission of NO_x by 31% and of PM10 by 26% in favour of the turbo roundabout. For the evening time when the traffic is definitely lighter, one can see an increase in average speed by 8% for the turbo roundabout and a decrease in the emission of NO_x by 21%, and of PM10 by 13% against the two-lane roundabout.

The emission values obtained at the micro-scale were also compared to the mesoscopic model in this study. The collation of the NO_x emission factor calculations showed differences ranging from 7 to 18% depending on the scenario. However, these results can be considered satisfactory. Further studies in respect of improvement in the performance of the mesoscopic model should focus on the correction of its calculation algorithms, mainly with regard to emissions other than those from vehicle exhaust systems.

Bibliography

[1] AL ALAMI, Y.R. Application of traffic emission models to the estimation of local pollutant hotspots in South Kensington. *1st Civil and Environmental Engineering Student Conference Energy*. 2012, **11**. Imperial College London.

[2] BIGAZZI, A., VAN LINT, J.W.C., KLUNDER, G. et al. Traffic data for local emissions monitoring at a signalized intersection. *13th International IEEE Conference "Intelligent Transportation Systems (ITSC)"*. Madeira Island, Portugal 2010.

[3] CSIKÓS, A., VARGA, I. Real-time modeling and control objective analysis of motorway emissions. *Proceedings of Ewgt 2012 – 15th Meeting of the Euro Working Group on Transportation*. 2012, **54**.

[4] FRANCO, V., KOUSOULIDOU, M., MUNTEAN, M. et al. Road vehicle emission factors development: A review. *Atmos. Environ*. 2013, **7**.

[5] JAWORSKI, A., LEJDA, K., MĄDZIEL, M. Analiza opóźnienia ruchu drogowego dla wybranych rozwiązań odnośnie pierwszeństwa przejazdu na skrzyżowaniu typu X. *Monografia* pod redakcją naukową Kazimierza Lejdy, Rzeszów 2016.

[6] MAYKUT, N.N., LEWTAS, J., KIM, E., LARSON, T.V. Source apportionment of PM 2.5 at an urban IMPROVE site in Seattle, *Washington. Environ. Sci. Technol.* 2003, **37**.

[7] NTZIACHRISTOS, L., GKATZOFLIAS, D., KOURIDIS, C., SAMARAS, Z. COPERT: a European road transport emission inventory model. *Inf. Technol. Environ. Eng*. 2009.

[8] QUEROL, X., VIANA, M., ALASTUEY, A. et al. Source origin of trace elements in PM from regional background, urban and industrial sites of Spain. *Atmos. Environ*. 2007, **41**.

[9] REXEIS, M., HAUSBERGER, S. Trend of vehicle emission levels until 2020 – prognosis based on current vehicle measurements and future emission legislation. *Atmos. Environ.* 2009, **43**.

[10] SMIT, R., MCBROOM, J. Development of a new high-resolution traffic emissions and fuel consumption model. *Road Transp. Res*. 2009, **18**(4).

[11] SMIT, R., POELMAN, M., SCHRIJVER, J. Improved road traffic emission inventories by adding mean speed distributions. *Atmos. Environ.* 2008, **42**(5).

[12] SMIT, R., SMOKERS, R., RABE, E. A new modelling approach for road traffic emissions: VERSIT+. *Transp. Res. Part D: Transp. Environ*. 2007, **12**(6).

[13] SMIT, R., SMOKERS, R., SHOEN, E., HENSEMA, A. A new modelling approach for road traffic emissions: VERSIT+ LD – background and methodology. *Report 06.ORPT. 016.1/RS, The Hague*. TNO Science and Industry, 2006.

Artur Jaworski, DEng. – Faculty of Mechanical Engineering and Aeronautics at Rzeszów University of Technology.

e-mail: *ajaworsk@prz.edu.pl*

Prof. Kazimierz Lejda, DSc., DEng. – Faculty of Mechanical Engineering and Aeronautics at Rzeszów University of Technology.

e-mail: *klejda@prz.edu.pl*

Maksymilian Mądziel, MSc. – Faculty of Mechanical Engineering and Aeronautics at Rzeszów University of Technology.

e-mail: *mmadziel@prz.edu.pl*

Article citation info:
KARPUKHIN, K., TERENCHENKO, A. The creation of energy efficient hybrid vehicles in the Russian Federation. 2017, **168**(1), 145-148. DOI: 10.19206/CE-2017-123

Kirill KARPUKHIN
Alexey TERENCHENKO

CE-2017-123

The creation of energy efficient hybrid vehicles in the Russian Federation

The paper shows the development of the NAMI Russian State Scientific Research Center associated with advanced research in the field of hybrid vehicles. The stages of design, creation and testing of hybrid vehicles with range extender system. The paper presents the results of bench and road tests of hybrid vehicles with range extender system. The peculiarities of creation and operation of hybrid vehicles for countries with difficult climatic conditions, for example, the Russian Federation.

Key words: *hybrid vehicle, range extender, traction battery, energy efficiency, climatic conditions*

1. Introduction

Individual mobility is a basic need of humans. Growing income goes hand in hand with more individual mobility. In early 2000, we had a total about 750 million vehicle, but in 2016, we have over 1 billion vehicle in the world. Currently most of the world's automotive countries link the solution of a complex ecological safety and problems of energy saving by regulating CO_2 emissions, as well as increasing adoption in the production of hybrid vehicles, which can significantly reduce the pollution on the planet. [1, 2].

According to the European Commission for Transport's forecasts, by 2020 7 per cent of passenger and light commercial transport in Europe is going to have electric drives, by 2030 this figure is going to increase to 31 per cent. The tendency to increase amount of hybrid vehicles and electric vehicles defines extension of geography of their use, inclusive of northern regions with low temperatures and long winters.

2. Main part

Electric transport is an integral part of our lives, but it has several significant shortcomings such as limited mileage on a single charge, the lack of well-developed infrastructure of charging stations, the complexity when operating in conditions of negative temperatures, etc., these disadvantages slow down its promotion in the global markets, especially in countries with difficult climate and long distances between cities. The Russian Federation is a country with a cold climate prevalent in most areas: average annual temperatures in the Northern and Central regions are in the range 0...–22°C that you can see on the temperature map presented in Figure 1.

While electric vehicle shall be operated over the full temperature range of the region in which it is used, the critical factor is the lowest temperature. The average winter temperature in Russia is Krasnodar –2°C, Moscow –6°C, Irkutsk –23°C. While in Moscow, winter temperatures can be below –30°C, and in Irkutsk – below –50°C (Fig. 2). Lithium-ion battery system can operate in a rather wide range of temperatures, but there are extrema, which is worth remembering all the time, especially in countries with cold climate and a lot of time zones, such as Russia.

In the Northern regions of Russia, the annual duration of the period of negative temperatures can reach 250-270 days. Electric and hybrid vehicles doesn't have the capability of temperature control of the traction batteries for their normal functioning in such conditions of temperature that negatively affects the durability of the traction batteries.

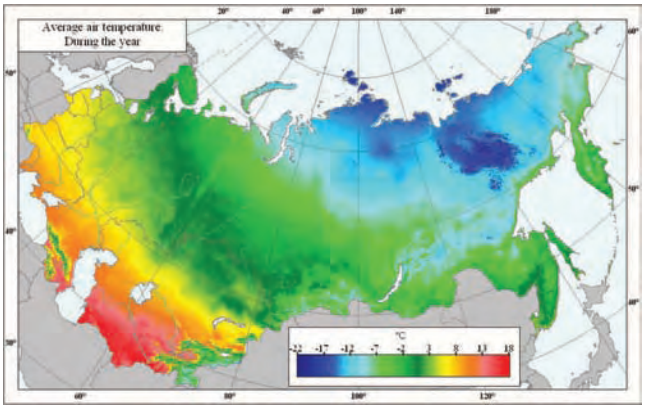

Fig. 1. Average air temperature during the year in Russia

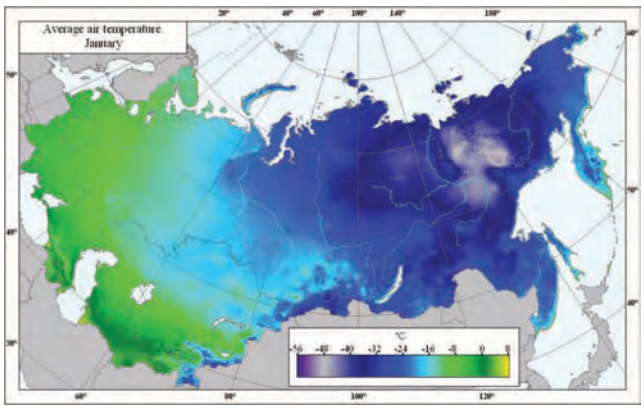

Fig. 2. Average minimum air temperature during the year in Russia

For example, in the instruction manual of the electric vehicle Tesla Model S indicate that to save battery you must fulfill the following conditions: the traction battery of an electric vehicle should be kept solely at zero temperature; avoid idle running car (30 minutes) in the cold; do not operate the electric vehicle at temperatures below –15°C; to warm up the electric vehicle after a long idle in the cold when you connect to the network and not from the battery. This determines the relevance of studying the properties of battery systems included in vehicles on electricity, at low temperatures.

Modern battery systems of hybrid and electric vehicles are designed, as a rule, on the basis of lithium – ion batteries of various types of electrochemical systems. Negative consumer characteristics of all lithium batteries is that they are very poorly adapted to sub-zero temperatures. They usually allow you to discharge at temperatures below –10...–20°C (reduction of the capacity and output of current), a charge – only at positive temperature.

At temperatures below +5°C, the charge current must be lowered. The charge is not valid when the temperature is below 0°C, in this case the external changes are not observed, but the chemical processes necessary for the correct operation of the battery will be broken, which can lead to permanent damage to the battery. During charging, at this temperature, the particles of lithium metal can be deposited on the anode. This coating of deposited lithium will not be lost when cycles of charge/discharge. Batteries with such a coating become less fault tolerant and can fail under vibration. [3–6].

In the world, developed and patented a large number of technical decisions concerning control systems and stabilization of the thermal state of the traction battery, having in its composition the elements of heating and cooling. In such devices are mainly used liquid temperature control system. Their disadvantages lie in the structural complexity. In addition, an emergency exists the possibility that the working fluid in the cavity of the battery container.

Frequently used air system the destination. Their design is virtually indistinguishable from liquid systems. The air system can be considered more promising, as the large heat capacity of the coolant compared to air in this case loses its relevance, given the relatively small magnitude of energy flow per unit volume, with temperature control of the battery.

Recently widely, especially in China, is under development that uses as the working parts of the thermostat thermoelectric probes such as Peltier elements. Such devices simplify the design of the battery have a higher energy performance.

As already mentioned, one of the key drawbacks that prevent widespread use of electric vehicles is the limited range of their actions. The existing problem is difficult to solve by increasing the capacity of the battery, as it leads to increase the cost of the vehicle (the vehicle) and weight gain, which in turn increases the energy consumption for overcoming the motion resistance forces. Besides the big battery has a long charge time (up to 7-8 hours). These shortcomings imposed on the climatic features of our country, exacerbate the problems hampering the popularization of electric vehicles.

The world's leading vehicle manufacturers and research organizations of the automotive industry, knowing about these problems, focus on the establishment of various systems of hybrid and electric vehicles, improvement of control algorithms.

Specialists of NAMI Russian State Scientific Research Center was developed an experimental model of a hybrid vehicle with a Range Extender system and innovative system of temperature control (Fig. 3) [7, 8]. As the combined power on this vehicle used the engine-generator set for extended range electric vehicles that don't have rigid kinematic connection with the drive shaft of the vehicle, in the world known as the Range Extender.

The Range Extender installed into the experimental prototype of the motor vehicle consists of a small operating volume internal combustion engine and electrical machine operating in a generator mode. This unit is experimental and allows to refine an algorithm and work out a method of definition of the Range Extender required capacity and energy capacity of the accumulator module, which will allow to use different variants of their arrangement on chassis of various class hybrid vehicles. Range Extender comprises the engine and the 20 kW/270 V generator.

Table 1. Technical characteristics of the Range Extender

Fuel type	Gasoline ≥ 90
Oil type	10W/30 SAE
Nominal voltage (DC)	270V DC
Maximum capacity [kW]	20 kW
Fuel efficiency [min]	0.5 l/kW·h
Range extender dimensions [mm]	667x451x698

The Range Extender has a transverse position in the vehicle's luggage compartment, on a place of the removed spare wheel well (Figures 4, 5).

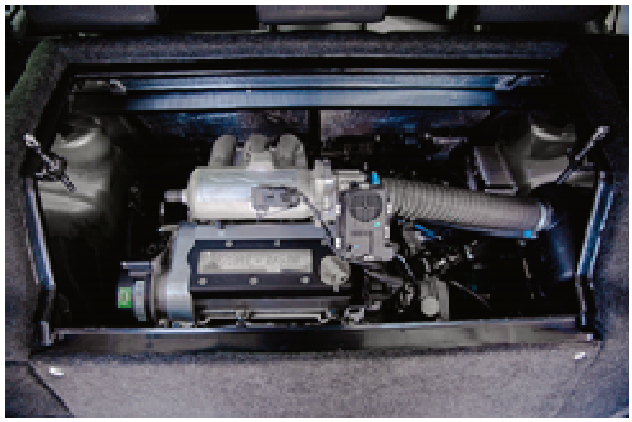

Fig. 3. Hybrid vehicle with Range Extender

The Range Extender is separated from the passenger compartment of the vehicle by special partitions equipped

with thermal insulating and noise absorbing materials. Control over the combined energy unit is performed via the information controlling interaction of the vehicle's electric traction drive, consisting of the electric machine, the invertor and the accumulator battery, and the Range Extender. The system's software includes the control over combined energy unit algorithm that was developed in MATLAB/Simulink and AVL Cruise, preliminary tested on a mathematical model of the vehicle with the combined energy unit (software-in-the-loop), as well as utility driver programs that perform data exchange and interaction of hardware and software parts of the control system.

Components composition and information connections of the combined energy unit control system are shown on the Figure 4. The arrows indicate directions of the information connections, above the arrows there are names of the used information protocols (RS-232, CAN). The combined energy unit control algorithm is in the controller that interacts with components of the electric traction drive control system – the electric machine's invertor and the Battery Management System (BMS), as well as with the Range Extender control unit. The control algorithm developed in the MATLAB/Simulink and AVL Cruise environment is translated into the C-language code, compiled and "flashed" into the combined energy unit controller. The control system included into the controller uses for its operation feedback signals that come from the combined energy unit's components via their control units.

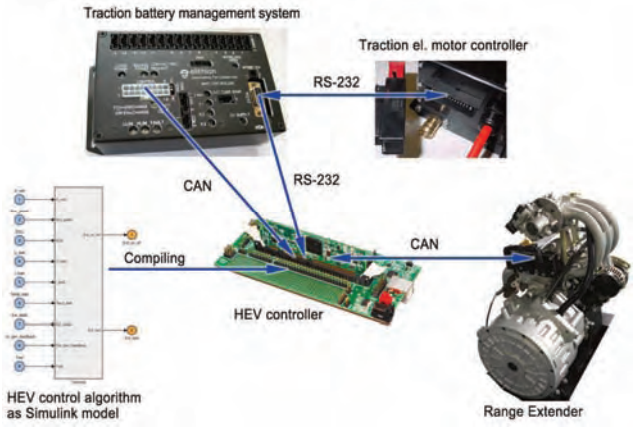

Fig. 4. Control system structure

For hybrid vehicle with Range Extender has been developed a system of accumulation and storage of electrical energy with innovative thermostatting's systems (Fig. 5).

The system temperature control consists of 26 of the battery cells placed in an airtight container. The container has an inner insulating coating and built-in temperature control device, built on two thermoelectric Converter Peltier and two SPAL fans. The system thermostat is powered by the onboard battery voltage of 12 V. In case of temperature increase in the battery pack above +20°C, at block enable control signal enable voltage. The signal U± is absent. Turn on the fan and the Peltier element operates in a cooling mode. The inclusion continues until the temperature drops below +20°C. If in conditions of low external temperatures the temperature of the battery decreases below +10°C, the control unit battery are formed signals enable voltage; U± and the Peltier element is switched on in heating mode. The advantage of Peltier element is small in size, the absence of any moving parts, as well as gases and liquids. Turning the direction of the current, perhaps as a cooling and heating – this allows for temperature control when ambient temperature is both above and below the temperature of the thermostat. Was carried out aerodynamic and thermal calculations temperature control system. It is possible to find the optimal layout of the battery module. The task of aerodynamic calculation was solved with the use of a complex of programs allowing to carry out solid modelling, and the integration of the movement of the air flow by the finite element method. Figure 6 shows how the airflow near the fans are distributed without significant turbulence, which minimizes the effect of surge.

Fig. 5. General view of the engine compartment with the developed system of accumulation and storage of electrical energy

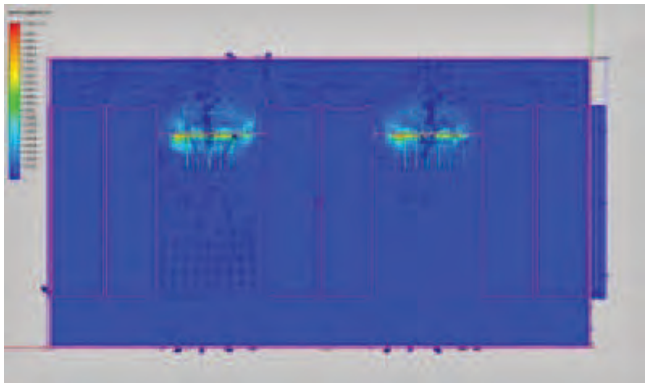

Fig. 6. Visualization of airflow near the fans

In the summer of 2016 hybrid vehicles with a Range extender system underwent comprehensive testing in the test Center "NAMI" (Fig. 7, 8).

The main results of the tests:

– maximum speed of the vehicle 134 km/h;
– regenerative braking from a speed greater than 40 km/h;
– emissions vehicle correspond to ecological class 5 (UNECE regulation No. 83);
– decrease in fuel consumption 12...14% in comparison with existing analogues hybrid vehicle;
– the energy content of the traction battery 23 kW/h;

– nominal voltage of the traction battery 305 V;
– the thermostating system ensures a working temperature range up to +12...+18°C at an external temperature of –40...+50°C.

Fig. 7. Fragment of bench tests

Fig. 8 Fragment tests in a heat chamber

3. Conclusions

1. Claimed by the manufacturers of electric performance, in particular the reserve and the required charging time, often not focused on countries with negative temperatures, and the middle Eastern climate, with excellent road and charging infrastructure and quality public services.
2. The results of the study allow to formulate the main aspects of ensuring the effective functioning of the battery systems of hybrid cars and electric vehicles in freezing conditions, so operation is not protected from the ambient temperature below +5°C battery systems are not desirable, as leading to accelerated degradation of the batteries.
3. Vehicles, having in its composition a heat-insulated battery, it is allowed to leave at negative external temperatures for a limited time, decreasing with decreasing temperature.
4. When you implement independent heating of the battery, for example, by using thermoelectric converters Peltier, the daily power consumption will be at –30°C of at least 1.6 kW·h. Therefore, if the time long-term Parking not known, hybrid and electric vehicles must be connected to the stationary power grid or hybrid vehicles to provide periodic startup to warm the engine and recharge the battery.
5. Developed temperature control system of the electric vehicle meant to be operated in difficult climatic conditions. The practical application of the developed principle of temperature control allows to provide the function of the battery in the most favorable temperature range 20–30°C, which in turn provides increased service life of battery is not less than 10–20%. The developed system thermostat will ensure the temperature within – 40 to +50°C

Bibliography

[1] International Energy Agency. Hybrid and electric vehicles. The electric drive delivers. 2015.

[2] MILLER, J. Propulsion systems for hybrid vehicles 2nd Edition. UK: The Institution of Engineering and Technology, 2010, 593.

[3] PESARAN, A. Battery thermal management in EVs and HEVs: issues and solutions. *National Renewable Energy Laboratory.* 1617 Cole Blvd. Golden, Colorado 80401. Advanced Automotive Battery Conference, Las Vegas, 2010.

[4] KARPUKHIN, K., TERENCHENKO, A., SHORIN, A., BAKHMUTOV, S., KURMAEV, R. Temperature control of the battery for hybrid or electric vehicle. *Biosciences Biotechnology Research Asia.* 2015, **12**(2), 1297-1301.

[5] KAZUKI, S., MASATOSHI, K., YOSHIYUKI, H. Hybrid vehicles, electric vehicles, fuel cell electric vehicles. Japan Automobile Research Institute, 2013, 11-13.

[6] WILEY, J. & Sons, Ltd. Encyclopedia of automotive engineering, 201, 2696.

[7] BAKHMUTOV, S., KARPUKHIN, K., TERENCHENKO, A., KURMAEV, R., KONDRASHOV, V., SKLYARINSKII, S. Production of the electric vehicle experimental prototype with the range extender. *Biosciences biotechnology research Asia.* 2015, **12**(Spl. Edn.), 533-538.

[8] KULIKOV, I., SHORIN, A., BAKHMUTOV, S., TERENCHENKO, A., KARPUKHIN, K. A Method of powertrain's components sizing for a range extended electric vehicle. *SAE Technical Paper* 2016-01-8096, 2016.

Kirill Karpukhin, DEng. – Department "Hybrid vehicle" NAMI Russian State Scientific Research Center.

e-mail: *K.Karpukhin@nami.ru*

Alexey Terenchenko, DEng. – Centre "Power Units" NAMI Russian State Scientific Research Center.

e-mail: *terenchenko@nami.ru*

Article citation info:
IDZIOR, M., CZAPLIŃSKI, E. Environmental aspects of the impact of the technical condition of motor vehicles on environmental pollution. *Combustion Engines*. 2017, **168**(1), 149-152. DOI: 10.19206/CE-2017-124

Marek IDZIOR
Edward CZAPLIŃSKI

CE-2017-124

Environmental aspects of the impact of the technical condition of motor vehicles on environmental pollution

The article presents selected aspects related to the influence of toxic components of exhaust gases from vehicle transport vehicles on environmental pollution and human health. The paper describes the quantitative structure of motor vehicles that are operating in Poland. The structure of used passenger cars that were imported from abroad and first registered in Poland was presented. The procedure for periodic control tests in exhaust emission diagnostic stations is also described. The results of the study allowed to distinguish a group of vehicles that did not meet the limits of pollution established by the legislator.

Key words: *exhaust, operation, research, cars, environment*

1. Aspects of environmental pollution by motor vehicles

The environmental pollution caused by motor vehicles is closely linked to the development of technology, and the technological revolution that has been observed for several decades in the world has led to an increase in the demand for energy. This triggers dangers, first of all the effects of burning all kinds of fuels. In the course of combustion, chemical compounds that are inactive for the environment, human life and animals are formed. Emissions to the atmosphere of large amounts of gases, mainly CO_2, produce a greenhouse effect resulting in a steady increase in the average temperature of the ecosphere and associated undesirable meteorological phenomena [1]. The industrial activity of society is a source of influence for the change of the natural environment, the fabrication and development of the manufacturing process results in the emergence of a new category of environmental influences, not only quantitatively but qualitatively. The development of new manufacturing processes, as a result of technical progress, has become the source of previously unknown environmental effects [2]. Transport in Europe is responsible for harmful levels of air pollutants and a quarter of greenhouse gas emissions in the European Union. According to a recent report by the European Environment Agency, many of the resulting environmental problems can be resolved by stepping up efforts to meet the new objectives of the European Union. Although air pollution has decreased in the last two decades, it is still a serious problem in many areas. "European standards" for vehicles did not reduce NO_2 emissions to levels set by law, although they generally contributed to significant improvements in air quality [3]. People living around high intensity roads are particularly exposed to excessive levels of pollution in the air. In 2010. The NO_2 level, in excess of the legal restrictions, was registered in 44% of roadside monitoring stations. The concentration of PM10 dust in these places exceeded the limits of 33%. These impurities have a direct effect on cardiovascular, lung, liver, spleen and blood [4].

Motor vehicles powered by internal combustion engines have the effect of polluting the atmosphere by emitting harmful substances such as carbon monoxide, hydrocarbons, nitrogen oxides, solids, and substances in low concentrations, such as aldehydes, Sulfur compounds, phosphorus and others. Substances that pollute the atmosphere are: engine exhaust gases, engine crankcase and fuel supply system [5].

Fig. 1. Air pollution in urban agglomerations [4]

2. Structure of motor vehicles in Poland

In Poland, in the recent period of time, along with the economic growth, the number of motor vehicles in continuous use increased. In December 2015, 27409106 units were registered in Poland. [7] All vehicles, trucks, buses, motorcycles and more (Fig. 2). The largest group of passenger cars is 20723423 [7], which accounts for 75.6% of the overall condition of vehicles in Poland (Fig. 3). There is a problem of ensuring proper technical condition of vehicles that are in service for many years. The average age of passenger cars in operation in December 2015. In Poland it was 15.5 years [6].

Their technical condition is checked once a year in diagnostic tests during compulsory control tests. Over the past period, the number of vehicles registered per 1000 inhabitants has risen to 653 in Poland. The highest growth was achieved in passenger cars, reaching 502 copies [6].

Most of the vehicles that are currently in service were not registered for the first time as new in the country, were used abroad and then imported to Poland. In 2003year 35736 units were imported, and in subsequent years, the number of imported cars increased significantly to an average of 700000 units per year, the most imported. In December 2008years

1103970 pcs. Until December 2015 the number of imported motor vehicles was 94522717 pieces [6].

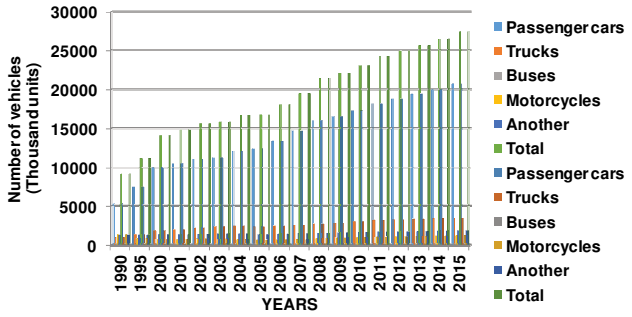

Fig. 2. Motor vehicles registered [7]

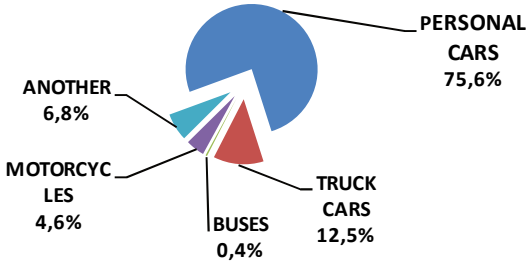

Fig. 3. Registered vehicles 2015 [8]

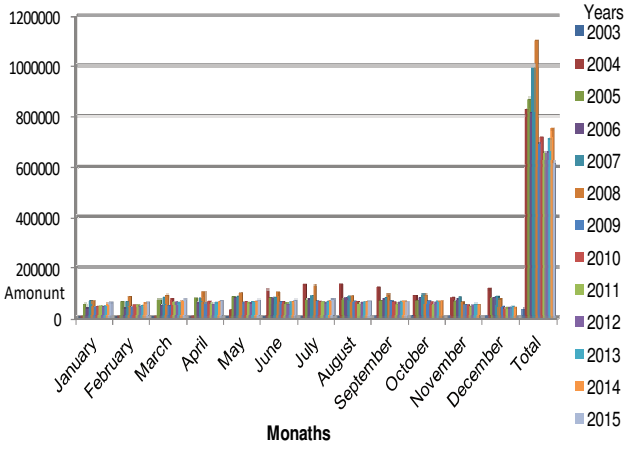

Fig. 4. Structure of used imported passenger cars [6]

3. Vehicle inspection in diagnostic stations

Existing legal regulations aim at guaranteeing road traffic safety participants only by vehicles that comply with accepted technical and safety standards.

Fig. 5. Diagnostic station [9]

Table 1. Levels of gaseous pollutants and air excess coefficient λ [12]

Lp	Vehicle	Engine speed	CO content in% volume of exhaust gas HC in ppm (particles per million) and λ for a vehicle						
			Until Sept. 1986	From 1 October 1986 to 30 June 1995	From 1 July 1995 to 30 April 2004			Since May 1 2004	
1	2	3	4	5	6	7	8	9	10
			CO	CO	CO	CH	λ	CO	λ
1	Motorcycle	Idle	5,5	4,5	4,5	-	-	*4,5*	-
2	Another motor vehicle	Idle	4,5	3,5	0,5	100	-	*0,3*	-
		2000 min^{-1} to 3000 min^{-1}	-	-	0,3	100	0,97-1,03	*0,2*	*0,97-1,03*

Fig. 6. Emission control [10]

Technical tests of vehicles are performed at the Vehicle Inspection Stations and consist of verifying that the vehicle meets the technical specifications of the regulations [12]. Measurement of gaseous emissions is carried out using a device designed to measure the concentrations of carbon monoxide (CO), carbon dioxide (CO_2), hydrocarbons (CH), oxygen (O_2), and lambda (λ).

Fig. 7. Gasbox Autopower emission control device [10]

Table 2. Gasbox Autopower technical specification [10]

Parameter	Value
Dimensions	460 x 200 x 250 mm
Weight	9 kg
Power supply	115–230 V
Power consumption	80 W
Control system	ETS lub ID < 4E
Technology	NDIR
Response time	< 15 s
Warm-up time	do 60 s

3.1. Measurement execution

Tests were carried out at the Vehicle Inspection Station on a randomly selected group of vehicles equipped with SI petrol engines fueled with petrol to determine the concentrations of the toxic exhaust gases of the used vehicles. The analysis was made according to the year of manufacture and mileage, which is the emission limit for engines mounted on vehicles. Concentration measurements were made at the gas emission test site, which is part of the compulsory equipment of the Vehicle Inspection Station [12]. Exhaust gas emission measurement was performed when the engine was heated above 70°C for engine oil and above 80°C for the coolant. The exhaust gas analyzer was introduced into the engine's exhaust system immediately before the measurement at a depth of at least 30 cm. The engine's crankshaft rotational speed was maintained for more than 15 seconds and then lowered to idle speed [12].

3.2. Findings

The test results presented [11] were made on a 120 vehicle group during mandatory inspection at a selected vehicle inspection station (SKP). Figure 9 shows the results of the measurement of the carbon monoxide (CO) content of exhaust gases from the engine, Made on low engine crankshaft rotation around 1000 rpm. The research shows that vehicles that were manufactured before 1995 do not meet the required pollution limits of about 36%, produced after 1995 does not meet about 30%, and vehicles that were produced after 2004 do not meet the requirements in about 10%.

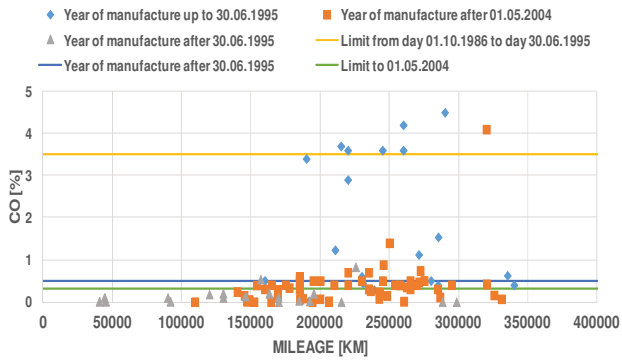

Fig. 8. CO test at idle [11]

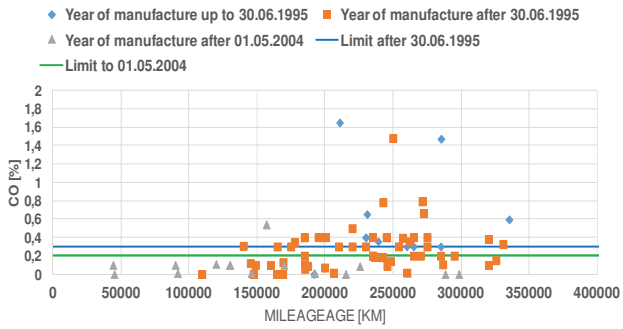

Fig. 9. CO study at elevated speed [11]

Figure 10 shows the test results (CO), which were made at elevated engine revolutions (2000-3000 rpm). Research shows that groups of vehicles that were produced after 1995 do not meet the required level of gaseous pollutants in about 28% while vehicles produced after 2004 in about 5%.

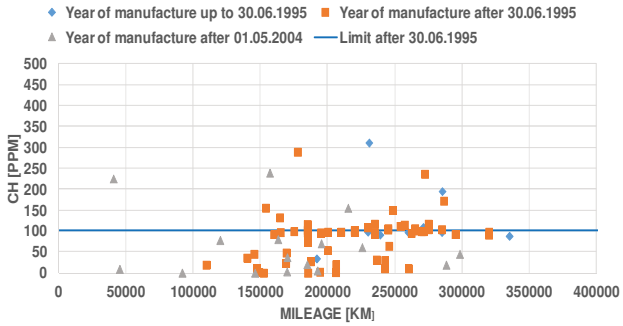

Fig. 10. Examination HC at idle [11]

The results of hydrocarbon (HC) research shown in Fig. 11 were made only for the group of vehicles that were produced between 1995 and 2004, as only this group of vehicles is subject to mandatory testing (HC). The research was done at a low crankshaft engine speed of around 1000 rpm, from the group of vehicles about 30% did not meet the requirements.

Hydrocarbon test at elevated engine crankshaft speed 2000-3000 rpm (Fig. 12). The research showed that a group of vehicles that do not meet the requirements is about 15%.

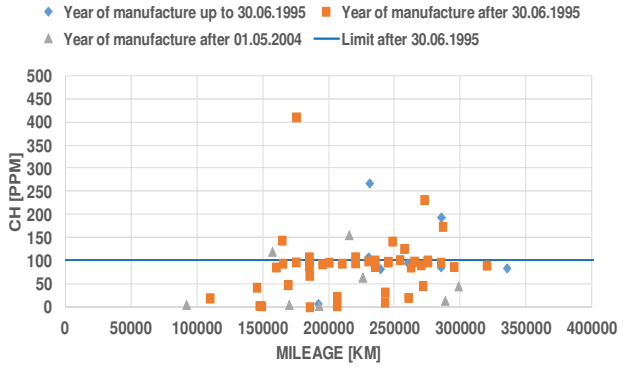

Fig. 11. HC test at elevated speed [11]

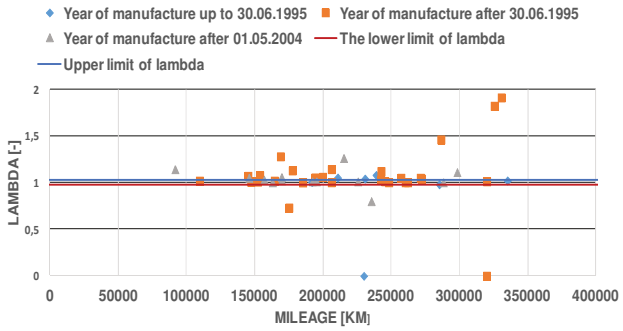

Fig. 12. Lambda study at idle [11]

The results of the measurement of the excess air ratio (lambda) are shown in Fig. 13. The tests were performed at low engine crankshaft speed of about 1000 rpm. The group of vehicles that were produced after 1995 did not meet the emission requirements in about 26%.

The measurement of the excess air ratio (lambda) was made at an increased engine speed (2000-3000 rpm). Results from the research they represent a group of vehicles manufactured after 1995 that do not meet the requirements of about 24% and vehicles manufactured after 2004 do not meet the required limits in about 5%.

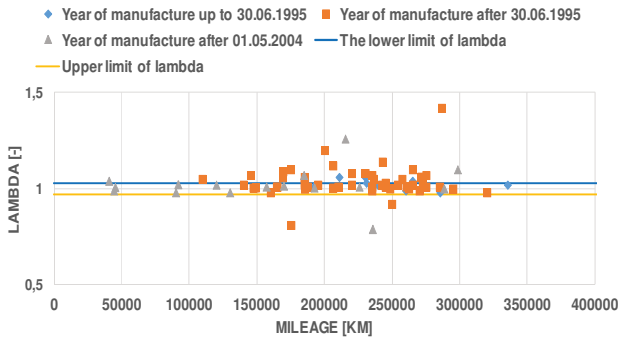

Fig. 13. Lambda study at elevated speed

4. Conclusion

The analysis of the number of vehicles in use in Poland shows that over 70% is over 10 years old. The average age of vehicles in 2015 was 15.5 years old. In the period from 2003 to 31 December 2015, 945,227 used cars were imported to the country, the average age brought in 2016 was about 12 years. During the periodic technical studies carried out, it has been shown that a significant proportion of the vehicles in service are not able to meet the required emissions limits. The research shows that the largest number of vehicles that do not meet emission limit values have been manufactured before 1995. The reason for not meeting the requirements of emission limit values for gas pollutants is too long car life and low technological advances of fuel supply systems and lack of modern exhaust aftertreatment systems.

Nomenclature

SI spark ignition engine
CO carbon monoxide
CH hydrocarbons
CO_2 carbon dioxide

Bibliography

[1] MERKISZ, J., PIELECHA, J. Emisja cząstek stałych ze źródeł motoryzacyjnych. *Wydawnictwo Politechniki Poznańskiej* 2014.
[2] JABŁOŃSKI, J. Technologie „zero emisji". *Wydawnictwo Politechniki Poznańskiej* 2011.
[3] www.eea.europa.eu/pl/pressroom/newsreleases/zanieczyszczenia związane z ruchem samochodowym 2015.10.24.
[4] www.eea.europa.eu/pl/pressroom/newsreleases/wielu-europejczykow-jest-nadal-narazonych 2015-10-24
[5] BIELACZYC, P., MERKISZ, J., PIELECHA, J. Stan cieplny silnika spalinowego a emisja związków szkodliwych. *Wydawnictwo Politechniki Poznańskiej* 2001.
[6] Opracowano na podstawie www.samar.pl 2016-02-14.
[7] Opracowanie własne na podstawie GUS – wyniki działalności 2016.
[8] www.pzpm.org.pl/Rynek-motoryzacyjny/Park-pojazdow-zarejestrowanych 2016.01.13.
[9] www.wsop.pl 2017.01.03.
[10] gazeo.pl/ 2017.01.14.
[11] Opracowanie na podstawie badań własnych w Stacji Diagnostycznej.
[12] Rozporządzenie Ministra Transportu, Budownictwa i Gospodarki Morskiej z dnia 26 czerwca 2012r. Dz.U. 2012.996 ze zmianami.

Prof. Marek Idzior, DSc., DEng. – Faculty of Machines and Transport at Poznan University of Technology

e-mail: *Marek.Idzior@put.poznan.pl*

Edward Czapliński, MSc. – Faculty of Machines and Transport at Poznan University of Technology

e-mail: *Edward.Czaplinski@put.poznan.pl*

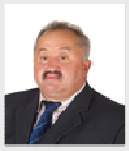

Article citation info:
OPALIŃSKI, M., TEODORCZYK, A., KALKE, J. The closed-cycle model numerical analysis of the impact of crank mechanism design on engine efficiency. *Combustion Engines*. 2017, **168**(1), 153-160. DOI: 10.19206/CE-2017-125

Marcin OPALIŃSKI
Andrzej TEODORCZYK
Jakub KALKE

CE-2017-125

The closed-cycle model numerical analysis of the impact of crank mechanism design on engine efficiency

The research presents a review and comparison of different engine constructions. Investigated engines included crankshaft engines, barrel engine, opposed-piston engines and theoretical models to present possible variations of piston motion curves.

The work comprises also detailed description of a numerical piston engine model which was created to determine the impact of the cycle parameters including described different piston motion curves on the engine efficiency. Developed model was equipped with Wiebe function to reflect a heat release during combustion event and Woschini's correlation to simulate heat transfer between the gas and engine components.Various scenarios of selected engine constructions and different working conditions have been simulated and compared. Based on the results it was possible to determine the impact of different piston motion curves on the engine cycle process and present potential efficiency benefits.

Key words: *piston motion, engine, simulation, efficiency, opposed*

1. Introduction

Most of the recent piston engines which are used in all types of business (automotive, aviation, marine and power) are presenting typical crankshaft mechanism where piston is connected to the crank shaft through a piston rod. Some of the constructions (e.g. RND 105 marine engine) includes additional connecting rod between the piston rod and crank shaft in order to decrease the piston side force but this design does not differ significantly from the first one in regards to the piston motion curve. Apart from that construction more and more companies are interested in new piston engine constructions. Most remarkable designs are those which are based on the opposed-piston (OP) engine concept. This design in general may provide reduced fuel consumption or increased power-to-weight ratio.

There are six main types of the OP engines [1]:

1. Crankless free piston engine
2. Single Crankshaft engines
3. Double Crankshaft engines
4. Multi Crankshaft engines
5. Rotary engines
6. Barrel engines

All of those constructions may be additionally divided for subtypes since there are different variants of the joints which can be applied for those engines.

This work focuses on the impact of different constructions on the piston motion. Different piston motion have impact on the local piston speed and thus the heat transfer. Also the different piston motion result in the different pressure profile, pressure derivative and therefore efficiency and other factors. Eight different construction have been selected to analyze the effect of different crank mechanism designs on the engine efficiency.

2. Review of different engine constructions

Selected engine construction for the analysis includes: typical crank shaft mechanism (STDE), crank shaft mechanism with added cam rod (EE), barrel engine (BE), single shaft opposed-piston engine (SSOP), single shaft OP engine with phasing (SSPOP), double shaft OP engine (DSOP), opposed piston barrel engine (BEOP) and the elliptical shape rotating cylinder (ERCOP). For each construction a piston motion equation was presented in subchapters 2.1–2.8.

2.1. Traditional crank shaft mechanism (STDE)

This design is world wide spread in all types of industries as it was stated at the beginning of the work. This construction will be used as the baseline for comparison purposes.

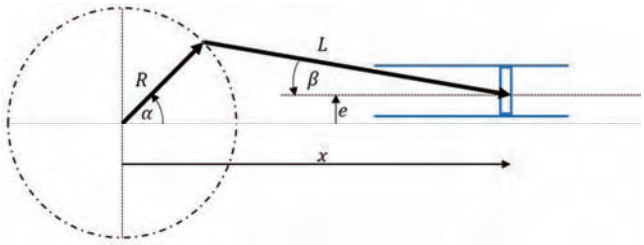

Fig. 1. STDE engine scheme

The equation for piston movement is as follows [2, 3]:

$$x = R\left(\cos\alpha + \frac{1}{\lambda}\sqrt{1-(\lambda\sin\alpha-\mu)^2}\right) \quad (1)$$

where: x – piston location, R – distance between crankshaft axis and piston rod crankshaft joint, L – length of the piston rod, α – crankshaft angle (CA), λ – is the R/L ratio, μ – is the e/L ratio.

The piston stroke may be directly calculated using following equation:

$$s = R\left(\sqrt{\left(\frac{1}{\lambda}+1\right)^2-\left(\frac{\mu}{\lambda}\right)^2}-\sqrt{\left(\frac{1}{\lambda}-1\right)^2-\left(\frac{\mu}{\lambda}\right)^2}\right) \quad (2)$$

2.2. Crank shaft mechanism with cam rod (EE)

This model of the engine was proposed by Rychter and Teodorczyk in 1985. The main advantage of this construction was variable compression ratio. The idea of this engine was to introduce additional eccentric rod between the crankshaft and piston rod with possible rotational move-

ment during engine work. The concept was analyzed for different relative rotational speeds between the crankshaft and eccentric rod [3–5].

1. $\omega_{rod} = \omega_{crankshaft}$
2. $\omega_{rod} = \pm\frac{1}{2}\omega_{crankshaft}$
3. $\omega_{rod} = \pm\omega_{crankshaft}$

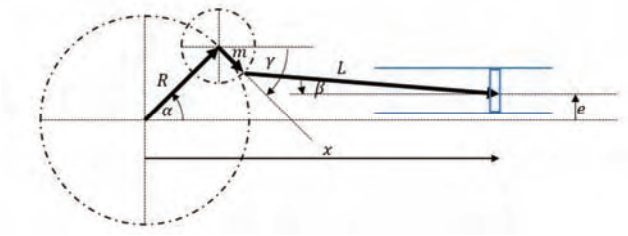

Fig. 2. EE engine scheme

For this engine the the piston motion curves is represented by following equation:

$$x = R\left(\cos\alpha + \frac{\delta}{\lambda}\cos\gamma + \frac{1}{\lambda}\sqrt{1-(\lambda\sin\alpha - \delta\sin\gamma - \mu)^2}\right) \quad (3)$$

where: m – length of the eccentric rod, δ – is the m/L ratio, other parameters are the same as for the STDE.

2.3. Barrel engine (BE)

The barrel engine, known also as axial engine, is a construction where cylinders are parallel to the crankshaft. This construction may be realized by cam, swash plate or wobble plate.

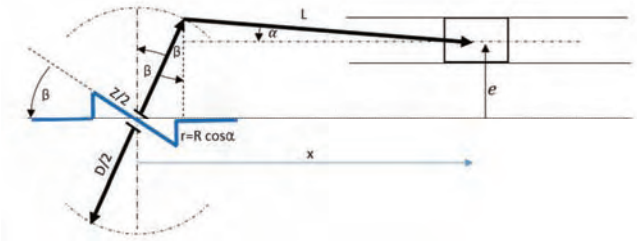

Fig. 3. BE engine scheme

Derived equation for the piston movement is expressed by the following formula:

$$x = \frac{DR\cos\alpha}{Z} + L\sqrt{1-\left(\frac{\frac{D}{2}\sqrt{1-\left(\frac{2R\cos\alpha}{Z}\right)^2}-e}{L}\right)^2} \quad (4)$$

where: Z – length of the crank, D – plate diameter, R – crank radius, e – distance between shaft axis and cylinder axis.

The stroke of the engine is represented by the formula:

$$s = 2\frac{DR}{Z} \quad (5)$$

2.4. Single shaft opposed-piston engine (SSOP)

The construction of SSOP engine reaches XIX century [1]. Single crankshaft is connected to two pistons through two crank rods with different lengths. The longer rod provides pulling force after combustion while the shorter rod pushes in the same time. This ensures well balanced design. Recently that type of engine construction is developed by the Ecomotors company [6].

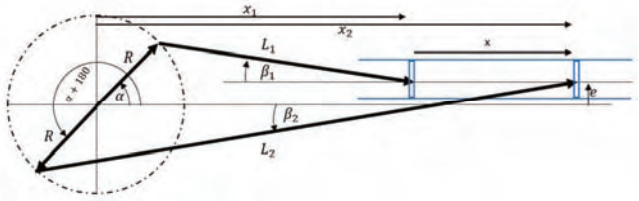

Fig. 4. SSOP engine scheme

The closed gas length is described by the following formula:

$$x = s - R\left(\frac{1}{\lambda_2}\sqrt{1-\lambda_2^2(\sin\alpha+\epsilon)^2} - 2\cos\alpha - \frac{1}{\lambda_1}\sqrt{1-\lambda_1^2(\sin\alpha-\epsilon)^2}\right) \quad (6)$$

where: λ_1, λ_2 – are ratios of $\frac{R}{L_1}$ and $\frac{R}{L_2}$ respectively, ϵ – is a ratio of $\frac{e}{R}$, other parameters are the same as for the STDE.

2.5. Single shaft opposed-piston engine with phasing (SSPOP)

This engine model is a derivative of the previous one. The concept provides additional geometrical parameters like different radii of the crankshaft (R_1, R_2) and angle shift between the cranks Δ.

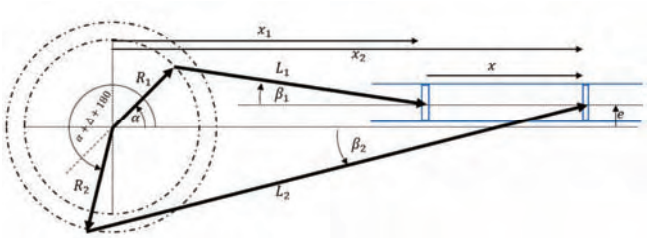

Fig. 5. SSPOP engine scheme

The equation for the captured gas length is:

$$x = s - R_2\left(\frac{1}{\lambda_2}\sqrt{1-\lambda_2^2(\sin(\alpha+\Delta)+\epsilon_2)^2} - \cos(\alpha+\Delta)\right) - R_1\left(\cos\alpha + \frac{1}{\lambda_1}\sqrt{1-\lambda_1^2(\sin\alpha-\epsilon_1)^2}\right) \quad (7)$$

where: λ_1, λ_2 – are the ratios $\frac{R_1}{L_1}$, $\frac{R_2}{L_2}$ respectively, ϵ_1, ϵ_2 – are the ratios $\frac{e}{R_1}, \frac{e}{R_2}$ respectively.

2.6. Double shaft opposed-piston engine (DSOP)

This type of engine contains two crankshafts which are driving via the piston rods two opposed pistons. Those shafts are coupled with gears, lay-shafts or chain to maintain the same movement. It is possible to provide in this construction phase shift for both crankshafts.

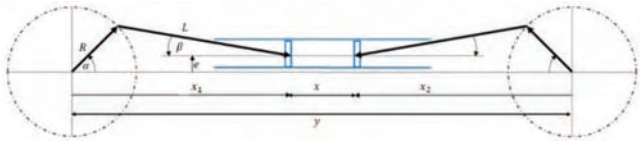

Fig. 6. DSOP engine scheme

The piston motion for this construction is the same as the motion for STDE engine with the difference that there are two pistons. So the geometrical parameters of the crankshaft construction are different for the same piston stroke. Additionally this construction may have for the same compression ratio and volume as the STDE lower piston speed for the same engine speed. Each of the piston from DSOP has to cover half of the distance with comparable STDE. That engine configuration is recently developed by the Achates Power company [7].

2.7. Opposed-piston barrel engine (BEOP)

This engine is a single shaft construction with all cylinders placed parallel to and around main shaft. The plates are located on opposite sides of the crankshaft.

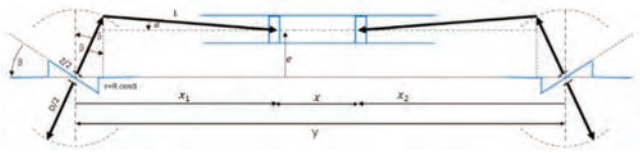

Fig. 7. BEOP engine scheme

The piston motion is the same as the BE construction with the same difference between the STD and DSOP - two pistons for one cylinder. This engine is recently developed at Warsaw University of Technology [8].

2.8. Elliptical rotating cylinder engine (ERCOP)

This engine is known also as a Coomber rotary engine [9] which was designed at the end of 19th century. The biggest advantage of this construction is elimination of piston side force and transferring it to the rollers which are moving on the elliptical guideway. The shape in general for that type of engine does not have to be an ellipse but this research will focus on that construction.

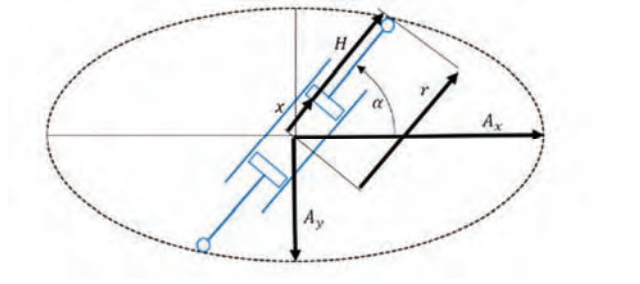

Fig. 8. ERCOP engine scheme

Derived equation for the combustion chamber lengths is presented by the formula:

$$x = \sqrt{\frac{A_y^2}{1-e^2\cos^2\alpha}} - H \tag{8}$$

where: A_y – the smallest ellipse radius, A_x – the biggest ellipse radius, H – the height of the piston with rollers, e – ellipse eccentricity described as:

$$e^2 = \frac{A_x^2 - A_y^2}{A_x^2} \tag{9}$$

Stroke can by calculated as the double difference between the maximum and minimum ellipse radii:

$$s = 2(A_x - A_y) \tag{10}$$

3. Piston motion curves

In order to compare all types of engines it was decided to provide for all constructions exactly the same geometrical dimensions. All models have the same piston bore, total piston stroke and compression ratio. Total piston stroke for all engines is the change of length of cylindrical volume of the gas for the compression and expansion process (maximum gas length decreased by minimum gas length). There was no differentiation between the compression and expansion ratios (like in the Atkinson cycle). It has to be noticed that for the opposed piston configuration determination of top dead center (TDC) and bottom dead center (BDC) may be addressed to the:

- minimal and maximal gas volume,
- TDC and BDC of the inlet piston position,
- TDC and BDC of the exhaust piston position,

For the need of this work the TDC and BDC will be associated with the gas volume regardless of the construction. The Table 1 presents selected engines' geometry parameters.

Table 1. Geometrical engine parameters for all configurations

Parameter	Unit	Value
Bore	mm	50
Stroke	mm	194
Volume of cyl	L	0.381

To obtain exactly the same stroke and CR for all engines the geometrical parameters were calculated based on the equations (1)–(10) prestented in the chapter 2. For those designs which stroke equation was not directly provided in this work the geometrical parameters were numerically determined to achieve required stroke and compression ratio. The stroke and compression ratio which were numericaly determined where accurate within 10^{-4}mm for stroke and 10^{-3} for CR.

The selected geometrical parameters were presetented in the Tables 2–9. All the parameters presented in the tables were rounded to 3 decimal places.

Table 2. Geometrical engine parameters for STDE

type	μ	λ	R
STDE_1	–0.1	0.2	96.493
STDE_2	–0.1	0.3	96.465
STDE_3	–0.1	0.4	96.420
STDE_4	0	0.2	97
STDE_5	0	0.3	97
STDE_6	0	0.4	97
STDE_7	0.1	0.2	96.493
STDE_8	0.1	0.3	96.465
STDE_9	0.1	0.4	96.420

The EE engine configuration presents very unique behaviour near the TDC. The compressed gas starts to expand for a while and just after TDC compresses once again. This situation appears when the angular position of the eccentric rod is twice bigger then crank angle ($\alpha_r = 2\alpha_c$). That means also that the eccentric rod rotates twice faster then crank angle.

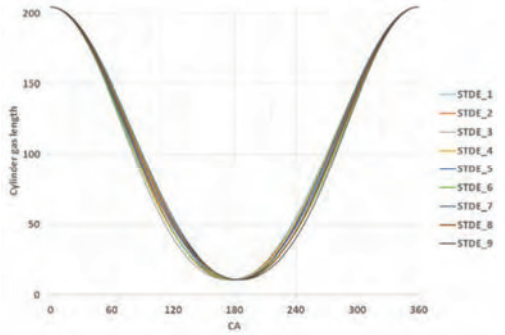

Fig. 8. STDE piston motion curves

Table 3. Geometrical engine parameters for EE

type	μ	λ	R	e_rod pos	δ
EE_1	–0.1	0.4	43.328	$\alpha_r = \alpha_c$	0.495
EE_2	–0.1	0.6	64.996	$\alpha_r = \alpha_c$	0.295
EE_3	–0.1	0.8	86.875	$\alpha_r = \alpha_c$	0.089
EE_4	0	0.4	42.135	$\alpha_r = 2\alpha_c$	0.544
EE_5	0	0.6	63.175	$\alpha_r = 2\alpha_c$	0.345
EE_6	0	0.8	84.272	$\alpha_r = 2\alpha_c$	0.144
EE_7	0.2	0.4	47.200	$\alpha_r = \alpha_c + 30^o$	0.567
EE_8	0.2	0.6	70.172	$\alpha_r = \alpha_c + 30^o$	0.365
EE_9	0.2	0.8	88.241	$\alpha_r = \alpha_c + 30^o$	0.136

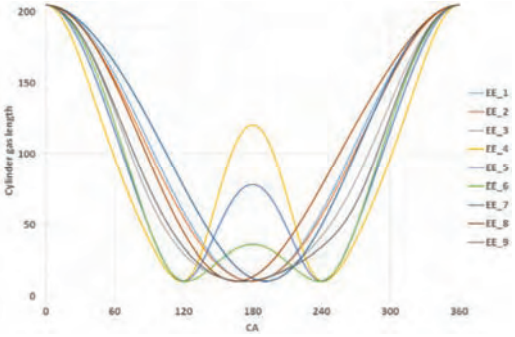

Fig. 9. EE piston motion curves

Table 4. Geometrical engine parameters for SSOP

type	λ_1	λ_2	R	ϵ
SSOP_1	0.2	0.148	48.493	–0.1
SSOP_2	0.3	0.196	48.485	–0.1
SSOP_3	0.4	0.234	48.493	–0.1
SSOP_4	0.2	0.148	48.485	0
SSOP_5	0.3	0.196	48.475	0
SSOP_6	0.4	0.234	48.5	0
SSOP_7	0.2	0.148	48.5	0.3
SSOP_8	0.3	0.196	48.5	0.3
SSOP_9	0.4	0.234	48.434	0.3

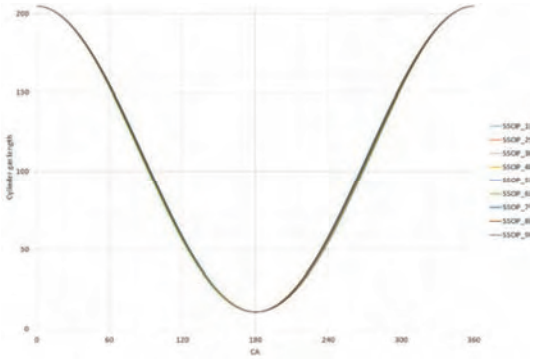

Fig. 10. SSOP piston motion curves

Table 5. Geometrical engine parameters for SSPOP

type	λ_1	λ_2	R_1	R_2	δ	ϵ_1	ϵ_2
SSPOP_1	0.225	0.193	45	55.312	–0.524	–0.1	–0.081
SSPOP_2	0.225	0.182	45	51.983	0	–0.1	–0.087
SSPOP_3	0.225	0.193	45	55.135	0.524	–0.1	–0.082
SSPOP_4	0.225	0.193	45	55.241	–0.524	0	0
SSPOP_5	0.225	0.182	45	52	0	0	0
SSPOP_6	0.225	0.193	45	55.241	0.524	0	0
SSPOP_7	0.225	0.193	45	55.135	–0.524	0.1	0.082
SSPOP_8	0.225	0.182	45	51.983	0	0.1	0.087
SSPOP_9	0.225	0.193	45	55.312	0.524	0.1	0.081

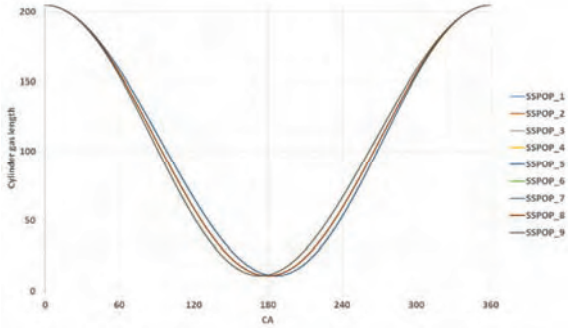

Fig. 11. SSPOP piston motion curves

Table 6. Geometrical engine parameters for ERCOP

type	A_x	A_y	H	e^2
ERCOP_1	400	303	297.611	0.426
ERCOP_2	350	253	247.611	0.477
ERCOP_3	300	203	197.611	0.542
ERCOP_4	250	153	147.611	0.625
ERCOP_5	200	103	97.611	0.735
ERCOP_6	150	53	47.611	0.875

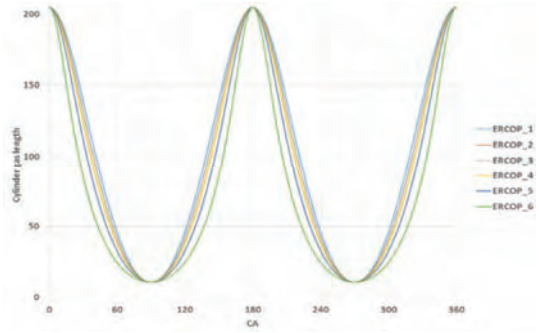

Fig. 12. ERCOP piston motion curves

Table 7. Geometrical engine parameters for BE

type	*Z*	*e*	*R*	*D*	*L*
BE_1	100	50	26.608	364.558	150
BE_2	100	75	23.789	407.759	150
BE_3	100	100	21.443	452.364	150
BE_4	200	100	42.886	452.364	150
BE_5	200	150	35.636	544.393	150
BE_6	200	200	30.368	638.822	150
BE_7	300	150	53.454	544.393	150
BE_8	300	225	42.381	686.629	150
BE_9	300	300	34.993	831.598	150

It can be noticed that during one rotation of the crankshaft there are 2 cycles of the engine for the ERCOP configuration. Due to significant difference between this piston motion and the rest of the engines it was decided to carry calculations such as only one compression and one

expansion appears in the piston motion for whole engine rotation. This can be comapared to the situation as if the ERCOP engine was working with twice lower engine speed then the other engines so the number of cycles within a particular time remains the same.

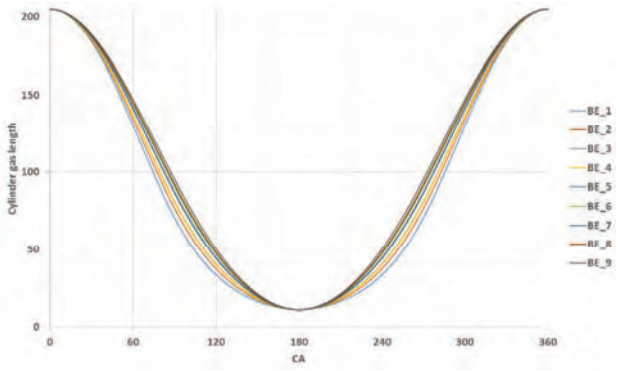

Fig. 13. BE piston motion curves

Table 8. Geometrical engine parameters for DSOP

type	μ	λ	R_1	R_2	ψ
DSOP_1	0.03	0.2	48.626	48.700	–10
DSOP_2	0.03	0.3	48.606	48.718	–10
DSOP_3	0.03	0.4	48.585	48.734	–10
DSOP_4	0.03	0.2	48.477	48.477	0
DSOP_5	0.03	0.3	48.476	48.476	0
DSOP_6	0.03	0.4	48.474	48.474	0
DSOP_7	0.03	0.2	48.626	48.700	10
DSOP_8	0.03	0.3	48.606	48.718	10
DSOP_9	0.03	0.4	48.585	48.734	10

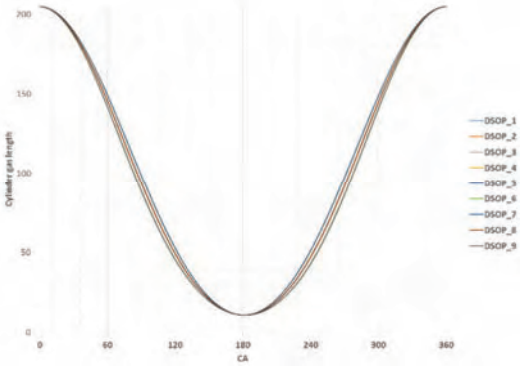

Fig. 14. DSOP piston motion curves

Table 9. Geometrical engine parameters for BEOP

type	Z	e	R	D	L
BEOP_1	100	50	12.367	392.157	150
BEOP_2	100	75	11.003	440.777	150
BEOP_3	100	100	9.905	489.675	150
BEOP_4	200	100	19.809	489.675	150
BEOP_5	200	150	16.496	588.027	150
BEOP_6	200	200	14.122	686.855	150
BEOP_7	300	150	24.744	588.027	150
BEOP_8	300	225	19.759	736.388	150
BEOP_9	300	300	16.435	885.301	150

Each of the engine piston motion curves for different geometrical parameters was presented in the Figures 8–15. Every equation for each engine was shifted in phase to maintain max gas volume at 0 deg CA. In most cases it resulted with the TDC apearing at 180 deg CA.

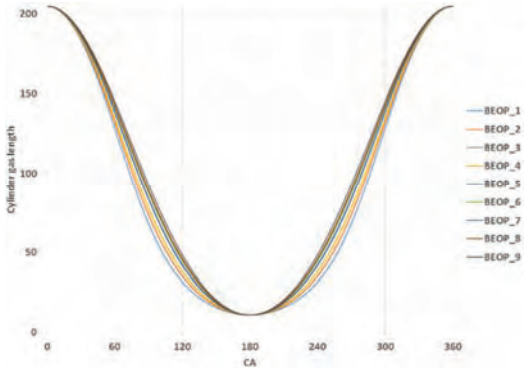

Fig. 15. BEOP piston motion curves

4. Model of the engine

All engines have been represented by a closed-cycle numerical model. The incylinder paramters where based on the ideal gas properties. The gas model was built based on the ideal gas mixture of the following species: nitrogen (N), oxygen (O_2), argon (Ar), carbon dioxide (CO_2), water (H_2O) and isooctane (C_8H_{18}). The molecular mass, volume and mass fractions where determined for each time step. The specific heat of the gas was determined based on the polynomal equations provided by NASA spec [10]. Pressure prediction was modeled by the following formula

$$\frac{dp_i}{d\Theta_i} = \left(\frac{dQ_{c,i}}{d\Theta_i} - \frac{dQ_{ht,i}}{d\Theta_i} - \frac{\gamma_i}{\gamma_i - 1} p_i \frac{dV_i}{d\Theta_i}\right) \frac{\gamma_i - 1}{V_i} \tag{12}$$

where: $\frac{dp_i}{d\Theta_i}$ – change of pressure at current step, $\frac{dQ_{c,i}}{d\Theta_i}$ – heat release at current step, $\frac{dQ_{ht,i}}{d\Theta_i}$ – heat transfer to walls at current step, $\frac{dV_i}{d\Theta_i}$ – change of gas volume at current step, p_i – current gas pressure, V_i – current gas volume, γ_i – current gas ratio of specific heats.

The model of the engine heat release was created based on the Woschni correlation with heat transfer coefficient described by the following formula:

$$h_{c,i} = 5b^{m_{ht}-1} p_i^{m_{ht}} w_i^{m_{ht}} T_i^{0.75-1.62m_{ht}} \tag{11}$$

where: b – pistone bore, p_i – pressure in current step, w_i – cylinder gas velocity in current step, T_i – gas temperature in current step, m_{ht} – constant equal to 0.8.

The combustion of the fuel mixture was based on complete combustion of isooctane with heat release based on the Wiebe expotential function:

$$x_{end,i} = 1 - \exp\left\{-\left[\left(2.302^{\frac{1}{m_c+1}} - 0.105^{\frac{1}{m_c+1}}\right)\left(\frac{\Theta_i - \Theta_{cstart}}{\Theta_{cdur}}\right)\right]^{m_c+1}\right\} \tag{12}$$

where: $x_{end,i}$ – amount of the fuel burned in particular time step, m_c – constant equal to 0.7, Θ_i – current angle (time), Θ_{cstart} – angle when 10% of fuel burned, Θ_{cdur} – duration of combustion from 10-90% of burned fuel.

The complete combustion model was based on the chemical reaction:

$$C_8H_{18} + 12.5O_2 \rightarrow 8CO_2 + 9H_2O \tag{13}$$

Fuel vapors were injected into the cylinder at the beginning of the engine cycle. The species' fractions and gas specyfic heat was updated for each additional fuel mass injected and timestep. The amount of fuel injected into the cylinder cycle starting paramters (p_0, T_0) and air-fuel equivalence ratio (λ). Based on that approach the amount of fuel injected for each engine is exactly the same when starting parameters are the same. Thus the power and efficiency of the engines depends mostly on the piston motion curve and combustion parameters. The power and efficiency were calculated based on the presented integral:

$$\eta_t = \frac{\int_{start}^{end} p_i dv_i}{m_{fuel} LHV} \tag{14}$$

where: p_i – is current gas pressure, dv_i – change of volume in calculation time step.

While the power of the engine was calculated based on the formula (2-stroke engine):

$$P = \eta_t m_{fuel}\, LHV\, N/60 \tag{15}$$

where: m_{fuel} – mass of fuel injected in one cycle, LHV-lower heat value of the fuel, N – engine speed.

There were 8 different configurations of engines investigated. Most of them were presented by 9 geometrical variations. In total there were 69 different piston motion curves implemented into the closed-cycle model. Two additional parameters have been selected to run calculations connected with the shape of the pressure profile in the cylinder: combustion duration (T_{cdur}) and start of combustion (T_{cstart}). The rest parameters remained unchanged. The Table 10 presents constant parameters for all engines calculations, while Table 11 presents 5 different setups for each piston motion curve, so in total there were 345 engine cases analyzed.

Table 10. Constant parameters for engine cycle simulations

Parameter	value	unit
Fuel lower calorific value (LHV)	47	MJ/kg
Air-fuel equivalence ratio (λ)	1.1	–
Engine speed	1500	rpm
Starting pressure	4	bar
Starting temperature	350	K
Mean piston surface temperature	580	K
Mean liner surface temperature	480	K
Volume content of water in air	1	%

Table 11. Variable parameters for engine cycle simulations

Setup	T_{cdur} (deg)	T_{cstart} (deg)
1	50	170
2	50	180
3	50	190
4	30	180
5	70	180

The closed cycle model did not include the scavenging process of the cylinder. The closed portion of volume of gas for each engine was exactly the same. The gas was 100% of fresh air (no residual gases) at the beginning and 100% of burned gas after combustion process.

5. Results

For each of the engine configuration and setup it was possible to plot the pressure, temperature, volume and all derivatives of the parameters for all timesteps. The major attention was paid to the engines' efficiency and power which were calculated with the equations 14 and 15.

From all results obtained for all engine configurations 3 of them were excluded. Those which excluded regarded 3 engine variations of configuration EE (particularly EE_4, EE_5 and EE_6). The calculations of these engine resulted in extremely high peak pressures (~700 bar) and peak temperatures (> 3000 K). For that high temperatures the amount of heat was so high that the heat losses exceeded fuel heat delivered. This unique engine design requires separate discussion to explain the reason of so high gas parameters.

Figure 16 presents a comparison of different engine configurations in regards to the efficiency. The presented efficiencies are the avarage efficiency of all engine geometrical variations for the particular combustion parameters setup (T_{cdur},T_{cstart}). For instance first column in Figure 16 presents the average efficiency of all gemetrical variations of STDE engine (STD_1, STD_2, …, STD_9) for the Setup 1 described in Table 11 (so for the T_{cdur} = 50 deg and T_{cstart} = 170 deg).

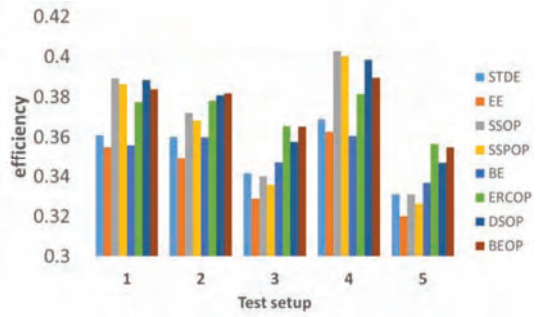

Fig. 16. Comparison of different setups on engine efficiencies

It can be noticed that the lowest engine efficiency was presented for the setup 5 by the EE engine (32.0%). The second lowest efficiency was also noticed for the setup 5 for the SSPOP engine configuration (32.6%). The highest efficiencies were observe for the SSOP engine and the second for the SSPOP, both for the latest combustion start (efficiency were equal to 40.3% and 40,0% respectively). It can be noticed that the behavior of the models was not linear. Higher impact on the efficiency was observed for the combustion duration (±20 deg variations) parameter than for the start of the combustion parameter (±10 deg variations). The BE engines presented lowest variations of efficiency which range was 33.7–36.0% for different setups.

The highest efficiency for the single engine configuration and variation was noted for the SSPOP_1. This model reached 40.6% for the setup 4. The lowest efficiency (excluding EE_5 to EE_7) for the particular variation was noted for the EE_8 configuration, setup 5 27.2%.

Figure 17 presents the comparison of averaged efficiency for all setups and variations for each design. Three lowest averaged efficiency are represented by the not opposed-piston configurations (STDE, EE, BE). This is connected with the reduced area of heat transfer for a cylinder (lack of engine head for OP designs). The difference between the BE and BEOP reaches 2.3 percentage points what gives 6.5% difference in regards to BE efficiency. Very similar

relative difference is between STDE and DSOP configurations. For those configuration the difference reaches 6.2%. The highest average efficiency was noted for the BEOP configuration (37.5%) with small difference to the DSOP engines (37.4%) and ERCOP engines (37.2%).

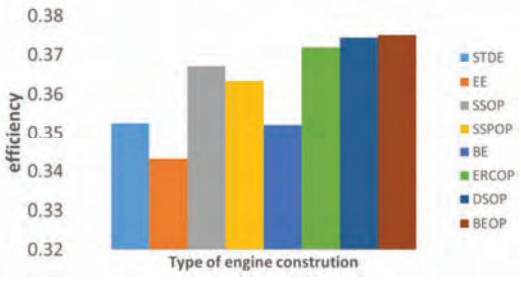

Fig. 17. Comparison of different engine configuration on efficiencies.

For each calculation maximum temperature and maximum pressure was collected. The plots presented at Figures 18 and 19 are showing the peak temperatures and peak pressures for each engine variation for setup 1 (Table 11).

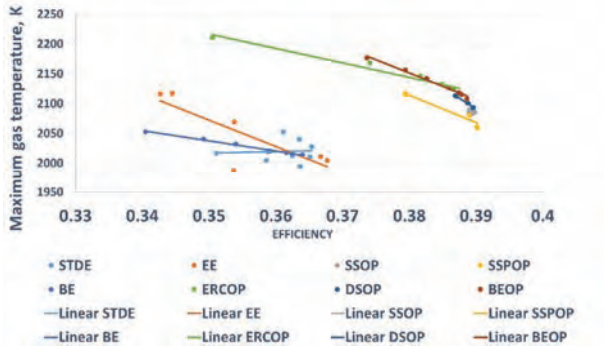

Fig. 18. Maximum gas temperatures for all designs

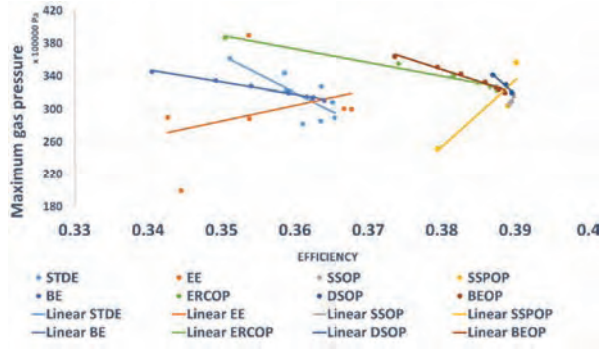

Fig. 19. Maximum gas pressures for all designs

In general the engine configurations shows that for lower peak values of the pressure and temperature the engine shows higher efficiency. Some of the configurations present very good trend for both parameters (BEOP, ERCOP, BE, SSOP, DSOP). The biggest variations are visible for the EE engine and it can be explained by the very different shape of piston curves in comparison to the rest of the engine designs.

The level of peak pressures for the conducted analysis reaches 390 bars while the peak temperatures are for most cases above 2000 K.

Average efficiency of all engine configurations and geometrical variations for setup 4 was 33.8% while for setup 5 was 38.3%.

6. Summary and conclusions

All engine configurations showed that it is beneficial to lower the time of combustion duration. The difference of the average efficiencies between setup 4 and setup 5 reached 5 percentage points. Those setups differs by one parameter which is combustion duration (70 deg CA, 30 deg CA respectively).

Most of the engines configurations presented trend that the lower combustion peak temperature appears in the closed cycle analysis the higher efficiency is. This phenomena can be connected with lower heat losses for the lower gas temperatures. For the whole cycle the wall temperature of the liner, piston and head (not OP engines) was set on the constant level and for those configurations where the peak temperature was higher the more heat was lost to the cooling system.

Regardless of the engine configuration the opposed piston engines proved to have, in general, higher efficiency exceeding for some cases 6% difference.

Optimization of piston motion curves may aid the process if increasing engine efficiency. It was showed that some of the curves indicated lower fuel consumption. The impact of the piston motion curves may be affected by other parameters such us combustion duration or start of combustion. The dependencies between the parameters and efficiency are not linear and the impact of them should be analyzed at the same time.

Acquired gas peak parameters were considered very high. This was connected with high starting pressure (4 bars) and compression ratio on the level of 19. Because of the high temperatures the loss of heat to the walls affected efficiency. In order to increase the efficiency the wall temperatures could be increase and the starting temperature could be lowered.

Due to very unique behavior of EE engine it is recommended to analyze this construction with separate parameters selected for this particular engine.

The construction of the ERCOP engine allows reaching the same number of cycles within particular time for twice lower speed than the other engines. This is a mitigation of the drawback of this construction. Since this design has a high inertia loads due to rotation of the cylinder lower speed may reduce the forces and stresses in this construction.

Nomenclature

CA crank angle
TCD top dead center
BDC bottom dead center
LHV fuel lower heating value
OP opposed-piston

Bibliography

[1] PIRAULT, J-P., FLINT, M. Opposed piston engines: Evolution, use and future applications. *SAE International*. Warrendale, 2010, 7-15.

[2] DZIERŻANOWSKI, P., ŁYŻWIŃSKI, M. Silniki tłokowe. *WKŁ*. Warszawa, 1981, 86-90.

[3] JĘDRZEJOWSKI, J. Mechanika układów korbowych silników samochodowych. *WKiŁ*. Warszawa, 1979, 16-47.

[4] RYCHTER, T. Analiza możliwości podwyższenia sprawności cieplnej silników tłokowych ZI. *Wydawnictwo PW*. Warszawa, 1986, 43-50.

[5] RYCHTER, T., TEODORCZYK, A. VR/LE engine with a variable R/L during a single cycle. *SAE Technical Paper 850206*.1985.

[6] HUO, M., HUANG, Y., HOFBAUER, P. Piston design impact on the scavengine and combustion in an opposed-piston, opposed-cylinder (OPOC) two-stroke engine. *SAE Technical Paper 2015-01-1269*. 2015.

[7] HEROLD, R., WAHL, M. et al. Thermodynamic benefits of opposed-piston two-stroke engines. *SAE Technical Paper 2011-01-2216*. 2011.

[8] KALKE J., OPALIŃSKI, M., SZCZECIŃSKI, M.. Opposed-piston engines: the future of internal combustion engines. *PhD Interdisciplinary Journal,* Gdańsk, 2014. 175-184.

[9] www.cedesign.net/steam/coomber.htm

[10] McBRIDE, B., ZEHE, M., GORDON, S., NASA Glenn coefficients for calculating thermodynamic properties of individual species *NASA/TP – 2002-211556,* 2003.

[11] PUDLIK, W., Termodynamika. *Wydawnictwo Politechniki Gdańskiej*. Gdańsk, 2007, 168.

Marcin Opaliński, MSc. – Faculty of Power and Aeronautical Engineering.

e-mail: *Marcin.Opalinski@itc.pw.edu.pl*

Prof. Andrzej Teodorczyk, DSc., DEng. – Faculty of Power and Aeronautical Engineering.

e-mail: *Andrzej.Teodorczyk@itc.pw.edu.pl*

Jakub Kalke, MSc. – Faculty of Power and Aeronautical Engineering.

e-mail: *Jakub.Kalke@itc.pw.edu.pl*

Article citation info:
SIADKOWSKA, K., MAJCZAK, A., BARAŃSKI, G. Studying a construction of piston for the aircraft CI engine. *Combustion Engines*. 2017, **168**(1), 161-167. DOI: 10.19206/CE-2017-126

Ksenia SIADKOWSKA
Adam MAJCZAK
Grzegorz BARAŃSKI

CE-2017-126

Studying a construction of pistons for the aircraft CI engine

This paper examines the selected constructions of piston for aircraft CI engines and discusses tendencies in a development of piston designs. The paper addresses the question of using new materials and coatings to improve quality of pistons and the study of heat transfer and methods to absorb heat from a piston by means of cooling ducts. The selected materials were examined in terms of their advantages and drawbacks. The paper discusses different shapes of piston heads and their impact on combustion as well as indicates other factors behind parameters of combustion and toxic emission like injector shape types, lubrication types and clearances in the combustion chamber.

Key words: *aircraft engine, piston, CI engine, opposed-piston engine, designing pistons*

1. Introduction

Compression-ignition engines are not common aircraft drive units but for many years it has been often successfully attempted to install them in the aircraft. Recently, some new constructions of pistons for compression ignition engines have been launched onto the market. In 2014, the first steel pistons for an automotive passenger CI application began to be sold [22]. Computational fluid dynamics enables heat transfer and combustion of a charge to be optimized. These are the tools that were not available for constructors in the last century, so engine manufacturers take older proven designs to improve them. Civil light aviation also uses aircraft with engines previously verified in automotive applications and which can become attractive solutions in civil aviation satisfy as they satisfy very demanding toxic emission standards and show low fuel consumption. The paper investigates piston designs dedicated to diesel engines. Small aircraft engines are very often based on verified automotive solutions so the focus is put on advances in automotive engines of a potential aviation application.

This paper follows an approach of critical analysis and investigates the known aviation and automotive piston constructions. Investigating non-scientific and commercial materials is purposeful to achieve a more comprehensive state-of-the-art about modern constructions of pistons as automotive applications to be successfully transferred to aviation.

2. Aircraft CI engines

When aircraft CI engines began to be developed in the 1940s, there were first turbojet and turboprop engines that successfully satisfied the needs of aviation at that time. Progress in automotive CI engines was reflected in aircraft engines so diesel aircraft engines were rediscovered in the 21st century.

Balicki et al. [1] claim that piston engines now frequently used in light and ultralight aviation by aeroclubs and for business, economic, rescue and recreation purposes technically represent a pre-war theory of operation, designing and technology of production, especially if regarded the progress in automotive engines. Low pressure injection engines are rare and frequently carburetors of a quite primitive construction are used. Ecological standards and climate change can significantly stimulate the progress in developing aircraft piston engines, even by transferring to them the achievements in automotive applications. Regardless of this, it is considered to introduce CI engines capable of running on one type of fuel.

Thielert Aircraft Engine GmbH, until its insolvency announced in 2008, was a recognized manufacturer of aircraft engines, including the Centurion range of aircraft CI engines. In 2013, the company was taken over by Continental Motors, Inc., owned in majority by China's AVIC International and renamed Technify Motors GmbH. Thielert's engines were mainly based on automotive turbo-diesel engines [14], however, for example, 180 original parts were designed for the Centurion 1.7, an inline-four engine [4]. The Centurion 1.7 was installed in the Piper, Cessna 172 and Diamond DA42 "Twin Star". The latter airplane, when the production of the Centurion 1.7 was suspended in 2009, was adapted by its manufacturer, Diamond Aircraft Industries, to the Lycoming gasoline engine and the turbodiesel Austro Engine E4 (Austro AE300) by Austro Engine GmbH. The bankruptcy of Thielert Aircraft Engine GmbH largely impacted the sales of the DA42 which since its launch onto the market in 2004, constituted 80% of the sales of 2-piston engine aircraft [15].

In 2009, the Italian manufacturer of light aircraft presented the Gemini100, a British diesel engine by Power Plant Developments, installed in the Tecnam P92. The Gemini100 is a compact opposed-piston engine of similar parameters to petrol engines (Gemini100: capacity – 1.6 l, power – 100 KM, weight – 70 kg, fuel consumption – 11–12 l of karosene/1h of flight; Rotax 912: 80-100 KM, 60 kg, 5000-5500 rpm, fuel consumption 15 l of petrol/1h of flight). The Gemini100 has been modified since 2006, and in 2015, it was announced that the research on this engine had been continued [18].

The Diesel V-8 Graflight by Engineered Propulsion Systems is another engine installed in a single-engine piston aircraft, the Cirrus SR22. This aircraft typically operates on the Continental IO-550-N 310 HP. In 2014, there was its first test flight. Manufacturer's representatives claimed that its time between overhaul (TBO) had been successfully extended up to 3000 hours and the engine would soon undergo certification procedures [17].

Fig. 1. Gemini100 engine [16]

The opposed-piston engine is a technologically interesting aircraft CI engine. The first opposed-piston engine was built in 1890, and since then have been used in ground, marine and aviation applications. Unlike the four-stroke engine, this type of engine doesn't need the head and valves which are considered to be the most expensive parts of standard engines. One of the most significant opposed-piston engines is the Junkers Jumo, designed and developed by Professor Hugo Junkers for the German army and civil aviation and manufactured between 1930 and 1945. In those days, the Junkers 205 and 207 showed unusual performance [13]. Other well-known opposed-piston engines include: Doxford (1920-1990), used in a wide range of ships, Kharkov 6TD (1932-current), used in Russian tanks, Fairbanks Morse 38D81/8 (1934-current), used in United States submarines, small marine freighters and trains, Rootes TS3 engine (1954-1972), used in the United Kingdom Commer truck, Napier Deltic engine (1954-current), used in high-speed trains and naval fast patrol boats, Rolls Royce K60 (1955-current), used in military applications, Leyland L60 (1960s-1995), used in the United Kingdom, produced Chieftain Battle Tank [13].

Junkers was working for 20 years to build an aircraft diesel engine and the Junkers Jumo 205 showed the best results and started the entire engine family. Figure 2 shows its design [24].

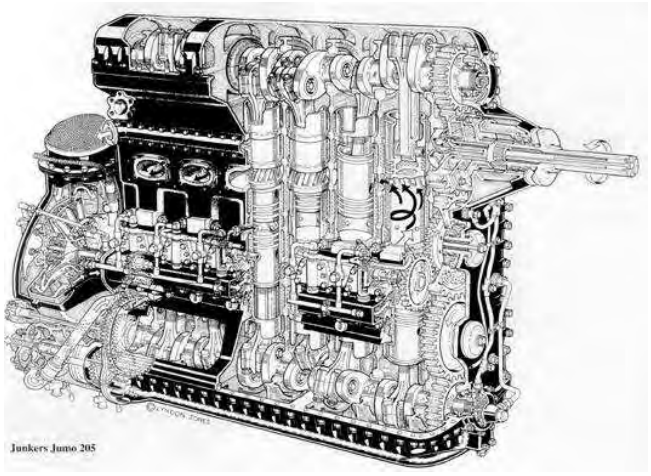

Fig. 2. Junkers Jumo 205 engine [24]

Despite their many advantages, opposed-piston engines had one disadvantage, i.e. high toxic emissions which suspended their progress for many years. Since the early 1980s, emission standards for all motor vehicles have eliminated all of the engines available at that time, mainly for their poor fuel injection system and a non-optimized geometry of their combustion chamber. Technological progress and up-to-date design methods have enabled this type of engine to be relaunched onto the market. With computational fluid dynamics and simulation software, these engines have been revived as a viable alternative and a product to fill a market gap [13].

In 2013, Achates Power was granted nearly U.S. $ 5 million from the United States Army to improve and develop a new engine based on the Junkers Jumo 205 design [2]. Actually, this engine can be further developed with today's advanced technologies.

3. Trends in designing pistons for CI engines

The piston in the compression ignition engine has varied tasks. It transmits the forces from and to an air-fuel mixture, shapes and seals the combustion chamber and releases heat generated by combustion. For many years, pistons have been typically made of aluminum alloys. In time, however, engines have been expected to be more efficient so their designs have had to be improved. Actually, the entire engine has been modified but this paper focuses on pistons and how they impact toxic emissions emitted by the CI engine. There are many methods to satisfy the increasingly strict toxic emission standards but the most frequently regarded solutions to be applied in pistons focused on changing their design, modifying shapes of the combustion chamber, using innovative nano-coatings or finding a more appropriate material or manufacturing technology.

David Adams, specialist from Ford's Dunton engine R&D centre in the United Kingdom, claims that already in 2012, there were strong tendencies to use steel pistons in diesel engines. Such a change, he says, is probably the most significant innovation in the use of new materials for automotive pistons. There have been the attempts to optimize aluminum-silicon alloy pistons with the use of additional alloying elements that improve the microstructure, stability and strength of the casting. However, the density of the material prevented from achieving lighter pistons, so the focus was put to find stronger materials to manufacture thinner sections and create better casting technology. Graphite coatings, almost standard for all types of pistons, have managed to reduce friction on the skirt and, to some extent, wear. Composite carbon-nanotube coatings, so far used on piston rings, are now also on the piston [12].

AVL's R&D work on pistons has been also focused on using steel for pistons, especially for high-power passenger car diesel engines where the maximum cylinder pressure reaches 200-220 MPa, whereas the limit for aluminum pistons is about 210 MPa. AVL has partially collaborated with suppliers to develop a steel piston as heavy as an aluminum one. They succeeded by special micro-friction welding processes in which the piston head and shaft were welded together under pressure by micro movement. AVL claims that welding two elements is more cost effective

than a complex casting. This type of technology is used for heavy-duty pistons [12].

4. Materials for pistons

Piston's tasks and loads applied to the piston – varied-load strength, correct thermal conductivity, rapid temperature changes, a correctly low friction coefficient – are the factors behind the choice of materials for the piston. If the piston is to be lightweight, low density materials are preferred. The most common material for pistons in most internal combustion engines is aluminum alloy which is preferred for its low weight, low mass production costs and strength under conditions that occur in the cylinder. Recently, CI engines have been more loaded so aluminum pistons frequently need to operate on the verge of their permissible loads. Therefore, designers have turned to steel which more high-temperature resistant and stronger. Rheinmetall Automotive Company reports that since 2014, the German company, Kolbenschmidt, has been the world's first supplier of steel pistons for passenger car diesel engines [22] and steel pistons with aluminum piston heads are capable of reducing fuel consumption and engine weight [21]. Properties of steel and its better than aluminum stability enable pistons to be smaller though stronger to higher loads. In addition, frictional forces are weaker than those in aluminum pistons. Better combustion conditions result not only from a changed material for the piston but also from the innovative patented LiteKS piston design that is able to reduce weight but not deteriorate strength as well as the use of nanomaterials (NanofriKS coating on the shaft).

a) Geometrical comparison of steel and aluminum pistons

b) Steel piston dedicated to CI engine vehicles

c) Steel piston dedicated to CI engine vehicles - cross section

d) Flow of oil in steel piston cooling channels

Fig. 3. Steel piston dedicated to diesel engines [20]

Rheinmetall Automotive AG's steel pistons are dedicated to compression-ignition engines in which cylinder pressure is more than 200 MPa and power higher than 100 kW/dm^3. Their weight is similar to that of aluminum pistons, and their smaller dimensions can reduce lateral and frictional forces and reduce fuel consumption by 2-3%. For their special design, they can be installed in the engine with a reduced core height**.** The optimized configuration of piston cooling and adapting combustion parameters can compensate for a relatively poor thermal conductivity of steel compared to that of aluminum and related higher temperatures on the surface of the combustion chamber. A large closed cooling channel is directly next to the area of critical temperatures so optimal cooling is provided. Favorable temperature distribution that occurs in the area around the piston reduces both carbonization of the ring groove and piston ring's wear. This patented design is a single-piece forged piston, which can guarantee a negligibly deformed ring groove [19].

Figure 4 shows the temperature distribution for two pistons made of different materials, operating under the same conditions. The cooling channel in the steel piston protects the piston ring by lowering its temperature even by 50°C compared to that of the aluminum piston. The highest temperature is in the upper and lower sections of the combustion chamber but it is higher by 30°C than in the aluminum piston [8].

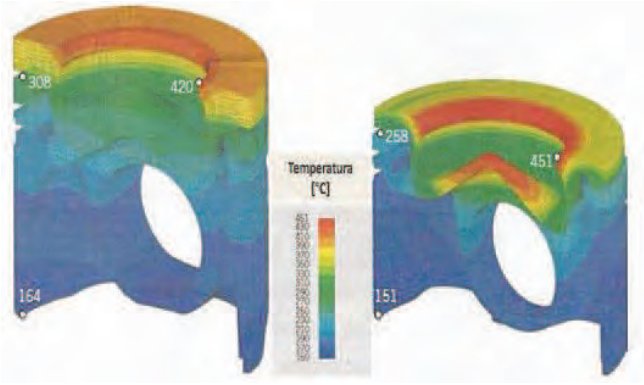

Fig . 4. Distributions of temperature in aluminum and steel pistons [8]

Figure 5 shows the distribution of safety factor, calculated from the load applied to pistons as a function of temperature. The stress in the aluminum piston is similar to the permissible stress level, whereas in the steel piston, there is a certain stress spare so there is no risk of surface cracks. The boundary temperatures on the combustion chamber surface in the steel piston start from 550°C [8].

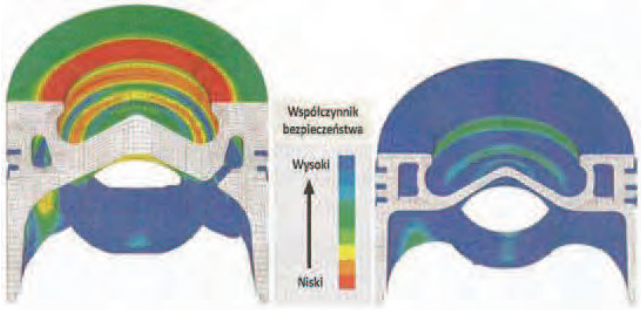

Fig. 5. Distributions of safety factor in aluminum and steel pistons [8]

The temperature of lubricating oil is not insignificant. If correctly regulated, it can reduce fuel consumption because the constant optimum temperature of the piston enables us to achieve such oil viscosity so that friction losses are reduced. Piston temperature can be indirectly controlled by changing oil temperature by regulating the oil flow. By controlling the oil flow, piston temperature can be modified within the range up to 50°C. The simulations by [6] to compare the capabilities of steel and aluminum pistons operating under the same conditions showed advantages and disadvantages of these solutions, see Table 1.

Table 1. Properties of steel pistons as in [6]

Advantages of steel pistons vs. aluminum ones	Disadvantages of steel pistons vs. aluminum ones
– higher temperature on the piston surface improves combustion, – reduced friction losses resulting from the smaller bearing piston surface and a lower thermal expansion, – better strength, – better strength to tribological wear, – the ability to reduce fuel consumption, – the ability to reduce toxic emissions, – the ability to increase the maximum cylinder pressure.	– lateral movements of the piston when the stroke begins and related piston strokes against the cylinder wall result in much wear of the piston skirt and a smooth section of the cylinder and increased noise, – high piston temperature can lead to carbonization of lubricating oil.

MAHLE's pistons are made of several different aluminum alloys. Pistons for CI engines are made of the eutectic alloy AlSi12Cu4Ni2Mg. The detailed composition and properties of this alloy have been provided in MAHLE's technical book [10, p. 67]. Aluminum-silicon pistons are usually cast but for special purposes forged as well. Forging changes the microstructure and properties of the element. Strength of pistons can be improved by the use of composite materials, namely aluminum alloys with a ceramic fiber, which can locally strengthen the most exposed sections, e.g. combustion chambers in the diesel engine. If aluminum pistons are not strong enough, iron-based materials can be used. This type of material can only locally reinforce the piston or iron or forged steel can be used for the entire piston. Pistons in heavy-duty diesel engines are chiefly made of cast iron. This material is used, for example, for monobloc pistons or composite piston skirts. Steel pistons can be made of two types of specially heat-treated steel: 42CrMo4 and 38MnVS6. This type of pistons are ideal for temperatures up to 450°C. When engines are tested, even higher temperatures of 500-550°C are possible, and then iron begins to peel as the result of its reaction with excess oxygen from an air-fuel mixture. If pistons operate at such temperatures, antioxidant coatings or other heat-resistant steels can be applied then. Generally, coatings prevent from a local melting of a material or its rubbing. In typical operating conditions, extra coatings are not necessary, but if there is extremal load – insufficient clearance due to the deformation of the cylinder, insufficient lubrication (at cold start, for elevated-temperature operation or used-oil operation), a new, not run-in engine, protective coatings prevent engine seizure. Samples of the coatings used by MAHLE are described in its technical book [10, pp. 79-81].

Cerit and Coban [3] examine the distribution of temperature and thermal loads acting on ceramic-coated aluminum pistons. The piston head was coated with magnesia stabilized zirconia powders. The temperature of the so coated piston is much higher than that of the non-coated one. The following figures show the test results.

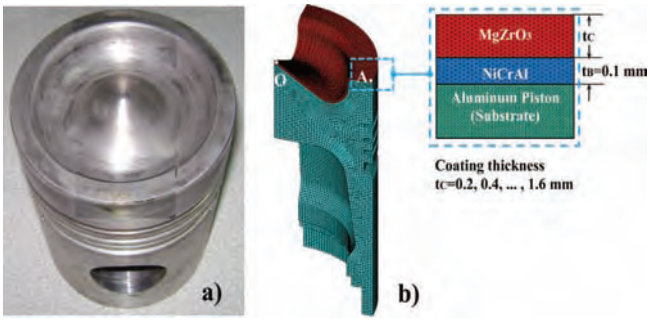

Fig. 6. Piston in the research: a) piston, b) coating mesh, coating composition and its parameters [3]

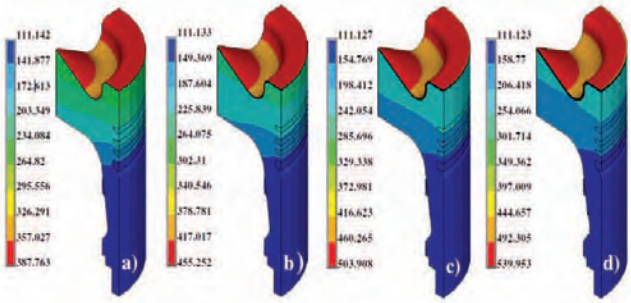

Fig. 7. Distribution of temperatures of the upper section of the coating for varied coating thickness: a) 0.4 mm, b) 0.8 mm, c) 1.2 mm, d) 1.6 mm [3]

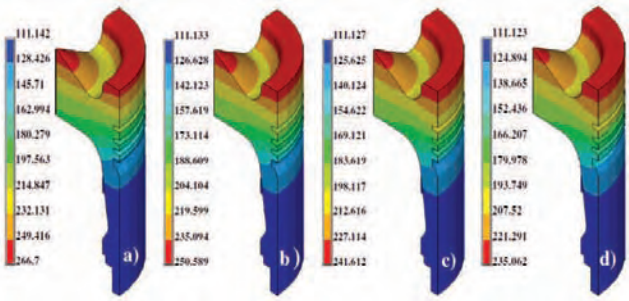

Fig. 8. Distribution of temperatures of the bottom section of the coating for varied coating thickness: a) 0.4 mm, b) 0.8 mm, c) 1.2 mm, d) 1.6 mm [3]

Higher temperatures in the combustion chamber are possible if coatings are applied to be a thermal barrier so engine's thermal efficiency increases. Decreasing piston temperatures under the coating improves engine performance. Clearly, the maximum thermal stress is a function of coating thickness. Maximum standard and tangential thermal stresses occur where the coating connects.

5. Cooling the piston

The piston is exposed to higher thermal loads because modern internal combustion engines are usually very loaded. Safe and reliable operation is possible if there is efficient cooling. A profile of CI engine piston temperature depends on the number and orientation of injection nozzles,

injection pressure, injection timing and combustion chamber geometry. Importantly, the increase in temperature is accompanied by the even by 80% decrease in material fatigue strength, and iron-based materials are much less sensitive to temperatures of up to 400°C. Depending on the method of cooling, the difference can be even up to 50°C. The method of cooling depends on the amount of heat to be released [10].

Certain interesting research on cooling CI engine pistons was done in China in 2016 [23]. The paper discusses a new method of theoretical calculations to design pistons. A model of a piston for the 16V280 CI engine was investigated. The highest temperature was on the edge of the combustion chamber.

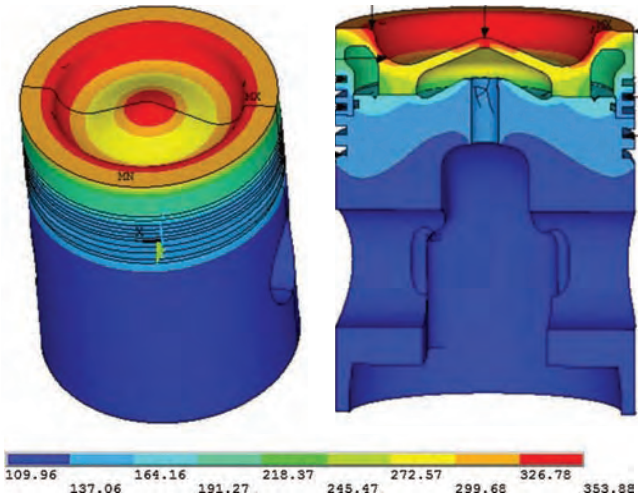

Fig. 9. Distribution of temperatures on the piston surface and inside the piston [23]

The distribution of piston head temperatures is very complex. The cooling method of cooling channels significantly impacts on cooling efficiency, and most of the heat from the piston is released to oil. The distribution of thermal stress in each measuring point is similar to that of mechanical stress so thermal stress cannot be ignored.

In the paper [5] investigated different piston configurations to find the most efficient cylinder air motion. Out of the examined shapes of the combustion chamber, the best one to achieve favorable conditions for combustion is a combustion chamber centrally mounted on the piston.

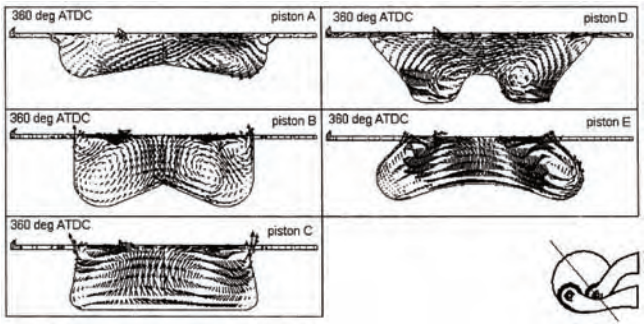

Fig. 10. Vectors of speed at TDC for 5 types of combustion chamber [9]

Payri et al. investigated in slightly more complex tests different configurations of the combustion chamber. Their research confirmed that piston geometry hardly impacts the in-cylinder flow during the intake stroke and the first part of the compression stroke unlike the shape of the combustion chamber which is important near TDC and in the early outlet stroke [9].

Another authors [11] discuss how combustion chamber turbulence and toxic emissions are impacted by shapes of the piston head and the injector nozzle. The figure below shows the combustion chamber geometry and the shape of the injectors to have been investigated.

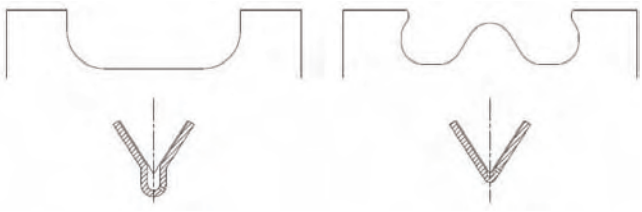

Fig. 11. Geometry of the combustion chamber and the nozzle endings; standard version – left, modified version – right [11]

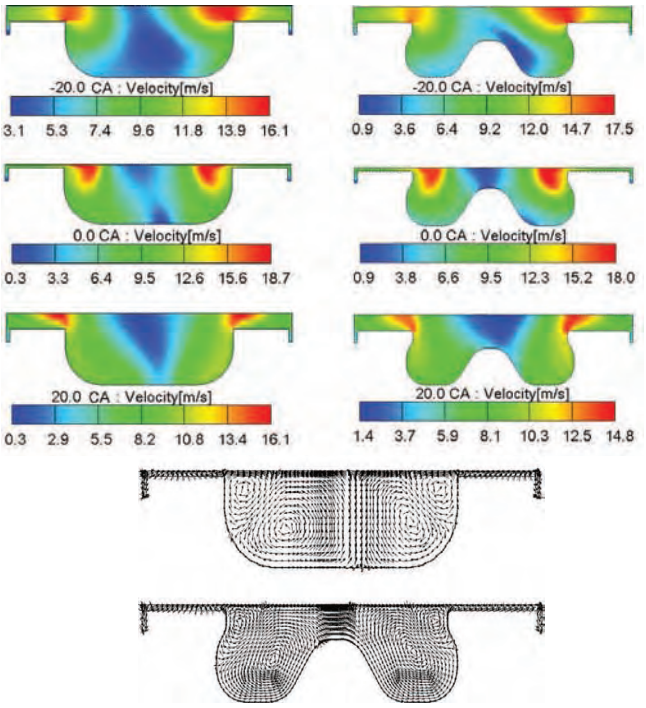

Fig. 12. Distribution of flow speed in the piston central section and vectors of speed in the piston central section at TDC [11]

The second configuration enabled lower toxic emissions. The CFD simulations showed that the shape of the combustion chamber was not so important as the changed shape of the injector. The author concludes that a negligible impact of the changed shape of the combustion chamber results from, e.g. a larger surface area and a large central projection inside the combustion chamber.

CFD tools have been used to develop further the shape of the combustion chamber, the geometry of the piston and fuel injection parameters in a new 2-liter ECOBlue CI engine mounted in the Ford Transit. It was the first time when the Ford had a mirror layout of intake channels so air could reach the first two cylinders by clockwise swirling and the latter two by counterclockwise swirling. This method ena-

bled better in-between cylinder air distribution, which significantly helped reduce emissions and fuel consumption (by 13% relative to the previous version) [7].

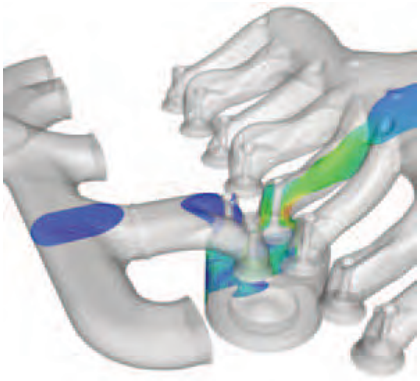

Fig. 13. CFD simulation in the ECOBlue [7]

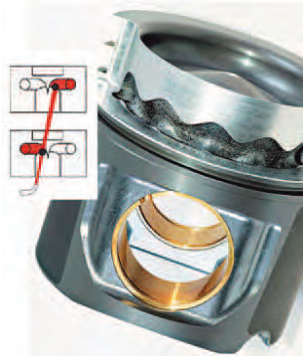

Fig. 14. Oil flow in the dual piston gallery [20]

Federal-Mogul Corporation has created a new piston design with a dual coolant loop gallery. The heat from the piston head is released more efficiently and operating temperature of the piston is lower. The following figure shows the oil flow. The figure depicts the upper and lower piston position when the coolant fills alternately the right and left piston gallery section. This type of solution has been applied in the Mercedes-Benz OM 500 [7].

6. Summary

The investigation on the construction of pistons dedicated to the compression-ignition engine focused on the development trends, especially in material applications and cooling improvement. The paper overviewed the history of aircraft compression-ignition engines and the factors behind the revived interest to improve this type of engines, and particularly piston-opposed engines. The higher permissible engine load has led to the solution of steel as alternative material. Steel pistons enable, among others, better combustion as higher temperatures on the piston surface and higher maximum cylinder pressure could be achieved. Such changes also require us to improve piston cooling. This paper discusses the solutions followed by certain automotive companies.

Acknowledgement

This work has been realized in the cooperation with The Construction Office of WSK "PZL-KALISZ" S.A." and is part of Grant Agreement No. POIR.01.02.00-00-0002/15 financed by the Polish National Centre for Research and Development.

Nomenclature

CFD	computational fluid dynamics	R&D	research&development
CI	compression ignition	TDC	top dead centre

Bibliography

[1] BALICKI, W., PĄGOWSKI, Z., SZCZECIŃSKI, S. et al. Drogi rozwoju napędów lotniczych. Prace Instytutu Lotnictwa. 2009, 199.

[2] BULLIS, K. An engine that uses one-third less fuel. www.technologyreview.com/s/509466/an-engine-that-uses-one-third-less-fuel/. 2013. (accessed 10-01-2017).

[3] CERIT, M., COBAN, M. Temperature and thermal stress analyses of a ceramic-coated aluminum alloy piston used in a diesel engine. International Journal of Thermal Sciences. 2014, **77**, 11-18.

[4] FRYŚ, A. Lotnicze silniki o zapłonie samoczynnym CENTURION 1,7 i 4,0. Silniki Spalinowe. 2005, **120**(1).

[5] GNANA SAGAYA RAJ, A., MALLIKARJUNA, J.M., GANESAN, V. Energy efficient piston configuration for effective air motion – a CFD study. Applied Energy. 2013 **102**, 347-354.

[6] ISKRA, A., BABIAK, M., WRÓBLEWSKI, E. Characteristics of friction losses of aluminum and steel pistons for diesel engine passenger car. Combustion Engines. 2015, **162**(3), 504-510.

[7] ŁYZIŃSKI, M. Unikalna konstrukcja tłoka silnikowego z podwójną galerią chłodzącą, Federal-Mogul, intercars.com.pl/pliki/PLK/wiad14.pdf (accessed 10-01-2017).

[8] OTTLICZKY, E., VOIGT, M., WEIMAR, H.J., WEIβ, E. Steel pistons for passenger car diesel engines. MTZ worldwide. 2011, **10**.

[9] PAYRI, F., BENAJES, J., MARGOT, X., GIL, A. CFD modeling of the in-cylinder flow in direct-injection diesel engines. Computers & Fluids. 2004, **33**, 995-1021.

[10] Pistons and engine testing. MAHLE GmbH (Ed.). Stuttgart 2012.

[11] PRASAD, B.V.V.S.U., SHARMA, C.S., ANAND, T.N.C., RAVIKRISHNA, R.V. High swirl-inducing piston bowls in small diesel engines for emission reduction. Applied Energy. 2011, **88**, 2355-2367.

[12] READ, K. Piston Perfect. Engine Technology International. 2012, **3**.

[13] WAHL, M. A historical look at opposed-piston engines. achatespower.com/opposed-piston-engine-history/ (accessed 10-01-2017).

[14] www.altair.com.pl/news/view?news_id=1328. Kto wykupi Thielerta? (accessed 10-01-2017).

[15] www.altair.com.pl/news/view?news_id=2164. Lepsze informacje Diamonda. Lotnictwo cywilne. 2008, (accessed 10-01-2017).
[16] www.altair.com.pl/news/view?news_id=2621. Nowy lotniczy diesel. Lotnictwo cywilne. 2009, (accessed 10-01-2017).
[17] www.dlapilota.pl/wiadomosci/avweb/pierwszy-lot-samolotu-z-s-ilnikiem-diesla-firmy-eps. Pierwszy lot samolotu z silnikiem Diesla firmy EPS. 2014, (accessed 10-01-2017).
[18] www.generalaviationnews.com/2015/04/29/superior-debuts-gemini-100-diesel/. Superior debuts Gemini 100 diesel. 2015, (accessed 10-01-2017).
[19] www.rheinmetall-automotive.com/en/press/press-kits/press-kits-detail/news/detail/News/innovative-components-for-clean-diesels/. Innovative components for "clean" diesels. 2013. (accessed 10-01-2017).
[20] www.rheinmetall-automotive.com/en/press/press-photos/ (accessed 10-01-2017).
[21] www.rheinmetall-automotive.com/fileadmin/media/kspg/Broschueren/Imagebroschueren/6280_Brosch_Kolbenschmidt_EN_web.pdf. Kolbenschidt Rheinmetall Automotive (accessed 10-01-2017).
[22] www.rheinmetall-automotive.com/fileadmin/media/kspg/Broschueren/Imagebroschueren/Rheinmetall_Automotive_company_info_en_web.pdf. Rheinmetall Automotive Company Information (accessed 10-01-2017).
[23] YAOHUI LU, XING ZHANG, PENGLIN XIANG, DAWEI DONG: Analysis of thermal temperature fields and thermal stress under steady temperature field of diesel engine piston. Applied Thermal Engineering. 2017, **113**, 796-812.
[24] ZACHAROW, A.V., Немецкие "предки" советских танковых дизелей, www.alexfiles99.narod.ru/library2/0001/jumo_and_5tdf_p1.htm (accessed 10-01-2017).

Ksenia Siadkowska, MEng. – Faculty of Mechanical Engineering at Lublin University of Technology.

e-mail: *K.Siadkowska@pollub.pl*

Grzegorz Barański, DEng. – Faculty of Mechanical Engineering at the Lublin University of Technology.

e-mail: *G.Baranski @pollub.pl*

Adam Majczak, MEng. – Faculty of Mechanical Engineering at the Lublin University of Technology.

e-mail: *A.Majczak@pollub.pl*

Article citation info:
GRABOWSKI, Ł., KARPIŃSKI, P., RUDZIK, D. Study on operating load of the compression ignition engine. 2017, **168**(1), 168-171.
DOI: 10.19206/CE-2017-127

Łukasz GRABOWSKI
Paweł KARPIŃSKI
Damian RUDZIK

CE-2017-127

Study on operating load of the compression ignition engine

Operation of car engines definitely shows varied values of parameters such as crankshaft speed or load. This paper presents the research and results on load and crankshaft speed in a compression ignition engine. Therefore, the research focused on an operation of a passenger car under urban and non-urban conditions. Our NI Diadem Analysis-based research referred to the data acquired by an OBD-II system. The results obtained enabled some layered charts to depict a frequency of operating states as specified by engine load and speed as well as histograms of these parameters in individual rides. Our investigation showed that operating conditions have an impact on engine operating states. In urban conditions, our engine operated within the range of 700-2000 rpm but idle was more than 50% of the time and load in most cases was not higher than 20%. In non-urban conditions, our engine operated within the range from 700 to 3000 rpm and load was up to 70%.

Key words: *compression ignition engine, load, operating condition*

1. Introduction

The share of car traffic in urban areas in developed and developing countries is increasing. This tendency has been confirmed by the release on road traffic in 2016 by the Great Britain's Department for Transport. This document shows that vehicle motor traffic (VMT) in urban areas was by about 5% higher than in 2007 and reached 31.4 billion vehicle miles, whereas vehicle motor traffic in non-urban areas increased by the same percentage to reach 58.5 billion vehicle miles [1].

Engine load and speed have an impact on service life of various engine components and fuel consumption [2, 3]. Moreover, toxic emissions of, e.g. particulates or nitrogen oxides are largely impacted if these operational parameters vary. A typical method to achieve combustion with low content of soot and nitrogen oxides and highly efficient operation is the use of the diesel particulate filter (DPF) and the exhaust gas recirculation (EGR) valve capable of increasing air fuel ratio. Another method is the RCCI burning which is a variation of the HCCI method and is capable of reducing toxic emissions and maintaining high thermal efficiency for medium and large loads [4]. It is, therefore, important to examine the most frequent operating states of a car engine in urban and non-urban conditions.

Toxic emissions emitted by various drive units can be compared by means of a CADC test driving cycle which relies on the statistical analysis of European real driving patterns, developed in an European project – ARTEMIS. Such a driving cycle covers three traffic situations: urban, non-urban and motorway. The authors [5, 6] claim that this approach is more reliable than the NEDC test procedure which is a laboratory-based defined speed change and a measurement of fuel consumption and toxic emissions.

While driving a car, there are varied loads so engine operation should be properly controlled. Such a control relies on transition from one to another operating point defined by speed, load and fuel consumption to achieve the best possible dynamic transition between operating states and the lowest possible specific fuel consumption [7].

The car engine operates under steady-state conditions but only in few traffic situations, e.g. in non-urban areas. The most frequent traffic operating conditions are transient conditions, e.g. the vehicle often speeds up and slows down in urban areas [8]. Certain experiments on how transient conditions impact the operation of a turbocharged diesel engine are discussed in [9].

Engine load is also impacted by ambient conditions, especially crosswind and headwind so a correct engine operation control should be accompanied by vehicle aerodynamics. The work [10] discusses the correlation between the coefficient of drag and speed and direction of wind for the truck.

Measured by means the PEMS system, emissions of nitrogen oxides and carbon dioxide have turned out to be higher for more varied topographically routes and more dynamic driving styles [11]. The PEMS system is a variation of the RDE test that relies on measuring emissions of toxic substances during real driving, regarding factors such as: speed, topography, ambient temperature, load. The NO_x emission is also reduced in non-urban areas [12]. The study [13] shows that energy consumption calculated from the TTV analysis for an up-and-down route is larger for compression-ignition engine than the electric engine.

This paper discusses the research results on engine operating states, i.e. load and crankshaft speed in urban and non-urban areas. The measurements were performed with a recording device that cooperates with an EOBD protocol compatible diagnostic connector.

2. Research object

The research object was a four-cylinder diesel engine 2.0 MZR-CD with a power of 100 kW (Fig. 1). The engine was mounted in the passenger car Mazda 6 wagon. The engine is directly fuel injected with a Common Rail system. The Euro 3 emission standards are satisfied by the solution of the engine cooperating with the diesel particulate filter (DPF). The engine is fitted with a variable-geometry turbocharger. The basic engine technical parameters are in Table 1.

Fig. 1. Research engine 2.0 MZR-CD

Table 1. 2.0 MZR-CD basic technical parameters

Year of production	2004
Cylinder capacity	1998 cm^3
Ignition type	CI
Injection type	Common Rail
Charge type	Variable-geometry turbocharger
Power	100 kW/136 hp (3500 rpm)
Torque	310 Nm (2000 rpm)
Engine mounting	transverse
Number of cylinders	4
Arrangement of cylinders	in-line
Camshaft location	SOHC (OHC)
Number of valves	16
Compression ratio	18:1
Bore	86 mm
Piston stroke	86 mm
Emission standard	Euro 3

3. Test bench

Load in the compression-ignition engine passenger car in urban and non-urban traffic is measured with the TEXA OBD Log (Fig. 2). Engine load value is directly available in OBD II information and it is expressed by percent. The recording device is capable of real-time registering engine parameters such as vehicle speed, crankshaft speed, coolant temperature, engine load, air mass flow, air temperature, intake air pressure, fuel pressure and battery voltage. There are also registered route-specific data like a vehicle identification number, route numbers, starting and ending hours. The recording device supports the following EOBD protocols which are in line with the J1850-41.6, J1850-10.4, ISO 9141-2 K/L, CAN (Control Area Network ISO 11898).

Fig. 2. TEXA OBD Log [14]

The device has been connected to the vehicle with an EOBD diagnostic connector. Entering the selected parameters was followed by transferring the data into the computer by a special software of OBD Log SW Suite. Data analysis were performed in NI Diadem software. A general diagram of data collection and investigation is depicted in Figure 3.

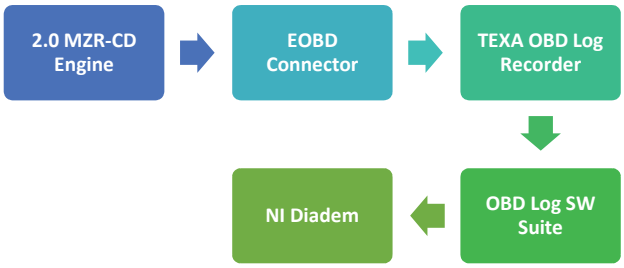

Fig. 3. Diagram of data collection and investigation

4. Research methodology

The vehicle with the connected DVR TEXA OBD Log operated on urban and non-urban routes of different lengths and varied loads. The recording device recorded the following parameters: engine load, coolant temperature, intake air pressure, crankshaft speed, vehicle speed, air temperature, air mass flow, pressure in the fuel rail, battery voltage.

A one-week driving tests were performed in urban and non-urban traffic and the data was recorded with a 5 Hz frequency. Ambient conditions were similar during each of the driving tests, and each of the drives was not less than 10 min. The tests were carried out in Lublin city and in Lublin province. Mean vehicle speed was 21 km/h in urban cycle and 52 km/h while driving non-urban cycle.

The NI Diadem software created the distribution of engine operating density at a specific engine speed and load. Our calculation was in line with a special script.

The results are given as histograms and contour plots. The load ranged from 0 to 100%, whereas the speed from 700 to 3,200 rpm. During analysis the measurement ranges were divided for load is 5%, whereas for crankshaft speed is 100 rpm.

5. Result examination

The first part shows the registered engine load and crankshaft speed as a function of driving time for the selected non-urban driving test.

The second part shows the contour plots of the frequency of engine load and the histograms of the engine load and the crankshaft rotational speed for the selected urban and non-urban driving tests. Because of many testing drives, this paper shows the data for one driving test under given traffic conditions only.

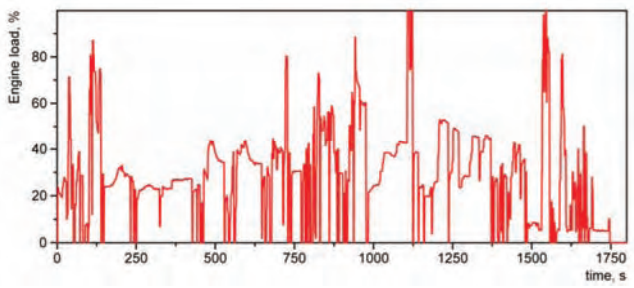

Fig. 4. Load as a function of driving time

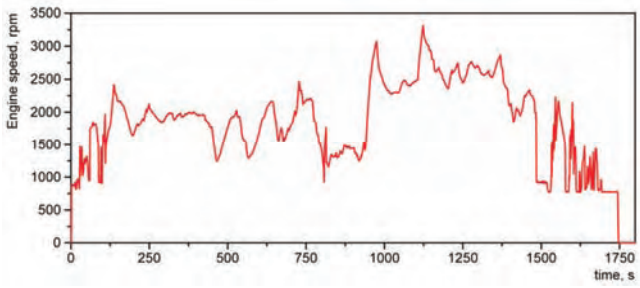

Fig. 5. Crankshaft speed as a function of driving time

The engine was at idle at first (about 750 rpm) and then the crankshaft speed increased as the vehicle accelerated to about 2,500 rpm (Fig. 4). Speed in the further part of the drive was not relatively constant as in the first period of time, i.e. 250-750 s it ranged from 1,400 to 1,700 rpm and later, i.e. 1,000-1,300 s increased and ranged between 2,300 and 2,600 rpm (Fig. 5).

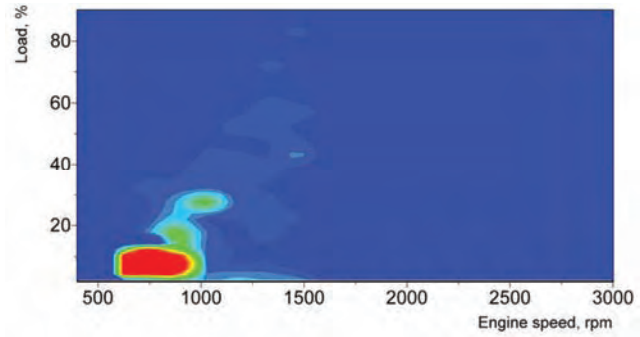

Fig. 6. Engine load frequency as a function of engine speed and load for urban traffic

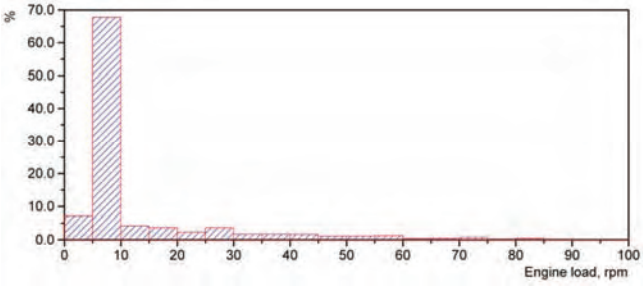

Fig. 7. Histogram of the engine load for urban traffic

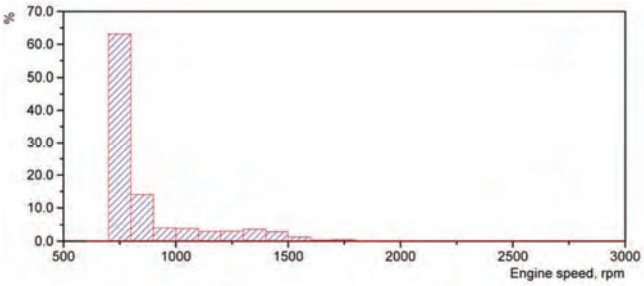

Fig. 8. Histogram for crankshaft speed for urban traffic

The load frequency as a function of speed and load is in Fig. 6 and the histograms of the frequency of engine load and speed for the selected urban test drive are in Figures 7 and 8, respectively.

The most frequent load of 0-10% corresponds to the idling speed of 700-900 rpm, which results from the fact that the vehicle often stopped during the urban drives because of heavier traffic, signal lights and other traffic disruptions. The most frequent load range for the research engine was 5-10% and the frequency of this range was about 68%. The urban engine load reached 80%, but the lowest frequency was in the load range of 75-80%. Idling speed, i.e. about 750 rpm, was most frequent, and the least frequent speed range was 1,875-2,000 rpm. The frequency of idling speed was about 63%. The urban engine speed range was 700-2,000 rpm.

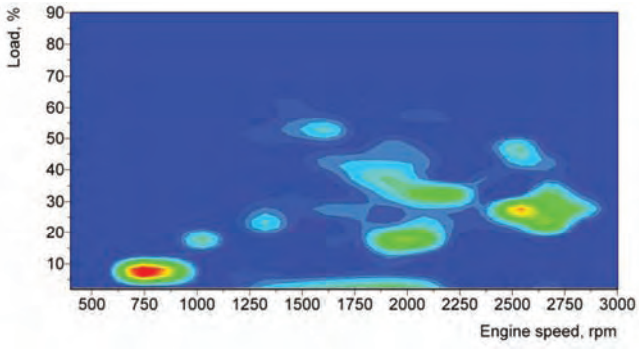

Fig. 9. Engine load frequency as a function of engine speed and load for non-urban traffic

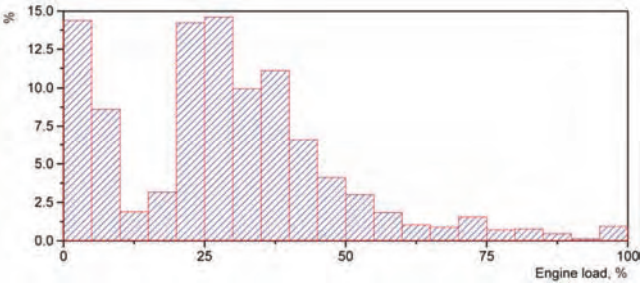

Fig. 10. Histogram for engine load in non-urban traffic

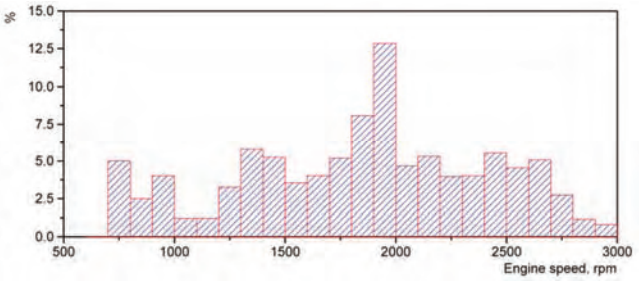

Fig. 11. Histogram for crankshaft speed in non-urban traffic

The load frequency as a function of speed and load is in Fig. 9 and the histograms of the frequency of engine load and speed for the selected non-urban test drive are in Figs 10 and 11, respectively.

The most frequent load ranges are: 0-10% – this range corresponds to the idling speed of 700-900 rpm and 20-30% – this range corresponds to the speed of 2,450-2,600 rpm. The former frequency results from the fact that the vehicle

often stopped in the non-urban drives because of traffic and other traffic disruptions. The latter one reflects constant-speed driving. The frequency of the 5-10% load range reached about 22%, whereas that of 20-30% was about 29%. The non-urban traffic engine load was nearly 100%, but the load range of 90-95% was least frequent. The most frequent speed was 1,875-2,000 rpm, and the frequency of this range was about 12,5%. The non-urban traffic crankshaft speed was within the range of 700-3,000 rpm.

6. Conclusions

The research aimed at specifying loads of the passenger car CI engine that operated in urban and non-urban traffic. It should be also noticed that obtained results concern one type of engine.

Installed in the Mazda 6 passenger car, the OBD Log device measured engine load.

Regarding the results, it can be claimed that the engine is loaded less in urban than non-urban traffic because of road conditions in the city like heavy traffic, signal lights and road works.

It can be concluded that the engine operates in urban traffic mainly at idle and a negligible load of about 5-10%, whereas in non-urban traffic it more often operates at higher speeds, i.e. 1,800-2,100 rpm and the larger load of 20-35%.

Nomenclature

DPF	diesel particulate filter
EGR	exhaust gas recirculation
EOBD	European On-Board Diagnostics
HCCI	homogeneous charge compression ignition
OBD	on-board diagnostics
PEMS	portable emission measurement system
RCCI	reactivity controlled compression ignition
RDE	real driving emission
TTW	tank-to-wheel
VGT	variable-geometry turbocharger
VMT	vehicle miles traveled

Bibliography

[1] Provisional Road Traffic Estimates, Department for Transport, Great Britain: January 2016–December 2016 Summary.

[2] QUIANFAN, X. Diesel engine system design. Woodhead Publishing Limited, 2011, 115.

[3] HEYWOOD, J.B. Internal combustion engine fundamentals. *McGraw-Hill Education*. 1988, 839.

[4] WANG, Y., YAO, M., LI, T. et al. A parametric study for enabling reactivity controlled compression ignition (RCCI) operation in diesel engines at various engine loads. *Applied Energy*. 2016, **175**, 389-402.

[5] BLANCO-RODRIGUEZ, D. Modelling and observation of exhaust gas concentrations for diesel engine control. *Springer*. 2014, 62-63.

[6] ANDRÉ, M. The ARTEMIS European driving cycles for measuring car pollutant emissions. *Science of The Total Environment*. 2004, **334-335**, 73-84.

[7] POSTRZEDNIK, S., STOPA, P., CIESIOŁKIEWICZ, A. The analysis of loading state of combustion engine in different variants of its work. *26 Międzynarodowa Konferencja Naukowa Silników Spalinowych. Nałęczów*, 2000, 235-244.

[8] RAKOPOULOS, C.D., GIAKOUNIS, E.G. Diesel engine transient operation – principles of operation and simulation analysis. Springer. 2009, 4.

[9] YUM, K.K., LEFEBVRE, N., PEDERSEN, E. An experimental investigation of the effects of cyclic transient loads on a turbocharged diesel engine. *Applied Energy*. 2017, **185**, 472-481.

[10] BARDEN, J., GEROVA, K. An on-road investigation into the conditions experienced by a heavy goods vehicle operating within the United Kingdom. *Transportation Research Part D*. 2016, **48**, 284-297.

[11] GALLUS, J., KIRCHNER, U., VOGT, R., BENTER, T. Impact of driving style and road grade on gaseous exhaust emissions of passenger vehicles measured by a Portable Emission Measurement System (PEMS). *Transportation Research Part D*. 2017, **52**, 215-226.

[12] KWON, S., PARK, Y., PARK, J. et al. Characteristics of on-road NOx emissions from Euro 6 light-duty diesel vehicles using a portable emissions measurement system. *Science of the Total Environment*, 2017, 576, 70-77.

[13] TRAVESSET-BARO, O., ROSAS-CASALS, M., JOVER, E. Transport energy consumption in mountainous roads. A comparative case study for internal combustion engines and electric vehicles in Andorra. *Transportation Research Part D*. 2015, **34**, 16-26.

[14] motofocus.pl/informacje/nowosci/6135/bez-zadnych-tajemnic-obd-log-texa

Łukasz Grabowski, DEng. – Faculty of Mechanical Engineering at the Lublin University of Technology.

e-mail: *L.Grabowski@pollub.pl*

Paweł Karpiński, MEng. – Faculty of Mechanical Engineering at the Lublin University of Technology.

e-mail: *Pawel.Karpinski@pollub.edu.pl*

Damian Rudzik, MEng. – Faculty of Mechanical Engineering at the Lublin University of Technology.

e-mail: *damianrud@gmail.com*

Article citation info:
OSIPOWICZ, T., ABRAMEK, F. The analysis of temperature disintegration on the body of fuel injector during research on test bench. *Combustion Engines*. 2017, **168**(1), 172-177. DOI: 10.19206/CE-2017-128

Tomasz OSIPOWICZ
Franciszek ABRAMEK

CE-2017-128

The analysis of temperature disintegration on the body of fuel injector during research on test bench

Article describes the results of researches fuel injectors on the test bench with using infrared camera. During researches has been verified various fuel injectors (working order and faulty). In results inner leaks fuel injectors have increased return dosages. Few elements influence on this. It is difficult to determine which element could be uses after disassemble. It is possible to determine the source of leaks during analysis decomposition of temperature fuel injector body.

Key words: *infrared camera, Common Rail system injector, injection and return dosages, fuel high pressure pump, CI engines*

1. Introduction

Using infrared camera by diagnosing Common Rail fuel injectors is innovative project and belongs to without invasion method of diagnostic.Without invasion method of diagnostic are effective, fast and not expensive. Normal diagnostic procedure of repairable injectors consists in disassemble and microscope researches. Microscope researches are very effective but time – consuming and expensive. This method is very helpful when it is noticeable that injector leaks but engineer is not sure where the leaks appear. It is possible to localize very fast damage area. There are many possibilities to use infrared camera to diagnose fuel system in CI – engines. It could be used to diagnose high pressure section in the fuel pump, adjusters and sensors, high pressure fuel pipes and rails. The good point of this type researches are short time and cheapness.

2. Infrared camera as diagnosing tools CI – engine injection systems

The main task of infrared camera is temperature measurement of researched object [7]. These type of researches are contactless and don't disrupt device work. So that it is very good diagnosing element. Temperature illustrates technical condition of device especially elements of fuel injection system such fuel pump or injectors [2]. The leakages on precision elements of injection system cause temperature rise. Main reason of faulty fuel injector work are leaks [3]. Injector during research on test bench heats up but in defect areas is very hot. Research protocol presents magnitude of injection and return dosages [4]. If dosages are wrong research worker don't know what is wrong. There are many elements in fuel injector which could be faulty. But when it is known the area of defect it could be very easy wrong element to diagnose. Defects of fuel injectors concern the precision elements and inner sealers usually. These parts are responsible for correct injector work. If something wrong is with these elements injectors dosages are wrong. The temperature on the injector body rise despite of leaks. When infra camera is used it could be easy find faulty elements because there will be higher temperature. Figure 1 presents electromagnetic Bosch fuel injector disassembly on spare parts. There are marked elements where temperature rises during leaks (A, B, C). Higher temperature occurs in injector coil because of work [5].

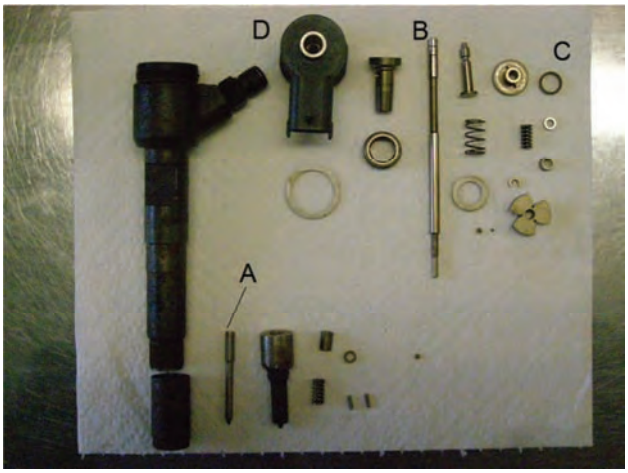

Fig. 1. Electromagnetic Bosch fuel injectors. A – precision element on injector needle, B – fuel injector steering valve, C – valve sealer, D – fuel injector coil

Figure 2 presents electromagnetic Bosch fuel injector researched infrared camera during test bench. There has been marked on the figure precision element on injector needle (A), fuel injector steering valve (B), valve sealer (C) and fuel injector coil (D). It is noticeable that higher temperature is on precision elements due to leaks and in the solenoid.

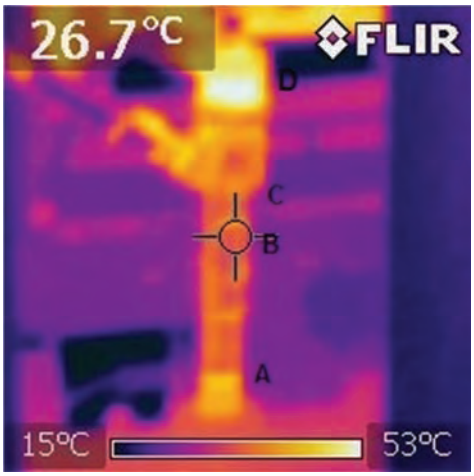

Fig. 2. Electromagnetic Bosch fuel injector on the infrared camera picture during test

There is possibility to analysis temperature injected fuel (Fig. 3) using infrared camera. Fuel temperature influences on corrosion, cavitation, erosion and friction phenomena. This parameter could be useful to determine phenomena inside injector nozzle.

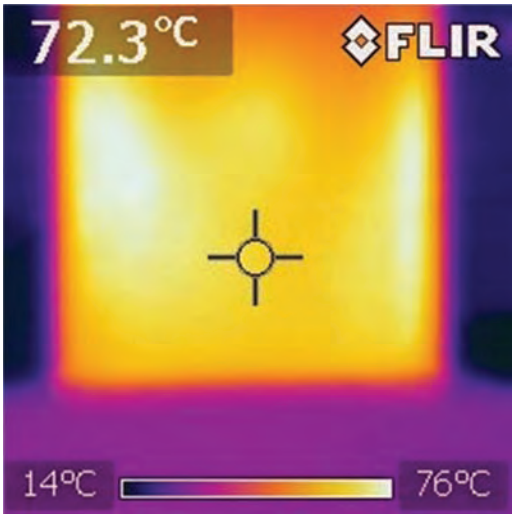

Fig. 3. Temperature of injection fuel

There is opportunity to research fuel injection pump especially high pressure section. If there are leaks it would be visible using infrared camera. Figure 4 presents the picture of high pressure injection pump during research on the bench.

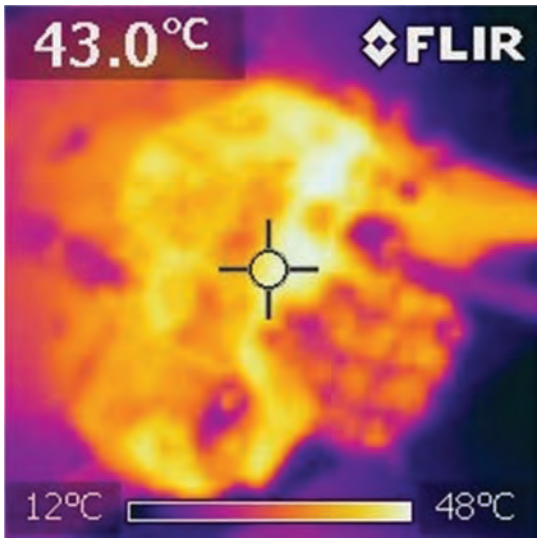

Fig.4. Temperature of fuel injection pump

3. Laboratory test

During laboratory tests has been used electromagnetic Delphi fuel injectors. Figure 5 presents researched injector disassembled on spare parts. There has been sectioned two areas. The first injector nozzle (A) and the second steering valve and electromagnetic coil areas (B). This areas determine fuel injector work parameters (injection and return dosages and injection delay). Catalogue number researched fuel injector were EJBR02201Z [6]. Researches has been made on STPiW 3 test bench (Fig. 7) by using infrared camera (Fig. 6). Infrared camera Flir i3 measures the temperatures 273–523 K (0–250°C). Measure deviation is ±2°C.

Fig. 5. Electromagnetic Delphi fuel injector dismantled on spare parts: A – injector nozzle area, B – steering valve and electromagnetic coil area

Fig. 6. Infrared camera Flir i3

Table 1 shows standard test of researched fuel injectors. There is noticeable that injectors 1 and 4 are damage. There are huge return dosages what influence on theirs parameters. Figure 7 presents test bench STPiW 3 with researched Delphi injectors and magnitude of return dosage test. There was taken two injectors third and fourth during researches with infrared camera. Studies has been taken into consideration two areas of injectors body nozzle (Fig. 8, 9) and steering valve with coil (fig. 10, 11). Tests have been made with 50, 80, 110 and 140 MPa system pressures. Figure 12 presents measured return dosage by pressure 140 MPa for faulty and good working injectors. There is noticeable in all instances considerable difference temperatures between injectors. Figures 13 and 14 present damage fuel injector precision elements: needle and steering valve.

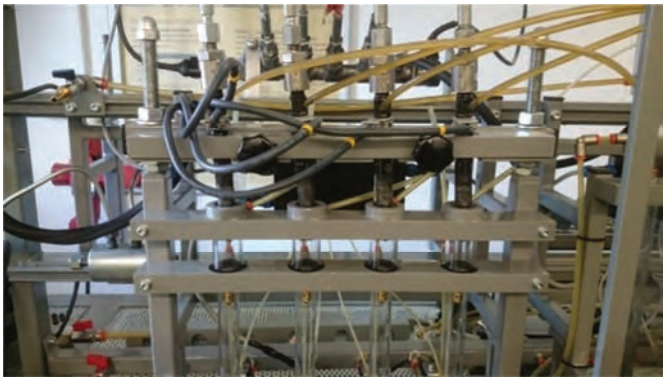
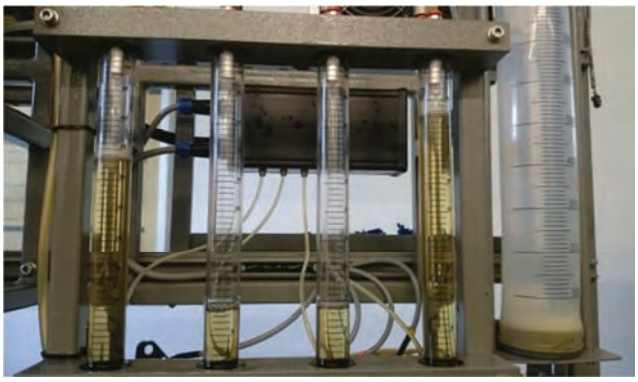

A B

Fig. 7. A – researched fuel injectors on test bench STPiW 3, B – the magnitudes of return dosages researched fuel injectors

Tab.1. Injection and return dosages standard test results

No.	Injection pressure [MPa]	Injection time [μs]		Range	Inj. 1	Inj. 2	Inj. 3	Inj.4
1	165	0	Injection	0.00–0.00	0.0	0.0	0.0	0.0
		60 s	Return	0.00–40.00	110.23	32.97	33.86	112.74
2	160	930	Injection	49.00–55.00	39.8	53.21	54.11	40.40
			Return	0.00–56.00	111.30	36.18	38.26	119.40
3	120	220	Injection	0.30–4.50	6.3	1.85	2.06	9.6
			Return	0.00–56.00	81.08	33.10	35.32	87.23
4	80	780	Injection	27.10–34.50	31.00	30.10	27.80	31.80
			Return	0.00–56.00	79.23	31.76	33.42	82.34
5	25	480	Injection	2.70–7.45	3.80	3.80	3.60	4.20
			Return	0.00–56.00	42.70	10.86	14.97	58.60
				Test pass	No	Yes	Yes	No

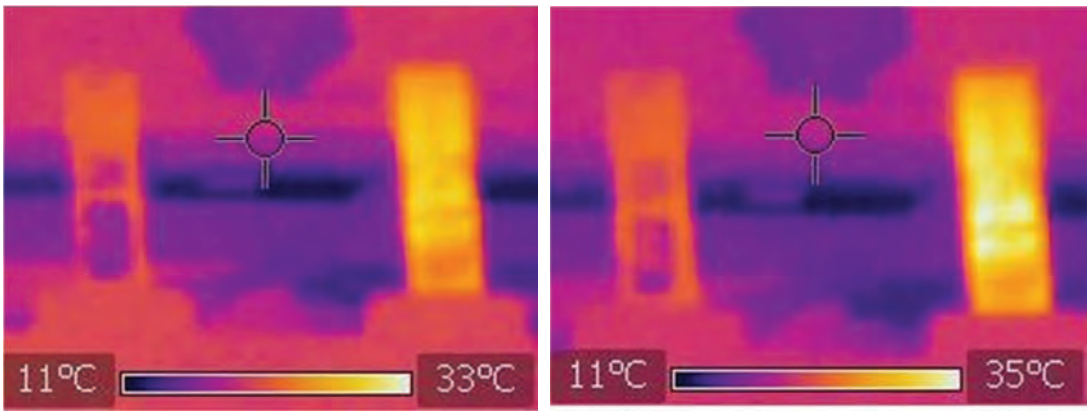

A B

Fig. 8. Pictures of nozzle areas from infrared camera for third and fourth injectors: A – fuel pressure 50 MPa, B – fuel pressure 80 MPa

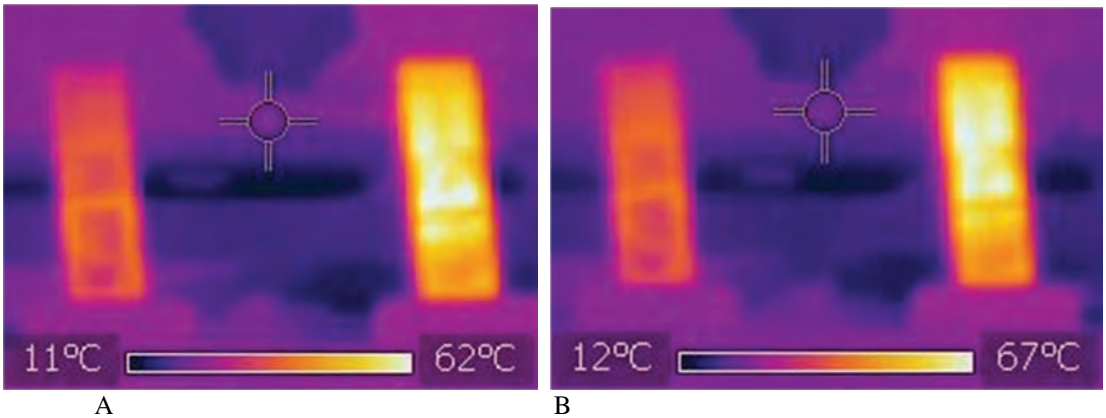

A B

Fig. 9. Pictures of nozzle areas from infrared camera for third and fourth injectors: A – fuel pressure 110 MPa, B – fuel pressure 150 MPa

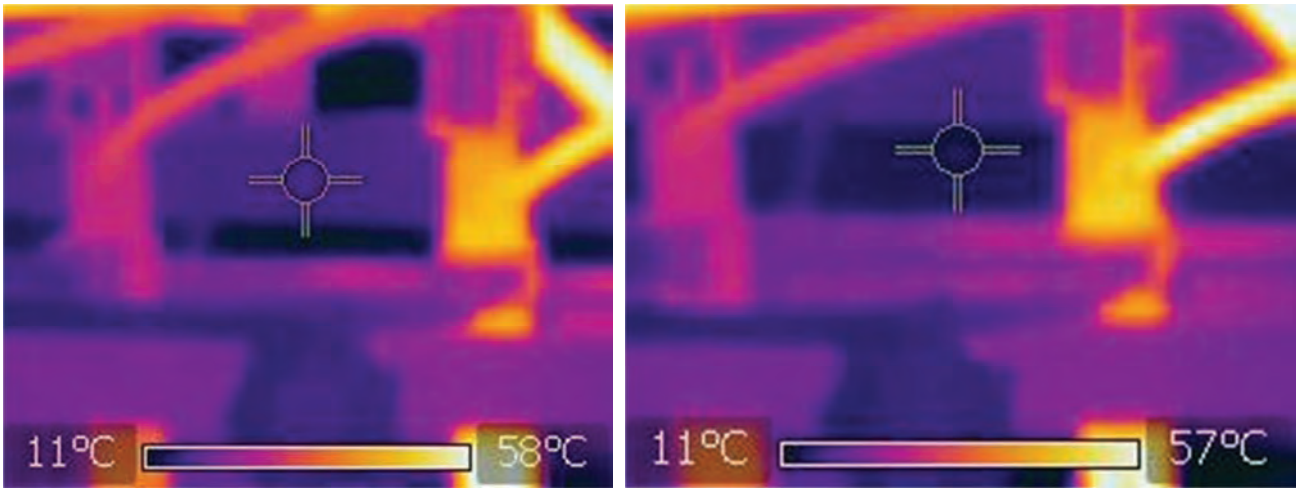

A B

Fig. 10. Pictures of steering valve and electromagnetic coil areas from infrared camera for third and fourth injectors: A – fuel pressure 50 MPa, B – fuel pressure 80 MPa

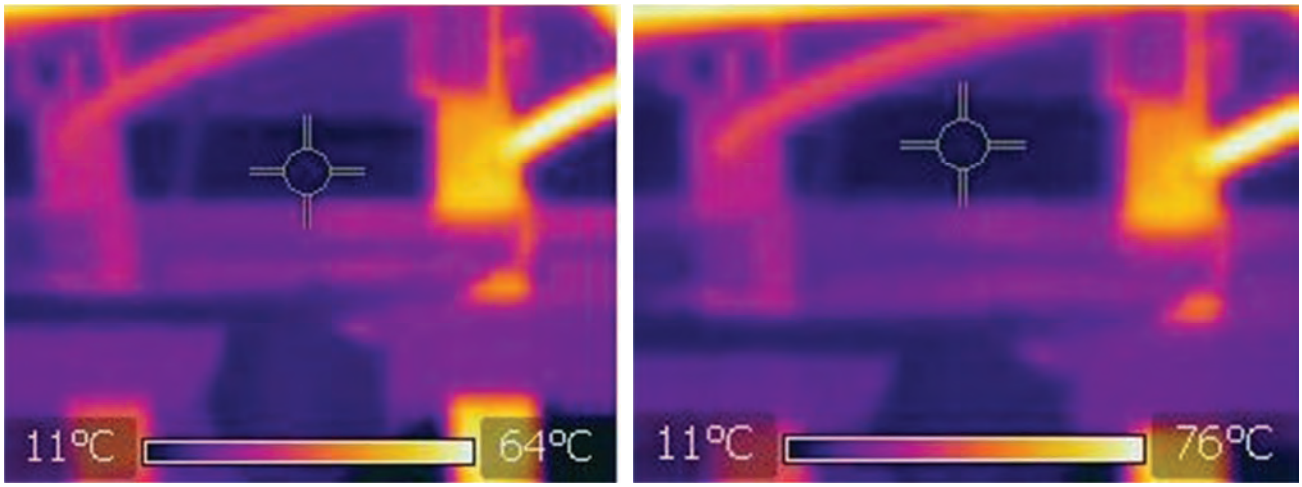

A B

Fig. 11. Pictures of steering valve and electromagnetic coil areas from infrared camera for third and fourth injectors: A – fuel pressure 110 MPa, B – fuel pressure 140 MPa

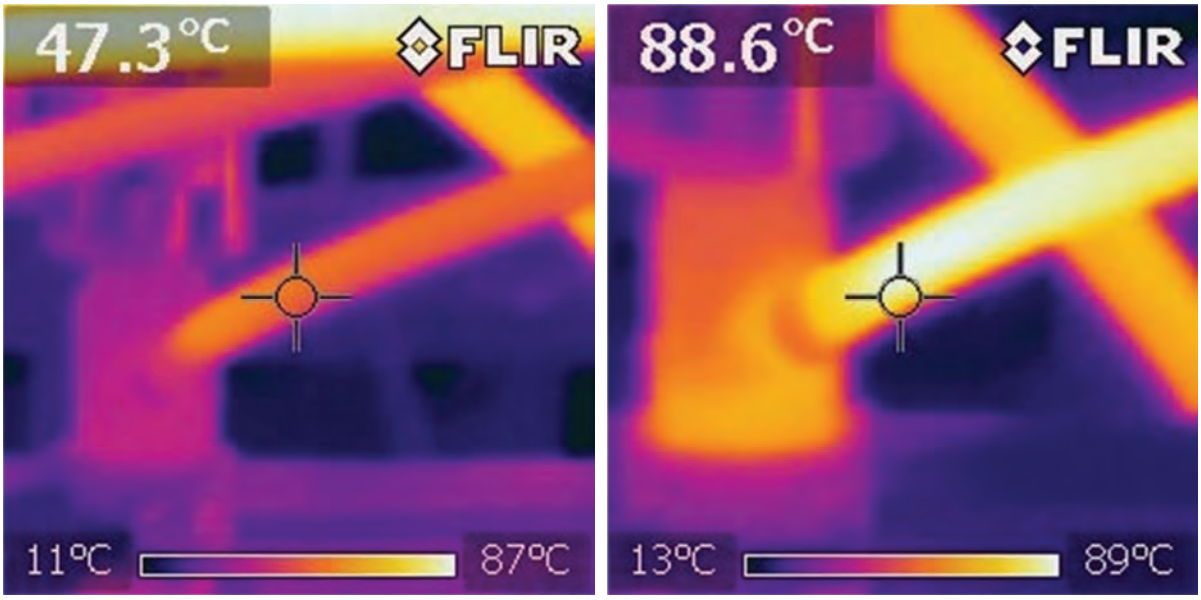

A B

Fig. 12. Temperature of return dosage: A – correct fuel injector, B – faulty fuel injector

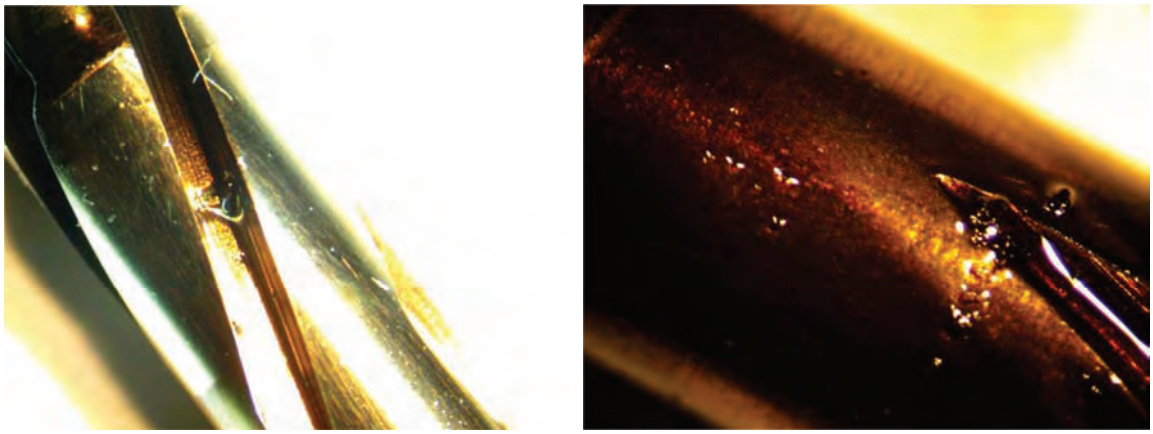

A B

Fig. 13. A, B Precision elements on damage injector needle

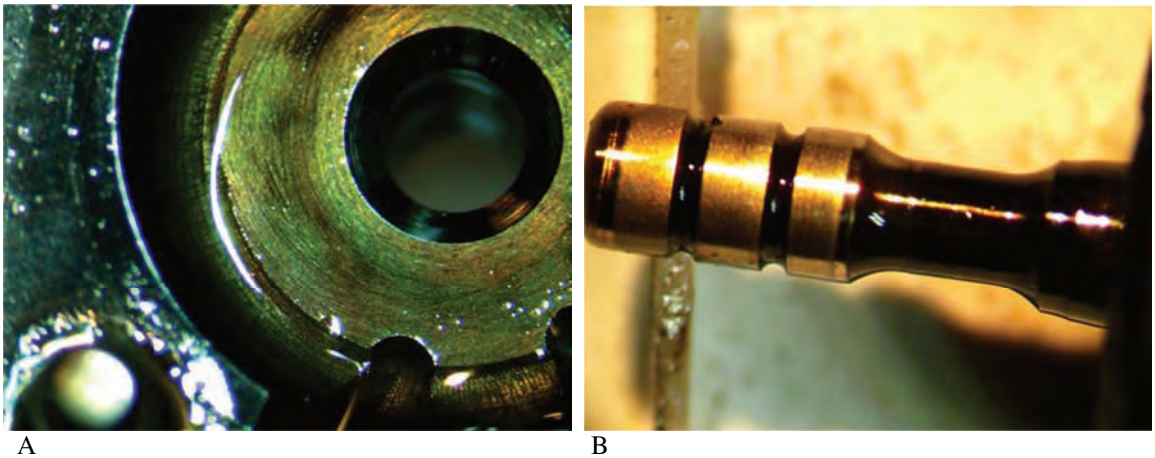

A B

Fig. 14. Damage injector steering valve A – valve section, B – piston

4. Conclusion

It is possible to state during analysis of research results that infrared camera could be useful during researches fuel injectors on the test bench. There happen very often that fuel injector is researched and the standard test shows its damage but engineer don't know where it occur. Fuel injector has few areas: nozzle with needle, steering valve with sealer and coil. When return dosage is to high it is hard to determine where the fault occurs. There is possibility to disassemble injector and use microscope to check precision elements but sometimes it is hard to find where the leaks are. It is easy to change all elements but then repair costs increase. Using infrared camera is very effective method without invasion of diagnostic during researches. There have been researched two areas of injectors during test. The first area was injector nozzle area. If the precision element on the injector needle is damage it will increase leaks. Temperature would be higher there (Fig. 8, 9). Infrared camera registers it. The same situation is with steering valve. Figure 12 presents the temperature difference between good working and faulty injectors. Return dosages amount 119.40 mm^3/H for faulty fuel injector and 38.26 mm^3/H for good working by 160 MPa test pressure. This difference is visible on infrared camera because the faulty injector has temperature of returning fuel 88°C (361 K) and good working 47°C (320 K). This is the result of internal leaks caused damages precision elements. The return dosage temperature increased about 87% by system pressure 160 MPa. For lower pressures 80 MPa temperature increased about 40%.

Figure 13 and 14 show damages precision elements. There are noticeable a lot of pollutants, metal filings, corrosion, temperature damages and pieces of fuel filter. Metal fillings come from fuel injection pump. In this case diagnostic process was very easy. Everything were visible. But sometimes there are instances where theoretical all elements are in norms but injector leaks. Using infrared camera to find this area is very helpful. There were researched injection fuel temperature on the test bench and fuel return dosages temperature for good working and faulty injectors. Injection temperatures were similar for both but return various due to leaks. The measurements have been carried starting through 40°C intake fuel to injectors. Than has been made one fuel injectors standard test to stabilize the temperature inside. After the test is it possible to make researches by using infrared camera. There is possibility to use this method to all modern fuel injectors. Every electromagnetic and piezoelectric fuel injectors start to heat during inner leaks.

Nomenclature

CI	compression ignition
CR	common rail system
µs	micro seconds

Bibliography

[1] AMBROZIK, A., AMBROZIK, T., ŁAGOWSKI, P. Fuel impact on emissions of harmful components of the exhaust gas from the CI engine during cold start up. *Eksploatacja i Niezawodnosc – Maintenance and Realiability.* 2015, **17**(1), 95-99.

[2] GÜNTHER, H. Common Rail – Systeme in der Werkstattpraxis. Technik, Prüfung, Diagnose. *Bad Wörihofen: KrafthandVerlag Walter Schultz GmbH*. 2012.

[3] KNEFEL, T. Ocena techniczna wtryskiwaczy Common Rail na podstawie doświadczalnych badań przelewów. *Eksploatacja i Niezawodnosc – Maintenance and Reliability.* 2012, **14**(1), 42-53.

[4] OSIPOWICZ, T., ABRAMEK, K.F., STOECK, T. Testing of modern common rail fuel injectors. *Combustion Engines*. 2015, **162**(3), 688-694.

[5] OSIPOWICZ, T. Diagnosing Common Rail fuel injectors using fuel micro – doses. *Teka. Commission of Motorization and Energetics in Agriculture.* 2015, **15**(1), 61-64.

[6] OSIPOWICZ, T. Analysis of the costs and cost – efficiency of regeneration of modern fuel injection systems in CI engines. *Econtechmod. An International Quarterly Journal.* 2016, **5**(2), 45-50.

[7] WIĘCEK, B., DE MEY, G. Termowizja w podczerwieni. Podstawy i zastosowania. *Wydawnictwo PAK*. 2011.

Tomasz Osipowicz, DEng. – Faculty of Mechanical Engineering and Mechatronics at West Pomeranian University of Technology.

e-mail: *Tomasz.Osipowicz@zut.edu.pl*

Karol F. Abramek, DSc., DEng. – Faculty of Mechanical Engineering and Mechatronics at West Pomeranian University of Technology.

e-mail: *Karol.Abramek@zut.edu.pl*

Article citation info:
LASOCKI, J., ORLIŃSKI, P., WOJS, M.K. et al. Hydroxyl radicals as an indicator of knocking combustion in the dual-fuel compression-ignition engine. *Combustion Engines*. 2017, **168**(1), 178-185. DOI: 10.19206/CE-2017-129

Jakub LASOCKI
Piotr ORLIŃSKI
Marcin Krzysztof WOJS
Marlena OWCZUK
Anna MATUSZEWSKA

CE-2017-129

Hydroxyl radicals as an indicator of knocking combustion in the dual-fuel compression-ignition engine

The occurrence of knocking combustion is one of the basic problems of dual-fuel compression-ignition engines supplied with diesel oil and gaseous fuel. In order to detect this phenomenon and evaluate its intensity, several methods are commonly used, including the analysis of pressure of working medium in the combustion chamber of the engine or vibrations of certain engine components. This paper discusses the concept of using mass fraction of hydroxyl radicals as the indicator of the occurrence of knocking combustion. Current knowledge on the conditions of hydroxyl radical formation in the engine combustion chamber has been systematized and the results of research on this subject have been presented. Theoretical considerations are illustrated by exemplary results of simulation studies of the combustion process in a dual-fuel compression-ignition engine supplied with diesel oil and methane. The conclusions drawn may be useful for the development of dual-fuel engine control systems.

Key words: *knocking combustion, dual-fuel engines, radicals, hydroxyl radicals*

1. Introduction

Compression-ignition (CI) engines, due to their favorable durability and efficiency, have been widely used in various applications, starting from industrial stationary power generators and engineering equipment, through agriculture, and ending up in the land and marine transportation sector. The market share of vehicles equipped with CI engines is continuously rising, especially in Europe, and the current trends show that they are getting more desirable in the foreseeable future across different categories, including light, heavy-duty and off-road vehicles [36].

However, despite clear advantages of CI engines, their emissions are difficult to control by classic aftertreatment of the oxygen-rich exhaust gases through the use of catalysts [16, 31]. Of all the substances formed in cylinders of CI engines, the most problematic are nitrogen oxides (NO_x) and particulate matter (PM) [23]. They cause air pollution, which is linked to serious health problems, especially respiratory and cardiovascular diseases [18]. The contribution of CI engines to total air pollution has been growing as a consequence of their increasing numbers in fleets and increasing distances travelled. Moreover, even with excellent fuel economy CI engines add to the increasing intensity of consumption of natural resources. The proven oil reserves, according to various studies [1, 12], will not sufficiently meet the expected growth of worldwide demand for the upcoming years. Environmental pollution problems, increasing energy demand and depleting oil reserves, associated with the use of fossil fuels, create growing opportunities for the use of alternative fuels [6, 7].

In the past few decades, valuable breakthroughs in the study on combustion and emission characteristics of various fuels have been made [11] and an increasing number of CI engines have been adapted to dual-fuel mode [25]. Numerous theoretical and empirical investigations have drawn attention towards gaseous fuels, i.e. natural gas (NG) and liquefied petroleum gas (LPG), as very promising candidates to play the role of essential energy source in the transportation sector in the near future [16].

In comparison with other alternative fuels, NG and LPG have some distinct and desirable advantages. Both gases can be supplied to the in-use engines without significant modifications [2, 14]. The dual-fuel mode can easily be reverted back to diesel-only operation [28]. CI engines supplied with NG or LPG have good thermal efficiency at high output. Unfortunately, at part load conditions there is a drop in efficiency and power output, when compared to engine supplied with diesel oil. With respect to ecological aspects, studies have shown that the use of NG and LPG in CI engines results in producing less polluting exhaust gases, if appropriate conditions are satisfied for its mixing and combustion [32]. In general, the greatest benefits can be achieved from reduction of NO_x and PM emissions. Another positive aspect of supplying CI engines with gaseous fuels is a big potential to lower noise emissions. All these advantages have prompted researchers to intensify their work on the further development of dual-fuel CI engines.

The combustion process in a dual-fuel engine is complex and combines the features of CI and spark-ignition (SI) engines [38]. Gaseous fuel, when inducted into the intake manifold or directly into the cylinder, easily mixes with fresh air and forms a homogeneous phase, which then can be ignited by a small amount of diesel oil called the pilot dose. Gaseous fuel acts as primary fuel since it is the main source of energy input to the engine. When compressed with air, it should not ignite spontaneously due to its high autoignition temperature. Diesel oil, injected near the end of compression stroke, should autoignite first and become a source of ignition for the combustion of gaseous fuel. However, if the percentage of inducted gaseous fuel is increased, the combustion process in dual-fuel engines can suffer from knocking, especially at high load [20, 21, 24, 30, 34, 42]. Knocking combustion involves autoignition of gaseous fuel-air mixture ahead of the advancing flame originated from the burning of diesel oil. Generated pressure oscilla-

tions cause deterioration of engine efficiency, increase in exhaust emissions and engine noise [22]. Severe knock leads to excessive wear of the engine and, in extreme cases, results in damage of the engine [22].

The problem of knock is widely recognized as a major obstacle for further improvement of dual-fuel CI engines supplied with gaseous fuels. Therefore, efficient methods of knock detection and evaluation of its intensity are needed. So far, several methods have been developed [22]. In the mass-produced engines the most commonly used method of knock detection employs vibration sensors, attached to certain engine components (typically engine block or head). The main drawback of this method is the susceptibility of the vibration signal to noise, especially at large engine speed [5]. Similar problem applies to the methods of engine knock detection based on direct measurement and analysis of in-cylinder pressure. In this case however, the fact of autoignition cyclic variability, even at the same in-cylinder pressure, must be taken into account [4]. One of the promising techniques used in engine knock detection involves determination of the quantity (e.g. mass fraction) of radicals existing in the in the combustion chamber [3, 15, 17, 19, 26, 27, 29, 33, 37, 40]. In order to acquire information about the quantity of radicals, chemical luminescence methods are widely used [3, 15, 17, 19, 29, 33, 37].

The focus of this paper is to discuss the mass fraction of hydroxyl radicals as an indicator of knocking combustion in the dual-fuel CI engine. Current state of the research on this issue has been reviewed and the results of simple simulations of the combustion process in dual-fuel CI engine, with particular emphasis on hydroxyl radicals formation, have been presented.

2. Hydroxyl radicals as an indicator of knocking combustion

The oxidation of hydrocarbon fuel in engine combustion chamber involves a variety of intermediate compounds, which reactions, in ideal conditions, lead to the final products, i.e. carbon dioxide (CO_2) and water (H_2O) [27]. The whole process is known to develop through a complex radical chain mechanism. The significant feature of this mechanism is branching of the chain, which makes combustion easy to self-accelerate, especially if intensified by the exothermic character of reaction. The autoignition of organic substances is strongly related to their exothermic oxidation chemistry, but the specific course of reaction is determined by the physical properties of the environment within which it takes place. The majority of alkanes follow a mechanism of oxidation, which is presented in Figure 1.

Complete mechanisms, which determine the existence of specific substances, have not been fully recognized yet, but the most important chemical reactions have been identified [10, 13, 29]. Initiation step of the mechanism of alkane oxidation, can be triggered by molecular oxygen (O_2), hydroxyl radical (OH) or hydroperoxyl radical (HO_2) according to the following reaction [27]:

$$RH + O_2/OH/HO_2 \rightarrow R + HO_2/H_2O/H_2O_2 \qquad (1)$$

Subsequent stages of alkane combustion involve large number of other radicals, e.g. hydridocarbon (CH), hydridooxidocarbon (HCO) and formaldehyde radical (HCHO) [29]. They have been identified as markers of different combustion phases, what makes it possible to detect engine knock based on intermediate radicals analysis [41].

As can be seen from previous studies, even though most of them concern SI engines, the concentration or mass fraction of hydroxyl radicals is found to be good indicator of knocking combustion. Shoji et al. [33] analyzed chemical luminescence emission of hydroxyl and other radicals inside engine cylinder. Under knocking combustion, hydroxyl radicals emerged earlier compared to normal combustion, and their quantity increased up to the occurrence of autoignition. Kawahara et al. [19] found that the fluctuations of hydroxyl radical emission intensity is synchronized with the in-cylinder pressure fluctuations (Fig. 2). Zhen et al. [40] observed that the changes of hydroxyl radical quantity were virtually the same with the changes of temperature. They stated that hydroxyl radicals play a major role during the transition from low-temperature chemistry to high-temperature autoignition. Merola and Vaglieco [26] proved that hydroxyl radicals were detected and correlated to the onset and the duration of knocking combustion. In the research of Azimov et al. [3], hydroxyl radicals emission intensity was evaluated as strong for knocking combustion cycles while in conventional combustion it could barely be detected. A similar conclusions were reached by Hashimoto et al. [15] and Itoh et al. [17], who reported that under non-knocking conditions hydroxyl radicals show relatively weak emission intensities, but for autoignition and knocking cycles these intensities gradually increase, compared to conventional cycle.

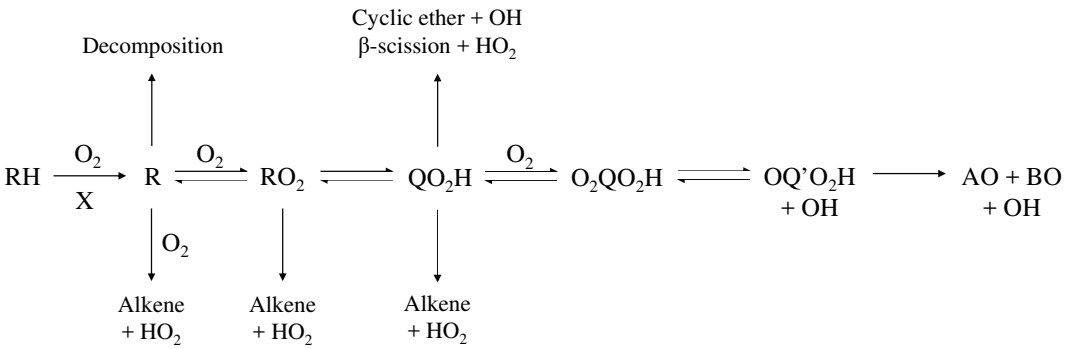

Fig. 1. Mechanism of alkane oxidation: RH – alkane, R – alkyl radical, OH – hydroxyl radical, HO_2 – hydroperoxy radical, X – various radicals, AO, BO – molecular oxygenated species [27]

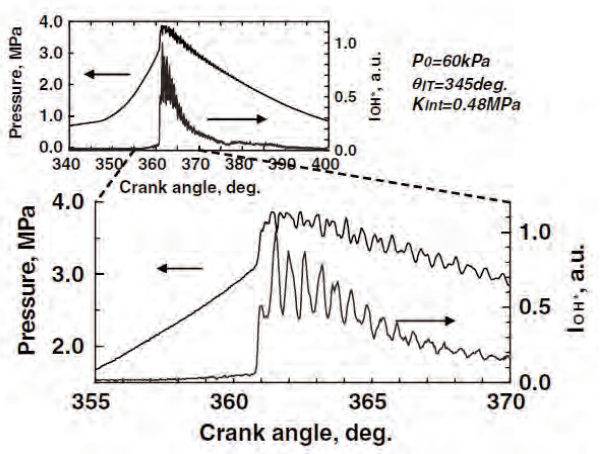

Fig. 2. Oscillation of the hydroxyl radical emission intensity – I_{OH^*} with the in-cylinder pressure [19]

3. Simulation of hydroxyl radicals formation during combustion in a dual-fuel engine

3.1. Model assumptions

As an example of the dependence of mass fraction of hydroxyl radical on engine operating conditions, simulation of the combustion process in a dual-fuel CI engine supplied with diesel oil and methane was performed. Numerical analysis was carried out using a one-dimensional model, developed in AVL BOOST software. The model was parametrized based on the specifications of Cummins B6-T590 engine (Table 1) and validated by comparison with empirically determined data.

Table 1. Specifications of Cummins B6-T590 engine [8, 9]

Parameter	Data
Type	Four-stroke, compression-ignition, turbocharged, water-cooled
Cylinder layout	In-line
Number of cylinders	6
Displacement volume	5883 cm^3
Bore	120 mm
Stroke	102 mm
Maximum power	103 kW @ (1,700–2,200) rpm
Maximum torque	565 N·m @ (1,500–1,600) rpm

Fuel supply system of the engine was modified to allow the delivery of gaseous fuel to the intake manifold, while pilot dose of diesel oil was injected directly into the cylinder. The idea behind the modifications was to make the engine run in dual-fuel mode, without introducing major changes of the construction. The general structure of the engine model developed in AVL BOOST is shown in Figure 3.

The main assumption for modeling of combustion in the proposed model was the differentiation of the combustion of diesel and methane. The parameters of the working medium in the cylinder, energy-related effects and mass fractions of species were the superposition of two individual combustion processes of varying dynamics. This approach is often used in research works on the combustion process of fuels with different physicochemical properties (e.g. Stelmasiak and Matyjasik [35]).

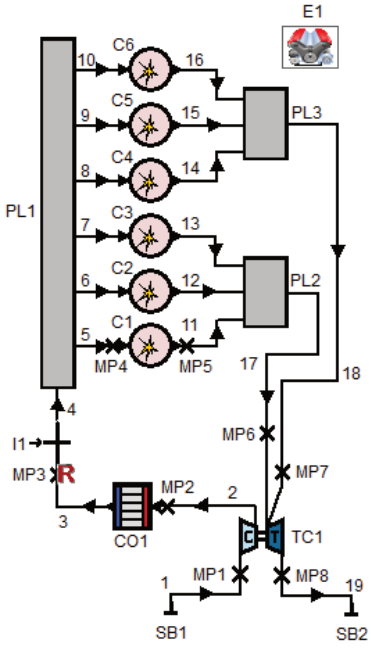

Fig. 3. The structure of the engine model developed in AVL BOOST: SB1, SB2 – system boundaries; MP1–MP8 – measuring points; TC1 – turbocharger; CO1 – air cooler; R – reference point for volumetric efficiency; I1 – gas injector; PL1–PL3 – plenums; C1–C6 – cylinders; E1 – engine, 1–18 – connecting pipes

The heat release rates were imposed by three-phase Wibe function, parametrized individually for the specific properties of methane and diesel oil. This function involves the fractions of heat for the kinetic combustion, diffusion combustion and afterburning stages, according to the general formulas [39]:

$$x_b = b_1 \cdot \left\{1 - \exp\left[-a \cdot \left(\frac{\alpha - SOC}{\alpha_z}\right)^{m_1+1}\right]\right\} + b_2 \cdot \left\{1 - \exp\left[-a \cdot \left(\frac{\alpha - SOC}{\alpha_z}\right)^{m_2+1}\right]\right\} + b_3 \cdot \left\{1 - \exp\left[-a \cdot \left(\frac{\alpha - SOC}{\alpha_z}\right)^{m_3+1}\right]\right\} \quad (2)$$

$$b_1 + b_2 + b_3 = 1 \quad (3)$$

where: α – crank angle, SOC – crank angle corresponding to the start of combustion, α_z – crank angle corresponding to combustion duration, a – completeness of combustion (for complete combustion a = 6.908), b_1 – mass fraction burnt coefficient for kinetic combustion, b_2 – mass fraction burnt coefficient for diffusion combustion, b_3 – mass fraction burnt coefficient for afterburning, m_1 – combustion rate for kinetic combustion, m_2 – combustion rate for diffusion combustion, m_3 – combustion rate for afterburning.

The crank angle corresponding to combustion duration (α_z), coefficients for mass fraction burnt (b_1–b_3) and combustion rates (m_1–m_3) were assumed separately for each fuel. The angle of the start of combustion, the same for both fuels, was determined by autoignition delay angle of diesel oil. The angles of the end of combustion of diesel and methane were different and set arbitrarily. The variables used

in the model allow independent simulation of the course of heat generation, separately for diesel oil and methane.

3.2. Model validation

The validation of the model was accomplished by comparing the simulated course of pressure of the medium inside the cylinder with the pressure measured empirically on the engine test bed. The empirical data used for model validation was obtained by the research team of Kruczyński et al. at Institute of Vehicles of Warsaw University of Technology. The data was published in papers [20, 21], where detailed conditions of the tests have been described.

The comparison was made for the same engine working conditions, defined by engine speed and load, with diesel oil, methane and air consumption as well as the parameters of the working medium introduced to the model. The independent variable parameters were described in section 3.1 of this paper. Their values were modified in order to ensure that the simulated course of pressure was sufficiently close to the measured one. Sample results of the comparison have been presented in Figure 4. They refer to engine speed of 1800 rpm, maximum load and two modes of fuel supply: single-fuel, with diesel oil only, and dual-fuel, with a mixture of diesel oil and 30% (w/w) of methane. The crankshaft rotation angle of 0 deg corresponds to the Top Dead Centre.

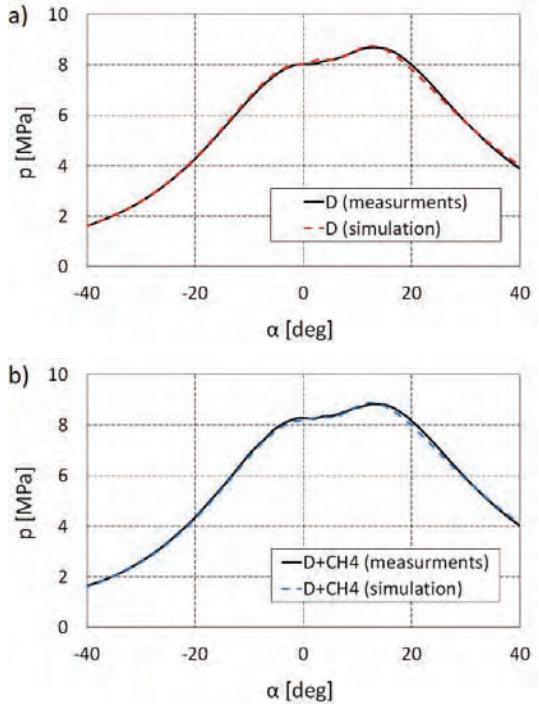

Fig. 4. Comparison of the pressure simulated and measured empirically (engine speed 1800 rpm, maximum load) for two cases of engine supply: a) with diesel oil – D, b) with a mixture of diesel oil and 30% (w/w) of methane – D + CH4

The comparison of the course of pressure has shown a sufficient conformity in all analyzed points. However, for a more in-depth assessment of the accuracy of the estimation of measured in-cylinder pressure by the model, absolute and relative errors have been calculated using the following formulas:

$$\Delta p = p_m - p_s \tag{4}$$

$$\delta p = (p_m - p_s)/p_m \tag{5}$$

where: Δp – absolute error, δp – relative error, p_m – measured in-cylinder pressure, p_s – simulated in-cylinder pressure.

Example error values, calculated for the pressure presented in Figs 4a and 4b, are shown in Fig. 5. Generally, for both engine supply modes, the absolute and relative errors can be rated as not large – their values do not exceed the range of (−0.15–0.2) MPa and (−3.0–3.0)% respectively. The smallest errors occur within the crankshaft angle corresponding to the compression stroke, while the largest follow active combustion and relate to the cylinder pressure drop. The analysis of absolute and relative errors confirms good quality of estimation of measured pressure by the developed model.

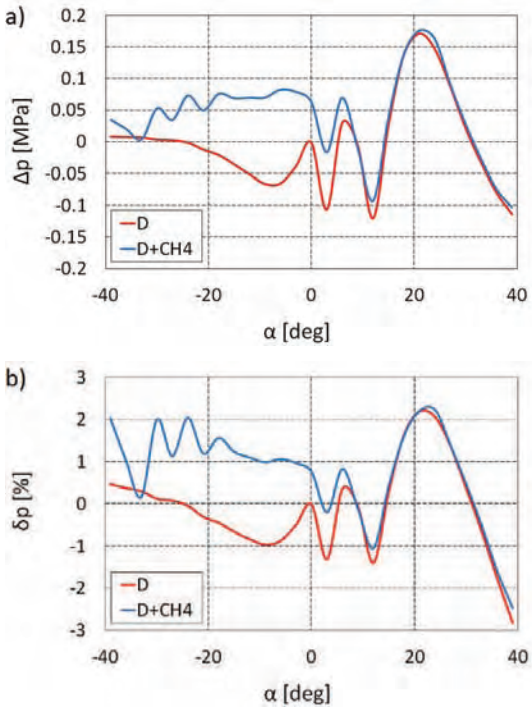

Fig. 5. Absolute (a) and relative (b) errors of the accuracy of the estimation of measured in-cylinder pressure by the model for two cases of engine supply with diesel oil – D and with a mixture of diesel oil and 30% (w/w) of methane – D + CH4

3.3. Simulation results and discussion

AVL BOOST contains a general species transport model, which allows the implementation of a kinetic model. The software solves species transport equations for an arbitrary number of chemical species. In this simulation, default kinetic model was extended to enable determination of hydroxyl radicals mass fraction. It has been proved, that increased quantity of hydroxyl radical in the interval between the initial point of ignition and the end of combustion indicates the higher probability of knock occurrence. The aim of the simulation was to evaluate the dependence of hydroxyl radicals mass fraction on the operating conditions of the engine, determined by the following parameters: methane content in fuel, engine speed and engine load.

The influence of methane content in fuel on mass fraction of hydroxyl radicals was investigated for five cases: D100 – pure diesel oil, 20CH4 – diesel oil with 20% (w/w)

of methane, 40CH4 – diesel oil with 40% (w/w) of methane, 60CH4 – diesel oil with 60% (w/w) of methane and 80CH4 – diesel oil with 80% (w/w) of methane. Figure 6 shows mass fraction of hydroxyl radicals obtained for engine working at 1800 rpm and 80% of maximum load.

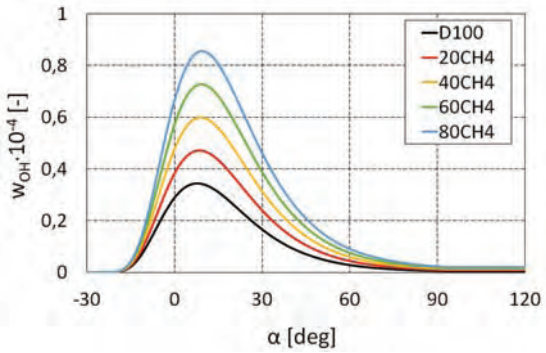

Fig. 6. Mass fraction of hydroxyl radicals – W_{OH} for various methane content in fuel supplying the engine (engine speed 1800 rpm, engine load 80%)

As shown in Fig. 6, it is clear that the increase in the mass fraction of hydroxyl radicals can be associated with an intensive combustion inside the cylinder, while the reduction is due to the ending of the combustion reaction chains. The mass fraction of hydroxyl radicals increases with the increase in methane content in engine fuel. A similar tendency can be observed for knocking intensity and methane content. According to the results of measurements performed on a test bench [21], under the same conditions of engine speed and load, knocking combustion occurred for 40% (w/w) of methane in fuel.

The effect of engine speed on the mass fraction of hydroxyl radicals was investigated within engine speed from the range of (1200–2200) rpm with 200 rpm step. Sample results, referring to 80% of maximum engine load and 40% (w/w) of methane content in fuel, are presented in Fig. 7.

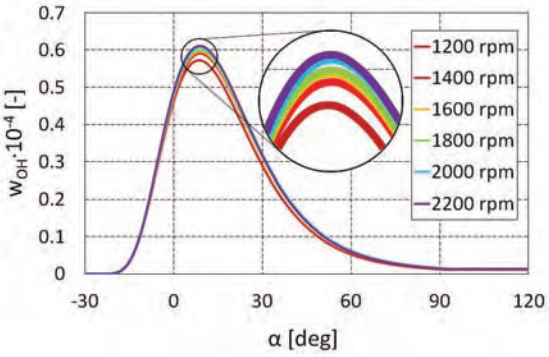

Fig. 7. Mass fraction of hydroxyl radicals – W_{OH} for various engine speed (engine load 80%, methane content in fuel 40% (w/w))

The difference in simulated mass fractions of hydroxyl radicals for various engine speed is not as significant as in the case of methane content of fuel, suggesting that the impact of engine speed on the knock is rather small. The same observation was made for all other cases of methane contents in the fuel. It should be noted, however, that the intensity of knocking in CI engines normally increases with engine speed, while in SI engines it is the other way round [42]. Dual-fuel CI engines combine the properties of both of them, and in this complex combustion process, other factors affecting knocking must be taken into account [32].

The relation between hydroxyl radical mass fraction and engine load was analyzed for 20%, 40%, 60%, 80% and 100% of maximum engine load, as shown in Fig. 8. The results refer to engine speed of 1800 rpm and 40% (w/w) methane content in the fuel.

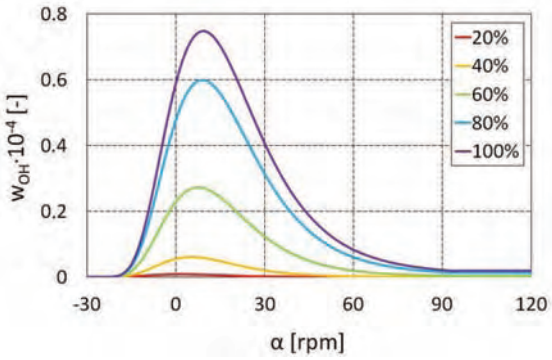

Fig. 8. Mass fraction of hydroxyl radicals – W_{OH} for various engine load (engine speed 1800 rpm, methane content in fuel 40% (w/w))

The impact of the engine load on hydroxyl radical mass fraction is significant. As the load increases, the mass fraction of hydroxyl radical increases. Analyzing the results shown in Fig. 8, it can be concluded that the knock probability decreases at the partial load. In the case of measurements performed on a test bench [21], under the same conditions of engine speed and methane content in fuel, knocking combustion occurred at 80% load. If the relationship between hydroxyl radical mass fraction and engine knock is considered, reduction of engine load would help to avoid knock.

Further examination of the effect of engine load includes variable content of methane in fuel. The results of the simulation, combining these two parameters, are shown in Fig. 9. The engine speed was set at 1800 rpm. Analysis of the results allows to state that engine working with (60–70)% of maximum load probably would not experience knocking combustion, since hydroxyl radical mass fraction is very low, regardless methane content in fuel. For other engine speeds similar results were obtained.

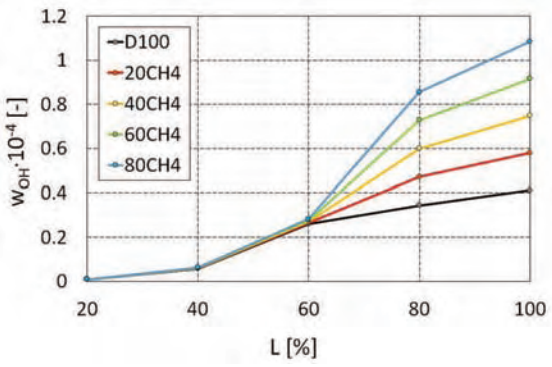

Fig. 9. The dependency of maximum hydroxyl radical mass fraction – W_{OH} on engine relative load and methane content in fuel (engine speed 1800 rpm)

3.4. Limitations of the study

Although the developed model has demonstrated good validity and reliability, providing sufficiently accurate estimations of the measured in-cylinder pressure in a certain dual-fuel CI engine, there are several limitations of this study that merit attention.

Like most of the engine knock simulation studies [39], this work is based on the semi-empirical model as well as simplified chemical reaction kinetics model implemented into commercial software. The implicit assumptions underlying the adopted model or simplified chemical reaction kinetics models may neglect some crucial factors determining the results of the simulation. For example, some chemical reaction species, involved in the combustion process, can be omitted. Therefore it is necessary to employ the detailed chemical reaction kinetics mechanisms to precisely investigate the autoignition mechanisms and combustion process.

Another aspect worth mentioning is the lack of quantitative dependence, of satisfactory accuracy, between knocking combustion and the mass fraction of hydroxyl radicals in engine cylinder. Previous studies have significantly contributed to general understanding of the connection between these two issues and confirmed a major role of hydroxyl radicals during knocking combustion. However, due to highly reactive and consequently short-lived nature of hydroxyl radicals, their mass fraction or concentration can be measured only in the flame zone directly in the combustion chamber [29]. Therefore the most widely used methods used to acquire information about the quantity of radicals are luminescence methods [29]. Optical emission accompanying combustion process cannot be however unequivocally identified with the quantity of radicals

In the context of the above, present study can be regarded as a preliminary work, that highlights some qualitative tendencies in terms of the relationship between mass fraction of hydroxyl radicals and the occurrence of knocking combustion.

4. Conclusions

The present state of research on the application of gaseous fuels in CI engines shows that it is one of the prominent and effective measures to overcome the crude oil scarcity and reduce exhaust emissions. While some technical aspects of dual-fuel CI engines have already reached proper degree of maturity, others are still in need for further development. Those include knocking combustion detection and evaluation. Based on a review of literature, concerning the formation of hydroxyl radicals during combustion process in engine cylinder, and results of numerical simulation of dual-fuel engine, supplied with methane and diesel oil, the following conclusions can be drawn:

- Hydroxyl radicals can act as an indicator of knocking combustion. With an increase in the mass fraction of hydroxyl radicals in the time interval between autoignition of diesel oil and the end of the combustion process, the probability of the occurrence of knock is also increasing.
- The amount of gaseous fuel, with respect to the dose of diesel oil, is a crucial factor determining the intensity of hydroxyl radicals formation in dual-fuel engine and – in consequence – the intensity of knocking combustion.
- Low to moderate load operation of dual-fuel engine restrains hydroxyl radicals formation and allow to reduce or avoid engine knock, even if gaseous fuel content is high.
- Simulation results suggest that engine speed has a minor effect on the hydroxyl radical mass fraction, despite the generally accepted fact that the effect of engine speed on the knocking combustion of conventional SI and CI engines is significant. This may mean that the developed model requires further improvements.

Nomenclature

20CH4	diesel oil with 20% (w/w) of methane
40CH4	diesel oil with 40% (w/w) of methane
60CH4	diesel oil with 60% (w/w) of methane
80CH4	diesel oil with 80% (w/w) of methane
α	crank angle
α_z	crank angle corresponding to combustion duration
Δp	absolute error
δp	relative error
A	completeness of combustion
AO, BO	molecular oxygenated species
b_1	mass fraction burnt coefficient for kinetic combustion
b_2	mass fraction burnt coefficient for diffusion combustion
b_3	mass fraction burnt coefficient for afterburning
C1–C6	cylinders (AVL BOOST model)
CH	hydridocarbon
CI	compression ignition
CO_2	carbon dioxide
CO1	air cooler (AVL BOOST model)
D	diesel oil
D100	pure diesel oil
D+CH4	mixture of diesel oil and methane
E1	engine (AVL BOOST model)
H_2O	water
HCO	hydridooxidocarbon
HCHO	formaldehyde radical
OH	hydroxyl radical
HO_2	hydroperoxyl radical
I1	gas injector (AVL BOOST model)
$I_{OH^\bullet}$	hydroxyl radical emission intensity
L	engine relative load
LPG	liquified petrolum gas
m_1	combustion rate for kinetic combustion
m_2	combustion rate for diffusion combustion
m_3	combustion rate for afterburning
MP1–MP8	measuring points (AVL BOOST model)
NG	natural gas
NOx	nitrogen oxides
O_2	oxygen
p	pressure

PL1–PL3	plenums (AVL BOOST model)
p_m	measured in-cylinder pressure
PM	particulate matter
p_s	simulated in-cylinder pressure
R	alkyl radical
R	reference point (AVL BOOST model)
RH	alkane
SB1, SB2	system boundaries (AVL BOOST model)
SOC	crank angle corresponding to the start of combustion
SI	spark ignition
TC1	turbocharger (AVL BOOST model)
W_{OH}	mass fraction of hydroxyl radicals
X	various radicals
x_b	heat release rate

Bibliography

[1] ABAS, N., KALAIR, A., KHAN, N. Review of fossil fuels and future energy technologies. *Futures*. 2015, **69**, 31-49.

[2] ASHOK, B., ASHOK, S.D., KUMAR, C.R. LPG diesel dual fuel engine – a critical review. *Alexandria Engineering Journal*. 2015, **54**, 105-126.

[3] AZIMOV, U., TOMITA, E., KAWAHARA, N. Combustion and exhaust emission characteristics of diesel micro-pilot ignited dual-fuel engine. In: *Diesel engine – combustion, emissions and condition monitoring*. Bari S. (Ed.). InTech, 2013.

[4] BALLAIS, R., GALLARDO-RIUZ, J.M., MEROLA, S.S. Optical diagnostics of the cycle-to-cycle variation in the kernel development and abnormal combustion: SI small engine. *Journal of KONES Powertrain and Transport*. 2010, **17**(2), 17-25.

[5] BRECQ, G., BELLETTRE, J., TAZEROUT, M. A new indicator for knock detection in gas SI engines. *International Journal of Thermal Sciences*. 2002, **42**, 523-532.

[6] CHMIELEWSKI, A., GUMIŃSKI, R., MĄCZAK, J., RADKOWSKI, S., SZULIM, P. Aspects of balanced development of RES and distributed micro cogeneration use in Poland: case study of a μCHP with Stirling engine. *Renewable and Sustainable Energy Reviews*. 2016, **60**, 930-952.

[7] CHMIELEWSKI, A., LUBIKOWSKI, K., MĄCZAK, J., SZCZUROWSKI, K. Geometrical model of cogeneration system based on a 1 MW gas engine. *Combustion engines*. 2015, **162**(1), 3-10.

[8] CUMMINS. *Operation and maintenance manual. Automotive, recreational vehicle, bus, and industrial 53.9 and 55.9 series engines*. Cummins Engine Company, 2000.

[9] FG INSIGHT. www.fginsight.com/vip/vip/ buyers-guide-case-ih-maxxum-mx135-tractor-3174

[10] GAYDON, A.G., WOLFHARD, H.G. *Flames, their structure, radiation and temperature*. London, 1979.

[11] GENG, P., CAO, E., TAN, Q., WEI, L. Effects of alternative fuels on the combustion characteristics and emission products from diesel engines: A review. *Renewable and Sustainable Energy Reviews*. 2017, **71**, 523-534.

[12] GOLDEMBERG, J., JOHANSSON, T.B., REDDY, A.K.N., WILLIAMS, R.H. Energy for the new millennium. *Ambio: A Journal of the Human Environment*. 2001, **30**, 330-337.

[13] GRIFFITHS, J.F., WHITAKER, B.J. Thermokinetic interactions leading to knock during homogenous charge compression ignition. *Combustion and Flame*. 2002, **131**, 386-399.

[14] HARRINGTON, J., MUNSHI, S., NEDELCU, C., OUELLETTE, P., THOMPSON, J., WHITEFIELD, S. Direct injection of natural gas in a heavy-duty diesel engine. *SAE Technical Paper*. 2002, 2002-01-1630.

[15] HASHIMOTO, S., AMINO, Y., YOSHIDA, K., SHOJI, H., SAIMA, A. Analysis of OH radical emission intensity during autoignition in a 2-stroke SI engine. In: *Proceedings of the 4th COMODIA*. 1998, 405-410.

[16] HEGAB, A.H., LA ROCCA, A., SHAYLER, P.J. Towards keeping diesel fuel supply and demand in balance: Dual-fuelling of diesel engines with natural gas. *Renewable and Sustainable Energy Reviews*. 2017, **70**, 666-697.

[17] ITOH, T., NAKADA, T., TAKAGI, Y. Emission characteristics of OH and C2 radicals under engine knocking. *JSME International Journal Series B*. 1995, **38**, 230-237.

[18] JAKUBIAK-LASOCKA, J., LASOCKI, J., SIEKMEIER, R., CHŁOPEK, Z. Impact of traffic-related air pollution on health. *Advances in Experimental Medicine and Biology*. 2015, **834**, 21-29.

[19] KAWAHARA, N., TOMITA, E., SAKATA, Y. Auto-ignited kernels during knocking combustion in a spark-ignition engine. *Proceedings of the Combustion Institute*. 2007, **31**, 2999-3006.

[20] KRUCZYŃSKI, S.W., ORLIŃSKI, P., WOJS, M.K., OWCZUK, M. Ocena możliwości spalania biogazu w silniku o zapłonie samoczynnym z dawką pilotującą oleju napędowego. *Zeszyty Naukowe Instytutu Pojazdów*. 2014, **100**(4), 103-111.

[21] KRUCZYŃSKI, S.W., ORLIŃSKI, P., WOJS, M.K., OWCZUK, M., MATUSZEWSKA, A. Ocena zjawiska spalania stukowego w dwupaliwowym silniku ciągnika rolniczego zasilanego dodatkowo biogazem. *Combustion Engines*. 2015, **162**(13), 639-646.

[22] LASOCKI, J. Engine knock detection and evaluation: a review. *Zeszyty Naukowe Instytutu Pojazdów*. 2016, **109**(5), 41-50.

[23] LLOYD, A.C., CACKETTE, T.A. Diesel engines: environmental impact and control. *Journal of the Air & Waste Management Association*. 2001, **51**, 809-47.

[24] LUFT, S. A dual-fuel compression ignition engine – distinctive features. *Combustion Engines*. 2010, **141**(2), 33-39.

[25] MATUSZEWSKA, A., OWCZUK, M., ZAMOJSKA-JAROSZEWICZ, A., JAKUBIAK-LASOCKA, J, LASOCKI, J., ORLIŃSKI, P. Evaluation of the biological methane potential of various feedstock for the production of biogas to supply agricultural tractors. *Energy Conversion and Management*. 2016, **125**, 309-319.

[26] MEROLA, S.S., VAGLIECO, B.M. Knock investigation by flame and radical species detection in spark ignition engine for different fuels. *Energy Conversion and Management*. 2007, **48**, 2897-2910.

[27] MOHAMED, C. *Autoignition of hydrocarbons in relation to engine knock*. PhD thesis. University of Leeds, 1997.

[28] PAPAGIANNAKIS, R.G., RAKOPOULOS, C.D., HOUNTALAS, D.T., RAKOPOULOS, D.C. Emission characteristics of high speed, dual fuel, compression ignition engine operating in a wide range of natural gas/diesel fuel proportions, *Fuel*. 2010, **89**, 1397-1406.

[29] PIERNIKARSKI, D., HUNICZ, J., KOMSTA, H. Detection of knocking combustion in a spark ignition engine using optical signal from the combustion chamber. *Eksploatacja i Niezawodnosc – Maintenance and Reliability*. 2013, **15**(3), 214-220.

[30] RÓŻYCKI, A. Granica spalania stukowego w dwupaliwowym silniku o zapłonie samoczynnym. *Czasopismo Tech-*

niczne z. 11. Mechanika. z. 7-M. Wydawnictwo PK, Kraków 2008.
[31] SAMOILENKO, D., CHO, H.M. Improvement of combustion efficiency and emission characteristics of IC diesel engine operating on ESC cycle applying variable geometry turbocharger (VGT) with vaneless turbine volute. *International Journal of Automotive Technology*. 2013, **14**(4), 521-528.
[32] SELIM, M.Y.E. Sensitivity of dual-fuel engine combustion and knocking limits to gaseous fuel composition. *Energy Conversion and Management*. 2004, **45**, 411-425.
[33] SHOJI, H., SAIMA, A., SHIINO, K., IKEDA, S. Clarification of abnormal combustion in a spark ignition engine. *SAE Technical Paper*. 1992, 922369.
[34] STELMASIAK, Z. Limitations of enrichment of gaseous mixture in dual fuel engines. *Eksploatacja i Niezawodnosc – Maintenance and Reliability*. 2014, **16**(4), 537-544.
[35] STELMASIAK, Z., MATYJASIK, M. Simulation of the combustion in a dual fuel engine with a divided pilot dose. *Silniki Spalinowe*. 2012, **151**(4), 43-54.
[36] THE INTERNATIONAL COUNCIL ON CLEAN TRANSPORTATION (ICCT). *European Vehicle Market Statistics*. Pocketbook 2014 Edition.
[37] TOSAKA, Y., SHOJI, H., SAIMA, A. A study of the influence of intermediate combustion products on knocking. *JSAE Review*. 1995, **16**, 233-238.
[38] WAGEMAKERS, A.M.L.M., LEERMAKERS, C.A.J. Review on the effects of dual-fuel operation, using diesel and gaseous fuels, on emissions and performance. *SAE Technical Paper*. 2012, 2012-01-0869.
[39] WIBE, I.I. Brennverlauf und Kreisprozeß von Verbrennungsmotoren *(Rate of heat release in cyclic process of internal combustion engines)*. Verlag Technik, Berlin 1970.
[40] ZHEN, X., WANG, Y., ZHU, Y. Study of knock in a high compression ratio SI methanol engine using LES with detailed chemical kinetics. *Energy Conversion and Management*. 2013, **75**, 523-531.
[41] ZHEN, X.D., WANG, Y., XU, S.Q., ZHU, Y.S., TAO, C.J., XU, T., SONG, M.Z. The engine knock analysis – an overview. *Applied Energy*. 2012, **92**, 628-636.
[42] ŻÓŁTOWSKI, A. Knock combustion in dual fuel diesel engine. *Journal of KONES Powertrain and Transport*. 2014, **21**(4), 547-553.

Jakub Lasocki, DEng. – Faculty of Automotive and Construction Machinery Engineering at Warsaw University of Technology.

e-mail: *J.Lasocki@simr.pw.edu.pl*

Piotr Orliński, DSc., DEng. – Faculty of Automotive and Construction Machinery Engineering at Warsaw University of Technology.

e-mail: *P.Orlinski@simr.pw.edu.pl*

Marcin Krzysztof Wojs, DEng. – Faculty of Automotive and Construction Machinery Engineering at Warsaw University of Technology.

e-mail: *Marcin.Wojs@simr.pw.edu.pl*

Marlena Owczuk, MEng. – Automotive Industry Institute in Warsaw, Department of Fuels and Renewable Energy.

e-mail: *M.Owczuk@pimot.eu*

Anna Matuszewska, DEng. – Automotive Industry Institute, Department of Fuels and Renewable Energy and in Cardinal Stefan Wyszynski University.

e-mail: *A.Matuszewska@pimot.eu*

Article citation info:
CIEŚLIKOWSKI, B., CYGNAR, M., JAKÓBIEC, J. Multifaceted diagnostic inference process for identifying the causes of self-ignition engine faults resulting from PM sediments. *Combustion Engines*. 2017, **168**(1), 186-190. DOI: 10.19206/CE-2017-130

Bogusław CIEŚLIKOWSKI
Mariusz CYGNAR
Janusz JAKÓBIEC

CE-2017-130

Multifaceted diagnostic inference process for identifying the causes of self-ignition engine faults resulting from PM sediments

Optimization of the fuel combustion process in a self-ignition engine with the multi-stage HPCR injection system sets the main trends in research on the thermodynamic stability of fuels, and the mechanisms of PM formation. The stages were indicated of the multifaceted diagnostic inference on the causes of failures of a turbocharger with variable geometry (VTG) which occur as a result of PM sedimentation in the nozzle area. An evaluation of the engine performance was conducted using a dedicated tester and an additional recording of the injector coil current characteristics with parallel readings of the fuel pressure variation in the reservoir. The indicated procedure established the underlying cause of the VTG compressor failure despite the absence of a recorded error code.

Key words: *VGT turbocharger, PM particulates, diagnostic tester, spectral analysis, error codes*

1. Introduction

The chemical formula of motor fuels is constantly evolving due to the requirements for combustion processes improvement, engine components cleanliness, and environmental protection, including propulsion system development [12].

Optimization of the fuel combustion process in a self-ignition engine with the multi-stage hydrocarbon fuel injection and fuels with added FAME biocomponents sets the main trends in fuel thermodynamic stability research, as well as the development of engine structures equipped with HPCRS. Oxidation resistance is one of the most important properties of fuel containing FAME components because of their low stability, resulting in products that jeopardize the sound functioning of the engine systems [13].

Fuels for compression-ignition engines, which meet the high requirements of modern diesel engine units equipped with HPCR high pressure fuel injection systems and catalytic exhaust after-treatment systems, must have appropriate physicochemical and utility properties.

The evolution of fuel quality, including biocomponents, requires continuing research which allows the identification of the quality and usability issues and indicates the possibilities for solving them. One of the important quality parameters closely related to the structure-group composition of fuels intended to power engines with self-ignition is their tendency for sediment formation. Some fuel properties such as high viscosity, low volatility, olefin content, aromatic compounds, and FAME biocomponents facilitate the formation of carbon deposits in the injector hole area, the combustion chamber, the turbocharger and the DPF system. A gradual growth of PM layers results in the loss of proper fuel spraying capability, the immobilization of the VTG turbocharger nozzle positioner, and the flue gas duct blockage in the DPF system [13].

The effects of these processes result in the occurrence of engine failures related to the record in the error code controller, the MIL indicator signaling, and switching to the engine's substitute operating characteristics. The complex nature of the error codes recording requires undertaking a multifaceted diagnostic inference process, as illustrated in the example of determining the causes of damage to a turbocharger with variable geometry (VTG). The profound analysis of the error codes recorded in the controller's memory conducted with the use a dedicated tester, along with a comparative evaluation of the "frozen frame" record and the current characteristics of the injector coil supply system against the backdrop of the fuel pressure record in the reservoir, allows to determine the cause of the fault.

2. Diagnostics of the self-ignition turbocharged engine (VTG)

The EDC system developed by Bosch is designed to control a self-ignition engine. This system, which monitors the turbocharger operation and controls the timing and the opening phases of the injectors, has been subject to continuous modifications (EDC 15, EDC 16, EDC 17) due to the introduction of further versions of the HPCRS. The vehicle's IT bus is used to communicate the EDC with the other controllers installed in the vehicle, and also to cooperate with external diagnostic testers through the OBD connector. In the case of the G9U 2.2 DCI engine which is being analyzed, the vacuum control system was used for the VTG turbocharger, consisting of a vacuum pump, a reservoir, an electrovalve, and an actuator which controls the nozzle positioner. The vehicle test run demonstrated a significant decrease in power and low acceleration values on each gear, indicating the VTG turbocharger damage. However, the identification of the faults of the indicated engine subassembly must be confirmed by a parametric analysis conducted with the use of the Clip probe with a dedicated interface for the vehicle of this make (Fig. 1) [9].

Fig.1. CLIP probe with the interface unit

The DF 301 error code referring to the "inlet air circuit" has been recorded in the controller memory. In the "infor-

mation" tab, the 1.DEF explanation indicates the low mass air flow in the engine air intake system. The "frozen frame" parameter reading was performed for the analysis of the engine's operating parameters at the time when the controller detected the fault (Fig. 2), which occurred at full load of the engine.

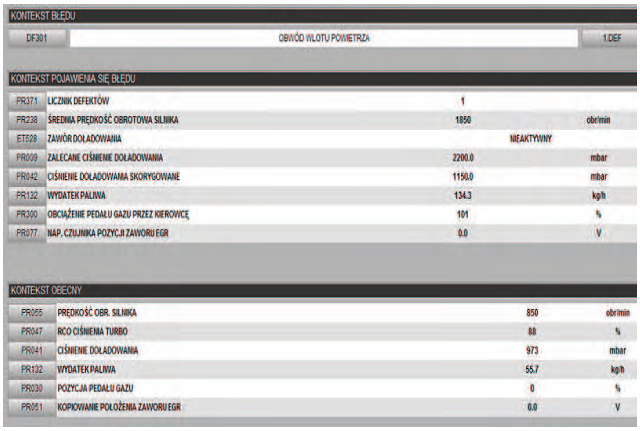

Fig. 2. Frozen frame recording when DF 301 error occurs

The difference was observed between the desired supercharging pressure values and the actual value generated by the pressure sensor in the air intake system behind the turbocharger. There was a large discrepancy between these values, with the difference increasing as the engine load increased. The condition is not always signaled by the MIL indicator, as it responds to the specificity of the engine controller software (EDC) [6]. The software differences correspond not only to the injection or turbocharger map, but also to the autodiagnostic system and the threshold value for error generation. Therefore, in case of a difference in supercharging pressures - actual and expected, the MIL indicator will not light up in each case. It is also necessary to know about the possible modifications to the original software for engine tuning purposes or for blocking a DPF bit frame or EGR valve [14]. Thus, checking the actual and expected supercharging pressures is an effective method for the initial confirmation of a fault in the engine charging system.

An important control parameter is also the voltage at the signal output of the flow meter, which allows to determine the possible power supply leaks when the turbocharger is operating properly. In the analyzed example (Fig. 3), with the air tight intake system, too low voltage of 3.56V occurred, compared to the required voltage of approx. 5V at the specified rotational speed.

The analysis conducted directly points to the possibility of VTG turbocharger's nozzle seizure as a result of accumulated particulate matter sediments, thus limiting their mobility. The tested engine did not show excessive lubricating oil consumption, which excludes the possibility of the sediments being formed from the residue of the excess lubricant burned. In this case, it is necessary to extend the scope of the diagnostic inference to the fuel injection regularity issue in the HPCR system despite the absence of an error indicating a system fault. The representative parameters of the system, primarily the corrective dose of the injectors, have been checked to assess the correctness of their operation. The increase in the corrective doses affects the excessive formation of solid particles, which also settle inside the turbine and contribute to the nozzle seizure. [7]. The measurement (Fig. 4) showed a large difference in the corrective doses of the injectors, but this does not directly imply their emergency condition. However, this fact is not indifferent to the VTG compressor and is undoubtedly one of the reasons behind the blocking of the nozzle controlling mechanism. Dose differences between injectors may also be related to the dynamic tightness of individual engine cylinders. The high value of the fuel correction for the 3rd cylinder is noteworthy.

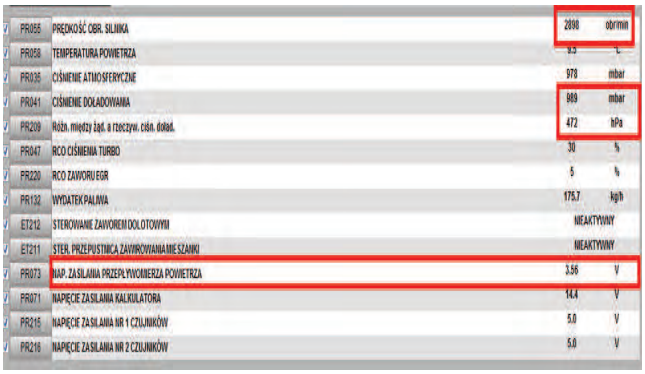

Fig. 3. Low voltage level of the flowmeter measuring system

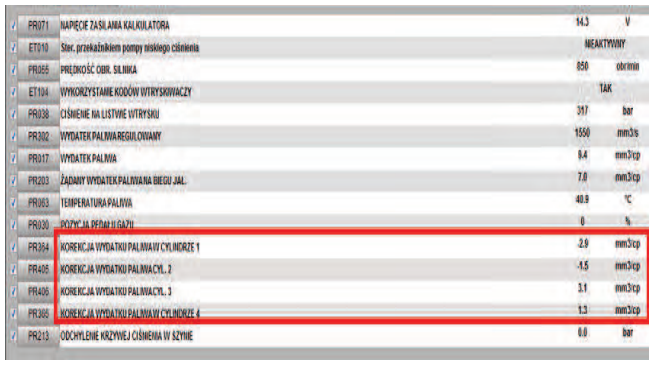

Fig. 4 Correction doses control for CR injectors.

An EDIA-5 analyzer (Fig. 5) which allows for the registration of injection control signals was used to investigate the causes of the fault. [11]. It is possible to view the control current characteristics for the four injectors with the reference of these values to the high pressure fuel sensor signal on the fuel rail (Fig. 6). The measurement allows the analysis of signal timing, amplitude and high pressure rise. Profound observation and interpretation of the injection timing characteristics and the pressure drop allows for the quick fault diagnosis.

The recorded characteristics show the high pressure maintenance conditions for the 3rd cylinder injector over the extended periods of time, suggesting the possibility of "clogging the atomizer openings". In this case, one aspect is worth noting of the injector damage condition in the absence of fault indications generated by the MIL indicator [15]. Contaminated fuel and improper filtering quality lead to permanent defects of the injector's ball control valve,

which cannot close the cross-channel leakage despite the EDC controller's failure to control the valve. The lower pressure in the control chamber of the injector causes an uncontrolled fuel injection. In this case, the controller will not register any fault, and the excess fuel contributes to the exhaustion smoke increase. Despite such a serious fault in the system – the MIL indicator on the instrument cluster [14] will not be activated.

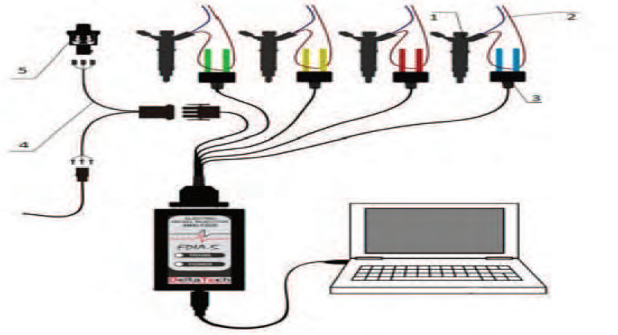

Fig. 5. Connection diagram of EDIA-5 analyzer [11]. 1 – injector, 2 – injector wires or dedicated connector, 3 – measuring probe, 4 – pressure sensor connection cable 5 – pressure sensor

Fig. 6. Current characteristics of injector coils and pressure in the fuel rail.

The last step is to erase the errors recorded in the controller's memory. This is an action that must always be performed after a repair or replacement of damaged components. Disassembly of the turbocharger confirmed the expected excess of the sediment in the lever and steering vanes area, and also the excessive deposits were found in the injector outlet zone (Fig. 7). After error deletion and a test run, the tester record showed no error codes.

Fig. 7. Residual sediments in the area of the levers positioning the exhaust nozzle blades and in the zone of injector outer openings

The above stages of the engine diagnostic process indicate the need to extend the interpretation of the fault states resulting from the recorded error codes with the use of a dedicated diagnostic kit. In this case replacing or repairing the VTG turbocharger would lead to a short-term improvement in the engine's operating condition, as the major malfunction results from improper fuel injection by the injector due to the sediment deposition in the exhaust zone. It is therefore desirable to fully visualize the performance parameters of interdependent systems and not to focus solely on the identified errors codes. The diagnostician should have the necessary knowledge to allow for accurate assessment of the engine damage, especially in the case of multi-mode functional analysis of engine systems.

3. Causes of IDID formation

The dangers arising from the formation of IDIDs involve the limitation to operation of the internal injectors' work units or their total blockage which results in the hydraulic dysfunction of these important engine components.

FAME's share in the diesel fuel also contributes to the formation of IDID by acid impurities, formed by the autocatalytic division of fatty esters with metal ions [1, 2]. Deposits formed this way can cause the surfaces of the interlocking elements to stick together, and intensify the corrosion processes. [8].

Particularly susceptible to the formation of the underlying sediments are PIBSI (Polyisobutylene bis Succinic Anhydride) with a high primary amine content in interaction with carboxy dimers of fatty acids. The resulting deposits are not soluble in commonly used organic solvents, which makes it difficult to analyze and determine their chemical structure.

Previous studies have also shown the potential for the formation of IDIDs from oxidation products of fuels. These products may especially occur in unstable diesel fuels containing FAME or may be a result of the aging of fatty acid esters present in lubricants [3, 4]. Multifunctional detergent-dispersant packs for diesel fuels, which contain a lot of additives, can interact and exhibit incompatibility manifested by turbidity and delamination. These issues require research into the component compatibility and stability.

It should be emphasized that the multifunctional detergent-dispersant additive package consists of a lubricant component, a corrosion inhibitor, a demulsifier, an antifoam additive, a cetane boost additive, an oxidation inhibitor, and a biocide.

The progress in the technology of detergent dispersant additives and their dosing level solves many of the problems discussed [2].

The multifunctional detergent dispersant package for advanced diesel engines must fulfill many functions protecting the HPCR high pressure fuel injection systems against internal IDIDs, atomizer blockage, wear and seizure of the high pressure fuel pump and also against corrosion of the fuel system. In addition, it should protect diesel fuel from oxidation, demonstrating the ability to wet metal surfaces and create a protective film that prevents highly adherent deposits and lacquers from settling, thereby keeping multi-turbo injectors clean [8].

4. Spectral analysis of sediments

Spectral analysis was performed of sediments from the fuel outlet openings of the HPCR injectors and from the turbocharger exhaust nozzle levers in order to determine the PM composition and their causes.

In the microscopic analysis of the deposit collected from the levers (Fig. 8), the sediment grains were observed, which were stained with a tarry substance. The sediment from the injection zone of the 3rd cylinder injector was characterized by a finer and "dry" structure with a visible fraction of the mineral material. The XRF ED X-ray fluorescence spectra were taken from the Oxford Instruments ED 2000 recorder, while the infrared IR spectra (FTIR) were recorded on the BIO-RAD FTS 175.

XRF (X-ray fluorescence) method was applied in the qualitative analysis and the sample of the sediments was taken after washing the analyzed zones with hexane (Fig. 9). On the basis of the assessment of band intensity changes for the identified elements, a qualitative assessment of the sedimentation was conducted. The presence of metals such as iron, zinc, chromium, nickel, and copper was found in the analyzed sediments. In addition, the presence of such elements as calcium and phosphorus and sulfur was noted. The presence of zinc, calcium and phosphorus results from the engine oil degradation, including the additive package. In addition, depressants also contain iron ions [8]. In the XRF spectrum for the sediments taken from the levers, a high intensity of iron bands was recorded. These impurities are mainly due to the corrosion processes of steel elements, whose structure is more susceptible to corrosive FAME. The relatively high intensity of the calcium and zinc bands was noted, indicating engine oil contamination as well as a significant share of the spectrum indicating nickel.

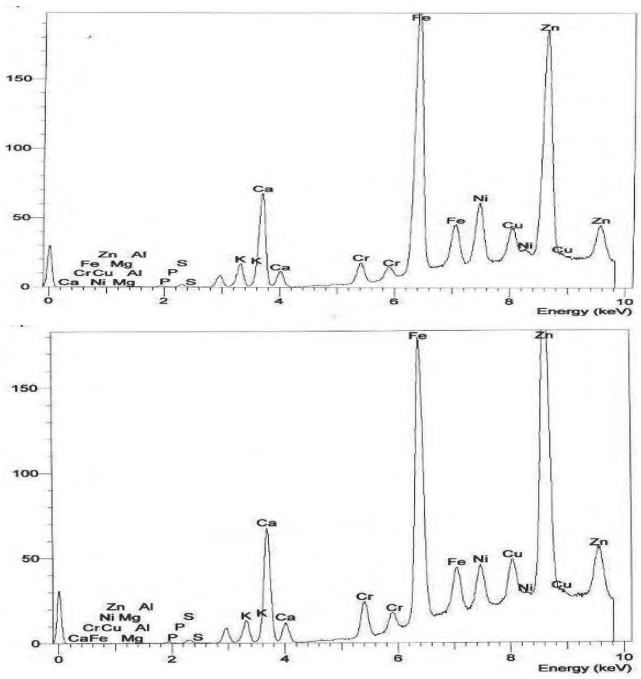

Fig. 8. XRF spectrum for sediments from the injector openings and nozzle levers

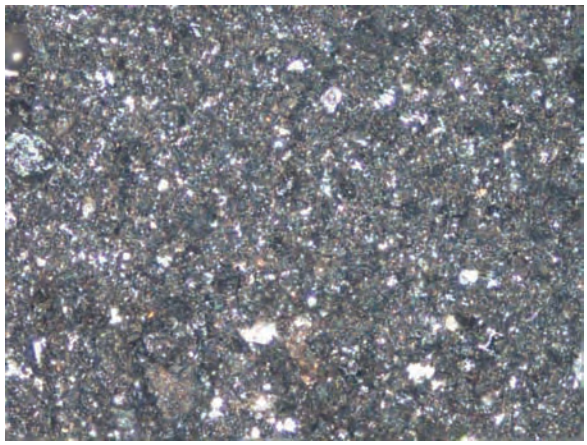

Fig. 9. Microscope image (magnification 100 ×, reflected light) of the sediment collected from the exhaust nozzle levers

After the sediments from the outer surface of the analyzed zones were washed with chloroform, the sample was analyzed in the infrared spectrum. The fuel residue and the engine oil residue were observed, as well as degradation products. The IR spectrum for the substances isolated in the 3rd opening of the injector is poorer (Fig. 10). At first a comparative analysis was conducted of hydrocarbon bands, i.e. the range of wave numbers: 2850–3000 cm^{-1}, 1464 cm^{-1}, 1377 cm^{-1}, 722 cm^{-1} [10]. In both cases, the background was more raised, which is related to the presence of soot. In addition, vibration bands typical for hydroxyl groups (about 3400 cm^{-1}) are present, which may be derived from the absorbed water, and also from the alcohol and carboxylic acids structures [10].

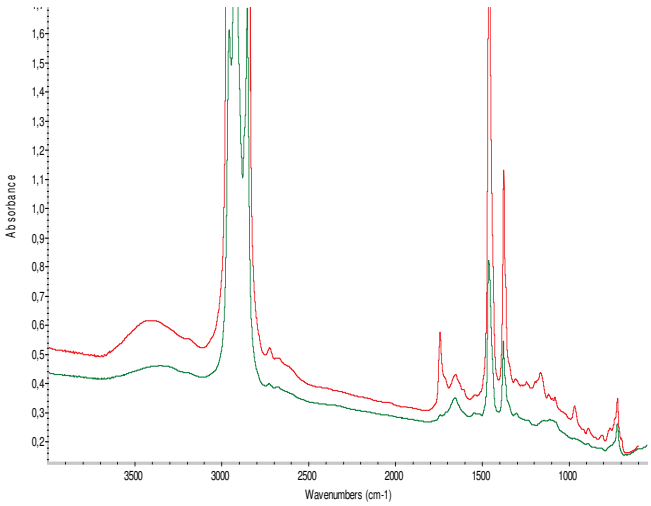

Fig. 9. Infrared spectrum of the soluble sediment from the injector openings (green) and nozzle levers (red)

The band in the range of about 1655 cm^{-1} in the diagnostic area of 2000–1600 cm^{-1} is also intensive, which indicates the presence of oxidation processes of organic compounds to carbonyl and carboxylic structures. The effects of these compounds on nitrogen oxides are related to the presence of hydrated carboxylic acid salts. These substances may also be derived from the oxidation and degra-

dation processes of the basic additives present in the engine oil.

The approx. 1630 cm^{-1} band is derived from other compounds containing C-O-NO_2 bonds, resulting from nitro-oxidation of engine oil components and fuel in contact with nitrogen oxides. The observed intense 1747 cm^{-1} band is related to the presence of esters, for which the representative ones are the relations of C=O (aliphatic) carbonyl groups with the bands in the 1750–1735 cm^{-1} range [5].

Conclusions

1. The presented stages of the diagnostic tests and inference for multi-symptom engine failure states, together with a wide analysis of the recorded error codes, guide the inference procedure towards the correct diagnostic decision.
2. An analysis of X-ray fluorescence spectrum with the energy dispersion in relation to determining the proportion of sedimentary elements, together with the infrared recording of the spectroscopy spectrum showed the proportion of organic compounds in solid PM.
3. Sediment retention leads to improper fuel spraying and dosing in the HPCR system, as well as blocking of the exhaust nozzle lever controllers, resulting in the OBD error code.
4. It is desirable to fully visualize the operating parameters of the interdependent systems and not to focus solely on the direct reading of the error codes indicated by the diagnostic tester.

Nomenclature

VTG	variable turbine geometry		
PM	particulate matter	DPF	diesel particulate filter
HPCRS	high pressure common rail system	EGR	exhaust gas recirculation
FAME	fatty acid methyl esters	IDID	internal diesel injector deposits

Bibliography

[1] CAPROTTI, R., BREAKSPEAR, A., KLAUSA, R. RME behaviour in current and future diesel fuel FIE. *SAE Technical Paper*. 2007, 2007-01-3982.

[2] CAPROTTI, R., BREAKSPEAR, A. et al. Detergency requirements of future diesel injection system. *SAE Technical Paper*. 2005, 2005-01-3901.

[3] CEC/TC 19 WG24; *Report of the ad-hoc incector sticikig task force* – 02 August 2011.

[4] CHAPMAN, L. Diesel soap – formation and realeted problems. *National Tanks Conference.* Boston MA, 2010.

[5] CIESLIKOWSKI, B. Spectral analysis of deposits from a catalytic converter of Diesel engine. *Combustion Engines.* 2011, **146**(3), 1-6.

[6] GUNTER, H. Układy wtryskowe Common Rail w praktyce warsztatowej: budowa, sprawdzanie, diagnostyka. Warszawa. *Wyd. Komunikacji i Łączności.* 2010.

[7] IDZIOR, M. et al. Analiza wpływu warunków eksploatacji na stan techniczny turbosprężarek doładowanych silników spalinowych. *Logistyka.* 2011, **3**, 1129-1139.

[8] JAKÓBIEC, J., STANIK, W., MAZANEK, A. Olej napędowy wg. Światowej Karty Paliw – wydanie piąte wrzesień 2013. *Logistyka*. 2014, **3**, 96-101.

[9] MERKISZ, J., MAZUREK, S. Pokładowe systemy diagnostyczne pojazdów. *Wyd. Komunikacji i Łączności.* Warszawa, 2007.

[10] SADLE, J. Spektroskopia molekularna. *Wydawnictwa Naukowo Techniczne,* Warszawa, 2002.

[11] PREISNER, L. Delta Tech Electronics EDIA5. *Materiały informacyjne Deltatech Electronics*, 2011.

[12] STANIK, W., JAKÓBIEC, J. Proekologiczny rozwój technologii silników o zapłonie samoczynnym; *Autobusy-Technika-Eksploatacja-Systemy transportowe*. 2013, **7-8**, 187-192.

[13] STANIK, W., JAKÓBIEC, J., WĄDRZYK, M. Wpływ stabilności termooksydacyjnej biokomponentów na pracę układu wysokociśnieniowego wtrysku paliwa typu Common Rail. *Logistyka*. 2015, **5**, 569-576.

[14] WĘGIEL, S. Zasilanie silników HDI. Poradnik serwisowy. **4**. 2004.

[15] WHITE, C., RANDALL, M. Kody usterek. *WKiŁ,* Warszawa 2008.

Bogusław Cieślikowski, DSc., DEng. – State University of Applied Sciences in Nowy Sącz, Poland.

Mariusz Cygnar, DSc., DEng. – State University of Applied Sciences in Nowy Sącz, Poland.

Janusz Jakóbiec, DSc., DEng. – University of Science and Technology, Krakow.

Article citation info:
MAGRYTA, P., PIETRYKOWSKI, K., MAJCZAK, A. Optimizing the geometry of the connecting rod in opposite pistons engine. *Combustion Engines*. 2017, **168**(1), 191-196. DOI: 10.19206/CE-2017-131

Paweł MAGRYTA
Konrad PIETRYKOWSKI
Adam MAJCZAK

CE-2017-131

Optimizing the geometry of the connecting rod in opposite pistons engine

The article presents the results of simulations research carried out, using Finite Element Method. The simulations were made in the Abaqus software. Studies were related to the reduction and improving of stress distribution in the connecting rod of opposite pistons combustion engine. The connecting rod has been developed in a 3D environment in the Catia software, then imported into the simulation tool, in which stress tests were performed. The connecting rod was subjected to a compression and stretching tests. Boundary conditions of forces used in simulation tests have been developed on the basis of the dynamic model created in the MSC Adams software. The study included nine iterations of geometric changes of connecting rod. Shape as well as properties such as parametric dimensions (rod length) were changed. The changes were dictated by the reduction of the maximum values of the stresses and the size of the fields with large stress values. As a result of the simulations, the improvement of the connecting rod strength was obtained by its geometrical change (which was obtained by reducing the stress fields).

Key words: *connecting rod, simulation, FEM, Abaqus, Catia v5*

1. Introduction

In aircraft propulsions systems, the new trends are for searching the solutions to reduce operating costs and mass of engines, while maintaining reliability. In the case of ultralight aircrafts, the essential feature of the propulsion system is the type of fuel that engine will be supplied. Particularly important feature, is its affordability and price of the fuel. Currently, most of the piston engines used in aviation are powered by AVGAS100LL fuel, which is expensive and increasingly difficult to access. Fuels available for most airports are JET-A and automotive fuels, such as ES95 and diesel fuel [2].

Some of aircraft engines used in aviation can be powered by diesel fuel and JET-A fuel. The advantage of those fuels is also low flammability and lower price compared to AVGAS100LL fuel. In addition, the specific fuel consumption in diesel engines is lower than in spark-ignition engines, which reduces the mass of fuel required to be used for the same fly mission distance, allowing greater mass to be carried in, despite the increased mass of the propulsion unit. These are the main advantages for the use of this type of the propulsion systems.

In addition, after analyzing the use of ultralight engines in aviation, in case of their cylinder system, it turned out that the dominant configuration of the engine, was the flat boxer cylinder system and the system with opposed pistons. The engines of this type are lighter, because the aligned cylinders/pistons counterbalance the inertia forces and there is no need to use additional balancing masses improving the rotation speed uniformity [8, 9]. Therefore, a system with opposing pistons was chosen based on the analysis for the engine design.

The designed connecting rod will be used in a Diesel engine. This engine will be characterized by opposing pistons positions. Ultimately, the propulsion unit will be used in the ultralight aircraft.

Because of the engine design, where the cylinders are located flat with pistons placed opposite, engine has to have two short crankshafts orientated against each other, which indirectly determines the connecting rod construction [3].

Because the engine is designed from the beginning, it is necessary to use advanced simulation tools to determine the dimensions and geometry of the main components of the crank-piston system.

2. Simulation research

The strength tests of the connecting rod were based on the Abaqus software, using the Finite Element Method. This method consists of solving differential equations based on the division of the domain (so-called discretization) into finite elements for which the solution is approximated by specific functions, and performing real calculations only for the nodes of that division [5]. This software allows to calculate the reduced strengths values for all compute nodes according to the mesh grid. To perform full strength calculations of a given element, it is needed to go through several steps necessary to build the correct model:

a) import of engine parts solid models,
b) modernization of solid models,
c) adding material properties,
d) arrangement of solid models,
e) interaction and correlation between elements,
f) adding restraints and forces acting on elements,
g) constructing a mesh grid,
h) computing process,
i) visualization and analysis of results.

At each stage, it is necessary to maintain the appropriate quality of research, so that reliable simulation results can be obtained. In order to optimize the connecting rod's shape, it has undergone several stages of strength calculations, any change in the design or geometry of the connecting rod resulted in the need to repeat all of the above mentioned steps.

In the first stage of the work, only the initial strength analysis was performed to verify the accuracy of the geometry and the selection of the appropriate mesh grid. The initial part of the article presents an introduction to simulation research involving the construction of a mesh grid and its verification in the form of a maximum load resulting from the force acting on the main engine components from

the combustion process. After the mesh grid was verified, the target model was constructed, based on the preliminary results [1].

2.1 Initial model

In the preliminary stage of the study, the model consist of the upper connecting rod part, cap, rod bushing, rod bearing inserts. All of the listed parts are shown in Fig. 1 and were previously imported into the Abaqus software.

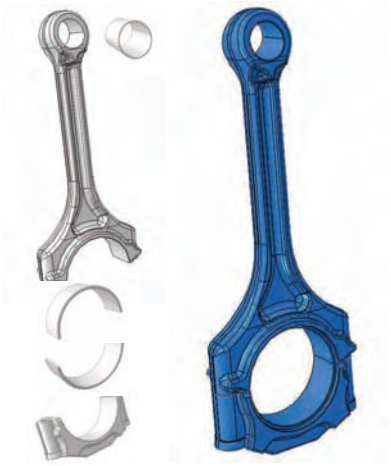

Fig. 1. Elements and assembly of the connecting rod

Due to the assembly of the connecting rod from several components it was necessary to give the contact properties on the contact surfaces between each elements. Contact properties were defined and assigned between such elements as:

a) upper part of connecting rod – cap,
b) upper part of connecting rod – rod bushing,
c) upper part of connecting rod – upper rod bearing insert,
d) cap - bottom rod bearing insert.

Figure 2 shows all contacts occurring in the model with reference to the above list.

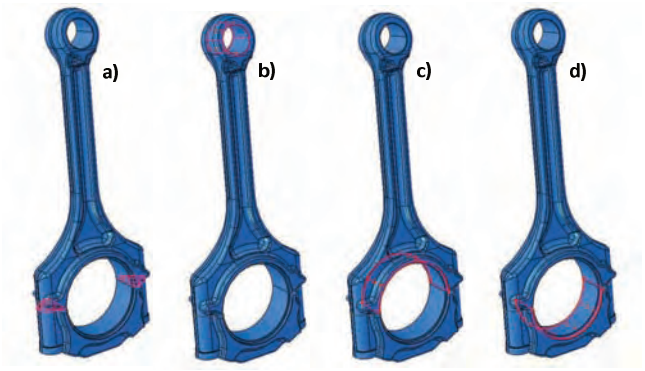

Fig. 2. Contact surfaces between individual elements

Due to the type of the connecting rod work process, it was decided to calculate its strength at the time of occurrence of the maximum force resulting from the combustion pressure. As conditions of restraint and conditions of forces acting on the connecting rod, it was decided to introduce the following:

a) fixation of the inner part of rod bearing inserts,
b) fixing the side surface of upper and lower part of the connecting rod,
c) fixing of the upper side surface of the connecting rod upper part,
d) fixing of the side surface of rod bushing,
e) force acting on the inner bottom side of the rod bushing.

All boundary conditions are presented in Fig. 3 with reference to the above list.

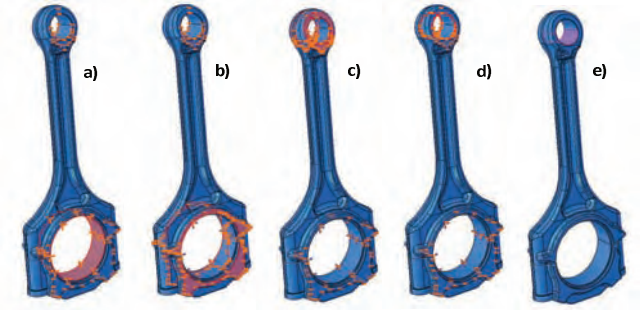

Fig. 3. Boundary conditions of restraints and forces acting on the model

As the material properties of the individual parts, it was decided to choose 40HNMA steel for the upper and lower connecting rods parts and Ti-3Al-8V-6Cr-4Mo-4Zr Beta C (TM) for all bushings [6, 4, 10]. The materials properties used in simulations are presented in Tables 1 and 2.

Table 1. 40HNMA steel material properties used for calculations

Material properties	Value
Poisson number	0.3
Density	7850 kg/m^3
Young module	207 GPa

Table 2. Ti-3Al-8V-6Cr-4Mo-4Zr Beta C (TM) material properties used for calculations

Material properties	Value
Poisson number	0.341
Density	8860 kg/m^3
Young module	110 GPa

In order to select the appropriate mesh grid, it was decided to conduct the optimization process of the grid in subsequent calculation steps. The initial size of the grid element was 4 mm and the final 1.1 mm (as shown in Fig. 4). Table 3 shows the size of the components and their number for all parts of the connecting rod.

For each of the cases, the generation of the mesh grid was performed and initial strength calculations were made to determine the accuracy of the mesh.

Table 3. Size and number of elements

Element size	Elements number				
	Upper part	Cap	Rod bushing	Upper rod bearing instert	Bottom rod bearing instert
4 mm	19535	8260	415	702	702
3 mm	27356	12221	683	1216	1216
2 mm	47686	23602	1488	2547	2547
1.5 mm	81415	43133	2782	5992	5992
1.2 mm	180374	92551	4763	11042	11042
1.1 mm	180374	92551	4763	11042	11042

Because some part of the connecting rod (bush and bearings inserts) are characterized by a small thickness, for the correctness of the calculation, the local density compaction of the mesh grid was decided in the next step. It is assumed that at least 3 mesh elements must be at the thickness of the thin-walled body, in order to avoid erroneous results, it was decided to use 5 elements. This operation was performed for all bushes and bearing inserts. Figure 5 shows the mesh grid view, generated for these parts using the local mesh compaction process.

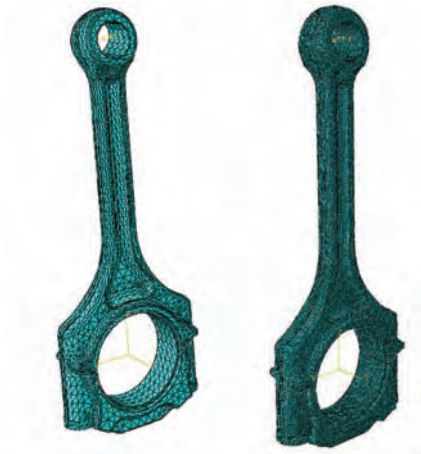

Fig. 4. Mesh grid view for 4 mm and 1.1 mm size of elements

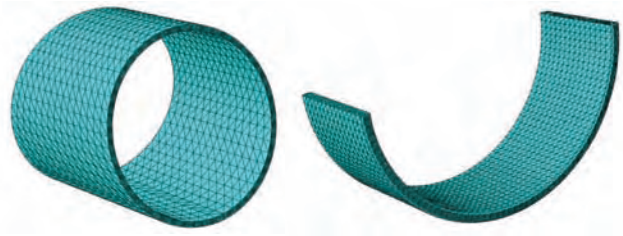

Fig. 5. Mesh grid with local density on bushing and bearing insertions

The rest of the elements have not been changed, and for the rod bushing, the new grid elements number was 10767 and for the upper and bottom rod bearing inserts was 17530. The prepared model has been subjected to the same calculation process. The main result of the presented initial simulation calculations is to determine the accuracy of the mesh grid. As it is clear from the preliminary calculations, the size of the element at 1.2-1.1 mm along with the local mesh density in the thin-walled components allows for reliable results. This means that the size of the grid element does not negatively affect the results of the simulation tests. The same model was used in the publication [7].

2.2 Main models

This section contains the results of the connecting rod strength calculations together with the history of changes in its geometry to reduce zones, where there is a dangerous stress area. Calculations were made in Abaqus software, and geometry changes after each calculation cycle were performed in Catia v5 software. In total, 8 connecting rod models and one target model were presented.

In order to reduce the time to optimize its geometric shape, it was decided to calculate the connecting rod only for compression. This mainly helped to change the shape of the constriction of the connecting rod I-beam. Boundary conditions and material properties are identical to those previously accepted for initial strength calculations. The same is the visualization of the computational grid selected for the models below. During the work on changing the geometry of the connecting rod, length of the rod has changed. In each case, the conditions of the loading force acting on the connecting rod were redefined and introduced into the calculation model.

To clearly presents the geometry changes of the connecting rod, it was decided to firstly present the results of the strength simulation of all 8 connecting rod models. After each model, geometric changes were included in the next release and all geometry models are presented together with the history of changes in their geometry, as well as final verification calculations for the target model at the end of the paper.

In order to shorten the calculation time in all models, it was decided to apply the restriction condition at the point of contact with the crankshaft and to give the compressive force acting along the connecting rod to the lower surface of the rod bushing. For a clear presentation of data, it was decided to set the same visualization parameters, i.e. the maximum stress was set at 300 MPa and the minimum at 0 MPa. This review, make it possible to compare the simulation results of the various models between each other.

Connecting rod – model 1

The model 1 contained a very small cross-sectional area of the I-beam and did not take into account the geometric requirements for the size of the rod bushing or rod bearing inserts. As we can see, the stresses in this model significantly exceeded 300 MPa, which was due to the too small cross-sectional area of the I-beam.

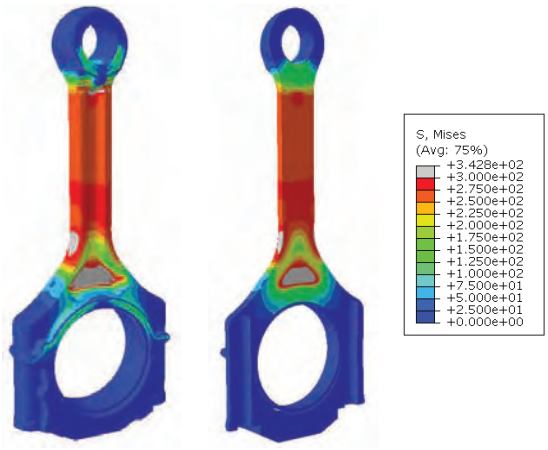

Fig. 6. Results of simulation of connecting rod model 1

Connecting rod – model 2

Model 2 has been significantly changed in comparison to model 1. The cross-sectional area of the I-beam was enlarged. The shape of the rod small and big end were completely changed. The geometrical changes were shown in Fig. 7. As shown in the figures, the stress level is significantly reduced but there are still local spots in the upper and lower parts of the connecting rod, where the stresses exceed 300 MPa.

Fig. 7. Geometric changes between model 1 (gray) and model 2 (yellow)

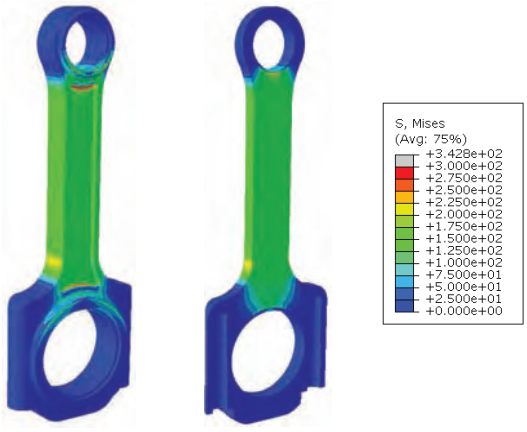

Fig. 8. Results of simulation of connecting rod model 12

Connecting rod – model 3

Model 3 has been changed in comparison to model 2 by changing the geometry of the rod small end and changing the geometry of the I-beam (mass reduction). The geometry changes are shown in Fig. 9. As shown in the figures, due to the mass reduction in the I-beam, the stress value is higher. By contrast, increasing the dimensions of the rod small end resulted in a more uniform distribution of stresses in this part.

Fig. 9. Geometric changes between model 2 (gray) and model 3 (yellow)

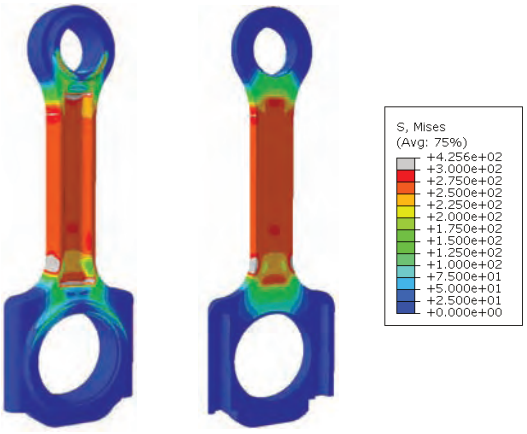

Fig. 10. Results of simulation of connecting rod model 3

Connecting rod – model 4

Model 4 has been changed in comparison to the model 3 by changing the geometry of I-beam and changing the outer curves describing the transition between I-beam and cap. The geometrical changes are shown in Fig. 11. As can be seen in the figures, changes in the shape of the outer lines between the I-beam and rod small end and cap, resulted in a change in the stress distribution.

Fig. 11. Geometric changes between model 3 (gray) and model 4 (yellow)

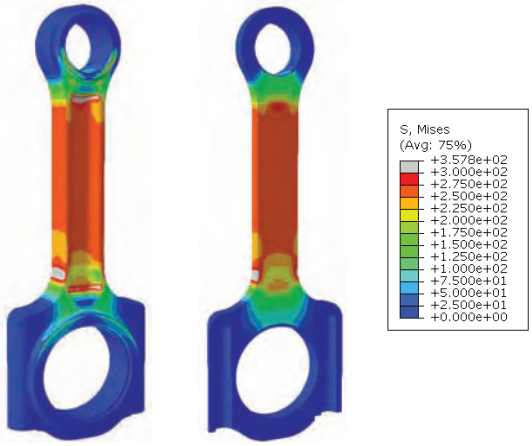

Fig. 12. Results of simulation of connecting rod model 4

Connecting rod – model 5

Model 5 has been significantly changed in comparison to model 4 in the geometry of I-beam, cap and small end. It was decided to accept a different width of the rod small end and different shape of the cap. The geometric changes are shown in Fig. 13. As can be seen in the figures presented below, the geometric changes introduced in model allow for significant reduction of stresses in the entire connecting rod geometry.

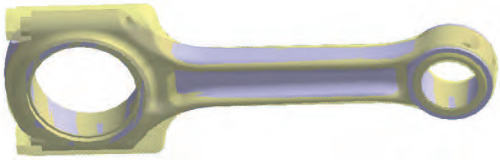

Fig. 13. Geometric changes between model 4 (yellow) and model 5 (grey)

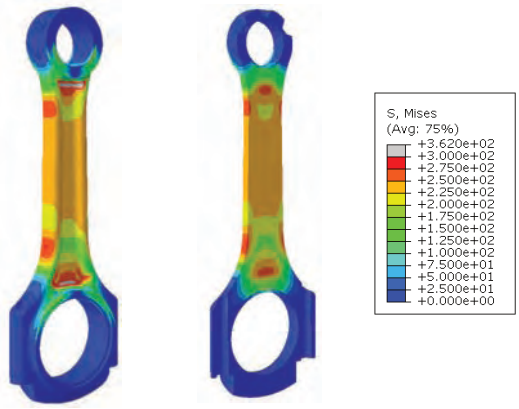

Fig. 14. Results of simulation of connecting rod model 5

Connecting rod – model 6

Model 6 has been changed in comparison to model 5 by changing the connecting rod length (from 145 to 125 mm). This change resulted from the changed of engine design assumptions. The geometry changes are shown in Fig. 15. As shown in the figures, the changes in the length of the connecting rod caused changes in the stress distribution in the connecting rod and the presence of high stresses on the outsides surfaces of the connecting rod.

Fig. 15. Geometric changes between model 5 (gray) and model 6 (yellow)

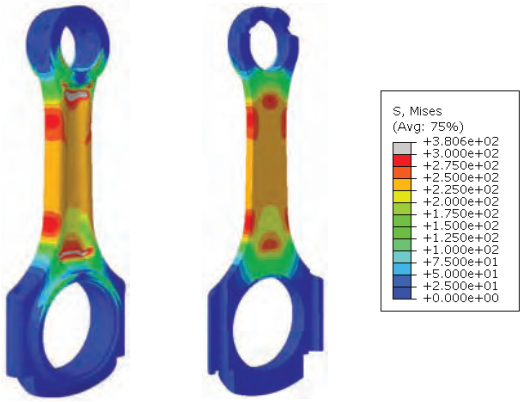

Fig. 16. Results of simulation of connecting rod model 6

Connecting rod – model 7

Model 7 has been slightly changed in comparison to model 6 by changing the geometry of the connecting rod I-beam. The presented geometric changes are shown in Fig. 17. As can be seen in the figures, the changes in the geometry of the connecting rod have reduced the field of occurrence of the value of the maximum stresses on the outside surfaces of the connecting rod.

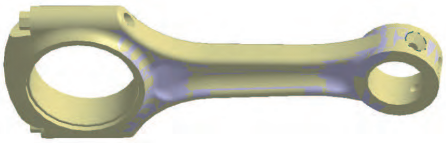

Fig. 17. Geometric changes between model 6 (yellow) and model 7 (gray)

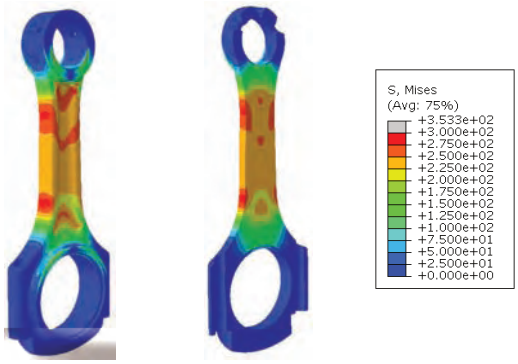

Fig. 18. Results of simulation of connecting rod model 7

Connecting rod – model 8

Model 8 has been changed in comparison to model 7 by changing the geometry of the I-beam and changing the connecting rod length (from 125 mm to 130 mm). This change resulted from the changed engine design assumptions. The geometrical changes are shown in Fig. 19. As shown in the figures, the changes made to the connecting rod have changed the distribution of the stresses that have accumulated in the outside surfaces of the I-beam.

Fig. 19. Geometric changes between model 7 (yellow) and model 8 (grey)

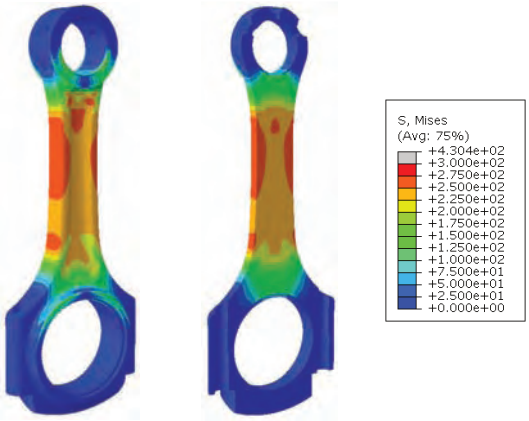

Fig. 20. Results of simulation of connecting rod model 8

Below, all intermediate versions of the connecting rod are shown as solid models.

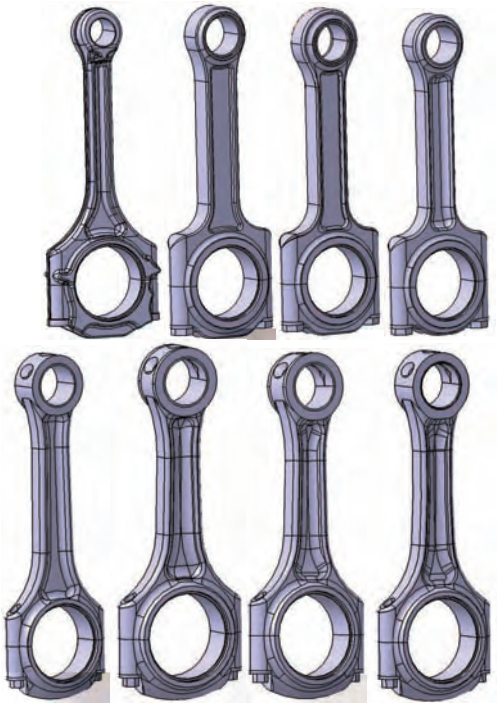

Fig. 21. All intermediate connecting rod models

5. Summary

As a result of the simulations, the geometry of the connecting rod has changed. Part of the change, in particular the change in the length of the connecting rod was dictated by the design process of the entire crank-piston system, on which the authors of the article had no influence on. Changing the length of the connecting rod between successive modes significantly influenced the stress distribution. As can be seen from the results of the simulations, the level of stress, was significantly reduced. This was due, to the change in cross section of the connecting rod I-beam, but also to the introduced of geometric changes (change of the outer lines). During the design process, the fields with the maximum stress values on both sides of the connecting rod were reduced. All of the presented results had the same range of stresses as presented in figures, which makes possible to compare the results presented in the article between each other. The publication does not show results for the connecting rod extension. Those studies were carried out in the next research step and did not show any dangerous area of stress.

The results of the research show that using modern numerical methods helps to shorten the design process. In addition, it allows to reduce the mass of the tested element by changing its geometry. Compared to analytical methods (where only the cross section of the connecting rod I-beam can be calculated to the compression condition), computer methods allow for the visualization of the stress distribution and the determination of dangerous locations in the geometry of the examined element.

Acknowledgement

This work has been realized in the cooperation with The Construction Office of WSK "PZL-KALISZ" S.A. and is part of Grant Agreement No. POIR.01.02.00-00-0002/15 financed by the Polish National Centre for Research and Development.

Nomenclature

FEM finite element method

Bibliography

[1] ABDUL-LATEEF, W. Finite element analysis of connecting rod using Nastran software. *The Iraqi Journal For Mechanical and Material Engineering*. 2012, **12**(2).
[2] FAROKHI, S. *Aircraft propulsion*, SBN: 978-1-118-80677-7, 2004.
[3] HEYWOOD, J.B. Internal combustion engine fundamentals. *McGraw-Hill*, USA, 1988.
[4] cartech.ides.com/datasheet.aspx?i=101&E=270 korbowód
[5] pl.wikipedia.org/wiki/Metoda_element%C3%B3w_sko%C5%84czonych
[6] JOSHI, P., UMAIRZAKI, M., FEM analysis of connecting rod of different materials using ANSYS. *International Journal of Engineering and Techniques.* 2015, **3**(1).
[7] MAGRYTA, P., PIETRYKOWSKI, K. The influence of load distribution in kinematic constraints of connecting rod on the results of the stress simulation. *Combustion Engines.* 2017.
[8] PIRAULT, J., FLINT, M. Opposed piston engines evolution, use and future applications. *SAE International*. ISBN 978-0-7680-1800-4.
[9] REGNER, G., JOHNSON, D., KOSZEWNIK, J., DION, E. et al. Modernizing the opposed piston, two stroke engine for clean, efficient transportation. *SAE Technical Paper*. 2013, 2013-26-0114.
[10] WELSCH, G., BOYER, R., COLLINGS, E.W. *Materials properties handbook: titanium alloys.* Metals Park, Ohio: ASM International, 1994.

Paweł Magryta, MEng. – Faculty of Mechanical Engineering at the Lublin University of Technology.

e-mail: *P.Magryta@pollub.pl*

Konrad Pietrykowski, DEng. – Faculty of Mechanical Engineering at the Lublin University of Technology.

e-mail: *K.Pietrykowski@pollub.pl*

Adam Majczak, MEng. – Faculty of Mechanical Engineering at the Lublin University of Technology.

e-mail: *A.Majczak@pollub.pl*

Article citation info:
AMBROSEWICZ-WALACIK, M., TAŃSKA, M. WALACIK, M. KOZŁOWSKI, M. Unconventional vegetable oils as raw material for biodiesel production. Combustion Engines. 2017, **168**(1), 197-200. DOI: 10.19206/CE-2017-132

Marta AMBROSEWICZ-WALACIK
Małgorzata TAŃSKA
Marek WALACIK
Michał KOZŁOWSKI

CE-2017-132

Unconventional vegetable oils as raw materials for biodiesel production

The aim of the study was to determine the possibility of using the unconventional vegetable oils for the biofuel production. The research material were cold-pressed oils from the seeds of milk thistle, hemp and evening primrose. After conducting the initial physico-chemical characteristics of oil samples, including the determination of sulphur content, acid number, viscosity at 40°C, density at 15ºC, oxidation stability and fatty acid composition, analysed oils have been subjected to the transesterification process. The produced methyl esters were further characterized by the above-mentioned features. Additionally, the temperatures of cold filter plugging point, cloud point and flash point were determined. On the basis of the conducted analyses it was demonstrated that the obtained oils, due to the high, far in excess of acceptable, values of the viscosity and density, and too low oxidative stability could not be used as a pure fuel. A similar conclusion was formulated in case of the produced methyl esters.

Key words: *unconventional vegetable oils, quality, fatty acids composition, biofuels production*

1. Introduction

Vegetable oils are widely used in the food, cosmetic, pharmaceutical, chemical industries, as good as in the fuel industry [1, 2]. These products can be obtained from many kind of plant species, however the world consumption is dominated by the soybean, palm, rapeseed, and sunflower oils [3]. It is believed that only the plant seeds, that occurs abundant and are characterized by the high oil content of appropriate quality are feasible for the biodiesel production. One of the most important factor determining the choice of an individual plant is its location, include climate and feedstock availability. The rapeseed and sunflower oils are predominantly used in Europe, while the palm oil predominates in the tropical countries. In turn, the soybean oil and animal fats are used in the United States [4].

On the other hand, as Chung cited by Torrey, the conventional sources no longer meet the increasing demands of the domestic and industrial sectors [5]. Therefore, the need for searching the other raw materials is existed. The usefulness of vegetable oils as raw materials for the biodiesel production is conditioned, among others, the species and variety, yield of seed and fat, and energy efficiency indicators [6–8]. Among the unconventional vegetable oils are these pressed from the seeds of milk thistle, hemp and evening primrose, which are widely known from their beneficial health properties.

Generally, authors of the presented work found that using the raw materials, that are commonly used for the medical, pharmaceutical and nutritional purposes, should be reduced in fuel industry. However, it should be remembered that these plants may occur on a contaminated soil, where different weed infestations and numerous pests are observed, and therefore their usage in the mentioned sectors would not be possible.

The milk thistle (*Silybum marianum* L.) is well known medical herb that is popular in the European traditional medicine, especially using during the treatment of different liver diseases. One the other hand, in Maroko that plant is considered as weed, that is abundantly available and is suitable for the control of environment pollutants [2, 9, 10]. The average oil content in that plant seeds ranges from 20 to 35%, what is similar to many other vegetable oils [11].

The evening primrose (*Oenothera biennis* L.) oil (18-25%) is one of the most important health- promoting specialty oil, and is being used in increasing amounts in the nutritional and pharmaceutical preparations [12]. It is classified as a "dietary supplement" under the Dietary Supplement Health and Education Act of 1994. As “Chemical Information Review Document for Evening Primrose Oil (*Oenothera biennis* L.)” reported nowadays it is cultivated in over 30 countries for its oil [13].

The hemp oil is derived from the seeds of *Cannabis sativa* (ranged from 25 to 35%) and contains significant amounts of the linolenic acid and linolenic acids [14, 15]. The cultivation of that plant is legally in Canada as a niche crop and is used mainly in the health food market [16]. As Leizer et al. found the additional presence of gamma-linolenic acid (GLA) in the hemp oil ultimately makes its nutritional value superior to the most comparable seed oils [17].

Taking into account the above the aim of the presented work was to determine the possibility of use the unconventional oils for the biofuels production.

2. Material and analytical methods

2.1. Material

The research material consisted of three samples of the commercial, cold-pressed oils from hemp, milk thistle and evening primrose seeds.

2.2. Analytical methods

The oil samples were characterized in terms of a viscosity at 40°C (PN-EN ISO 3104), density at 15°C (PN-EN ISO 12185), acid value (PN-EN14104:2004P), oxidative stability (PN-EN ISO 6885:2016-04P) and fatty acids composition (PN-EN ISO 12966-4:2015-07E).

After conducting the physico-chemical characteristics of the oils the double-base transestrification process was carried out. In the first stage of reaction 200 g of oil was heated to 60°C and then a solution of potassium methoxide was

added (by using methanol in a ratio of oil = 1: 6 (v/v) and KOH in an amount of 1% based on the weight of oil). The reaction was carried out in 60°C for 40 min. In the first stage of process ¾ of the total amount of potassium methoxide was added and in second one ¼. Then the reaction mixture was subjected to the separation for 24 h. After the complete separation, the upper ester phase was poured into glass flasks and the second stage of reaction was conducted in 60°C for 30 min. After the second step of the transestrification the ester phase was isolated as described above.

The methyl esters obtained from different vegetable oils were determined in terms of the sulphur content (as above), acid value (ISO 14104), viscosity at 40°C (as above), the density at 15°C (as above), oxidative stability (ISO 14112), temperature of flash point (PN-EN ISO 3679) and temperature of cold point and the cold filter plugging point (EN 116).

3. Results and discussion

The obtained vegetable oils were characterized by the high values of the viscosity and density, however typical for the oils pressed from seeds of these plant species. The oil sample obtained from milk thistle seeds was characterized by the highest value of mentioned parameters (respectively, 59.54 mm^2/s and 927 kg/m^3). In turn, lower, however similar, values were noticed for the samples of evening primrose and hemp oils. A similar tendency was observed in case of the acid value, that determines the hydrolysis degree (Table 1). The oil of milk thistle was the most hydrolysed, as indicated the increased values of acid value (10.07 mh KOH/g) and %FFA (5.035%). The degree of hydrolysis of other two samples were lower, however approx. 2-fold higher that the recommended value (< 3 mg KOH/g) [18]. The stated for all samples the high hydrolysis degree allowed to decide, which method of the transesterification (single, double) should be used. Taking into consideration a weak quality of oils and an economic aspect, authors of the presented work decided to use the double-base transesterification.

The oxidative stability and fatty acids composition were typical for the oils pressed from seeds of these plant species [2, 13, 14, 19–21] (Table 1). The hemp oil, with high share of polyunsaturated acids (especially gamma linolenic), was characterized by the lowest resistance to the oxidation, while significantly higher the milk thistle oil, that was characterized by the highest share of saturated acids (palmitic, stearic, arachidic and behenic acids). It should be remembered that the fatty acids profile of raw materials does not change during the transesterification process [22], therefore, stated for the analysed samples low oxidative stability will be determined the low value of that discriminant for the produced methyl ester samples.

Table 1. Characterization of the analysed oils

Discriminates	Oil samples		
	milk thistle	evening primrose	hemp
Viscosity at 40 °C (mm^2/s)	59.54	30.21	27.67
Density at 15 °C (kg/m^3)	927	924	925
Acid value (mg KOH/g)	10.07	6.67	6.32
% FFA	5.035	3.335	3.160
Oxidative stability (h)	4.62	1.38	1.22
Fatty acids composition (%):			
miristic		–	0.74
palmitic	10.28	7.97	8.78
palmitoleic	-	0.03	0.11
stearic	6.30	2.08	3.67
oleic	23.09	6.75	15.49
linoleic	50.72	76.08	52.90
linolenic	0.44	7.09	16.36 (include, 0.46 alfa-linoleic, and 15.90 gamma-linoleic)
stearidonic	–	–	0.34
arachidic	4.72	–	0.71
eicosenoic	1.06	–	0.40
behenic	3.09	–	0.28
erucic	0.19	–	0.22

The transestrification process of the analysed oils significantly contributed to the reduction of the viscosity (approx. 6.5-fold) and density values (Table 2), whereby two of samples (evening primrose and hemp oils) met the requirements of the UE standard EN 14214. On the other hand, the values of these parameters for the milk thistle oil significantly exceeded the required values. That sample was also characterized by the highest, and therefore unacceptable, values of the temperature of cloud point and temperature of cold filter plugging point, which could contribute to the hindered engine work in lower temperatures. What is more, all of the analysed ester samples were characterized by too low oxidative stability and too high values of acid value. The only features that fulfilled the standard requirements were the temperature of flash point (> 101°C) and sulphur content (< 10 ppm).

Sanford et al., analysing different unconventional sources for the biodiesel production, among others, oils from hemp and evening primrose seeds found similar results as these in presented work [23]. Additionally, the main features determined for the milk thistle biodiesel were almost on the same level, compared to these obtained by Ullah et al [24]. Moreover, Li et al., analysing the feasibility of converting *Cannabis sativa* L. oil into the biodiesel,

also found that methyl esters of that sample were characterized by the suitable values of the viscosity, density, sulphur content and flash point [25]. However, as it was also stated, values of the cloud point and temperature of cold filter plugging were too high. What is more, in Alcheikh work, it is presented, that the biodiesel produced from hemp oil was also characterized by the poor oxidative stability [26].

Table 2. Characteristics of the prepared methyl esters

Discriminants	Methyl esters obtained from different oils		
	milk thistle	evening primrose	hemp
Viscosity at 40°C [mm^2/s]	8.87	4.67	3.92
Density at 15°C [kg/m^3]	898	888	884
Flash point [°C]	> 160	> 160	> 160
Cloud point [°C]	–5	–4	–6
Cold filter plugging point [°C]	–6	–5	–7
Acid value [mg KOH/g]	0.32	0.66	1.11
Sulphur content [ppm]	1.96	2.23	2.54
Oxidative stability [h]	4.78	1.44	1.32

Rizwanul Fattah et al. found, that mentioned features do not disqualify analysed oils as a raw material for the fuel purposes, because these discriminants may be easily improved with the chemical additives, such as antioxidants, that are commonly used to inhibit the oxidative degradation of biodiesel [27].

What is more, as Nwadike et al. found increased viscosity of biodiesel (in case of milk thistle biofuel) may be decrease by either blending with a conventional diesel oil or other biodiesel characterized by the lower share of saturated methyl esters [28].

Conclusions

Commonly used for the medical, pharmaceutical and nutritional purposes the hemp, milk thistle and evening primrose oils should not be generally used in the fuel industry, due to their beneficial health properties. One the other hand, in case of the possible deficiency of widely used oleic raw materials, such as rapeseed, sunflower and soybean, seeds of that plant species could be used to the methyl esters production. However, it should be remembered that an addition of different compounds, such as antioxidants, would be needed, due to the low oxidative stability of these oils, and therefore the produced methyl esters. What is more, in case of the milk thistle oil it would be necessary to prepare a blend with lees viscous diesel oil, because as a pure fuel characterized by too high viscosity it would not be suitable for the Diesel engines.

Bibliography

[1] DUGO, G., PERA, L., TORRE, G.L., GIUFFRIDA, D. Determination of Cd(II), Cu(II), Pb(II), and Zn(II) content in commercial vegetable oils using derivative potentiometric stripping analysis. *Food Chemistry*. 2004, **87**, 639-645

[2] ISMAILI, S.A, HARKAR, H., GHARBY, S. et al. Chemical composition of two non-conventional oils in Morocco: Melia azadirachta and Silybum marianum (L.). *Journal of Materials and Environmental Sciences*. 2016, **7**(6), 2208-2213.

[3] STEVENSON, D.G., ELLER, F.J., WANG L. et al. Oil and tocopherol content and composition of pumpkin seed oil in 12 cultivars. *Journal of Agricultural Food Chemistry*. 2007, **55**, 4005-4013.

[4] KNOTHE, G., KRAHL, J., VAN GERPEN, J. The biodiesel handbook *AOCS Press*, Champaign, USA 2005.

[5] CHUNG, K-H. Transesterification of Camellia japonica and Vernicia fordii seed oils on alkali catalysts for biodiesel production. *Journal of Industrial and Engineering Chemistry*. 2010, **16**(4), 506-509.

[6] HEIMANN, S. Aktualne problemy dotyczące badania odmian rzepaku na cele konsumpcyjne oraz biopaliw i makuchy. Forum producentów roślin zbożowych, kukurydzy i rzepaku. *Polagra – Forum* 2002, 47-52.

[7] JANKOWSKI, K., BUDZYŃSKI, W. Energy potential oilseed crops. *Electronic Journal of Polish Agricultural Universities, Agronomy*. 2003, **6**(2).

[8] BUDZYŃSKI, W., BIELSKI, S. Surowce energetyczne pochodzenia rolniczego. Cz. 1. Biokomponenty paliw płynnych. *Acta Scientarium Polonorum seria Agricultura*. 2004, **3**(2), 5-14.

[9] FRASCHINI, F., DEMARTINI, G., ESPOSTI, D. Pharmacology of silymarin. *Clinical Drug Investigation*. 2002, **22**(1), 51-65.

[10] KURKIN, V.A. Saint-Mary thistle: a source of medicinals. *Pharmaceutical Chemistry Journal*. 2003, **37**(4), 189-202.

[11] RAMASAMY, K., AGARWAL, R. Multitargeted therapy of cancer by Silymarin. *Cancer Letters*. 2008, **269**, 352-362.

[12] CHRISTIE, W.W. The analysis of evening primrose oil. *Industrial Crops and Products*. 1999, **10**, 73-83.

[13] Chemical Information Review Document for Evening Promrose (Oenotheta biennis L.) [CAS No. 90028-66-3]. 2009, 1-38.

[14] DEFERNE, J.L., PATE, D.W. Hemp seed oil: A source of valuable essential fatty acids. *Journal of the International Hemp Association*. 1996, **3**(1), 4-7.

[15] Hemp Seed Oil, 22 October 2009, www.bulknaturaloils.com/plantoil/alphalinoleic/hempseedoil.html

[16] JESSEN, H. Hemp biodiesel: when the smoke clears." Biodiesel Magazine. February, 2007. www.biodieselmagazine.com/articles/1434/hemp-biodiesel-when-the-smoke-clears

[17] LEIZER, C., RIBNICKY, D., POULEV, A. et al. The composition of hemp seed oil and its potential as an important source of nutrition. *Journal of Nutraceuticals, Functional & Medical Foods*. 2000, **2**(4), 35-53.

[18] PN-90/R-66151. Rośliny przemysłowe oleiste. Ziarno rzepaku i rzepiku podwójnie ulepszonego.

[19] CALLOWAY, J.C., LAAKKONEN, T.T. Cultivation of Cannabis oil seed varieties in Finland. *Journal of the International Hemp Association*. 1996, **3**(1), 32-34.

[20] ULUATA, S., ÖZDEMIR, N. Antioxidant activities and oxidative stabilities of some unconventional oilseeds. *Journal of American Oil Chemistry Society*. 2012, **89**(4), 551-559.

[21] PRESCHA, A., GRAJZER, M., DEDYK, M., GRAJETA, H. The antioxidant activity and oxidative stability of cold-pressed oils. *Journal of American Oil Chemistry Society*. 2014, **91**(8), 1291-1301.

[22] RAMOS, M.J., FERNÁNDEZ, C.M., CASAS, A. et al. Influence of fatty acid composition of raw materials on biodiesel properties. *Bioresource Technology*. 2009, **100**(1), 261-268.

[23] SANFORD, S.D., WHITE, J.M., SHAH, P.S. et al. Feedstock and biodiesel characteristics report. 2009, 1-136. biodiesel.org/reports/20091117_gen-398.pdf.
[24] ULLAH, K., AHMAD, M., QIU, F. Assessing the experimental investigation of milk thistle oil for biodiesel production using base catalyzed transesterification. *Energy*. 2015, **89**, 887-895.
[25] LI, S-Y., STUART, J.D., PARNAS, R.S. The feasibility of converting Cannabis sativa L. oil into biodiesel. *Bioresource Technology*. 2010, **101**(21), 8457-8460.
[26] ALCHIKH, A. Advantages and challegnes of hemp biodiesel production: A comparison of hemp vs. other crops commonly used from biodiesel production. Master's Energy System, Faculty of Engineering ans Sustainable Development. University of Gävle, 2015, 1-31.
[27] RIZWANUL FATTAH, I. M., MASJUKI, H.H. et al. Effect of antioxidants on oxidation stability of biodiesel derived from vegetable and animal based feedstocks. *Renewable & Sustainable Energy Reviews*. 2014, **30**, 356-370.
[28] NWADIKE, I., YAHAYA, M., O'DONNELL, S. et al. Cold flow properties and kinematic viscosity of biodiesel. *Universal Journal of Chemistry*. 2013, **1**(4), 135-141.

Marta Ambrosewicz-Walacik, DEng. – Faculty of the Technical Sciences, University of Warmia and Mazury in Olsztyn.

e-mail: *Marta.Ambrosewicz@uwm.edu.pl*

Marek Walacik, DEng. – Faculty of Geodesy, Geospatial and Civil Engineering, University of Warmia and Mazury in Olsztyn.

e-mail: *Marek.Walacik@uwm.edu.pl*

Małgorzata Tańska, DEng. – Faculty of Food Sciences, University of Warmia and Mazury in Olsztyn.

e-mail: *M.Tanska@uwm.edu.pl*

Michał Kozłowski, MSc. – Faculty of the Technical Sciences, University of Warmia and Mazury in Olsztyn.

e-mail: *Michal.Kozłowski@uwm.edu.pl*

INSTYTUT TECHNICZNY WOJSK LOTNICZYCH

ul. Księcia Bolesława 6, 01-494 Warszawa, skr. poczt. 96
tel.: 261 851 300; tel./faks: 261 851 313
www.itwl.pl e-mail: poczta@itwl.pl

Tomograf komputerowy (CT) – badanie nieniszczące NDT

Instytut Techniczny Wojsk Lotniczych oferuje usługi z zakresu badań tomografem komputerowym. Badania prowadzone są na tomografie typu v/tome/x m 300 firmy GE o max. mocy lampy 300kV/500W. Urządzenie posiada również lampę do nanotomografii o mocy 80kV/15W.

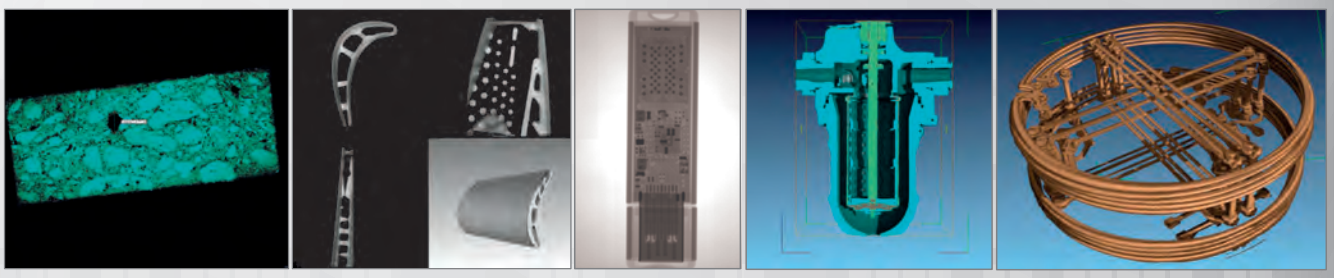

Prowadzimy prace badawcze obejmujące swym zakresem materiały takie jak:

- stopy tytanu
- stale
- materiały kompozytowe
- beton
- guma

Urządzenie umożliwia prowadzenie badań z zakresu:

- wykrywania defektów o rozmiarach powyżej 0,5 µm z wykorzystaniem lampy 180 kV
- materiałów o bardzo dużej gęstości (np. łopatki turbin silników lotniczych) z wykorzystaniem lampy o mocy 300 kV
- układy elektroniczne (scalone)
- materiały pirotechniczne
- złożone agregaty lotnicze

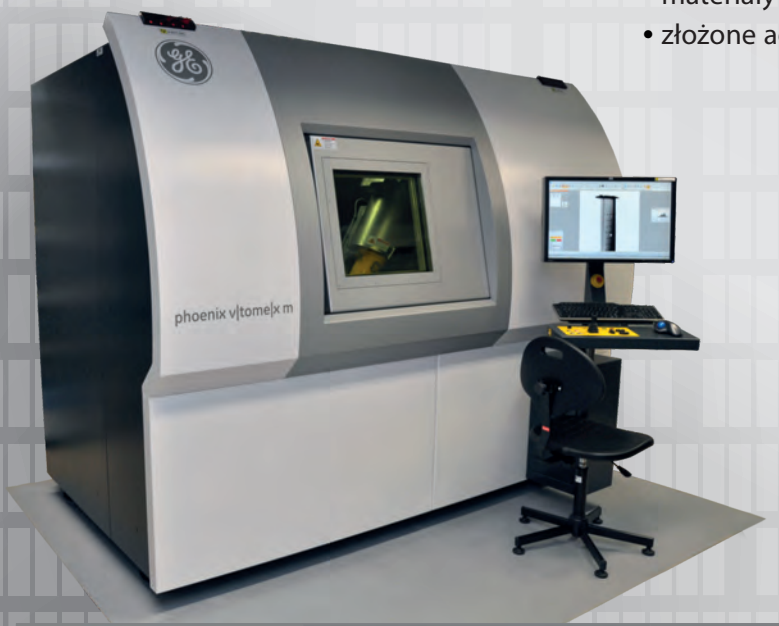

Masa badanych elementów do 50 kg.
Wymiary orientacyjne 50×50×60 cm.

Posiadamy wysoko wykwalifikowany, certyfikowany personel.

Kontakt bezpośredni:
Zakład Silników Lotniczych
tel.: +48 261 851 334; fax: +48 261 851 338
e-mail: jaroslaw.spychala@itwl.pl

Zapraszamy do współpracy!

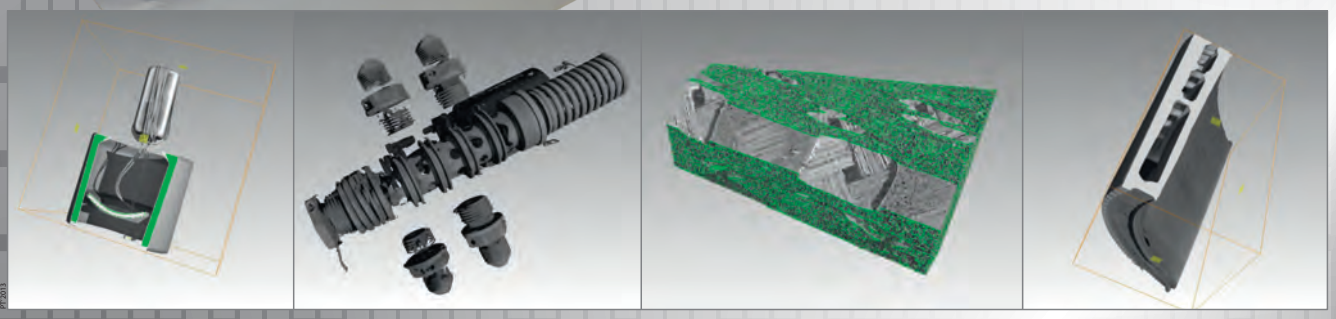

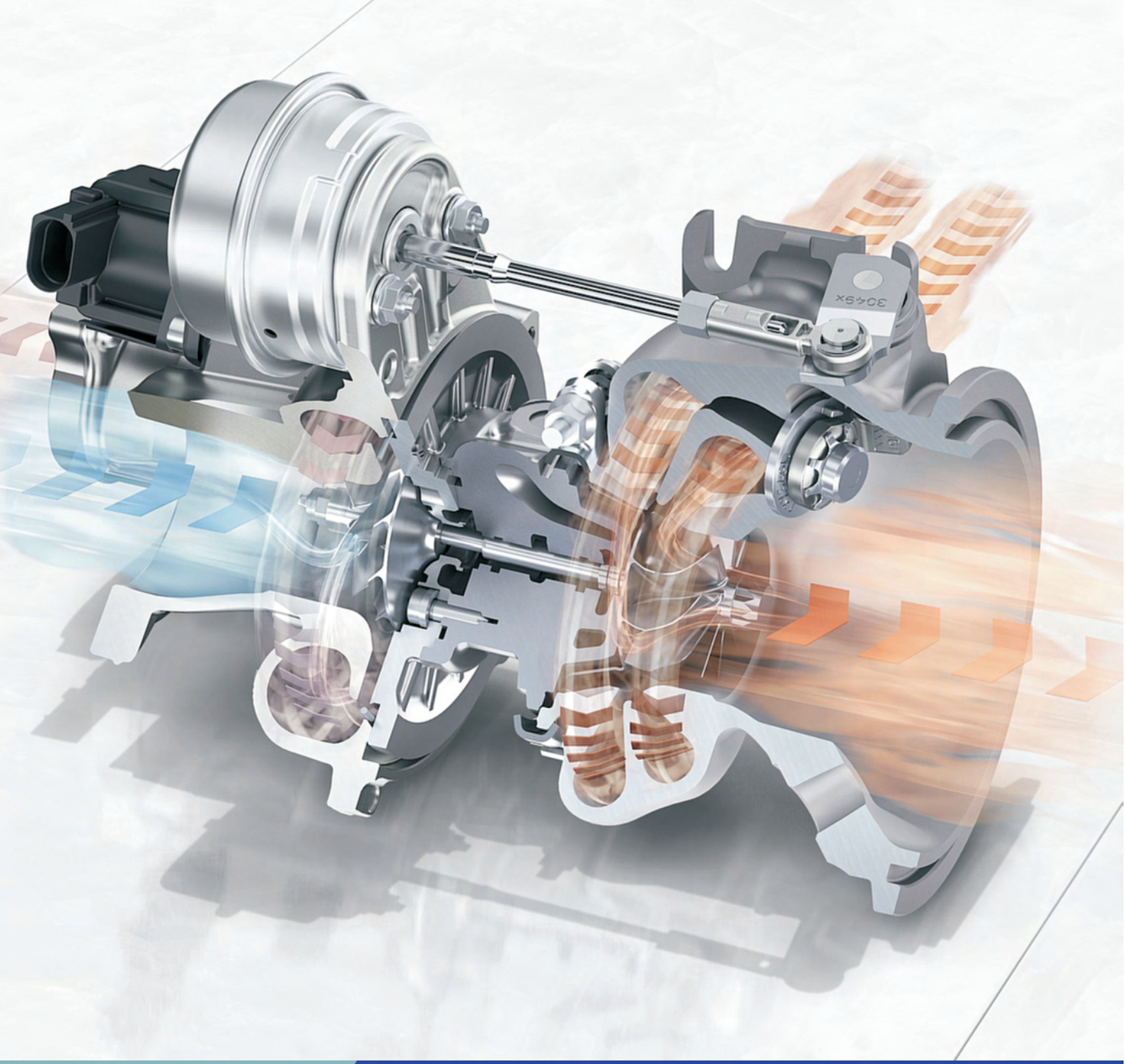

Publisher:

Polish Scientific Society of Combustion Engines

Combustion Engines

Polskie Towarzystwo Naukowe Silników Spalinowych

ISSN: 2300-9896

www.combustion-engines.eu